

Photoproduction of $\eta\pi$ -pairs off nucleons

Inauguraldissertation

zur

Erlangung der Würde eines Doktors der Philosophie
vorgelegt der
Philosophisch-Naturwissenschaftlichen Fakultät
der Universität Basel

von

Alexander Käser

aus Rheinfelden, Deutschland

Basel, 2017

Originaldokument gespeichert auf dem Dokumentenserver der Universität Basel
edoc.unibas.ch

Genehmigt von der Philosophisch-Naturwissenschaftlichen Fakultät auf Antrag von

Prof. Dr. B. Krusche

Prof. Dr. V. Metag

Basel, 18. April 2017

Prof. Dr. Martin Spiess
Dekan

Abstract

In this work, photoproduction of $\eta\pi$ meson pairs off protons and neutrons, bound in the deuteron, and off free protons was investigated. The data were taken at the Mainzer Microtron MAMI during 4 beam-times in 2007 and 2009, using liquid hydrogen and deuterium targets. Additionally, longitudinally polarized dButanol data and carbon data were analyzed using data from 5 beam-times carried out from 2013-2016. A longitudinally polarized electron beam of up to 1.5 GeV, was converted to circularly polarized photons via a bremsstrahlung process. The photons were energy-tagged with the Glasgow tagging spectrometer and reached energies up to 1.4 GeV.

Final state particles were detected in a nearly 4π covering electromagnetic calorimeters, consisting of the Crystal Ball and TAPS detectors.

Charged particles were identified with a dedicated Particle Identification Detector in the CB and veto detectors in TAPS.

The center of mass energy W was determined from the final state particles, using a kinematic reconstruction to remove effects of Fermi motion inside the deuteron, and covers energies from ≈ 1600 MeV - 1900 MeV.

For the reactions $\gamma p \rightarrow \eta\pi^0 p$, $\gamma p(n) \rightarrow \eta\pi^0 p(n)$, $\gamma n(p) \rightarrow \eta\pi^0 n(p)$, $\gamma p \rightarrow \eta\pi^+ n$, $\gamma p(n) \rightarrow \eta\pi^+ n(n)$, and $\gamma n(p) \rightarrow \eta\pi^- p(p)$ total cross sections, angular distributions for different coordinate systems, mass distributions of $N\eta$, $N\pi$ and $\eta\pi$ have been extracted as well as beam helicity asymmetries and are compared to theoretical predictions.

Also, total cross sections were extracted for the inclusive reactions $\gamma N(N) \rightarrow \eta\pi^0(N)$ and $\gamma N(N) \rightarrow \eta\pi^\pm(N)$ and for the coherent reaction $\gamma d \rightarrow \eta\pi^0 d$.

Additionally, the double polarization observable E and the helicity dependent cross sections $\sigma_{1/2}$ and $\sigma_{3/2}$ were extracted for the $\eta\pi^0$ channels.

The shapes of the extracted observables are almost identical for reactions on quasi-free protons and neutrons. Compared to the results of the reactions on free protons, the results of quasi-free protons are reduced by FSI effects. The shapes of the quasi-free proton results agree nicely with the free proton results, if the total cross section is divided out.

Ratios of total cross sections on quasi-free protons and neutrons are in agreement with the assumption, that $\eta\pi$ photoproduction is dominated by a sequential decay cascade of the form $\Delta^* \rightarrow \Delta(1232)3/2^+ \eta \rightarrow \pi\eta N$. Also the invariant mass distributions support this assumption, and additionally the angular distributions are in good agreement with model predictions that only take the $\Delta(1700)3/2^-$ resonance into account.

Contents

1. Introduction	15
1.1. Photoproduction of pseudoscalar mesons	19
1.1.1. CGLN amplitudes	19
1.1.2. Multipole Expansion	20
1.1.3. Helicity amplitudes	21
1.1.4. Isospin amplitudes	23
1.2. Polarization Observables	26
1.3. Complete Experiments	28
1.4. Extraction of Resonance Parameters	30
1.5. Previous Results	31
1.6. Motivation	36
2. Experimental Setup	38
2.1. MAMI	39
2.2. Electron and photon beams	42
2.3. Glasgow Photon Tagger	43
2.4. Crystal Ball	45
2.5. Particle Identification Detector	46
2.6. TAPS	47
2.7. Targets	49
2.7.1. Liquid Deuterium/Hydrogen Target	49
2.7.2. Frozen Spin Target	50
2.7.3. Carbon Target	53
2.8. Measurement of the target polarization	54
2.9. Measurement of electron polarization	56
2.9.1. Mott Measurement	57
2.10. Measurement of the photon polarization	58
2.11. Data Acquisition	58
2.11.1. Tagger	58
2.11.2. CB	59
2.11.3. TAPS	60
2.12. Trigger	60
2.13. Software	62
2.13.1. AcquRoot	62
2.13.2. A2 GEANT	63
2.13.3. OSCAR	64

2.13.4. Pluto	65
2.13.5. CaLib	65
2.14. Beam-time Overview	65
2.14.1. Hydrogen and Deuterium Data	65
2.14.2. D-Butanol Data	66
2.14.3. Carbon Data	66
2.15. Target Polarization	66
3. Event Reconstruction	69
3.1. Tagger	69
3.2. Crystal Ball	69
3.3. TAPS	70
4. Calibration	73
4.1. Energy Calibration	73
4.1.1. CB energy calibration	73
4.1.2. TAPS energy calibration	75
4.1.3. PID energy calibration	77
4.1.4. PID angle calibration	78
4.1.5. TAPS Veto energy calibration	78
4.1.6. CB LED Calibration	79
4.1.7. TAPS LED Threshold Calibration	79
4.1.8. Tagger energy calibration	80
4.2. Time Calibration	81
4.2.1. CB time calibration	81
4.2.2. TAPS time calibration	83
4.2.3. Tagger time calibration	84
4.2.4. PID and Veto time calibration	84
4.3. Calibration of the Simulation	85
4.3.1. Energy Resolution	85
4.3.2. Angular resolutions	86
5. Analysis	88
5.1. Kinematics in the participant-spectator model	88
5.2. Event Selection	90
5.2.1. Analysis of $\gamma p(n) \rightarrow \eta\pi^0 p(n)$	91
5.2.2. Analysis of $\gamma n(p) \rightarrow \eta\pi^0 n(p)$	91
5.2.3. Analysis of $\gamma N(N) \rightarrow \eta\pi^0(N)$	91
5.2.4. Analysis of $\gamma p(n) \rightarrow \eta\pi^+ n(n)$	92
5.2.5. Analysis of $\gamma n(p) \rightarrow \eta\pi^- p(p)$	92
5.2.6. Analysis of $\gamma N(N) \rightarrow \eta\pi^\pm(N)$	92
5.2.7. Analysis of $\gamma p \rightarrow \eta\pi^0 p$	93
5.2.8. Analysis of $\gamma p \rightarrow \eta\pi^+ n$	93
5.2.9. Analysis of $\gamma d \rightarrow \eta\pi^0 d$	93

5.2.10. Reconstruction of η and π^0 mesons	94
5.2.11. Reconstruction of η -mesons from 3 neutral hits	95
5.2.12. Confidence Levels	95
5.3. Discrimination of charged particles	98
5.4. Energy correction of η and π^0 mesons	101
5.5. Background rejection	103
5.5.1. Pulse Shape Analysis	104
5.5.2. Coplanarity Cut	107
5.5.3. Missing Mass Cut	117
5.5.4. η Invariant Mass	128
5.5.5. π^0 Invariant Mass	140
5.6. Time Of Flight	148
5.7. Nucleon polar angle	152
5.8. Fermi Momentum	153
5.9. Time cuts	155
5.9.1. Photon coincidence time	155
5.9.2. Tagger Random Coincidences	155
5.10. Software Trigger	156
5.10.1. CB energy sum trigger	156
5.10.2. Multiplicity trigger	157
5.11. Detection efficiency correction	158
5.12. Nucleon detection efficiency correction	161
5.13. Photon Flux	163
5.13.1. Tagging efficiency	164
5.13.2. E_γ dependent Flux	165
5.13.3. W dependent Flux	167
5.14. Extraction of the true center of mass energy W	168
5.15. Extraction of the Beam Helicity Asymmetry I^\odot	169
5.16. Extraction of total cross sections	172
5.17. Extraction of the yields	173
5.18. Extraction of angular distributions	173
5.19. Extraction of mass distributions	174
5.20. Extraction of the double polarization observable E	174
5.20.1. Carbon Subtraction	175
5.20.2. Extraction of helicity dependent cross sections	178
5.21. Empty target subtraction	179
5.22. Merging of Data sets	180
5.23. Systematic uncertainties	180
5.23.1. Reaction independent systematic uncertainties	181
5.23.2. Reaction dependent systematic uncertainties	181
5.23.3. Summation of systematic uncertainties	182
5.23.4. Uncertainties related to polarized data	184

6. Results	187
6.1. Total cross sections	187
6.1.1. Cross sections for $\eta\pi^0$ channels	188
6.1.2. Cross sections for $\eta\pi^\pm$ channels	190
6.1.3. Cross-section for $\eta\pi^0$ coherent	192
6.1.4. Ratios of total cross sections of quasi-free reactions	193
6.2. $\cos(\theta_\eta)$ distributions	194
6.2.1. $\eta\pi^0$ channels	194
6.2.2. $\eta\pi^\pm$ channels	195
6.3. Invariant Mass Distributions	196
6.3.1. $\eta\pi^0$ channels	197
6.3.2. $\eta\pi^\pm$ channels	198
6.4. Angular Distributions	199
6.4.1. $\eta\pi^0$ channels	199
6.4.2. $\eta\pi^\pm$ channels	201
6.5. Helicity Asymmetries	203
6.5.1. $\eta\pi^0$ channels	204
6.5.2. $\eta\pi^\pm$ channels	207
6.6. Double polarization observable E	209
6.7. Helicity dependent cross sections	212
6.8. Conclusions	214
A. Appendix 1	215
A.1. Efficiencies	216
A.1.1. $\eta\pi^0$ channels	216
A.1.2. $\eta\pi^\pm$ channels	219
A.2. Differential Cross sections	222
A.2.1. $\eta\pi^0$ channels	222
A.2.2. $\eta\pi^\pm$ channels	224
A.3. Determination of $\Delta m_{\gamma_i \gamma_j}$	225
B. Data tables	227
B.0.1. Total Cross Sections	227
B.0.2. Total Cross Sections as function of W	236
B.0.3. Invariant Mass Distributions	242
B.0.4. Angular Distributions of the η in the CM System	278
B.0.5. Angular Distributions of the π in the Helicity System	282
B.0.6. Angular Distributions of the Pion in the Canonical System	290
B.0.7. Helicity Asymmetries	298
B.0.8. Double Polarization Observable E as Function of E_γ	310
B.0.9. Double Polarization Observable E as Function of W	311
B.0.10. Helicity Dependent Cross Sections as Function of E_γ	312
B.0.11. Helicity Dependent Cross Sections as Function of W	314

List of Figures

1.1.	Oscillator model	16
1.2.	Coupling Constant	17
1.3.	Resonance spectra	17
1.4.	Cross sections for total photo absorption	18
1.5.	Level scheme	25
1.6.	Coordinate System	26
1.7.	Feynman Graphs	30
1.8.	Cross section decomposition	31
1.9.	Previous Results: Total Cross Section	32
1.10.	Previous Results: Angular and IM Distributions	33
1.11.	Previous Results: Invariant Mass Distributions	34
1.12.	Previous Results: Beam-Target Asymmetry	35
1.13.	Previous Results: Beam-Helicity Asymmetry	36
2.1.	Schematic Overview of the Detector Setup	38
2.2.	Floorplan of the MAMI facility	40
2.3.	Racetrack Microtrons functionality	41
2.4.	Schematic drawing of the HDSM functionality	42
2.5.	Schematic view of the Glasgow photon tagger	45
2.6.	Photo of CB	46
2.7.	Photos of the PID	47
2.8.	Configuration of TAPS	49
2.9.	Target Cell	50
2.10.	Zeeman levels	51
2.11.	Polarization for several Temps and B-fields	52
2.12.	Dilution refrigerator	53
2.13.	Carbon Target	54
2.14.	NMR levels	54
2.15.	NMR Signal	55
2.16.	Target polarization values	56
2.17.	Mott polarimeter	57
2.18.	Beam polarization values	58
2.19.	CB electronics	60
2.20.	Schematic view of the trigger electronics	62
2.21.	Visualization of the exp. setup in GEANT	64
2.22.	NMR Coils	67

2.23. Larmor-frequencies	68
2.24. Magnetic field inhomogeneities	68
3.1. TAPS shower depth	71
3.2. Cluster Sizes	72
4.1. CB low energy calibration	75
4.2. BaF ₂ spectrum	76
4.3. PSA Spectrum in TAPS	77
4.4. PID angular Calibration	78
4.5. CB LED Calibration	79
4.6. TAPS Calibration	80
4.7. Tagger Calibration	81
4.8. Fermi momentum distribution	83
4.9. Time Calibration	84
4.10. Energy resolution of the CB and TAPS detectors	85
4.11. Angular resolution of CB	87
4.12. Angular resolution of TAPS	87
5.1. Participant spectator model	89
5.2. TOF in TAPS	94
5.3. Confidence levels for neutral channels	96
5.4. Confidence levels for charged channels	97
5.5. Confidence levels for dButanol	97
5.6. PiC identification	99
5.7. Pion correction function	100
5.8. π^- energy correction	101
5.9. π^+ energy correction	101
5.10. η and π^0 correction	102
5.11. $\gamma\gamma$ invariant masses	103
5.12. PSA spectra of q.f. excl. $\eta\pi^0$	104
5.13. PSA spectra of q.f. excl. $\eta\pi^\pm$	105
5.14. PSA spectra of $\eta\pi$	105
5.15. PSA spectra of $\eta\pi$ for reactions on free protons	106
5.16. PSA spectra of q.f. excl. $\eta\pi^0$ for dButanol	106
5.17. Coplanarity for the $\eta\pi^0 p(n)$ final state	108
5.18. Coplanarity for the $\eta\pi^0 n(p)$ final state	109
5.19. Coplanarity for the $\eta\pi^0 d$ final state	110
5.20. Coplanarity for the $\eta\pi^0 p$ final state (free)	111
5.21. Coplanarity for the $\eta\pi^+ n(n)$ final state	112
5.22. Coplanarity for the $\eta\pi^0 p(p)$ final state	113
5.23. Coplanarity for the $\eta\pi^0 p$ final state	114
5.24. Coplanarity for the $\eta\pi^0 p(n)$ final state for dButanol	115
5.25. Coplanarity for the $\eta\pi^0 n(p)$ final state for dButanol	116

5.26. Missing Mass for the $\eta\pi^0 p(n)$ final state	118
5.27. Missing Mass for the $\eta\pi^0 n(p)$ final state	119
5.28. Missing Mass for the $\eta\pi^0(N)$ final state	120
5.29. Missing Mass for the $\eta\pi^0 d$ final state	121
5.30. Missing Mass for the $\eta\pi^0 p$ final state (free)	122
5.31. Missing Mass for the $\eta\pi^+ n(n)$ final state	123
5.32. Missing Mass for the $\eta\pi^- p(p)$ final state	124
5.33. Missing Mass for the $\eta\pi^\pm(N)$ final state	125
5.34. Missing Mass for the $\eta\pi^+ n$ final state (free)	126
5.35. Missing Mass for the $\eta\pi^0 p(n)$ final state for dButanol	127
5.36. Missing Mass for the $\eta\pi^0 n(p)$ final state for dButanol	127
5.37. Invariant mass of the η for the $\eta\pi^0 p(n)$ final state	129
5.38. Invariant mass of the η for the $\eta\pi^0 n(p)$ final state	130
5.39. Invariant mass of the η for the $\eta\pi^0(N)$ final state	131
5.40. Invariant mass of the η for the $\eta\pi^0 d$ final state	132
5.41. Invariant mass of the η for the $\eta\pi^0 p$ final state (free)	133
5.42. Invariant mass of the η for the $\eta\pi^+ n(n)$ final state	134
5.43. Invariant mass of the η for the $\eta\pi^- p(p)$ final state	135
5.44. Invariant mass of the η for the $\eta\pi^\pm(N)$ final state	136
5.45. Invariant mass of the η for the $\eta\pi^+ n$ final state (free)	137
5.46. Invariant mass of the η for the $\eta\pi^0 p(n)$ final state for dButanol	138
5.47. Invariant mass of the η for the $\eta\pi^0 n(p)$ final state for dButanol	139
5.48. Invariant mass of the π^0 for the $\eta\pi^0 p(n)$ final state	141
5.49. Invariant mass of the π^0 for the $\eta\pi^0 n(p)$ final state	142
5.50. Invariant mass of the π^0 for the $\eta\pi^0(N)$ final state	143
5.51. Invariant mass of the π^0 for the $\eta\pi^0 d$ final state	144
5.52. Invariant mass of the π^0 for the $\eta\pi^0 p$ final state	145
5.53. Invariant mass of the π^0 for the $\eta\pi^0 p(n)$ final state for dButanol	146
5.54. Invariant mass of the π^0 for the $\eta\pi^0 n(p)$ final state for dButanol	147
5.55. Time-Of-Flight for π^0 final states	149
5.56. Time-of-Flight for π^\pm final states	150
5.57. Time-of-Flight for inclusive and coherent reactions	150
5.58. Time-of-Flight for reactions on free protons	151
5.59. Time-of-Flight for π^0 final states	151
5.60. Nucleon polar angles	152
5.61. Fermi momentum distributions	154
5.62. Photon coincidence time	155
5.63. Random time	156
5.64. CB Energy Sum	157
5.65. Detection efficiency for qf. $\eta\pi$ channels	159
5.66. Detection efficiency comparison	160
5.67. Detection efficiency as function of E_γ	161
5.68. Detection efficiencies as function of W	161
5.69. Nucleon Efficiency Correction	163

5.70.	Electron counts and tagging efficiency	164
5.71.	Photon Fluxes as function of E_γ	166
5.72.	Tagger P2	167
5.73.	W dependent Flux	168
5.74.	Reaction and production plane	171
5.75.	Coordinate Systems for Angular Distributions	174
5.76.	Determination of the dilution factor	177
5.77.	Determination of the dilution factor	177
5.78.	Empty target cross sections	180
5.79.	Systematic Errors as function of W	183
5.80.	Systematic Errors as function of E_γ	183
5.81.	Systematic Errors as function of W	184
5.82.	Systematic Errors as function of E_γ	184
6.1.	Cross Sections as function of E_γ	188
6.2.	Cross Sections as function of W	189
6.3.	Cross Sections as function of E_γ	190
6.4.	Cross Sections as function of W	191
6.5.	Coherent Cross Section	192
6.6.	Ratios of CS	193
6.7.	Differential Cross Sections	194
6.8.	Coherent Cross Section	195
6.9.	Mass Distributions for $\eta\pi^0$ channels	197
6.10.	Mass Distributions for $\eta\pi^\pm$ channels	198
6.11.	Φ distributions for $\eta\pi^0$	199
6.12.	$\cos(\theta)$ distributions for $\eta\pi^0$	200
6.13.	Φ distributions for $\eta\pi^\pm$	201
6.14.	$\cos(\theta)$ distributions for $\eta\pi^\pm$	202
6.15.	Helicity asymmetries for $\eta\pi^0$ with model predictions	204
6.16.	Helicity asymmetries for $\eta\pi^0$ with fits to the data	205
6.17.	Fit parameters	206
6.18.	Helicity asymmetries for $\eta\pi^\pm$ with model predictions	207
6.19.	Helicity asymmetries for $\eta\pi^\pm$ with fits to the data	208
6.20.	Fit parameters	209
6.21.	Double Polarization Observable E as function of W	210
6.22.	Double Polarization Observable E as function of E_γ	211
6.23.	Comparison of sums of hel. dep. cross sections	211
6.24.	Helicity dependent cross sections as function of W	212
6.25.	Helicity dependent cross sections as function of E_γ	213
A.1.	Efficiency comparison for $\eta\pi^0$ channels	216
A.2.	Efficiency as function of $\cos(\theta_{\eta\pi}^*)$ for E_γ	217
A.3.	Efficiency as function of $\cos(\theta_{\eta\pi}^*)$ for W	218
A.4.	Efficiency comparison for $\eta\pi^\pm$ channels	219

A.5. Efficiency as function of $\cos(\theta_{\eta\pi}^*)$ for E_γ	220
A.6. Efficiency as function of $\cos(\theta_{\eta\pi}^*)$ for W	221
A.7. Diff. cross section as function of $\cos(\theta_{\eta\pi}^*)$ for E_γ	222
A.8. Diff. cross section as function of $\cos(\theta_{\eta\pi}^*)$ for W	223
A.9. Diff. cross section as function of $\cos(\theta_{\eta\pi}^*)$ for E_γ	224
A.10. Diff. cross section as function of $\cos(\theta_{\eta\pi}^*)$ for W	225

List of Tables

1.1.	Quarks in the standard model	16
1.2.	Multipole amplitudes	21
1.3.	Double polarization observables	26
2.1.	Magnetic moments	51
2.2.	Parameters of the hydrogen and deuterium beam-times.	65
2.3.	Parameters for the dButanol beam-times.	66
2.4.	Parameters of the carbon beam-times.	66
5.1.	Event cluster conditions	91
5.2.	Target parameters	172

Acknowledgments

First and foremost I would like to express my gratitude to my supervisor Prof. Dr. Bernd Krusche for letting me join his research group and the invaluable support through the work of my PhD. Also a big thank you to Prof. Dr. Volker Metag for agreeing to be my co-referee. I also want to thank the past and present members of our group: I. Jaegle, F. Pheron, Y. Maghrbi, R. Trojer, R. Rostomyan, I. Keshelashvili, D. Werthmüller, M. Oberle, M. Dieterle, L. Withhauer, T. Strub, N. Walford, M. Günther, S. Abt, S. Lutterer, S. Garni and D. Ghosal for your support, valuable discussions and the fun times we had, especially the barbecues. Last but certainly not least I want to thank my family and friends for their support and patience during the last years.

1. Introduction

Up until the 1930s nucleons were considered to be pointlike, similar to electrons. Therefore, the magnetic moment of the proton was expected to be $\mu_N = eh/2\pi m_p c$, where e is the elementary charge, h is Planck's constant, m_p is the proton mass and c is the speed of light. Similarly, the neutron was expected to have a magnetic moment of 0. In 1933 measurements by Stern and Frisch [1], found the magnetic moment of the proton to be $\mu_p = 2.79\mu_N$ and therefore significantly different from the expected value. Additionally, the magnetic moment of the neutron was found to be [2] $\mu_n = -1,91\mu_m$. These were the first hints, that nucleons might not be pointlike as expected. This assumption was confirmed by [3] by measurements of the charge radius of protons, which was found to be $\sqrt{\langle r^2 \rangle} \approx 0.74$ fm. In 1953 Anderson [4] found the first nucleon resonance in pion-proton scattering at the Chicago Cyclotron. This resonance is today known as the $P_{33}(1232)$ or $\Delta(1232)3/2^+$ resonance and many more resonances were to follow.

Today a common way to notate nucleon resonances is the following:

$$L_{2I2J}(M), \quad (1.1)$$

where L denotes the angular momentum of the decay into a πN system, I is the isospin of the resonance, J is the spin of the resonance, M is the mass of the resonance in MeV. The particle data group [5] moved to a slightly different notation:

$$I(W)J^P, \quad (1.2)$$

where I is the isospin (N for $I=1/2$, Δ for $I=3/2$), W is the mass in MeV and J^P are total angular momentum and parity. For example the $P_{33}(1232)$ resonance is written in this notation as $\Delta(1232)3/2^+$, and the $D_{33}(1700)$ as $\Delta(1700)3/2^-$.

In 1964 Gell-Mann [6] introduced quarks as the fundamental constituents of hadrons. In this model baryons consist of three quarks and mesons consist of a quark-antiquark pair. Over the following years the constituent quark model was adapted and enhanced, and several new models were developed to gain a better understanding of the resonance spectrum. An overview over recent constituent quark models is given in [7].

family	flavor	charge	spin	mass
1st	up	2/3	1/2	~ 2,3 MeV
	down	-1/3	1/2	~ 4,8 MeV
2nd	charm	2/3	1/2	~ 1,3 GeV
	strange	-1/3	1/2	~ 95 MeV
3rd	top	2/3	1/2	~ 170 GeV
	bottom	-1/3	1/2	~ 4,6 GeV

Table 1.1.: The six quarks of the standard model. Numerical values from [5]

What all these models have in common is, that they predict more resonances, than have experimentally been observed. It is not clear if the explanation for these missing resonances phenomenon is caused by the theoretical or the experimental side.

The number of predicted resonances is closely related to the number of degrees of freedom in a model. Models which treat nucleons as consisting of three equal quarks, predict the most excited states. Some models reduce the complexity of this three-body approach by treating the nucleon as a quark-diquark system. Due to the reduced number of degrees of freedom these models predict fewer resonances.

Another approach is to treat the nucleon as being composed of two independent oscillators as depicted in Fig. 1.1. Nucleon resonances can than be described as excitations of these oscillators. However, the number of resonances predicted by this model is still too large.

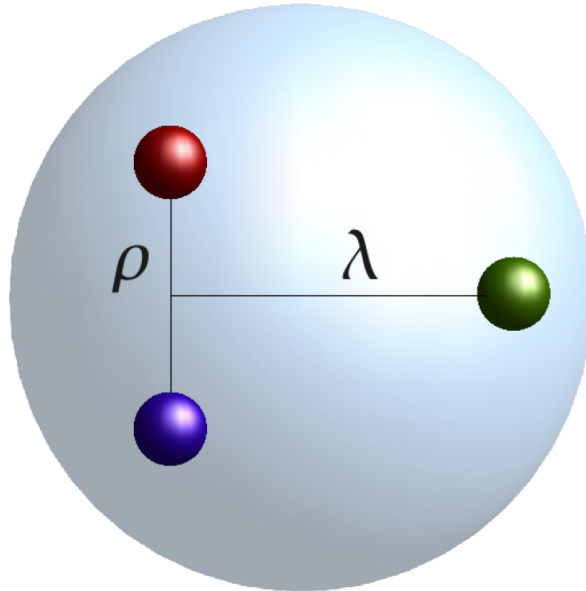


Figure 1.1.: Illustration of a model treating the nucleon as system of the oscillators ρ and λ . Fig. taken from [8]

Another ansatz that has proven itself in other fields, perturbation theory, cannot be applied because of a distinct feature of the strong interaction. The coupling constant α_s is indeed not constant as is shown in Fig. 1.2, but varies with the momentum transfer Q . For small values of Q α_s becomes increasingly large, therefore higher order terms in α_s can no longer be expected to vanish.

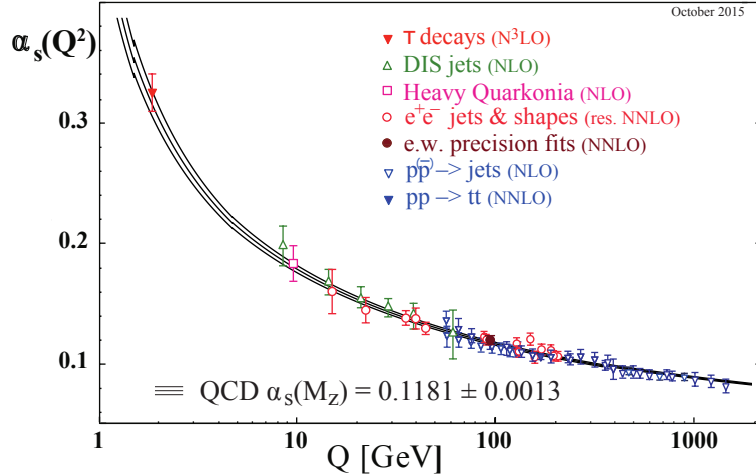


Figure 1.2.: Strong coupling constant α_s as function of the momentum transfer Q . [5]

On the experimental side it could be that certain resonances have not been observed because until 20 years ago, most experiments were performed with meson beams impinging on nuclear targets. Resonances that couple only weakly to mN cannot be observed this way. Therefore, photoexcitation experiments have become more important to search for resonances that couple strongly to γN .

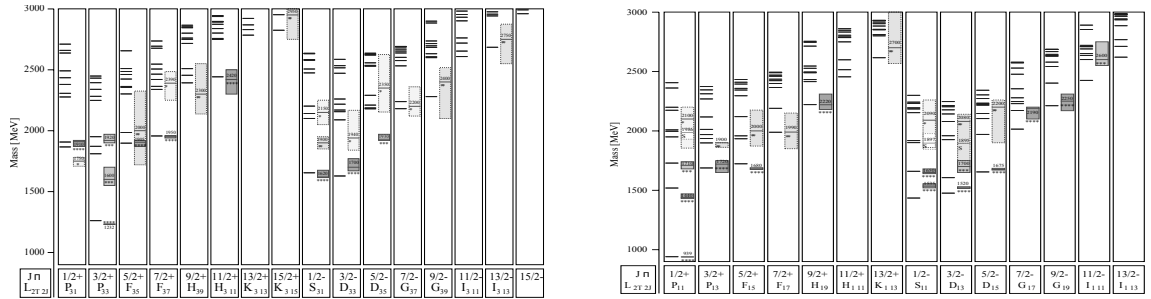


Figure 1.3.: Calculated positive and negative parity resonance spectrum for isospin $I=3/2$ on the left and isospin $I=1/2$ on the right. The predicted masses are shown on the left of each column, the experimentally observed resonance position is shown on the right. The box size corresponds to the experimental uncertainty. The darker shaded a box, the more reliable is the resonance. Figure taken from [9].

The total photoabsorption cross section on nucleons is shown in Fig. 1.4. Numerous different nucleon resonances can contribute to the cross section. Due to the broad shapes and strong overlaps it is challenging to identify specific resonances and extract information about them. The choice of a suitable reaction, that has only contributions from few resonances simplifies the extraction of resonance parameters. For example η photoproduction is strongly dominated by the $S_{11}(1535)$ and therefore allows a precise study of this resonance [10].

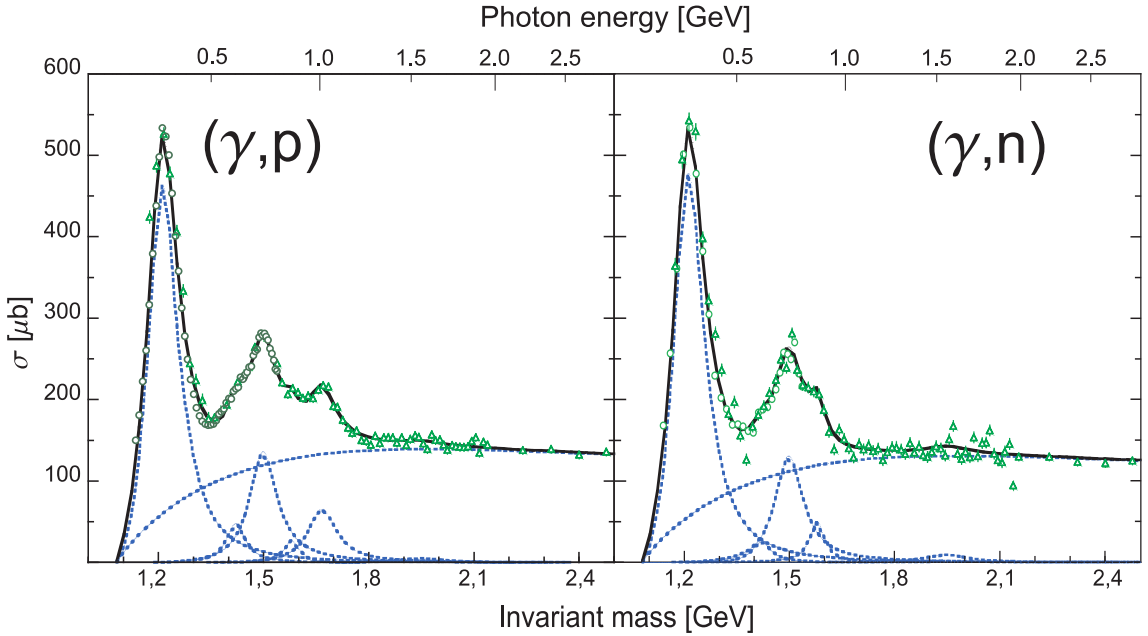


Figure 1.4.: Cross sections of the total photoabsorption on protons (left) and neutrons (right). Green points: measured data. Blue dashed lines: Fit of Breit Wigner shapes of nucleon resonances and background. Figure taken from [10].

1.1. Photoproduction of pseudoscalar mesons

1.1.1. CGNL amplitudes

The simplest case of photoproduction is the production of a single pseudoscalar meson. This process can be described by the following formula:

$$\gamma + N \rightarrow m + N', \quad (1.3)$$

where a photon γ impinges on a nucleon N and produces a meson m and a final state nucleon N' .

In scattering theory the scattering matrix S is used to describe the transition of the initial state $|i\rangle$, here $(\gamma + N)$, into the final state $|f\rangle$, here $(m+N')$.

The square of the absolute value of the matrix element S_{if} equals the probability of the transition to occur:

$$P(|i\rangle \rightarrow |f\rangle) = |S_{if}|^2. \quad (1.4)$$

Included in the S matrix are the aspects of the transition like interaction, reaction phase space and four-momentum conservation.

The matrix elements S_{if} are given by:

$$S_{if} = \frac{\delta^4(p_{N'} + p_m - p_N - p_\gamma)}{(2\pi)^2} \cdot \sqrt{\frac{M_N^2}{4E_{N'}E_mE_NE_\gamma}} \cdot i\mathcal{M}_{if}, \quad (1.5)$$

where $p_j = (E_j, \vec{p}_j)$ denotes the 4 vector of particle j and \mathcal{M} are Lorentz invariant matrix elements. They can be expressed by Pauli spinors χ :

$$\mathcal{M}_{fi} = \frac{4\pi W}{M_N} \langle \chi(N') | \mathcal{F} | \chi(N) \rangle, \quad (1.6)$$

where W is the center of mass energy:

$$W = \sqrt{s} = \sqrt{(p_\gamma + p_N)^2}, \quad (1.7)$$

and \mathcal{F} is a 2×2 matrix given by the Chew-Goldberger-Nambu-Low (CGNL) parametrization [11]:

$$\begin{aligned} \mathcal{F} = & i\vec{\sigma} \cdot \vec{\epsilon} F_1 + (\vec{\sigma} \hat{p}_m)(\vec{\sigma} \cdot (\hat{p}_\gamma \times \vec{\epsilon})) F_2 \\ & + i(\vec{\epsilon} \cdot \hat{p}_\gamma)(\hat{p}_m \cdot \vec{\epsilon}) F_3 + i(\vec{\sigma} \cdot \hat{p}_m)(\hat{p}_m \cdot \vec{\epsilon}) F_4, \end{aligned} \quad (1.8)$$

With the unit vectors $\hat{p}_\gamma = \vec{p}_\gamma / |\vec{p}_\gamma|$ and $\hat{p}_m = \vec{p}_m / |\vec{p}_m|$, the polarization vector of the photon $\vec{\epsilon}$. The vector $\vec{\sigma}$ contains the Pauli matrices.

With the CGNL amplitudes F_i , the unpolarized cross section can be parametrized:

$$\begin{aligned}
\frac{p_\gamma^*}{p_m^*} \frac{d\sigma}{d\Omega} = & \left[|F_1|^2 + |F_2|^2 + \frac{1}{2}|F_3|^2 + \frac{1}{2}|F_4|^2 + \text{Re}(F_1 F_3^*) \right] \\
& + [\text{Re}(F_3 F_4^*) - 2\text{Re}(F_1 F_2^*)] \cdot \cos(\theta_m^*) \\
& - \left[\frac{1}{2}|F_3|^2 + \frac{1}{2}|F_4|^2 + \text{Re}(F_1 F_4^*) + \text{Re}(F_2 F_3^*) \right] \cdot \cos^2(\theta_m^*) \\
& - [\text{Re}(F_3 F_4^*)] \cdot \cos^3(\theta_m^*).
\end{aligned} \tag{1.9}$$

where '*' denotes the center of mass system for p_γ^* , p_m^* and θ_m^* but complex conjugate for F_i^* .

The CGNL amplitudes F_i can be expressed through derivatives of Legendre polynomials $P'_l(\cos\theta)$, $P''_l(\cos\theta)$ and the multipole amplitudes $E_{l\pm}$, $M_{l\pm}$ described in section 1.1.2 [12]:

$$\begin{aligned}
F_1(\theta_m^*) &= \sum_{l=0}^{\infty} [lM_{l+} + E_{l+}] P'_{l+1}(\cos(\theta_m^*)) + [(l+1)M_{l-} + E_{l-}] P'_{l-1}(\cos(\theta_m^*)) \\
F_2(\theta_m^*) &= \sum_{l=0}^{\infty} [(l+1)M_{l+} + lM_{l-}] P'_l(\cos(\theta_m^*)) \\
F_3(\theta_m^*) &= \sum_{l=0}^{\infty} [E_{l+} - M_{l+}] P''_{l+1}(\cos(\theta_m^*)) + [E_{l-} + M_{l-}] P''_{l-1}(\cos(\theta_m^*)) \\
F_4(\theta_m^*) &= \sum_{l=0}^{\infty} [M_{l+} - E_{l+} - M_{l-} - E_{l-}] P''_l(\cos(\theta_m^*)),
\end{aligned} \tag{1.10}$$

1.1.2. Multipole Expansion

The excitation of an intermediate N^* resonance from a nucleon N via a photon γ can be described by angular momenta and parity. The photon with spin \vec{s}_γ ($s=1$) and relative orbital angular momentum \vec{l} and total angular momentum $L_\gamma = \vec{s}_\gamma + \vec{l}$ couples to the nucleon N with spin \vec{J}_N ($J=1/2$) and parity P_N and produces a resonance N^* with spin J_{N^*} and parity P_{N^*} . P_{N^*} is then given by:

$$P_{N^*} = P_N \cdot P_\gamma = P_\gamma \tag{1.11}$$

For the spin of the resonance the following rule applies:

$$|L_\gamma - J_N| \leq J_{N^*} \leq |L_\gamma + J_N| \tag{1.12}$$

Assuming that the resonance decays to the nucleon ground state by emission of the pseudo-scalar meson m with spin 0 and relative angular momentum L_m , the following rule applies:

For the spin and parity this rules apply:

$$|L_m - J_N| \leq J_{N^*} \leq |L_m + J_N|, \tag{1.13}$$

and

$$P_{N^*} = P_N \cdot P_m \cdot (-1)^{L_m} = P_N \cdot (-1)^{L_m+1}. \quad (1.14)$$

Comparing equation 1.11 with 1.12 and 1.13 with 1.14 yields:

$$\begin{aligned} J_{N^*} &= |L_\gamma \pm \frac{1}{2}| = |L_m \pm \frac{1}{2}| \\ P_{N^*} &= P_\gamma = (-1)^{L_m+1}, \end{aligned} \quad (1.15)$$

where the \pm are independent.

Parity and angular momentum conservation then lead to:

$$\begin{aligned} EL : L &= L_m \pm 1 \\ ML : L &= L_m \end{aligned} \quad (1.16)$$

For pseudo-scalar photoproduction the notation $E_{l\pm}$ and $M_{l\pm}$ is used. M denotes magnetic multipoles, E denotes electric multipoles, $l=L_m$ is the relative orbital momentum between the meson and the nucleon in the final state and the \pm sign indicates if the nucleon spin has to be subtracted from or added to l to get the total angular momentum J_{N^*} .

Examples of the lowest order multipoles are given in table 1.1.2. From there can also be seen, that resonances with J_{N^*} can be excited by one electrical and one magnetic multipole, respectively. Resonances with $J_{N^*} = \frac{1}{2}^+$ ($\frac{1}{2}^-$) can only be excited by the M_{1-} (E_{0+}) multipole.

photon M-pole	initial State (L_γ^P, J_N^P)	interm state J_{im}^P	final state (J_N^P, L_N^P)	multipole	$\frac{p_\gamma^* d\sigma}{p_m^* d\Omega}$
E1	$1^-, \frac{1}{2}^+$	$\frac{1}{2}^-$	$(\frac{1}{2}^+, 0^-)$	E_{0+}	$ E_{0+} ^2$
		$\frac{3}{2}^-$	$(\frac{1}{2}^-, 2^-)$	E_{2-}	$\frac{1}{2} E_{2-} ^2 (5 - 3x^2)$
M1	$1^+, \frac{1}{2}^+$	$\frac{1}{2}^+$	$(\frac{1}{2}^+, 1^+)$	M_{1-}	$ M_{1-} ^2$
		$\frac{3}{2}^+$	$(\frac{1}{2}^+, 1^+)$	M_{1+}	$\frac{1}{2} M_{1+} ^2 (5 - 3x^2)$
E2	$2^+, \frac{1}{2}^+$	$\frac{3}{2}^+$	$(\frac{1}{2}^+, 1^+)$	E_{1+}	$\frac{9}{2} E_{1+} ^2 (1 + x^2)$
		$\frac{5}{2}^+$	$(\frac{1}{2}^+, 3^+)$	E_{3-}	$\frac{9}{2} E_{3-} ^2 (1 + 6x^2 - 5x^4)$
M2	$2^-, \frac{1}{2}^+$	$\frac{3}{2}^-$	$(\frac{1}{2}^+, 2^-)$	M_{2-}	$\frac{9}{2} M_{2-} ^2 (1 + x^2)$
		$\frac{5}{2}^-$	$(\frac{1}{2}^+, 3^+)$	M_{2+}	$\frac{9}{2} M_{2+} ^2 (1 + 6x^2 - 5x^4)$

Table 1.2.: Lowest order multipole amplitudes for pseudo-scalar meson photoproduction. p_γ^* and p_m^* are photon and meson momentum in the CM system, respectively.

1.1.3. Helicity amplitudes

A different parametrization of \mathcal{F} is possible by means of initial and final state helicity. The helicity λ of a particle is defined as:

$$\lambda = \frac{\vec{s} \cdot \vec{p}}{|\vec{p}|} \quad (1.17)$$

In case of the photoproduction of pseudo-scalar mesons this definition leads to $\lambda_m = 0$ for mesons, $\lambda_\gamma = \pm 1$ for photons and $\nu_{if} = \pm 1/2$ for initial and final state nucleons. This allows for $2 \times 2 \times 2 = 8$ Matrix elements $H_{\nu_f, \mu} = \langle \nu_f | T | \lambda_\gamma \nu_i \rangle$ ($\mu = \nu_i - \lambda_\gamma$) of which, due to parity conservation, only 4 are independent [12]:

$$\begin{aligned} H_1 &= H_{(1/2), (3/2)} = H_{-(1/2), -(3/2)} \\ H_2 &= H_{(1/2), (1/2)} = -H_{-(1/2), -(1/2)} \\ H_3 &= H_{-(1/2), (3/2)} = -H_{(1/2), -(3/2)} \\ H_4 &= H_{(1/2), -(1/2)} = H_{-(1/2), (1/2)} \end{aligned} \quad (1.18)$$

The relation between CGLN and helicity amplitudes is given by:

$$\begin{aligned} H_1(\Theta, \Phi) &= -\frac{1}{\sqrt{2}} e^{i\Phi} \sin \Theta^* \cos \frac{\Theta^*}{2} (F_3 + F_4) \\ H_2(\Theta, \Phi) &= \sqrt{2} \cos \frac{\Theta^*}{2} ((F_2 - F_1) + \frac{1}{2}(1 - \cos \Theta^*)) (F_3 - F_4) \\ H_3(\Theta, \Phi) &= \frac{1}{\sqrt{2}} e^{2i\Phi} \sin \Theta^* \sin \frac{\Theta^*}{2} (F_3 - F_4) \\ H_4(\Theta, \Phi) &= \sqrt{2} e^{i\Phi} \sin \frac{\Theta^*}{2} ((F_1 + F_2) + \frac{1}{2}(1 + \cos \Theta^*)) (F_3 + F_4) \end{aligned} \quad (1.19)$$

A second possible decomposition by means of partial waves is given by [13]:

$$\begin{aligned} H_1(\theta, \phi) &= \frac{1}{\sqrt{2}} e^{i\phi} \sin \theta \cos \frac{\theta}{2} \sum_{l=0}^{\infty} [B_{l+} - B_{(l+1)-}] (P_l''(\cos \theta) - P_{l+1}''(\cos \theta)) \\ H_2(\theta, \phi) &= \sqrt{2} \cos \frac{\theta}{2} \sum_{l=0}^{\infty} [A_{l+} - A_{(l+1)-}] (P_l'(\cos \theta) - P_{l+1}'(\cos \theta)) \\ H_3(\theta, \phi) &= \frac{1}{\sqrt{2}} e^{2i\phi} \sin \theta \sin \frac{\theta}{2} \sum_{l=0}^{\infty} [B_{l+} - B_{(l+1)-}] (P_l''(\cos \theta) + P_{l+1}''(\cos \theta)) \\ H_4(\theta, \phi) &= \sqrt{2} e^{i\phi} \sin \frac{\theta}{2} \sum_{l=0}^{\infty} [A_{l+} - A_{(l+1)-}] (P_l'(\cos \theta) - P_{l+1}'(\cos \theta)), \end{aligned} \quad (1.20)$$

where the helicity elements $A_{l\pm}$ and $B_{l\pm}$ describe the transition to final states with meson relative orbital angular momentum 1 and total angular momentum $J = l \pm 1/2$. $A_{l\pm}$ refers to initial states with helicity $1/2$, $B_{l\pm}$ refers to initial states with helicity $3/2$. The relation between the helicity amplitudes and the CGLN multipoles is given by:

$$\begin{aligned}
A_{l+} &= \frac{1}{2}((l+2)E_{l+} + lM_{l+}) \\
A_{l+1} &= \frac{1}{2}((-lE_{(l+1)-} + (l+2)M_{(l+1)-})) \\
B_{l+} &= E_{l+} - M_{l+} \\
B_{(l+1)-} &= E_{(l+1)-} + M_{(l+1)-}
\end{aligned} \tag{1.21}$$

The advantage of this last representation is the close connection between helicity amplitudes and electromagnetic resonance couplings [12]:

$$\begin{aligned}
A_{1/2} &= \sqrt{2\pi\alpha/k} \langle N^*, J_z = \frac{1}{2} | J_{em} | N, S_z = -\frac{1}{2} \rangle \\
A_{1/2} &= \sqrt{2\pi\alpha/k} \langle N^*, J_z = \frac{3}{2} | J_{em} | N, S_z = \frac{1}{2} \rangle
\end{aligned} \tag{1.22}$$

Assuming a Breit-Wigner shape for the resonances 1.22 reads:

$$\begin{aligned}
A_{1/2} &= \mp \frac{1}{C_{Nm}} \sqrt{(2J+1)\pi} \frac{q^* M_R \Gamma_R^2}{k^* m_N \Gamma_m} \text{Im}\{(A_{l\pm}(W=M_R))\} \\
A_{3/2} &= \pm \frac{1}{C_{Nm}} \sqrt{(2J+1)\pi} \frac{q^* M_R \Gamma_R^2}{k^* m_N \Gamma_m} \sqrt{(2J-1)(2J+3)/16} \text{Im}\{(B_{l\pm}(W=M_r))\}
\end{aligned}, \tag{1.23}$$

where m_N is the nucleon mass, M_R is the mass of the resonance and Γ_R is the decay width, Γ_m is the partial decay width of the decay channel of interest and C_{Nm} is the Clebsch-Gordan coefficient of the decay of the resonance into the relevant state.

For a spin of $J = 1/2$ $A_{3/2}$ vanishes. Therefore, spin 1/2 resonances have only a $A_{1/2}$ coupling, whereas resonances with spin $J \geq 3/2$ have $A_{1/2}$ and $A_{3/2}$ couplings.

1.1.4. Isospin amplitudes

A complication of meson photoproduction is the isospin since it is only conserved at the hadronic vertex (or vertices for multi meson production) but not at the electromagnetic vertex. At the em. vertex isoscalar ($\Delta I=0$) and isovector ($\Delta I = 0, \pm 1$) components of the electromagnetic current can be present. The transition operator can be separated into an isoscalar part \hat{S} and an isovector part \hat{V} . With this separation three independent matrix elements can be built: the isoscalar A^{IS} , isovector A^{IV} and the isospin changing A^{V3} :

$$\begin{aligned}
A^{IS} &= \left\langle \frac{1}{2}, \pm \frac{1}{2} \middle| \hat{S} \middle| \frac{1}{2}, \pm \frac{1}{2} \right\rangle \\
\mp A^{IV} &= \left\langle \frac{1}{2}, \pm \frac{1}{2} \middle| \hat{V} \middle| \frac{1}{2}, \pm \frac{1}{2} \right\rangle \\
A^{V3} &= \left\langle \frac{3}{2}, \pm \frac{1}{2} \middle| \hat{V} \middle| \frac{1}{2}, \pm \frac{1}{2} \right\rangle,
\end{aligned} \tag{1.24}$$

using the notation $\langle I_f, I_{f3} | \hat{A} | I_i, I_{i3} \rangle$ to describe the transition from the initial state with total isospin I_i and the 3-component I_{i3} to the final state with isospin I_f and 3-component I_{f3} [10].

The isospin amplitudes for single π photoproduction can then be written as:

$$\begin{aligned} A(\gamma p \rightarrow \pi^0 p) &= +\sqrt{\frac{2}{3}} A^{V3} + \sqrt{\frac{1}{3}} (A^{IV} - A^{IS}) \\ A(\gamma n \rightarrow \pi^0 n) &= +\sqrt{\frac{2}{3}} A^{V3} + \sqrt{\frac{1}{3}} (A^{IV} + A^{IS}) \\ A(\gamma p \rightarrow \pi^+ n) &= -\sqrt{\frac{1}{3}} A^{V3} + \sqrt{\frac{2}{3}} (A^{IV} - A^{IS}) \\ A(\gamma n \rightarrow \pi^- p) &= +\sqrt{\frac{1}{3}} A^{V3} - \sqrt{\frac{2}{3}} (A^{IV} + A^{IS}) \end{aligned} \quad (1.25)$$

From eq. 1.25 it can be seen, that the isospin structure of the excitation of Δ resonances is different from the excitation of N^* resonances. The excitation of Δ resonances is the same for protons and neutron since only the isospin changing amplitude A^{V3} can contribute. Excitations of N^* resonances involve the A^{IS} and A^{IV} amplitudes so that generally the electromagnetic couplings are different for protons and neutrons.

To unambiguously determine the three amplitudes, measurements on the proton and additionally on the neutron are needed. Since there are no free neutrons, light nuclei have to be used as neutron targets. This introduces additional uncertainties due to nuclear effects like Fermi motion and final state interactions. The deuteron is especially suited as target nucleus, because of the low binding energy and its well understood nuclear structure. Cross sections off the neutron can then be extracted assuming quasi free kinematics as explained in section 5.1.

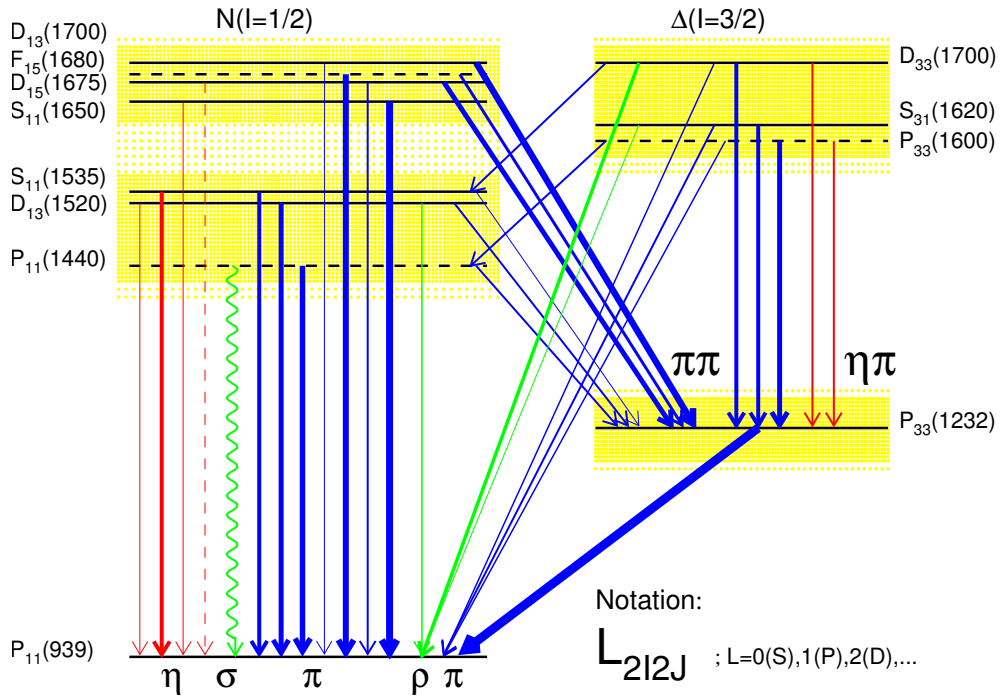


Figure 1.5.: Low lying excited states of the nucleon. Left side: $I=1/2 N^*$ resonances. Right-hand side: $I=3/2 \Delta^*$ resonances. Arrows indicate typical decay modes, the width corresponds to the branching ratio.

1.2. Polarization Observables

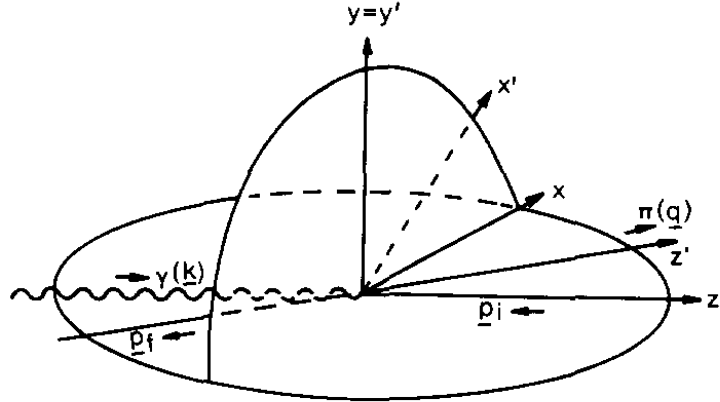


Figure 1.6.: Coordinate system used to define polarization observables: $x = y \times z$, $x' = y \times z'$, $y = k \times q / |k \times q|$, $y' = y$, $z = k / |k|$, $z' = q / |q|$. k : photon momentum. q : meson momentum. Figure taken from [14].

Polarized beams and targets allow to extract a multitude of observables. These observables can be grouped as follows: Single polarization observables (S -type) and double polarization observables. The latter can be divided into three subgroups:

$$\begin{array}{lll} \text{Beam-Target } \mathcal{BT} & \text{Beam-Recoil } \mathcal{BR} & \text{Target-Recoil } \mathcal{TR} \\ E, F, G, H & O_x, O_z, C_x, C_z & T_x, T_z, L_x, L_z \end{array}$$

Table 1.3.: Double polarization observables according to [15].

The S -type observable contain the unpolarized cross section σ_0 , the beam asymmetry Σ , the target asymmetry T and the recoil polarization P . With these observables the most general form of the total cross section of photoproduction of a single pseudoscalar meson is given by [15]:

$$\begin{aligned}
d\sigma^{B,T,R}(\vec{P}_\gamma, \vec{P}_T, \vec{P}_R) = & d\sigma_0[1 - P_L^\gamma P_y^T P_{y'}^R \cos(2\Phi_\gamma)] \\
& + \hat{\Sigma}[-P_L^\gamma \cos(2\Phi_\gamma) + P_y^T P_{y'}^R] \\
& + \hat{T}[P_y^T - P_L^\gamma P_{y'}^R \cos(2\Phi_\gamma)] \\
& + \hat{P}[P_{y'}^R - P_L^\gamma P_y^T \cos(2\Phi_\gamma)] \\
& + \hat{E}[-P_c^\gamma P_z^T + P_L^\gamma P_x^T P_{y'}^R \sin(2\Phi_\gamma)] \\
& + \hat{G}[P_y^L P_z^T \sin(2\Phi_\gamma) + P_c^\gamma P_x^T P_{y'}^R] \\
& + \hat{F}[P_c^\gamma P_x^T + P_L^\gamma P_z^T P_{y'}^R \sin(2\Phi_\gamma)] \\
& + \hat{H}[P_L^\gamma P_x^T \sin(2\Phi_\gamma) - P_c^\gamma P_z^T P_{y'}^R] \\
& + \hat{C}_{x'}[P_c^\gamma P_{x'}^R - P_L^\gamma P_y^T P_{z'}^R \sin(2\Phi_\gamma)] \\
& + \hat{C}_{z'}[P_c^\gamma P_{z'}^R + P_L^\gamma P_y^T P_{x'}^R \sin(2\Phi_\gamma)] \\
& + \hat{O}_{x'}[P_c^\gamma P_{x'}^R \sin(2\Phi_\gamma) + P_c^\gamma P_y^T P_{z'}^R] \\
& + \hat{O}_{z'}[P_L^\gamma P_{z'}^R \sin(2\Phi_\gamma) - P_c^\gamma P_y^T P_{x'}^R] \\
& + \hat{L}_{x'}[P_z^T P_{x'}^R + P_L^\gamma P_x^T P_{z'}^R \cos(2\Phi_\gamma)] \\
& + \hat{L}_{z'}[P_z^T P_{z'}^R + P_L^\gamma P_x^T P_{x'}^R \cos(2\Phi_\gamma)] \\
& + \hat{T}_{x'}[P_x^T P_{x'}^R - P_L^\gamma P_z^T P_{z'}^R \cos(2\Phi_\gamma)] \\
& + \hat{T}_{z'}[P_x^T P_{z'}^R - P_L^\gamma P_z^T P_{x'}^R \cos(2\Phi_\gamma)],
\end{aligned} \tag{1.26}$$

where P_i^T is the degree of polarization of the target in direction of i , P_i^R is the degree of polarization of the recoil nucleon in direction of i , P_L^γ is the degree of linearly photon polarization, P_c^γ is the degree of circular photon polarization, Φ is the angle of transverse polarization and σ_0 is the unpolarized cross section. In the used notation \hat{A} does not denote the observable A , but the product of the observable with the cross section σ_0 . This profile functions are chosen because they are most simply determined by the CGNL amplitudes [15].

Equation 1.26 can be simplified if only circularly polarized photon beams and a linearly polarized target with polarization parallel to the photon beam are considered:

$$d\sigma(P_c^\gamma, P_z^T) = \frac{1}{2} d\sigma_0(1 - EP_c^\gamma P_z^T). \tag{1.27}$$

One of the tasks of this work was to extract the double polarization observable E which is defined as follows:

$$E = \frac{\sigma_{1/2} - \sigma_{3/2}}{\sigma_{1/2} + \sigma_{3/2}}, \tag{1.28}$$

where the index $1/2$ denotes anti-parallel and $3/2$ denotes parallel photon and nucleon spins.

In terms of helicity amplitudes, E can be written as:

$$E = \frac{1}{2}(-|H_1|^2 + |H_2|^2 + |H_3|^2 + |H_4|^2)\rho \quad (1.29)$$

or in terms of CGLN amplitudes [15]:

$$E = Re\{F_1^*F_1 + F_2^*F_2 - 2\cos\theta^*F_1^*F_2 + \sin^2\theta^*(F_2^*F_3 + F_1^*F_4)\}\rho, \quad (1.30)$$

where ρ is a phase space factor.

1.3. Complete Experiments

As can be seen in section 1.1.1, four complex amplitudes are needed to extract the unpolarized cross section for the photoproduction of a single pseudoscalar meson. A set of measurements that allow to determine the amplitudes unambiguously is called 'complete experiment'. The knowledge of the differential cross section only provides information on the sum of the absolute squares of these amplitudes. To gain information on the phases between the amplitudes, the measurement of polarization observables is required.

In 1997 Chiang and Tabakin [16] showed that eight carefully chosen observables, each depending on two kinematic values, are sufficient to unambiguously determine the reaction amplitudes.

If only one pseudoscalar meson is produced, the whole reaction can be described in a single plane, that contains the incoming photon, the meson and the recoil nucleon. In the photoproduction of meson pairs, which has more degrees of freedom, two distinct planes have to be constructed as depicted in Fig. 5.74. Therefore, two meson production allows access to more observables. For example the beam helicity asymmetry I^\odot (see section 5.15) can be determined with only a circularly polarized photon beam.

A 'disadvantage' of the photoproduction of meson pairs is, that the formalism is generally more complicated, since there, problems with a three body final state have to be considered. If in a two-body decay the energy or angle of one particle is known, the corresponding value of the second particle can immediately be determined. This is in contrast to three-body decays where the remaining energy (or angle) can be continuously distributed between the two remaining particles. Additionally, there are many ways to couple the angular momenta of the individual particles to the total angular momentum, what makes a partial wave expansion challenging [17].

Formally, the photoproduction of two pseudoscalar mesons m_1 and m_2 on a nucleon N is described by:

$$\gamma(k) + N(p_1) \rightarrow m_1(q_1) + m_2(q_2) + N'(p_2), \quad (1.31)$$

where the values in parentheses are the respective 4-momenta. Additionally, one can define the following values:

$$\begin{aligned}
s &= (k + p_1)^2 \\
t &= (k - q)^2 = (p_2 - p_1)^2 \\
q &= (q_1 + q_2) = -p_2 \\
s_{m_1 m_2} &= (q_1 + q_2)^2 = q^2 \\
s_{N m_1} &= (p_2 + q_1)^2 \\
s_{N m_2} &= (p_2 + q_2)^2
\end{aligned} \tag{1.32}$$

These variables fulfill the relation:

$$s_{m_1 m_2} + s_{N m_1} + s_{N m_2} = s - 2m_N^2 - m_{m_1} - m_{m_2} \tag{1.33}$$

The whole process can be described by 5 kinematic variables, usually two Lorentz-invariants and three angles are chosen.

In 2005 Roberts and Oed [18] showed that at least 15 observables as functions of five kinematic values have to be measured in order to determine the reaction amplitudes unambiguously. The magnitude of the amplitudes alone requires knowledge of 8 observables, the extraction of the phases requires additional 7 observables. A complete experiment would include the measurements of the unpolarized cross section, single, double and even triple polarization observables which require the measurement of recoil polarization. Therefore, a complete experiment for photoproduction of meson pairs is rather unrealistic at this moment.

Additional information on the formalism of the polarization observables in the production of $\eta\pi$ pairs can be found in [19].

1.4. Extraction of Resonance Parameters

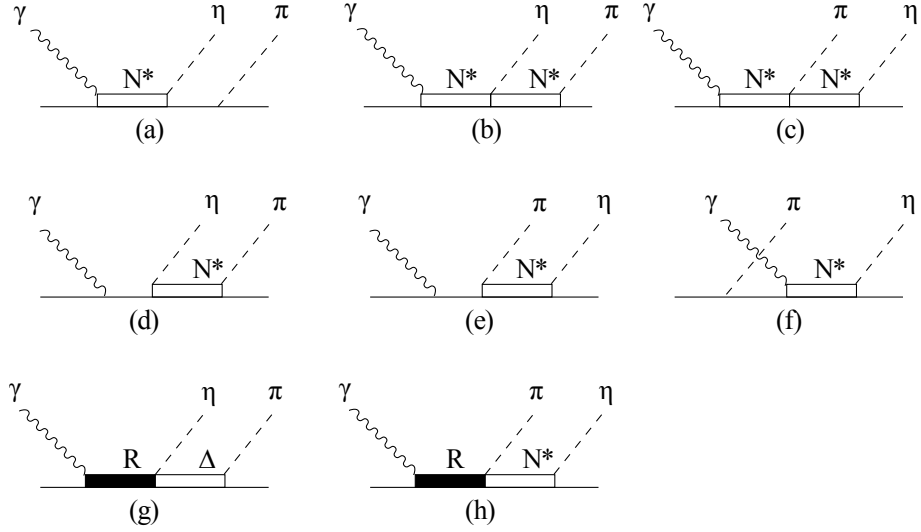


Figure 1.7.: Feynman Graphs that are included in the model of [20]. These model calculations will be compared to the experimental results in section 6. Fig. taken from [20].

The experimental results of this work will be compared to model calculations within an isobar model from Fix et al. [20].

In this model, resonance propagators are described with non-relativistic energy dependent Breit-Wigner curves:

$$G_R(W) = \frac{\Gamma_R/2}{W_R^2 - W - i \cdot \Gamma_R/2}, \quad (1.34)$$

where W_R is the position of the resonance and Γ_R is the resonance width. Resonances included in the full model are: $D_{33}(1700)$, $P_{33}(1600)$, $P_{31}(1750)$, $F_{35}(1905)$, $P_{33}(1920)$, $D_{33}(1940)$. However, the calculations shown in section 6 only take the $D_{33}(1700)$ into account.

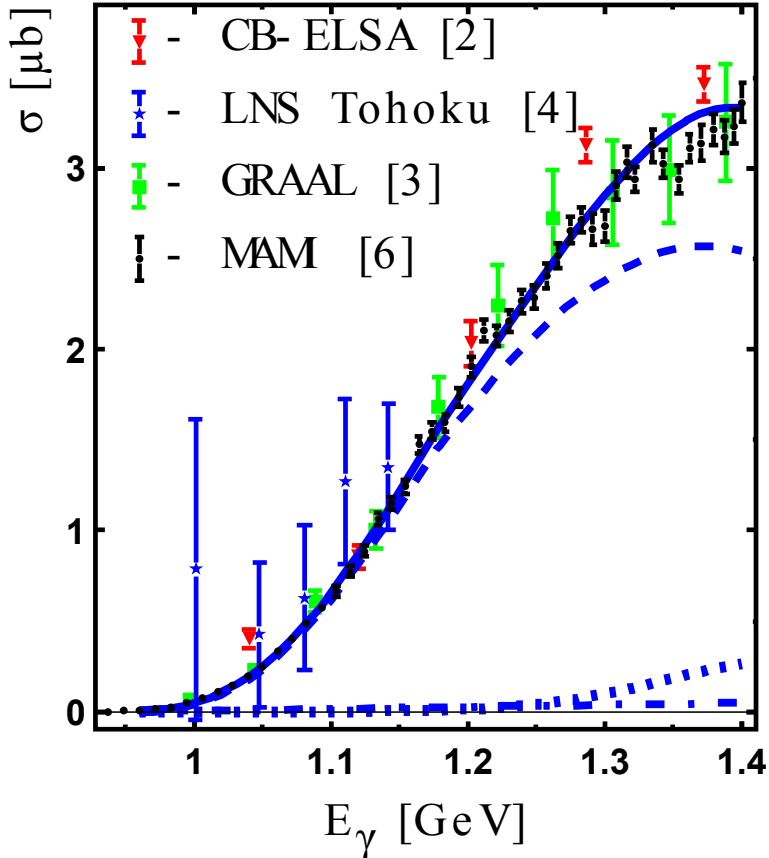


Figure 1.8.: Comparison of the cross section $\gamma p \rightarrow \eta\pi^0 p$ to model calculations. Points: experimental data. Solid blur line: full calculation. Dashed blue line: contributions from the D_{33} partial wave. Blue dotted line: contribution from P_{33} . Blue dashed dotted line: non resonant contributions. Fig. taken from [20].

Non-resonant contributions like Born terms (diagrams a-f in Fig. 1.7) are parametrized using effective Lagrangians.

These parameterizations are then fitted to experimental data.

1.5. Previous Results

Up until now, experimental results were only available for the reaction $\gamma p \rightarrow \eta\pi^0 p$ on free protons. Experiments have been performed at MAMI in Mainz [17] [21] [22] [23] [24], ELSA in Bonn [25] [26] [27] [28], GRAAL in Grenoble [29] and Sendai in Japan [30].

Results for the total cross sections are shown in Fig. 1.9. The threshold of the reaction is ≈ 930 MeV from where the cross section exhibits a steep rise to $\approx 3.2 \mu b$, where it stays up to energies of 2.5 GeV. The data are compared to calculations of the BnGa model

[25], [31], that show a clear dominance of the formation of a $\Delta\eta$ intermediate state in the energy range from threshold up to 1.5 GeV. Several independent works [20], [32], [33], [22], [25] agree with this assumption, and also conclude, that nonresonant background terms are negligible (see for example Fig. 1.8).

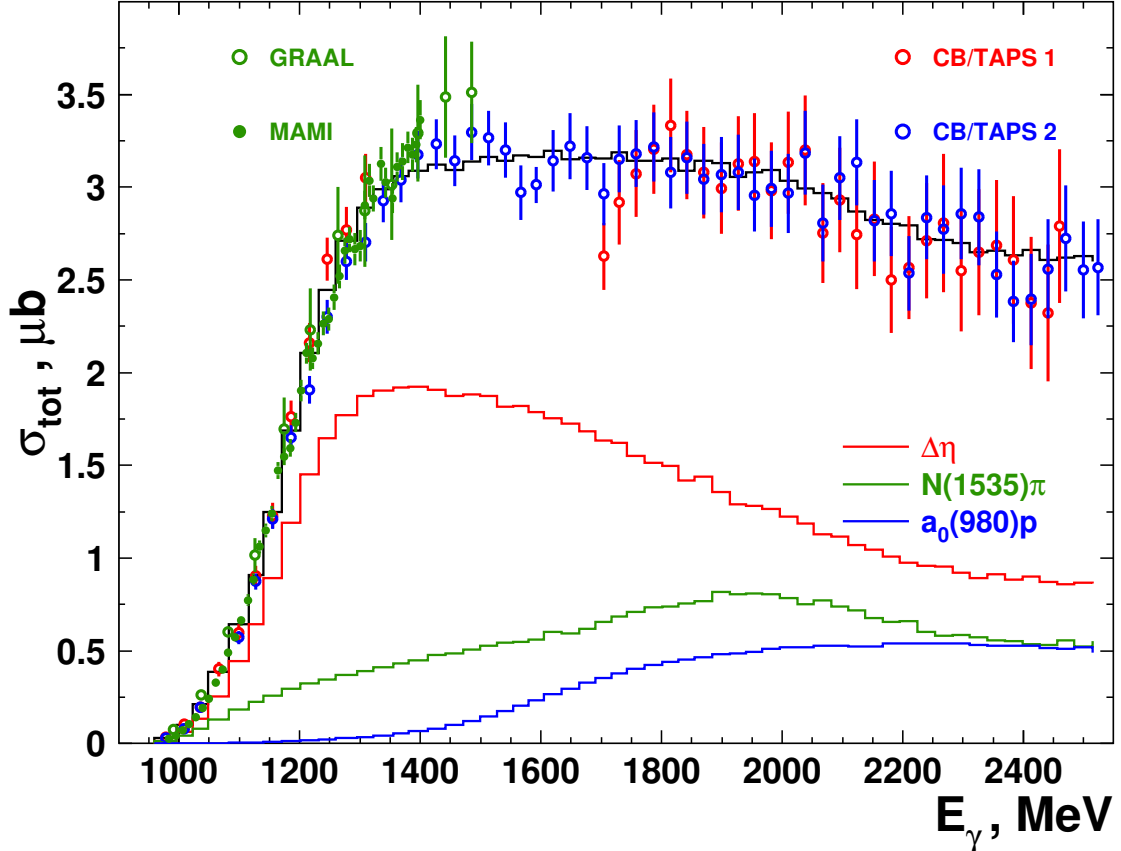


Figure 1.9.: Total cross section of the reaction $\gamma p \rightarrow \eta\pi^0 p$. The experimental data are from Crystal Ball/TAPS at MAMI [22] (open green circles), CBELSA/TAPS [25] (CBTAPS 1, open red and blue circles) and GRAAL [29] (open green circles). The red, green and blue lines show the contributions of $\Delta\eta$, $N(1535)1/2^-\pi$, and $a_0(980)p$ to the total fit shown in black, based on calculations from BnGa. Figure taken from [34]

Figure 1.10 shows on the left-hand side angular distributions of the π^0 in different coordinate systems (see section 5.18). The right-hand side shows invariant mass distributions of the $\pi^0 p$ and ηp subsystems. All distributions are compared to a model prediction that only takes the D_{33} resonance into account. With this assumption, the model is able to reproduce the experimental results nicely.

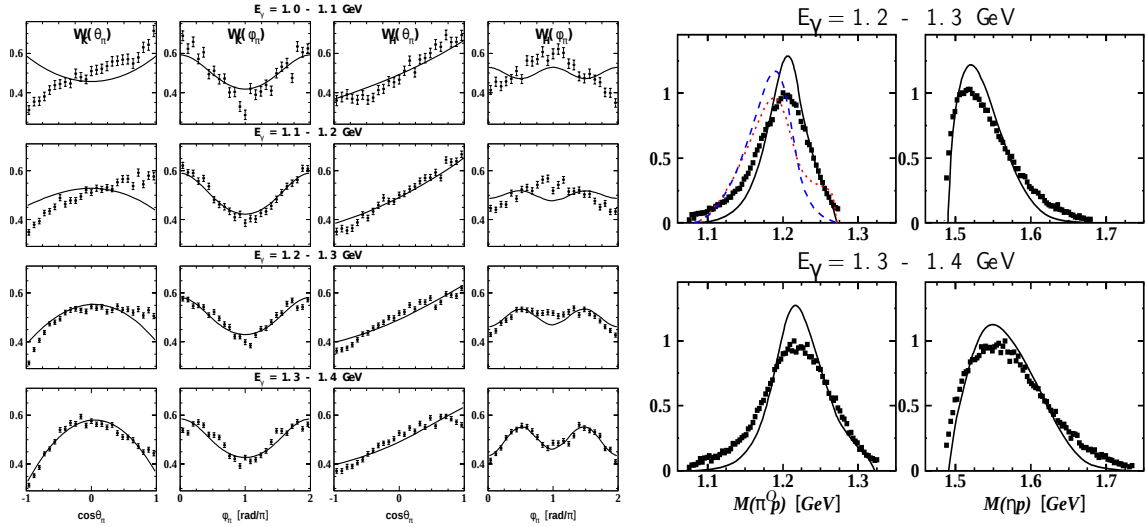


Figure 1.10.: Angular distributions (left) and invariant mass distributions. Solid lines are model predictions that only take the D_{33} partial wave into account. Blue dashed curve: model with only P_{33} contribution. Red dotted line: model with only D_{35} contributions. Taken from [22].

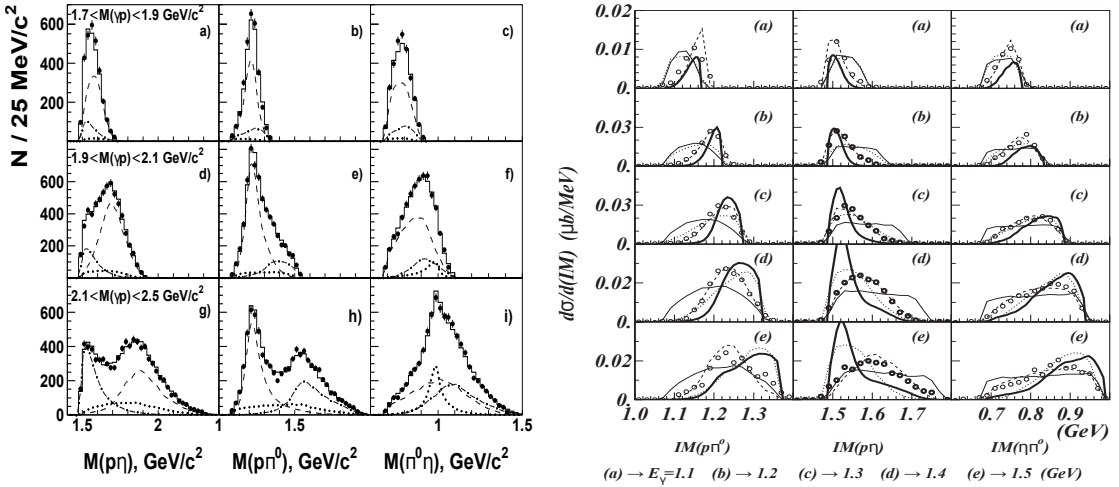


Figure 1.11.: Left-hand side: data and fits from [28]. Solid lines: best fit to the data. Dashed lines: contribution from $\Delta\eta$. Dash-dotted lines: contributions from $S_{11}\pi$. Dotted lines: contributions from $a_0(980)$. Right-hand side: Open circles: data from [29]. Thin black line: model with 3-body phase space. Dashed lines: model with $\Delta\eta$. Dotted lines: $S_{11}\pi$. Thick black lines: model from [32].

Similar findings were made in [28] and [29], shown in the left-hand and right-hand side of 1.11, respectively.

The top row on the left-hand side of Fig. 1.11 corresponds to the same energy range covered in [22] and also in this work. Again the $\Delta\eta$ intermediate state dominates the distributions. At higher energies contributions from $S_{11}\pi$ start to play a role.

In [29] also the beam asymmetry Σ was extracted, and similar to the invariant mass distributions the $\Delta(1700)3/2^-$ was essential for the agreement between data and model calculations.

More polarization observables for the reaction $\gamma p \rightarrow \eta\pi^0 p$ have been investigated in [23], namely the target and beam target asymmetries, and were compared to the model from [20]. Figure 1.12 shows the beam-target asymmetry P_x^\odot as function of the azimuthal angles of the final state particles and as function of the final state two-body invariant masses. The red dashed line in the first column represents a parametrization that assumes the reaction to take place exclusively via formation of an intermediate $\Delta\eta$ pair and the helicity amplitudes of $\gamma N \rightarrow \Delta(1700)3/2^-$ to be identical.

This parameterization is in good agreement with the full model and the experimental data.

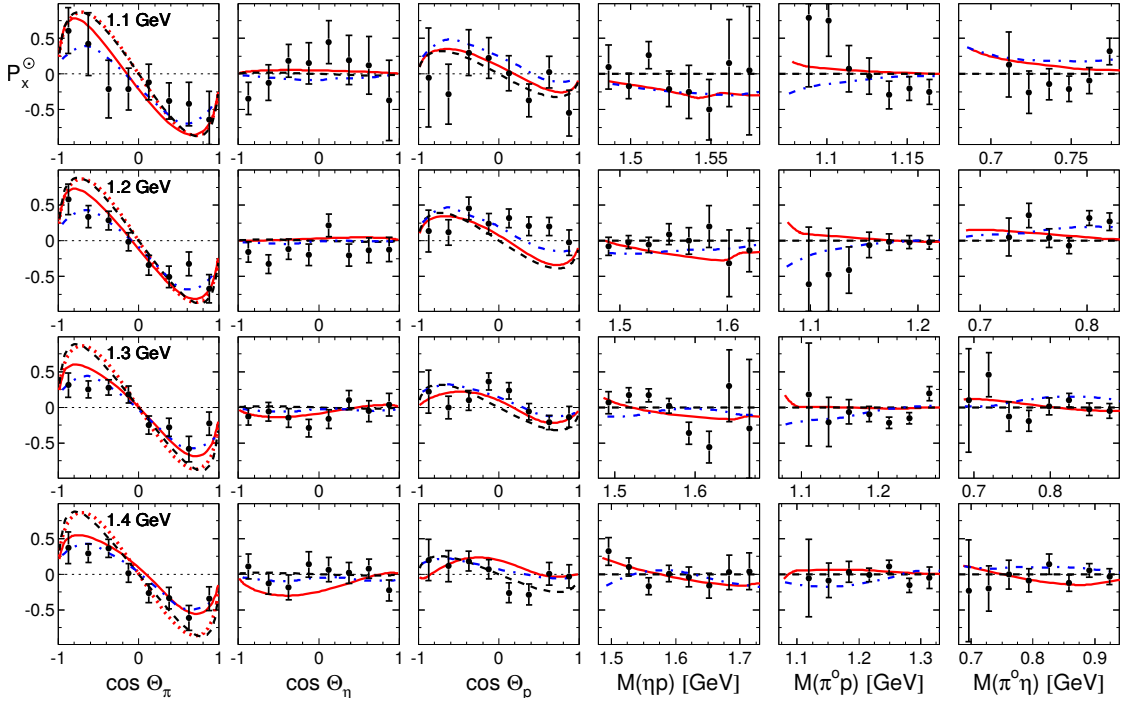


Figure 1.12.: Beam-target asymmetry P_x^\odot as function of the azimuthal angles of the final state particles and as function of the final state two-body invariant masses. The solid red lines show model predictions from [20], the dashed lines are predictions, that only include the D_{33} partial wave. The red dashed line show a parametrization, that in addition treats the helicity amplitudes $A_{3/2}$ and $A_{1/2}$ as identical. Figure taken from [23].

The beam-helicity asymmetry I^\odot was investigated in [35]. Again, the data were compared to model predictions from [20]. The aim was to investigate the role of positive parity resonances that would manifest in the asymmetry via interference with the dominant D_{33} partial wave.

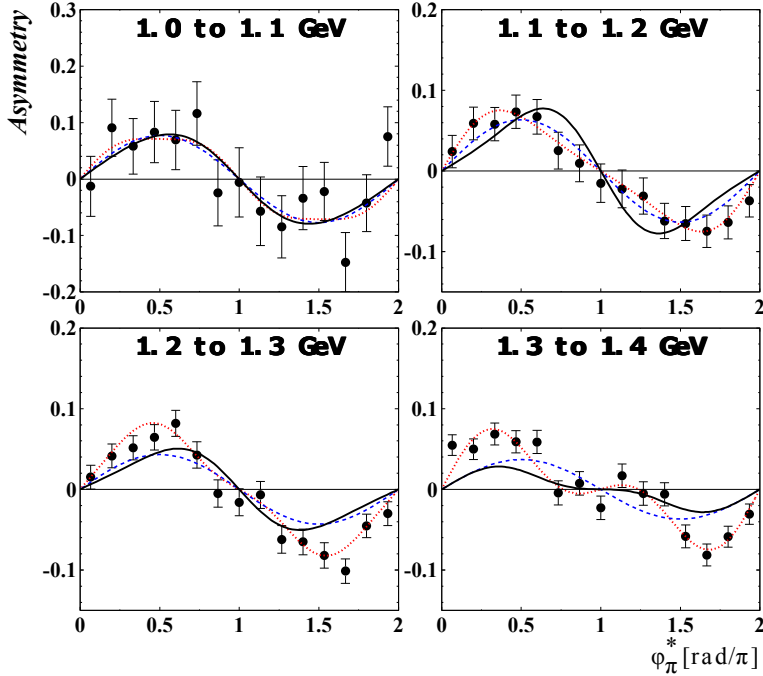


Figure 1.13.: Beam-helicity asymmetry I^\odot as function of the angle ϕ between the reaction and production plane (see Fig. 5.74). The dotted line shows a Fourier expansion, the solid line shows a prediction based on the full model of [20], the dashed line shows a prediction based solely on the D_{33} amplitude. Figure taken from [35].

Further indications of the importance of the D_{33} are given in [24]

In summary, it is well established that the D_{33} partial wave plays a dominant role in $\eta\pi^0$ photoproduction on free protons. In the threshold region it is populated via the $\Delta(1700)3/2^-$ and at higher energies probably via the $\Delta(1940)3/2^-$.

1.6. Motivation

Photoproduction of meson pairs gained increasing interest in the past years because it allows to examine cascade decays of the form $R^* \rightarrow R + m_1 \rightarrow N + m_1 + m_2$, where R^* is a high energetic resonance, R is a resonance with less energy than R^* , $m_{1,2}$ are mesons and N denotes a nucleon. These reactions allow the investigation of resonances that couple only weakly to the nucleon ground state.

In this work the photoproduction of $\eta\pi$ pairs was investigated. The isoscalar nature of the η meson allows only transitions of the form $\Delta^* \rightarrow \Delta^{(*)}\eta$ or $N^* \rightarrow N^{(*)}\eta$ as shown in Fig. 1.5.

This allows two forms of cascade decays:

$$\gamma N \rightarrow N^* \rightarrow \pi N^* \rightarrow \pi\eta N \quad (1.35)$$

and

$$\gamma N \rightarrow \Delta^* \rightarrow \eta\Delta \rightarrow \pi\eta N. \quad (1.36)$$

These are shown as diagrams (g) and (h) in Fig. 1.7. The background diagrams (a)-(f) have been found to be negligible (see section 1.5). In case of $\eta\pi^0$ production on free protons (see next section) it was found, that the reaction takes predominantly place via decays of the form 1.36. Near the threshold region the dominant contributions come from the $\Delta(1700)3/2^-$ and at higher energies from the $\Delta(1940)3/2^-$.

The isospin amplitudes for $\eta\pi$ photoproduction can easily be deduced from equation 1.25, because due to the isoscalar η meson they are equal to the amplitudes for single π production:

$$\begin{aligned} A(\gamma p \rightarrow \eta\pi^0 p) &= +\sqrt{\frac{2}{3}}A^{V3} + \sqrt{\frac{1}{3}}(A^{IV} - A^{IS}) \\ A(\gamma n \rightarrow \eta\pi^0 n) &= +\sqrt{\frac{2}{3}}A^{V3} + \sqrt{\frac{1}{3}}(A^{IV} + A^{IS}) \\ A(\gamma p \rightarrow \eta\pi^+ n) &= -\sqrt{\frac{1}{3}}A^{V3} + \sqrt{\frac{2}{3}}(A^{IV} - A^{IS}) \\ A(\gamma n \rightarrow \eta\pi^- p) &= +\sqrt{\frac{1}{3}}A^{V3} - \sqrt{\frac{2}{3}}(A^{IV} + A^{IS}) \end{aligned} \quad (1.37)$$

For the excitation of Δ resonances from the nucleon ground state only the isospin changing amplitude A^{V3} can contribute, while $A^{IS} = A^{IV} = 0$. Therefore, in case of a cascade decay of the form 1.36, the total cross sections should obey the following relations:

$$\sigma(\gamma p \rightarrow \eta\pi^0 p) = \sigma(\gamma n \rightarrow \eta\pi^0 n) = 2\sigma(\gamma p \rightarrow \eta\pi^+ n) = 2\sigma(\gamma n \rightarrow \eta\pi^- n). \quad (1.38)$$

One of the aims of this work was to extract the cross sections of eq. 1.37 to investigate the isospin structure of $\eta\pi$ production.

2. Experimental Setup

This chapter will give a summary of the components used in the experimental setup that was used to obtain the data analyzed in this work. Figure 2.1 shows a schematic view of this setup. The primary electron beam from the MAMI accelerator [36] [37] enters from the left-hand side, where it impinges on a radiator. There, the electrons produce photons via bremsstrahlung. The scattered electrons are then deflected in the magnetic field of the Glasgow tagger [38], [39], where they are energy tagged to reconstruct the energy of the bremsstrahlung photons. These photons are collimated and hit the target situated in the center of the Crystal Ball detector [40], [41], [42]. For the identification of charged particles in the CB, the target is surrounded by the Particle Identification Detector (PID, [40], [43]). The Two Armed Photon Spectrometer (TAPS, [44], [45]) is used as a forward wall. For the identification of charged particles in TAPS each individual element is equipped with a thin veto detector [46].

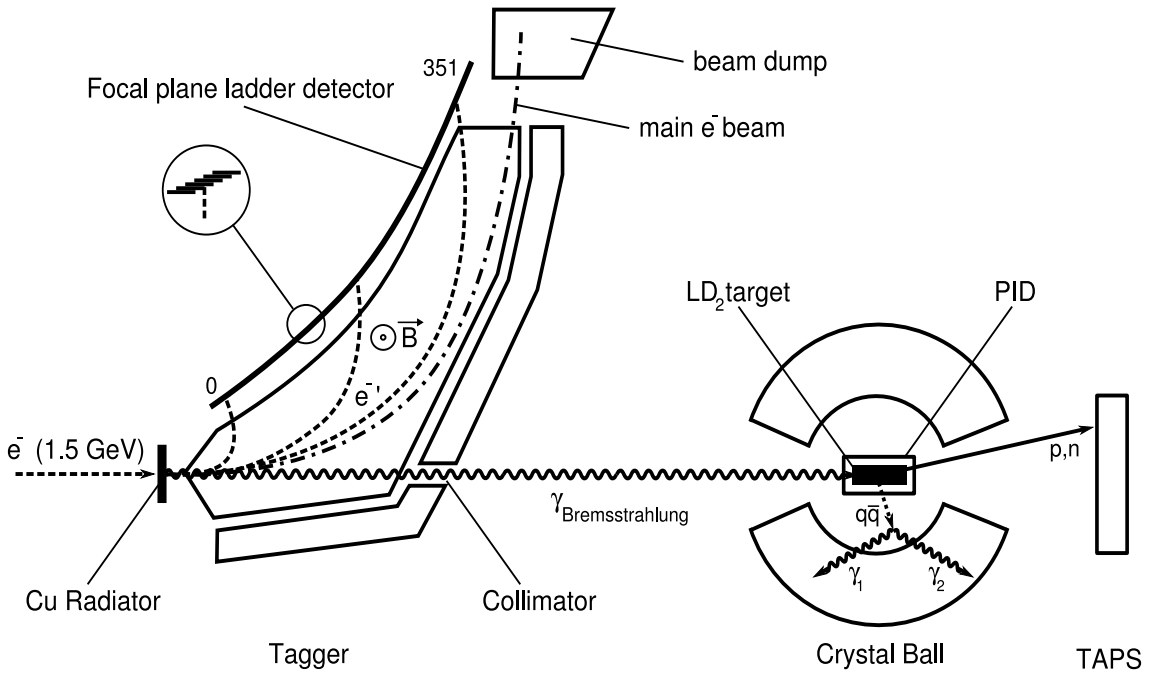


Figure 2.1.: Schematic overview over the experimental Setup. Figure taken from [47].

2.1. MAMI

The MAinzer Microtron (MAMI) [36], [37] is an electron accelerator facility, that consists of 4 individual microtrons. It can produce polarized and unpolarized electron beams up to an energy of 1.6 GeV. Though the electrons are accelerated in bunches, the interval between each bunch is small enough to be seen by the detectors as a continuous wave. Unpolarized electrons are produced by a thermionic electron gun, polarized beams are produced with circularly polarized laser-light that strikes a semiconductor crystal (GaAsP), which generates linearly polarized photoelectrons [48]. Polarization-rates reach up to 85%. Subsequently, the electron beams are preaccelerated to 611 keV and directed into the injector linear accelerator (LINAC) which brings them to an energy of 3.97 MeV. From the LINAC they are injected into the first RaceTrack Microtron (RTM) to reach 14.86 MeV of energy.

RTMs consist of one LINAC and in each stage of 2 dipole magnets with homogeneous fields. The magnets are used to bend the electron trajectories 180° on both sides of the system, so they can be fed into the LINAC again. Each of these turn adds a constant amount of energy to the electrons and thus increases the radii in the magnetic fields. The electrons are extracted, when they reach the outermost trajectory which corresponds to the maximum energy of the respective RTM.

Two additional RTMs continue to accelerate the beam to 180 MeV and then to 855 MeV, which is the maximum energy of MAMI-B [49].

In 2006 the latest upgrade to MAMI was installed, to reach energies up to 1.6 GeV. Due to space limitations it was not possible to build a fourth RTM, because the needed dipole magnets would have had to be about 6 times larger than the magnets of RTM3. To circumvent this, the Harmonic Double-Sided Microtron (HDSM) was built [37]. The HDSM utilizes 4 magnets in the corners of the apparatus, each deflecting the electrons 90° . In both of the long sides of the apparatus one LINAC is installed. With this upgrade (MAMI-C), MAMI can produce high quality electron-beams, with low emittance and a maximum current of $100 \mu\text{A}$.

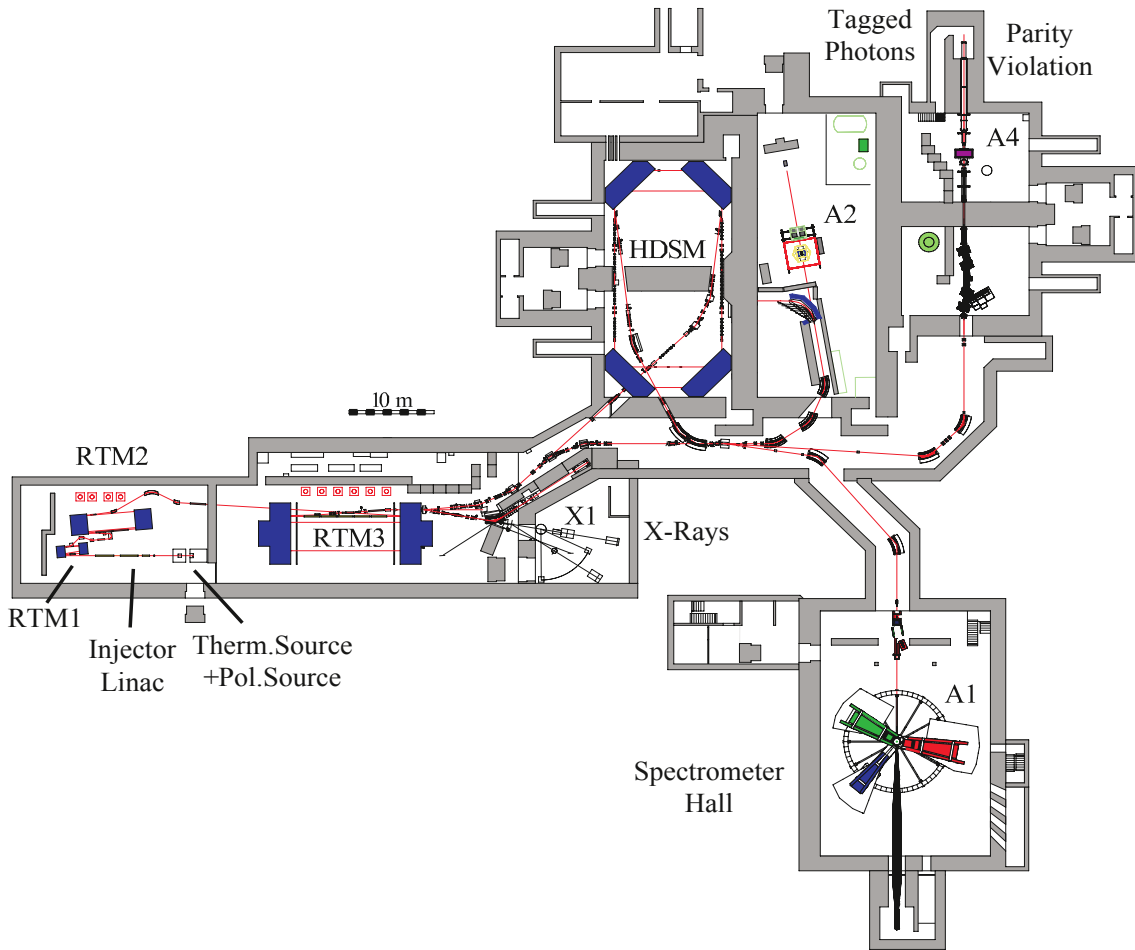


Figure 2.2.: Floorplan of the MAMI facility from [36]. The bottom left side shows the electron sources and the injector LINAC. Electrons are then accelerated in the RTMs 1-3 and the HDSM. From the HDSM the electrons were led to the A2 hall, where the detector systems used in this work are located.

Figure 2.2 shows schematically the RTM cascade at MAMI.

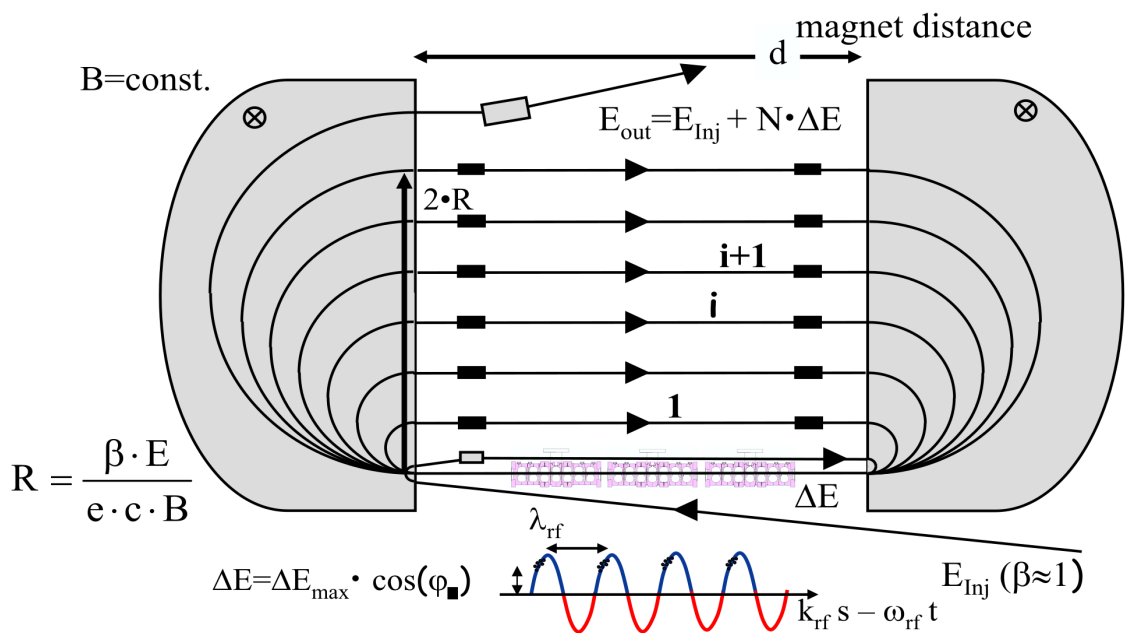


Figure 2.3.: Schematic that shows the basic functionality of a RTM. The bottom middle part shows the LINAC that is used to increase the electron energy by the amount ΔE in each turn. The shaded areas on the left and right side denote the bending magnets. Figure taken from [36].

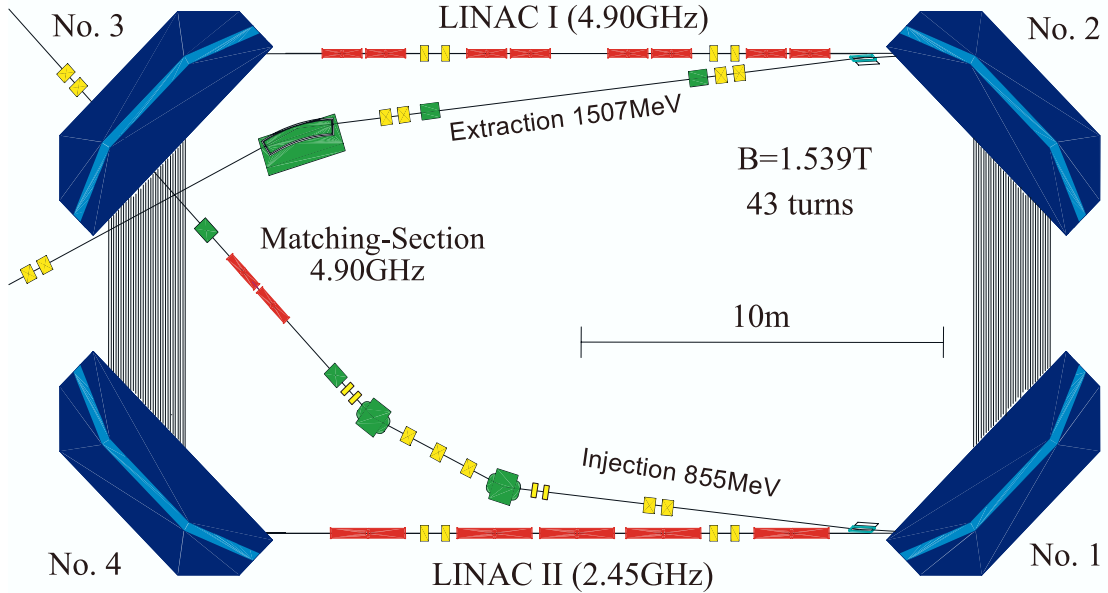


Figure 2.4.: Schematic drawing of the HDSM. Figure taken from [36].

2.2. Electron and photon beams

In the context of this work, only circularly polarized photon beams were used to produce $\eta\pi^0$ pairs. Linearly polarized photons were not used and therefore will not be discussed. A detailed discussion can be found in [50], [51].

The MAMI facility can produce unpolarized and polarized electron beams, using two different electron sources. Unpolarized electrons are produced with a simple thermionic electron gun, but the process of generating polarized electrons is more complicated.

Linearly polarized light is produced by a Titanium-Sapphire Laser. An adjustable $\lambda/4$ plate ("Pockels"-cell) is used to convert the linear polarization to circular polarization. This Pockels cell switches its optical axes if the polarity of the voltage over the cell is inverted, thus allowing to flip the helicity of the laser-light. The laser-light is then used for the optical pumping of longitudinally polarized electrons of a GaAsP (gallium arsenide phosphor) semiconductor, where the polarization of the electrons depends on the polarization of the laser-light.

After acceleration the electron beam has to be converted to a photon beam, which is achieved via incoherent bremsstrahlung in a radiator foil. If the electron beam was not polarized, the scattering in the radiator will lead to unpolarized photons, while the scattering of longitudinally polarized electrons will result in circularly polarized photons [52], [48]. To eliminate intrinsic asymmetries in the helicity of the photon beam, the

helicity was flipped with the Pockels-cell at a frequency of $\approx 1\text{Hz}$.

The degree of polarization for the photons is then given by the Olsen-Maximon formula [53]:

$$P_\gamma = P_{e^-} \frac{4x - x^2}{4 - 4x + 3x^2}, \quad (2.1)$$

where $x = E_\gamma / E_e$ is the ratio of the photon- and electron energy and P_{e^-} is the degree of polarization of the electrons.

In case of this work a $10\mu\text{m}$ copper foil, and a thin Vacoflux 50 foil, which is an iron cobalt alloy, were used. In the bremsstrahlung process, the electrons interact with the coulomb-field of nuclei and are decelerated, leading to the emission of photons. Due to the mass difference between electrons and nuclei, the kinetic energy of the recoiling nucleus can be neglected, and the photon-energy is then given by energy conservation:

$$E_\gamma = E_e - E'_e \quad (2.2)$$

where E_e is the energy of the electron before and E'_e is the energy after the bremsstrahlung process.

The cross section for incoherent bremsstrahlung in a medium with atomic number Z is given by the Bethe-Heitler formula [54], [55]:

$$d\sigma_{BH} = 4Z^2 \alpha a_0^2 \frac{dE_\gamma}{E_\gamma} \frac{E'_e}{E_0} \left[\frac{E_0}{E'_e} + \frac{E'_e}{E_0} - \frac{2}{3} \right] \left[\ln \left(\frac{2E'_e E_0}{E_\gamma} \right) - \frac{1}{2} \right] \quad (2.3)$$

where α is the electromagnetic fine structure constant and a_0 is the Bohr radius. From equation 2.3 can be seen, that the cross section has a $1/E_\gamma$ dependence.

The mean photon opening angle can be calculated by:

$$\sqrt{\langle \Theta_\gamma^2 \rangle} \simeq \frac{m_{e^-}}{E_0} \quad (2.4)$$

From equation 2.4, with an energy of 1.5 GeV follows, that the mean opening angle is 0.34mrad . This means, that most photons are emitted in forward direction with respect to the direction of the electron-beam. For a clear definition of the photon beam, a lead collimator with an opening of 4 mm was used, what resulted in a spot diameter of $\approx 1.3\text{ cm}$ on the target. The loss of photons due to the collimator can later be corrected by measuring the tagging efficiency (see section 5.13.1).

2.3. Glasgow Photon Tagger

The energy of the scattered electrons, that is needed to calculate the photon energy (eq. 2.2) was determined with the Glasgow photon tagger. The tagger uses a $\approx 1.9\text{T}$ magnetic field to deflect scattered and unscattered electrons. Unscattered electrons (that means electrons, that did not produce a photon in the radiator) are bent by $\approx 79^\circ$ and led to a shielded beam dump where also a Faraday cup is installed to measure

the electron current. Scattered electrons are deflected with different radii, according to their respective energy. For energies of 5 to 93% of the maximum energy, electrons can be detected in a ladder of 353 EJ-200 scintillators, installed in the focal plane. The scintillator bars are overlapping, thus allowing a coincidence analysis of adjacent elements. Each scintillator is 80 mm long and 2 mm thick. Widths vary from 9 to 32 mm to keep the energy coverage per element constant.

The combination of 2 overlapping scintillators to 1 logical detector results in 352 logical ladder elements, with energy resolutions of 2 to 5 MeV. Each scintillator is read out by individual Hamamatsu R1635 photomultiplier tubes (PMTs). To eliminate influence from the taggers magnetic field, the PMTs are shielded with steel plates.

A high beam intensity can saturate or even damage the scintillators. Especially the elements that register the lowest photon energies (highest electron energies) are effected by this, due to the $1/E_\gamma$ dependence on the photon energy distribution. Therefore, only the scintillators 1 (high photon energy) to 272 (low photon energy) were used. This allowed the detection of photons in an energy range from 400 MeV to 1400 MeV.

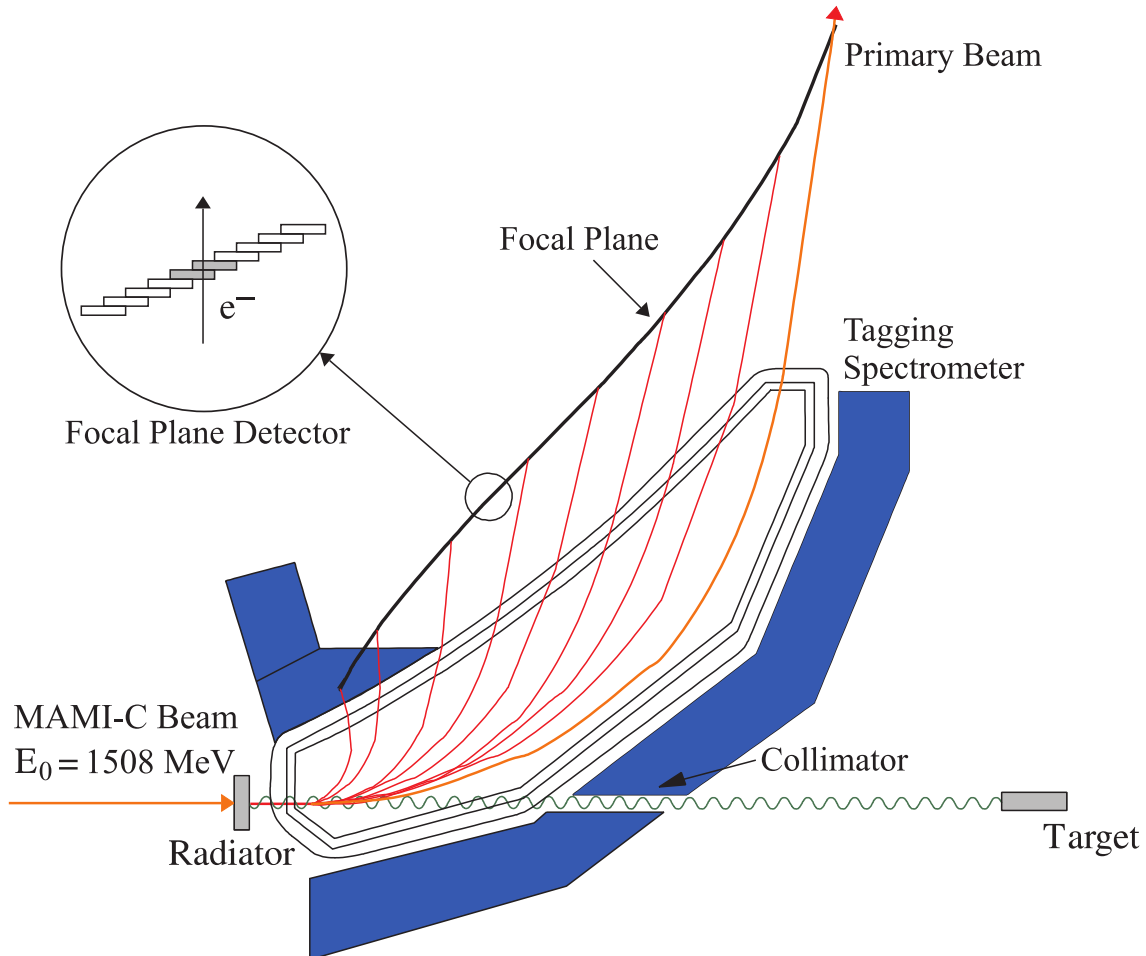


Figure 2.5.: Schematic view of the Glasgow photon tagger. From [52]

2.4. Crystal Ball

The basic geometry of CB corresponds to a regular icosahedron. This is a polyhedron with 20 faces in the form of equilateral triangles. For CB each of this major triangles is subdivided into 4 minor triangles, each containing nine triangularly shaped scintillator crystals. To account for the electron-beam entrance and exit windows, 24 crystals in forward and backward direction were removed respectively. In total, CB consists of 672 scintillators. The crystals are made from thallium doped sodium iodide ($\text{NaI}(\text{Tl})$), shaped in form of a truncated triangular pyramid with a length of 40.6 cm (see the left-hand side of Fig. 2.6). Due to the geometry of CB, 11 slightly different shapes are used. With these crystals two hemispheres with inner and outer radii of 25.3 cm and 66 cm were formed. These hemispheres are separated by 2 stainless steel plates of 1.5 mm thickness in the equatorial region as well as an adjustable air gap. The two hemispheres

can be aligned so that the center of the target cell is aligned with the geometric center of CB. Both hemispheres are evacuated to protect the hygroscopic NaI(Tl) crystals from moisture, and also for mechanical stability. Optical isolation between crystals is achieved by individual wrapping with Mylar foil and reflector paper. The readout of each crystal is performed by individual SRC L50B01 photomultipliers, optically coupled to the crystals by glass windows. This coupling causes a small signal loss due to air gaps between crystal-glass and glass-photocathode. CB covers $\approx 95\%$ of the 4π solid angle, what makes it an excellent tool for the investigation of multi photon final states. Photons deposit their energy via the production of electromagnetic showers, which typically spread over 13 adjacent crystals (the center plus 12 neighbors) in CB and contain 98% of the photon's energy. Charged pions with energies up to 240 MeV can be stopped in the crystals, the maximum energy for protons is 425 MeV and for photons it is 1 GeV.

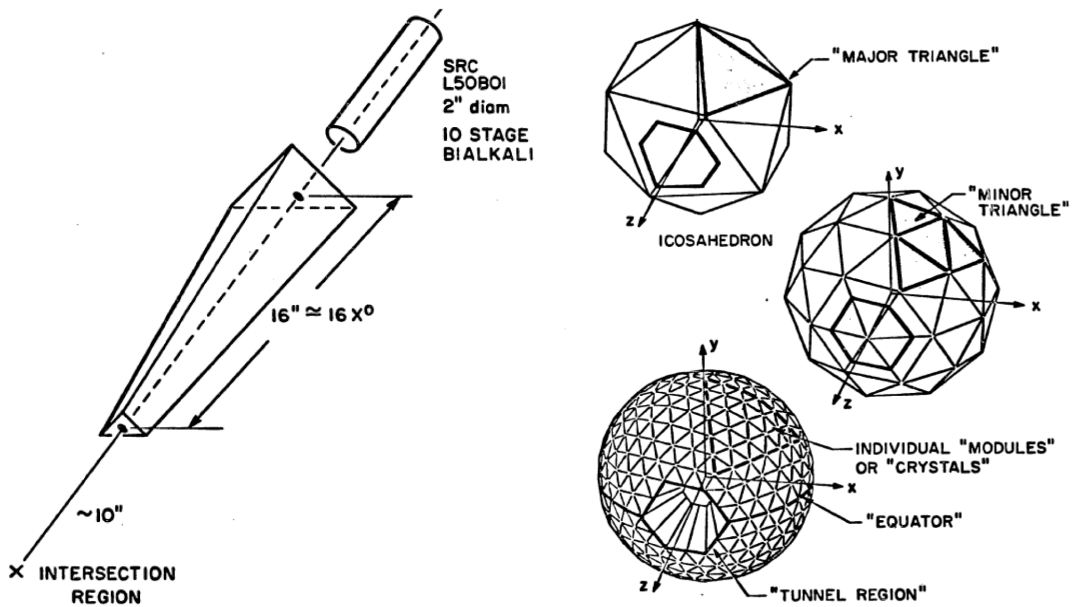


Figure 2.6.: Schematic picture of the Crystal Ball and its composition. Left-hand side: Basic geometry of a single crystal. Right-hand side: geometric composition of the CB. Figures from [56].

2.5. Particle Identification Detector

The Particle Identification Detector (PID) consists of 24 EJ-204 plastic scintillators, each 500 mm long, 15.3 mm wide, and 4 mm thick with a trapezoid cross-sectional area. They are arranged in a cylindrical shape with 10 cm diameter surrounding the target cell. The readout is performed by individual Hamamatsu H3164-10 photomultipliers coupled to their respective scintillator via a lucid light guide. For optical isolation, elements are

wrapped in aluminum foil and additionally black Tedlar (polyvinyl fluoride). To avoid additional material between the target and CB or TAPS the electronics are installed in upstream direction from the target at angles $\Theta > 160^\circ$. Installed at its nominal position the PID covers the complete solid angle of the CB. In this work, the PID was the only inner detector used. The second inner detector, a Multi Wire Proportional Chamber (MWPC) was installed, but not operational during all measurements. The PID was used as a veto detector to discriminate between charged and neutral particles. This is necessary, since CB only measures energy, but does not give information about the charge of a detected particle. In Addition, the PID can be used to separate protons, electrons and charged pions by E- ΔE measurements (see section 5.3).

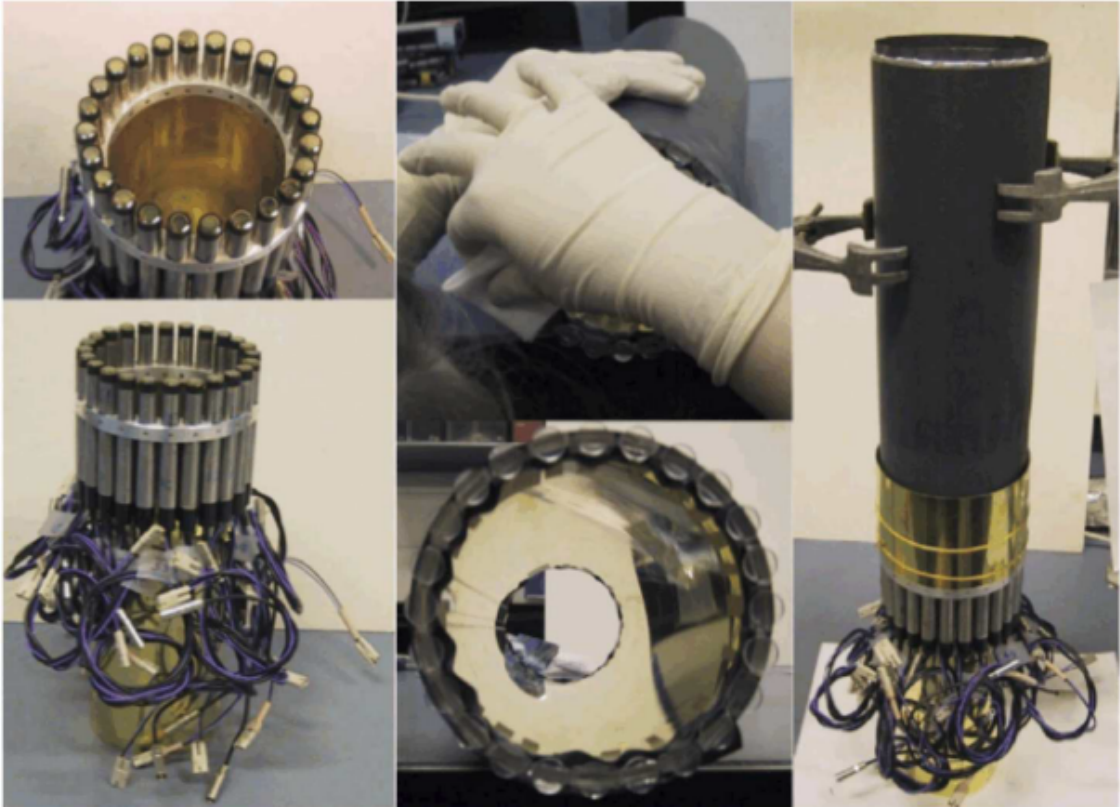


Figure 2.7.: Photos of the PID. The pictures on the left show the PMTs used for readout. The Photo on the right show the PID elements wrapped in Tedlar and connected to the PMTs. Taken from [43].

2.6. TAPS

The Two Arms Photon Spectrometer (TAPS) was installed as a forward wall, to cover the exit hole of the CB. For the December 2007 beam-time TAPS consisted of 384 BaF₂

crystals. These crystals are hexagonally shaped, 25 cm long (12 radiation lengths) and have a diameter of 5.9 cm. In case of this work, TAPS was configured in a hexagonal shape, with 11 rings and 6 sectors as shown in Fig. 2.8.

Each crystal was read out by an individual Hamamatsu R2059-01 PMT.

Optical isolation was achieved by individually wrapping the crystals in VME2000 reflector foil and additionally aluminum foil.

The maximum energy of protons to be stopped in a BaF₂ crystal is 380 MeV, the maximum energy for charged pions is 185 MeV. One feature of BaF₂ is its 2 components scintillation light, distinguished by their respective decay times. The fast component decays in $\tau = 0.9\text{ns}$, whereas the slow component decays in $\tau = 650\text{ns}$. This property can be used in a Pulse Shape Analysis (PSA) to distinguish between photons and hadrons (see section 5.5.1), since these particles deposit their energy in different ways. The fast component is also responsible for the high time resolution of TAPS (up to $\Delta\tau \approx 0.17$ ns for a single element, while the slow component is responsible for the high energy resolution.

Before the beam-times in 2009, the BaF₂ crystals in the two innermost rings were replaced with crystals made from lead tungstate (PbWO₄). The PbWO₄ crystals have a trapezoidal shape, so that one BaF₂ crystal can be replaced by 4 PbWO₄ crystals. Due to the fast decay time ($\tau \approx 10\text{ns}$) the PbWO₄ can handle the high rates at small forward angles better than the BaF₂. Also, the higher density of PbWO₄ allows the use of smaller crystals what results in better granularity and therefore higher resolution. Altogether the 18 BaF₂ crystal in the two innermost rings of TAPS were replaced by 72 PbWO₄ crystals. Each of the PbWOs is 20 cm long (22 radiation lengths) and the readout is performed by Photonics XP1911 PMTs.

Unfortunately the advantages of PbWO₄ could not be used because the elements were not yet fully functional during the measurements of this work, what resulted in an acceptance hole of TAPS in the inner two rings.

For the discrimination of charged particles, each TAPS element and each group of 4 PbWO₄ is equipped with a 5 mm thick EJ-204 plastic scintillator. Each scintillator is connected to a Hamamatsu H6568 PMT with a wavelength-shifting fiber. A more detailed discussion is given in [46].

TAPS 2009: view from target

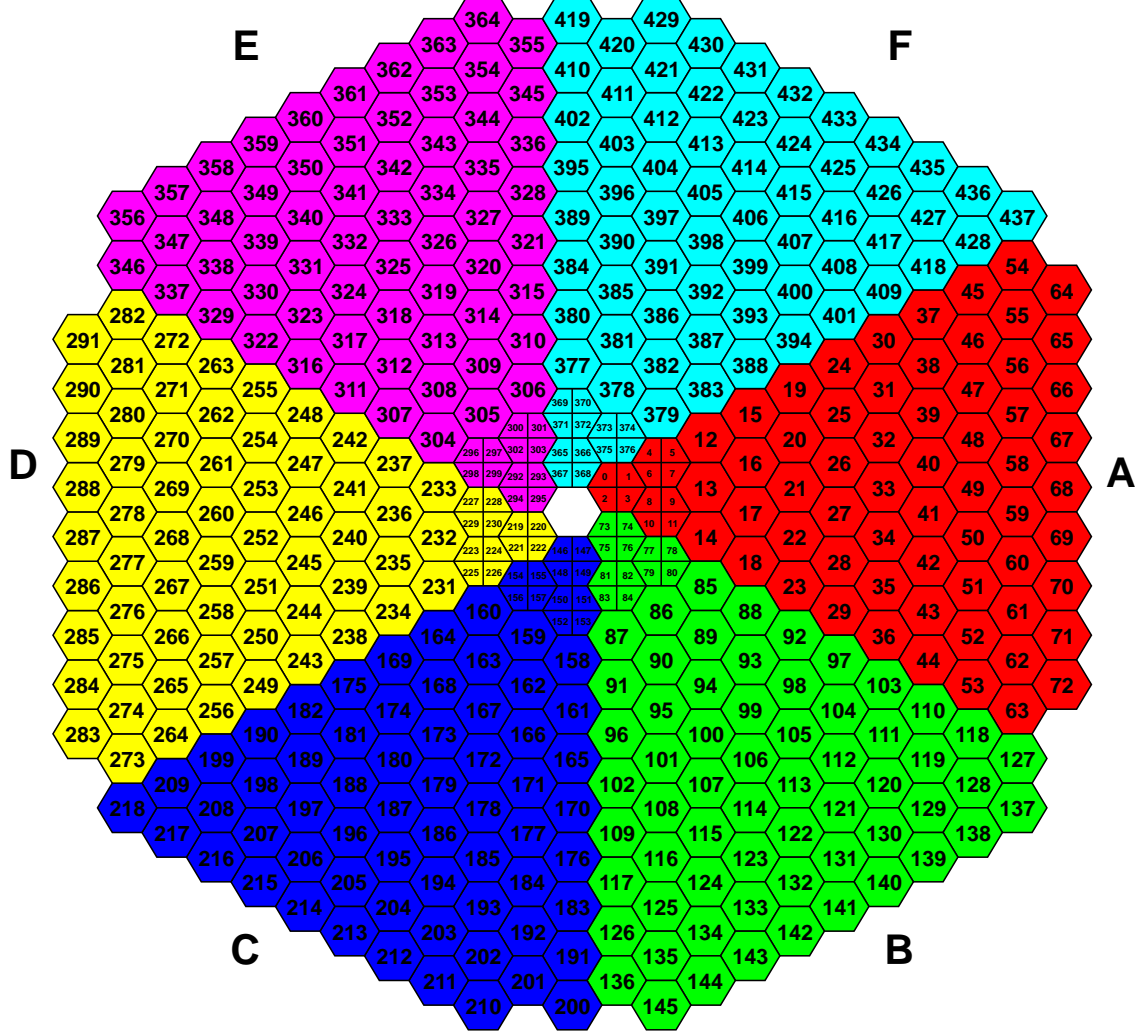


Figure 2.8.: Geometry of the TAPS detector, with the 6 logical sectors. The picture shows the version for the experiments from 2009 with the inner two rings made from PbWO₄

2.7. Targets

2.7.1. Liquid Deuterium/Hydrogen Target

The target container shown in Fig. 2.5 is a cylinder of 4 cm diameter made from 125 μm Kapton. The length of the target can be adjusted with different entrance windows adapters. For this work targets with lengths of 10 cm (lH_2 , April 2009), 4.72 cm (lD_2 December 2007 and February 2009) and 3.02 cm (lD_2 , May 2009) were used.

The targets were kept at a temperature of $T = 20\text{K}$ and a pressure of 1080 mbar.

Both values were closely monitored during the experiments and thermic isolation was achieved by wrapping the target in eight layers of super isolating foil (8 μm Mylar and 2 μm aluminum).



Figure 2.9.: Photo of the target cell for the deuterium/hydrogen targets. Taken from [57]

2.7.2. Frozen Spin Target

To determine the double polarization observable E , in addition to the polarized photon beam, also the target nucleons had to be polarized.

For an ensemble of spin J particles in a magnetic field \vec{B} , their energy levels split up in $2J+1$ sub-levels. The spacing ΔE between the sub-levels is given by:

$$\Delta E = -g m \mu B_z, \quad (2.5)$$

where g is the Lande-factor, μ is the magnetic moment and $m = -j, -j+1, \dots, j$ is the magnetic quantum number. For protons and neutrons, this leads to 2 energy levels as shown on the left side of Fig 2.10 while deuterons have 3 energy levels (right side of 2.10).

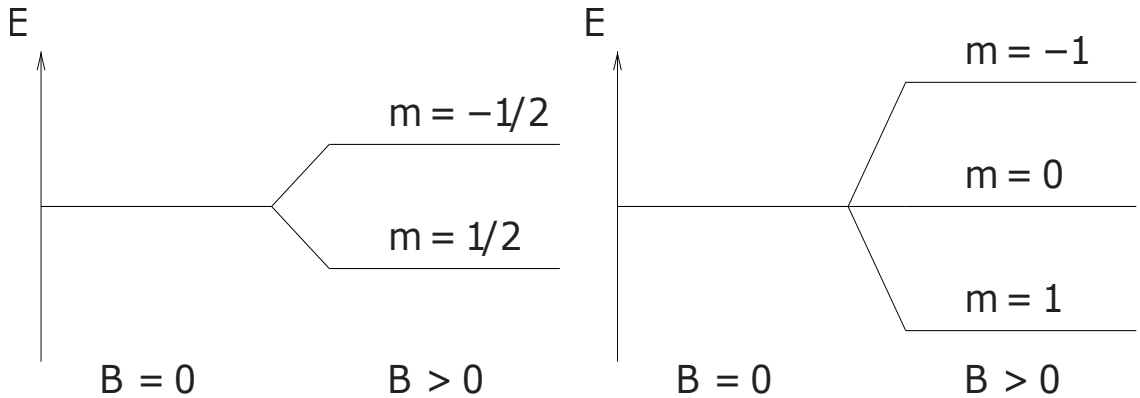


Figure 2.10.: Split-up of energy levels of particles that carry a magnetic momentum, in an external magnetic field, according to the Zeeman-effect. Taken from [58].

In thermal equilibrium the populations of these levels are Boltzmann distributed:

$$\frac{N(E + \Delta E)}{N(E)} = e^{\frac{\Delta E}{k_b T}} \quad (2.6)$$

where $k_B = 8.617 * 10^{-5} eV/K$ is the Boltzmann constant and T is the temperature. The degree of polarization P_J is then given by [58]:

$$P_J = \frac{1}{J} \frac{\sum_{m=-J}^J m e^{\frac{m\mu_B}{k_b T}}}{\sum_{m=-J}^J e^{\frac{m\mu_B}{k_b T}}} \quad (2.7)$$

Figure 2.11 show the polarization for several particles. The g-factors and magnetic moments are given in table 2.1.

	g-factor	μ
electrons	-2.0023	μ_B
protons	5.5857	μ_N
deuterons	0.8574	μ_N

Table 2.1.: g-factor and magnetic moment for several particles with Bohr magneton $\mu_B = 5.7884 \cdot 10^{-11} MeV T^{-1}$ and nuclear magneton $\mu_N = 3.1525 \cdot 10^{-14} MeV T^{-1}$. Values from [59].

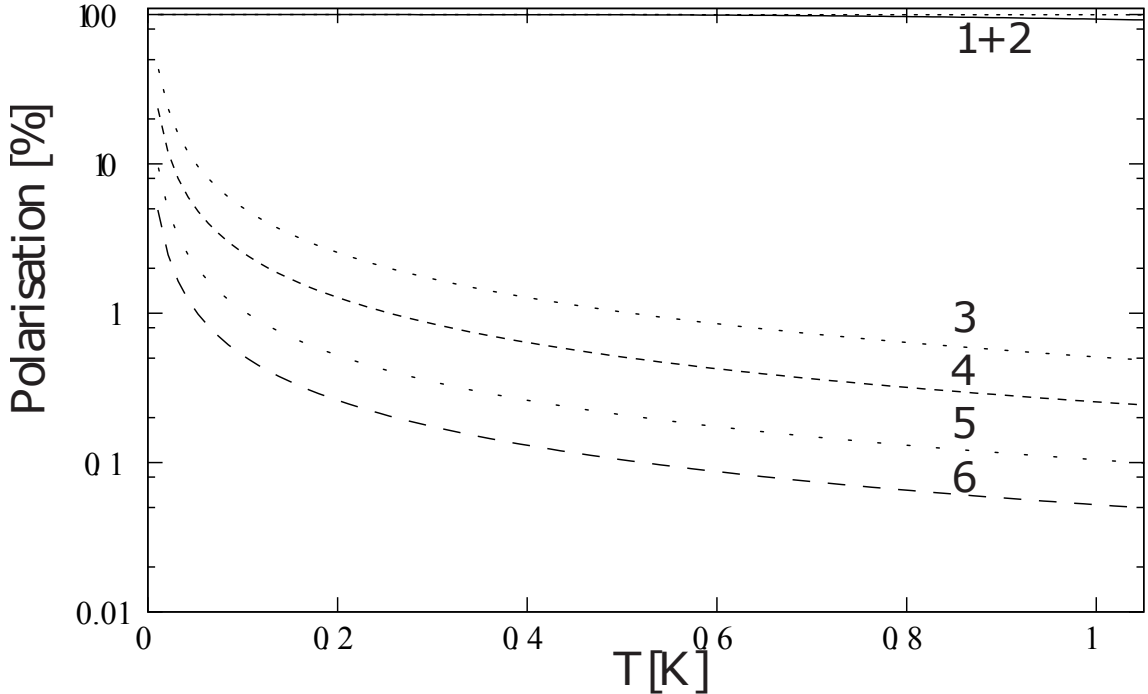


Figure 2.11.: Degree of polarization as function of temperature. Curves 1 and 2: electrons at 5 T and 2.5 T. Curves 3 and 4: protons at 5 T and 2.5 T. Curves 5 and 6: deuterons at 5 T and 2.5 T. Taken from [58].

From Fig. 2.11 one can see, that the needed conditions to polarize electrons to almost 100% are rather moderate with magnetic fields of ≈ 2 T and temperatures of about 1 K. However these conditions are in no way suited to reach high degrees of polarization of nucleons. Temperatures of about 0.1 K and field strength of about 20 T would be needed, which is technically not feasible.

Instead, the technique of dynamic nucleon polarization is used. This method uses microwave radiation to transfer the high degree of polarization of electrons to nucleons. To achieve a preferably high electron polarization, the dButanol was doped with the paramagnetic trityl radical Finland D36.

Depending on the frequency of the microwave radiation, the deuterons can then be polarized parallel or anti-parallel to an external magnetic field.

Detailed explanations of this technique are given in [58], [60].

The cooling of the target was achieved with the $^3\text{He}/^4\text{He}$ dilution refrigerator shown in Fig. 2.12. Before data taking, the target was placed in a magnetic field of ≈ 2.5 T and cooled down to ≈ 0.025 K to polarize the electrons in the trityl radicals. Then the target was irradiated with a microwave frequency to transfer the electron polarization to the deuterons. After the desired polarization was reached, the magnet was removed and a small holding coil with a field of ≈ 0.6 T was installed around the target, so it could be put inside the detector setup.



Figure 2.12.: Photograph of the ${}^3\text{He}$ / ${}^4\text{He}$ dilution refrigerator. Taken from [61].

2.7.3. Carbon Target

For background measurements a target made of carbon foam as shown in Fig. 2.13 was used. This allowed to modify the density so that the number of carbon nuclei matches the number of carbon nuclei inside the dButanol target. Therefore, a density of 0.57 g/cm³ was chosen. During the carbon runs, the experimental conditions were the same as for the dButanol target, except the temperature. To avoid damage to the carbon target, it was not cooled down.



Figure 2.13.: Photograph of the carbontarget. Taken from [62].

2.8. Measurement of the target polarization

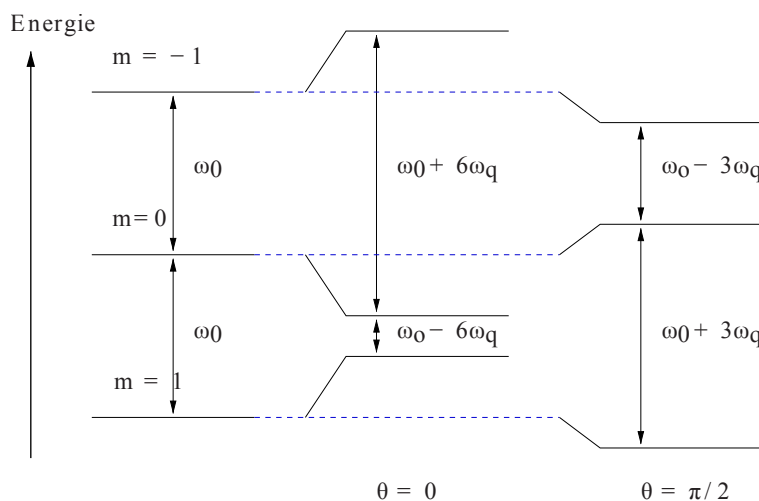


Figure 2.14.: Shift of the Zeeman levels in dButanol. Taken from [58].

The degree of target polarization is determined via Nuclear Magnetic Resonance (NMR). A coil with a few windings is installed around the target as shown on the left-hand side of Fig. 2.22. This coil acts as die inductive part of an RCL resonant circuit which operates at a resonance frequency close to the nuclear Larmor-frequency. Applying a radiofrequency near the Larmor-frequency induces a level transition with $\Delta m = \pm 1$ in a few nuclei. However, this only holds true for a pure deuterium target. Because of the chemical bindings in dButanol, there are additional fieldgradients which interact with the quadrupole moment of the deuteron. This causes shifts of the energy levels and therefore different frequencies ω_{\pm} are needed to induce level transitions with $m = \pm 1$ [58].

$$\omega_{\pm} = \omega_0 \pm 3\omega_q, \quad (2.8)$$

where ω_q describes the shift in the resonance frequency caused by the interaction of the field gradients with the deuterons' quadrupole moment. The NMR spectra in Fig. 2.15 show two peaks corresponding to the two resonance frequencies ω_{\pm} . For higher degrees of polarization, the spectra become more and more asymmetric since the different energy levels have different occupation numbers. From the occupation number of the $\Delta m = \pm 1$ levels $N_{\pm 1}$, the polarization can be deduced via:

$$P_T = \frac{r^2 - 1}{r^2 + r + 1} \quad (2.9)$$

where $r = \sqrt{N_1/N_{-1}}$.

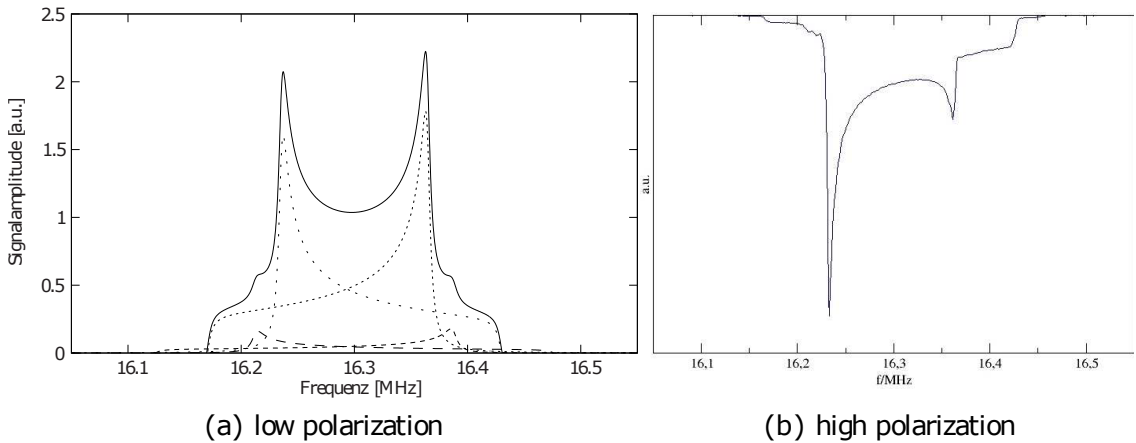


Figure 2.15.: Examples of NMR signals. The lefthand side shows contributions of carbon-deuteron bindings (dotted lines with high peaks) and oxygen-deuteron bindings (dashed lines with small peaks). The solid line corresponds to the sum of all 4 contributions. The righthand side shows a NMR signal at a polarization value of $P = 81.5\%$ and $B=2.5$ T. Taken from [63].

Using the NMR technique, the target polarization was determined before and after data taking and when the target was re-polarized or the direction of the polarization was switched. The polarization values during data taking were then calculated from the initial polarization P_i assuming an exponential decay:

$$P(t) = P_i e^{-\frac{t}{\tau}} \quad (2.10)$$

where τ is the relaxation time. Figure 2.16 shows the target polarizations for the analyzed beam-times as function of the run number.

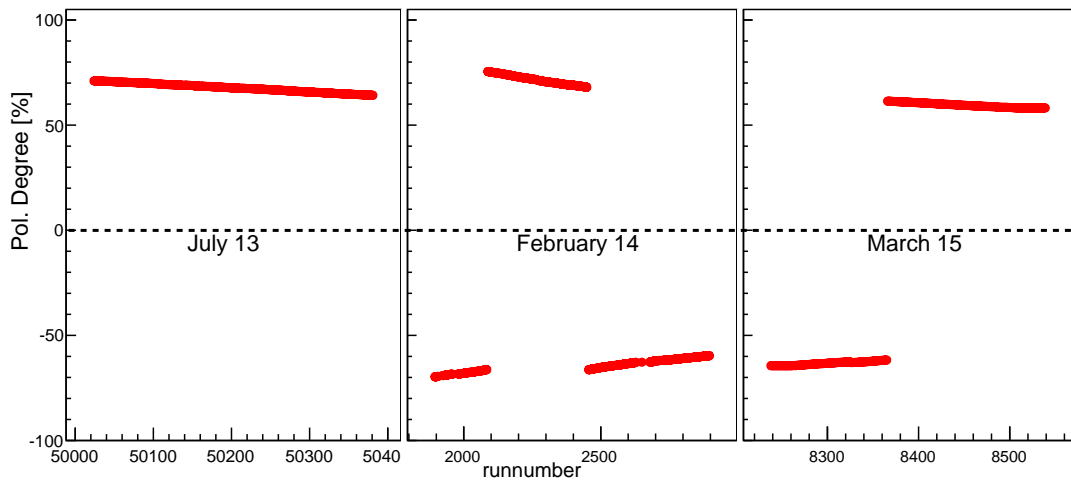


Figure 2.16.: Values of the target polarization.

2.9. Measurement of electron polarization

The electron polarization can be determined using Mott measurements at the stage of the LINAC, and during data taking using a Møller measurement. Since the polarizations values used in this work were determined only with the Mott measurement, the Møller measurement will not be described. A detailed explanation can be found in [64].

2.9.1. Mott Measurement

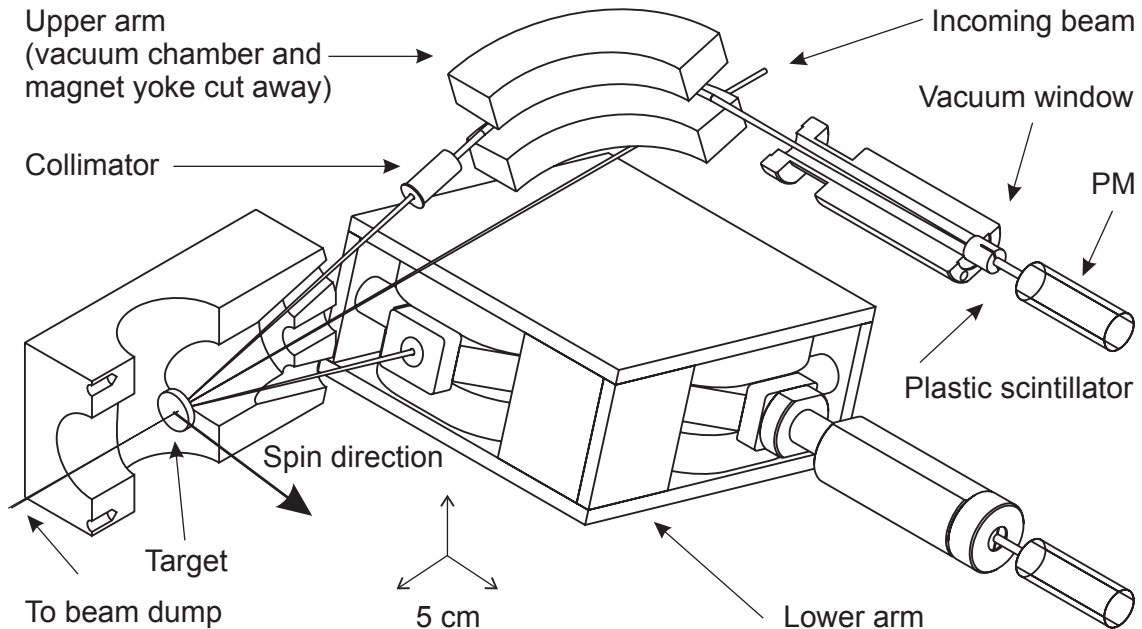


Figure 2.17.: Mott polarimeter. [65]

The Mott polarimeter used to determine the electron beam polarization is located behind the injector LINAC of MAMI where the electrons have an energy of 3.65 MeV. Dedicated runs had to be performed because the electron-beam has to be deflected into the polarimeter, therefore no data taking was possible during these runs.

Inside the polarimeter a thin, unpolarized gold foil is used to scatter the electrons. Depending on their spin, electrons will be deflected in one of two directions, where they can be detected by two counters located at fixed scattering angles of $\Theta = \pm 164^\circ$. The degree of electron polarization can then be determined from the ratio of detected electrons in both detectors:

$$A = \frac{N_1 - N_2}{N_1 + N_2} \quad (2.11)$$

To minimize systematic effects electrons with positive and negative helicity were used. The asymmetry reads then:

$$A = \frac{\sqrt{N_1^+ N_2^-} - \sqrt{N_1^- N_2^+}}{\sqrt{N_1^+ N_2^-} + \sqrt{N_1^- N_2^+}} \quad (2.12)$$

The electron polarization is then given by:

$$P = \frac{A}{S}, \quad (2.13)$$

where S is a function called analyzing power or Sherman function. It depends on the scattering angle, energy and atomic number of the target material, and can be calculated from theory.

For very high beam energies, the polarization has to be corrected by a factor of $k=1.0551$ [66].

The electron polarizations for the analyzed beam-times are shown in Fig. 2.18.

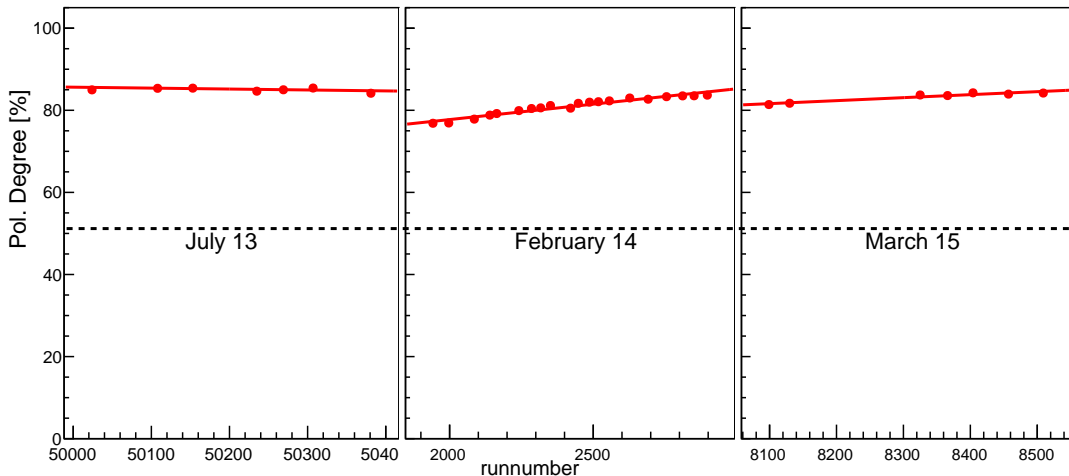


Figure 2.18.: Values of the target polarization.

2.10. Measurement of the photon polarization

If the electron degree of polarization is known, the photon polarization can be calculated with equation 2.1.

2.11. Data Acquisition

All detector elements are read out with photomultiplier tubes (PMTs). The PMTs produce an electrical signal proportional to the amount of scintillating light in each element. These analogue signals are then converted to digital values to be stored for further analysis.

2.11.1. Tagger

Precise timing information for the tagger is needed to correlate hits in the tagger elements to events in the detectors. Signals from the tagger elements above a discriminator threshold are led to a CATCH TDC (COMPASS Accumulate, Transfer and Control

Hardware Time to Digital Converter, see below). The CATCH TDCs store the time information of all electron hits in the tagger per event.

In addition, the signals are sent to a FASTBUS scaler, that counts the individual number of electrons per tagger element.

The energy deposited in the tagger elements is only needed for calibration, so it is not written to the data stream during normal data taking.

2.11.2. CB

The signals of all 672 NaI(Tl) crystals are led to an active splitter in 42 groups of 16 adjacent crystals to build the sum of the analog signals, that is used for the energy sum trigger (see below).

Then the signal is split into 2 parts. One part of the signal is delayed by 300 ns and sent to a sampling ADC, where it is integrated and also the pedestal is subtracted. The other part of the signal is led to two Leading Edge Discriminators (LEDs) where it is tested against two thresholds.

If the low threshold is reached, the signal is led to CATCH TDCs.

The outputs of the high threshold are used for the multiplicity trigger.

The signals of the PID elements are amplified and also split. One part of the signal is led to ADCs for integration to get energy information, the second part is led to CATCH TDCs to get the timing information.

Crystal Ball Trigger

Front End Electronics

J.R.M.Annand

14th September, 2004

Updated 10th November 2008

Updated 9th September 2011

- A: Uppsala 16 chan analogue fan out
- B: Uppsala 16 chan discriminator I2C control
- C: LeCroy 428F NIM analogue Fan In/Out
- D: LeCroy 4413 16 chan CAMAC discriminator
- E: LeCroy 623B NIM discriminator
- F: EG&G Ortec 474 Timing Filter Amp
- G: Mz-KPh VUCAM CAMAC prescale
- H: CAEN CF208 CAMAC CFD
- J: LeCroy 612 NIM x10 amplifier
- K: Mz-KPh NIM ECL-to-LVPECL
- L: LeCroy 4516 CAMAC logic
- M: LeCroy 429A NIM OR
- N: LeCroy 4616 ECL -> NIM

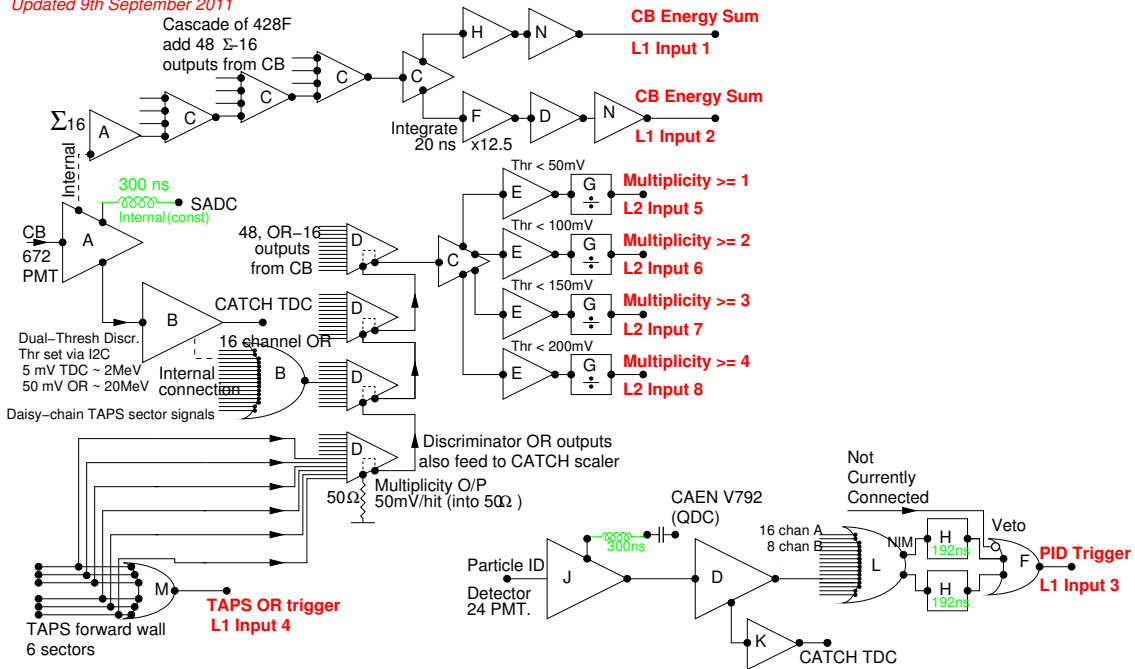


Figure 2.19.: Schematic view of the CB electronics, taken from [67]

2.11.3. TAPS

The signals of the TAPS elements are split and led to two discriminators. A Constant Fraction Discriminator (CFD) checks if a signal is above the noise level (usually around 3 MeV). Signals that pass the CFD are led to Time to Amplitude Converters (TACs) for time measurement and Charge to Digital Converters (QDCs) to get energy information. To account for the two light components of the BaF₂ crystals, the signals are integrated over a long interval of 2 μs and a short interval of 40 ns. The readout of the vetoes works similar.

2.12. Trigger

During readout of the detectors and digitalization, the data acquisition cannot record new events. To keep this dead-time low, several conditions can be implemented, that must be fulfilled by an event in order to be stored for further analysis. These trigger conditions are chosen in a way that only events of possible interest are stored for the offline analysis.

The first level trigger (L1) is based on the total deposited energy in the CB. The analog

signals of the CB crystals are summed up and tested against a threshold value by a Leading Edge Discriminator (LED). If the threshold is not reached, the event is rejected. In this work the energy sum trigger was set to around 300 MeV for all beam-times, what mainly suppresses single pion events which are produced at a very high rate and thus would occupy the data acquisition.

The second level trigger applies a condition of the multiplicity of an event. Every crystal in the CB is assigned to a logical group of 16 adjacent crystals. If one crystal in a group registers an energy above a certain threshold (\approx 30 MeV for this work), the group adds to the multiplicity.

The multiplicity trigger can also be applied to TAPS. The TAPS crystals are divided in 6 logical groups of 64 adjacent elements. If one crystal in a group registers an energy above the LED1 threshold, the group adds to the multiplicity.

The multiplicity trigger provides only an approximate number of particles. If two particles are detected in the same logical group they are counted as one. Also, if one particle deposits its energy in a cluster that is spread over multiple logical groups, it can be counted several times.

For the beam-times of December 2007 and May 2009 the multiplicity trigger was set to M2+, what requires events to have 2 multiplicity hits or more. In the beam-times of February 2009 and April 2009 the trigger was set to M3+.

Figure 2.20 shows a schematic view of the trigger electronics.

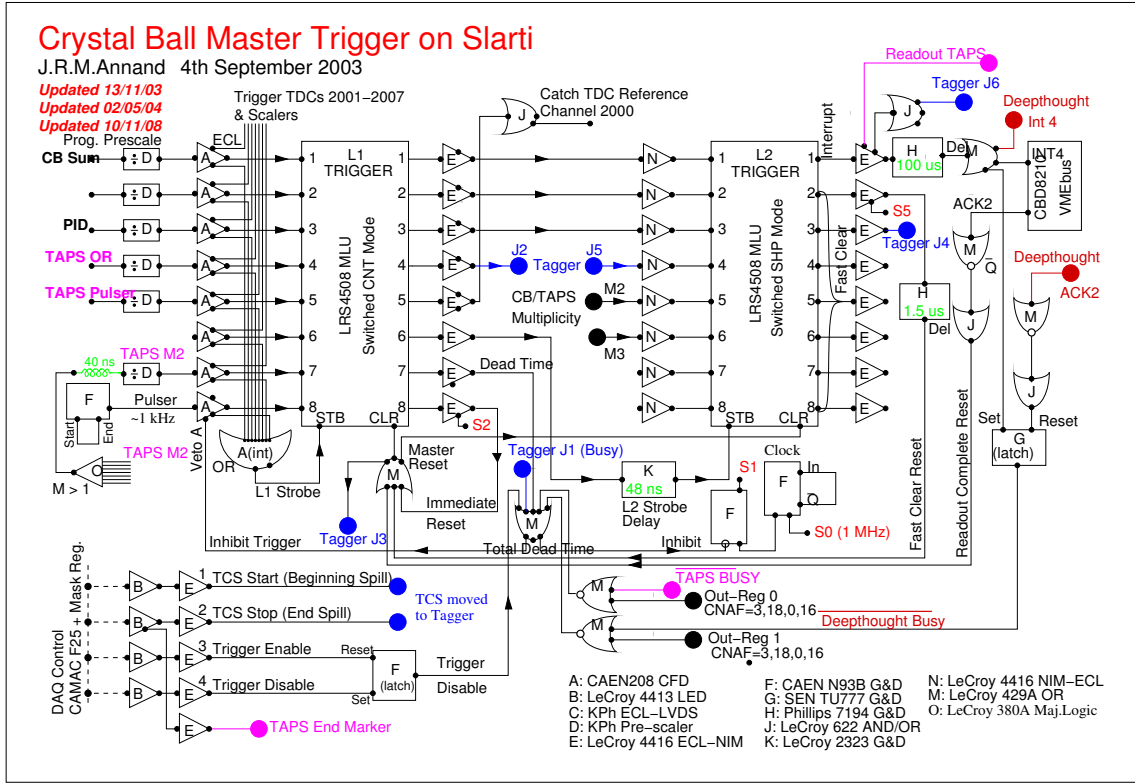


Figure 2.20.: Schematic view of the trigger electronics, taken from [67]

2.13. Software

The following sections will give a description of the different software packages, that were used to produce and analyze the raw data and Monte Carlo Simulation files. The main packages are AcquRoot, A2GEANT, OSCAR and CaLib.

2.13.1. AcquRoot

AcquRoot is a software package created for the A2 collaboration by John Annand [68]. It is written in C++ and based on the ROOT framework provided by CERN [69]. The core components of AcquRoot include ACQU, which was used to obtain the experimental data used in this work, the AcquRoot analyzer, that was used to presort the data, and the MC event generator AcquMC, which was not used in this work. Both ACQU for experimental data and the A2 simulation for simulated data produce binary files, that can be decoded with the AcquRoot analyzer. The object oriented approach of AcquRoot allows to implement each detector in individual classes, derived from base classes which provide common functionality. The configuration is done with individual ASCII files, that can easily be modified for different experimental setups. Basically also the calibration can be handled with ASCII files. For this work however a more

flexible and powerful framework called CaLib was used which uses MySQL databases for calibration [47].

A preselection of the calibrated data was performed with very rough cuts, to exclude unneeded event classes from the further analysis what resulted in a considerable speedup.

2.13.2. A2 GEANT

For Monte Carlo simulations the A2 simulation package was used [70]. It is based on GEANT4 (GEometry ANd Tracking) provided by CERN [71], [72]. GEANT4 is written in C++ and used to simulate the interaction of particles with various materials for a wide energy range. A2 GEANT contains a detailed model of the experimental setup with respect to the geometry and materials of the detector systems, as depicted in Fig. 2.21.

The setup was modeled as detailed as possible, to allow a realistic tracking of particles through the detectors. This is needed for a precise determination of the detection efficiency.

GEANT4 provides several physics lists to model particle interactions at various energies [73]. It was found in [47] that simulations that used the Bertini cascade models (QGSP_BERT) combined with the high precision neutron package (_HP) resembled the experimental data the best. For this work, GEANT was used in the version 4.9.6.

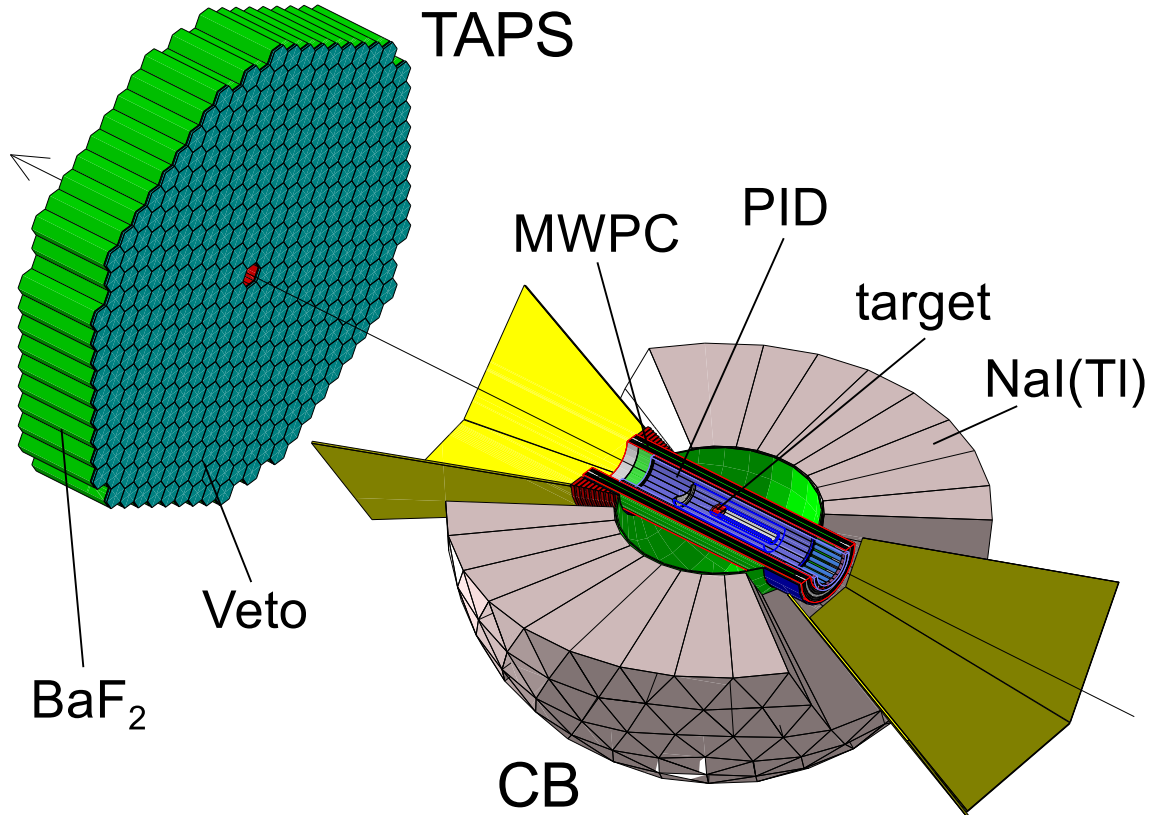


Figure 2.21.: Visualization of the experimental setup, implemented in GEANT4. The top half of CB is not shown.

2.13.3. OSCAR

OSCAR (OSCAR Simplifies Coding and Analyzing with Root) is a library of C++ classes developed by D. Werthmüller [47] which provide many additional functions to ROOT. Functionality is distributed over several modules:

- A2: basic meson reconstruction for several event classes, presort functionality
- analysis: Analysis classes for reaction channels
- graph: plotting and visualization of data
- utils: basic input/output, data format for cross sections
- MC: classes for MC event generation

OSCAR was used for the analysis of the presorted data, where each reaction was analyzed with an individual class.

2.13.4. Pluto

The MC event-generators in this work were created with PLUTO 5.41, developed by the HADES collaboration for heavy ion and hadronic reactions [74]. Pluto is written in C++ and based on ROOT. Since PLUTO did not support reactions on quasi-free nucleons carrying a Fermi momentum, a plug-in was developed by M. Dieterle [63] and L. Witthauer [75]. PLUTO can combine simple reactions to complex reaction channels and cascade decays. Particle properties like decay channels and branching ratios are stored in an internal database.

2.13.5. CaLib

The calibration library CaLib was used for calibration of the data (see chapter 4) It is written in C++ and uses the AcquRoot framework. Calibration values for the detectors and their elements are stored in MySQL databases. It also provides classes for the interaction with AcquRoot.

2.14. Beam-time Overview

The data sets analyzed in this work were taken during different beam-times, all which had slightly different conditions, thus making it necessary to calibrate and analyze each data set individually. An Overview of beam-time parameters can be seen in tables 2.2 - 2.4. More details on the different targets are given in table 5.2.

2.14.1. Hydrogen and Deuterium Data

	Dec 07	Feb 09	Apr 09	May 09
amount [GB]	424	532	795	416
electron energy [MeV]	1508	1508	1558	1558
electron current [nA]	10	5	10	4.5
tagger mag. field [T]	1.8321770	1.8281117	1.889231	1.89601
trigger mult	M2+	M3+	M2+	M2+
E-sum trigger	>300	>300	>300	>300
target material	LD ₂	LD ₂	LH ₂	LD ₂
target length [cm]	4.72 ± 0.05	4.72 ± 0.05	10 ± 0.1	4.72 ± 0.05
radiator	10 μm Cu	10 μm Cu	10 μm Cu	Møller
beamspot size on target [cm]	1.3	1.3	1.3	1.3

Table 2.2.: Parameters of the hydrogen and deuterium beam-times.

2.14.2. D-Butanol Data

	Jul 2013	Feb 2014	Mar 2015
amount [GB]	717	1300	938
electron energy [MeV]	1558	1558	1558
electron current [nA]	8.3	9-10	9
tagger mag. field [T]	1.832	1.828	1.889
trigger mult	M2+	M2+	M2+
E-sum trigger	>250	>250	>250
target material	dButanol	dButanol	dButanol
target length [cm]	2.0 ± 0.05	2.0 ± 0.05	2.0 ± 0.05
radiator	Møller	Møller	Møller
beamspot size on target [cm]	0.9	0.9	0.9

Table 2.3.: Parameters for the dButanol beam-times.

2.14.3. Carbon Data

	Feb 2014	May 2016
amount [GB]	300	400
electron energy [MeV]	1558	1558
electron current [nA]	8.3	12
tagger mag. field [T]	1.832	1.888
trigger mult	M2+	M2+
E-sum trigger	>250	>290
target material	Carbon	Carbon
target length [cm]	2.0 ± 0.05	2.0 ± 0.05
radiator	Møller	Møller
beamspot size on target [cm]	0.9	0.9

Table 2.4.: Parameters of the carbon beam-times.

2.15. Target Polarization

During the PhD-works of Dr. Manuel Dieterle [63] and Dr. Lilian Witthauer [75], some issues with the target polarization have been discovered. The observable E should be close to 1 in the threshold region of single η photoproduction, according to theoretical models and measured data. However, [75] found E to be significantly lower than 1. Extensive checks, described in the mentioned PhD theses ruled out any other probable cause besides the target polarization.

The polarization was investigated during the March 2015 beam-time in the bachelor thesis work of [76]. Therefore, two new NMR coils as shown in Fig. 2.22 were used to investigate the polarization on the surface and in the center of the target. Measurements

with these coils revealed substantial differences in the polarization values on the targets surface and center, namely lower polarization values in the center.



Figure 2.22.: NMR coils as of May 2015. Left-hand side: surface coil, right-hand side: in-beam coil. Figure taken from [77].

There are two possible causes for these different polarization values. The first one is 'beam-heating', where the photon-beam locally heats the target by producing electron-positron pairs and destroys the polarization. This possibility, however, was excluded by measurements of the polarization during the beam-time. If beam-heating was the cause of depolarization, the target center should lose its polarization faster than the outside of the target, however this was not observed.

The second possibility are inhomogeneities in the field of the polarization magnet. These would lead to a position dependent splitting of Zeeman levels and therefore position dependent Larmor-frequencies as depicted in Fig. 2.23.

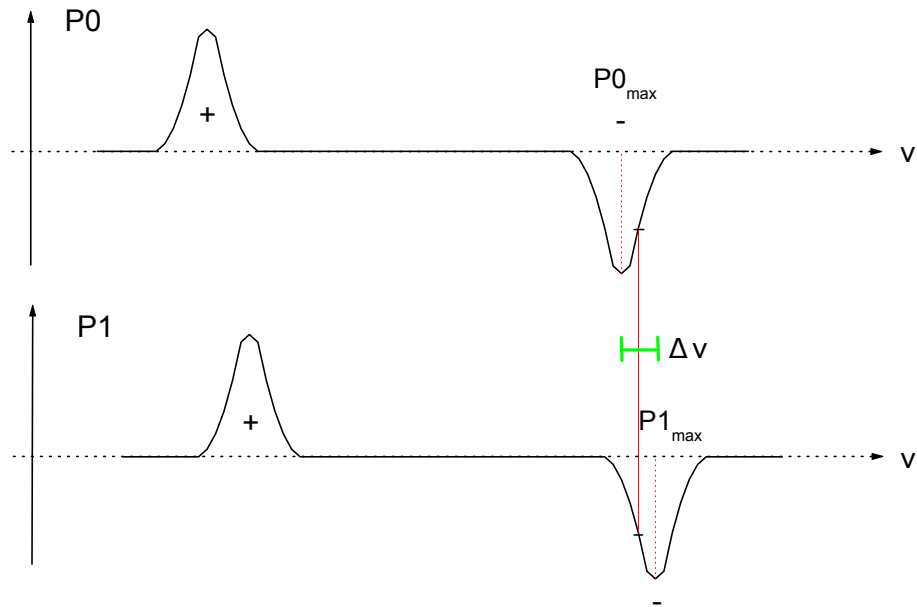


Figure 2.23.: Different frequencies are needed to reach maximum polarizations at the positions P_0 and P_1 . Figure taken from [76].

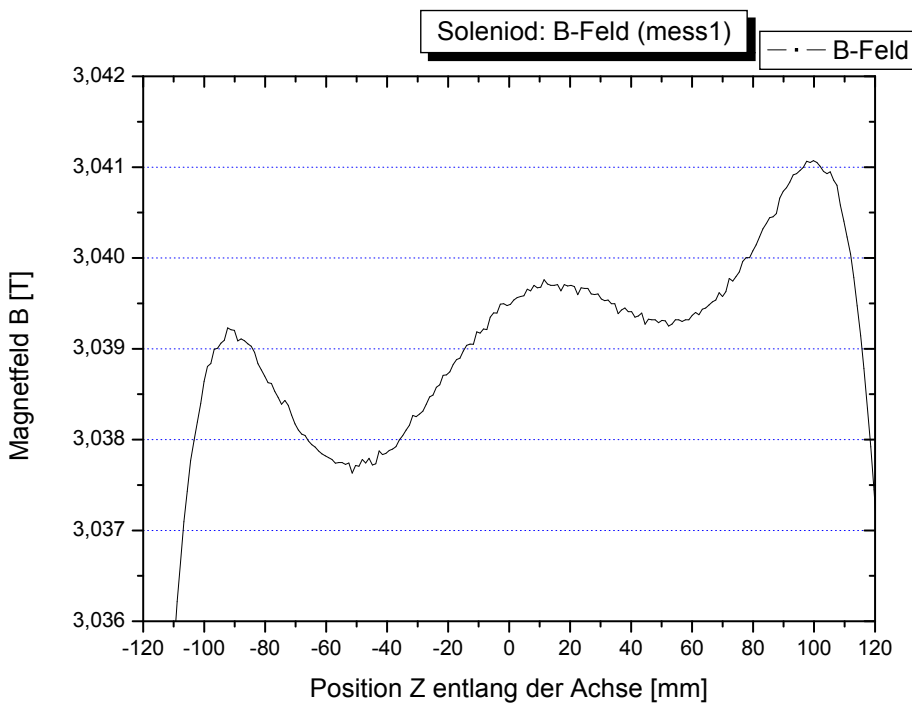


Figure 2.24.: Magnetic field inhomogeneities in z-direction. Figure taken from [78].

3. Event Reconstruction

This section describes how the signals from the detector systems are used to reconstruct events. In this step the nature of the particles belonging to an event is reconstructed as well as their energies, spatial positions and timing information. The reconstruction is straight forward if a particle deposits its complete energy in a single detector element. It is more complicated if the energy is spread over a cluster of multiple elements.

3.1. Tagger

As described in section 2.3 the tagger was used to measure the energy of scattered electrons E'_e and subsequently to determine the energy of the bremsstrahlung photon E_γ . With the energy of the MAMI electron beam E_e the relation is:

$$E_\gamma = E_e - E'_e \quad (3.1)$$

The energy E'_e can be determined from the number of the tagger element that registered an electron hit. This correlation between tagger element and energy was established by performing an energy calibration as described in section 4.1.8.

For each event, a list of tagger elements and the corresponding timings is created. The time values are stored by multi-hit TDCs. No clustering algorithm is needed for the tagger, because a coincidence condition was applied to only two neighboring elements.

3.2. Crystal Ball

The clustering in CB was done with a dedicated algorithm. In most cases, a photon detected in CB distributes 98% of its energy over a cluster of 13 crystals, formed by the center crystal and its 12 direct neighbors [40].

A list of all elements that detected a hit is created and sorted by energy. The crystal with the highest energy is treated as logical center of the cluster and the time of this crystal is set as the time of the cluster. Then the energies of the up to 12 neighboring crystals are checked. If the energy E_i of an adjacent crystal is higher than a threshold of 2 MeV, it is added to the cluster's energy. So the cluster energy $E_{cluster}$ is given by the sum of the energies E_i

$$E_{cluster} = \sum_{i=1}^N E_i, \quad (3.2)$$

where N is the number of crystals belonging to a cluster (13 in maximum). If a crystal contributes to a cluster it is removed from the list, because each crystal is only allowed to contribute to one cluster. The number of clusters per event was limited to 12, and the minimum energy per cluster was set to 20 MeV.

For all found clusters the cluster position $\vec{r}_{cluster}$ was calculated from the individual crystal positions \vec{r}_i by energy-weighting them:

$$\vec{r}_{cluster} = \frac{\sum_{i=1}^N \sqrt{E_i} \vec{r}_i}{\sum_{i=1}^N \sqrt{E_i}} \quad (3.3)$$

Once all clusters in the CB were found, they were checked for possible coincidences with the PID to distinguish between charged and neutral particles. A hit in CB was marked as charged when a hit in a PID element with a difference in azimuthal angle $\Delta\Phi < 15^\circ$ was found.

The PID delivers no information about the polar angle Θ . In theory this can lead to the misidentification of neutral particles as charged, if a neutral particle is detected in the azimuthal region covered by a PID element that was hit by a charged particle. However, an investigation using simulated data, did show no problems with this effect.

3.3. TAPS

The clustering algorithm of TAPS starts like the one of the CB with an energy ordered list of hit elements that detected an energy exceeding the CFD threshold. Again the element with the highest energy is set as the logical center of the cluster, and the time of this element is used as time of the cluster. The algorithm then checks the adjacent crystals of the center and adds their energy to the cluster energy. In contrast to CB the algorithm then continues to check the neighboring elements of clusters members until no more crystals with the needed minimum energy are found. The total cluster energy was calculated similar to eq. 3.2. The minimum cluster energy was set to 20 MeV, the maximum number of clusters per event to 8.

For the position of a cluster logarithmic weights are calculated [79]:

$$W_i = \max \left\{ 0, W_0 + \ln \left(\frac{E_i}{E_{cluster}} \right) \right\} \quad (3.4)$$

$$\vec{r}_{cluster} = \frac{\sum_{i=1}^N W_i \vec{r}_i}{\sum_{i=1}^N W_i} \quad (3.5)$$

The value of $W_0 = 5$ was determined in [45] using MC simulations.

The horizontal positioning of the TAPS elements cause particles do not hit the crystals face on, but with a skewed trajectory. Therefore, the cluster position has to be corrected

for the distance d that a particle travels inside a crystal before producing the shower [80]:

$$d = \ln \left(\frac{E_{cluster}}{E_{crit}} \right) + 1.2X_0, \quad (3.6)$$

where X_0 is the radiation length and E_{crit} is the critical energy. The values for BaF₂ are 2.05 cm and 12.78 MeV respectively.

The correction for the coordinates is then given by:

$$x' = x - x \left(\frac{s}{d} + 1 \right)^{-1} \quad (3.7)$$

$$y' = y - y \left(\frac{s}{d} + 1 \right)^{-1} \quad (3.8)$$

where s is the flight-path as shown in Fig. 3.1.

Also, because of the skewed trajectory, charged particles do not always hit the veto in front of a cluster's central element, but the veto of a different cluster member. Therefore, the vetoes of all cluster members were checked for coincidence with the central BaF₂ crystal. If a coincidence was found, the hit was marked as charged.

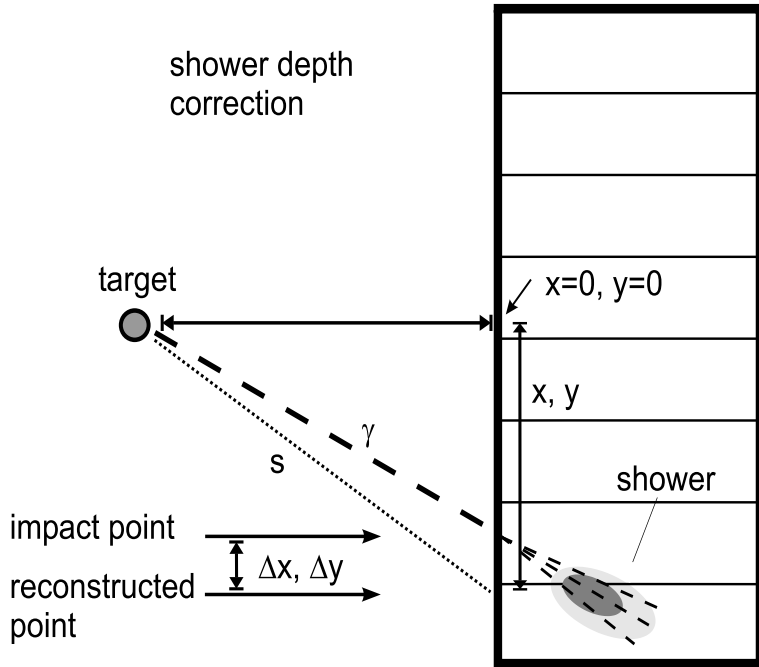


Figure 3.1.: Correction of the shower depth in TAPS. Figure taken from [81].

An overview of the typical clusters sizes of particles detected in the CB and TAPS detectors is shown in Fig. 3.2.

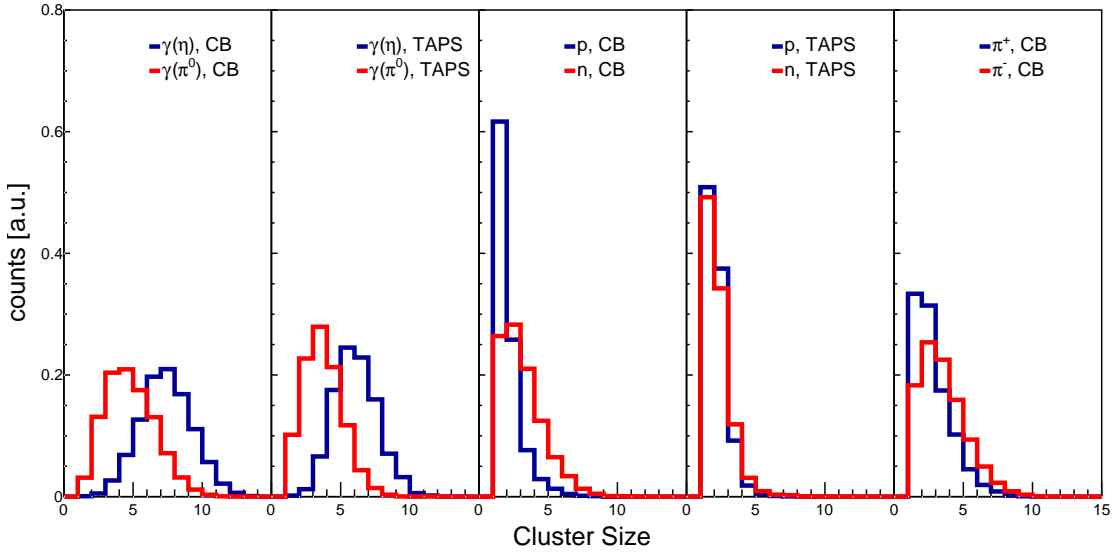


Figure 3.2.: Elements per cluster for the detected particles. From left to right: Photons from the η decay in blue, photons of the π^0 decay in red for photons in CB. The second picture shows the same for photons in TAPS. The third and fourth pictures show nucleons detected in CB and TAPS respectively. Protons are shown in blue, neutrons in red. The last picture shows charged pions detected in CB. π^+ in blue, π^- in red. Charged pions in TAPS were not considered in the analysis (see section 5.3).

High energetic photons deposit their energy mainly via electromagnetic showers. With increasing energy the showers become larger, both laterally and in depth, therefore the clusters of photons originating from a η decay, that have more energy, produce bigger clusters than photons from a π^0 decay.

Charged particles deposit their energy by ionizing the detector material. This produces small clusters. For example protons often deposit their energy in just 1 or 2 neighboring crystals.

Neutrons deposit their energy via (in)elastic scattering or via nuclear reactions that produce secondary particles. In general the deposited energy is not correlated to the initial energy of neutrons [82]. This is also visible in section 5.6, where no correlation between the Time-Of-Flight of neutrons and their deposited energy can be seen.

4. Calibration

For analysis, the raw signals from the detectors have to be converted into physical quantities. Timing information is provided by Time to Digital Converters (TDCs), the energy information is stored with Analog to Digital Converters (ADCs).

4.1. Energy Calibration

Particles depositing energy in scintillators cause the scintillators to emit light. The scintillation light is amplified in PMTs and converted into an electric charge. Charge to digital converters (QDCs) convert this charge into a digital value. In first order, the amount of charge c is proportional to the deposited energy E_{dep} :

$$E_{dep} = g \cdot (c - p), \quad (4.1)$$

where g is the conversion gain [MeV/channel] and p is the pedestal [channel]. The pedestal is the return value of the QDC when no energy was deposited in the corresponding crystal (base signal). The goal of the energy calibration is to find g and p for each detector element.

4.1.1. CB energy calibration

The energy calibration of the CB was done in several steps. Before the actual data acquisition a rough low energy calibration is performed using a $^{241}Am/^{9}Be$ source that emits monochromatic photons of 4.438 MeV and neutrons with energies between 0 and 10 MeV. This source is placed in CB and the gains of all QDCs are adjusted so that the 4.438 MeV of the emitted photons corresponded to the same ADC channel for each crystal (see Fig. 4.1). The pedestals for each QDC are then recorded and hardware thresholds are set accordingly.

This method is only valid for low energetic photons. Since the photons that are measured in an experiment can have much higher energies, a different calibration has to be performed to determine the gains. This was done using experimental data, with photons from the reaction $\gamma p \rightarrow \pi^0 p$.

For a free proton target, as in the April 2009 beam-time, the reaction is kinematically over-determined. With the energy of the incoming photon and the mass of the target nucleon, the center of mass energy can be calculated. From that, with the masses of the pion m_π and the recoil proton m_p , the energy of the pion and also of its decay photons can be calculated from kinematics [83]. A comparison of the measured energy and the corresponding calculated value allows to adjust the conversion gains until the two values agree. A detailed explanation of the procedure can be found in [84].

For heavier targets the reaction is no longer over-determined, due to Fermi motion. Instead, the peak position of the π^0 meson in the 2γ invariant mass spectrum was used. The invariant mass of two photons, γ_1 and γ_2 is given by:

$$\begin{aligned} m_{\gamma_1\gamma_2} &= \sqrt{(p_{\gamma_1} + p_{\gamma_2})^2} \\ &= \sqrt{(E_{\gamma_1} + E_{\gamma_2})^2 - (\vec{p}_{\gamma_1} + \vec{p}_{\gamma_2})^2} \\ &= \sqrt{2E_{\gamma_1}E_{\gamma_2} \cdot (1 - \cos(\Psi_{\gamma_1\gamma_2}))}, \end{aligned} \quad (4.2)$$

where $p_{\gamma_{1/2}}$ are the photon 4-vectors, $E_{\gamma_{1/2}}$ are the photon energies, $\vec{p}_{\gamma_{1/2}}$ are the corresponding photon momenta and $\Psi_{\gamma_1\gamma_2}$ is the opening angle between the two photons.

If one photon was detected in a cluster with the central element i and the second photon somewhere else, the invariant mass was calculated and filled into a histogram versus the element number i .

The resulting distribution is fitted with a sum of a Gaussian and a polynomial function, to determine the peak position. Then the gain for the crystal is adjusted to align the peak position to its nominal value of 134,9766 MeV [5]. Since the change of the gain of one crystal influences all possible clusters that contain this crystal, this procedure had to be repeated iteratively until all gains converged.

After this high energy calibration the π^0 peak is located at its nominal position for each crystal. However, the peak of the η is shifted from its correct position because the decay photons of the η usually have higher energies than the decay photons of the π^0 . This shift is caused by energy dependent shower losses, for example in crystals at the edges of CB and applied thresholds. The high energy calibration corrects these effects for photons that have typical energies from decaying pions.

The relative energy loses are smaller for higher photon energies and thus over-corrected in case of photons coming from an η decay. To account for this overcorrection a second order function is applied to the deposited energy E_{dep}

$$E' = k_0 E_{dep} + k_1 E_{dep}^2 \quad (4.3)$$

where E' is the corrected energy, and k_0 and k_1 are determined by shifting the η and π^0 peak positions in their respective invariant masses to the correct positions.

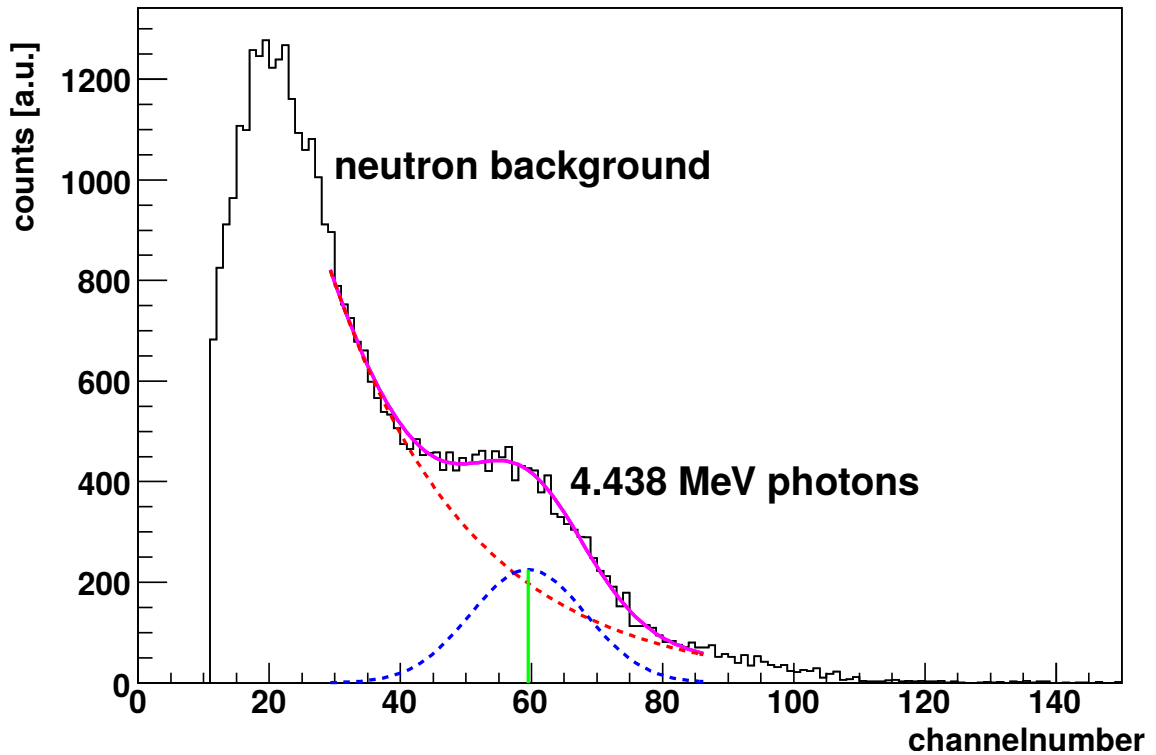


Figure 4.1.: Energy spectrum of a single NaI crystal obtained with a $^{241}Am/^{9}Be$ source (black line). Red curve: exponential background function. Dashed blue curve: Gaussian fit to the photon peak. Magenta curve: Total fitting function. Green line: Position of the photon peak. Figure adapted from [85].

4.1.2. TAPS energy calibration

As for the CB detector, the calibration of TAPS includes several steps. Again a rough calibration was performed before the data acquisition to set the hardware thresholds. For the offline analysis additional steps were necessary.

For the rough calibration cosmic muon radiation was used. Cosmic muons are minimum ionizing and deposit about 6.45 MeV/cm in the BaF₂ crystals [86]. Since all crystals in TAPS are arranged horizontally, muons pass the same distance in every crystal (5.8 cm) and hence deposit the same amount of 37.7 MeV in each crystal. Fig. 4.2 show a typical spectrum. The peak position is determined with a Gaussian fit and the pedestal position can easily be seen. From equation 4.1 the gain can be calculated.

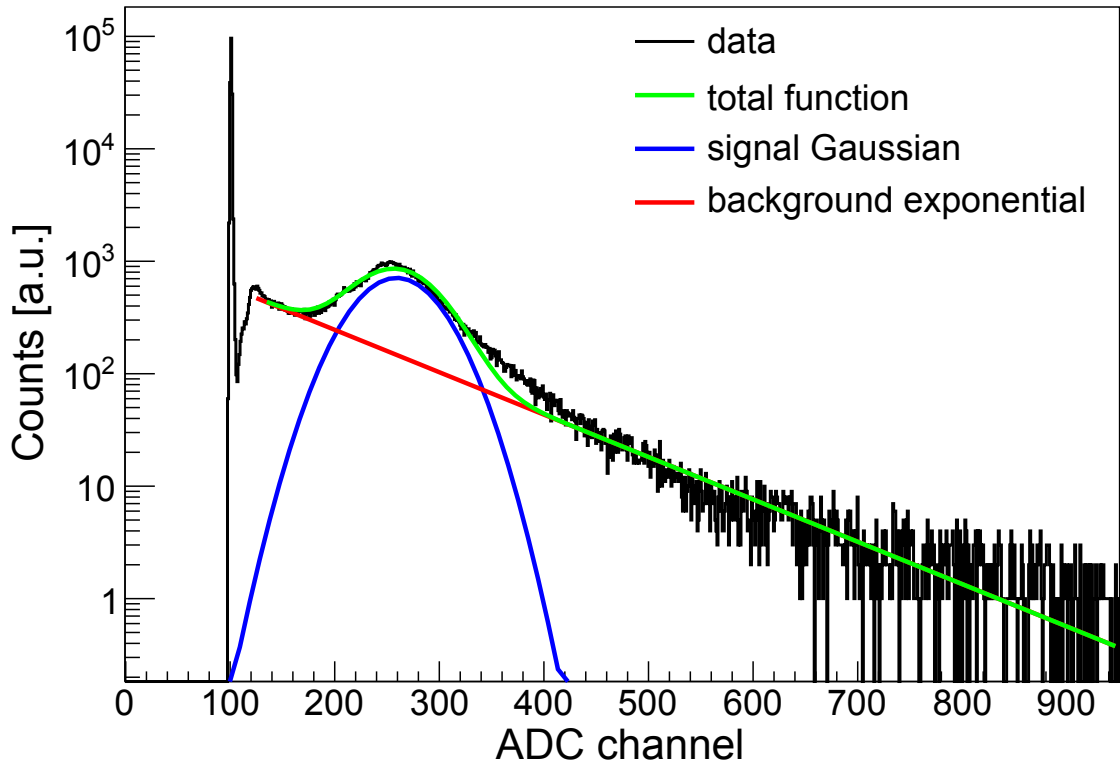


Figure 4.2.: Typical spectrum for the energy deposition of cosmic radiation in a single BaF₂ crystal. The pedestal peak around channel 100 corresponds to 0 MeV, the cosmics peak around channel 250 corresponds to 37.7 MeV. Figure taken from [47].

For the offline calibration the pedestals were determined from the raw spectra of the ADCs. For the gains the same procedure as for CB was applied with one modification. Only one photon was requested to be in TAPS, the second photon was requested to be detected in the CB. Again requesting one photon in TAPS and one in CB the quadratic energy correction was done in the same way as for CB.

The above mentioned procedure was done for the standard (long) integration gate of the BaF₂ crystals. To use the short gate information, an additional calibration step was required. First the radius r_{PSA} and the angle Φ_{PSA} were calculated:

$$r_{PSA} = \sqrt{E_s^2 + E_l^2} \quad (4.4)$$

$$\Phi_{PSA} = \arctan\left(\frac{E_s}{E_l}\right) \quad (4.5)$$

where E_s and E_l are the results of integrating the deposited energy over the short and long gate of the central element of each cluster in TAPS, respectively. When plotting r_{PSA} against Φ_{PSA} nucleons and photons form distinct band like structures, which allow

for the discrimination between these kinds of particles. The Φ_{PSA} position of the photon-band was determined for a low energy range ($0 \text{ MeV} < r_{PSA} < 50 \text{ MeV}$) and a high energy range ($500 \text{ MeV} < r_{PSA} < 600 \text{ MeV}$) by fitting Gaussians to the projections of the photon-band for both energy regions respectively. Since E_l is known, E_s can be calculated and the pedestals and gains can be adjusted in a way that $E_l = E_s$ for photons what means that photons are located at $\Phi_{PSA} = 45^\circ$ for all PSA radii.

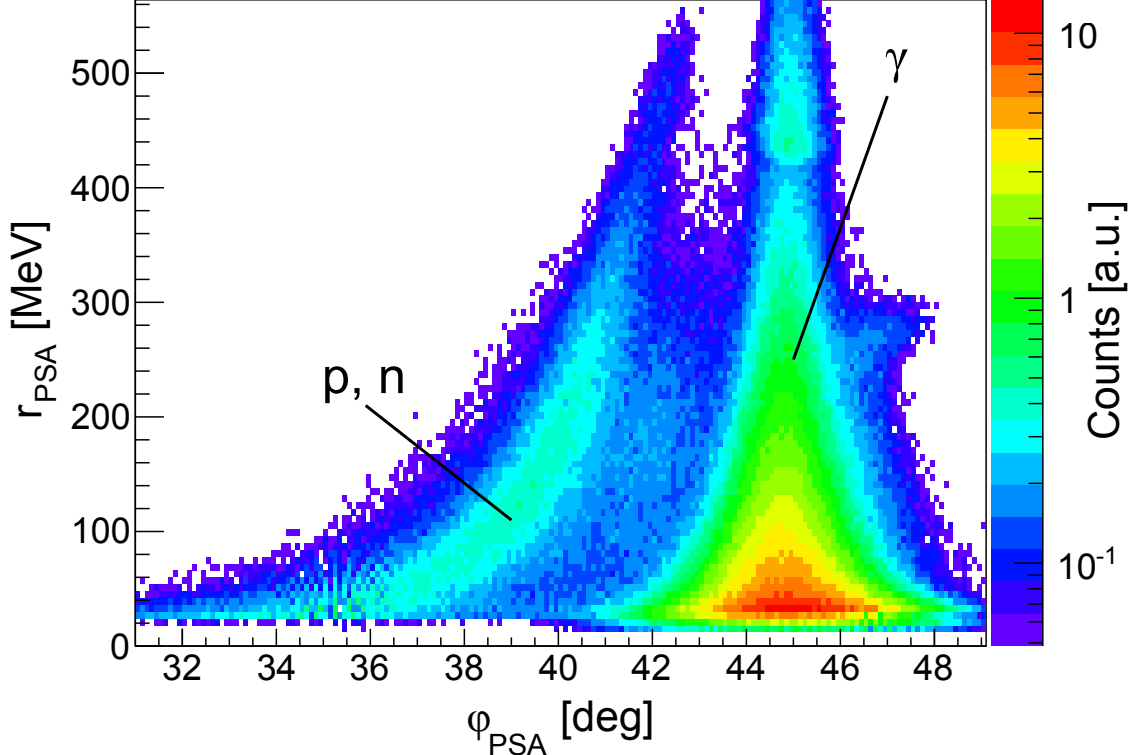


Figure 4.3.: PSA spectrum of the TAPS BaF_2 crystals. Nucleons can be seen in the banana shaped structure below 42° , photons are distributed around 45° . Taken from [47].

4.1.3. PID energy calibration

The PID energy was calibrated with the energy deposition of protons. First proton events were simulated and for every PID element, the deposited energy in this element was plotted against the energy deposited in the CB.

For experimental data the $\pi^0 p$ final state was selected and the raw ADC values of the PID were plotted against the proton energy in the PID. The energy in the PID elements could not be used since this would have required an initial calibration.

Subsequently, the histograms were projected for several bins of CB energy and the proton peak was fitted with a Gaussian to determine the peak-position. This was done for simulated and experimental data.

Then the peak positions of simulated data were plotted against experimental data and fitted with a linear function to establish the dependency between the ADC values and the corresponding energies.

The y-intercept of the fitting function then equals the pedestal value, the gain value corresponds to the slope of the function.

Since this procedure relies on the identification of charged hits in the CB (see section 3.2), the PID azimuthal calibration has to be performed before the energy calibration. A detailed explanation of the energy calibration can be found in [87].

4.1.4. PID angle calibration

For maintenance of the target, the MWPCs or the PID itself, the PID can be removed. When it is reinstalled, the correlation between PID elements and CB elements in the Φ angle has to be redetermined.

Events with exactly one hit in the PID and one cluster in CB are selected and for each PID element a histogram is filled with the Φ angle from the CB hit (see Fig. 4.4). The large coincidence peak is fitted with a combination of a Gaussian and a polynomial function for the background, to determine the peak position. Peak positions are then plotted against the PID elements and fitted with a linear function from which the exact angle of each PID element can be determined. The smaller peak in Fig. 4.4 is caused by events where a charged and a neutral particle are emitted back-to-back, and the charged particle stops in the PID. Hence, there is a difference in Φ of 180°.

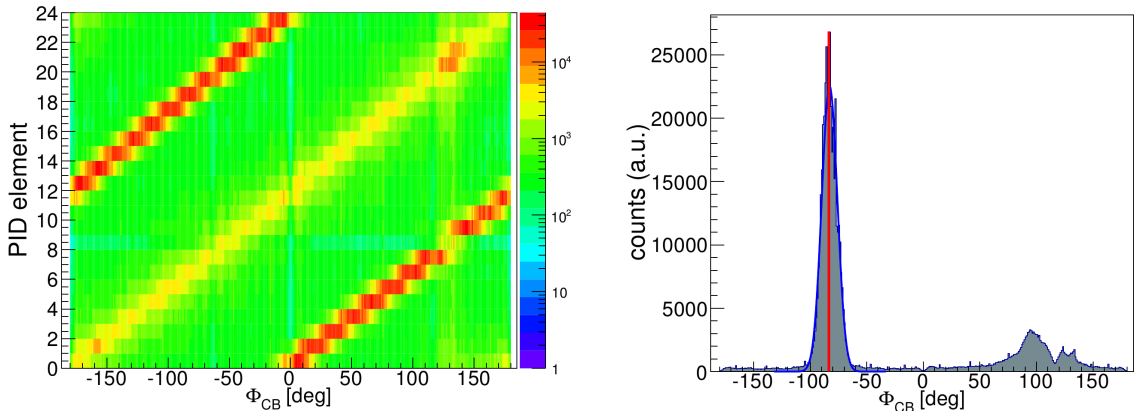


Figure 4.4.: The left-hand side shows the PID element as function of the CB Φ angle for one hit in the PID and one hit in CB. The right-hand side shows the Projection for one PID element. The prominent coincidence peak is fitted with a Gaussian to determine the exact position. Taken from [88]

4.1.5. TAPS Veto energy calibration

The pedestals for each veto were determined from experimental data using the raw ADC spectra. The gains were determined in the same way as for the PID by comparing

experimental and simulated data.

4.1.6. CB LED Calibration

As described in section 2.12 the CB LED thresholds are important for the multiplicity trigger. The information which elements exceeded the threshold is not stored in the data, therefore the values have to be reconstructed.

The CB is divided into 42 blocks of 16 neighboring elements. For each block, the element that detected the maximum energy was determined because these elements have most likely passed the thresholds. The same was done for the 6 TAPS sectors, since they were also allowed to contribute to the multiplicity.

Depending on the used multiplicity trigger conditions (in this work M2+ and M3+), the two or three elements with the highest energies of all blocks were determined and their energies were filled in histograms for the corresponding elements. The resulting spectra show a steep rise, as can be seen on the left-hand side of Fig. 4.5. The derivatives of these spectra were fitted with Gaussians to extract the exact peak position and therefore the LED value, as shown on the righthand-side of 4.5.

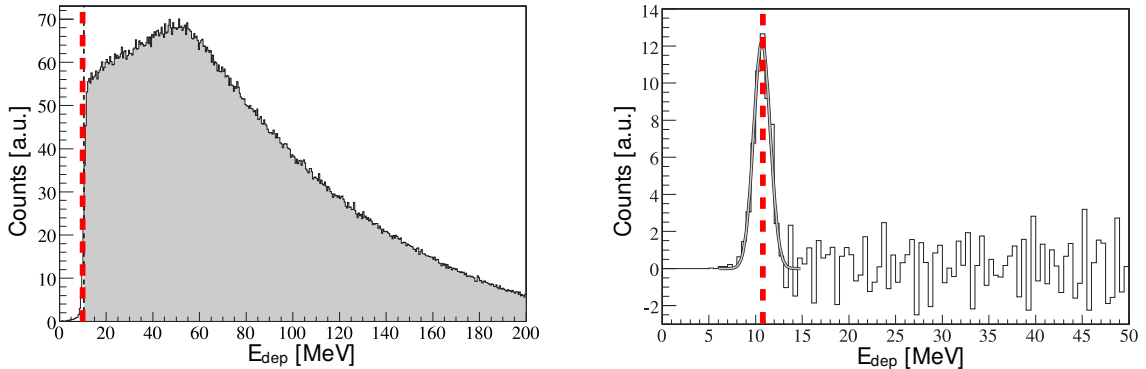


Figure 4.5.: Taken from [63].

4.1.7. TAPS LED Threshold Calibration

The values of the TAPS LED thresholds can be set for each individual element separately. For this work, the thresholds of all elements were set to around 30 MeV. The exact values were determined with the cosmics calibration. In principle the method from section 4.1.6 could also be applied to TAPS, but since the LED patterns of TAPS are stored in the data, they are used to determine the LED thresholds.

Two energy spectra were created. The first one contained the energy of all hits in the element, the second one contained only hits in the element with a coincident LED hit. In the ratio of the histograms a step-like rise can be seen, that is caused by the threshold (left side of Fig. 4.6). The derivative of the histogram was fitted with a Gaussian to determine the exact value of the threshold (right side Fig. 4.6).

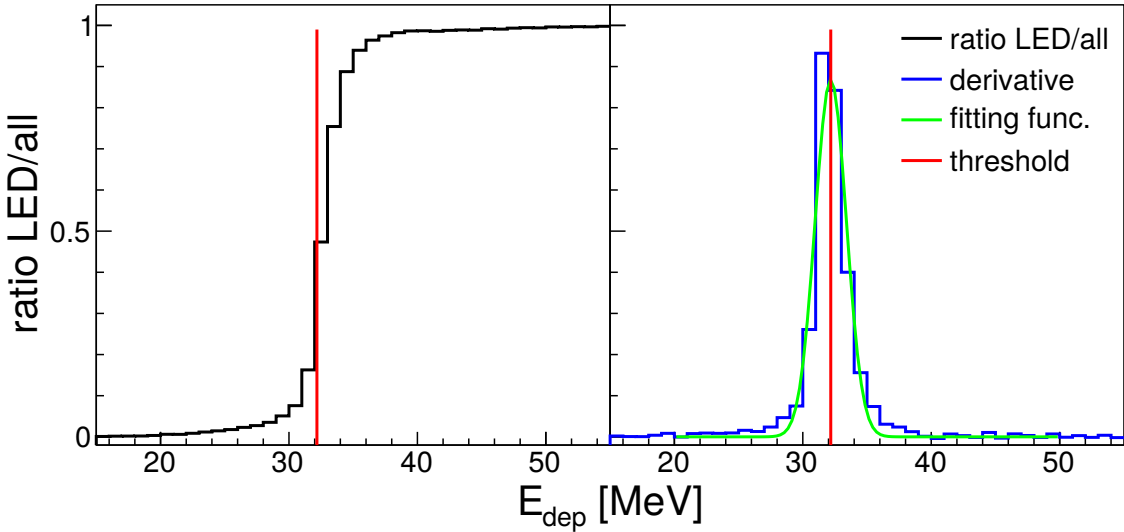


Figure 4.6.: Taps LED Calibration. The left-hand side shows the ratio of LED hits and all hits, the right-hand side shows the derivative. The red line indicates the threshold position. Taken from [47]

4.1.8. Tagger energy calibration

To calibrate the tagger, the energy of the electron beam from MAMI and the field strength of the tagger's dipole magnet have to be known. Both values are very stable during a beam-time and can be precisely monitored.

For a given magnetic field strength, several tagger calibration measurements were performed with a low intensity electron beam, that was bent into the focal plane detectors, without hitting the radiator first. Small variations of the field strength allow to steer the electron beam to a specific tagger channel. This was done for several electron beam energies and tagger channels (see Fig. 4.7). The interpolation for all tagger channels is done by the program ugcav2ua [38]. It calculates the tagger energy calibration from the known magnetic field strength, using a uniform field map, and the electron beam energy.

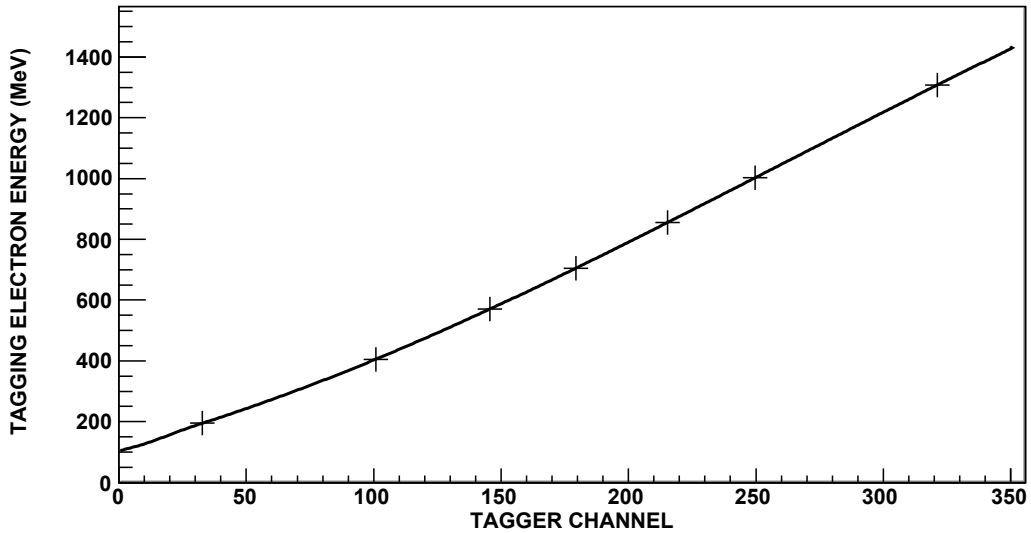


Figure 4.7.: Tagger Energy Calibration. Taken from [38].

4.2. Time Calibration

For coincidence measurements, well calibrated time information is crucial. Timing information is returned in form of a channel number by Time to Digital Converters (TDCs). In general the correlation between a channel number and the corresponding time is given by:

$$t = g(c - o), \quad (4.6)$$

where t is the time [ns], g is a conversion gain [time/channel number], c is the channel number and o [channel number] is an offset that can be chosen freely. In general o is chosen in way, that the coincidence time between any two given detector elements is 0. The goal of the time calibration is to find the values for g and o . The conversion gain is an intrinsic value for a TDC and usually supplied by the manufacturer.

4.2.1. CB time calibration

For each CATCH TDCs, the gain is a fixed value of 117 ps per channel, so only the offset values, but also some corrections had to be determined.

At first, for each cluster in the CB the time difference between the cluster members and the respective central element was calculated and filled into a histogram for every central element. The resulting distribution was fitted with a Gaussian to determine the mean values and new offsets were calculated using:

$$o'_i = o_i + \frac{\bar{t}_i}{g_i}, \quad (4.7)$$

where o_i is the old offset, \bar{t}_i is the mean time, and g_i is 0.117 ns/channel. This step was repeated until all time peaks were aligned at 0 ns.

Due to the leading edge discriminators and the slow rise time of the NaI(Tl) crystals there is a strong dependence between the time and the deposited energy as shown in Fig. 4.8. This time walk had to be corrected in order to enhance the time resolution. The correction was done by plotting the time difference between CB and tagger for all elements of CB as function of the deposited energy and fitting it with the following formula.

$$t(E) = p_0 + \frac{p_1}{(E + p_2)^{p_3}}, \quad (4.8)$$

where p_0, \dots, p_3 are fit parameters. These parameters were calculated for every crystal individually the correction was applied via:

$$t' = t - t(E). \quad (4.9)$$

After the time walk correction the coincidence time between the elements was aligned back to 0 again, like in the first step of the time calibration.

Since the tagger time was used as a reference, the corresponding calibration had to be done first.

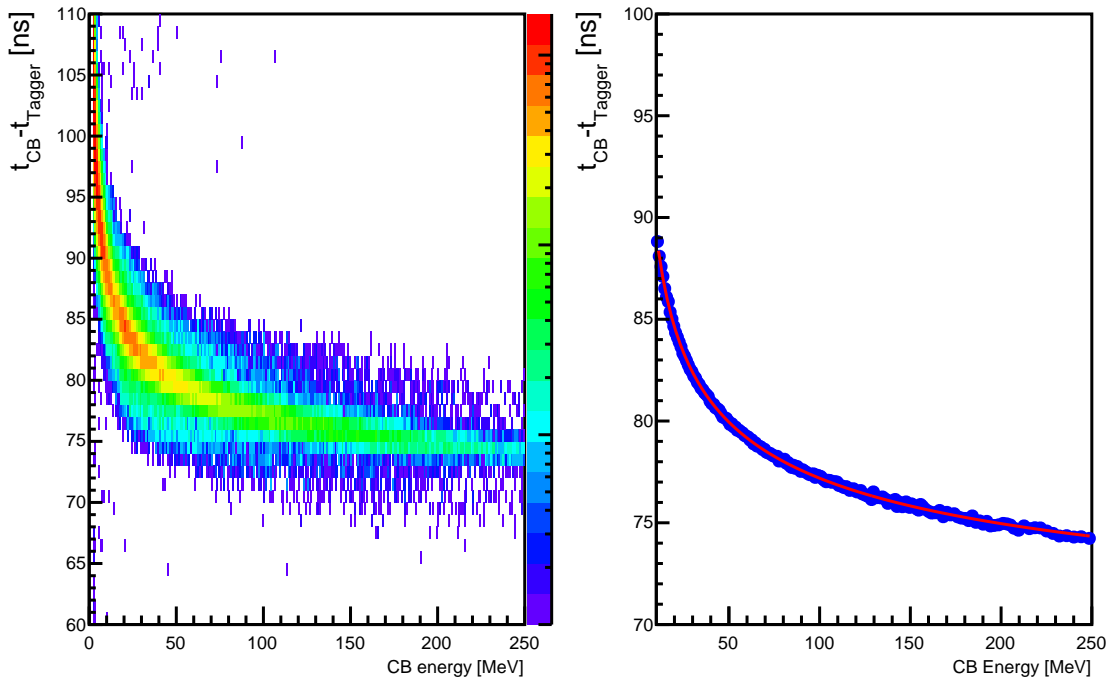


Figure 4.8.: Left-hand side: Time difference between the CB and the tagger as function of the energy deposited in CB. Right-hand side: The blue circles correspond to the peak positions of several energy intervals. The red curve is a fit to the data using eq. 4.8.

4.2.2. TAPS time calibration

The BaF₂ crystals of TAPS have an excellent intrinsic time resolution. In combination with the rather long distance from the target (≈ 1.5 m), TAPS could be used for Time-Of-Flight (TOF) analyses (see section 5.6).

A time walk correction was not necessary for TAPS because of the very fast rise-time of the BaF₂ crystals and the use of CFDs, since this kind of discriminator generally does not show time walk effects.

The TAPS gains are usually calibrated before an experiment. To do so, the common stop signal of all TAPS elements was delayed by installing different cables of known lengths and delays. Cosmics measurements were taken with and without the delay cables installed. The difference in the known delays was then plotted against the difference of the pedestal positions and fitted linearly for every crystal. The conversion gain is then given by the slope of the fitting function.

Offsets were calibrated the same way as for CB.

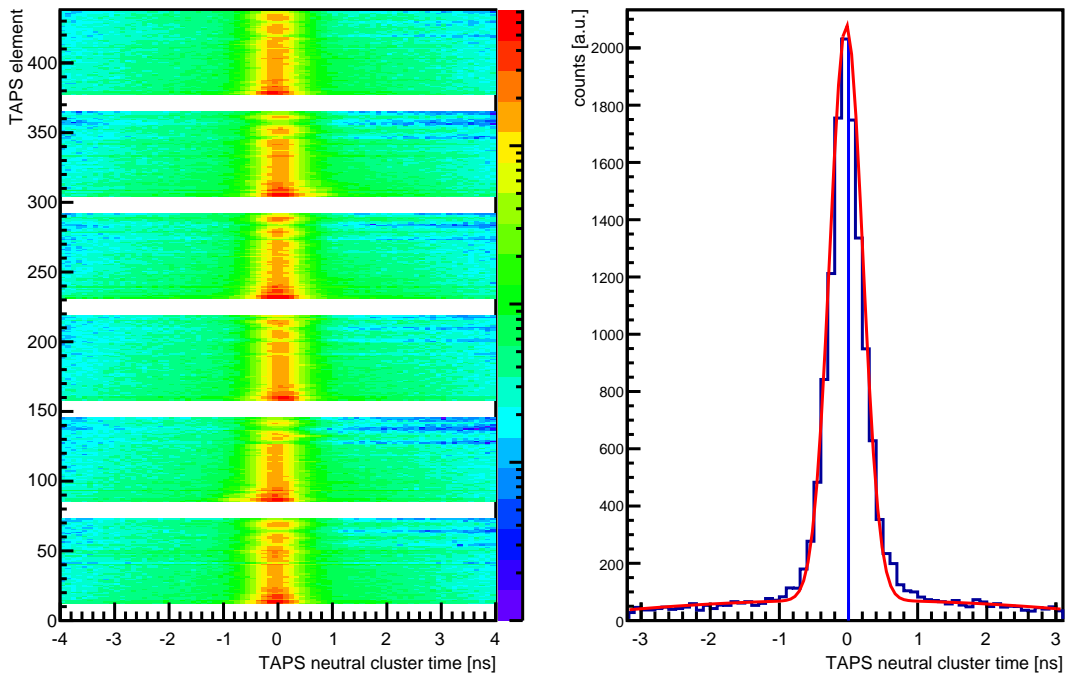


Figure 4.9.: Left-hand side: Time difference between TAPS and the tagger for all TAPS elements. Right-hand side: Projection for a single element.

4.2.3. Tagger time calibration

The CATCH TDCs of the tagger have a fixed conversion gain of 0.117 ns/channel. Therefore, only the offsets had to be calibrated.

This was done by plotting the time difference between all neutral clusters in TAPS and hits in the tagger, individually for every tagger channel. The positions of the coincidence peaks were extracted and new offsets were calculated using eq. 4.7. Since the timing of a tagger channel does not depend on other channels, this calibration needed only one iteration.

4.2.4. PID and Veto time calibration

The timing information of the PID and the vetoes was not used in this work. Hence, only a rough calibration was performed to align the relative timings between the individual elements, so all coincidence peaks are positioned at zero.

4.3. Calibration of the Simulation

For the simulated data, no time calibration was necessary since coincidence is always given in the simulation. Therefore, only energy calibrations for the detectors had to be performed. For the thresholds the same values as for the experimental data were used. The high energy calibration and quadratic energy correction were performed the same way as for experimental data to shift the peak positions of π^0 and η mesons in the invariant mass to their nominal masses.

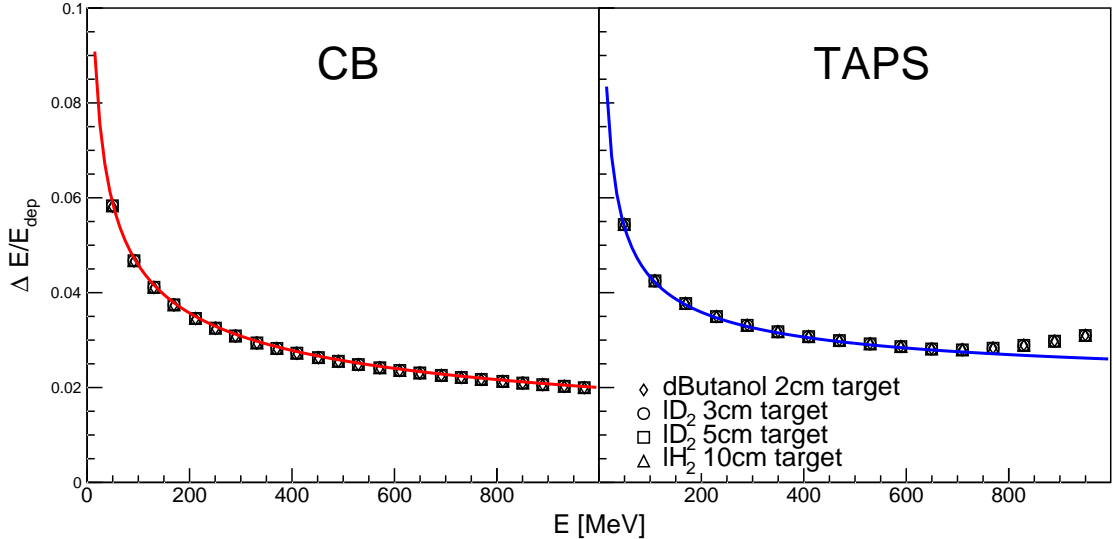


Figure 4.10.: Energy resolutions of the CD and TAPS detectors. The solid lines show the parameterizations given in eqs. 4.10 and 4.10. the open symbols show the resolutions obtained from simulations of different target cells.

4.3.1. Energy Resolution

The deposited energies of photons in the CB and TAPS detectors were artificially smeared in the simulated data, to achieve the same resolutions as in experimental data. The experimentally determined resolutions can be parametrized as follows [89], [45]:

$$\frac{\Delta E}{E} = \frac{2\%}{(E[\text{GeV}])^{0.36}} \quad (\text{CB}) \quad (4.10)$$

$$\frac{\Delta E}{E} = 1.8\% + \frac{0.8\%}{(E[\text{GeV}])^{0.5}} \quad (\text{TAPS}) \quad (4.11)$$

To determine the resolutions of simulated data, isotropically distributed photons with random energies up to 1 GeV were simulated for each detector setup. The deposited energy and resolution were determined by fitting Gaussians with low energy tails to the measured spectra [45].

The resulting energy resolutions after smearing are shown in Fig. 4.10 as function of the deposited energy and compared to the experimentally determined resolutions. An excellent agreement between the resolution of the simulation and the parametrization can be seen over the whole energy range in CB, and also for TAPS up to energies of about 800 MeV, were a small deviation can be seen. This is most likely caused by the method used to determine the resolution, described in [45]. There, a collimated photon beam with a maximal energy of 790 MeV impinged on a TAPS block. Since the photons in the simulation were not collimated, the resolutions might deviate from eq. 4.11. However, this deviation is no problem in the context of this work since the decay photons of η - and π^0 mesons do not reach this energies. The equations 4.10 and 4.11 were also used in the χ^2 test to reconstruct η - and π^0 -mesons, were the absolute energy error has to be known (see sec. 5.2.10).

4.3.2. Angular resolutions

The angular resolutions also had to be known to determine the absolute angular error in the χ^2 test (see A.3. The same simulation of isotropically distributed photons as for the determination of the energy resolution was used. The difference between generated and reconstructed polar and azimuthal angle was determined as function of the polar angle and the errors $\Delta\Theta$ and $\Delta\Phi$ could be extracted. Figures 4.11 and 4.12 show the corresponding resolutions for the CB and TAPS, respectively. A clear dependence on the target length can be seen for the resolution of the polar angle Θ in the CB. This is caused by a wider distribution of the reaction vertex in the z direction for a longer target cell, what results in different lengths of the flightpaths parallel and perpendicular to the z axis and thus worsens the polar angle resolution.

Since the target diameter does not change with length, the azimuthal angle resolution is not affected.

The right-hand side of Fig. 4.12 shows the influence of the PbWO₄ crystals on the TAPS Θ resolutions. Since the PbWO₄ crystals were not functional for the beam-times of 2009, no angle information was available for the 2 inner rings, what caused a sudden decrease in the resolution at smaller angles.

For both detectors a decrease in the angular resolutions can be seen at very large and very low angles. This is caused by an energy loss at the very edges of the detectors.

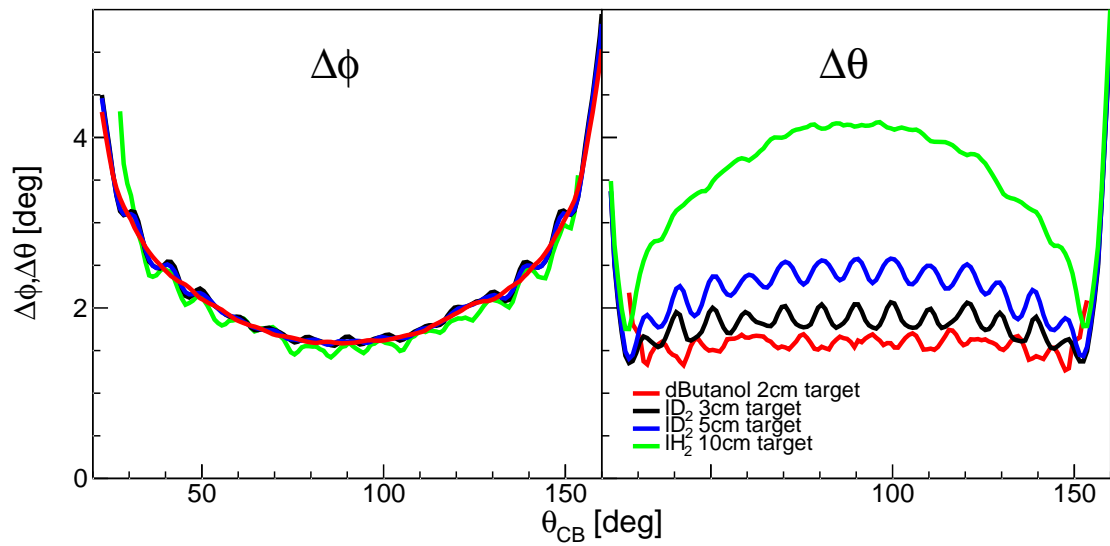


Figure 4.11.: Angular resolutions for photons in the CB, obtained from simulation.

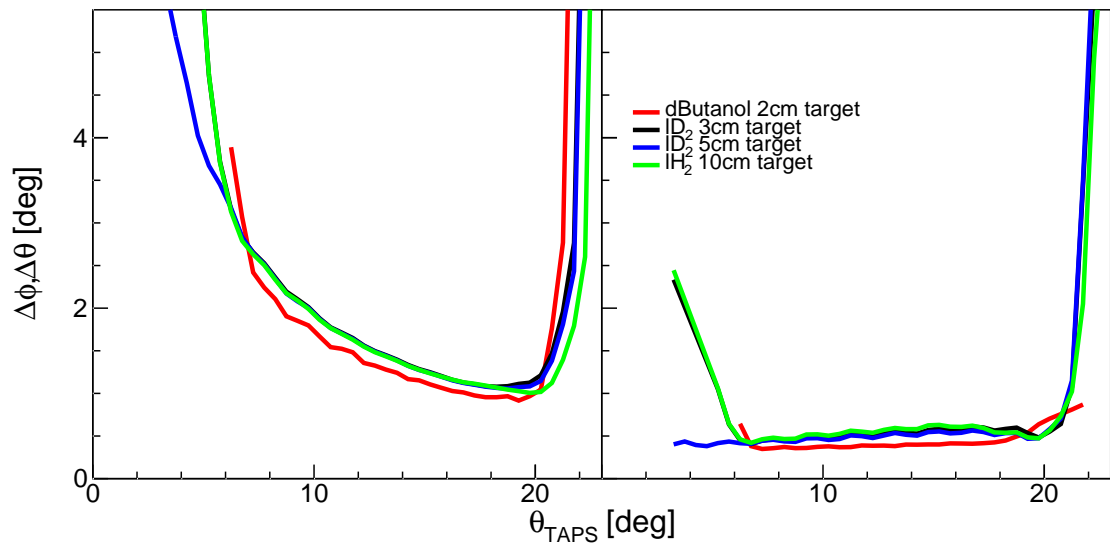


Figure 4.12.: Angular resolutions for photons in TAPS, obtained from simulation.

5. Analysis

After the calibration of the detector system the actual analysis of the reactions of interest can start. This chapter will give an overview of the steps needed to extract total and differential cross sections as well as asymmetries and polarization observables. In this work the following reactions were analyzed:

$\gamma p(n) \rightarrow \eta\pi^0 p(n)$	quasi-free exclusive $\eta\pi^0$ photoproduction off the proton
$\gamma n(p) \rightarrow \eta\pi^0 n(p)$	quasi-free exclusive $\eta\pi^0$ photoproduction off the neutron
$\gamma N(N) \rightarrow \eta\pi^0(N)$	quasi-free inclusive $\eta\pi^0$ photoproduction off the deuteron
$\gamma p(n) \rightarrow \eta\pi^+ n(n)$	quasi-free exclusive $\eta\pi^+$ photoproduction off the proton
$\gamma n(p) \rightarrow \eta\pi^- p(p)$	quasi-free exclusive $\eta\pi^-$ photoproduction off the neutron
$\gamma N(N) \rightarrow \eta\pi^\pm(N)$	quasi-free inclusive $\eta\pi^\pm$ photoproduction off the deuteron
$\gamma d \rightarrow \eta\pi^0 d$	coherent $\eta\pi^0$ photoproduction off the deuteron
$\gamma p \rightarrow \eta\pi^0 p$	exclusive $\eta\pi^0$ photoproduction off the free proton
$\gamma p \rightarrow \eta\pi^+ n$	exclusive $\eta\pi^+$ photoproduction off the free proton

Initial state nucleons in brackets denote the spectator nucleon, final state nucleons in brackets mean, that a coincident detection was not required in the analysis. Protons are denoted by 'p', neutrons by 'n', deuterons by 'd' and 'N' can denote a proton or a neutron.

The basic principle of the analysis is the same for all mentioned reaction channels. First events are selected based on the number of neutral and charged clusters. Then a χ^2 test is performed to reconstruct neutral mesons from their decay photons, and identify nucleon candidates. A PSA test is performed to separate photons from nucleons in TAPS.

Afterwards a series of kinematic cuts are applied to reject unwanted background reactions, as described below.

5.1. Kinematics in the participant-spectator model

In the participant-spectator-model for the deuteron it is assumed, that quasi-free reactions take place solely on one nucleon, the participant. The second nucleon, the spectator, does not take part in the reaction, and remains in its initial state.

A schematic view is shown in Fig. 5.1.

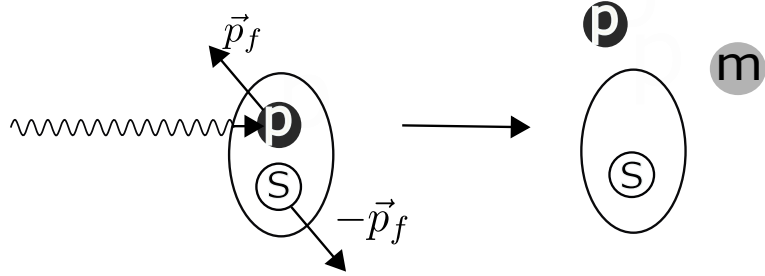


Figure 5.1.: Simplified view of the participant-spectator model. The left side shows the participant p with Fermi momentum \vec{p}_f being impinged by a photon, and the spectator s with Fermi momentum. The righthand side shows the recoiled participant and a meson m that was produced in the reaction.

In the initial state the participant carries the Fermi momentum \vec{p}_F and the energy E_p . The spectator's energy is given by E_S and since the deuteron is at rest, it has to carry the Fermi momentum $-\vec{p}_F$. The small binding energy of the deuteron of ≈ 2.2 MeV is neglected in this model. Assuming energy and momentum conservation, the 4-vector of the deuteron in the initial state is then given by:

$$p_D = p_P + p_S = \begin{pmatrix} E_P \\ \vec{p}_F \end{pmatrix} + \begin{pmatrix} E_S \\ -\vec{p}_F \end{pmatrix} = \begin{pmatrix} m_D \\ 0 \end{pmatrix} \quad (5.1)$$

The energy of the spectator is given by:

$$E_S = \sqrt{m_S^2 + \vec{p}_F^2} \quad (5.2)$$

The energy of the participant can then be approximated by:

$$E_P = m_D - E_S = m_D - \sqrt{m_S^2 + \vec{p}_F^2} \neq \sqrt{m_P^2 + \vec{p}_F^2} \quad (5.3)$$

what means, that the participant is off-shell.

With the incoming photon 4-vector $p_\gamma = (E_\gamma, \vec{p}_\gamma) = (E_\gamma, 0, 0, E_\gamma)$ and the 4-vector of the participant p_P the center of mass energy $W = \sqrt{s}$ can be calculated. s is given as the square of the sum of the initial state 4-vectors.

$$s = (p_\gamma + p_P)^2 = E_\gamma^2 + 2E_\gamma E_P + E_P^2 - (\vec{p}_\gamma + \vec{p}_P)^2 \quad (5.4)$$

Inserting E_P yields:

$$s = m_D^2 + m_S^2 + 2E_\gamma(m_D - \sqrt{m_S^2 + \vec{p}_F^2}) - 2m_D\sqrt{m_S^2 + \vec{p}_F^2} - 2E_\gamma p_{F,z}. \quad (5.5)$$

From equation 5.5 the energy of the recoil nucleon can be calculated from the 4-vector of the $\eta\pi$ system $p_M = p_\eta + p_\pi$ and the polar and azimuthal angles of the recoil nucleon.

Again assuming energy and momentum conservation and neglecting the deuterons binding energy, the sum of the 4-vectors in the initial state has to equal the sum of the 4-vectors in the final state:

$$\begin{pmatrix} E_\gamma \\ \vec{p}_\gamma \end{pmatrix} + \begin{pmatrix} m_D \\ 0 \end{pmatrix} = \begin{pmatrix} E_M \\ \vec{p}_M \end{pmatrix} + \begin{pmatrix} E_R \\ \vec{p}_R \end{pmatrix} + \begin{pmatrix} E_S \\ \vec{p}_S \end{pmatrix}, \quad (5.6)$$

where the values for E_γ , E_M , m_D , m_P , m_S , θ_M , ϕ_M , θ_P and ϕ_P are known from the analysis. The kinetic energy of the recoil nucleon $T_R = E_R - m_R$ can then be calculated via:

$$T_R = \frac{-(BC - 2A^2m_P) + \sqrt{(BC - 2A^2m_P)^2 - C^2(B^2 - A^2)}}{2(B^2 - A^2)}. \quad (5.7)$$

with the following definitions:

$$\begin{aligned} A &:= p_{M,x} \sin(\theta_P) \cos(\phi_P) + p_{M,y} \sin(\theta_P) \cos(\phi_P) + (p_{M,z} - E_\gamma) \cos(\theta_P) \\ B &:= E_M - E_\gamma - m_D \\ C &:= (E_M + m_P - E_\gamma - m_D)^2 - (m_S^2 + p_M^2 + E_\gamma^2 - 2E_\gamma p_{M,z}) \end{aligned}$$

The details of this derivation are given in [63]. This reconstruction of the recoil nucleons kinetic energy is necessary, because the energy information of the detector setup is less precise for nucleons than for photons.

5.2. Event Selection

The first step, after events have been reconstructed as described in section 3, is to assign event classes to certain reaction channels. Event classes are identified by the number of neutral and charged clusters, that should correspond to the particles in a reaction's final state. Table 5.2 shows a summary of the reactions and the according event classes, analyzed in this work. The following sections give a very brief overview over the investigated reactions, and the main sources of background contributions. These background reactions were also investigated with MC simulations to determine their influence on coplanarity, missing mass and invariant mass spectra. The most probable sources of background were determined by fitting a sum of the simulated lineshape of the signal and background reactions to the experimental data. The background reactions, that in addition to the simulation of the signal, reproduce the lineshape of the experimental data best, are given in sections 5.2.1-5.2.9, and are also shown in the spectra of sections 5.5.2 - 5.5.5.

The elimination of background contributions will be discussed in section 5.5.

Reaction channel	required clusters	
	Neutral	Charged
$\gamma p(n) \rightarrow \eta\pi^0 p(n) \rightarrow 4\gamma p(n)$	4	1
$\gamma n(p) \rightarrow \eta\pi^0 n(p) \rightarrow 4\gamma n(p)$	5	0
$\gamma N(N) \rightarrow \eta\pi^0(N) \rightarrow 4\gamma(N)$	4 5 4	1 0 0
$\gamma p(n) \rightarrow \eta\pi^+ n(n) \rightarrow 2\gamma\pi^+ n(n)$	3	1
$\gamma p(n) \rightarrow \eta\pi^- p(p) \rightarrow 2\gamma\pi^- p(p)$	2	2
$\gamma N(N) \rightarrow \eta\pi^\pm(N) \rightarrow 2\gamma\pi^\pm(N)$	2 3 2	1 1 2
$\gamma d \rightarrow \eta\pi^0 d \rightarrow 4\gamma d$	4	1
$\gamma p \rightarrow \eta\pi^0 p \rightarrow 4\gamma p$	4	1
$\gamma p \rightarrow \eta\pi^+ n \rightarrow 2\gamma\pi^+ n$	3	1

Table 5.1.: Conditions on the number of clusters, that need to be fulfilled by an event to enter into the analysis. For the quasi-free inclusive reactions multiple conditions can be fulfilled, that are connected via a logical 'or'.

5.2.1. Analysis of $\gamma p(n) \rightarrow \eta\pi^0 p(n)$

The analysis of $\gamma p(n) \rightarrow \eta\pi^0 p(n)$ requires the decay photons of the mesons to be detected as well as the recoil proton. Therefore, all events with 4 neutral clusters and one charged cluster are selected.

The main sources of background in this reaction come from the following reactions that have the same final states:

- $\gamma p(n) \rightarrow 2\pi^0 p$
- $\gamma d \rightarrow \eta\pi^0 d$

5.2.2. Analysis of $\gamma n(p) \rightarrow \eta\pi^0 n(p)$

The analysis of $\gamma n(p) \rightarrow \eta\pi^0 n(p)$ requires the decay photons of the mesons to be detected as well as the recoil neutron. Therefore, all events with 5 neutral clusters are selected.

The main source of background in this reaction comes from the following reaction that has the same final state:

- $\gamma p(n) \rightarrow 2\pi^0 n$

5.2.3. Analysis of $\gamma N(N) \rightarrow \eta\pi^0(N)$

The analysis of $\gamma N(N) \rightarrow \eta\pi^0(N)$ requires the decay photons of the mesons to be detected, while the detection of the recoil nucleon is optional. Therefore, no condition on the coplanarity can be applied.

The main sources of background in this reaction come from the following reactions that have the same final state:

- $\gamma p(n) \rightarrow 2\pi^0 p$
- $\gamma n(p) \rightarrow 2\pi^0 n$
- $\gamma d \rightarrow \eta\pi^0 d$

5.2.4. Analysis of $\gamma p(n) \rightarrow \eta\pi^+ n(n)$

The analysis of $\gamma p(n) \rightarrow \eta\pi^+ n(n)$ requires the decay photons of the η meson to be detected as well as the π^+ and the recoil neutron. Therefore, all events with 3 neutral clusters and one charged cluster are selected. A dE-E analysis as described below was used to identify the charged pion.

The main source of background in this reaction comes from the following reaction that has the same final state:

- $\gamma p(n) \rightarrow \pi^0\pi^+ n$

5.2.5. Analysis of $\gamma n(p) \rightarrow \eta\pi^- p(p)$

The analysis of $\gamma p(n) \rightarrow \eta\pi^+ n(n)$ requires the decay photons of the η meson to be detected as well as the π^- and the recoil proton. Therefore, all events with 2 neutral clusters and 2 charged clusters are selected.

To separate charged pions and protons a dE-E analysis as described below was applied. If both charged particles were detected in the CB, their deposited energy in the PID was compared to the deposited energy in the CB as seen in Fig. 5.6. It was requested that one particle is located in the pion band, the other one in the proton band. If only one charged particle was detected in the CB, it was requested to be located in the pion band. Events were rejected if both particles were detected in TAPS, because there it is not possible to distinguish charged pions efficiently from protons. The fibers used to collect the scintillation light have a diameter of 1 mm and cannot collect all the light. Additional loss is caused by the small bending radius ($R=26$ mm) that prevents total reflection inside the fibers. In summary these effects lead to a reduced energy resolution of the vetoes.

The main source of background in this reaction comes from the following reaction that has the same final state:

- $\gamma n(p) \rightarrow \pi^0\pi^- p$

5.2.6. Analysis of $\gamma N(N) \rightarrow \eta\pi^\pm(N)$

The analysis of $\gamma N \rightarrow \eta\pi^0(N)$ requires the decay photons of the eta to be detected, as well as the charged pion, while the detection of the recoil nucleon is optional. Therefore, no condition on the coplanarity can be applied.

The main sources of background in this reaction come from the following reactions that have the same final states:

- $\gamma p(n) \rightarrow \eta p$
- $\gamma p(n) \rightarrow \pi^0 p$

5.2.7. Analysis of $\gamma p \rightarrow \eta\pi^0 p$

The analysis of $\gamma p \rightarrow \eta\pi^0 p$ requires the decay photons of the mesons to be detected as well as the recoil proton. Therefore, all events with 4 neutral clusters and one charged cluster are selected.

The main source of background in this reaction comes from the following reaction that have the same final state:

- $\gamma p(n) \rightarrow 2\pi^0 p$

For consistency, the invariant mass W was reconstructed from the final state in the further analysis.

5.2.8. Analysis of $\gamma p \rightarrow \eta\pi^+ n$

The analysis of $\gamma p \rightarrow \eta\pi^+ n$ requires the decay photons of the η meson to be detected as well as the π^+ and the recoil neutron. Therefore, all events with 3 neutral clusters and one charged cluster are selected. A dE-E analysis as described below was used to identify the charged pion.

The main sources of background in this reaction come from the following reactions that have the same final state:

- $\gamma p \rightarrow \pi^0 \pi^+ n$
- $\gamma p \rightarrow 2\pi^0 p$

5.2.9. Analysis of $\gamma d \rightarrow \eta\pi^0 d$

The analysis of $\gamma d \rightarrow \eta\pi^0 d$ requires the decay photons of the mesons to be detected as well as the recoil deuteron. Therefore, all events with 4 neutral clusters and one charged cluster are selected. To separate protons from deuterons a Time-Of-Flight vs energy cut was applied as shown in Fig. 5.2, were a clear deuteron Time-of-Flight band is visible. The Time-of-Flight technique was also used to calculate the energy of the recoil deuteron as described in section 5.6.

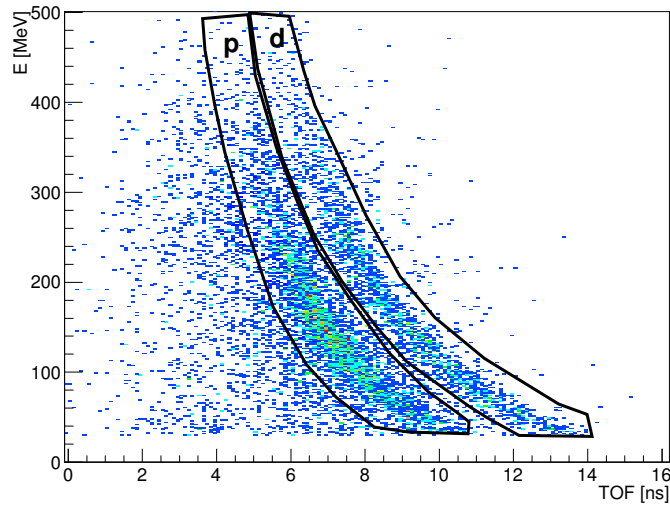


Figure 5.2.: Time-of-Flight in TAPS. The proton ("p") and deuteron ("d") bands can be seen clearly.

5.2.10. Reconstruction of η and π^0 mesons

Both, the η and the π^0 meson decay into 2 photons with probabilities of 39.31% for the eta and 98.82% for the pion [5]. Since it is impossible to know which photons originated from the decay of which meson, a statistical method has to be applied to find the most probable combination of photons. This is done with a χ^2 test. For each event χ^2 values are calculated with the following formulae, for each of the 3 possible combinations of photon pairs composed of 2 photons:

$$\chi_1^2 = \left(\frac{m_{\gamma_i\gamma_j} - m_\eta}{\Delta m_{\gamma_i\gamma_j}} \right)^2 + \left(\frac{m_{\gamma_k\gamma_l} - m_{\pi^0}}{\Delta m_{\gamma_k\gamma_l}} \right)^2 \quad (5.8)$$

$$\chi_2^2 = \left(\frac{m_{\gamma_i\gamma_j} - m_{\pi^0}}{\Delta m_{\gamma_i\gamma_j}} \right)^2 + \left(\frac{m_{\gamma_k\gamma_l} - m_\eta}{\Delta m_{\gamma_k\gamma_l}} \right)^2 \quad (5.9)$$

Here $m_{\gamma_i\gamma_j}$ denotes the invariant mass of the photon pair $\gamma_i\gamma_j$, m_{η/π^0} is the nominal η/π^0 mass, $\Delta m_{\gamma_i\gamma_j}$ is the error in the invariant mass, and for the indices one has $i, j, k, l = 1, 2, 3, 4$ and $i \neq j \neq k \neq l$.

The invariant mass of the photon pair $\gamma_1\gamma_2$ is given by:

$$m_{\gamma_1\gamma_2} = \sqrt{2E_{\gamma_1}E_{\gamma_2} \cdot (1 - \cos(\phi_{\gamma_1\gamma_2}))}, \quad (5.10)$$

with the photon energies E_{γ_1, γ_2} and the opening angle between the two photons $\phi_{\gamma_1\gamma_2}$. The errors $\Delta m_{\gamma_i\gamma_j}$ depend only on the errors of the energy ΔE , polar angle $\Delta\Theta$ and azimuthal angle $\Delta\Phi$ and can thus be calculated for each combination as explained in section A.3.

The combination with the smallest χ^2 value has the highest probability to be the 'right' combination, and thus the mesons will be reconstructed from the corresponding photon pairs using energy and momentum conservation:

$$\begin{pmatrix} E_\eta \\ \vec{p}_\eta \end{pmatrix} = \begin{pmatrix} E_{\gamma_i} \\ \vec{p}_{\gamma_i} \end{pmatrix} + \begin{pmatrix} E_{\gamma_j} \\ \vec{p}_{\gamma_j} \end{pmatrix},$$

$$\begin{pmatrix} E_{\pi^0} \\ \vec{p}_{\pi^0} \end{pmatrix} = \begin{pmatrix} E_{\gamma_k} \\ \vec{p}_{\gamma_k} \end{pmatrix} + \begin{pmatrix} E_{\gamma_l} \\ \vec{p}_{\gamma_l} \end{pmatrix},$$

where (E_η, \vec{p}_η) is the four-vector of the η -meson, $(E_{\pi^0}, \vec{p}_{\pi^0})$ is the four-vector of the π^0 -meson and $(E_{\gamma_i,j,k,l}, \vec{p}_{\gamma_i,j,k,l})$ are the four-vectors of the 4 final state photons.

In case of 5 neutral particles in the final state, the same procedure is applied. There are 15 possible photon pair combinations with one leftover particle. χ^2 values are calculated for the pair combinations and the most probable combinations is used to form the $\eta\pi^0$ pair, while the leftover particle is treated as the neutron candidate. In this case, for the indices the following holds true: $i, j, k, l = 1, 2, 3, 4, 5$ and $i \neq j \neq k \neq l$.

5.2.11. Reconstruction of η -mesons from 3 neutral hits

For $\eta\pi^\pm$ production the reconstruction of the η is easier.

If there are only 2 neutral clusters in an event, the reconstruction of the η meson is trivial.

$$\begin{pmatrix} E_\eta \\ \vec{p}_\eta \end{pmatrix} = \begin{pmatrix} E_{\gamma_1} \\ \vec{p}_{\gamma_1} \end{pmatrix} + \begin{pmatrix} E_{\gamma_2} \\ \vec{p}_{\gamma_2} \end{pmatrix}.$$

If there are 3 neutral particles, the χ^2 is calculated for the 3 possible pair combinations:

$$\chi^2 = \left(\frac{m_{\gamma_i\gamma_j} - m_\eta}{\Delta m_{\gamma_i\gamma_j}} \right)^2 \quad (5.11)$$

The combination that minimizes the χ^2 value is used to reconstruct the η -meson, the leftover neutral particle is treated as neutron candidate. The reconstruction of charged pions is described in the next section.

5.2.12. Confidence Levels

The quality of the particle reconstruction with the χ^2 tests is reflected in the distributions of the χ^2 values. For k independent values x_i that are distributed according to a normal distribution with mean values μ_i and standard deviations σ_i , the χ^2 distribution is defined as:

$$\chi^2 = \sum_{i=1}^k \left(\frac{x_i - \mu_i}{\sigma_i} \right)^2. \quad (5.12)$$

The corresponding probability density function is then given by [90]:

$$f(\chi^2, k) = \frac{(\chi^2)^{k/2-1} \cdot e^{-\chi^2/2}}{2^{k/2} \cdot \Gamma(k/2)}, \quad (5.13)$$

where $\Gamma(k/2)$ is the Gamma function and k denotes the degrees of freedom.

Closely related to the χ^2 distribution is the confidence level. The confidence level $W(\chi^2, k)$ is defined as the probability that a random value x^2 that is distributed according to $f(\chi^2, k)$ is greater than a given χ^2 :

$$W(\chi^2) = P(x^2 \geq \chi^2). \quad (5.14)$$

Therefore, a high χ^2 corresponds to a small confidence level and vice versa.

Figures 5.3 - 5.5 show the confidence levels for the event classes investigated in this work. The top rows show the distributions before the analysis cuts, the lower rows show the distributions with the cuts applied.

Fig. 5.3 shows reactions with $\eta\pi^0$ pairs for deuterium targets, Fig. 5.5 shows the distributions for the reactions on dButanol targets, and Fig. 5.4 shows the distributions for $\eta\pi^+$ pairs. In the reaction $\gamma n(p) \rightarrow \eta\pi^- p$ no χ^2 test has to be performed since there are only 2 neutral clusters involved. For the same reason the χ^2 distribution of $\gamma p(n) \rightarrow \eta\pi^+ n$ equals the distribution of $\gamma N(N) \rightarrow \eta\pi^\pm(N)$. Therefore, these reactions are not shown.

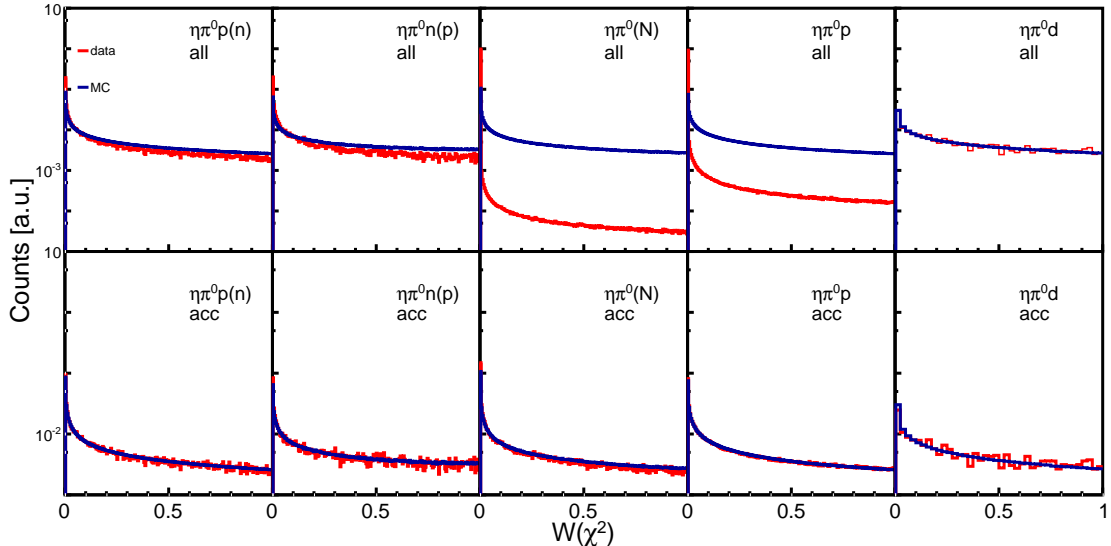


Figure 5.3.: Normalized confidence level distributions of reactions with $\eta\pi^0$ pairs in the final state. Experimental data are shown in red, simulated data are shown in blue.

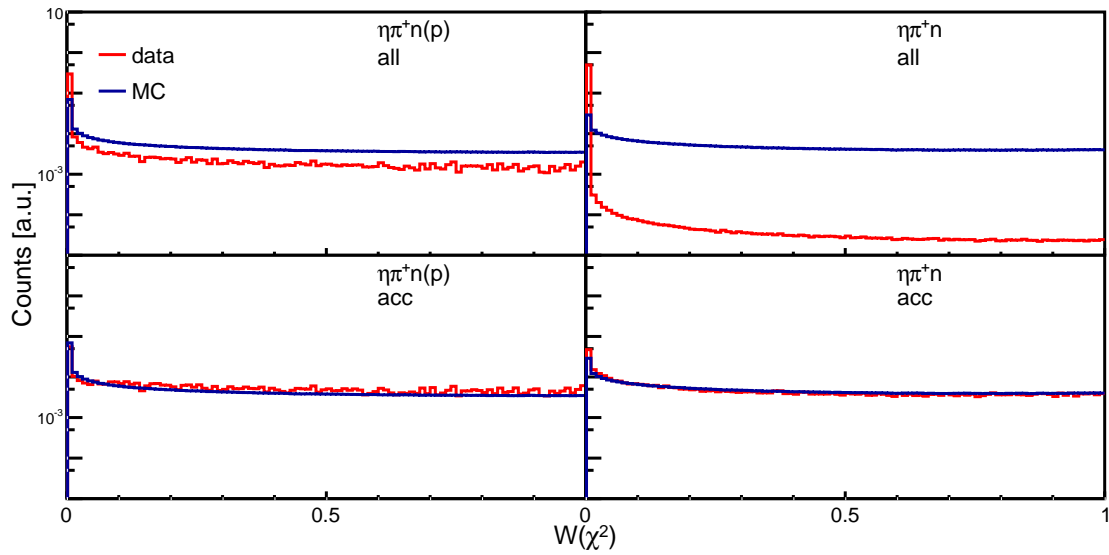


Figure 5.4.: Normalized confidence level distributions of reactions with $\eta\pi^+$ pairs in the final state. Experimental data are shown in red, simulated data are shown in blue.

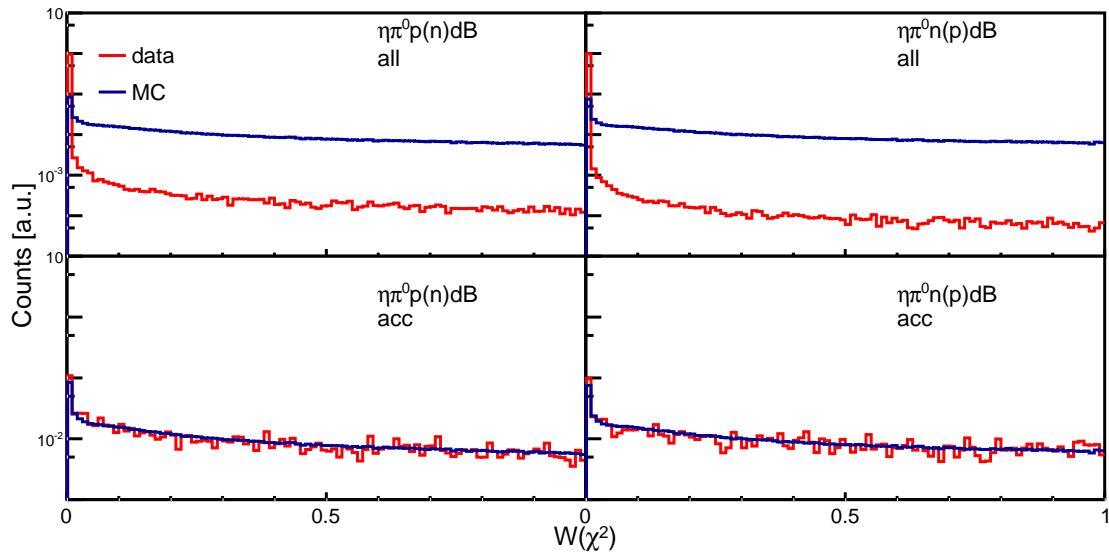


Figure 5.5.: Normalized confidence level distributions of reactions with $\eta\pi^0$ pairs in the final state (for dButanol targets). Experimental data are shown in red, simulated data are shown in blue.

For all channels there is a more or less pronounced discrepancy between simulated and experimental data, if no cuts are applied. This is caused by the background contributions in the experimental data that cause 'wrong' χ^2 values. After cuts are applied there

is excellent agreement between experimental and simulated data. This is especially important since the simulated data do not contain background contributions that could contaminate the χ^2 distributions.

Alltogether, it seems that the event selection is equivalent for simulation and experimental data and effects like combinatorial background are well under control.

5.3. Discrimination of charged particles

The classification in charged and neutral clusters itself does provide no additional information on charged particles, it especially does not distinguish between charged pions and protons. To identify charged pions the energy deposited in the PID was plotted against the energy deposited in the CB for each charged particle. The corresponding spectra can be seen in Fig. 5.6 which show the typical band-like structures. At low PID energies the pion band can be seen. Above the proton band is visible, that shows a strong dependence on the CB energy.

For several bins of CB energy the proton band was projected and fitted with a Gaussian, to determine the peak position and width. Then a cut at the -1.5σ position of the proton peak was determined. Particles that lie below the cut are considered to be charged pions, particles above are treated as protons. The cut is shown as red line in Fig. 5.6. After this classification, the 4-vectors of the charged particles were calculated.

$$p_{cp} = \begin{pmatrix} E_c \\ \vec{p}_c \end{pmatrix} * \frac{m_{cp}}{|p_c|}, \quad (5.15)$$

where $p_c = (E_c, \vec{p}_c)$ is a 4-vector constructed with the energy E_c and momentum \vec{p}_c of the cluster, and m_{cp} is the nominal value of the particles mass.

In principle a Time-of-Flight analysis could be done for charged particles in TAPS to identify pions, but for higher energetic protons, the bands strongly overlap and a clear separation of pions is not possible.

The Time-of-Flight analysis is also not possible for the CB because of the small flight distance from the target to the detector of about 25 cm and the not sufficiently good time resolution of the NaI crystals.

Hence, the only method to identify charged pions was the dE-E analysis for PID and CB.

This means however that charged pions detected in TAPS were excluded from the analysis. This does affect the reaction phase space, but since the CB covers about 95% of 4π this is a minor effect.

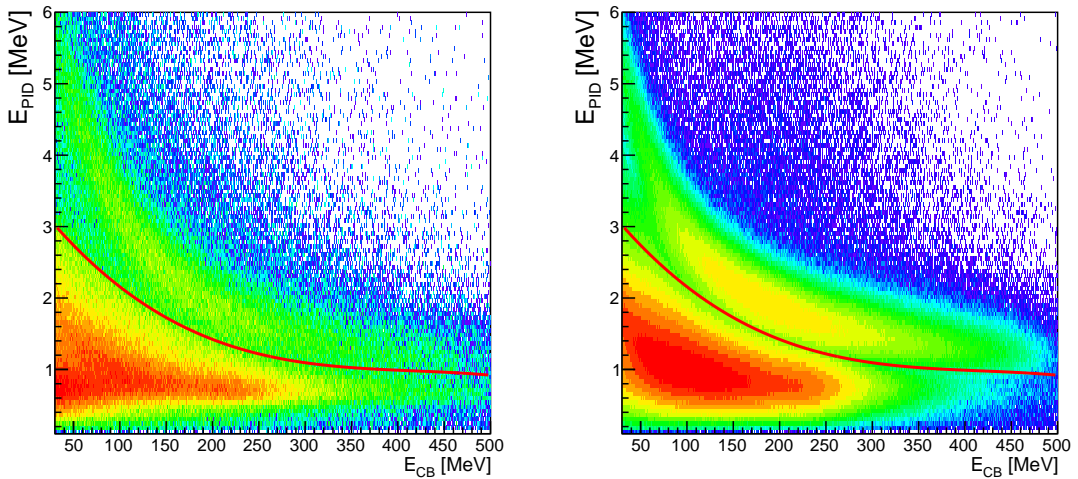


Figure 5.6.: The left-hand side shows the energy deposited in the PID against the energy in the CB for the reaction $\gamma n(p) \rightarrow \eta\pi^-p$ for experimental data. The red line represents the cut between pions and protons. Particles below the line are considered to be pions, particles above the line are considered to be protons. The right-hand side shows the same for simulated data.

The upper rows in Figs. 5.8 and 5.9 show the deposited energy in the CB plotted versus the generated energy of simulated π^- and π^+ respectively. A deviation from the line that represents $E_{gen} = E_{det}$ is clearly visible. This deviation is caused by the fact, that photons have been used to calibrate the CB energy information.

Since precise energy information of the pions is crucial for the reconstruction of the center of mass energy (see section 5.14) a correction function was determined and applied to simulated and experimental data.

For the correction function the difference $E_{gen}-E_{det}$ is divided by E_{det} and then plotted versus E_{det} .

Figure 5.7 shows the resulting distribution.

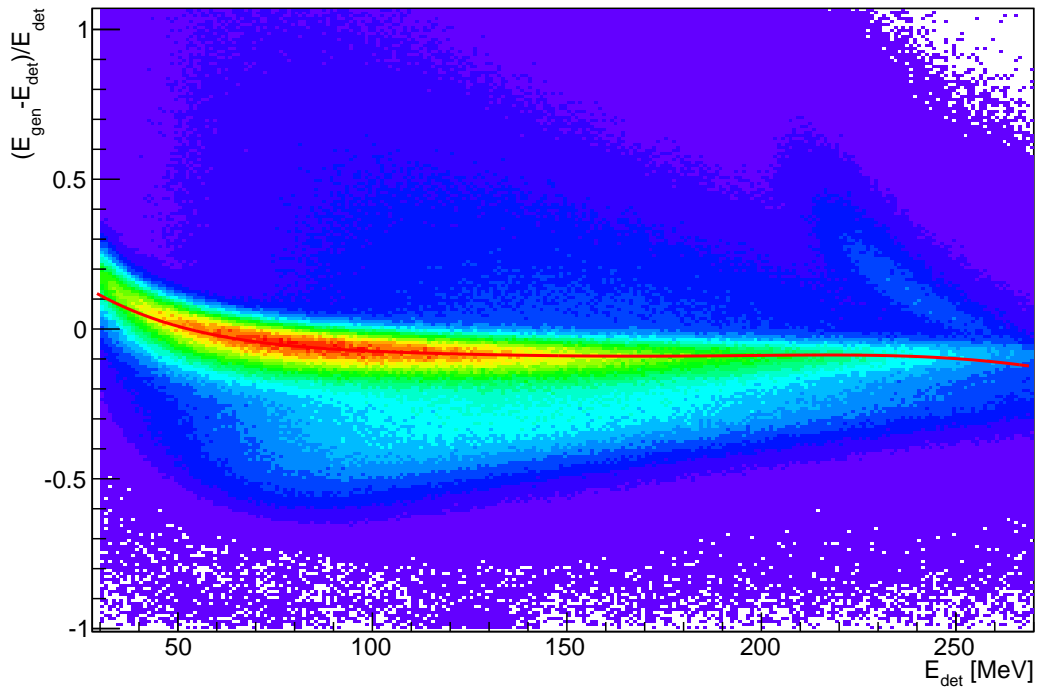


Figure 5.7.: Distribution of the correction-factor as a function of the detected energy of the pion in the CB. The histogram was projected for several bins of energy that were fitted with Gaussians to determine the position. The red line is a fit to the positions.

This distribution is then projected and fitted with a combination of a Gaussian and a polynomial to determine the peak position as function of E_{det} . The peak positions are then fitted with a polynomial, that is used as correction function f_{cor} in the analysis in the following way.

$$E_{cor} = E_{det} + f_{cor}(E_{det})E_{det} \quad (5.16)$$

Inserting $f_{cor}(E_{det}) = \frac{E_{gen} - E_{det}}{E_{det}}$ immediately returns $E_{cor} = E_{gen}$ in case of the simulation.

The corresponding distributions with the corrected energy are shown in the lower rows of Figs. 5.8 and 5.9.

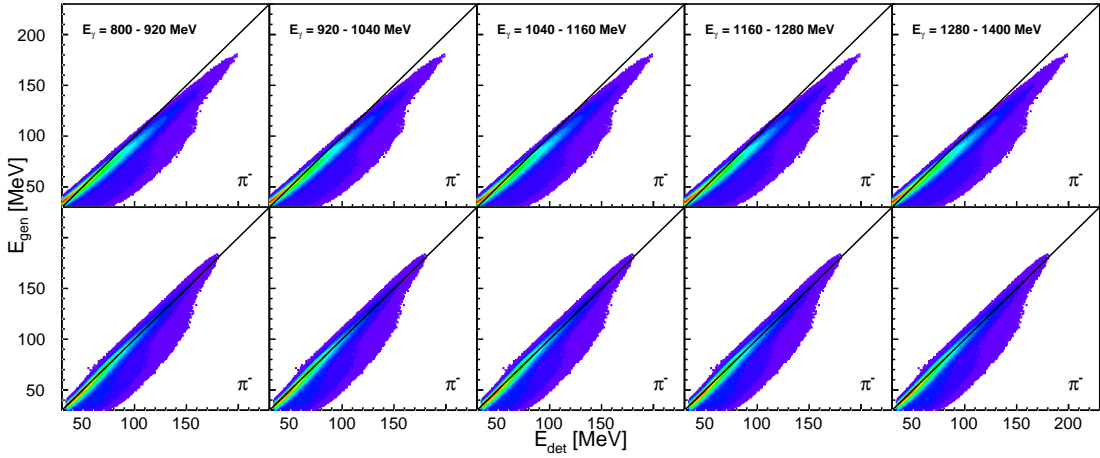


Figure 5.8.: Generated energy of π^- mesons versus the detected energy for simulated data for 5 bins of photon energy. The upper row shows the distribution before the correction described in the text, the lower row shows the distributions after the correction. The solid line represents $E_{det} = E_{gen}$.

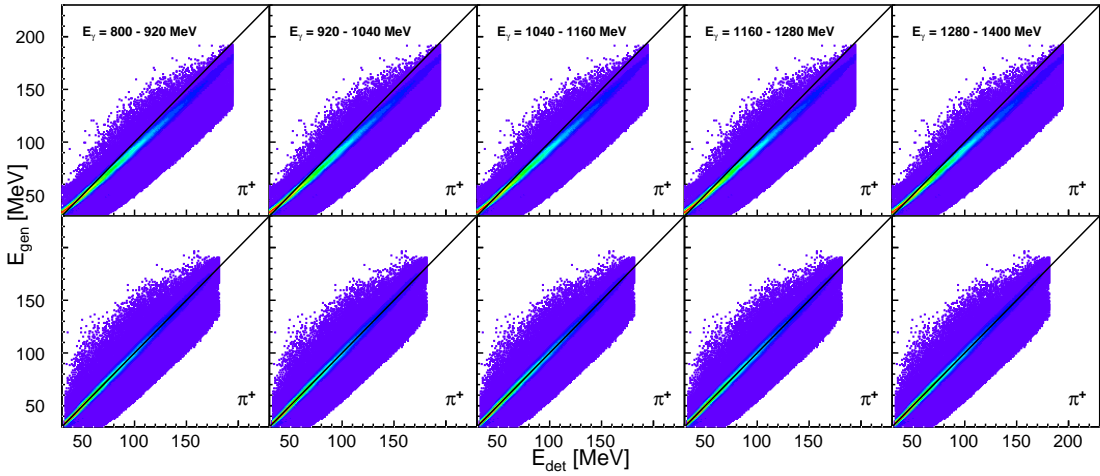


Figure 5.9.: Same as Fig. 5.8 but for π^+ mesons.

After this correction the same technique, described in section 5.14 could be used to determine the kinetic energy of the recoil nucleon, for reactions with neutral and charged pions, thereby minimizing systematic differences between the respective analyzes.

5.4. Energy correction of η and π^0 mesons

The invariant masses of η and π^0 mesons are shown in Fig. 5.10. The average values of the distributions are close to the values given in the literature. However, the values for

each event can vary in the width of the peaks. This could lead to smearing of signals, for example the missing mass. To avoid this, and enhance the energy resolution, the energies of η and π^0 mesons are scaled to fulfill $E_{cor}^2 = p_{cor}^2 + m_i^2$, where m_i is the literature value of the η or π^0 mass, respectively.

$$E_{cor} = \frac{m_i}{m_{\gamma\gamma}} E$$

$$\vec{p}_{cor} = \frac{\sqrt{E_{cor}^2 - m_i^2}}{|\vec{p}|} \vec{p}, \quad (5.17)$$

where m_i is the literature value of the mass of the η or π meson and $m_{\gamma\gamma}$ is the invariant mass of the corresponding photon pair.

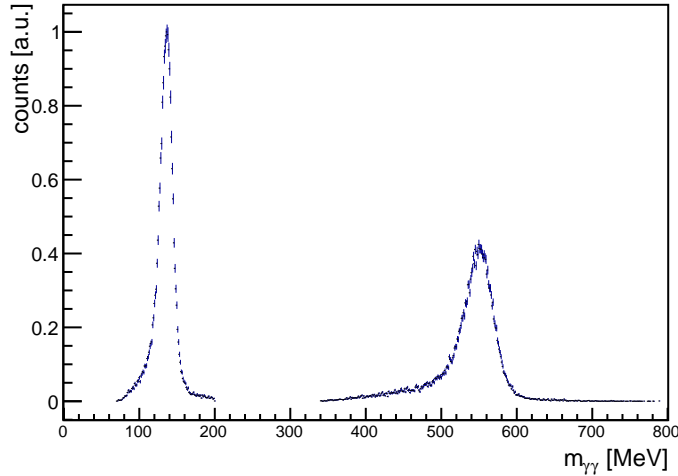


Figure 5.10.: Invariant mass of the η and π^0 mesons.

A detailed derivation of eqs. 5.17 is given in [91].

5.5. Background rejection

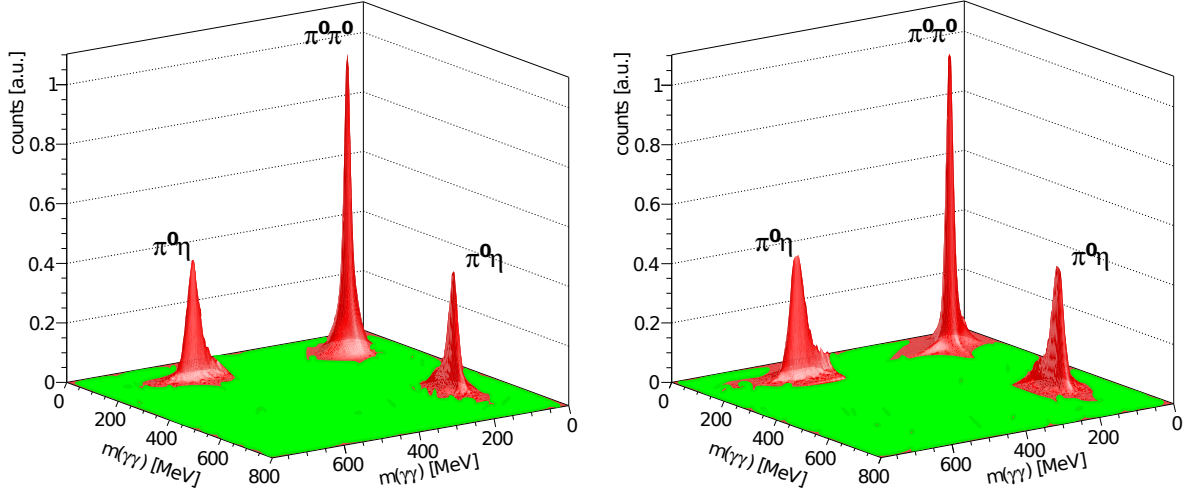


Figure 5.11.: Spectra of the invariant masses of the best combinations of 4 and 5 photons to $\eta\pi^0$ and $2\pi^0$ pairs. Right-hand side: exclusive reaction on quasi-free protons. Left-hand side: exclusive reaction on quasi-free neutrons. The $\eta\pi^0$ peaks are enhanced by a factor of 50.

Up to this point in the analysis, the most probable combinations of photon pairs to mesons as well as nucleon candidates have been identified. The next step is to distinguish between 'true' events, that originate from the reactions of interest, and background reactions. Background originates from reactions that end up in similar final states as reactions of interest. The dominant background contributions to the $\eta\pi$ channels come from the corresponding $\pi\pi$ channels, where the η is replaced by a π^0 . These reactions have the exact same final states as the $\eta\pi$ channels and much larger cross sections (detailed information about 2π photoproduction can be found in [88] and [63]).

Additional reactions can end up in the same final states because of misidentification of charged particles as neutral (and vice versa) due to the <100% efficiency of the veto and PID detectors, or mis-identifications of charged pions and protons. For example a lot of background to the inclusive reaction $\gamma N(N) \rightarrow \eta\pi^\pm(N)$ comes from the ηp final state as can be seen in Fig 5.33. Here the proton is misidentified as a charged pion. Reactions can also end up in the same final states if particles are completely lost due to inefficiencies in the detector systems.

The following sections describe the techniques that were used to reject as much background contributions as possible, while not removing too much good events.

5.5.1. Pulse Shape Analysis

The first cut that is applied to the data after the χ^2 test is the PSA cut. It is used to discriminate photons from nucleons.

For each BaF₂ crystal a Gaussian was fitted to a projection of the photon band to determine the cut position. To pass the cut, photons of an event were required to lie within a $\pm 3\sigma$ area around the mean value. In Figs. 5.12 - 5.16, the shown cuts represent the global average of the individual cut positions. The photon bands are located at angles of 45° and after the kinematic cuts, there is barely any contamination visible for the quasi free exclusive reactions. There is more background visible for reactions with a neutron in the final state, what is caused by the possible misidentification of a neutron as a photon during the χ^2 test. The exclusion zone for nucleons was chosen at PSA radii $r_{PSA} < 85$ MeV and $r_{PSA} > 380$ MeV. In the area between, high energetic nucleons can be located, that punch through the detector [63]. Therefore, no cut was applied in this region.

The PSA information is not available in the simulation, therefore the PSA cuts were chosen very conservatively. The upper rows of Figures 5.12 - 5.16 show the PSA spectra right after the χ^2 test, the lower rows show the spectra after all analysis cuts have been applied, to compare which events are actually affected by the PSA cuts.

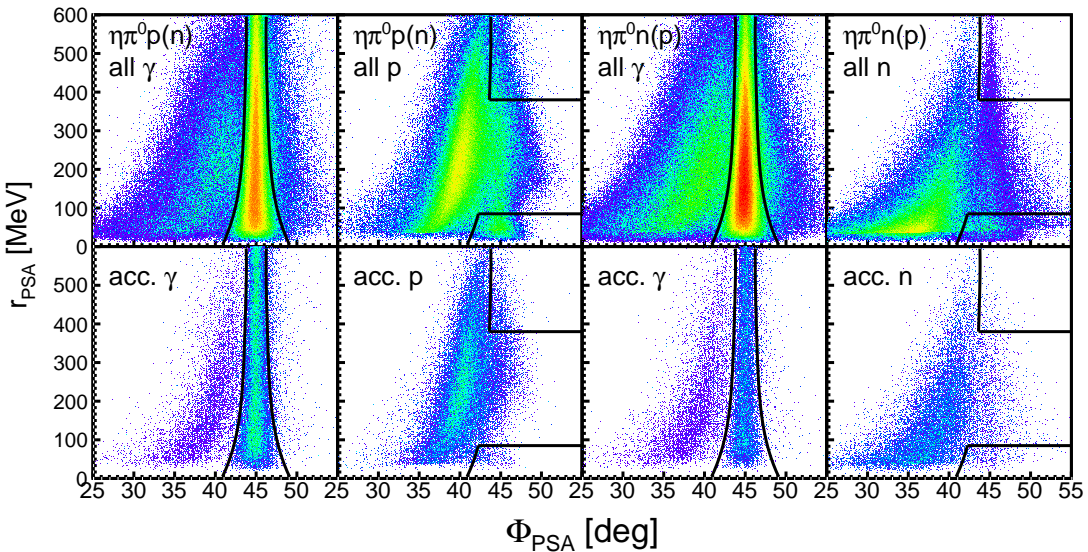


Figure 5.12.: PSA spectra of the quasi-free exclusive photoproduction of $\eta\pi^0$ pairs. The top row shows the raw spectra without kinematic cuts, the bottom row shows the spectra after applying all kinematic cuts (see below). The solid lines show the positions of the PSA-Cuts.

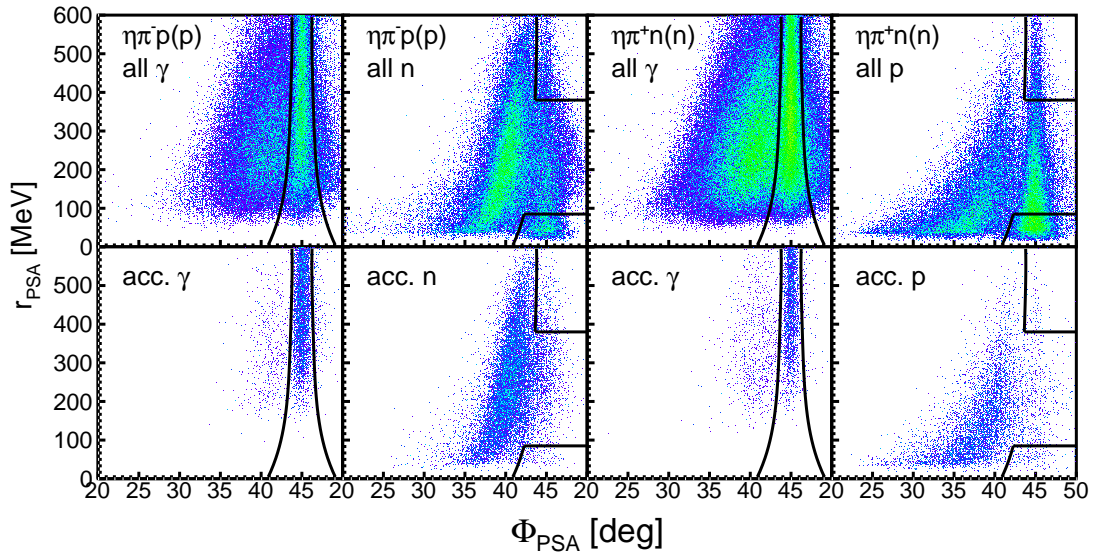


Figure 5.13.: PSA spectra of the quasi-free exclusive photoproduction of $\eta\pi^\pm$ pairs. The top row shows the raw spectra without kinematic cuts, the bottom row shows the spectra after applying kinematic cuts. The solid lines show the positions of the PSA-Cuts.

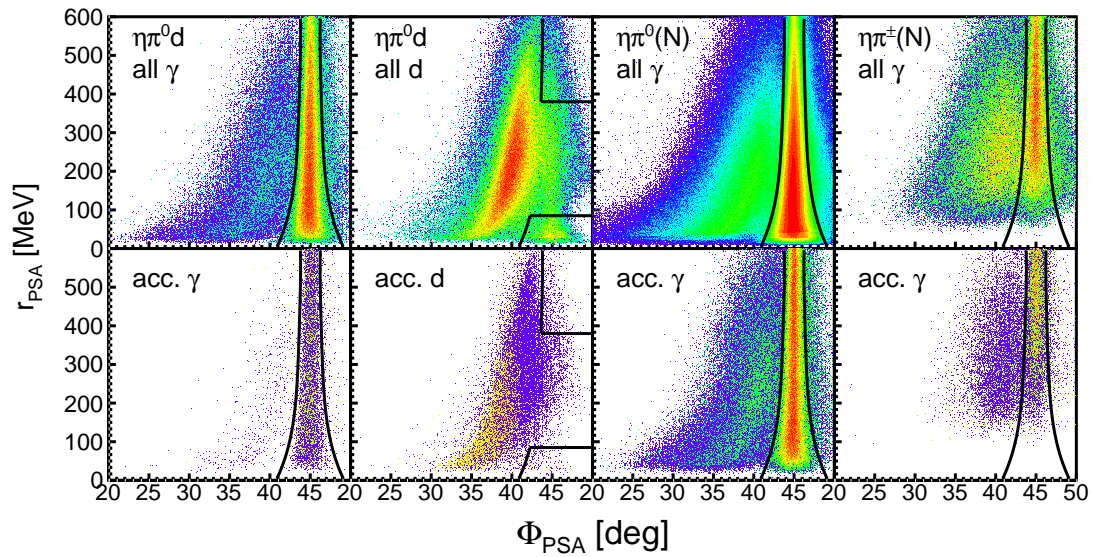


Figure 5.14.: PSA spectra of the coherent reaction $\eta\pi^0d$, the quasi-free inclusive reaction $\eta\pi^0(N)$ and the quasi-free inclusive reaction $\eta\pi^\pm(N)$. The top row shows the raw spectra without kinematic cuts, the bottom row shows the spectra after applying kinematic cuts. The solid lines show the positions of the PSA-Cuts.

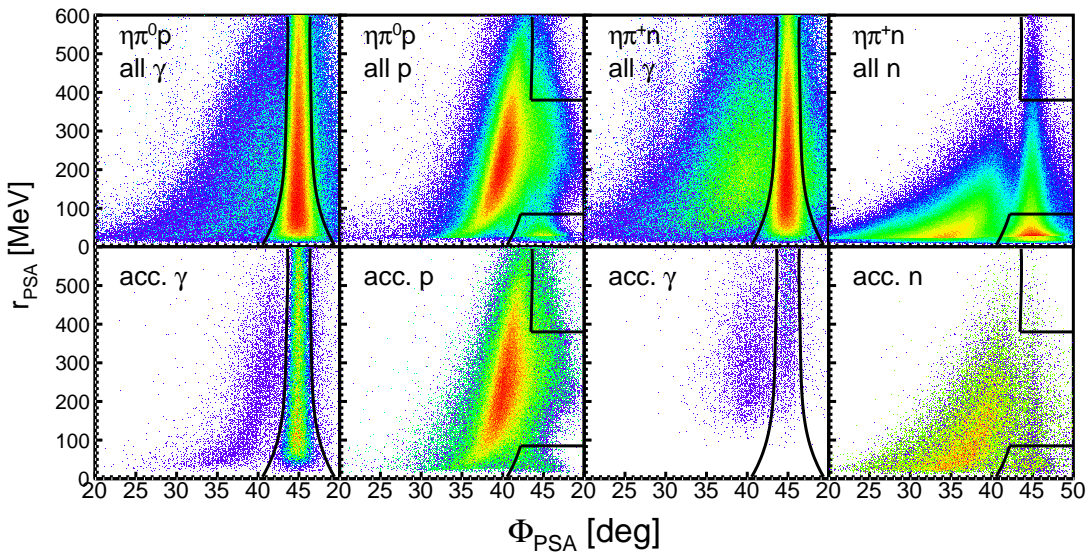


Figure 5.15.: PSA spectra of the reactions on free protons. The top row shows the raw spectra without kinematic cuts, the bottom row shows the spectra after applying kinematic cuts. The solid lines show the positions of the PSA-Cuts.

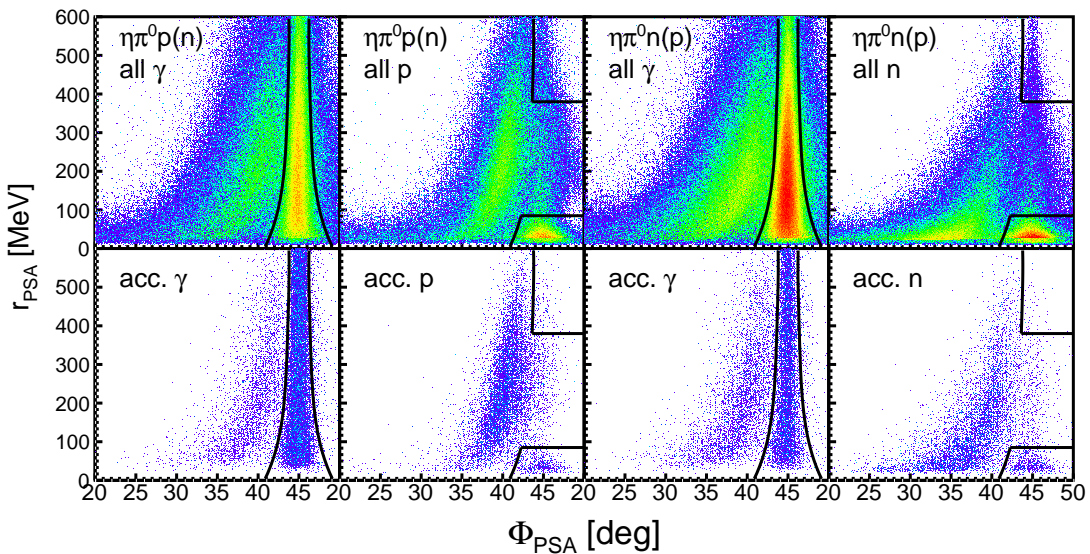


Figure 5.16.: PSA spectra of the quasi-free exclusive photoproduction of $\eta\pi^0$ pairs for the dButanol data. The top row shows the raw spectra without kinematic cuts, the bottom row shows the spectra after applying analysis cuts. The solid lines show the positions of the PSA-Cuts.

5.5.2. Coplanarity Cut

For the exclusive channels, where the recoil nucleons have to be detected, a condition on the difference in azimuthal angle between the $\eta\pi$ system and the recoil nucleon can be applied.

The situation is easier for single meson photoproduction. In this case, the meson lies in the plane that is spanned by the incident photon and the recoil nucleon due to momentum conservation. If it is also assumed, that the target is at rest, the difference in the azimuthal angle $\Delta\Phi$ in the cm system has to be 180° , but since the nucleons inside the deuteron are not at rest but carry small Fermi momentum, the $\Delta\Phi$ distributions will be smeared out.

The Lorentz boost transforming the cm frame to the laboratory frame takes place along the z-axis, since the target is at rest, and the incoming photon moves in z-direction. Since Φ is independent of z, the difference on Φ can be calculated directly in the laboratory frame.

For three-body final states, this condition is not directly applicable. Therefore, in this work the η and π mesons were combined to one 'effective' meson resulting in a quasi-two-body system, so that the co-planarity condition with the recoil nucleon could be applied.

$$\begin{aligned}\Delta\phi &= \phi_{\eta\pi} - \phi_N && \text{if } \phi_{\eta\pi} - \phi_N \geq 0 \\ \Delta\phi &= \pi - |\phi_{\eta\pi} - \phi_N| && \text{if } \phi_{\eta\pi} - \phi_N < 0,\end{aligned}$$

The co-planarity spectra are shown in Figs. 5.17 - 5.23, where a rough cut on the invariant-masses of the mesons was applied $110 \text{ MeV} \leq m_\pi \leq 160 \text{ MeV}$, $500 \text{ MeV} \leq m_\eta \leq 600 \text{ MeV}$). Since the width of the $\Delta\Phi$ distributions is highly energy dependent, the co-planarity cut was determined as a function of the photon energy.

For the quasi free reactions, there is almost no background visible with exception of the $\eta\pi^+$ channel. In this channel the co-planarity cut was set at $\pm 3\sigma$ with respect to the peak, to reject background. For the remaining quasi-free channels, the cut positions were set at $\pm 4\sigma$.

The free $\eta\pi^0$ reaction as well as the coherent reaction on the deuteron are also almost background free, thus wide cuts were chosen at $\pm 4\sigma$. For the free $\eta\pi^+$ reaction the cut positions were chosen at $\pm 3\sigma$ to reject the small background contribution.

Figures 5.24 and 5.24 show the coplanarity spectra of the reactions on the butanol, compared to the deuterium. The dButanol spectra are somewhat broader than the corresponding deuterium spectra. This broadening is caused by the larger Fermi-momentum in the dButanol (see Fig 5.61).

For all spectra, the experimental data are shown as red triangles. MC simulations of the reactions of interest are shown as blue solid lines. MC Simulations of background reactions are shown in green. The experimental data were fitted with the sum (black) of the signal simulation and the background contributions.

$$\gamma p(n) \rightarrow \eta\pi^0 p(n)$$

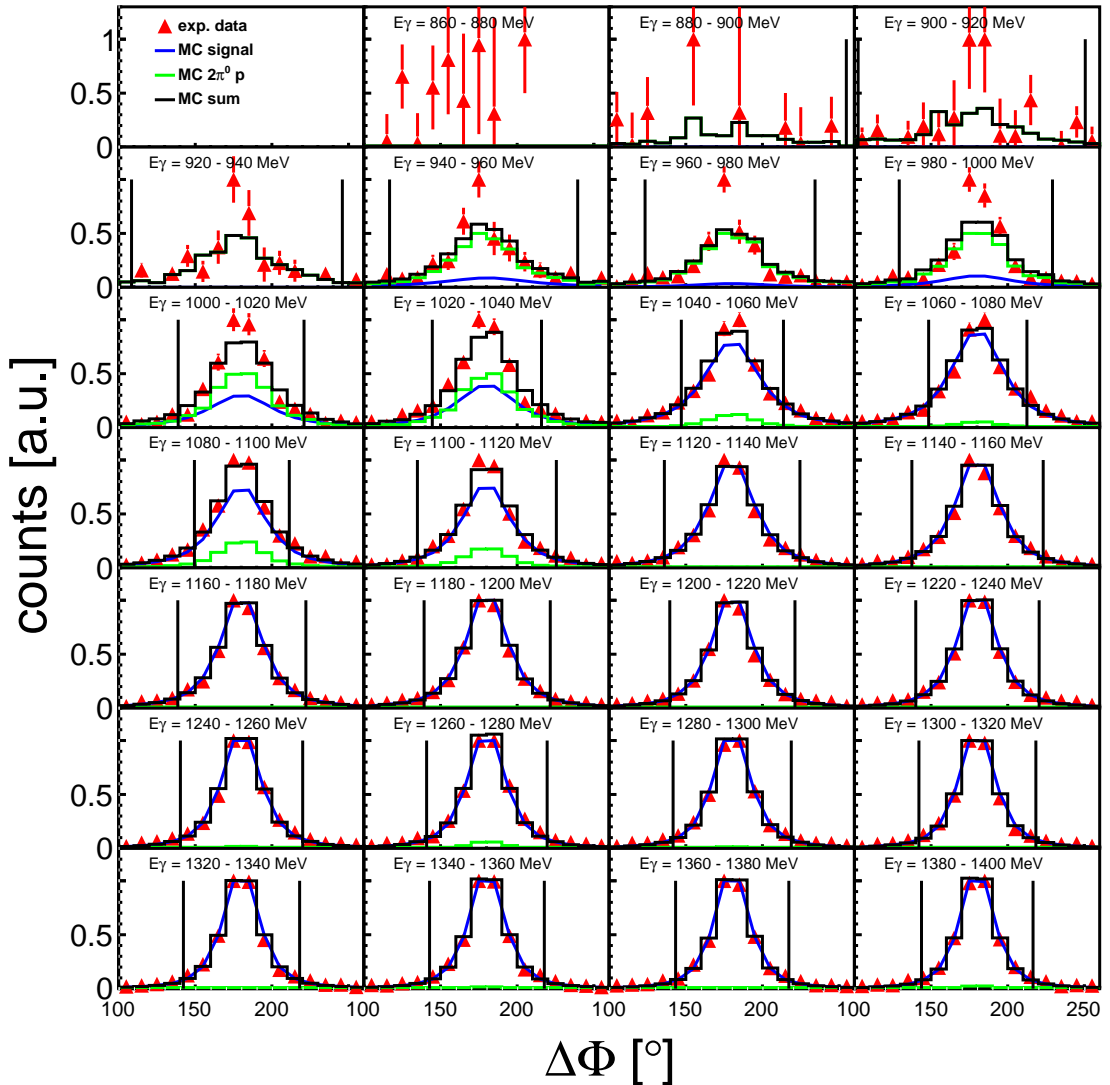


Figure 5.17.: Spectrum of the Φ difference between the combined meson system and the recoil nucleon of the reaction $\gamma p(n) \rightarrow \eta\pi^0 p(n)$. Red triangles: experimental data. Blue solid line: simulated data of the reaction. Green solid line: simulated background reaction $\gamma p(n) \rightarrow \pi^0\pi^0 p(n)$. Black solid line: sum of the simulated data. Vertical lines: cut positions.

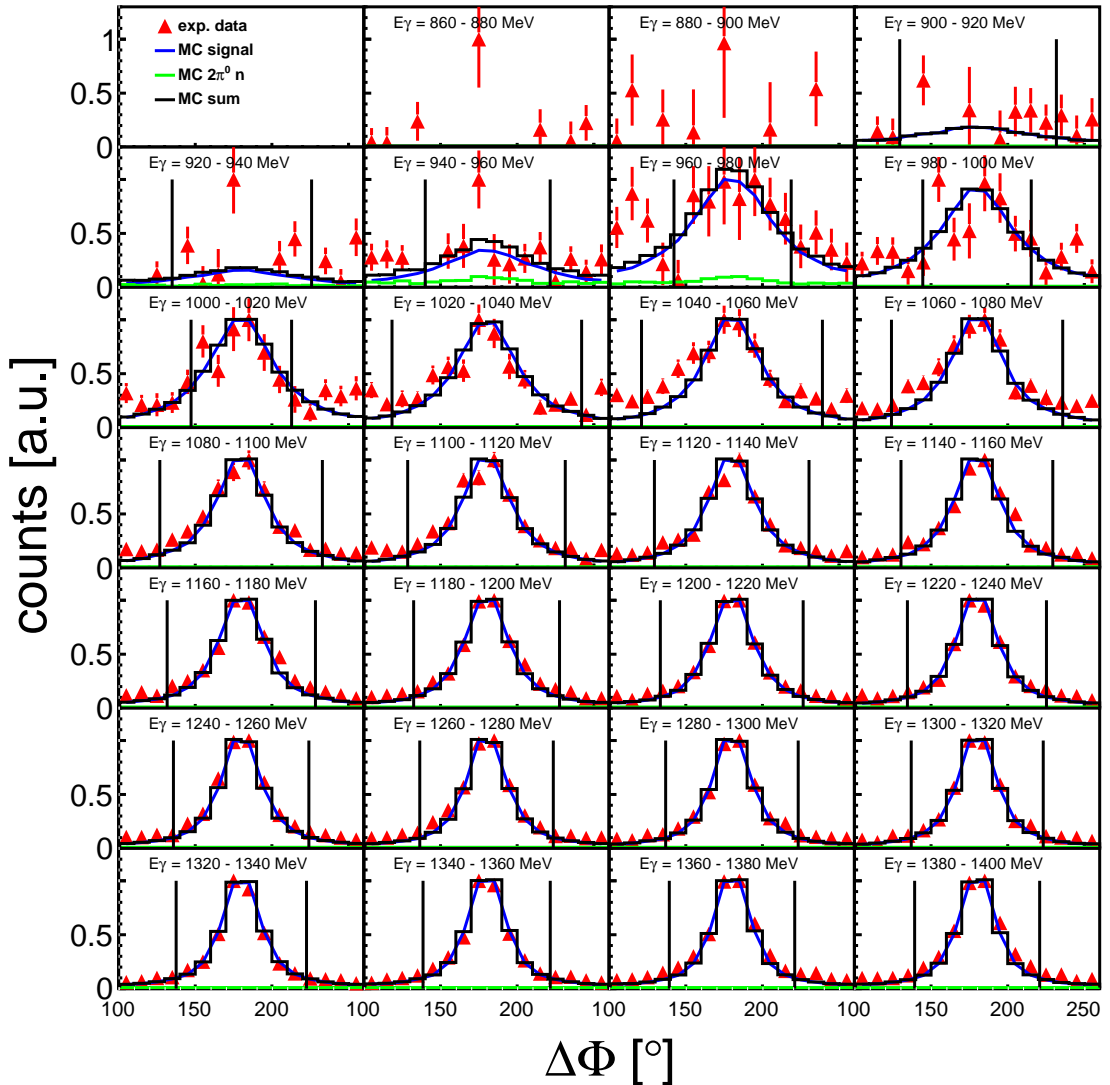
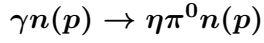


Figure 5.18.: Spectrum of the Φ difference between the combined meson system and the recoil nucleon of the reaction $\gamma n(p) \rightarrow \eta\pi^0 n(p)$. Red triangles: experimental data. Blue solid line: simulated data of the reaction. Green solid line: simulated background reaction $\gamma n(p) \rightarrow \pi^0\pi^0 n(p)$. Black solid line: sum of the simulated data. Vertical lines: cut positions.

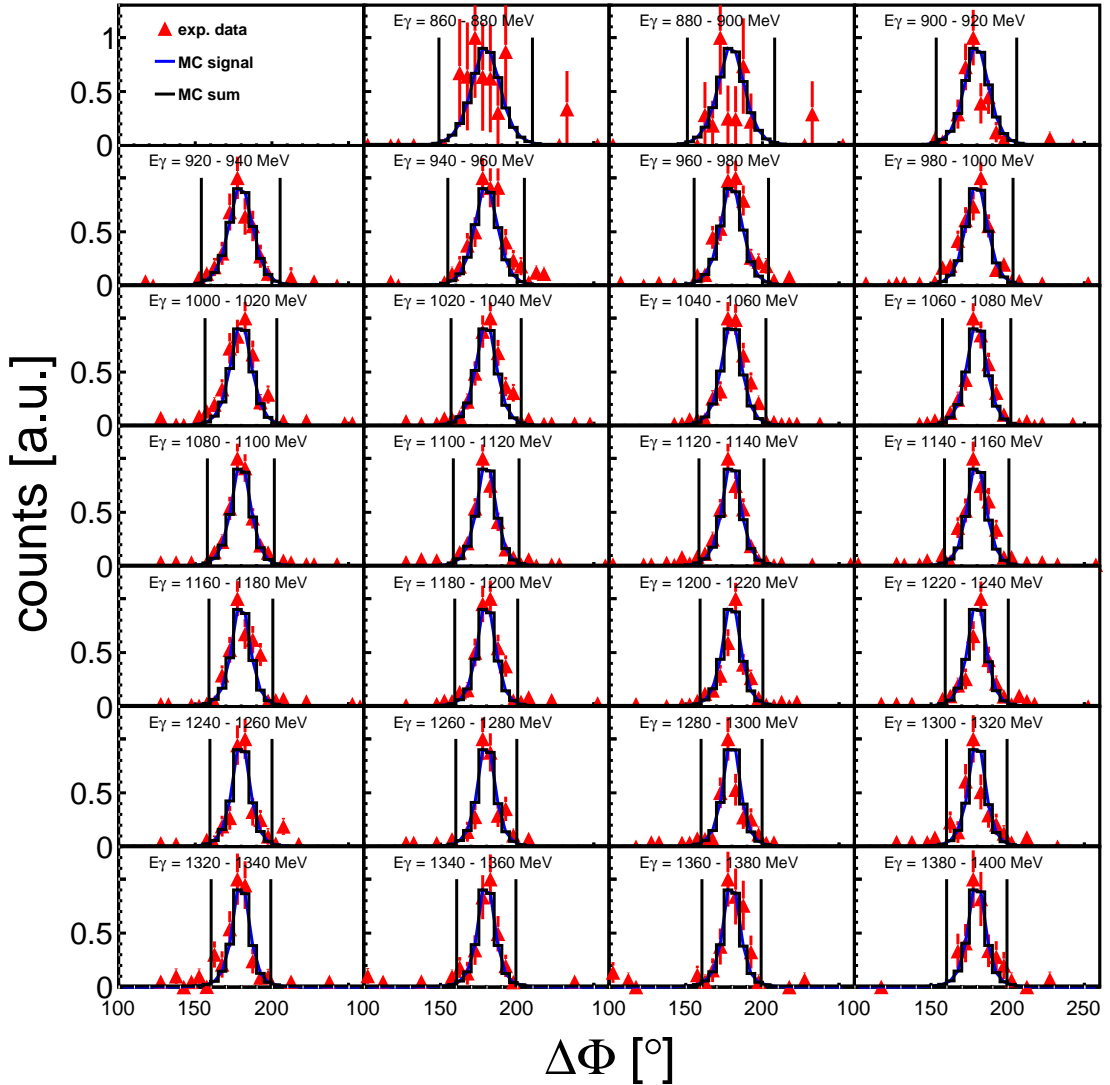
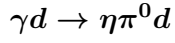


Figure 5.19.: Spectrum of the Φ difference between the combined meson system and the recoil deuteron of the reaction $\gamma d \rightarrow \eta\pi^0d$. Due to the absence of Fermi motion, the peaks are narrower than in the spectra of the quasi free reactions. Red triangles: experimental data. Blue solid line: simulated data of the reaction. Green solid line: simulated background reaction $\gamma p(n) \rightarrow \pi^0\pi^0p(n)$. Black solid line: sum of the simulated data. Vertical lines: cut positions.

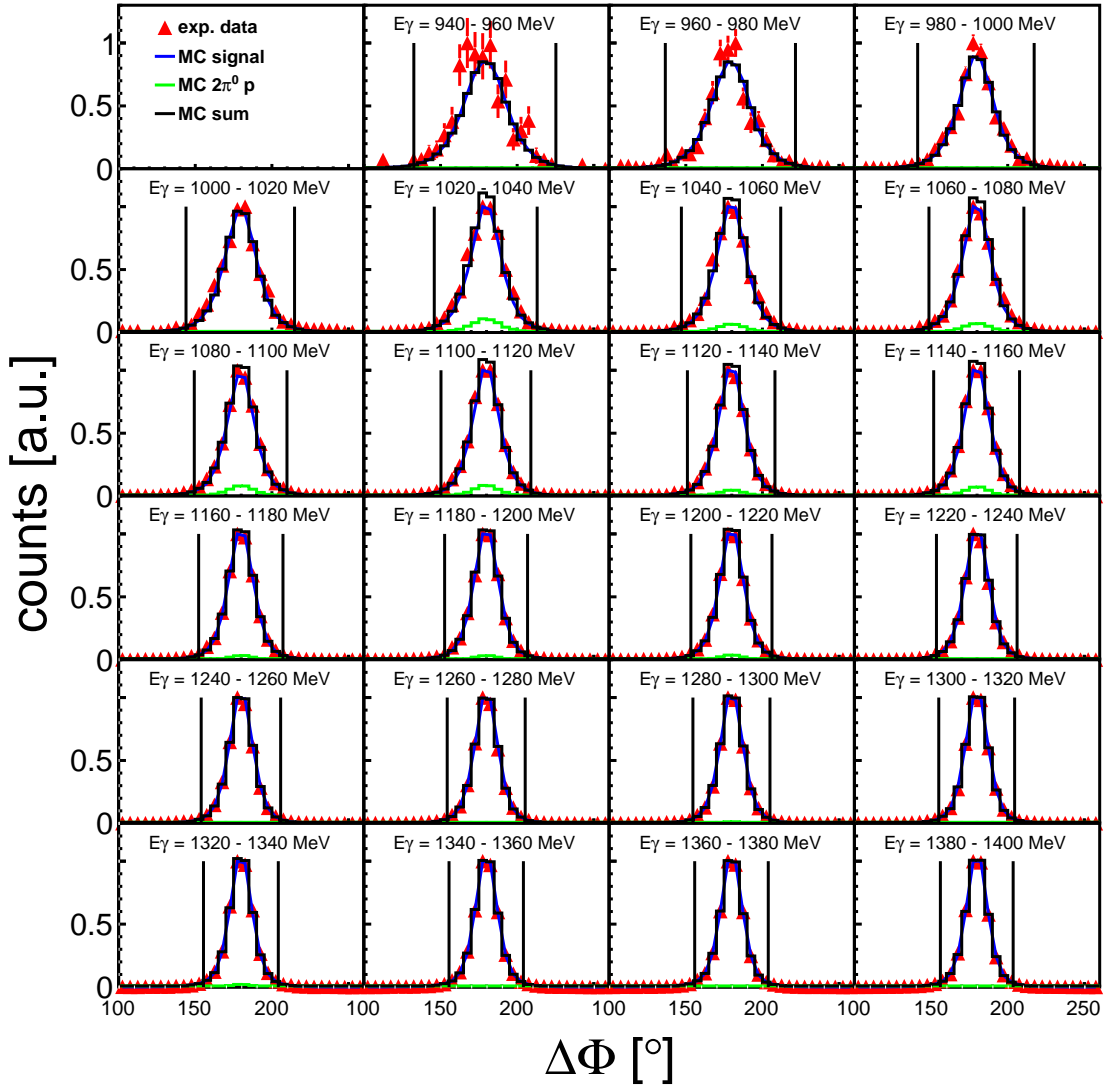
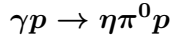


Figure 5.20.: Spectrum of the Φ difference between the combined meson system and the recoil nucleon of the reaction $\gamma p \rightarrow \eta\pi^0 p$. Due to the absence of Fermi motion, the peaks are narrower than in the spectra of the quasi free reactions. Red triangles: experimental data. Blue solid line: simulated data of the reaction. Green solid line: simulated background reaction $\gamma p \rightarrow \pi^0\pi^0 p$. Black solid line: sum of the simulated data. Vertical lines: cut positions.

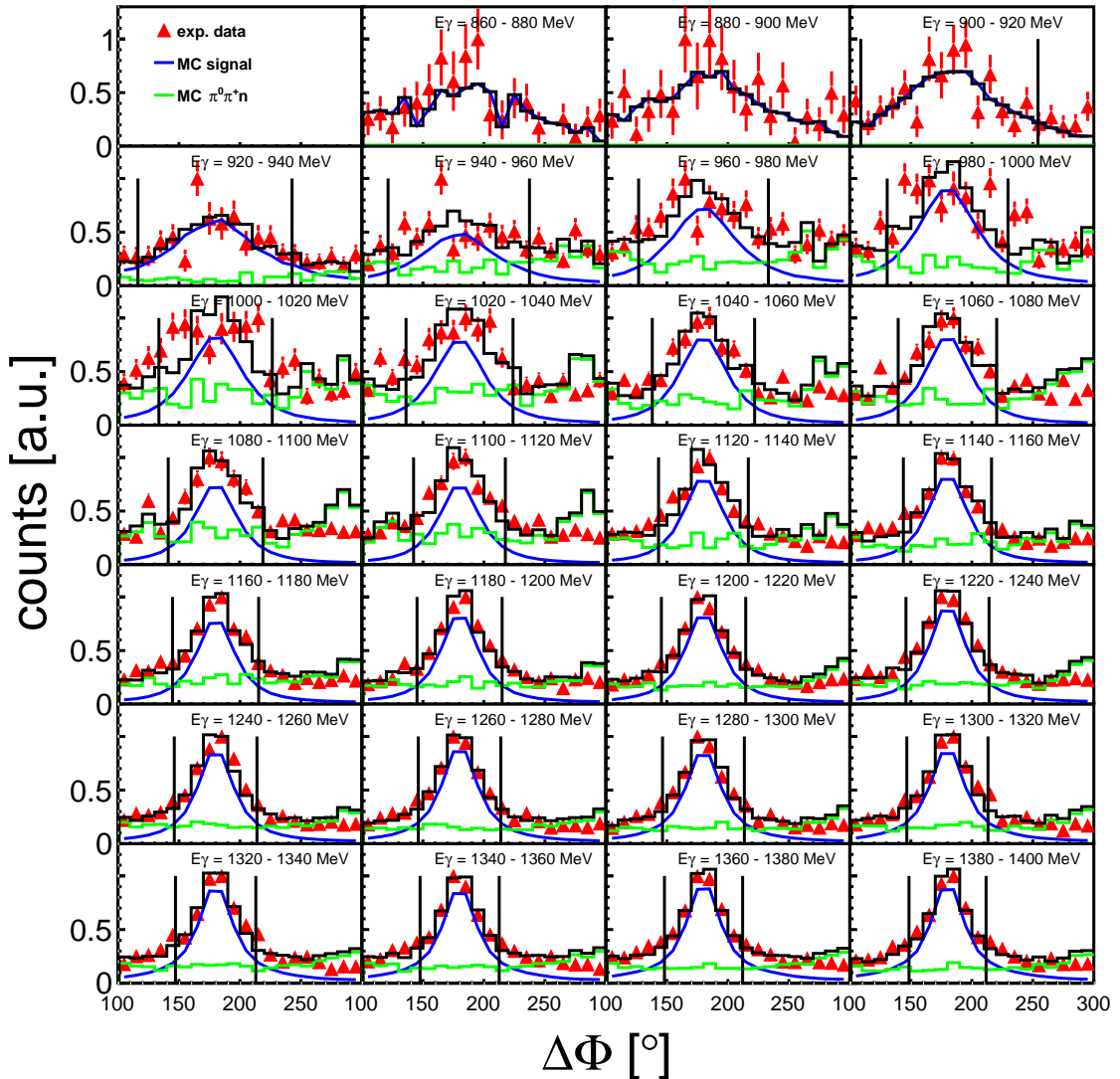
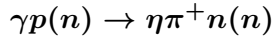


Figure 5.21.: Spectrum of the Φ difference between the combined meson system and the recoil nucleon of the reaction $\gamma p(n) \rightarrow \eta\pi^+ n(n)$. Red triangles: experimental data. Blue solid line: simulated data of the reaction. Green solid line: simulated background reaction $\gamma p(n) \rightarrow \pi^0\pi^+p(n)$. Black solid line: sum of the simulated data. Vertical lines: cut positions.

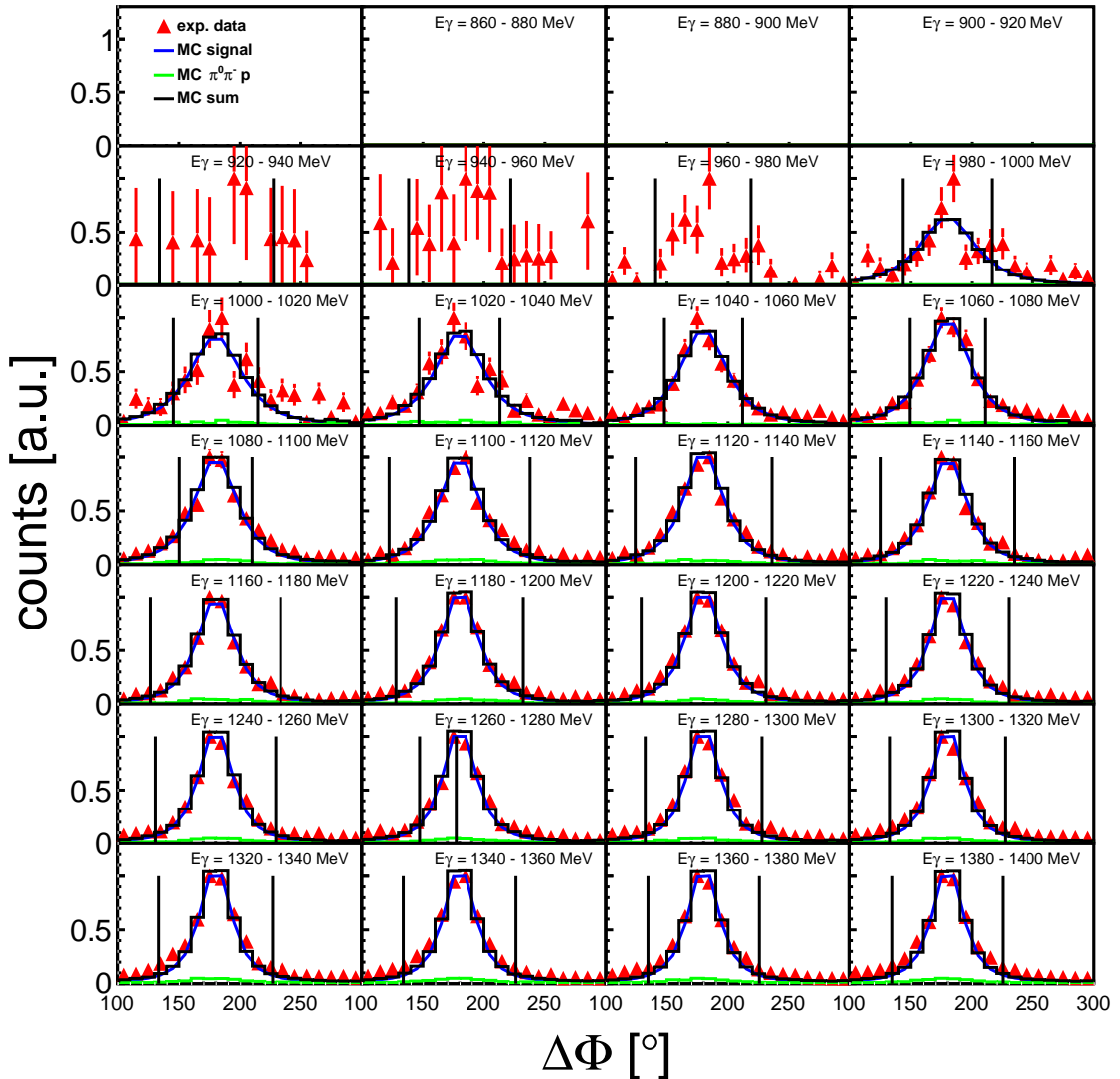
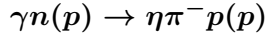


Figure 5.22.: Spectrum of the Φ difference between the combined meson system and the recoil nucleon of the reaction $\gamma n(p) \rightarrow \eta\pi^- p(p)$. Red triangles: experimental data. Blue solid line: simulated data of the reaction. Green solid line: simulated background reaction $\gamma n(p) \rightarrow \pi^0\pi^- p(p)$. Black solid line: sum of the simulated data. Vertical lines: cut positions.

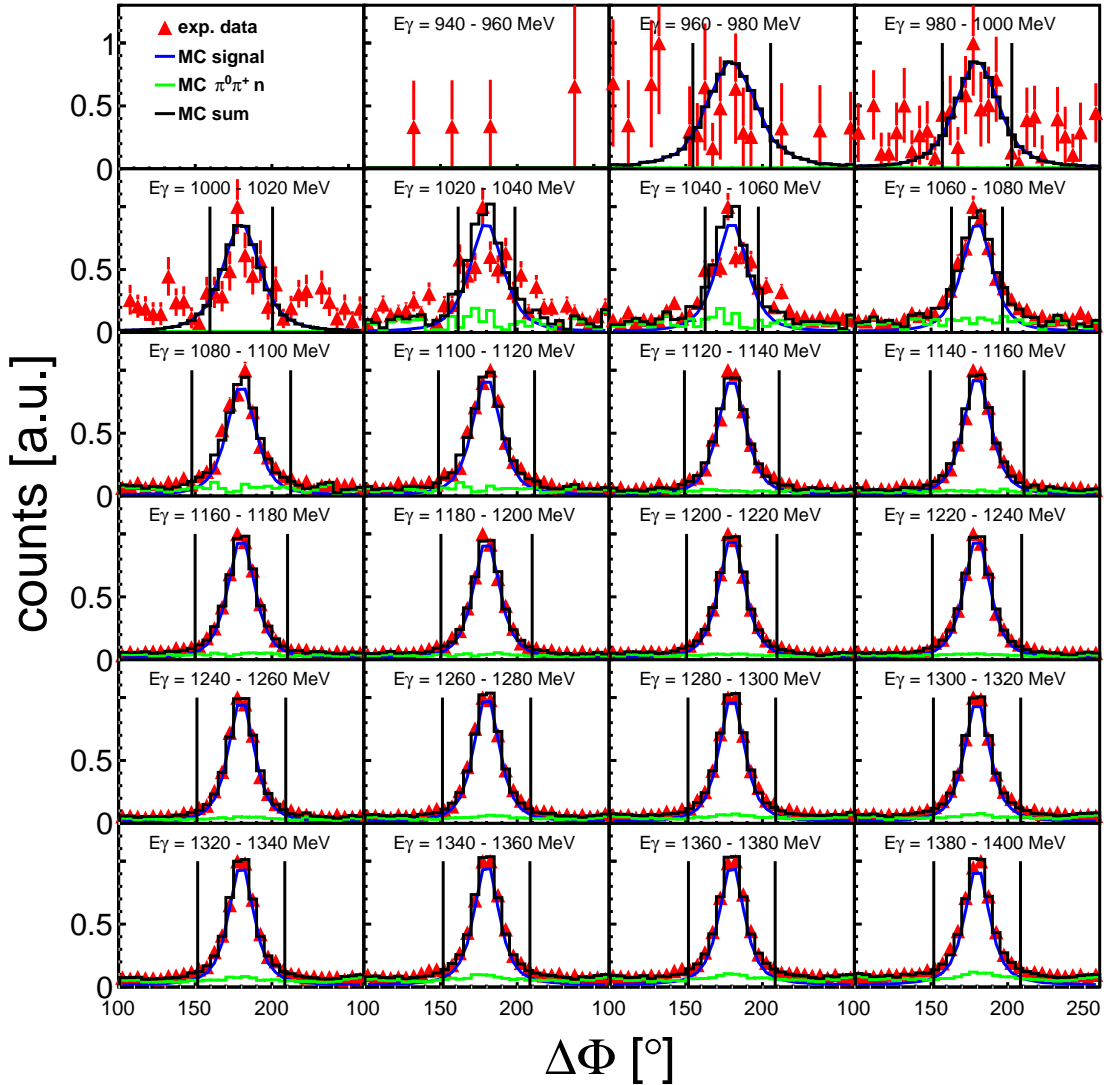
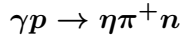


Figure 5.23.: Spectrum of the Φ difference between the combined meson system and the recoil nucleon of the reaction $\gamma p \rightarrow \eta\pi^+n$. Red triangles: experimental data. Blue solid line: simulated data of the reaction. Green solid line: simulated background reaction $\gamma p \rightarrow \pi^0\pi^+p$. Black solid line: sum of the simulated data. Vertical lines: cut positions.

$\gamma p(n) \rightarrow \eta\pi^0 p(n)$ for dButanol

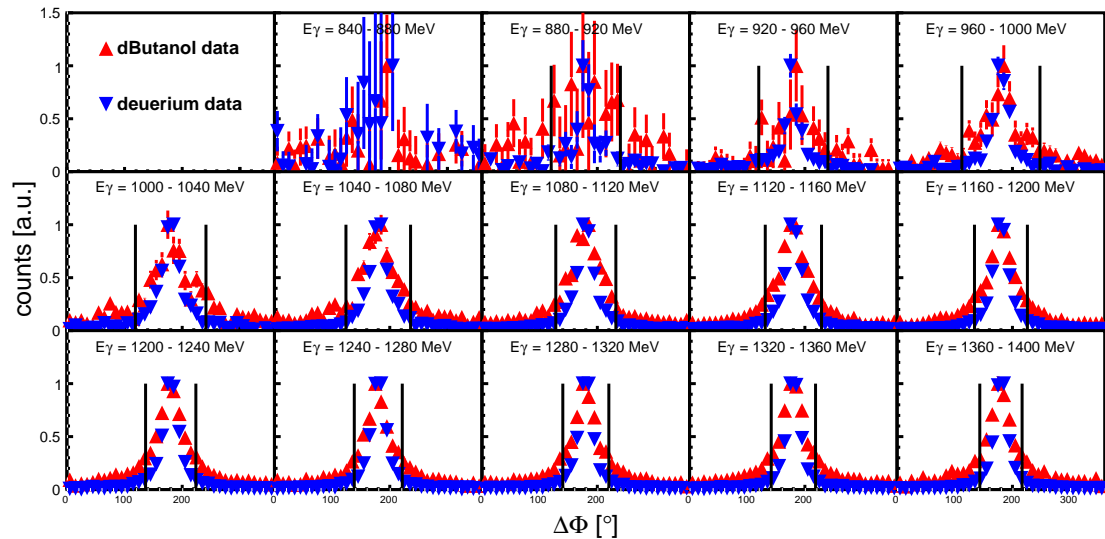


Figure 5.24.: Spectrum of the Φ difference between the combined meson system and the recoil nucleon of the reaction $\gamma p(n) \rightarrow \eta\pi^0 p(n)$ on dButanol. Red triangles: polarized butanol data. Blue triangles: unpolarized deuterium data. Vertical lines: cut positions.

$\gamma n(p) \rightarrow \eta\pi^0 n(p)$ for dButanol

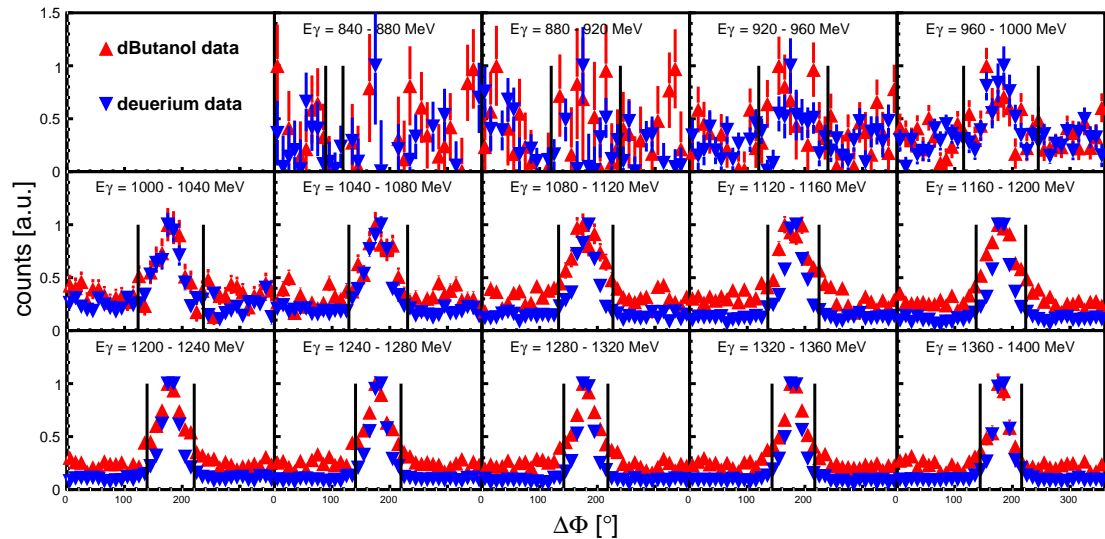


Figure 5.25.: Spectrum of the Φ difference between the combined meson system and the recoil nucleon of the reaction $\gamma p(n) \rightarrow \eta\pi^0 p(n)$ on dButanol. Red triangles: polarized butanol data. Blue triangles: unpolarized deuterium data. Vertical lines: cut positions.

5.5.3. Missing Mass Cut

Another method to identify the reactions of interest and to remove unwanted background contributions, is the investigation of the missing mass.

The missing mass is defined as:

$$M = \sqrt{\left(\sum_i p_i^{IS} - \sum_j p_j^{FS} \right)^2} = \sqrt{\left(\sum_i E_i^{IS} - \sum_j E_j^{FS} \right)^2 - \left(\sum_i \vec{p}_i^{IS} - \sum_j \vec{p}_j^{FS} \right)^2}, \quad (5.18)$$

where $p_i = (E_i^{IS}, \vec{p}_i^{IS})$ is the four vector of the i-th particle in the initial state and $p_j = (E_j^{FS}, \vec{p}_j^{FS})$ is the four vector of the j-th particle in the final state.

In this work the recoil nucleon, even when detected, was treated as missing, hence the missing mass was calculated via:

$$M = \sqrt{(E_\gamma + m_P - E_\eta - E_\pi)^2 - (\vec{p}_\gamma - \vec{p}_\eta - \vec{p}_\pi)^2}, \quad (5.19)$$

where E_γ and \vec{p}_γ are the energy and momentum of the incident photon, E_η and \vec{p}_η are the energy and momentum of the η , E_π and \vec{p}_π are energy and momentum of the π and m_P is the mass of the participating nucleon, that is assumed to be at rest. If the mesons were correctly identified and originated from the reaction of interest the missing mass distributions should peak at the nominal participant nucleon mass.

For all reaction channels the nominal mass of the participant was subtracted from M to align the resulting distributions at zero.

$$\Delta M = M - m_P \quad (5.20)$$

The resulting missing mass spectra and the used cuts for all investigated reactions are shown in Figs. 5.26 - 5.34 in the following sections. The spectra were filled with applied coplanarity cut and a rough invariant mass cut ($110 \text{ MeV} \leq m_\pi \leq 160 \text{ MeV}$, $500 \text{ MeV} \leq m_\eta \leq 600 \text{ MeV}$).

Figures 5.35 and 5.36 compare the butanol spectra to the deuterium spectra. Again broadening due to the higher Fermi-momentum of the dButanol is visible.

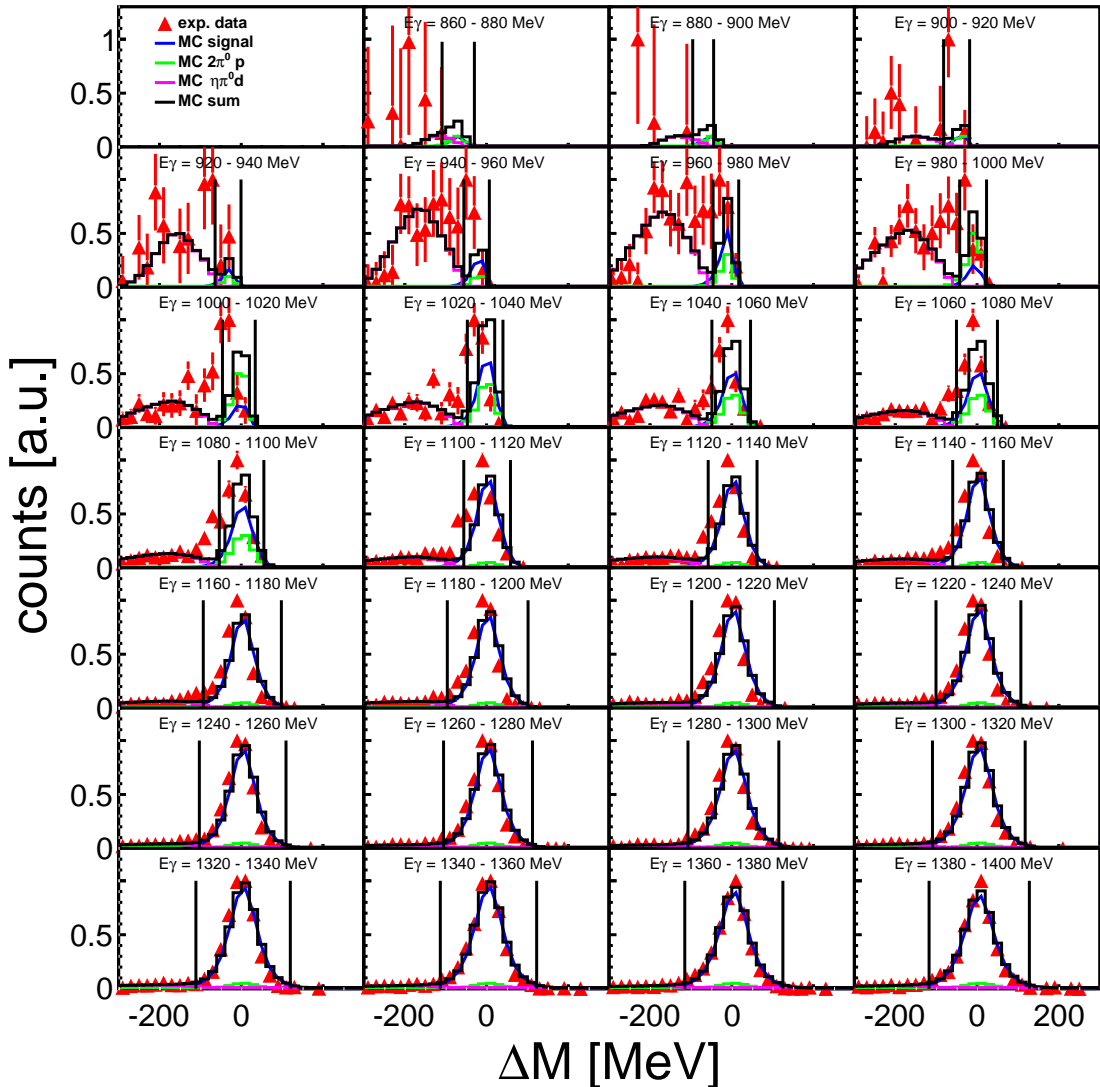
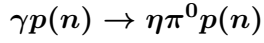


Figure 5.26.: Missing mass spectrum of the reaction $\gamma p(n) \rightarrow \eta\pi^0 p(n)$. Red triangles: experimental data. Blue solid line: simulated data of the reaction. Green solid line: simulated background reaction $\gamma p(n) \rightarrow \pi^0\pi^0 p(n)$. Magenta solid line: simulated background reaction $\gamma d \rightarrow \eta\pi^0 d$. Black solid line: sum of the simulated data. Vertical lines: Cut positions.

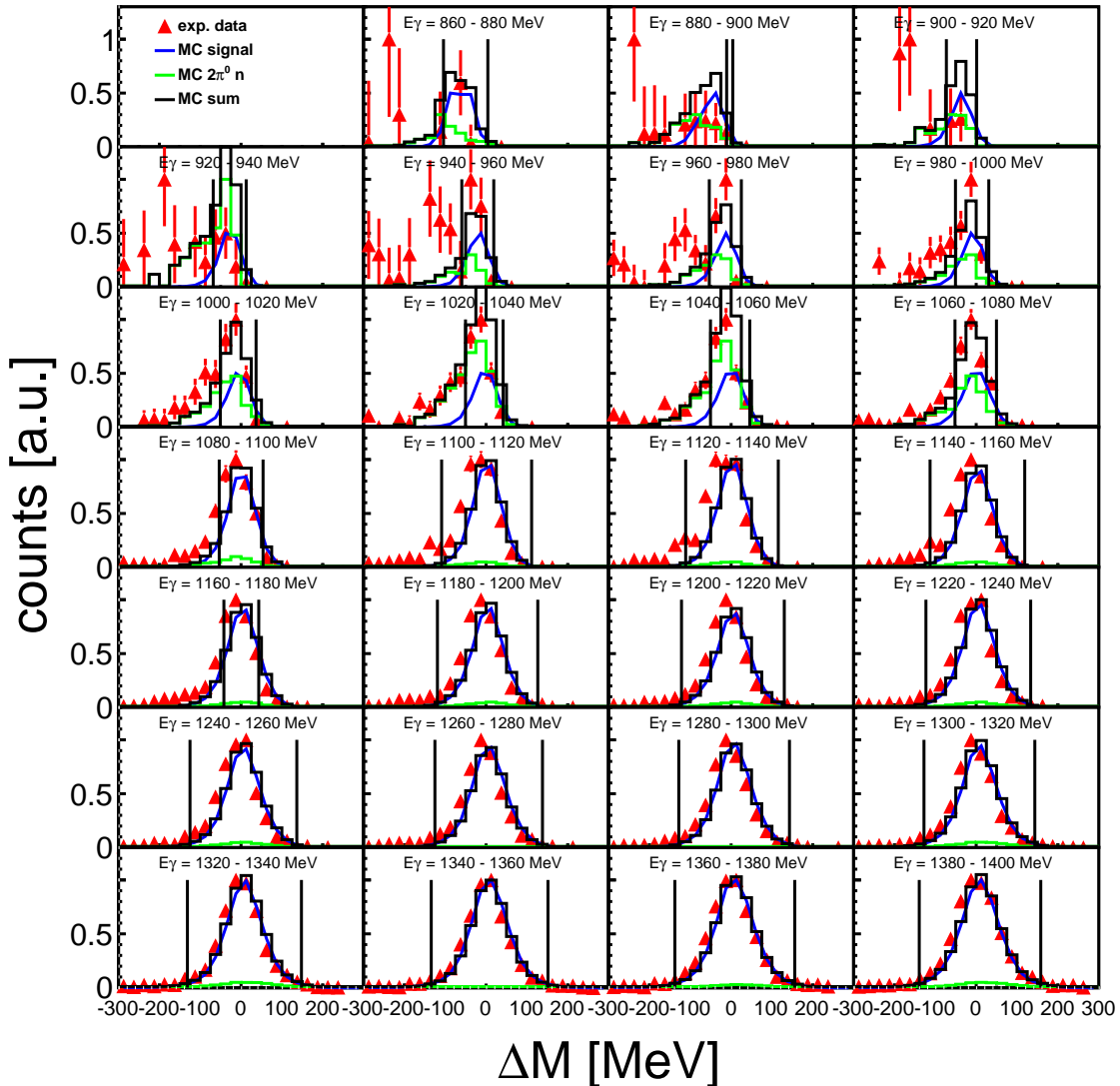
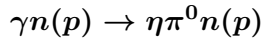


Figure 5.27.: Missing mass spectrum of the reaction $\gamma n(n) \rightarrow \eta\pi^0 n(p)$. Red triangles: experimental data. Blue solid line: simulated data of the reaction. Green solid line: simulated background reaction $\gamma n(p) \rightarrow \pi^0\pi^0 n(p)$. Black solid line: sum of the simulated data. Vertical lines: cut positions.

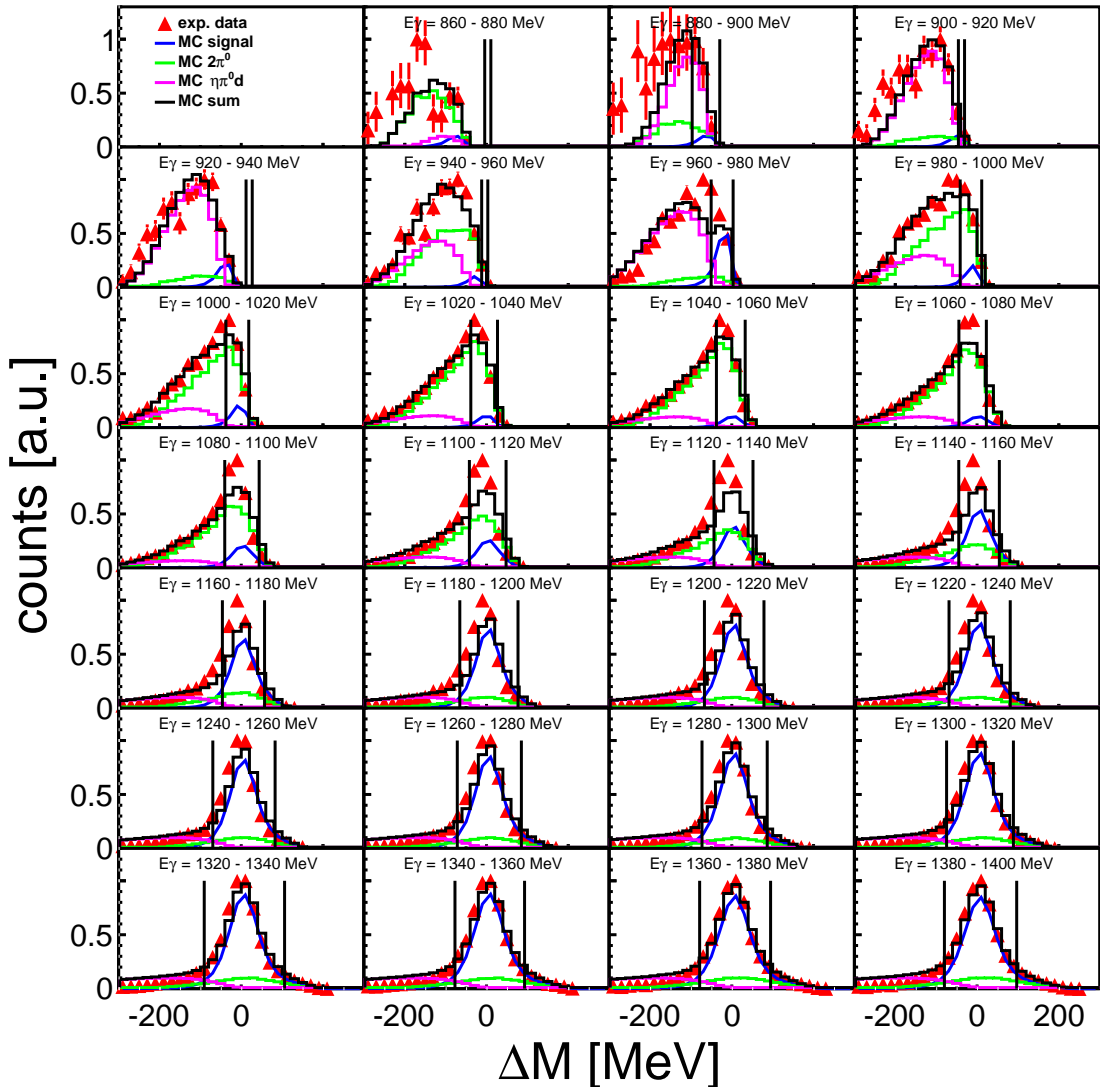
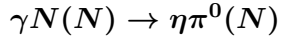


Figure 5.28.: Missing mass spectrum of the reaction $\gamma N(N) \rightarrow \eta\pi^0(N)$. Red triangles: experimental data. Blue solid line: simulated data of the reaction. Green solid line: simulated background reaction $\gamma p(n) \rightarrow \eta\pi^0 p(n)$. Magenta solid line: simulated background reaction $\gamma d \rightarrow \pi^0\pi^0 d$. Black solid line: sum of the simulated data. Vertical lines: cut positions.

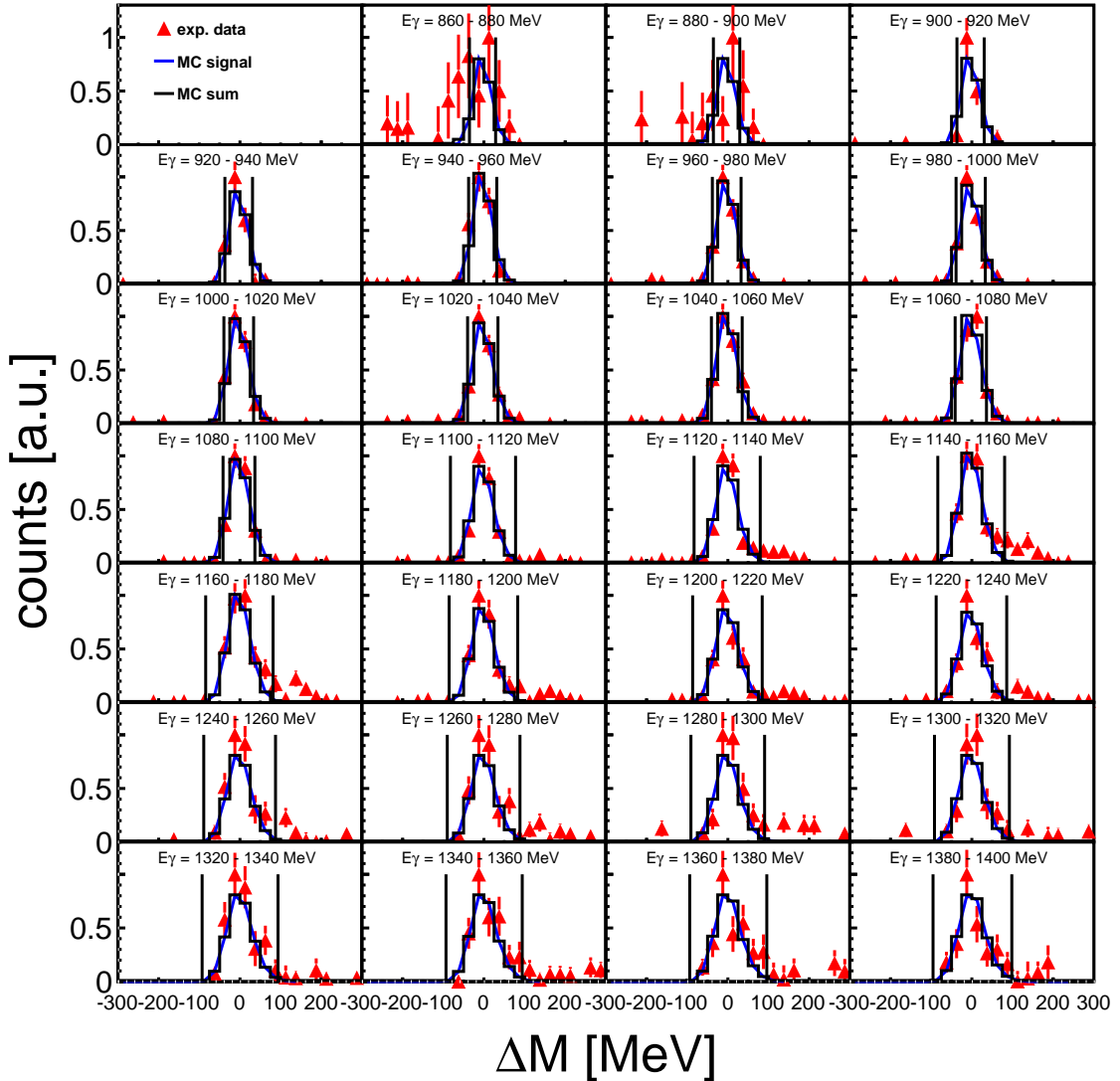
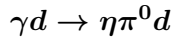


Figure 5.29.: Missing mass spectrum of the reaction $\gamma d \rightarrow \eta\pi^0d$. Due to the absence of Fermi motion, the peaks are narrower than in the spectra of the quasi free reactions. Red triangles: experimental data. Blue solid line: simulated data of the reaction. Green solid line: simulated background reaction $\gamma p(n) \rightarrow \pi^0\pi^0p(n)$. Black solid line: sum of the simulated data. Vertical lines: cut positions.

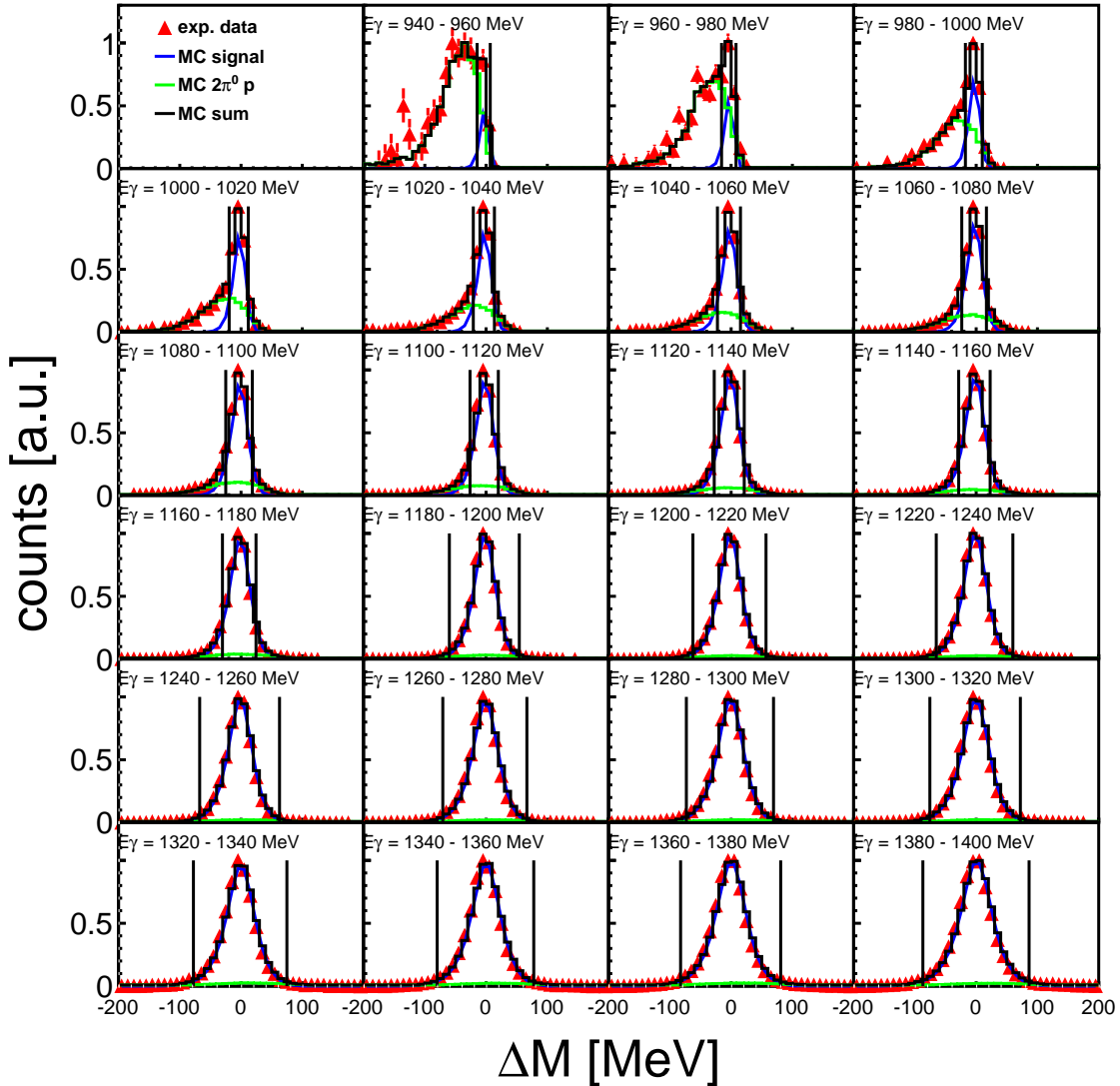
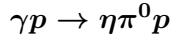


Figure 5.30.: Missing mass spectrum of the reaction $\gamma p \rightarrow \eta\pi^0 p$. Due to the absence of Fermi motion, the peaks are narrower than in the spectra of the quasi free reactions. Red triangles: experimental data. Blue solid line: simulated data of the reaction. Green solid line: simulated background reaction $\gamma p \rightarrow \pi^0\pi^0 p$. Black solid line: sum of the simulated data. Vertical lines: cut positions.

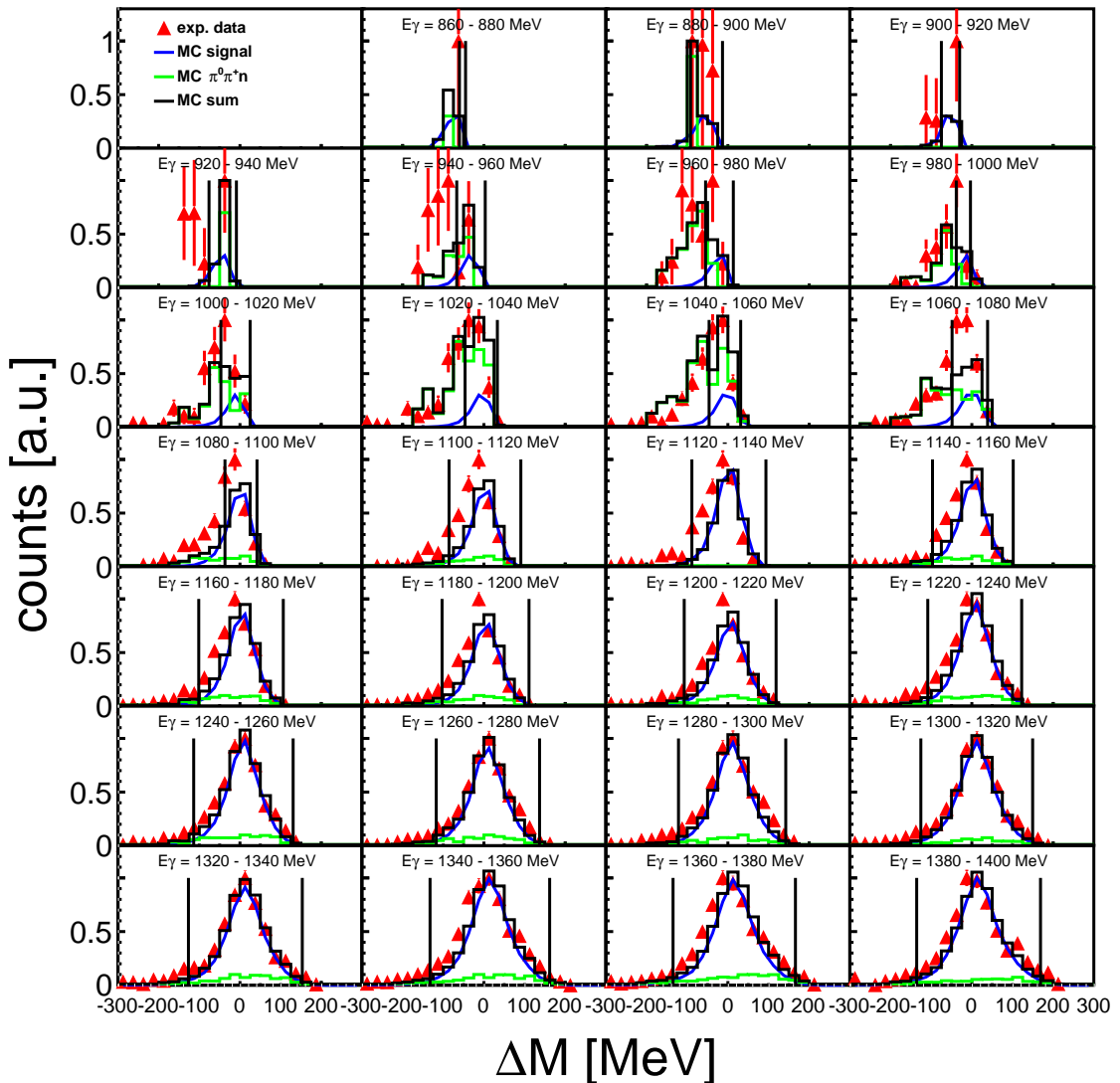
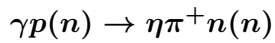


Figure 5.31.: Missing mass spectrum of the reaction $\gamma p(n) \rightarrow \eta\pi^+ n(n)$. Red triangles: experimental data. Blue solid line: simulated data of the reaction. Green solid line: simulated background reaction $\gamma p(n) \rightarrow \pi^0\pi^+p(n)$. Black solid line: sum of the simulated data. Vertical lines: cut positions.

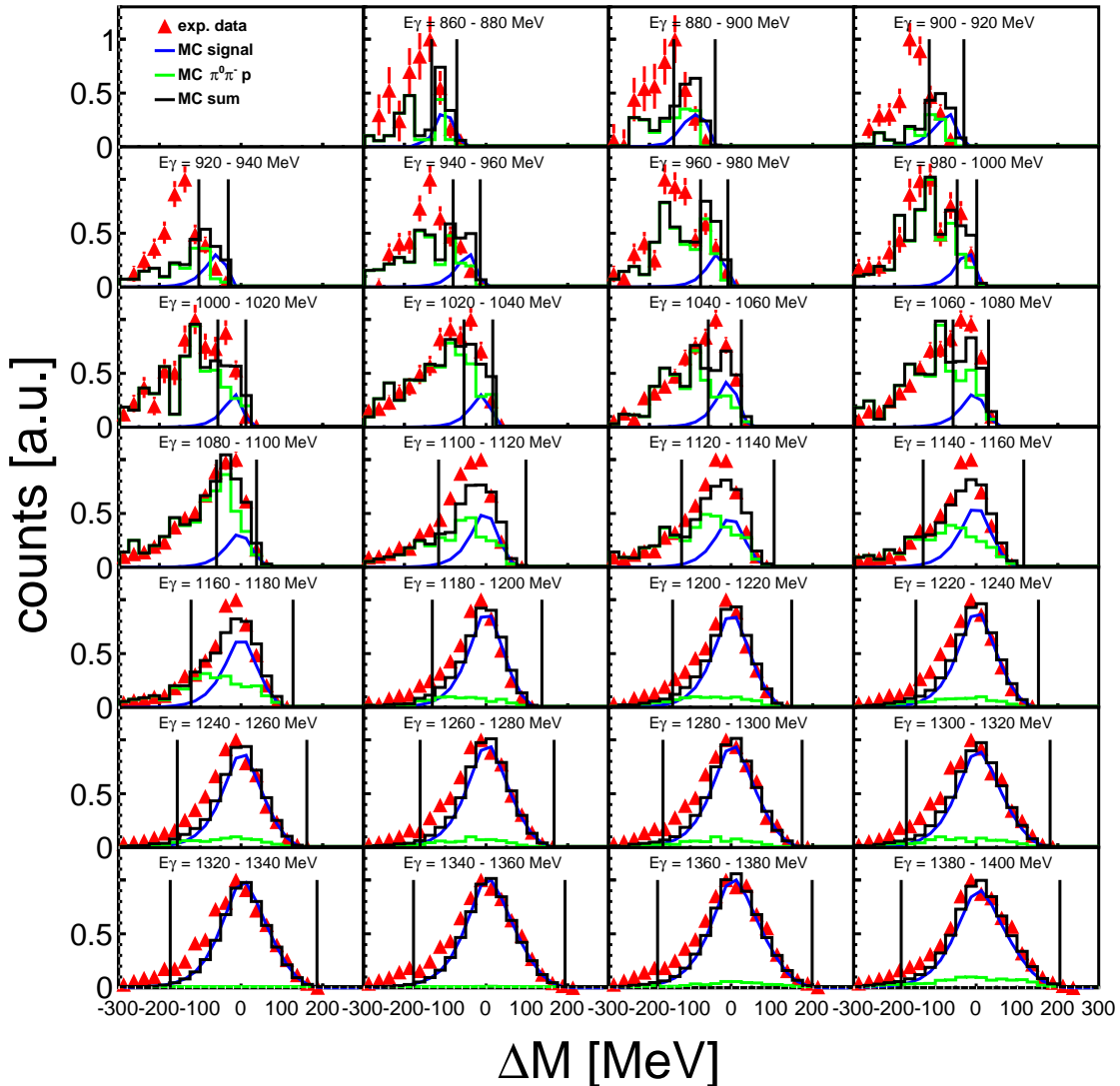
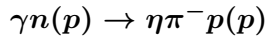


Figure 5.32.: Missing mass spectrum of the reaction $\gamma n(p) \rightarrow \eta\pi^- p(p)$. Red triangles: experimental data. Blue solid line: simulated data of the reaction. Green solid line: simulated background reaction $\gamma n(p) \rightarrow \pi^0\pi^- p(p)$. Black solid line: sum of the simulated data. Vertical lines: cut positions.

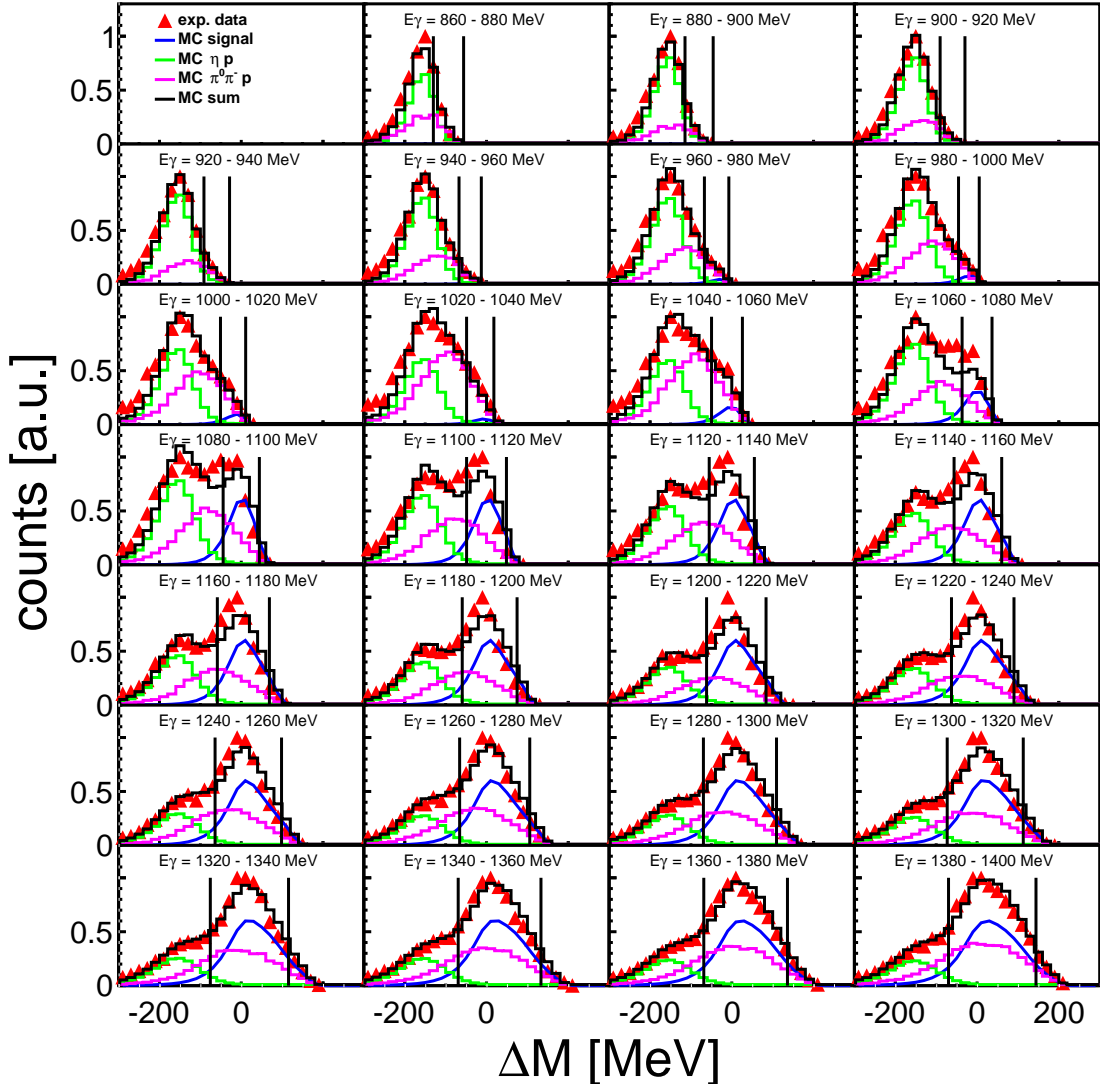
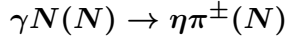


Figure 5.33.: Missing mass spectrum of the reaction $\gamma N(N) \rightarrow \eta\pi^\pm(N)$. Red triangles: experimental data. Blue solid line: simulated data of the reaction. Green solid line: simulated background reaction $\gamma p(n) \rightarrow \eta p(n)$. Magenta solid line: simulated background reaction $\gamma p(n) \rightarrow \pi^0 p(n)$. Black solid line: sum of the simulated data. Vertical lines: cut positions.

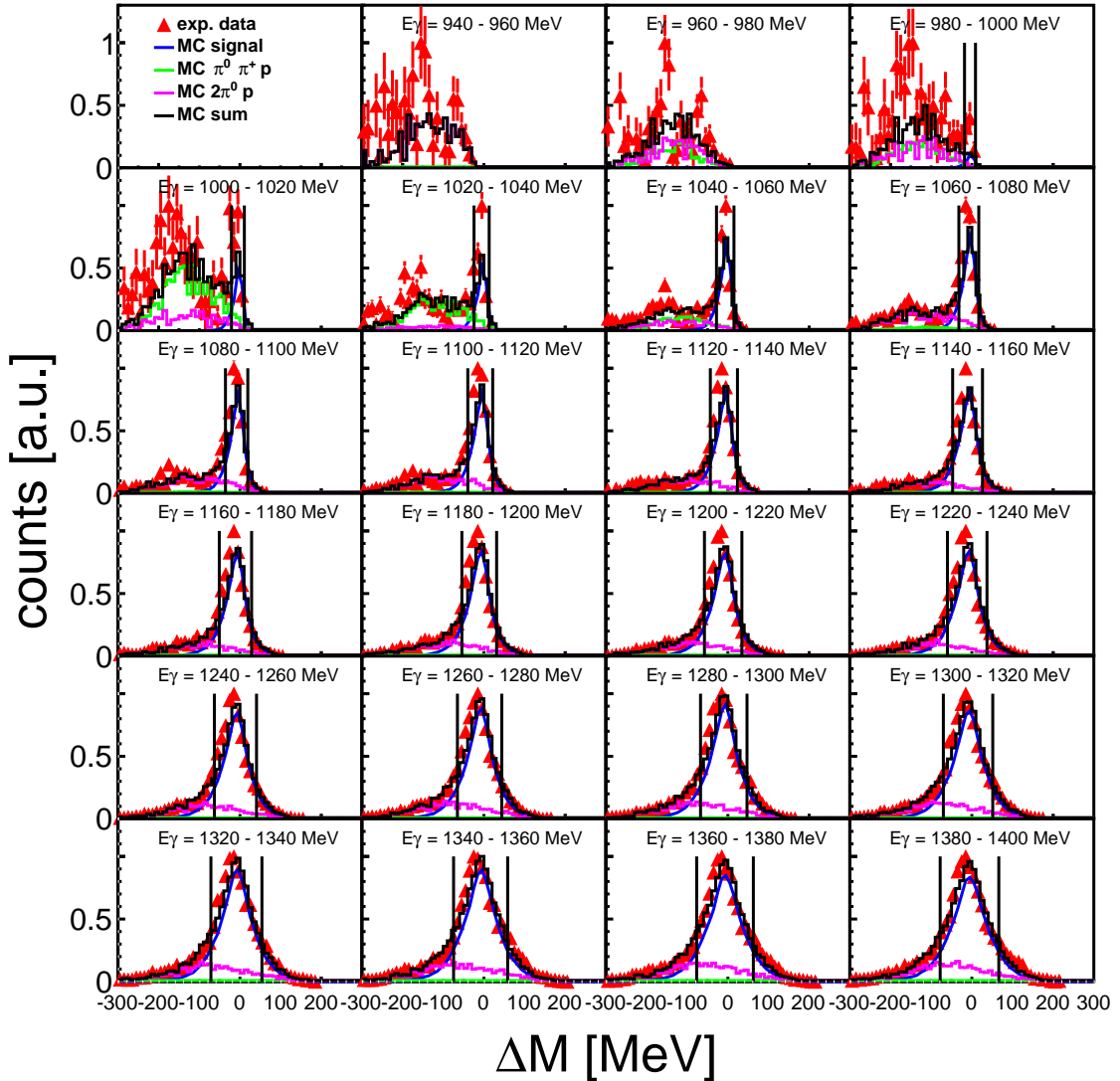
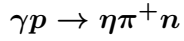


Figure 5.34.: Missing mass spectrum of the reaction $\gamma p \rightarrow \eta\pi^+n$. Red triangles: experimental data. Blue solid line: simulated data of the reaction. Green solid line: simulated background reaction $\gamma p \rightarrow \pi^0\pi^+p$. Magenta solid line: simulated background reaction $\gamma p \rightarrow \pi^0\pi^0p$. Black solid line: sum of the simulated data. Vertical lines: cut positions.

$\gamma p(n) \rightarrow \eta\pi^0 p(n)$ for dButanol

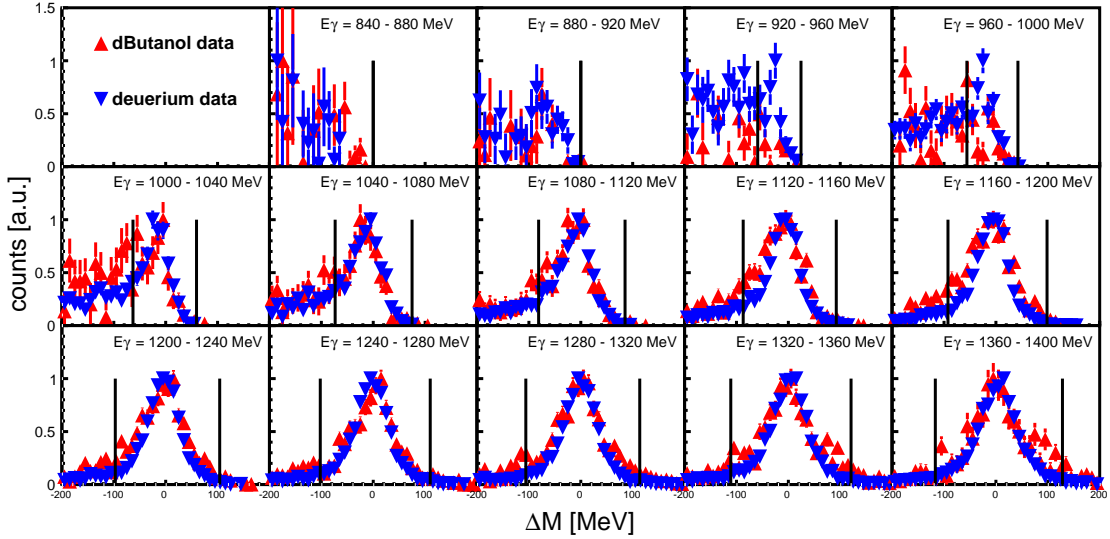


Figure 5.35.: Spectrum of the missing mass of the reaction $\gamma p(n) \rightarrow \eta\pi^0 p(n)$ on dButanol. Red triangles: polarized butanol data. Blue triangles: unpolarized deuterium data. Vertical lines: cut positions.

$\gamma n(p) \rightarrow \eta\pi^0 n(p)$ for dButanol

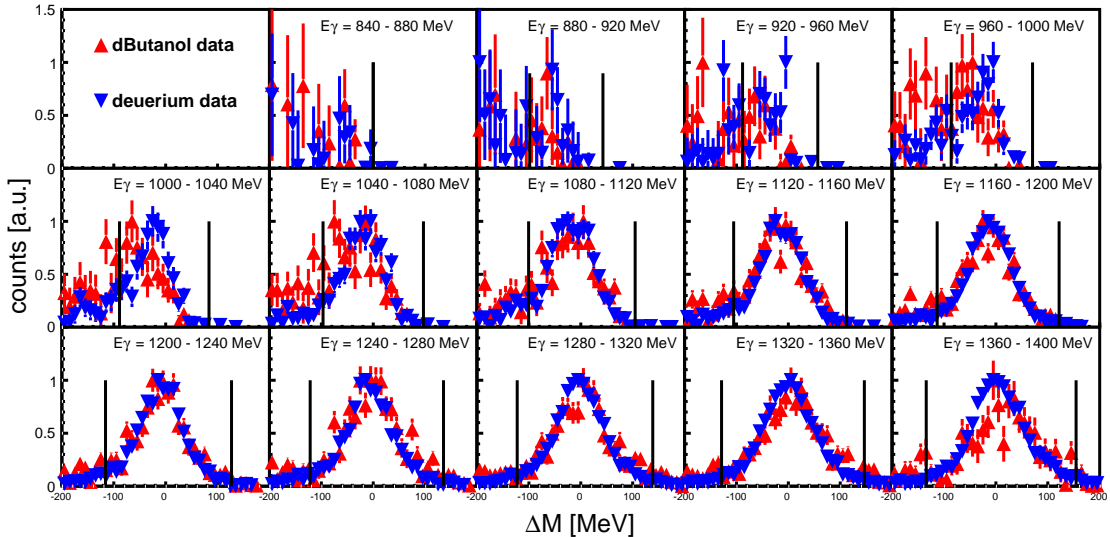


Figure 5.36.: Spectrum of the missing mass of the reaction $\gamma n(p) \rightarrow \eta\pi^0 n(p)$ on dButanol. Red triangles: polarized butanol data. Blue triangles: unpolarized deuterium data. Vertical lines: cut positions.

5.5.4. η Invariant Mass

Figures 5.37 - 5.45 show the η invariant mass for all analyzed channels after all kinematic cuts have been applied. Since only the 2 photon decay of the η was taken into account, the invariant mass can be extracted using eq. 4.2.

The spectra for the $\eta\pi^0$ channels are practically background-free, especially for photon energies greater than 1000 MeV. The spectra for the $\eta\pi^\pm$ channels are also almost clean. In the spectra of the $\eta\pi^- p$ final state (Fig. 5.43) there is still a little background at lower invariant masses. This is most likely caused by the two charged particles in the final state. Due to this, there is a larger probability that pions are misidentified as protons, and vice versa. The same behavior but more pronounced is visible in the quasi-free inclusive spectra (Fig. 5.44). Again, the background comes most likely from the $\pi^0\pi^- p$ channel, that sits right under the peak in the missing mass spectra 5.33 and can not be completely eliminated by the missing mass cut. Contamination from the ηp production could be removed by the missing mass cut.

Figures 5.46 and 5.47 compare the spectra of reactions on the dButanol to reactions on deuterium. Since only the information of the decay photons was used to determine the invariant mass, the larger Fermi-momentum of the dButanol does not affect the spectra. Therefore, the shape of the dButanol spectra is the same as for the deuterium spectra.

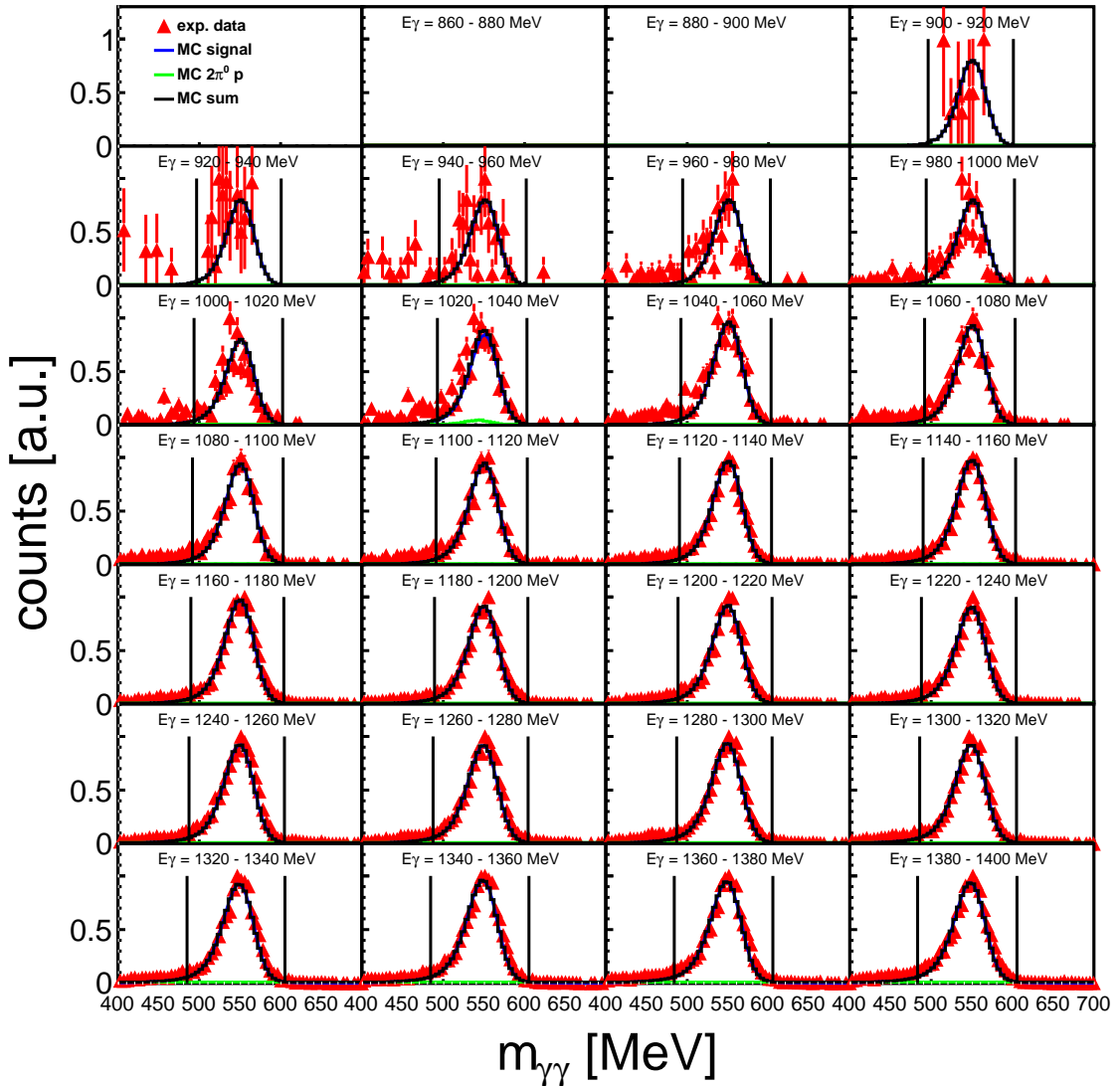
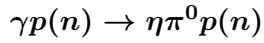


Figure 5.37.: Spectrum of the invariant mass of the 2 photons from the η decay of the reaction $\gamma p(n) \rightarrow \eta\pi^0 p(n)$. Red triangles: experimental data. Blue solid line: simulated data of the reaction. Green solid line: simulated background reaction $\gamma p(n) \rightarrow \pi^0\pi^0 p(n)$. Black solid line: sum of the simulated data. Vertical lines: cut positions.

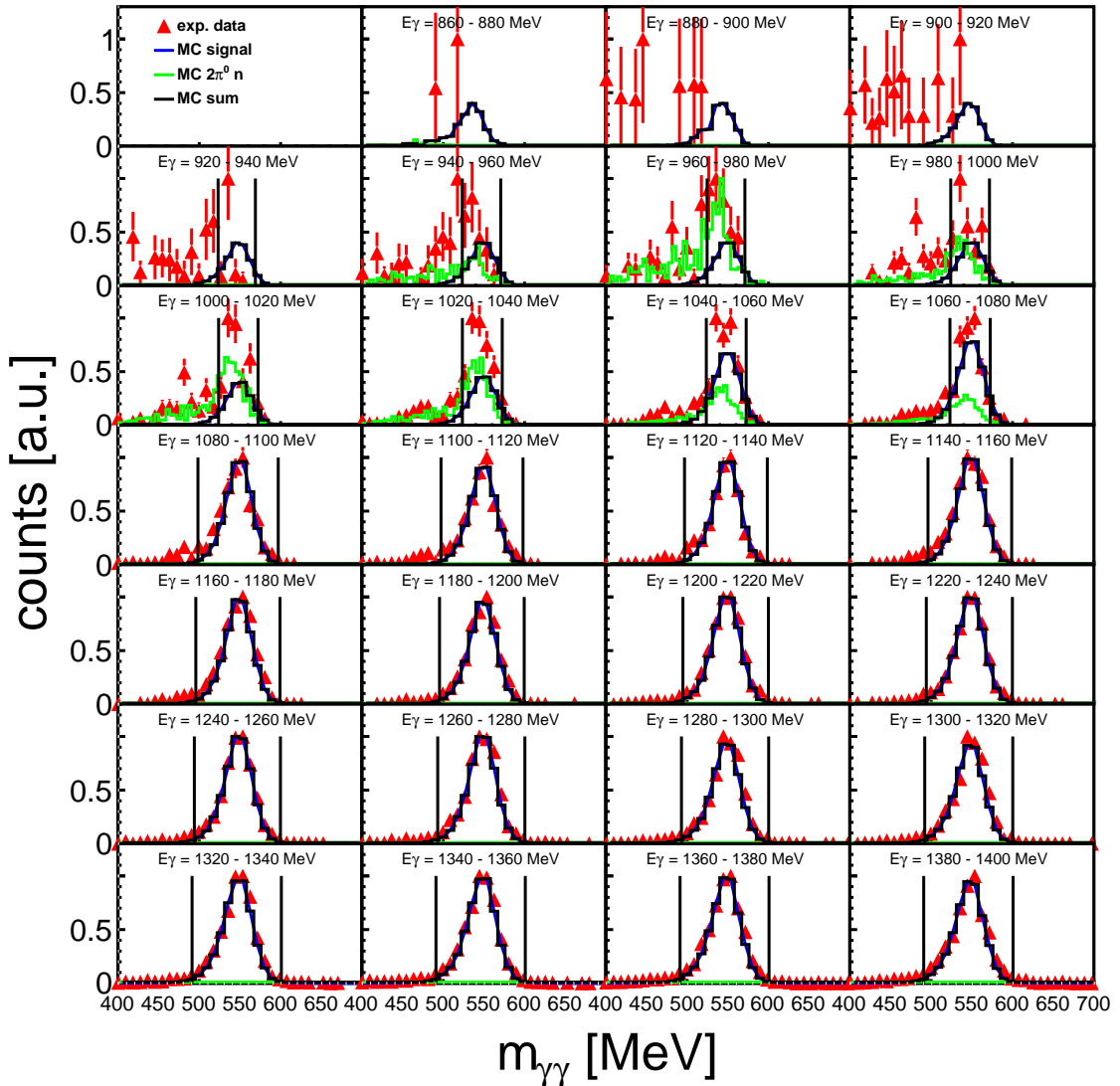
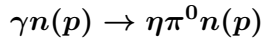


Figure 5.38.: Spectrum of the invariant mass of the 2 photons from the η decay of the reaction $\gamma n(p) \rightarrow \eta\pi^0 n(p)$. Red triangles: experimental data. Blue solid line: simulated data of the reaction. Green solid line: simulated background reaction $\gamma n(p) \rightarrow \pi^0\pi^0 n(p)$. Black solid line: sum of the simulated data. Vertical lines: cut positions.

$$\gamma N(N) \rightarrow \eta\pi^0(N)$$

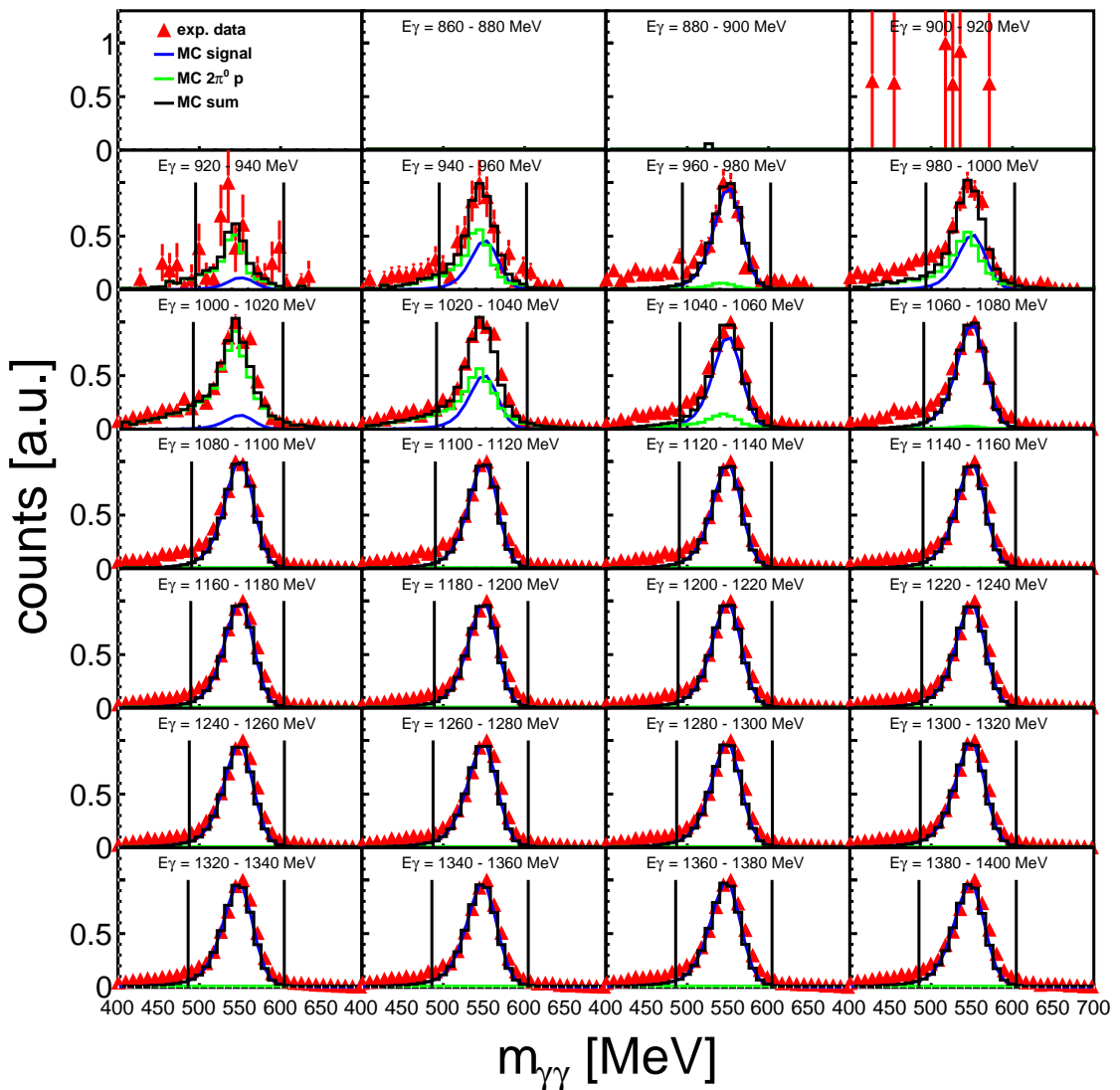


Figure 5.39.: Spectrum of the invariant mass of the 2 photons from the η decay of the reaction $\gamma N(N) \rightarrow \eta\pi^0(N)$. Red triangles: experimental data. Blue solid line: simulated data of the reaction. Green solid line: simulated background reaction $\gamma p(n) \rightarrow \pi^0\pi^0 p(n)$. Black solid line: sum of the simulated data. Vertical lines: cut positions.

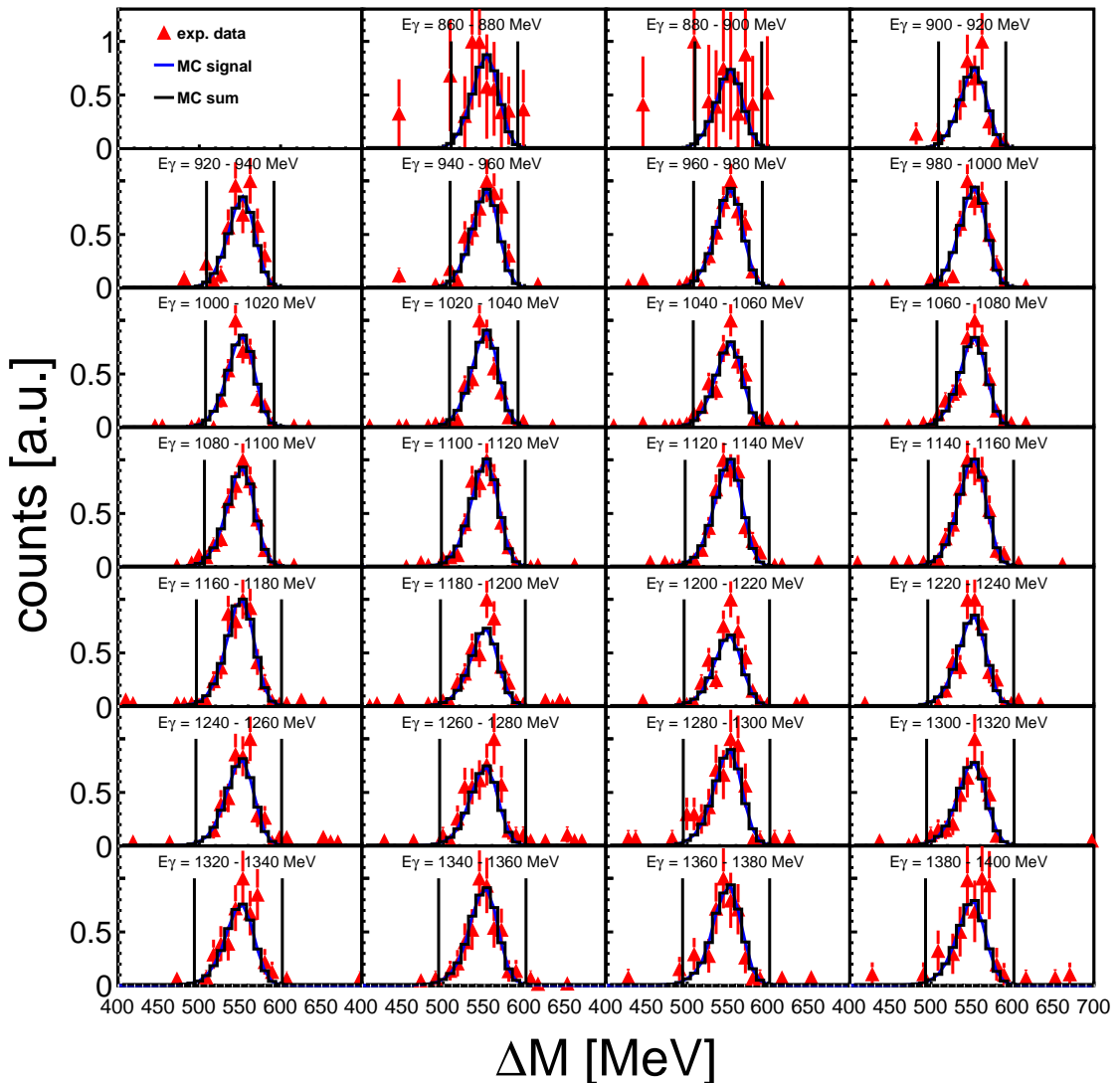
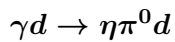


Figure 5.40.: Spectrum of the invariant mass of the 2 photons from the η decay of the reaction $\gamma d \rightarrow \eta\pi^0d$. Red triangles: experimental data. Blue solid line: simulated data of the reaction. Green solid line: simulated background reaction $\gamma p(n) \rightarrow \pi^0\pi^0p(n)$. Black solid line: sum of the simulated data. Vertical lines: cut positions.

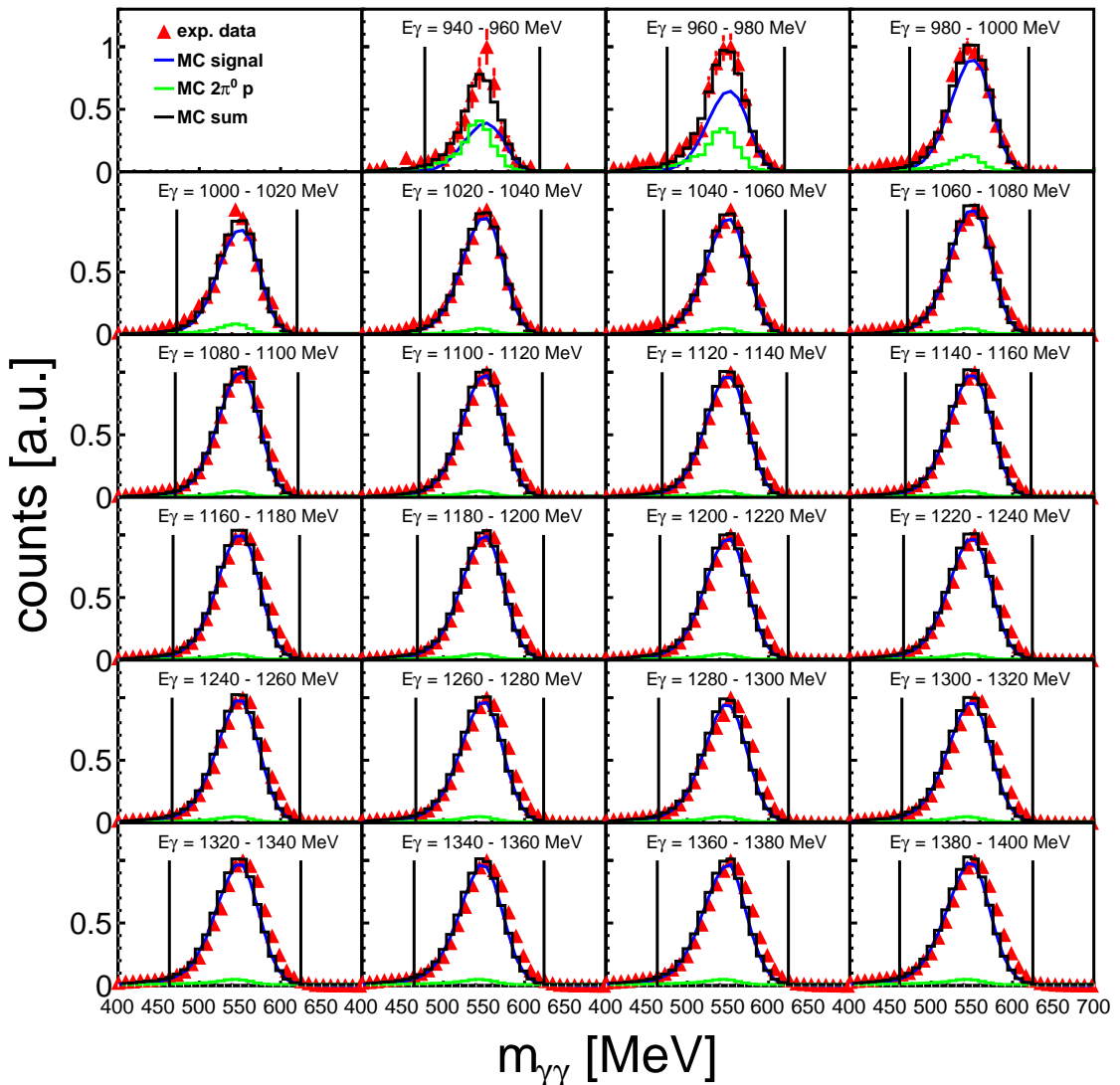
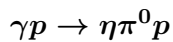


Figure 5.41.: Spectrum of the invariant mass of the 2 photons from the η decay of the reaction $\gamma p \rightarrow \eta\pi^0 n$. Red triangles: experimental data. Blue solid line: simulated data of the reaction. Green solid line: simulated background reaction $\gamma p \rightarrow \pi^0\pi^0 p$. Black solid line: sum of the simulated data. Vertical lines: cut positions.

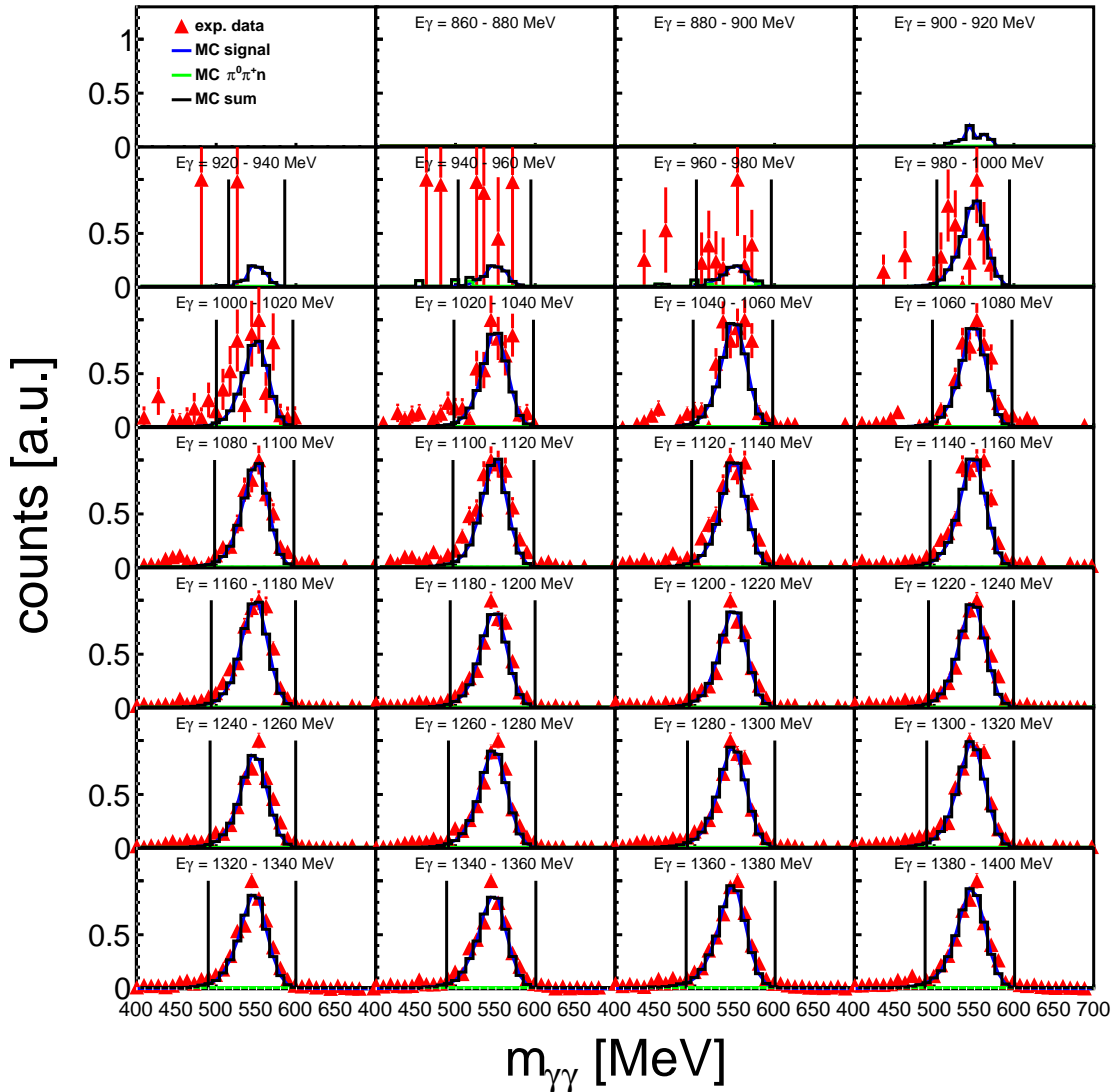
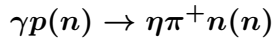


Figure 5.42.: Spectrum of the invariant mass of the 2 photons from the η decay of the reaction $\gamma p(n) \rightarrow \eta\pi^+ n(n)$. Red triangles: experimental data. Blue solid line: simulated data of the reaction. Green solid line: simulated background reaction $\gamma p(n) \rightarrow \pi^0\pi^+p$. Black solid line: sum of the simulated data. Vertical lines: cut positions.

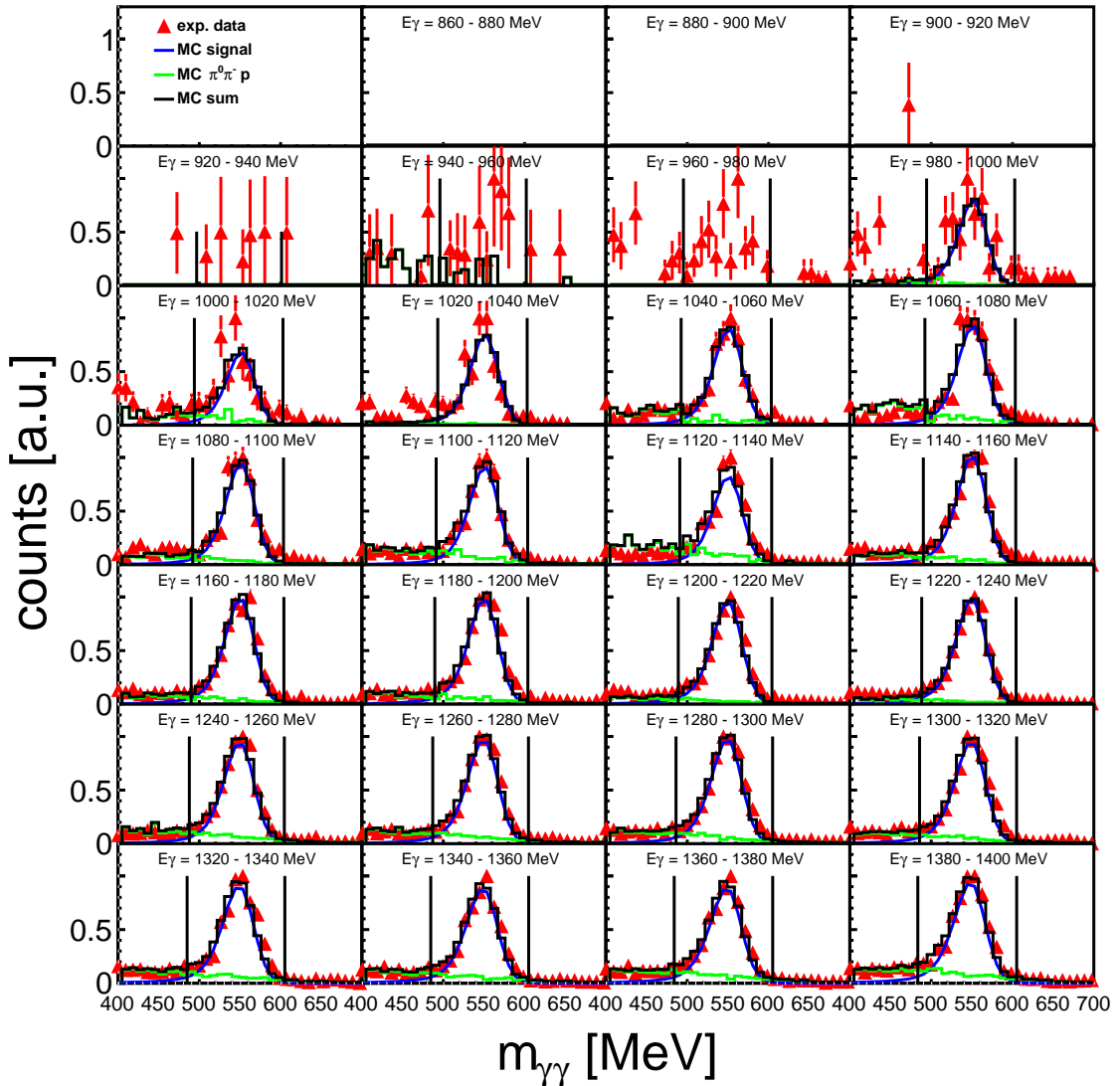
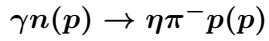


Figure 5.43.: Spectrum of the invariant mass of the 2 photons from the η decay of the reaction $\gamma n(p) \rightarrow \eta\pi^- p(p)$. Red triangles: experimental data. Blue solid line: simulated data of the reaction. Green solid line: simulated background reaction $\gamma n(p) \rightarrow \pi^0\pi^- p(p)$. Black solid line: sum of the simulated data. Vertical lines: cut positions.

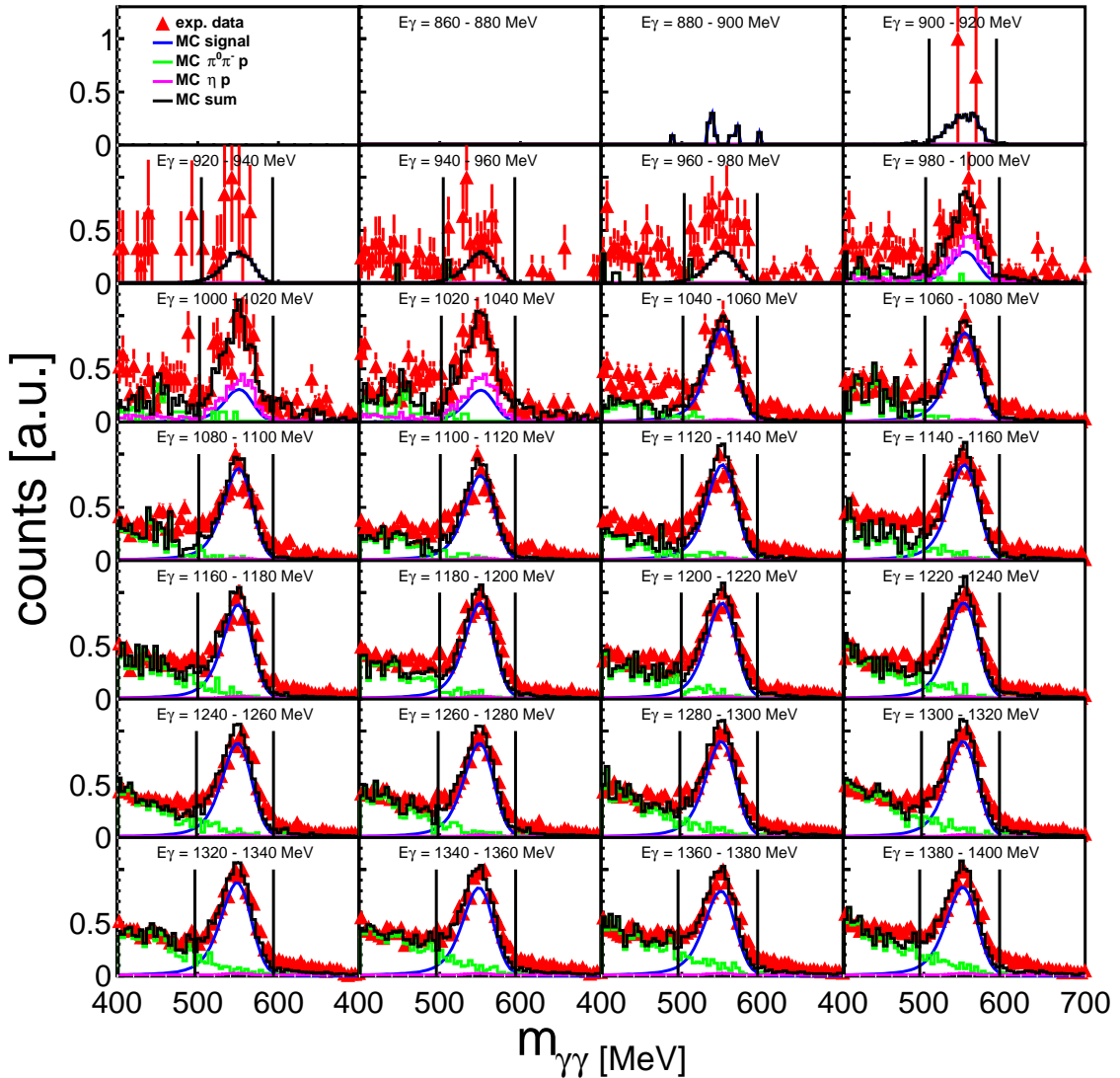
$\gamma N(N) \rightarrow \eta\pi^\pm(N)$


Figure 5.44.: Spectrum of the invariant mass of the 2 photons from the η decay of the reaction $\gamma N(N) \rightarrow \eta\pi^\pm(N)$. Red triangles: experimental data. Blue solid line: simulated data of the reaction. Green solid line: simulated background reaction $\gamma n(p) \rightarrow \pi^0\pi^+\pi^-n$. Magenta solid line: simulated background reaction $\gamma p(n) \rightarrow \eta p(n)$. Dark green solid line: simulated background reaction $\gamma p(n) \rightarrow \pi^0p(n)$. Black solid line: sum of the simulated data. Vertical lines: cut positions.

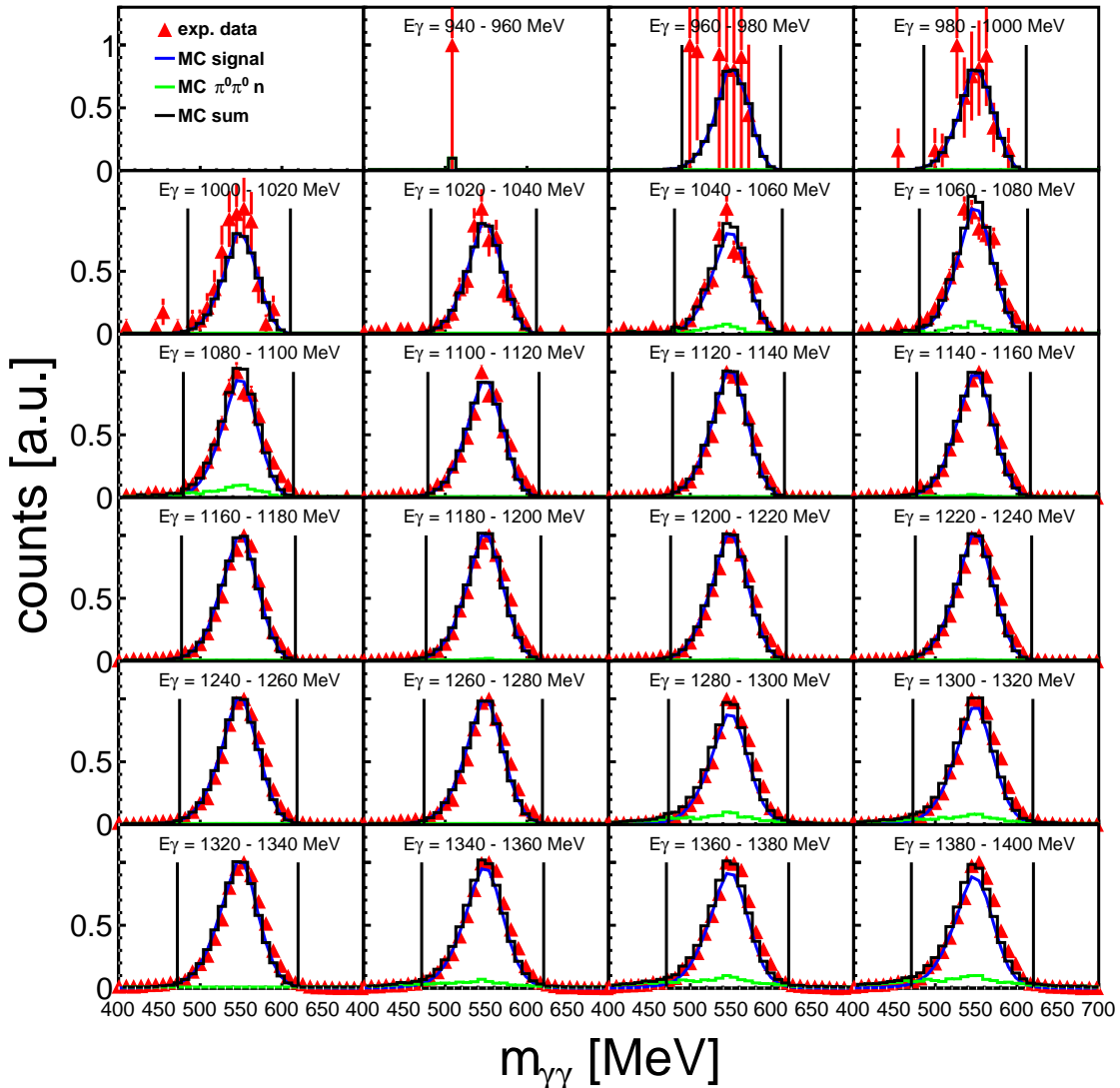
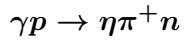


Figure 5.45.: Spectrum of the invariant mass of the 2 photons from the η decay of the reaction $\gamma p \rightarrow \eta\pi^+n$. Red triangles: experimental data. Blue solid line: simulated data of the reaction. Green solid line: simulated background reaction $\gamma p(n) \rightarrow \pi^0\pi^+p$. Black solid line: sum of the simulated data. Vertical lines: cut positions.

$\gamma p(n) \rightarrow \eta\pi^0 p(n)$ for dButanol

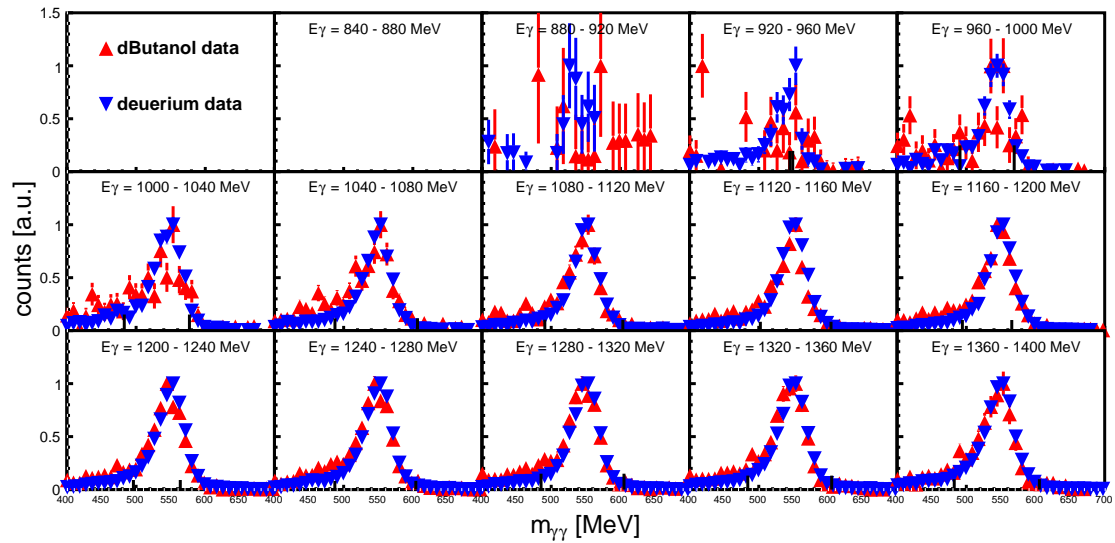


Figure 5.46.: Spectrum of the invariant mass of the 2 photons from the η decay of the reaction $\gamma p(n) \rightarrow \eta\pi^0 p(n)$ on dButanol. Red triangles: polarized butanol data. Blue triangles: unpolarized deuterium data. Vertical lines: cut positions.

$\gamma n(p) \rightarrow \eta\pi^0 n(p)$ for dButanol

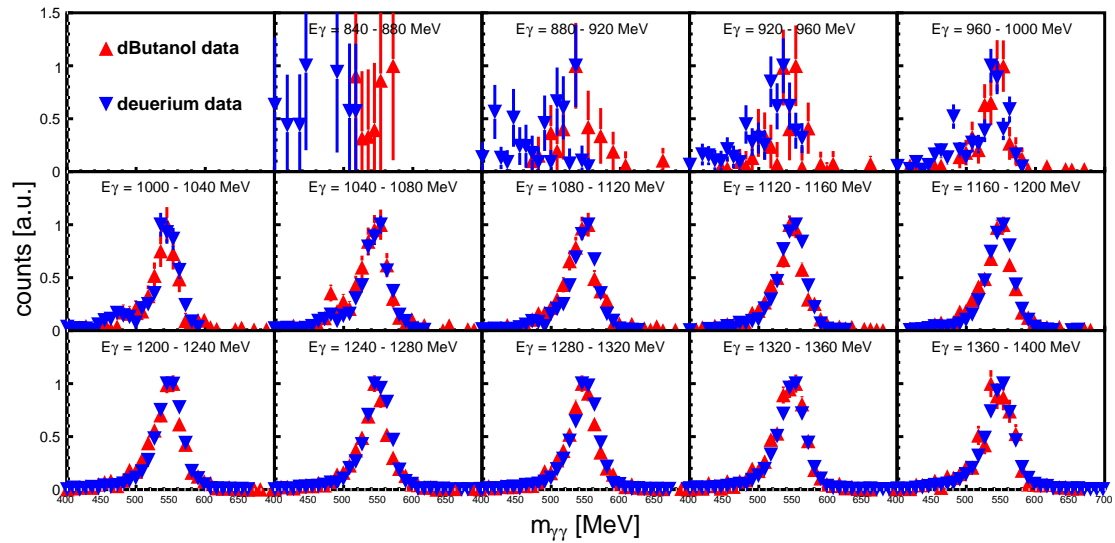


Figure 5.47.: Spectrum of the invariant mass of the 2 photons from the η decay of the reaction $\gamma p(n) \rightarrow \eta\pi^0 p(n)$ on dButanol. Red triangles: polarized butanol data. Blue triangles: unpolarized deuterium data. Vertical lines: cut positions.

5.5.5. π^0 Invariant Mass

Figures 5.48 - 5.52 show the π^0 invariant mass for the deuterium data. Since the mass of the π^\pm mesons was always set to the nominal value during the reconstruction (see section 5.3), no mass spectra for these channels are shown. Figures 5.54 and 5.54 show the spectra of dButanol compared to the deuterium spectra. Similar to the spectra for the invariant-mass of the η no influence of the dButanols Fermi-momenta is visible.

$$\gamma p(n) \rightarrow \eta\pi^0 p(n)$$

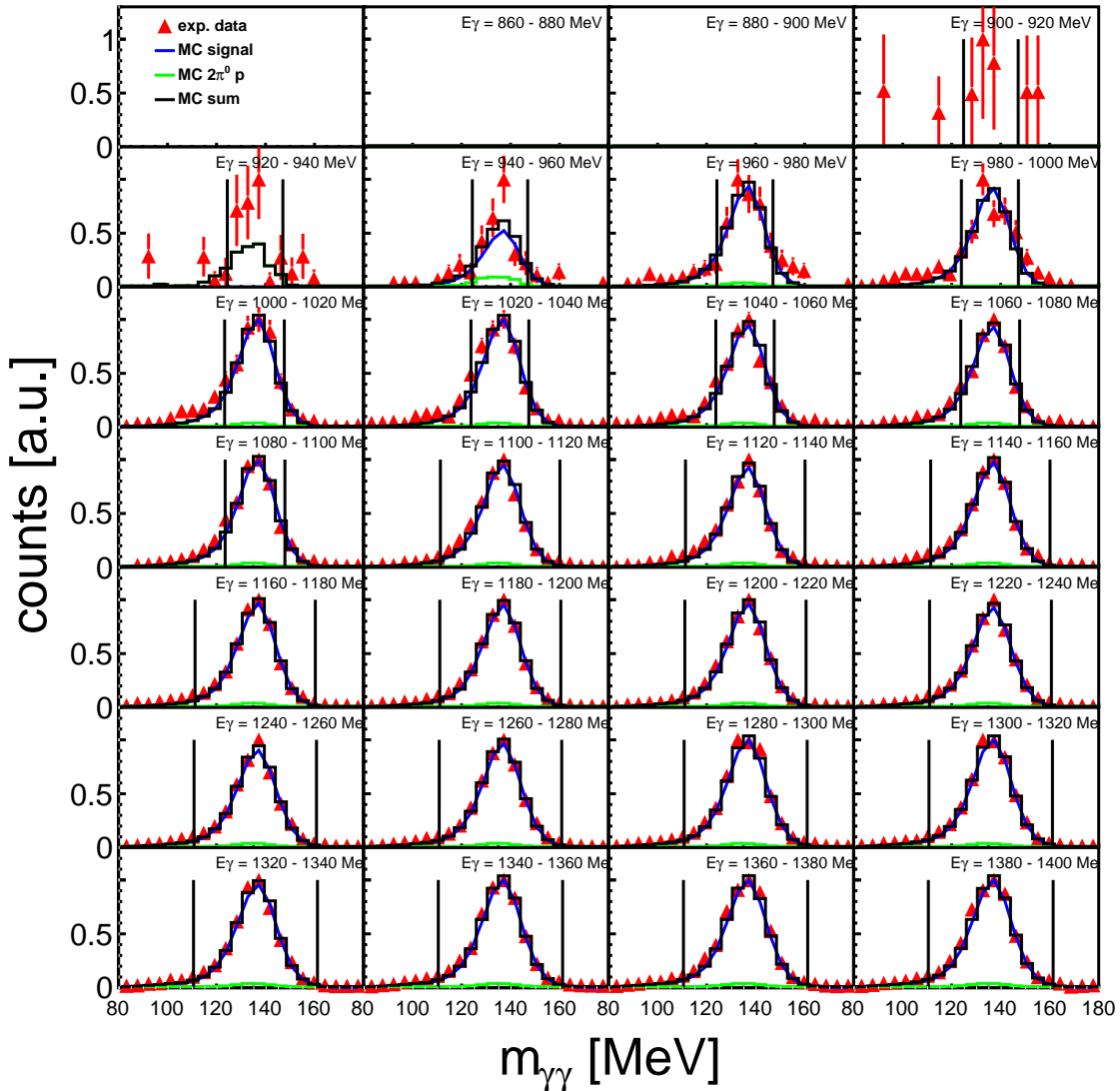


Figure 5.48.: Spectrum of the invariant mass of the 2 photons from the π^0 decay of the reaction $\gamma p(n) \rightarrow \eta\pi^0 p(n)$. Red triangles: experimental data. Blue solid line: simulated data of the reaction. Green solid line: simulated background reaction $\gamma p(n) \rightarrow \pi^0\pi^0 p(n)$. Black solid line: sum of the simulated data. Vertical lines: cut positions.

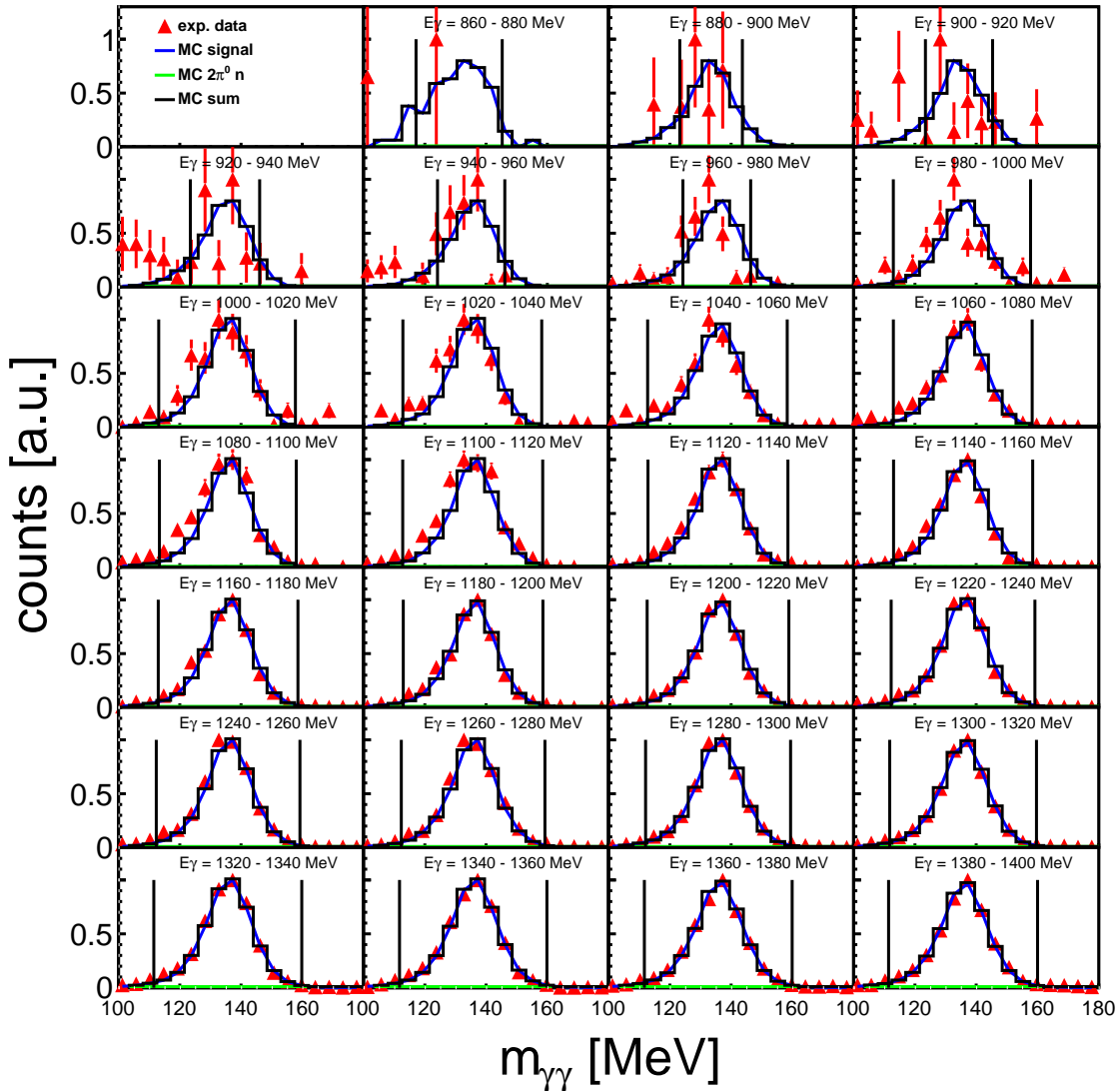
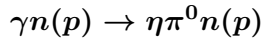


Figure 5.49.: Spectrum of the invariant mass of the 2 photons from the π^0 decay of the reaction $\gamma n(p) \rightarrow \eta\pi^0 n(p)$. Red triangles: experimental data. Blue solid line: simulated data of the reaction. Green solid line: simulated background reaction $\gamma n(p) \rightarrow \pi^0\pi^0 n(p)$. Black solid line: sum of the simulated data. Vertical lines: cut positions.

$$\gamma N(N) \rightarrow \eta\pi^0(N)$$

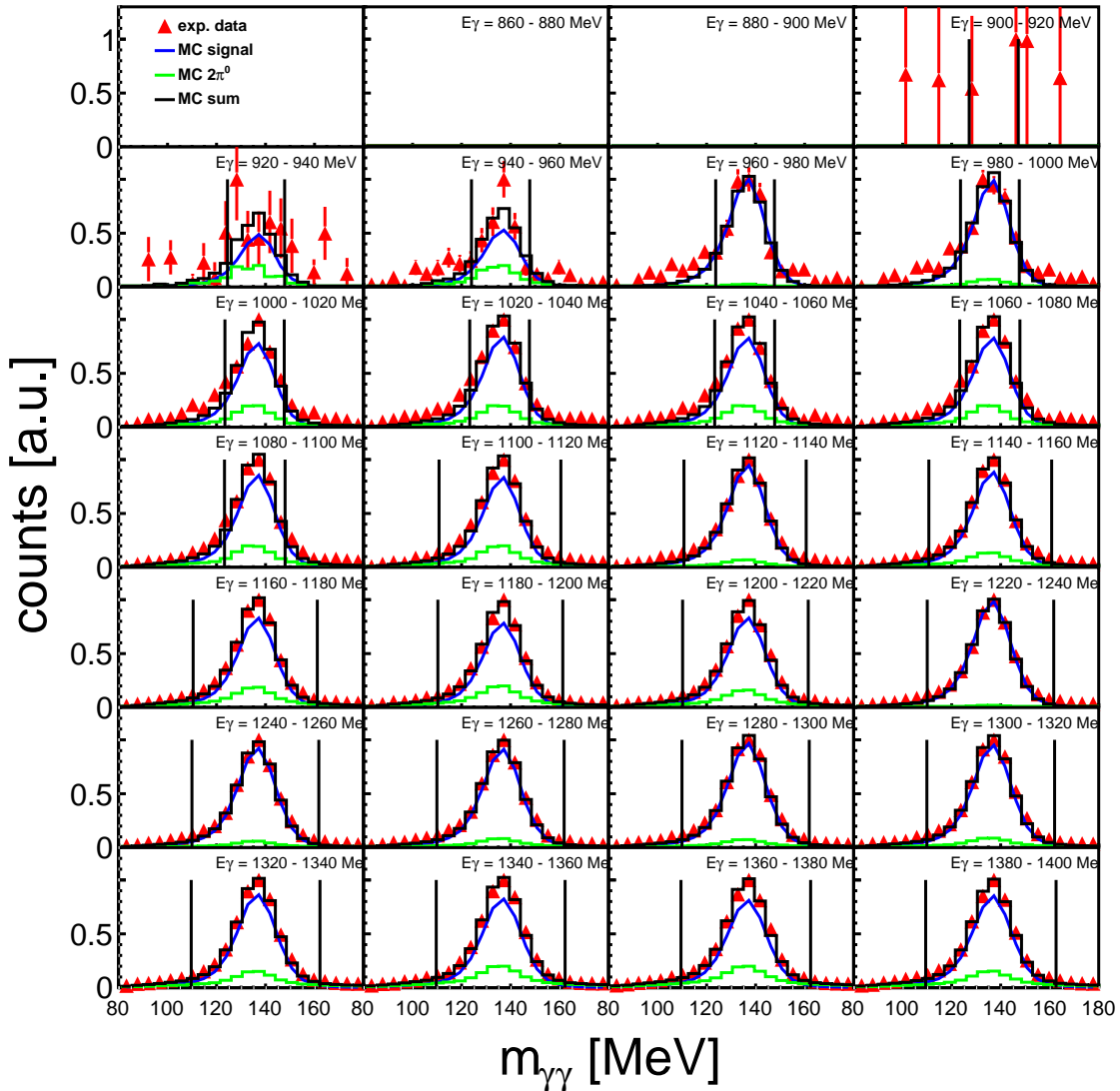


Figure 5.50.: Spectrum of the invariant mass of the 2 photons from the π^0 decay of the reaction $\gamma N(N) \rightarrow \eta\pi^0(N)$. Red triangles: experimental data. Blue solid line: simulated data of the reaction. Green solid line: simulated background reaction $\gamma N(N) \rightarrow \eta\pi^0(N)$. Black solid line: sum of the simulated data. Vertical lines: cut positions.

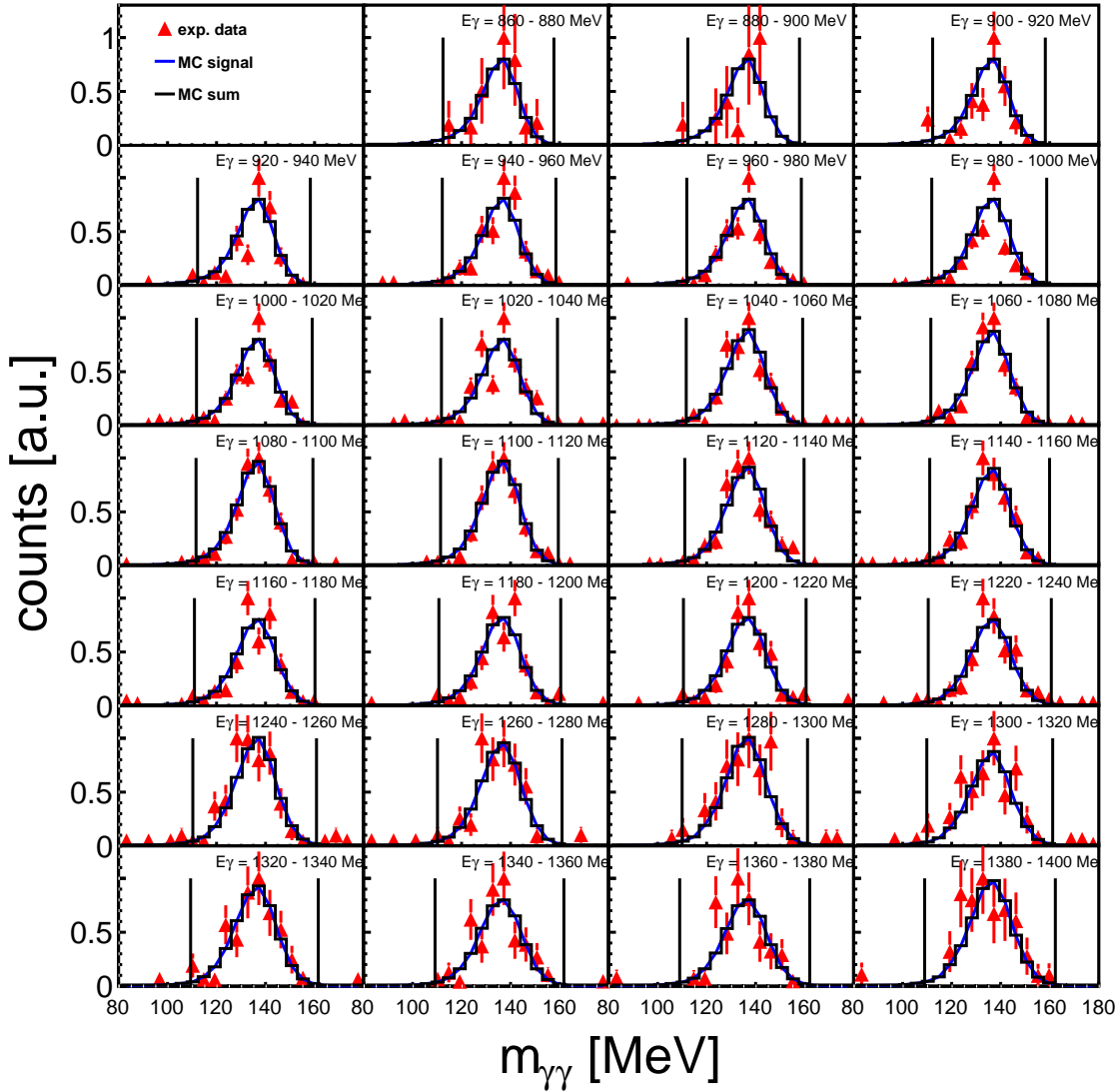
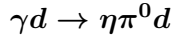


Figure 5.51.: Spectrum of the invariant mass of the 2 photons from the π^0 decay of the reaction $\gamma d \rightarrow \eta\pi^0d$. Red triangles: experimental data. Blue solid line: simulated data of the reaction. Green solid line: simulated background reaction $\gamma p(n) \rightarrow \pi^0\pi^0p(n)$. Reactions on quasi free protons and neutrons did contribute. Black solid line: sum of the simulated data. Vertical lines: cut positions.

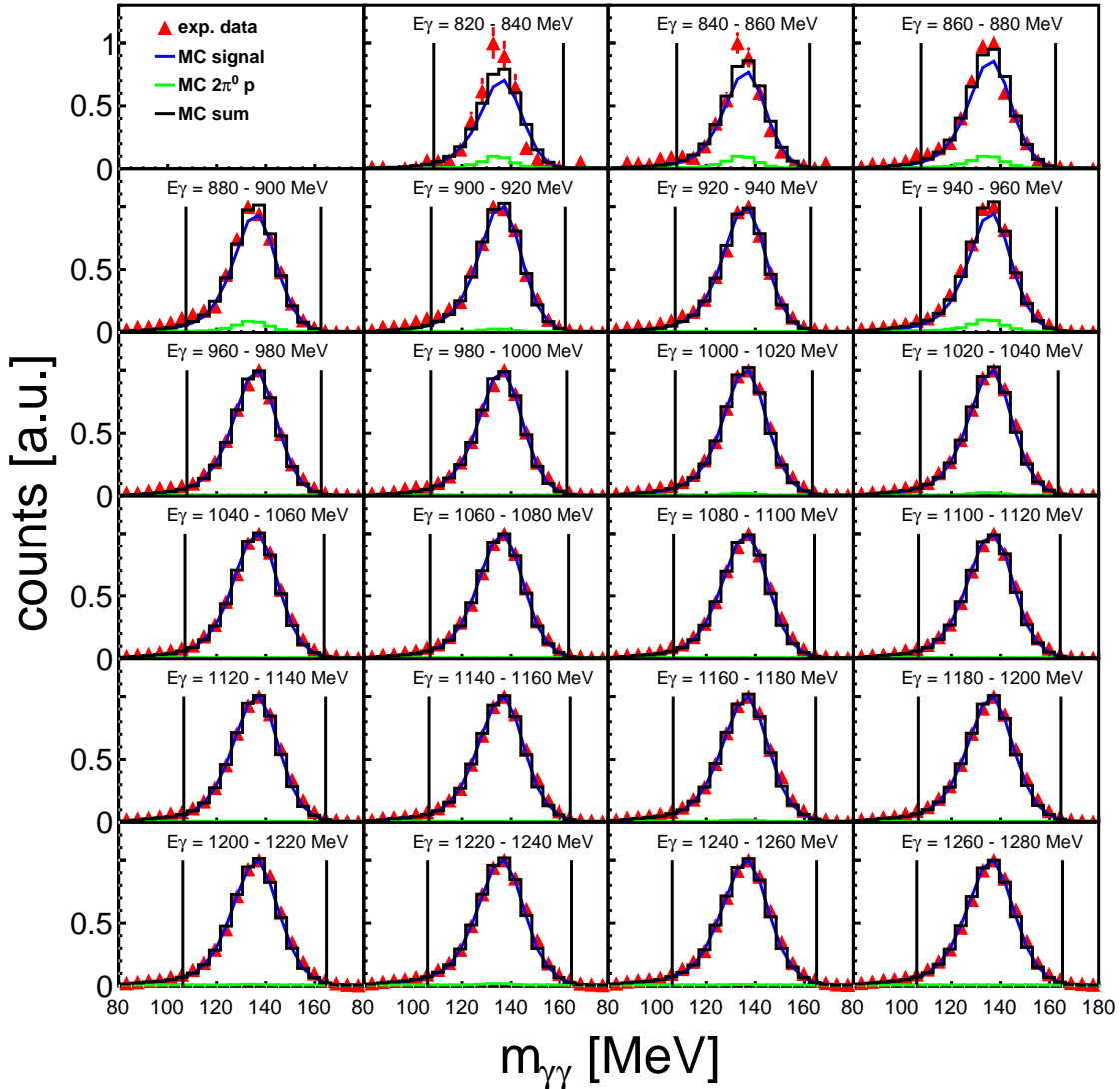
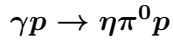


Figure 5.52.: Spectrum of the invariant mass of the 2 photons from the π^0 for the $\gamma p \rightarrow \eta\pi^0 p$. Red triangles: experimental data. Blue solid line: simulated data of the reaction. Green solid line: simulated background reaction $\gamma p \rightarrow \pi^0\pi^0 p$. Black solid line: sum of the simulated data. Vertical lines: cut positions.

$\gamma p(n) \rightarrow \eta\pi^0 p(n)$ for dButanol

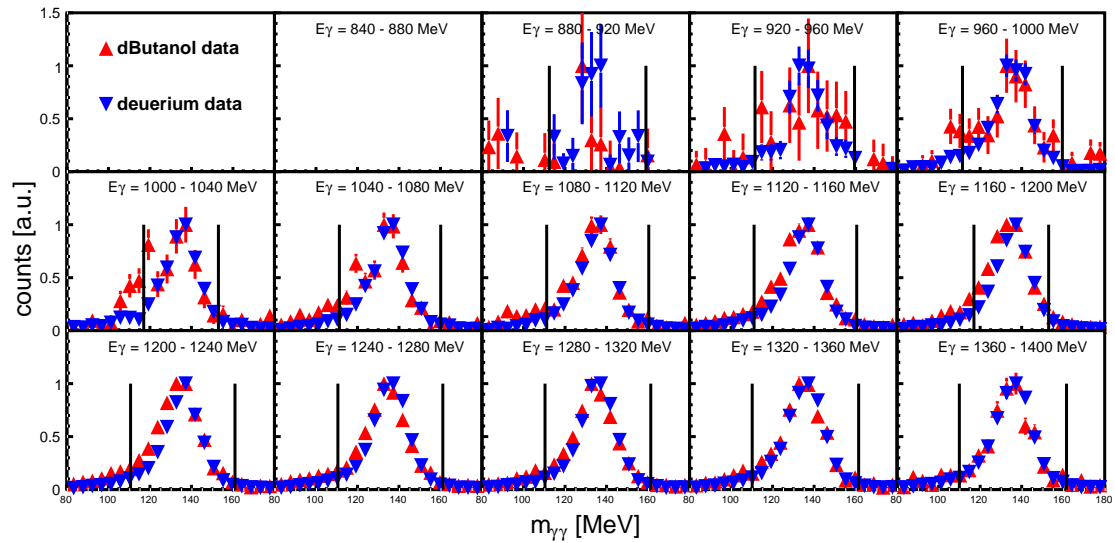


Figure 5.53.: Spectrum of the invariant mass of the 2 photons from the π^0 decay of the reaction $\gamma p(n) \rightarrow \eta\pi^0 p(n)$ on dButanol. Red triangles: polarized butanol data. Blue triangles: unpolarized deuterium data. Vertical lines: cut positions.

$\gamma n(p) \rightarrow \eta\pi^0 n(p)$ for dButanol

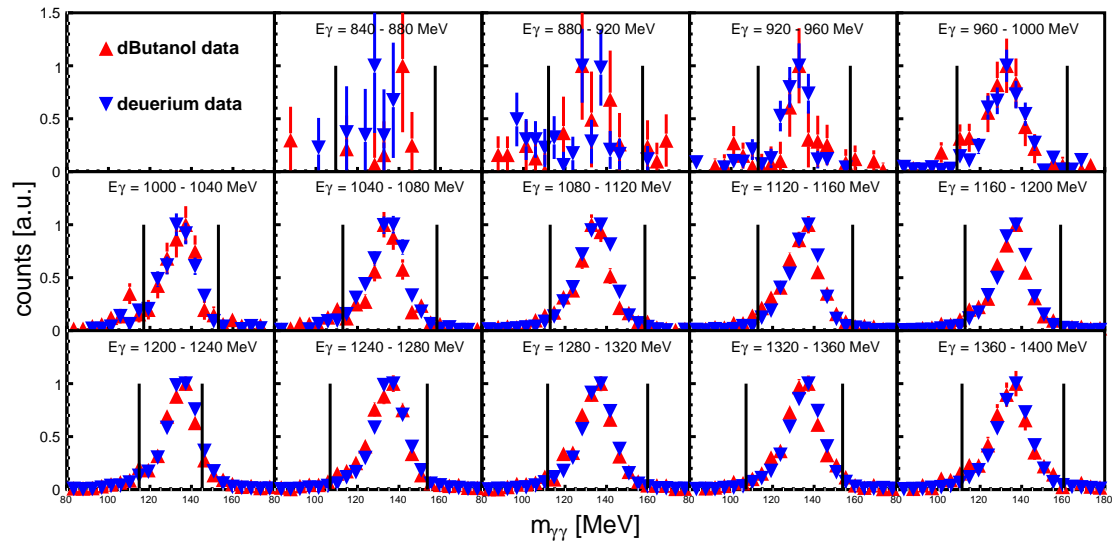


Figure 5.54.: Spectrum of the invariant mass of the 2 photons from the π^0 decay of the reaction $\gamma p(n) \rightarrow \eta\pi^0 p(n)$ on dButanol. Red triangles: polarized butanol data. Blue triangles: unpolarized deuterium data. Vertical lines: cut positions.

5.6. Time Of Flight

For the particles detected in TAPS a Time-Of-Flight (TOF) analysis could be performed because of the good time resolution of the BaF₂ crystals and the sufficient distance from the target of about 1.5 m. The TOF analysis is particularly suited to distinguish between photons and nucleons and also protons from neutrons.

For each particle the TOF value is calculated:

$$TOF = \frac{\Delta t}{s} + \frac{1}{c} \left[\frac{ns}{m} \right], \quad (5.21)$$

where s is the flight-path of the particle, c is the speed of light and Δt is the time difference between a hit in TAPS and the tagger. The tagger was chosen as reference because of the better time resolution compared to the CB.

Because of the calibration method, where all photon time differences were located at zero an additional offset of 1/c has to be added to the TOF.

Since the flight paths 's' are different for every particle, the TOF was normalized to one meter, hence the unit ns/m and the TOF corresponds to the inverse of the particle's velocity.

The TOF can also be used to calculate the kinetic energy of the recoil particle via:

$$T_R = m_R(\gamma - 1) = m_R \left(\sqrt{\frac{1}{1 - \beta^2}} \right) \quad (5.22)$$

$$\beta = \frac{v}{c} = \frac{1}{TOF \cdot c}, \quad (5.23)$$

where m_R is the mass of the recoil particle.

Figs. 5.59 - 5.57 show the TOF plotted against the deposited energy E in TAPS for each investigated reaction. Each plot is labeled with the particles in the corresponding final states. The top row in all plots shows the spectra after the χ^2 test and PSA cuts, before all analysis cuts are applied, therefore they still contain contributions from background reactions.

Before the cuts are applied, the nucleon spectra show some contamination at TOF values around 3.3 ns and small energies, that stem from wrongly assigned photons in the neutron spectra, and electrons in the proton spectra. These contaminations can successfully be removed by kinematic cuts.

The proton spectra additionally show a cumulation of events at energies between 250 MeV and 500 MeV and TOF values of 4-5 ns. These are very high energetic protons, that punch through the detector and therefore do not deposit their total energy in the crystals.

The photons spectra before cuts are free from contributions of different particles, but contain a big amount of photons from background reactions. After cuts the spectra show much fewer entries, but the location and shape of the photon bands does not change.

The lower rows of 5.59 - 5.57 show the spectra after the analyses cuts are applied (acc.).

The photon and proton spectra are clean and the proton spectra show the typical banana-like band-structure. This is caused by the fact, that low energetic nucleons have a large TOF, while high energetic nucleons have a small TOF.

For neutrons there is no clear correlation between TOF and deposited energy. This is caused by different possibilities of neutrons to deposit their energy in the detector elements(see sec. 3.3).

Remarkable is the clear separation of the proton and deuteron bands shown in fig 5.57, what allowed a clean identification of the coherent reaction on the deuteron. A larger plot is shown in Fig. 5.2.

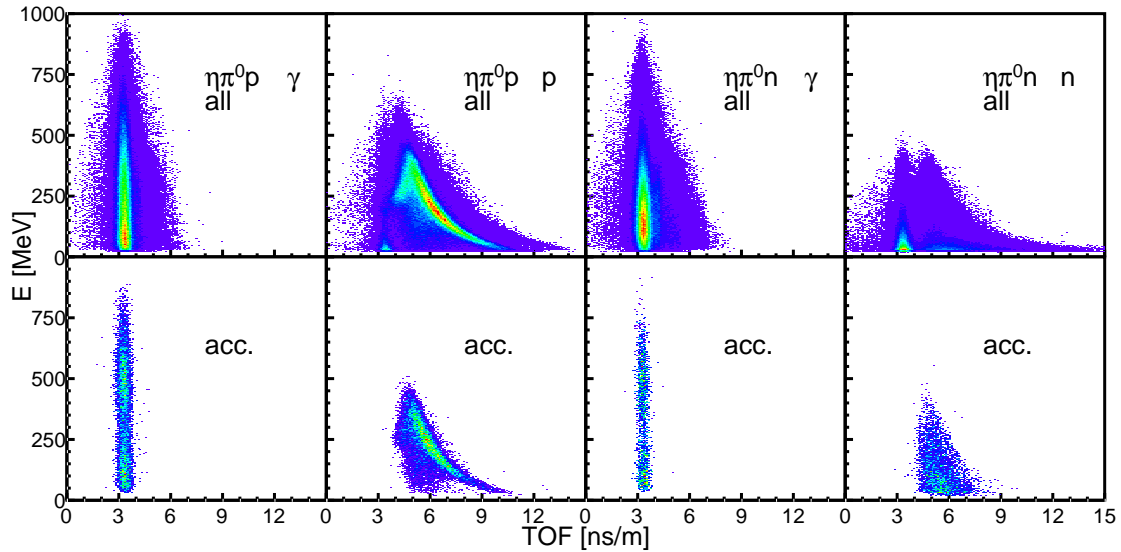


Figure 5.55.: Energy deposited in TAPS vs. Time-of-Flight (TOF). The upper row shows the spectra before all kinematic cuts, the lower row shows the spectra for events that were accepted into the analysis i.e. with all kinematic cuts applied. Shown are spectra for quasi-free reactions with neutral pions.

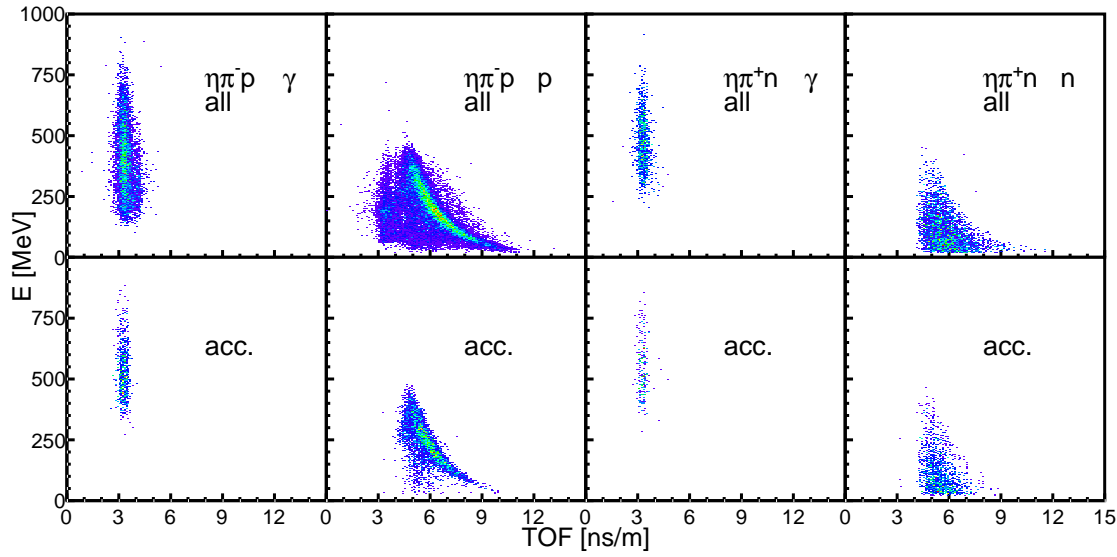


Figure 5.56.: Energy deposited in TAPS vs. Time-of-Flight (TOF). The upper row shows the spectra before all kinematic cuts, the lower row shows the spectra for events that were accepted into the analysis i.e. with all kinematic cuts applied. Shown are spectra for quasi-free reactions with charged pions.

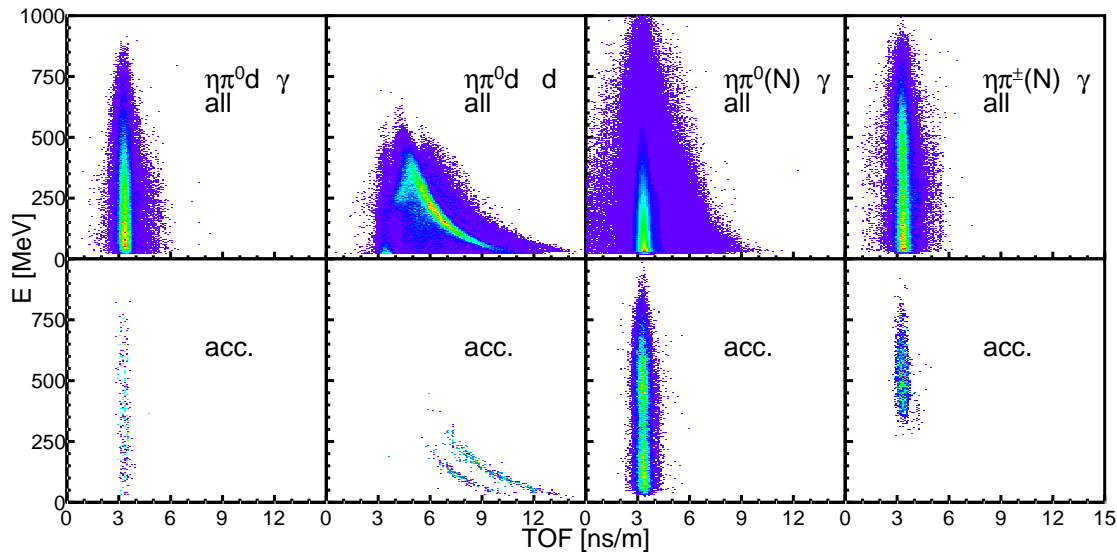


Figure 5.57.: Energy deposited in TAPS vs. Time-of-Flight (TOF). The upper row shows the spectra before all kinematic cuts, the lower row shows the spectra for events that were accepted into the analysis i.e. with all kinematic cuts applied. Shown are spectra for coherent and inclusive reactions.

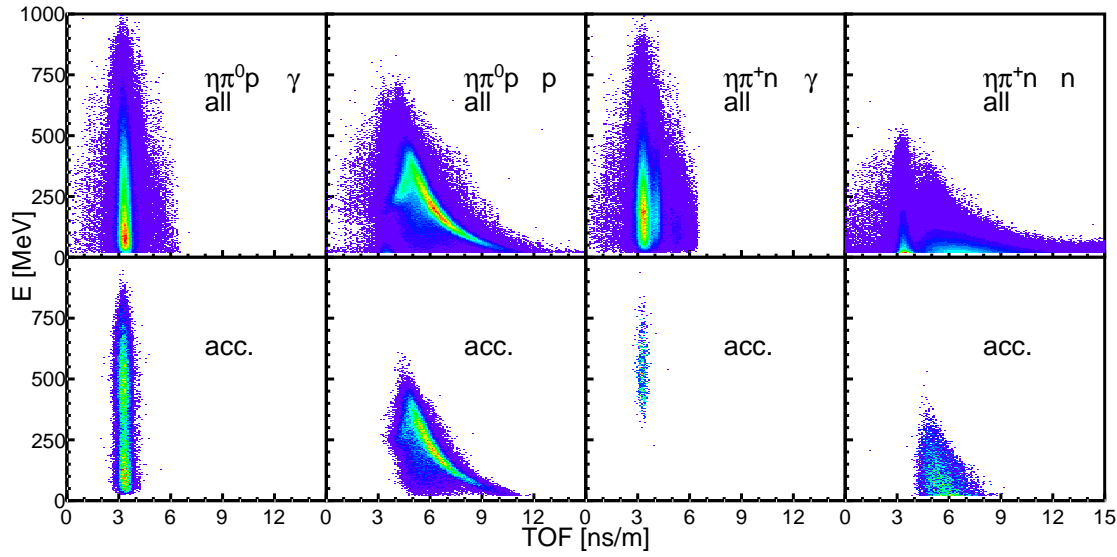


Figure 5.58.: Energy deposited in TAPS vs. Time-of-Flight (TOF). The upper row shows the spectra before all kinematic cuts, the lower row shows the spectra for events that were accepted into the analysis i.e. with all kinematic cuts applied. Shown are spectra for reactions on free protons

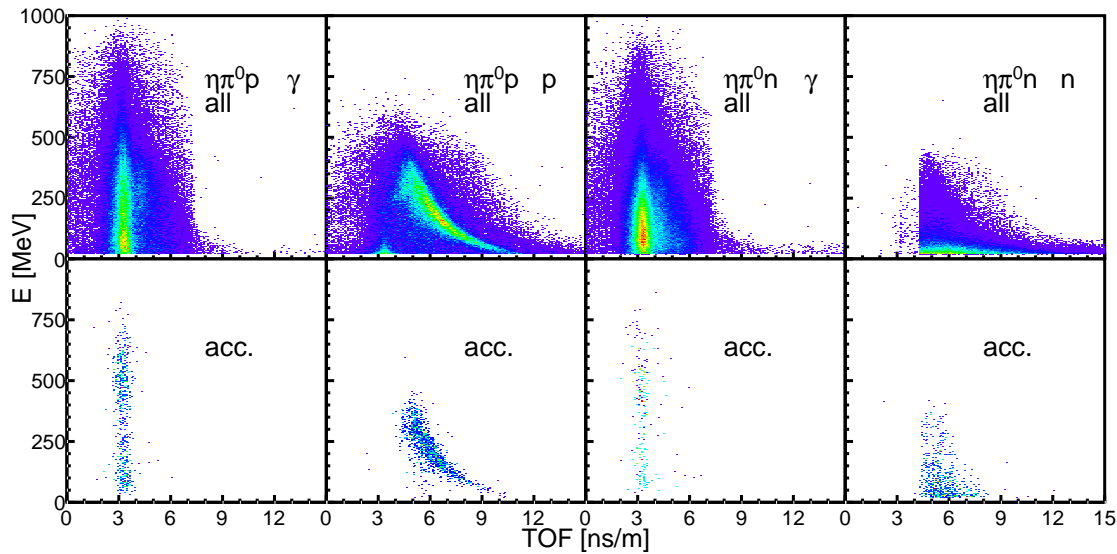


Figure 5.59.: Energy deposited in TAPS vs. Time-of-Flight (TOF). The upper row shows the spectra before all kinematic cuts, the lower row shows the spectra for events that were accepted into the analysis i.e. with all kinematic cuts applied. Shown are spectra for quasi-free reactions with neutral pions for the dButanol data.

5.7. Nucleon polar angle

For quasi free kinematics, neglecting high Fermi momenta, the polar angle of nucleons is kinematically limited. Figure 5.60 shows a comparison between experimental and simulated data. The distributions start at 5° , where nucleons are detected in TAPS. Since the two inner rings were not functional, no particles could be detected at lower angles. The gap between TAPS and the CB is clearly visible at 22° .

The fluctuations in the distribution come from the segmentation of the detectors and the rather small cluster sizes of nucleons that can be seen in Fig. 3.2.

A cut on the polar angle was set at 45° , where the distributions start to deviate significantly.

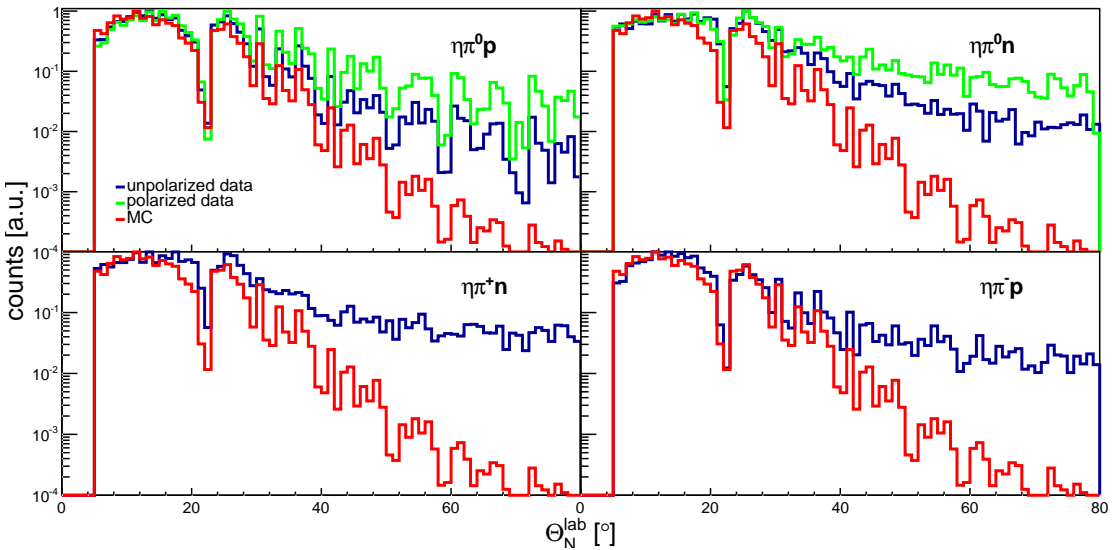


Figure 5.60.: Spectra of the polar angles of recoil nucleons in the lab frame after all analysis cuts. Deuterium data are shown in blue, the corresponding MC simulations are shown in red, dButanol data are shown in green.

During the December 2007 beam-time the PID was not located at its usual position, but was shifted for about 15 cm in beam direction. This lead to problems with the identification of charged particles in the CB since the PID did not cover the whole polar angle of the CB anymore. Due to this there was an angular region where all detected particles were marked as neutral, whether they had a charge or not. This presented a problem to the analysis since wrongly assigned clusters would have influence on the event selection. For example $\eta\pi^0p$ events could be wrongly assigned to the $\eta\pi^0n$ channel if the recoil nucleon was wrongly identified.

For the channels with charged pions the situation is even worse. $\gamma p(n) \rightarrow \eta\pi^+n(n)$ events would be completely lost if the pion was misidentified as neutral particle. $\gamma n(p) \rightarrow \eta\pi^-p$ events could either end up in the $\gamma p(n) \rightarrow \eta\pi^+n(n)$ channel if the proton or the pion is marked as neutral, since the detector system cannot distinguish between π^+ and π^-

Additionally, the shift of the PID lead to problems with the determination of the nucleon detection efficiency, which needs hydrogen data that were measured under the same conditions as the deuterium data. But since there was no hydrogen data with a shifted PID, the nucleon detection efficiency could not reliably be extracted for the December 2007 beam-time.

These problems lead to the decision to completely reject events where the recoil nucleon candidate was detected in the range $15^\circ < \Theta < 27^\circ$.

5.8. Fermi Momentum

Equation 5.6 can be used to extract the momentum p_S of the spectator nucleon. Since the spectator does not take part in the reaction, its momentum has to be the same in the initial and the final state. Momentum conservation then yields:

$$\vec{p}_\gamma + \vec{p}_P^{IS} + \vec{p}_S^{IS} = \vec{p}_m + \vec{p}_P^{FS} + \vec{p}_S^{FS}, \quad (5.24)$$

and therefore

$$\vec{p}_F = \vec{p}_P^{FS} + \vec{p}_m - \vec{p}_\gamma \quad (5.25)$$

The corresponding distributions extracted from experimental data are shown in Fig. 5.61 for the quasi-free exclusive reaction channels and compared to theoretical predictions using the Paris NN potential [92]. The general shape of the distribution of the data is well reproduced by the model, however the peak positions are slightly shifted. This is most likely caused by the finite resolution of the detector setup. The same behavior was seen in [47]. Also visible are the larger Fermi momenta in the dButanol data, which are caused by the heavy nuclei surrounding the deuterons.

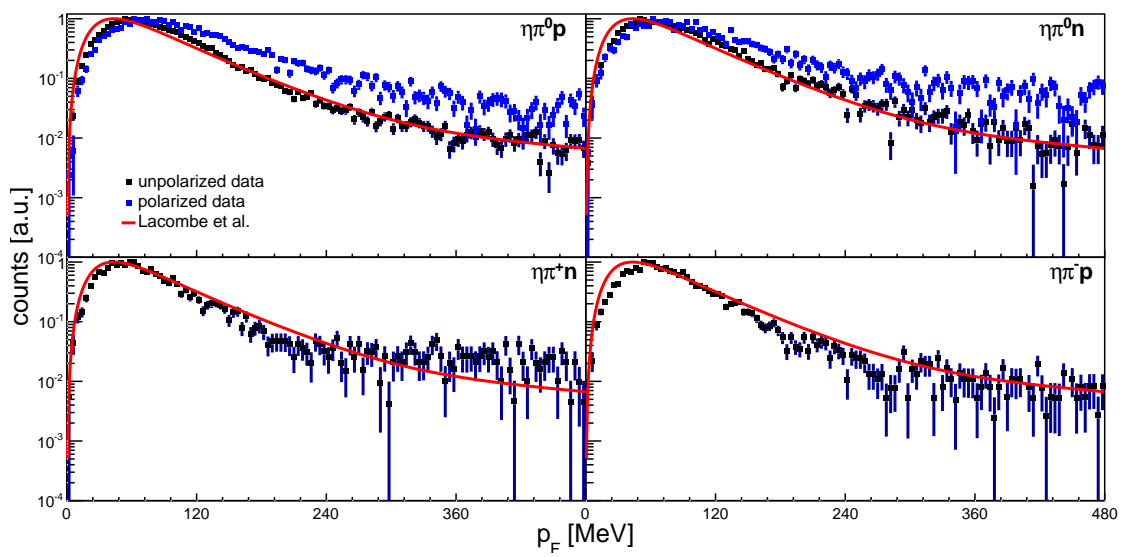


Figure 5.61.: Distribution of the Fermi momentum. Experimental data are shown in black, compared to the parametrization of the deuteron wave function of [92] in red. The y-axis is shown logarithmically.

5.9. Time cuts

5.9.1. Photon coincidence time

A condition on the time difference of photons was implemented, to ensure they belong all to the same event. The corresponding spectra are shown in Fig. 5.62. Since the spectra are practically background free, very wide cut positions were chosen.

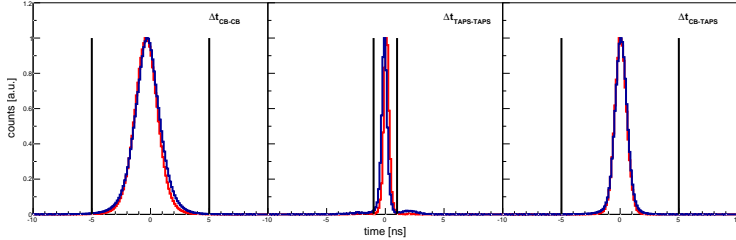


Figure 5.62.: Time difference of detected photons after the χ^2 test (blue) and after the analysis cuts (red). Left-hand side: CB-CB. Middle: TAPS-CB. Right-hand side: TAPS-TAPS. The vertical black lines indicate the cut positions.

5.9.2. Tagger Random Coincidences

During the time window of an event (gate), all electrons that hit the tagger ladder are stored. During the beam-times used in this work an average of 30 electrons was registered per event, but only one can be correlated to the bremsstrahlung photon that caused a reaction in the target. This means that the energy of the incoming photon beam cannot be known on an event-by-event basis. To compensate this a statistical method is applied to subtract background coming from random coincidences from all quantities that include information of the photon beam energy. A detailed description of the method can be found in [93].

A sideband subtraction is used to remove the random background. It is based on the assumption of time coincidence between the "true" electron in the tagger, and the signals of the photons in the detectors. The detector time was determined by averaging the hit times of the decay photons from η and π^0 mesons. If one or more photon was detected in TAPS, only their timing information was used, because of the better time resolution of TAPS. This can be seen in Fig. 5.63 in form of the narrower peak in the TAPS spectrum. The constant flat background in the spectra is caused by uncorrelated electrons in the tagger. Assuming a pure random distribution of the uncorrelated electrons, their contribution to the background windows (red areas) $[t_1, t_2]$ and $[t_5, t_6]$ and the prompt windows $[t_3, t_4]$ should be the same. In the analysis the subtraction was implemented by filling the same histogram with different weights for events in the prompt windows $[t_3, t_4]$ and the background windows $[t_1, t_2]$ and $[t_4, t_5]$. The weight for events in the prompt windows was set to $w_p = 1$ and the weight for random coincidences was calculated via:

$$w_r = \frac{t_4 - t_3}{(t_2 - t_1) + (t_6 - t_5)} \quad (5.26)$$

The number of true entries N_t corresponding to the green areas in Fig. 5.63 is then calculated from the number of prompt entries N_p corresponding to the whole area under the peak via:

$$N_t = N_p + \sum_{i=1}^{N_r} w_r = N_p + w_r N_r \quad (5.27)$$

and the statistical error is given by

$$\Delta N_t = \sqrt{N_p + w_r^2 N_r} \quad (5.28)$$

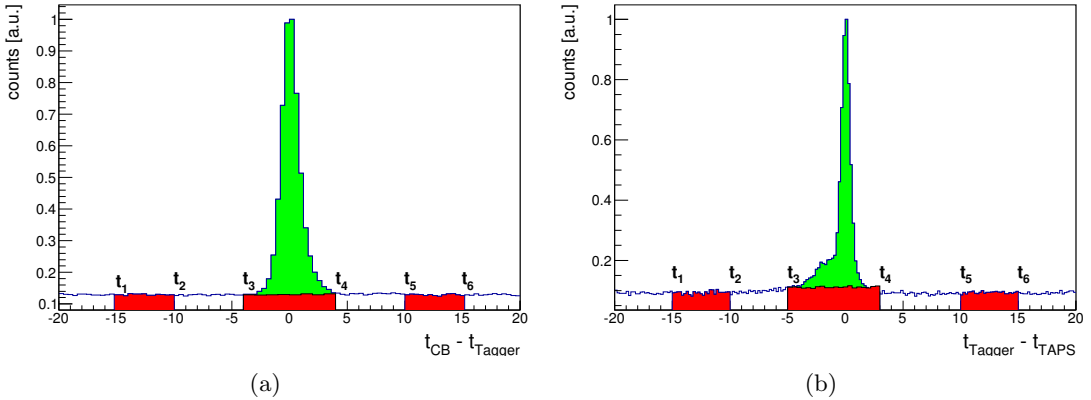


Figure 5.63.: random time

From equation 5.28 can be seen, that the statistical error is minimized by choosing large windows for the random background. The described procedure was only necessary for experimental data, since in the MC simulation there are no multiple electron hits per event.

5.10. Software Trigger

5.10.1. CB energy sum trigger

The energy-sum trigger checks the sum of the deposited energies of the particles in CB against a threshold value. Since the analog signals are used to determine the sum, the calibrated energies cannot be used for the software trigger. From the individual calibration gains of the 672 NaI crystals an average gain is calculated, that is used to decalibrate the energy information, thus reconstructing the analog signals. A detailed

description is given in [51] and [85]. The same procedure using the same values was applied to experimental and simulated data.

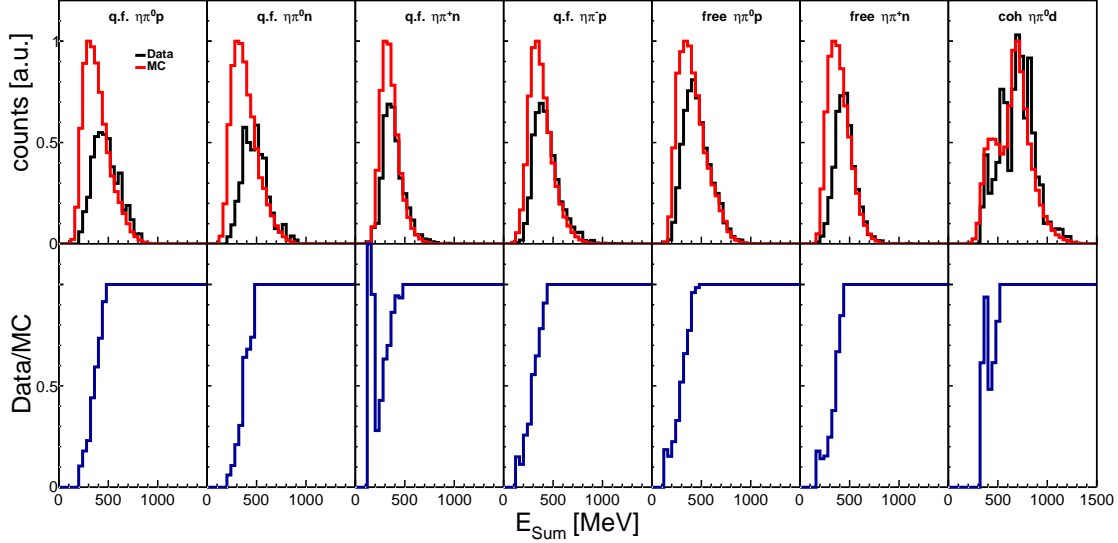


Figure 5.64.: CB energy sum for the exclusive reactions. The top row shows the distribution from experimental data in black and the distributions from simulated data in red. The bottom row shows the ratio of experimental data to simulated data.

Figure 5.64 shows the distributions of the CB energy sum for the exclusive channels. The distributions are normalized in the descending slope. It is evident, that for all channels events with a low energy sum are suppressed in the experimental data compared to the simulation because of the hardware trigger. To compensate for this, the ratio of experimental and simulated data was calculated, as shown in the lower row of Fig. 5.64. The resulting distribution was set constantly to 1, after the ratio first reached this value, and is referred to as cumulative distribution function (CDF).

The simulated data were then weighted with a factor $f_{MC} < 1$ directly taken from the CDF.

5.10.2. Multiplicity trigger

The multiplicity trigger was done in the same way as for experimental data. The CB is divided into 45 logical groups of 16 neighboring elements, and one block contributes to the multiplicity trigger if at least one element registers a signal above threshold.

TAPS was divided into 6 sectors that were tested against the LED1 threshold. The inner 3 rings of TAPS were rejected from the trigger decision to reduce electromagnetic background, and also the outermost ring was excluded due to shower loses and therefore wrong energy information. For the thresholds, the same values as for experimental data were used.

5.11. Detection efficiency correction

The detection efficiency of the detector setup is needed to normalize the results. For every reaction channel an individual efficiency was determined. As described in section 2.13.2, GEANT4 was used for the simulation of the reactions that were generated by PLUTO. For the liquid deuterium and deuterated butanol targets, the nucleons were generated with a momentum corresponding to the Fermi momentum distribution of deuterium. To account for the energy dependence of the bremsstrahlung process, simulated events were weighted with $1/E_\gamma$.

The target volume was either filled with liquid hydrogen, liquid deuterium or deuterated Butanol, and the reaction vertex was chosen randomly inside the volume of the target cell.

To reproduce the experimental conditions, the setup of every beam-time was implemented individually in the simulation. Also, the same detector thresholds and trigger conditions were applied as for experimental data. Additionally, the energy information was smeared as described in section 4.3 to account for the experimental resolution. The simulated data were then analyzed with the same software as experimental data. Furthermore, defective elements in the detectors that were rejected during the analysis of experimental data were also rejected in the simulation.

The detection efficiency was then determined using simulated events, by dividing the number of detected events N_{det} by the number of generated events N_{gen} .

$$\epsilon(E, \cos(\Theta_{\eta\pi,det}^*)) = \frac{N_{det}(E_{det}, \cos(\Theta_{\eta\pi,det}^*))}{N_{gen}(E_{gen}, \cos(\Theta_{\eta\pi,gen}^*))} \quad (5.29)$$

Again the energy E can be either E_γ or W. Since the energies and angles are not necessarily the same for generated and detected events, equation 5.29 yields effective efficiencies, that can have values greater than 1. These effective efficiencies have been found to better describe resolution effects close to threshold, than efficiencies that only rely on the information of the generated particles.

Since it is well established that the $\Delta\eta$ intermediate state plays a crucial role in the $\gamma p \rightarrow \eta\pi^0$ reaction, it was decided to compare phase space simulations with simulations that include a sequential decay. Figure 5.65 shows detection efficiencies as function of W for the quasi-free exclusive channels. The choice of the decay mode seems to have almost no effect on the efficiencies since phase space and simulations via a Δ resonance are in good agreement.

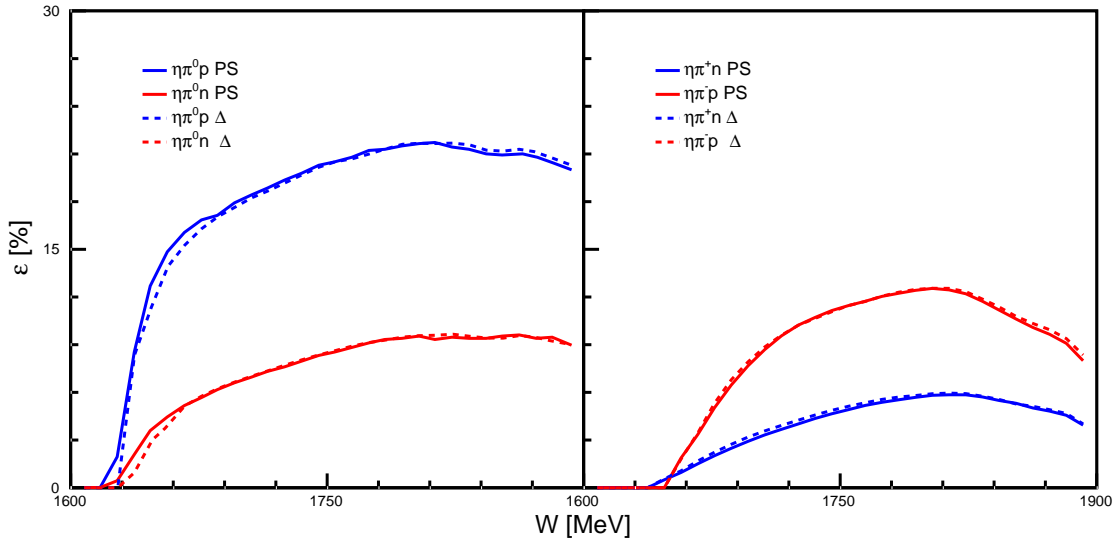


Figure 5.65.: Detection efficiency as function of the final state center of mass energy W for reactions with neutral pions in the final state. Solid lines: Simulations using a $\Delta\eta$ intermediate state. Dashed lines: Simulations using pure phase space. Reactions on the quasi-free proton are shown in red, reactions on the quasi-free neutron are shown in blue.

In addition, Fig. 5.66 shows mass distributions of the nucleon pion system. Results that were extracted using phase space simulations (green triangles) are compared to results from simulations using a sequential decay (blue triangles). Also shown are the line-shapes of the corresponding simulations with the same color coding.

The results extracted with both types of simulations are in good agreement, and since the line-shape of the simulations with a $\Delta\eta$ intermediate state describes the data much better, it was decided to use these simulations to normalize the results from free and quasi-free reactions. For the coherent reactions a pure phase space simulation was used.

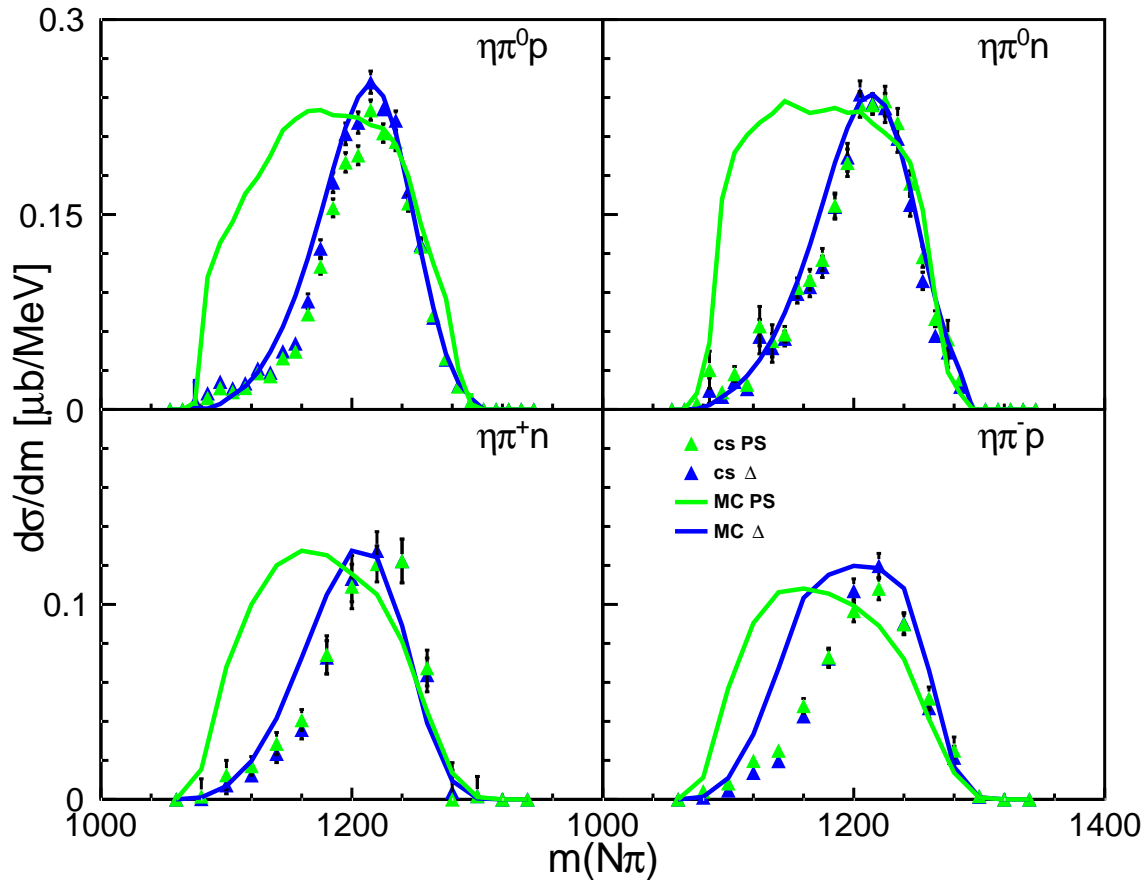


Figure 5.66.: Differential cross sections as function of the combined Nucleon-pion invariant mass. Blue Symbols: Cross sections extracted with a simulation that includes a $\Delta\eta$ intermediate state. Green Symbols: Cross sections extracted with a simulation that uses pure phase space. Solid lines: Line shapes of the used simulations, scaled to the corresponding data.

The detection efficiencies for all analyzed channel, as functions of E_γ and W , integrated over the whole angular range, are shown in Figs. 5.67 and 5.68.

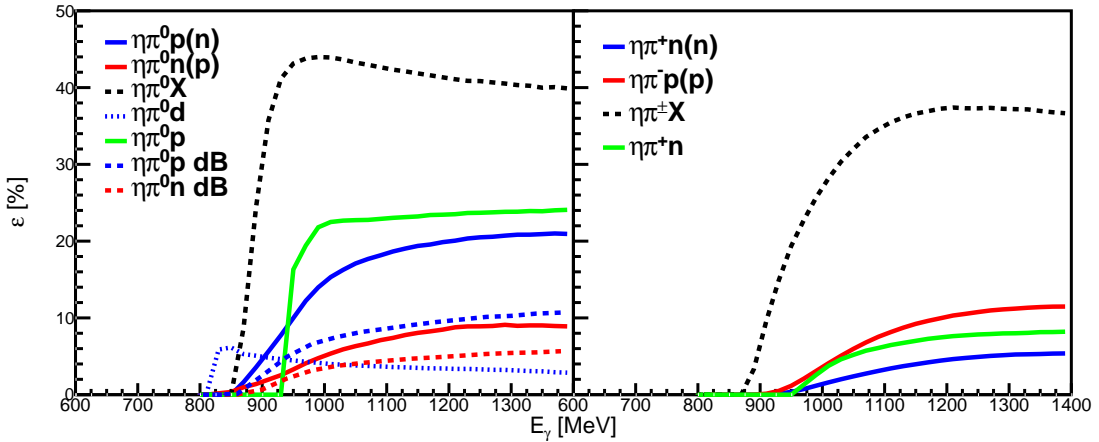


Figure 5.67.: Detection efficiencies as function of E_γ . The left side shows reactions with neutral pions in the final state, the right side shows reactions with charged pions in the final state.

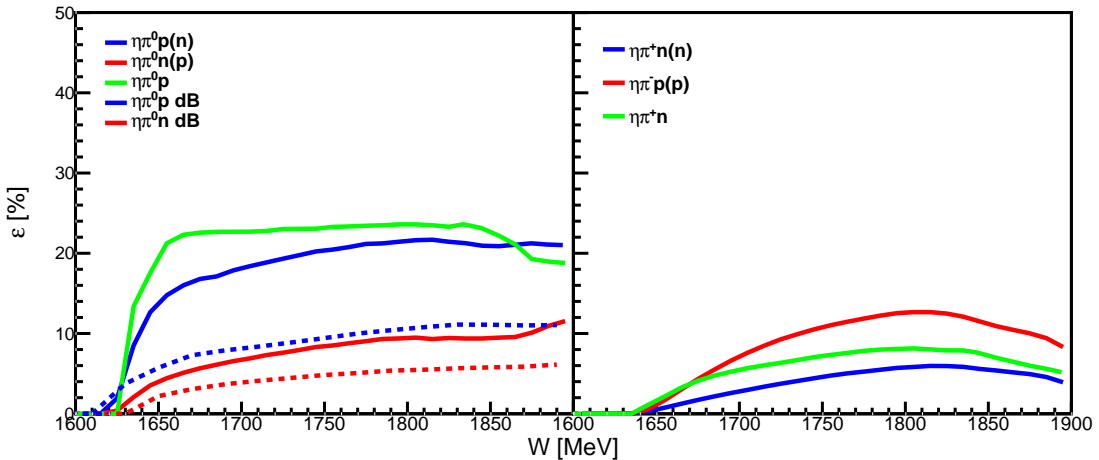


Figure 5.68.: Detection efficiencies as function of W . The left side shows reactions with neutral pions in the final state, the right side shows reactions with charged pions in the final state.

Figures show the detection efficiencies as functions of E_γ and W for all analyzed channels.

5.12. Nucleon detection efficiency correction

In [47] it was found that the detection efficiency determined with simulations had to be corrected with experimental data from a hydrogen target, to yield a precise nucleon detection efficiency. A correction is necessary to compensate for imperfections in the implementation of the experimental setup in GEANT and inefficiencies in the PID and

the TAPS vetoes. The following reactions were analyzed on the Apr 2009 beam-time to extract the corrections:



The most straightforward choice to extract the neutron detection efficiency $\gamma p \rightarrow \pi^+ n$ could not be used because the beam-time was taken using an M3+ trigger, but the reaction only has two particles in the final state. Additionally, the lack of photons in the final state leads to a worse time resolution, and hence worse random background subtraction in the tagger.

The reactions $\gamma p \rightarrow \eta \pi^0 p$ and $\gamma p \rightarrow \eta \pi^+ n$ are in principle suited to determine the nucleon detection efficiencies. But tests have shown that due to the very low cross section and insufficient statistics, the correction factor could not reliably be extracted. [63] compared the corrections extracted from $\gamma p \rightarrow \eta p$ and $\gamma p \rightarrow \pi^0 \pi^0 p$ and found, that the extracted corrections do not depend on the reaction. Therefore, the above mentioned reactions were chosen.

For both, experimental and simulated data, the nucleon detection efficiencies $\epsilon_p^d(T_p, \theta_p)$ and $\epsilon_n^d(T_n, \theta_n)$ were calculated by calculating the ratio of events where the recoil nucleon was detected, and all events (sum of events where the recoil nucleon was detected and events where it was not detected):

$$\begin{aligned} \epsilon_p^d(T_p, \theta_p) &= \frac{N(\pi^0 \pi^0 p)}{N(\pi^0 \pi^0 p) + N(\pi^0 \pi^0)} \\ \epsilon_n^d(T_n, \theta_n) &= \frac{N(\pi^+ \pi^0 n)}{N(\pi^+ \pi^0 n) + N(\pi^+ \pi^0)} \end{aligned} \quad (5.32)$$

The kinetic energy T_N and polar angle Θ_N of the nucleon in the lab frame were calculated using kinematics, as described in section 5.1, regardless if the recoil nucleon was detected or not.

From the efficiencies a correction factor $f_c(T_N, \Theta_N)$ was calculated

$$f_c(T_N, \Theta_N) = \frac{\epsilon_N^{MC}(T_N, \Theta_N)}{\epsilon_N^d(T_N, \Theta_N)}, \quad (5.33)$$

where ϵ^{MC} denotes the efficiency determined for the simulation, and ϵ^d denotes the efficiency for experimental data.

This correction factor was then applied to the detection efficiencies explained in section 5.11.

Figure 5.69 shows the correction factors for the proton and neutron detection efficiency for different Θ_N bins as function of T_N

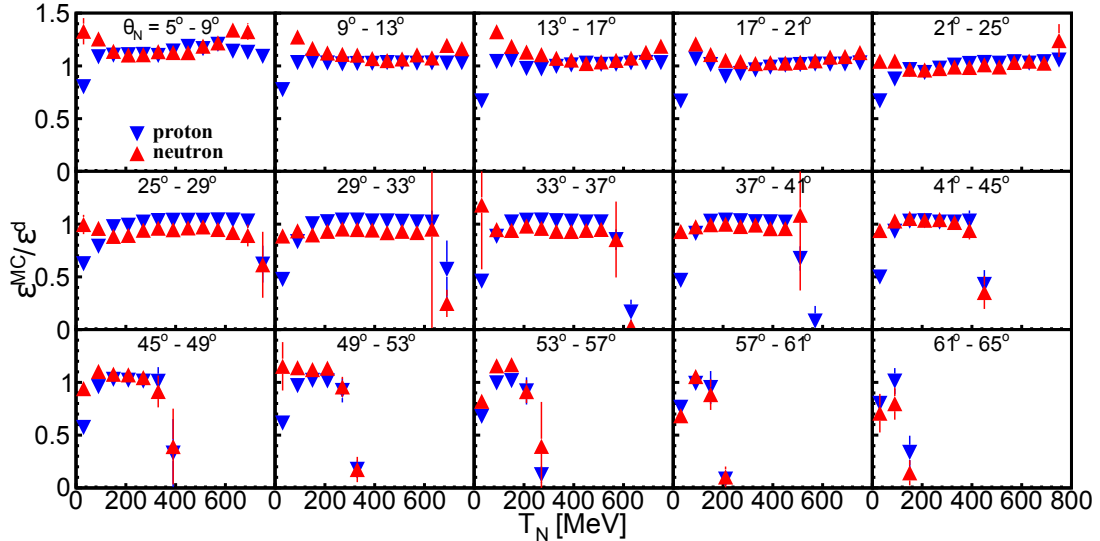


Figure 5.69.: Correction factor f_c for the nucleon detection efficiency. The correction for proton is shown in red, the correction for neutron in blue. Taken from [88].

For small nucleon energies and polar angles clear deviation from 1 can be seen. Nucleons in this region are detected in TAPS.

The described method to extract the correction factors does only work if the hydrogen beam-time has the same detector setup as the beam-times that need correction. This was the fact for the beam-times of Feb 2009 and May 2009, but not for December 2007 where the PID was shifted. Applying the same cut on the polar angle in the hydrogen beam-time is not suited to compensate this shift because of the different material budget. Therefore, the detection efficiency of the Dec 2007 beam-time could not be corrected in the affected area and the corresponding bins were excluded for the extraction of final results.

The nucleon detection efficiency correction seems to work reliably. In the results a comparison of the inclusive cross section $\gamma p \rightarrow \eta\pi^0$ from [22] with the exclusive cross section of $\gamma p \rightarrow \eta\pi^0 p$ of this work is shown, and the results are in excellent agreement.

5.13. Photon Flux

For a correct total normalization of observables it is important to know the exact number of photons, that impinged on the target. This photon-flux is determined from the number of electrons that were detected in one tagger channel $N_{e^-}(c)$ and the tagging efficiency of the corresponding channel $\epsilon_{tagg}(c)$.

$$N_\gamma(c) = N_{e^-}(c) \cdot \epsilon_{tagg}(c) \quad (5.34)$$

During the data acquisition $N_{e^-}(c)$ is constantly measured by scalers modules and stored for analyses.

These scales were only counting when the DAQ was not occupied with the readout of the detectors. During readout the detectors are not able to register new events, so in order to count the correct number of electrons, the scalers had to be inhibited when the DAQ was busy.

For the tagging efficiency measurements (see section 5.13.1) a dedicated taggerDAQ was used that operates independent of the DAQ for the regular data taking. The busy times of the two DAQ systems are different and therefore a correction had to be applied to the electron scalers using the lifetime of the tagger Γ_{tagg} and the lifetime of the other detectors Γ_{det} :

$$N'_{e^-} = N_{e^-} \frac{\Gamma_{det}}{\Gamma_{tagg}} \quad (5.35)$$

For the beam-times of this work, this correction was in the order of 25% - 30%. A detailed description can be found in [39].

5.13.1. Tagging efficiency

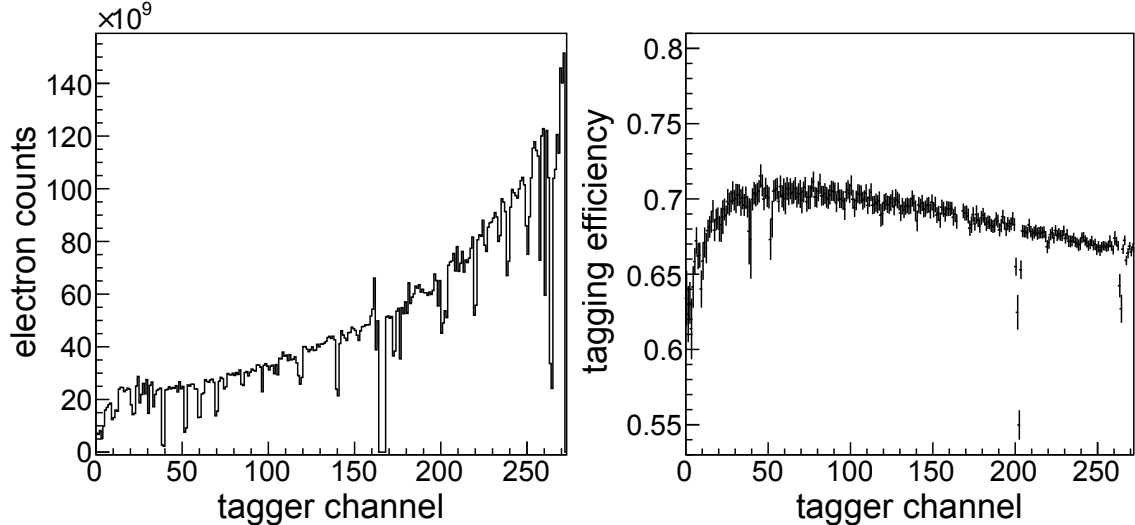


Figure 5.70.: Left-hand side: Electron counts per tagger channel detected by the scalers.
Right-hand side: Average tagging efficiency per tagger channel. Data from May 2009 beam-time. Figures taken from [47].

To determine the tagging efficiency, the normal data taking was paused to perform dedicated tagging efficiency runs at low beam intensities. A lead glass detector is inserted into the beam-line, that has a photon detection efficiency of nearly 100% so that the number of photons reaching the target could be determined. The low intensity is also needed to avoid random coincidences in the tagger. Since the tagging efficiency depends strongly on the size of the collimator that is used to focus the photon beam, and also

the electron energy, but only weakly on the photon beam intensity, it is assumed that the determined tagging efficiencies are also valid at high beam intensities.

At the low intensities of the tagging efficiency runs, there is a considerable amount of background contamination coming from cosmic radiation and activated material close to the tagger. To determine the amount of background events, two measurements are taken without beam, before and after the tagging efficiency run. The two background runs are averaged and subtracted from the events of the tagging efficiency run.

Average tagging efficiencies for all tagger channels of the May 2009 beam-time can be seen in Fig. 5.70.

Since the beam-quality and position are not constant over a beam-time, but can vary, also the tagging efficiency varies over time. Thus, the dedicated tagging efficiency runs were not sufficient to determine the averaged tagging efficiency.

To account for the time dependence, the photon beam was led to the P2 ionization chamber that is installed permanently at the end of the beam-line. The P2 counts are proportional to the photon flux on the target. Together with the counts in the tagger scalers a relative tagging efficiency over the whole beam-time could be determined by building the ratio between the P2 and tagger counts $r_{P2,tagg}$.

The relative efficiency could then be normalized with the efficiencies from the dedicated runs as shown in Fig. 5.72 to extract the time dependent tagging efficiency for each tagger channel:

$$\epsilon_{tagg}(c, t) = \frac{\bar{\epsilon}_{tagg}(c)}{\bar{\epsilon}_{tagg}} r_{P2,tagg}(t)_{norm} \quad (5.36)$$

The average efficiency of a tagger channel is given by:

$$\bar{\epsilon}_{tagg}(c) = \frac{1}{N_m} \sum_{i=1}^{N_m} \epsilon_i(c), \quad (5.37)$$

where $\epsilon_i(c)$ is the efficiency of the c -th channel in the i -th tagging efficiency measurement. The global average of the tagging efficiency is given by:

$$\bar{\epsilon}_{tagg} = \frac{1}{N_c} \sum_{c=1}^{N_c} \bar{\epsilon}_{tagg}(c) \quad (5.38)$$

The normalization of the tagger/P2 ratio to the absolute measurements was done by a χ^2 minimization.

5.13.2. E_γ dependent Flux

Knowing the number of electrons per tagger channel and the tagging efficiency, the number of photons that reached the target can be calculated with equation 5.35. To get the photon flux as a function of the photon energy E_γ these values have to be converted to photons per energy bin. This was done with the bin overlap method described in [47], which takes the different energy coverage of the tagger elements into account.

The energy binning was chosen identical to that of the excitation function histograms that were used to extract cross sections.

A typical spectrum is shown on the left side of Fig. 5.71. The bins at just below 900 MeV that show a notably lower count-rate come from broken tagger channels, that were omitted in the analysis.

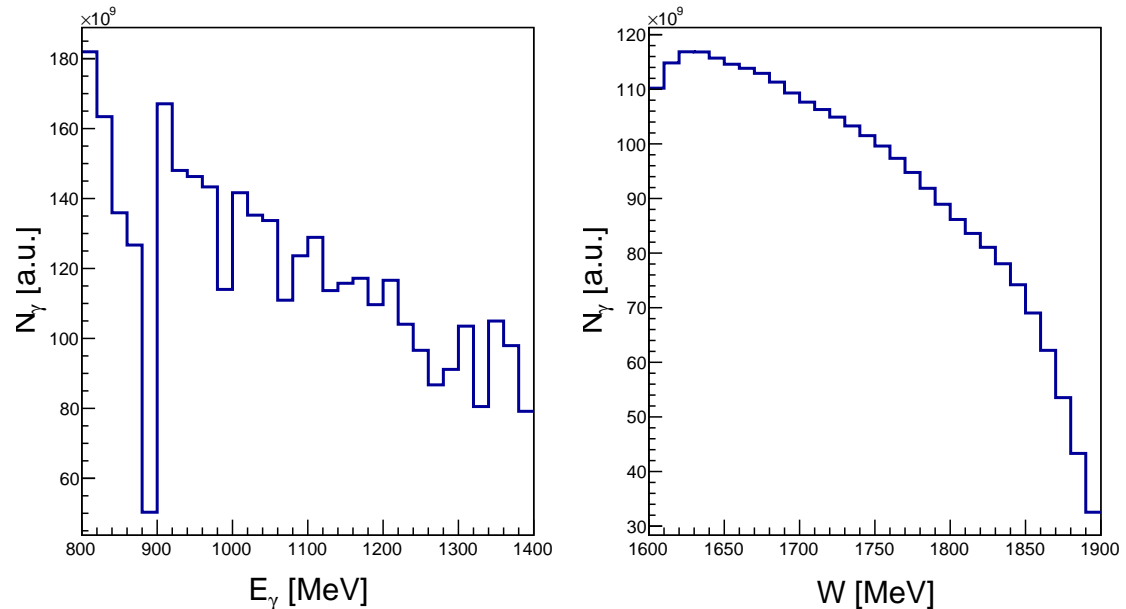


Figure 5.71.: Photon fluxes that impinged of the target. Left-hand side: Flux as function of the incident photon beam energy E_γ . Right-hand side: Flux as function the final state center of mass energy W . Data from the May 2009 beam-time

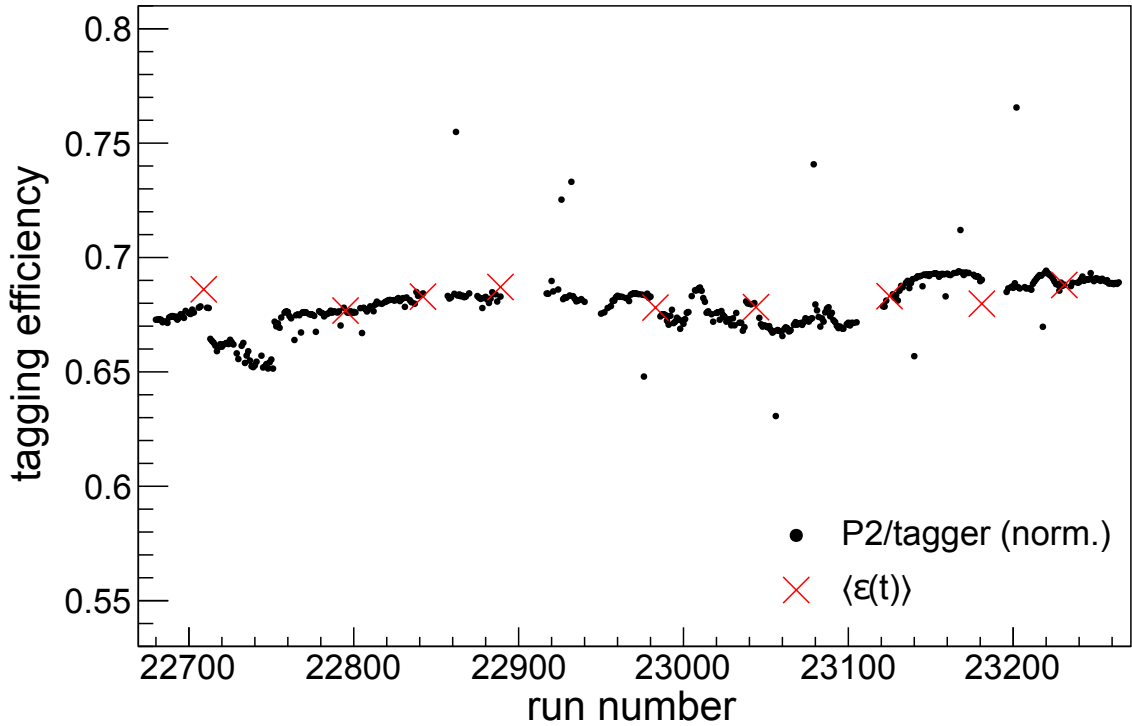


Figure 5.72.: Black points: normalized tagger/P2 ratio. Red crosses: tagging efficiency measurements. Taken from [47].

5.13.3. W dependent Flux

For the normalization of observables as function of the final state invariant mass W , the flux has to be converted into the number of photons per W bin. For the reactions on the free proton, this is straightforward, since E_γ can easily be converted into W with equation 5.39.

For the calculation of the W -dependent flux for reactions on nucleons that carry a Fermi momentum, the situation is more complicated. Due to the Fermi momentum different photon energies can contribute to the same bin of W as depicted in Fig. 5.73.

The used algorithm determines the W -distribution by sampling. For each tagger channel a large number n ($\sim 10^6$) of possible W values is determined via equation 5.5 by using the photon energy of the tagger channel and a random momentum, chosen from the deuteron Fermi momentum distribution from [92]. The possible values are weighted with N_γ/n and filled in a histogram, again using the bin overlap method.

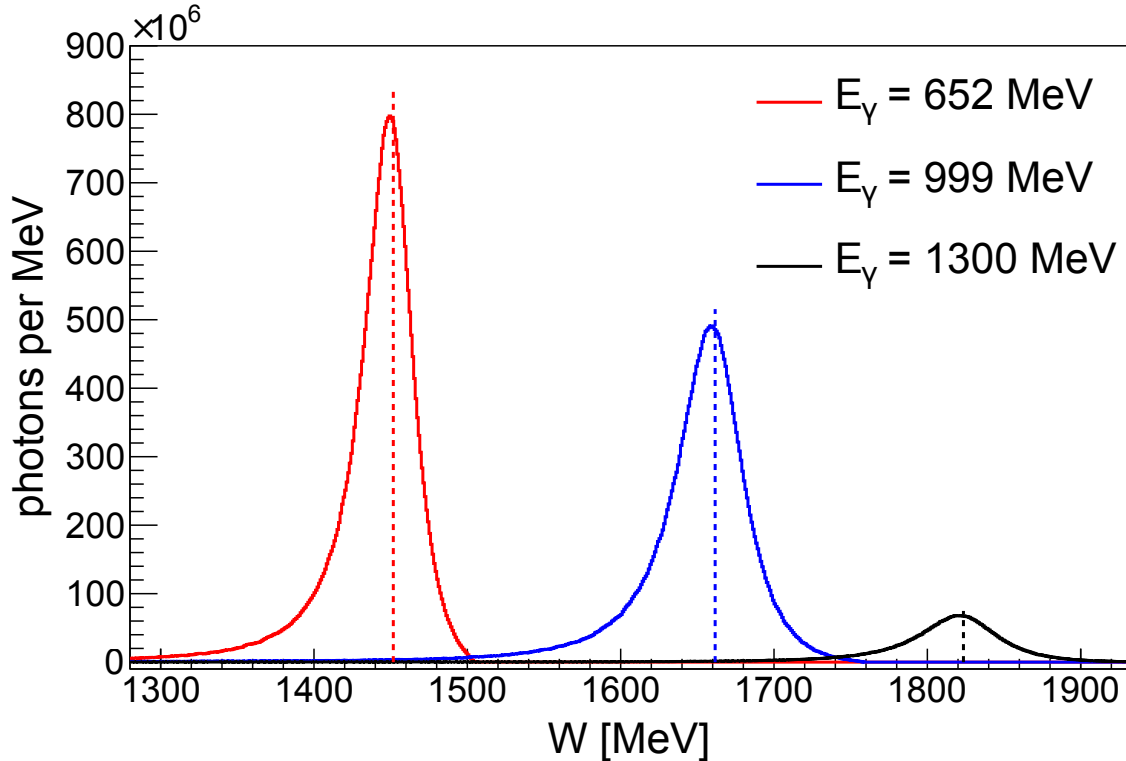


Figure 5.73.: Dashed lines: positions of $W = \sqrt{2E_\gamma m_N + m_N^2}$. Taken from [47].

5.14. Extraction of the true center of mass energy W

With a precise tagger calibration it is straightforward to get the energy of the incoming photons E_γ and therefore it is an obvious choice to extract observables in bins of or as function of E_γ as is shown in section 6.1 for the total cross sections. However, this does not account for the Fermi momentum of nucleons bound in nuclei.

In case of reactions on free nucleons, the center of mass energy W can be calculated from the initial state if the participant nucleon is assumed to be at rest:

$$\begin{aligned} W &= \sqrt{s} = \sqrt{(P_\gamma + P_P)^2} \\ &= \sqrt{2m_T E_\gamma + m_T^2}, \end{aligned} \tag{5.39}$$

where $P_\gamma = (E_\gamma, \vec{p}_\gamma)$ is the 4-vector of the incoming photon and $P_P = (m_T, 0, 0, 0)$ is the 4-vector of the participant.

Extracting cross sections with this assumption will lead to free cross sections folded with Fermi motion.

To account for the Fermi momentum in quasi-free reactions W has to be reconstructed from the reactions final state particles, in case of this work the η and π mesons and the

recoil nucleon.

$$W = \sqrt{s} = \sqrt{(P_\eta + P_\pi + P_N)^2} \quad (5.40)$$

The detection of nucleons and charged pions is less precise than the detection of photons since the detector setup is highly optimized for the detection of photons, what leads to a lower detection efficiency for nucleons. Furthermore, the position reconstruction is less precise for nucleons since they deposit their energy in smaller clusters than photons. In addition, the neutrons kinetic energy cannot reliably be reconstructed from its deposited energy as mentioned in section 5.5.1.

Therefore, a kinematic reconstruction of the kinetic energy of the recoil nucleon is used that relies on the meson 4-vectors and the recoil nucleons position (see equation 5.7).

5.15. Extraction of the Beam Helicity Asymmetry I^\odot

Polarization observables have proven to be very sensitive to reaction mechanisms, making them well suited for tests of model calculations.

The beam-helicity asymmetry $I^\odot(\Phi)$ is defined as follows:

$$I^\odot(\Phi) = \frac{d\sigma^+ - d\sigma^-}{d\sigma^+ + d\sigma^-} \quad (5.41)$$

where $d\sigma^+$ and $d\sigma^-$ are differential cross sections calculated for the two possible spin states of the circularly polarized photon beam, and Φ describes the angle between the production and the reaction plane in the cm system (see Fig. 5.74).

Φ can unambiguously be determined by the following relations:

$$\cos(\Phi) = \frac{(\vec{k} \times \vec{q})(\vec{q} \times \vec{p})}{|\vec{k} \times \vec{q}| |\vec{q} \times \vec{p}|} \quad (5.42)$$

$$\sin(\Phi) = -\frac{((\vec{k} \times \vec{q}) \times \vec{q})(\vec{q} \times \vec{p})}{|(\vec{k} \times \vec{q}) \times \vec{p}| |\vec{q} \times \vec{p}|}, \quad (5.43)$$

where \vec{k} is the momentum of the incoming photon γ , $\vec{q} = \vec{p}_1 + \vec{p}_2$ is the sum of the momenta of particles p_1 and p_2 , and \vec{p}_1 is the momentum of particle p_1 . All vectors are defined with respect to the γN cm system.

Many normalization factors are equal in the numerator and denominator of equation 5.41 and cancel out for the calculation of I^\odot and equation 5.41 simplifies to:

$$I^\odot(\Phi) = \frac{1}{P_\gamma} \frac{N^+(\Phi)/\epsilon - N^-(\Phi)/\epsilon}{N^+(\Phi)/\epsilon + N^-(\Phi)/\epsilon} \quad (5.44)$$

where N^\pm denotes the count rates of the respective spin states, ϵ is the detection efficiency, and P_γ is the degree of polarization of the photon beam. The difference in photon flux of both polarization states is at the 0.05% level and was not taken into account.

For integration over bigger phase space regions, the efficiency does not cancel out in the ratio and has to be taken into account.

Three different permutations of (p_1, p_2, p_3) can be chosen and hence 3 different asymmetries have been extracted:

- I_1^\odot with $(p_1, p_2, p_3) = (\eta, \pi, N)$ and angle Φ_1 .
- I_2^\odot with $(p_1, p_2, p_3) = (\pi, N, \eta)$ and angle Φ_2 .
- I_3^\odot with $(p_1, p_2, p_3) = (\eta, N, \pi)$ and angle Φ_3 .

Parity conservation leads to a symmetry condition for all the asymmetries I^\odot :

$$I^\odot(\Phi_i) = -I^\odot(2\pi - \Phi_i) \quad (5.45)$$

Furthermore, the asymmetries can be expanded into a sine series

$$I^\odot(\Phi) = \sum_{n=1}^{\infty} A_n \sin(n\Phi), \quad (5.46)$$

that can be fitted to the results.

The polarization transfer from the electron beam to the photon beam can be described by a relation given by Olsen and Maximon [94]:

$$P_\gamma = P_{e^-} \frac{4x - x^2}{4 - 4x + 3x^2}, \quad (5.47)$$

with the degree of electron polarization P_e^- and the relative photon energy $x = E_\gamma/E_e^{max}$.

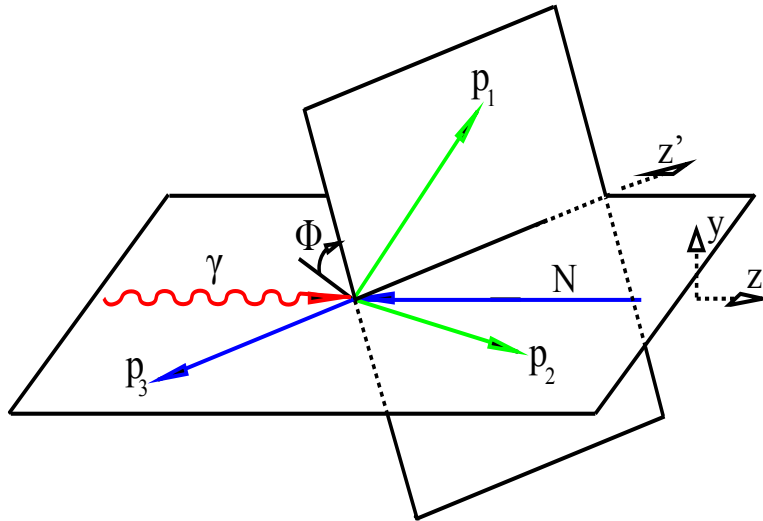


Figure 5.74.: Illustration of how the momentum vectors span the planes, used to determine the Φ angle. p_1 , p_2 and p_3 are a permutation of the recoil nucleon and the π and η mesons in the final state. The reaction plane is spanned by the momentum of the incident photon γ and the momentum of particle p_3 , the production plane is built by the momenta of particles p_1 and p_2 . All vectors are in the cm system.

5.16. Extraction of total cross sections

The unpolarized differential cross section $d\sigma/d\Omega$ as function of the energy E and the polar angle of the combined $\eta\pi$ system $\cos(\Theta_{\eta\pi}^*)$ can be written as:

$$\frac{d\sigma}{d\Omega}(E, \cos(\Theta_{\eta\pi}^*)) = \frac{N(E, \cos(\Theta_{\eta\pi}^*))}{N_\gamma(E) \cdot \epsilon(E, \cos(\Theta_{\eta\pi}^*)) \cdot \Gamma_r^\eta/\Gamma \cdot \Gamma_r^\pi/\Gamma \cdot \Delta\Omega \cdot n_t} \quad (5.48)$$

with the following definitions:

$N(E, \cos(\Theta_{\eta\pi}^*))$	yields as function of E and $\cos(\Theta_{\eta\pi}^*)$
E	E_γ or W
$\cos(\Theta_{\eta\pi}^*)$	the polar angle of the $\eta\pi$ system in the cm frame
$N_\gamma(E)$	number of incoming photons
$\Delta\Omega$	solid angle covered by $\cos(\Theta_{\eta\pi}^*)$ in [sr]
Γ_r^η/Γ	branching ratio for the decay $\eta \rightarrow 2\gamma = 39,41 \pm 0,2\%$
Γ_r^π/Γ	branching ratio for the decay $\pi^0 \rightarrow 2\gamma = 98,82 \pm 0,03\%$
$\epsilon(E, \cos(\Theta_{\eta\pi}^*))$	detection efficiency
n_t	target surface density in [b^{-1}]

The target density n_t was calculated via

$$n_t = \frac{f_{fill} \cdot \rho_t \cdot l_t \cdot N_A}{M_t}, \quad (5.49)$$

where ρ_t is the density of the target material, l_t is the target length, N_A is Avogadro's constant, and M_t is the molar mass. The filling factor f_{fill} gives the fraction of the volume, that is actually filled with target material. For the liquid targets $f_{fill} = 1$ holds, but for the dButanol f_{fill} is smaller, because the target volume is filled with spherical Butanol beads.

	Dec 07	Feb 09	Apr 09	May 09	Mar 15	Feb 14
Material	lD ₂	lD ₂	lH ₂	lD ₂	dButanol	Carbon
Length [cm]	4.72	4.72	4.72	3.02	2	2
f_{fill}	1	1	1	1	0.6	1
ρ_t [g/cm ³]	0.1623	0.1623	0.071	0.1623	1.1	0.57
M_{mol} [g/mol]	2.014	2.014	1.008	2.014	84.1923	12.011
n_t [b^{-1}]	0.23039	0.23039	0.422	0.14741	0.09442	0.05659

Table 5.2.: Target parameters. The targets for all dButanol beam-times were the same, therefore only the March 2015 beam-time is shown as example.

For convenience the total cross section was calculated as function of $\cos(\Theta)$ instead of Θ itself. With the substitution $\Theta \rightarrow \cos(\Theta)$ and hence $d\cos(\Theta) = -\sin(\Theta)d\Theta$, the solid angle bin $\Delta\Omega$ becomes constant for all bins and reads:

$$\Delta\Omega = \frac{4\pi}{N_b} \quad (5.50)$$

where N_b is the number of $\cos(\Theta)$ bins.

The total cross section can then be extracted by integrating the differential one:

$$d\sigma(E) = \int \frac{d\sigma}{d\Omega}(E, \cos(\Theta_{\eta\pi}^*)) d\Omega \approx \frac{4\pi}{N_b} \sum_{i=1}^{N_b} \frac{d\sigma}{d\Omega}(\cos(\Theta_{\eta\pi}^*)) \quad (5.51)$$

5.17. Extraction of the yields

The yields $N(E, \cos(\Theta_{\eta\pi}^*))$ of section 5.16 correspond to the number of correctly identified events of the reaction of interest. They were extracted in the following way: If an event passed all kinematical cuts, it was checked if the reconstructed pion mass was within the right limits. If so, the corresponding eta mass was filled into a histogram as function of energy as shown in section 5.5.4. For the unpolarized data 5 $\cos\theta$ bins were chosen, for the polarized data 1 $\cos\theta$ bin was used.

The resulting spectra were fitted with a combination of the simulated line-shape of the signal and simulated background contributions. Final yields then correspond to the integral of events under the signal peak within the used invariant mass cuts.

5.18. Extraction of angular distributions

Differential cross sections have been extracted as functions of $\cos(\Theta)$ and Φ of the pion in the nucleon-pion rest-frame for the free and quasi-free reactions in deuterium data. Two different coordinate systems, depicted in Fig. 5.75, were chosen to extract the differential cross sections.

In the canonical frame, the z' axis is chosen parallel to the photon beam direction, whereas it is parallel to the direction of the pion-nucleon system's momentum for the helicity frame.

In both systems, the y' axis is chosen as:

$$y' = \frac{\mathbf{p}_\eta \times \mathbf{k}_\gamma}{|\mathbf{p}_\eta \times \mathbf{k}_\gamma|}, \quad (5.52)$$

and the x' axis lies in the reaction plane and is oriented in a way that results in a right-handed coordinate frame.

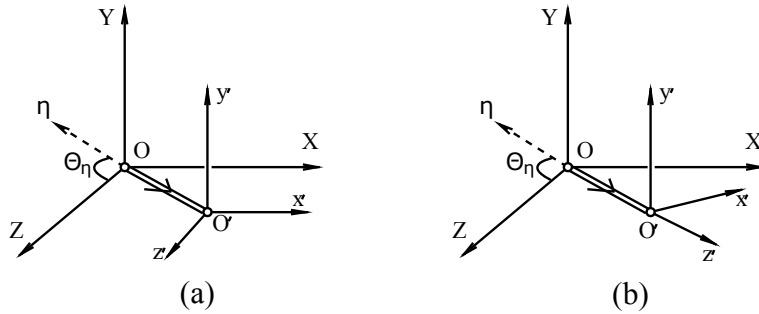


Figure 5.75.: Coordinate systems used to extract the angular distributions. The left-hand side shows the canonical system, with the z' axis in direction of the photon beam, the right-hand side depicts the helicity system with the z' axis in direction of the pion nucleon momentum.

In addition, differential cross sections were extracted as function of $\cos(\Theta_\eta^*)$ (section 6.2) and $\cos(\Theta_{\eta\pi}^*)$ (section A.2) in the global γ -nucleon CM system.

The resulting distributions are shown in section 6.4

5.19. Extraction of mass distributions

Distributions of meson-meson and meson-nucleon invariant masses were extracted as the magnitudes of the combined meson-meson and meson-nucleon 4-vectors. The results are shown in section 6.3.

5.20. Extraction of the double polarization observable E

The double polarization Observable E is defined as:

$$E = \frac{\sigma_{1/2} - \sigma_{3/2}}{\sigma_{1/2} + \sigma_{3/2}} = \frac{\sigma_{diff}}{\sigma_{sum}}, \quad (5.53)$$

where $\sigma_{1/2}$ and $\sigma_{3/2}$ denote the cross sections for events where the photon-spin and target spin are aligned anti-parallel and parallel, respectively.

For measurements on a dButanol target with a polarization degree of deuterons p_t and a circularly polarized photon beam of degree p_γ equation 5.53 can be written as:

$$E = \frac{1}{p_\gamma p_t} \frac{\frac{N_1^{dB}}{n_1^{dB} F_1^{dB}} - \frac{N_3^{dB}}{n_3^{dB} F_3^{dB}}}{\frac{N_1^{dB}}{n_1^{dB} F_1^{dB}} + \frac{N_3^{dB}}{n_3^{dB} F_3^{dB}}}, \quad (5.54)$$

where $N_1^{dB} = N_{1/2}^{dB}$ and $N_3^{dB} = N_{3/2}^{dB}$ are the count-rates of events with helicity $1/2$ and $3/2$. F_1^{dB} and F_3^{dB} are the corresponding photon fluxes, and n_1^{dB} and n_3^{dB} are the

normalization factors consisting of the detection efficiency ϵ , target density ρ and the branching ratio Γ_i/Γ .

Assuming that the detection efficiencies for both helicity states are equal, the normalization factors cancel out in the ratio. Additionally, it was assumed that the photon fluxes are equal: $F_1^{dB} = F_3^{dB} = F^{dB}/2$, where F^{dB} is the total flux on the dButanol target.

These assumptions simplify equation 5.54 to:

$$E = \frac{1}{p_\gamma p_t} \frac{(N_1^{dB} - N_3^{dB})/\frac{F^{dB}}{2}}{(N_1^{dB} + N_3^{dB})/\frac{F^{dB}}{2}} \quad (5.55)$$

However, the yields N_1^{dB} and N_3^{dB} are contaminated by contributions from the carbon and oxygen nuclei inside dButanol. This background contributes equally to both of the helicity states. Therefore, the difference of the dButanol yields can be written as:

$$N_1^{dB} - N_3^{dB} = N_1 + \frac{N_{CO}}{2} - N_3 + \frac{N_{CO}}{2} = N_1 - N_3, \quad (5.56)$$

where, N_1 and N_3 are the yields of the deuterium and N_{CO} are the yields of the carbon and oxygen.

For the sum of the dButanol yields the following equation can be found:

$$N_1^{dB} + N_3^{dB} = N_1 + \frac{N_{CO}}{2} + N_3 + \frac{N_{CO}}{2} = N_1 + N_3 + N_{CO}, \quad (5.57)$$

With eq. 5.56 and eq. 5.57 eq. 5.54 can be written as [75]:

$$E = \frac{1}{p_\gamma p_t} \frac{N_1 - N_3}{(N_1 + N_3 + N_{CO})N_\gamma^{dB}/2 - D \cdot (N^C F_\gamma^C/2)}, \quad (5.58)$$

where N^C are the carbon yields and D is the dilution factor (see section 5.20.1).

A second way to extract E can be used with the relation $\sigma_{1/2} + \sigma_{3/2} = 2\sigma_{unpol}$. Equation 5.53 can then be written as:

$$E = \frac{\sigma_{diff}}{2\sigma_{unpol}}. \quad (5.59)$$

This way of extracting E does not rely on the subtraction of the carbon content, since it cancels out in the denominator and the unpolarized cross sections were extracted using deuterium targets. It requires however the precise knowledge of the unpolarized cross sections, but since these cross sections were extracted as part of this work too, this method of extracting E is rather straightforward. In the following the method used to extract E according to eq. 5.58 will be called "version 1", eq. 5.59 will be referred to as "version 2".

5.20.1. Carbon Subtraction

For the determination of the carbon background dedicated beam-times were carried out, with the same experimental conditions as for the dButanol, but with a carbon target of comparable density. For a proper background subtraction, the relative contributions

of carbon and oxygen nuclei to the dButanol, also called dilution factor, has to be determined. This was done by comparing missing mass distributions of dButanol data, carbon data and deuterium data. If the individual data sets are properly normalized, the spectra of carbon and deuterium should add up to the dButanol.

Missing mass distributions are especially suited for this comparison, as contributions from different nuclei are well separated, due to different Fermi momenta.

The target density of deuterons inside the dButanol is given by:

$$n_t^{d,dB} = 10 \cdot n_t^{dB}, \quad (5.60)$$

since there are 10 deuterons per dButanol molecule.

Assuming that the cross section scales with the nuclear surface area $A^{2/3}$ [95], the contributions of the oxygen can be approximated with carbon by $(M_O/M_C)^{2/3}$ and the corresponding target density of carbon and oxygen in dButanol is given by:

$$n_t^{CO,dB} = \left(4 + \left(\frac{M_O}{M_C} \right)^{2/3} \right) n_t^{dB} \quad (5.61)$$

The contribution of ^3He and ^4He that surrounded the dButanol beads for cooling, can be calculated via:

$$n_t^{He} = \frac{((1-f)L_{dB} + L_{end})\rho_{He}N_A}{M_{He}}, \quad (5.62)$$

where L_{end} describes the size of the end-caps of the target and $\rho_{He} = 0.14 \text{ g/cm}^3$. With the approximation of helium with carbon, the target density of helium inside the dButanol is given by:

$$n_t^{He,dB} = \left(\frac{M_{He}}{M_C} \right)^{2/3} \cdot n_t^{He} \quad (5.63)$$

The normalization of the missing mass spectra was done with these normalization factors:

$$f_d = \frac{1}{n_t^d \epsilon_{dB} N_\gamma^{dB} \Gamma_i / \Gamma} \quad (5.64)$$

$$f_{dB} = \frac{1}{n_t^{dB} \epsilon_{dB} N_\gamma^{dB} \Gamma_i / \Gamma} \quad (5.65)$$

$$f_C = \frac{1}{n_t^C \epsilon_{dB} N_\gamma^C \Gamma_i / \Gamma} \cdot \frac{n_t^{CO,dB} + n_t^{He,dB}}{n_t^{dB}} \quad (5.66)$$

The corresponding distributions are shown for reactions on quasi-free protons and neutrons in Figs. 5.76 and 5.77 respectively.

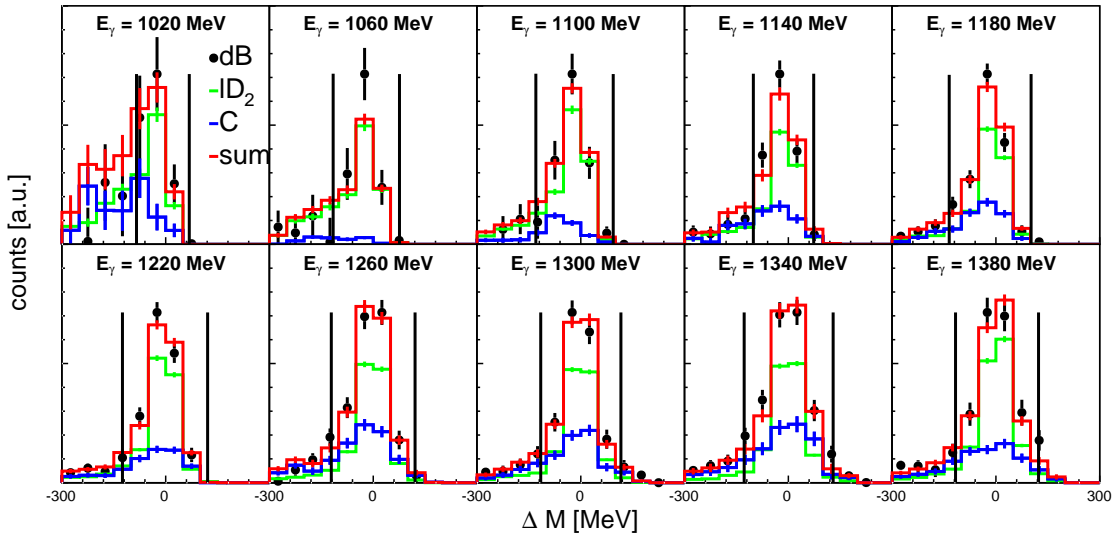


Figure 5.76.: Missing mass spectra for the reaction $\gamma p(n) \rightarrow \eta\pi^0 p$ on dButanol. The data from the dButanol target are shown in black. Contributions from deuterium are shown in green, contributions from the carbon target are shown in blue. The sum of deuterium and carbon contributions are shown in red.

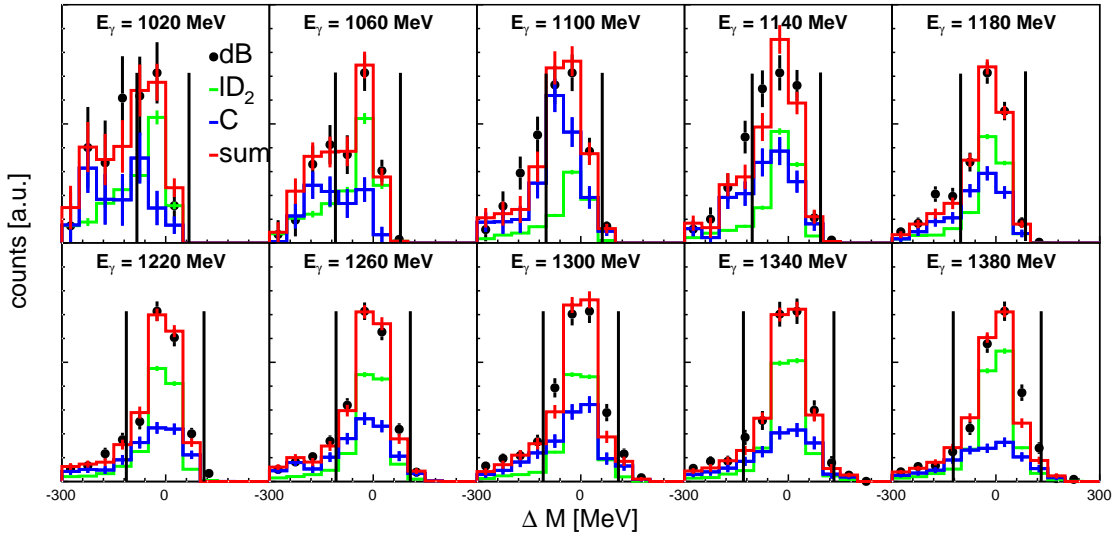


Figure 5.77.: Missing mass spectra for the reaction $\gamma n(p) \rightarrow \eta\pi^0 n$ on dButanol. The data from the dButanol target are shown in black. Contributions from deuterium are shown in green, contributions from the carbon target are shown in blue. The sum of deuterium and carbon contributions are shown in red.

For the longitudinally polarized dbutanol data only one data set with a carbon target was available. Since the statistics was hardly enough to determine the carbon contributions, it was decided to also use the carbon runs of the May 2016 beam-time. This beam-time was operating with a transversely polarized target, but since the holding field was turned off for the carbon runs, the only difference to the Feb 2014 beam-time was a different holding coil. Therefore, the systematic differences between the two carbon measurements are expected to be negligible.

5.20.2. Extraction of helicity dependent cross sections

Once the double polarization observable E is known it can be used to extract the helicity dependent cross-sections $\sigma_{1/2}$ and $\sigma_{3/2}$ via:

$$\begin{aligned}\sigma_{1/2} &= \sigma_{unpol}(1 + E) \\ \sigma_{3/2} &= \sigma_{unpol}(1 - E)\end{aligned}\tag{5.67}$$

Results extracted with these formulae will be denoted as 'version 1'.

It is also possible to extract the cross sections from the difference and sum:

$$\begin{aligned}\sigma_{1/2} &= \frac{\sigma_{sum} + \sigma_{diff}}{2} \\ \sigma_{3/2} &= \frac{\sigma_{sum} - \sigma_{diff}}{2}\end{aligned}\tag{5.68}$$

where again a subtraction of the carbon content in σ_{sum} is needed. Results extracted with these formulae will be denoted as 'version 2'.

If σ_{sum} is replaced by $2\sigma_{unpol}$ a third version to extract the helicity dependent cross-sections is possible without a carbon subtraction:

$$\begin{aligned}\sigma_{1/2} &= \frac{2\sigma_{unpol} + \sigma_{diff}}{2} \\ \sigma_{3/2} &= \frac{2\sigma_{unpol} - \sigma_{diff}}{2},\end{aligned}\tag{5.69}$$

Results extracted with these formulae will be denoted as 'version 3'.

It is also possible to directly extract the helicity dependent cross sections without a detour [63]:

$$\begin{aligned}\sigma_{1/2} &= \frac{N_{1/2}(1 + p) - N_{3/2}(1 - p)}{2Fnp} \\ \sigma_{3/2} &= \frac{N_{3/2}(1 + p) - N_{1/2}(1 - p)}{2Fnp},\end{aligned}\tag{5.70}$$

Results extracted with these formulae will be denoted as 'version 4'.

With the cross sections extracted according to equation 5.70, the observable E can also be directly determined according to Eq. 5.53. Results for E that were extracted using Eq. 5.70 are labeled 'version 3'.

5.21. Empty target subtraction

As mentioned above, the targets are surrounded by a target container made of Kapton, a polyimide which contains hydrogen, oxygen, nitrogen and carbon nuclei. So in addition to the nuclei inside the target, reactions can take place on the nuclei of the Kapton, and thus contribute to cross sections. Therefore, the amount of events coming from the target windows has to be determined and subtracted from the cross sections.

To estimate the contributions from the target window, empty target runs were performed during the April 2009, May 2009 and December 2007 beam-times. The empty target runs of December 2007 could not be used due to a normalization problem [47]. Overall there are 8 empty target runs for the May 2009 beam-time (deuterium) and 13 for the beam-time of April 2009 (hydrogen). These runs were analyzed in the same way as the productions runs, and the same cuts were applied. Yields were extracted and normalized as described above to calculate cross sections for the target windows.

Due to the limited amount of data, and the very low cross sections of the $\eta\pi$ reactions, the empty target cross sections were extracted for one $\cos(\Theta_{\eta\pi}^*)$ bin and 5 energy bins for E_γ and W. The resulting cross sections are shown in Fig. 5.78.

The contributions to the total cross sections were estimated to be in the order of 5 %. For the double polarization observable E no empty target subtraction was performed, since the same target container was used for dButanol and Carbon measurements therefore the empty target contribution is removed with the carbon subtraction. In the numerator the empty target contribution cancels out since it contributes equally to both spin configurations.

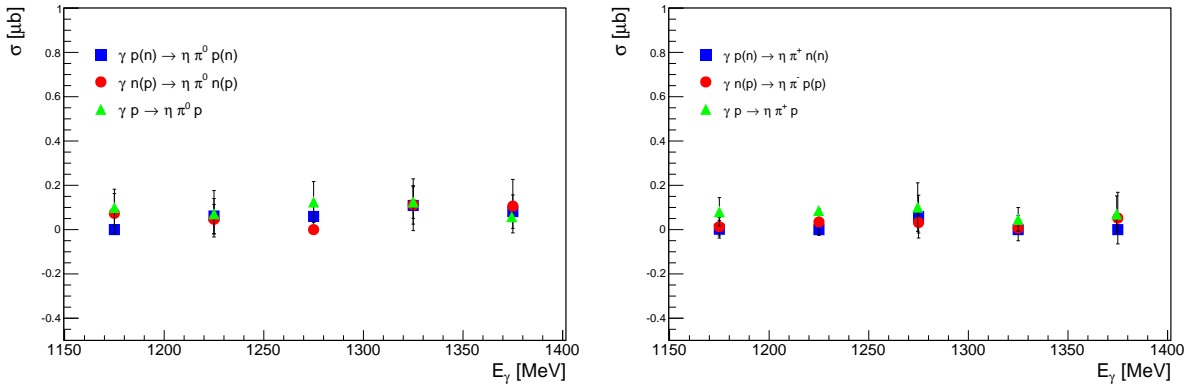


Figure 5.78.: Cross sections extracted from data using empty targets. The left-hand side shows cross sections for the neutral channels, the right-hand side shows cross sections for reactions with charged pions.

5.22. Merging of Data sets

The results of this work were obtained using data from several different beam-times. For the final results, individual cross sections were averaged, weighted with their statistical errors. For the polarized results the averages of σ_{diff} and σ_{sum} were determined.

$$\langle \sigma \rangle = \frac{\sum_{i=1}^n \frac{\sigma}{\Delta\sigma_i^2}}{\sum_{i=1}^n \frac{1}{\Delta\sigma_i^2}} \quad (5.71)$$

$$\langle \Delta\sigma \rangle = \frac{1}{\sqrt{\sum_{i=1}^n \frac{1}{\Delta\sigma_i^2}}} \quad (5.72)$$

5.23. Systematic uncertainties

The following sections will give an overview of the sources of systematic uncertainties introduced by the analysis steps and experimental conditions. Since the experimental conditions are the same for all reactions, the corresponding uncertainties have only to be determined once, while analysis-related errors have to be determined for each reaction individually.

5.23.1. Reaction independent systematic uncertainties

Target length

The target surface density is directly proportional to the length of the target cell (see eq. 5.49). The main uncertainty is related to a deformation of the inner target window [57].

The target length of Dec 2007 and Feb 2009 is given as (4.76 ± 0.05) cm, the values for Apr 2009 and May 2009 are (10.0 ± 0.08) cm and (3.02 ± 0.03) cm respectively. This lead to an average uncertainty of 1.1%.

Empty target

The relative empty target contributions (see section 5.21) seem to be independent of energy, although it is difficult to establish given the limited amount of empty target data. However, the same conclusion was drawn in the works of [63], [88], [47] and [75] that analyzed different reactions in the same data sets. Finally, it was assumed that half the empty target contribution corresponds to the systematic uncertainty.

Photon Flux

The main uncertainty in the determination of the photon flux comes from the tagging efficiency measurement (see 5.13.1). It was estimated to be in the order of 2.8% in [47].

5.23.2. Reaction dependent systematic uncertainties

Kinematic Cuts

The choice of the kinematic cuts also influences systematic uncertainties since they change the event selection. Signal to background ratios can be changed, simulated data could be handled differently than experimental data etc.

To estimate the influence, the positions of all cuts were varied by $\pm 3\%$ and cross sections were extracted with the modified cuts. Then the errors were calculated from the averaged deviations of the cross section data.

Crystal Ball Energy Sum

The CDF applied to the CB energy sum affects events with CB energy sums below ≈ 400 MeV. To estimate the systematic errors, cross section were extracted using the CDFs explained in section 5.10.1 and compared to cross section, that were extracted with a cut on the energy sum $E_{Sum} > 450$ MeV. Again, half of the deviation was used as the systematic error.

Nucleon Detection Efficiency

For the exclusive reactions, also the nucleon detection efficiency influences the results. To estimate the uncertainty, cross sections of the exclusive (recoil nucleon is required)

and inclusive (recoil nucleon is not required) reactions were compared. If the nucleon detection is accurate the following equations should hold true:

- $\sigma(\gamma N(N) \rightarrow \eta\pi^0(N)) = \sigma(\gamma p \rightarrow \eta\pi^0 p) + \sigma(\gamma n \rightarrow \eta\pi^0 n) + \sigma(\gamma d \rightarrow \eta\pi^0 d)$
- $\sigma(\gamma N(N) \rightarrow \eta\pi^\pm(N)) = \sigma(\gamma p \rightarrow \eta\pi^+ n) + \sigma(\gamma n \rightarrow \eta\pi^- p)$

For reactions on the free proton these relations read:

- $\sigma(\gamma p \rightarrow \eta\pi^0(N)) = \sigma(\gamma p \rightarrow \eta\pi^0 p)$
- $\sigma(\gamma p \rightarrow \eta\pi^+(N)) = \sigma(\gamma p \rightarrow \eta\pi^+ n)$

Any deviations from these relations can be attributed to the nucleon detection efficiency. Thus, for reactions on the deuteron, the difference between inclusive and the sum of the exclusive cross sections was calculated, while for reactions on free protons the difference between exclusive and inclusive cross-sections was determined. Finally, the half of these differences were assumed to be the systematic uncertainty of the nucleon detection efficiency.

ΔE - E analysis

The discrimination of charged particles also contributes to the systematic errors. To estimate it, the cut described in section 5.3 was shifted by $\pm 3\%$ and the deviations of cross sections were compared.

5.23.3. Summation of systematic uncertainties

The uncertainties of the above mentioned sources were combined individually for all investigated channels. Assuming that the errors are independent they were summed up quadratically:

$$\Delta_{sys}(E) = \sqrt{\sum_{i=1}^n (\Delta_{sys}^i(E))^2}, \quad (5.73)$$

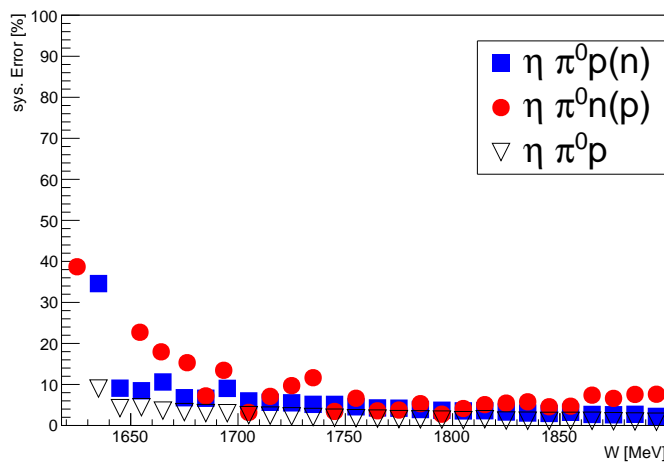


Figure 5.79.: Systematic Errors as function of the final state center of mass energy W for reactions with neutral pions. Blue squares: $\gamma p(n) \rightarrow \eta\pi^0 p(n)$. Red circles: $\gamma n(p) \rightarrow \eta\pi^0 n(p)$. Hollow triangles: $\gamma p \rightarrow \eta\pi^0 p$.

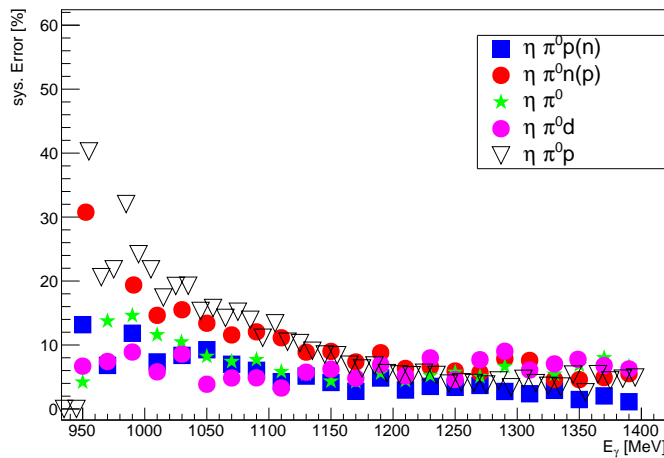


Figure 5.80.: Systematic Errors as function of the incoming photon energy E_γ for reactions with neutral pions. Blue squares: $\gamma p(n) \rightarrow \eta\pi^0 p(n)$. Red circles: $\gamma n(p) \rightarrow \eta\pi^0 n(p)$. Green stars: $\gamma d \rightarrow \eta\pi^0$. Magenta circles: $\gamma d \rightarrow \eta\pi^0 d$. Hollow triangles: $\gamma p \rightarrow \eta\pi^0 p$.

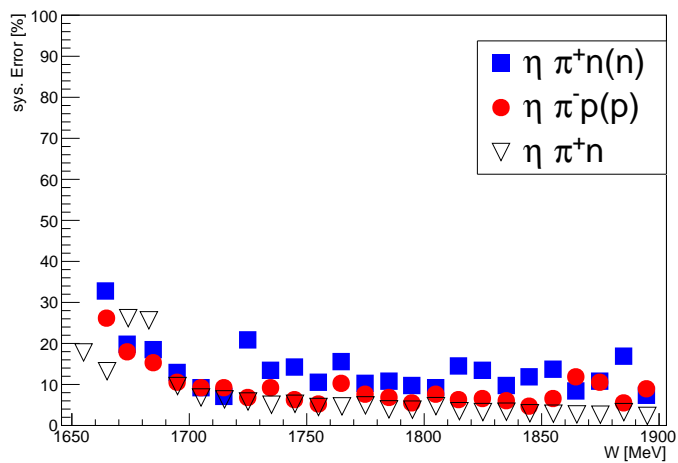


Figure 5.81.: Systematic Errors as function of the final state center of mass energy W for reactions with charged pions. Blue squares: $\gamma p(n) \rightarrow \eta\pi^+n(n)$. Red circles: $\gamma n(p) \rightarrow \eta\pi^-p(p)$. Hollow triangles: $\gamma p \rightarrow \eta\pi^+n$.

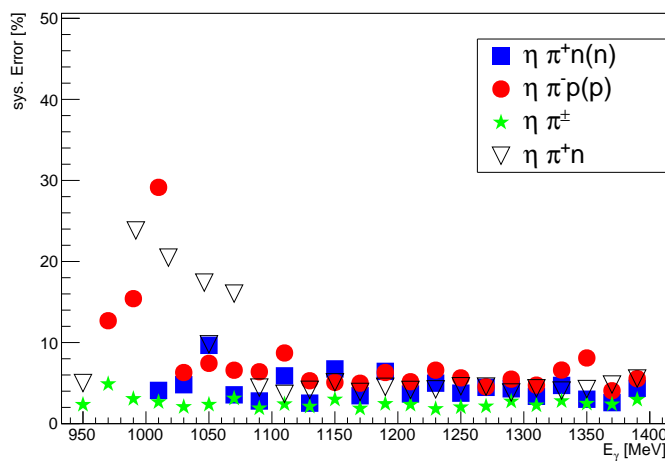


Figure 5.82.: Systematic Errors as function of the incoming photon energy E_γ for reactions with neutral pions. Blue squares: $\gamma p(n) \rightarrow \eta\pi^+n(n)$. Red circles: $\gamma n(p) \rightarrow \eta\pi^-p(p)$. Green stars: $\gamma d \rightarrow \eta\pi^\pm$. Hollow triangles: $\gamma p \rightarrow \eta\pi^+n$.

5.23.4. Uncertainties related to polarized data

The uncertainties described above also apply to the polarized data. However, in the determination of the double polarization observable E most of these uncertainties cancel out in the ratio. Uncertainties that do not cancel, for example uncertainties from the

carbon subtraction, where estimated by comparing the differences between the extraction methods.

$$\Delta E = \frac{1}{2} \max\{\Delta E_{12}, \Delta E_{13}, \Delta E_{23}\}, \quad (5.74)$$

where $\Delta E_{ij} = |E_i - E_j|$ is the absolute value of the difference between results of E determined with method i and j, respectively.

The systematic uncertainties of the helicity dependent cross sections were determined accordingly:

$$\Delta \sigma_{1/2} = \frac{1}{2} \max\{\Delta \sigma_{1/2}^{12}, \Delta \sigma_{1/2}^{13}, \Delta \sigma_{1/2}^{23}\} \quad (5.75)$$

$$\Delta \sigma_{3/2} = \frac{1}{2} \max\{\Delta \sigma_{3/2}^{12}, \Delta \sigma_{3/2}^{13}, \Delta \sigma_{3/2}^{23}\} \quad (5.76)$$

where $\Delta \sigma_{1/2}^{ij} = |\sigma_{1/2}^i - \sigma_{1/2}^j|$ is the absolute value of the difference of results of $\sigma_{1/2}$ determined with versions i and j respectively. This method takes uncertainties related to the carbon subtraction, analysis cuts, flux determination and nucleon detection efficiency into account.

Target polarization

Uncertainties related to issues with the target polarizations (see section 2.15) were determined in [75] by a renormalization of E in the threshold region of η photoproduction. The difference between the minimal and maximal scale factor was taken as the systematic uncertainty. A value of $\Delta P_T = \pm 10\%$ was found.

Photon polarization

The systematic uncertainties affecting the degree of photon polarization come from the Mott measurements described in section 2.9.1. The main sources of uncertainties are [65]:

- Determination of the electron spin angle, due to bending of the electron beam before extraction to the A2 hall (1.1 %).
- Admixture of transversely polarized electrons (2.2 %).
- finite thickness of the Mott radiator (1.1 %)
- statistical errors (0.2 %).

Overall, a value of $\Delta P_\gamma = 2.7\%$ was assumed.

Total systematic uncertainty

The systematic uncertainties from the target and beam polarizations were summed quadratically:

$$\Delta P = \sqrt{P_T^2 + P_\gamma^2} \approx 10.4\%. \quad (5.77)$$

The total systematic uncertainty of the helicity dependent cross sections and the observable E were then determined via:

$$\Delta E^{tot} = \sqrt{\Delta E^2 + \Delta P^2} \quad (5.78)$$

$$\Delta \sigma_{1/2}^{tot} = \sqrt{\Delta \sigma_{1/2} + \Delta P^2} \quad (5.79)$$

$$\Delta \sigma_{3/2}^{tot} = \sqrt{\Delta \sigma_{3/2} + \Delta P^2} \quad (5.80)$$

6. Results

In this chapter, the final results obtained in this work will be presented. Total cross sections have been extracted as function of the incoming photon energy E_γ and as function of the final state invariant mass W . In addition differential cross sections as well as helicity asymmetries have been extracted for several bins of W . The final state invariant mass was reconstructed from the final state particles for all reactions (see section 5.14). Section 6.1 will show the extracted total cross sections, differential cross sections will be shown in sections 6.2 - 6.4 and helicity asymmetries can be found in section 6.5. Each of these sections will be split in two parts, the first containing results for reactions with neutral pions in the final state, while results with charged pions will be shown in the second part. Results for the double polarization observable E are shown in section 6.6, results for the helicity dependent cross sections are shown in section 6.7.

6.1. Total cross sections

This section shows the total cross sections of all analyzed channels as function of E_γ in Figs. 6.1 and 6.3, and as function of W in Figs. 6.2 and 6.4. The cross section of the coherent reaction will be shown in Fig. 6.5.

To test the analysis, free proton data were analyzed and compared to previous results of $\eta\pi^0$ production from [22]. As can be seen in Fig. 6.2, the results from this work (green triangles) are in excellent agreement with earlier results (open circles).

All Figs. show almost perfect agreement between quasi-free proton (blue squares) and neutron (red circles) data which is in accordance with the assumption, that the reactions take predominantly place via a cascade decay of the form $\Delta^* \rightarrow \eta\Delta(1232) \rightarrow \eta\pi N$.

The comparison between free and quasi-free proton data shows clear indication for FSI effects, that are responsible for the lower cross sections on quasi-free protons. FSI effects seem to be more pronounced for $\eta\pi^0$ channels than for reactions with charged pions in the final state. The same can be seen in single pion production [12].

The comparison of quasi-free inclusive and exclusive cross sections in Figs. 6.1 and 6.4 allows to check the quality of the nucleon detection efficiencies. Ideally the sum of quasi-free proton and neutron cross sections (and the coherent cross section in case of $\eta\pi^0$ production) should be equal to the inclusive cross section. Any deviations point to a systematic problem with the nucleon detection.

As can be seen, the sum of the quasi-free cross sections agree very well with the inclusive cross sections. The deviations are below the 5% level. This comparison is not possible for cross sections as function of W since the recoil nucleon has to be detected in order to reconstruct the final state invariant mass. Therefore, no inclusive cross sections can

be extracted since the analysis does not explicitly ask for the recoil nucleons for this reaction channels (see table 5.2) in section 5.2.

6.1.1. Cross sections for $\eta\pi^0$ channels

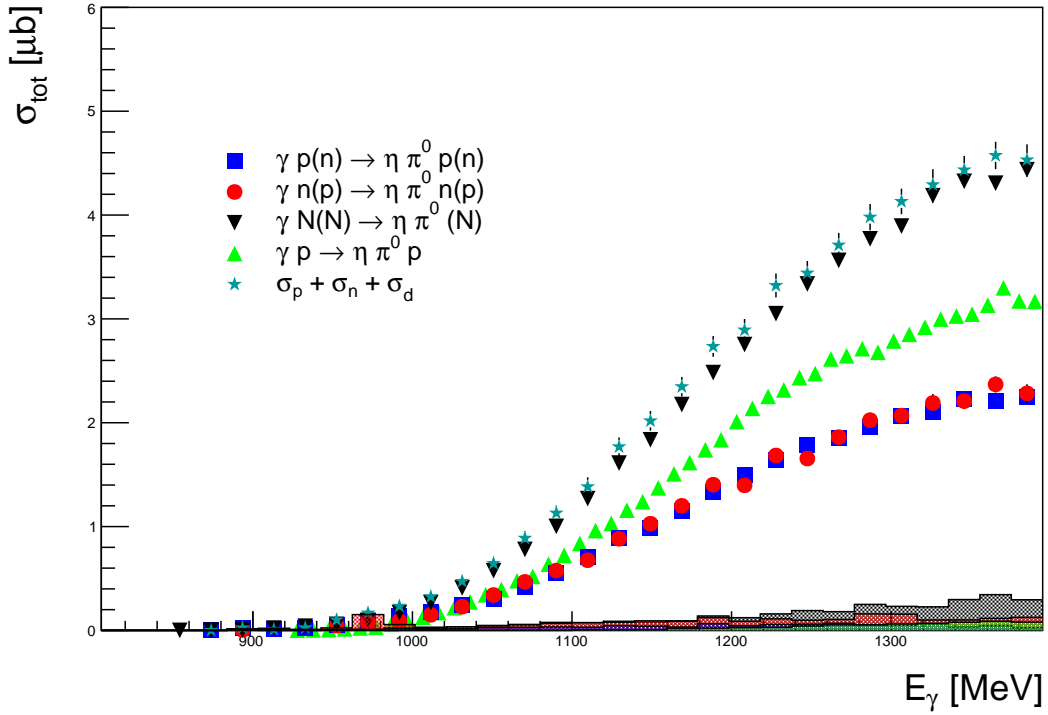


Figure 6.1.: Total cross sections for $\eta\pi^\pm$ production as functions of the incident photon energy E_γ . Blue: Exclusive reaction on quasi-free protons. Red: Exclusive reaction on quasi-free neutrons. Magenta: Exclusive reaction on free protons. Green: sum of the cross sections of the reactions on quasi-free protons and neutrons. Black: Inclusive reaction on quasi-free protons and neutrons. The shaded areas show the systematic uncertainties.

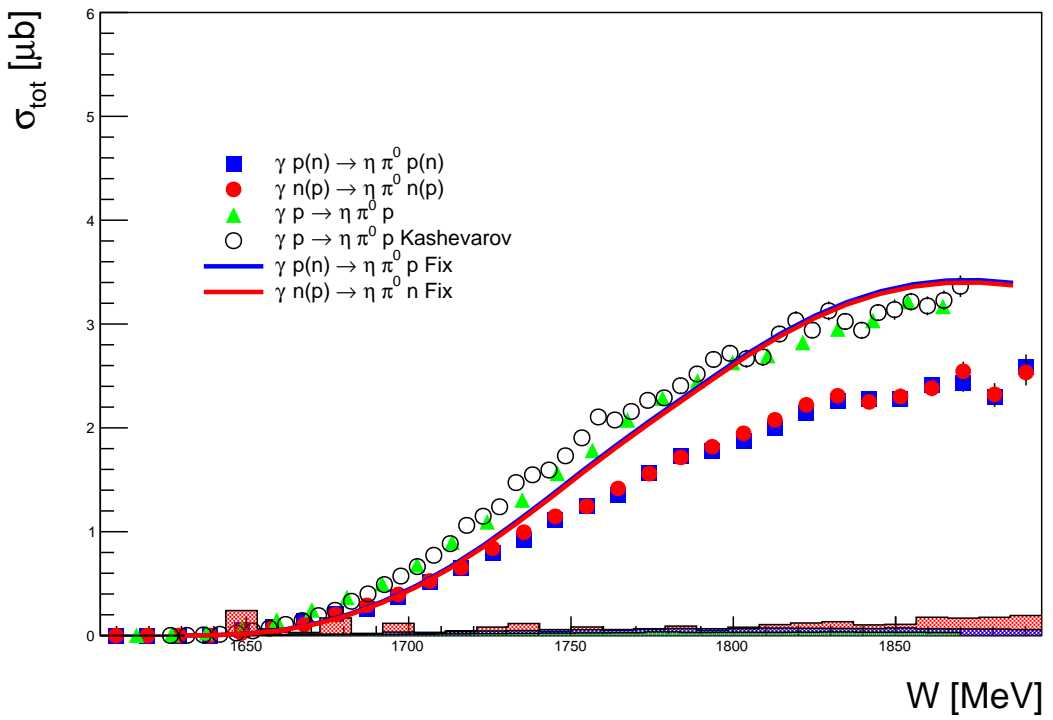


Figure 6.2.: Total cross sections for $\eta\pi^\pm$ production as functions of the final state invariant mass W . Blue: Exclusive reaction on quasi-free protons. Red: Exclusive reaction on quasi-free neutrons. Green: Exclusive reaction on free protons. Open black: Inclusive reactions on free protons from [22]. Solid lines: Theoretical predictions with the same color coding as experimental results. The shaded areas show the systematic uncertainties.

6.1.2. Cross sections for $\eta\pi^\pm$ channels

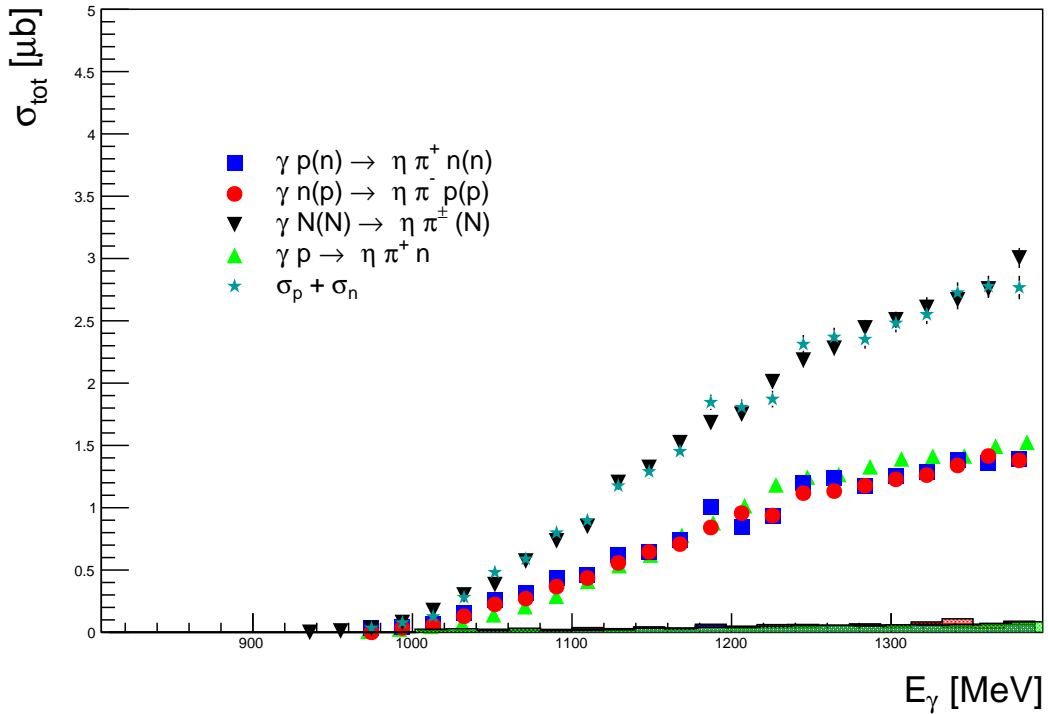


Figure 6.3.: Total cross sections for $\eta\pi^\pm$ production as functions of the incident photon energy E_γ . Blue: Exclusive reaction on quasi-free protons. Red: Exclusive reaction on quasi-free neutrons. Magenta: Exclusive reaction on free protons. Green: sum of the cross sections of the reactions on quasi-free protons and neutrons. Black: Inclusive reaction on quasi-free proton and neutrons. The shaded areas show the systematic uncertainties.

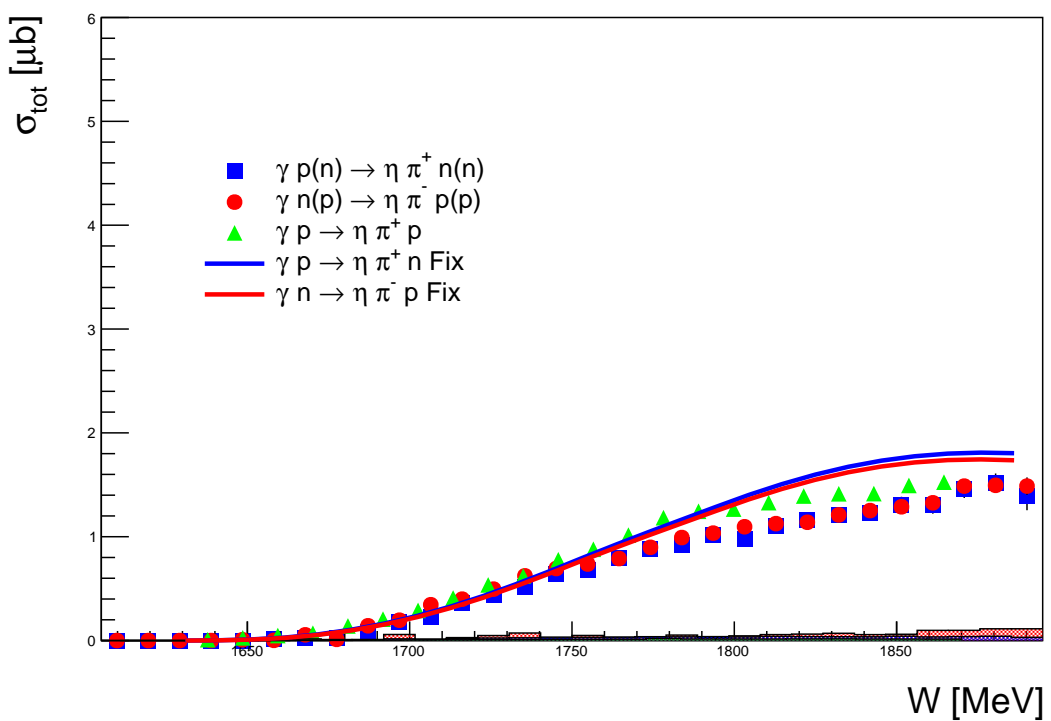


Figure 6.4.: Total cross sections for $\eta\pi^\pm$ production as functions of the final state invariant mass W . Blue: Exclusive reaction on quasi-free protons. Red: Exclusive reaction on quasi-free neutrons. Green: Exclusive reaction on free protons. Solid lines: Theoretical predictions with the same color coding as experimental results. The shaded areas show the systematic uncertainties.

6.1.3. Cross-section for $\eta\pi^0$ coherent

The deuteron has isospin $I = 0$. The coherent amplitude of $\eta\pi^0$ production is proportional to the sum of the amplitudes of the quasi-free reactions:

$$A(\gamma d \rightarrow \eta\pi^0 d) \propto A(\gamma p \rightarrow \eta\pi^0 p) + A(\gamma n \rightarrow \eta\pi^0 n) \quad (6.1)$$

If the expressions from equations 1.37 are inserted in eq. 6.1, it follows immediately, that the isoscalar component A^{IS} cancels out. Therefore, the isoscalar excitation of N^* resonances is forbidden. The total cross section of the reaction is compared to model predictions from [21] in Fig. 6.5. The model only includes Δ resonances and the good agreement with experimental data is another hint, that N^* resonances only play a minor role in $\eta\pi$ photoproduction.

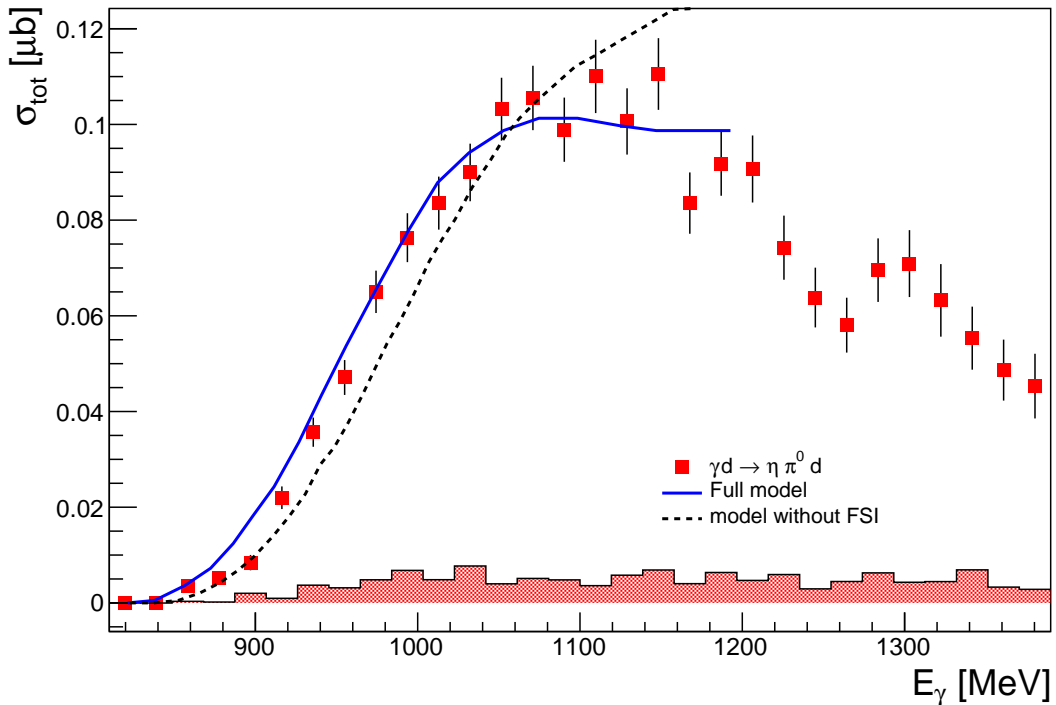


Figure 6.5.: Red squares: total cross section of the reaction $\gamma d \rightarrow \eta\pi^0 d$. Solid blue line: model prediction from [21] including FSI. Dashed black line: model prediction from [21] without FSI. The shaded area shows the systematic uncertainty.

6.1.4. Ratios of total cross sections of quasi-free reactions

The ratios of the total cross sections were determined and are shown as function of W in Fig. 6.6. It can be seen, that the relations of equation 1.37 hold excellently what is a strong hint that $\eta\pi$ photoproduction takes dominantly place via a decay of the form 1.36, and that N* resonances play only a minor role in the investigated energy range. However, exact quantum number of the involved Δ resonances cannot be derived from the cross section ratios.

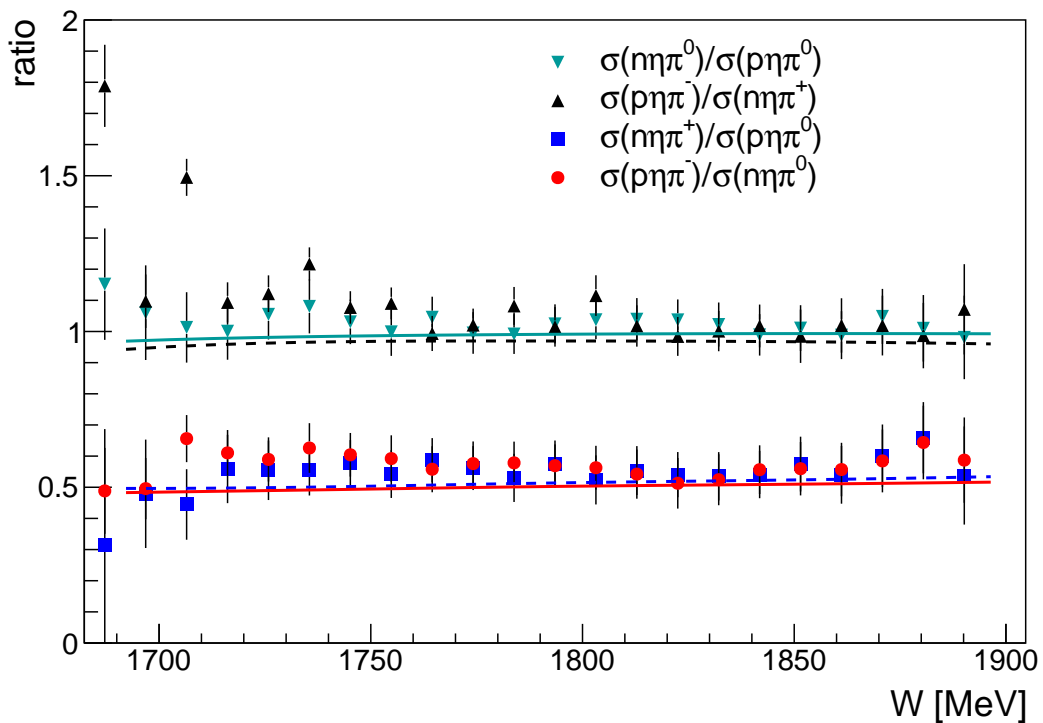


Figure 6.6.: Ratios of cross section as function of W. Blue show the ratio of the cross sections of the quasi-free reactions off the proton, red show the ratio of the cross sections of the reactions off quasi free neutrons, black shows the reaction of the cross sections with neutral pions in the final state, and cyan shows the ratio of the cross sections with charged pions in the final states. In the legend, the respective final state particles are denoted. The solid and dashed lines describe the ratios of the theoretically predicted cross sections, with the same color coding.

6.2. $\cos(\theta_\eta)$ distributions

This section describes the differential cross sections as function of the azimuthal angle of the η meson θ_η in the γN center of mass frame, for 4 bins of W . The differential cross sections are normalized to the total cross sections to remove possible FSI effects and to simplify comparisons between free and quasi-free results. After this renormalization the results of the free proton agree nicely with the results of the quasi-free reactions, indicating that FSI effects only influence the absolute magnitude of the cross-sections, but not the shape. Also, the experimental results agree reasonably with the model predictions. For both isospin channels, the distributions are almost isotropically flat for energies near the threshold. This is in accordance with [22] [28], since the $\Delta(1700)3/2^-$ is the only candidate that decays to $\eta\Delta$ in a relative s-wave state.

6.2.1. $\eta\pi^0$ channels

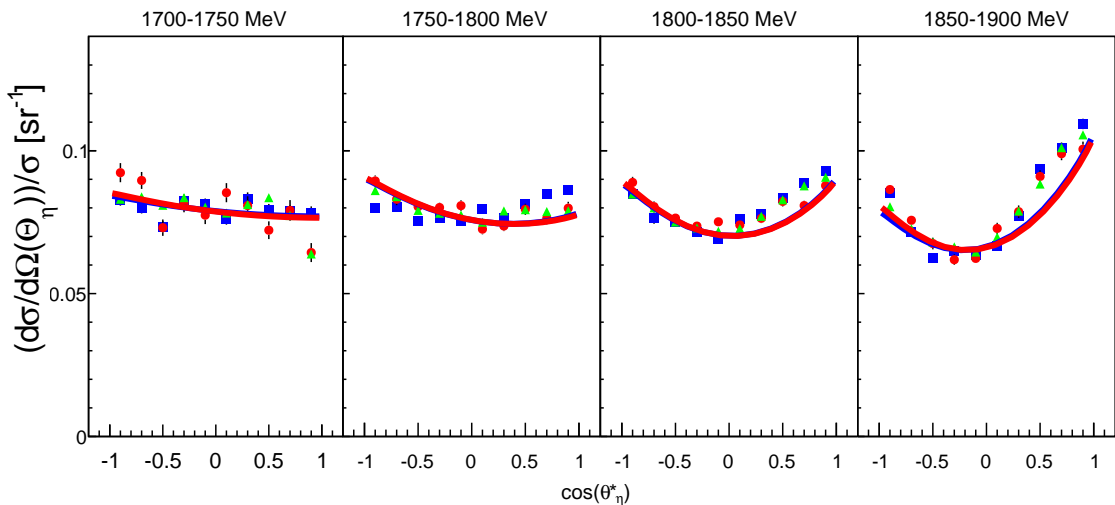


Figure 6.7.: Differential cross sections for the production of $\eta\pi^0$ pairs in the γN center of mass system. Blue: exclusive reaction on quasi-free protons. Red: Exclusive reaction on quasi free neutrons. Green: Exclusive reaction on free protons. Solid lines: Theoretical predictions from [20]. Results overlap, so they might be difficult to distinguish.

6.2.2. $\eta\pi^\pm$ channels

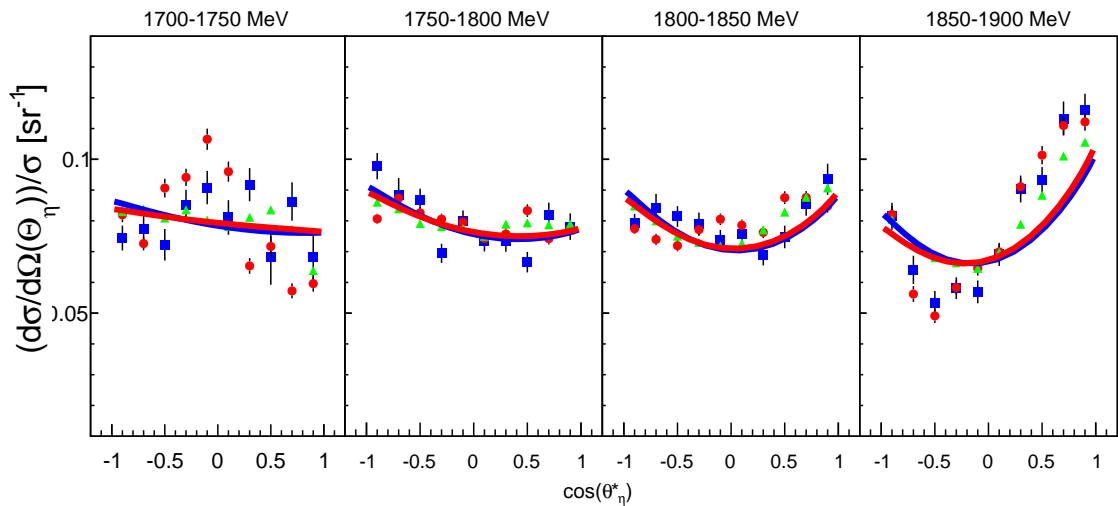


Figure 6.8.: Differential cross sections for the production of $\eta\pi^\pm$ pairs in the γN center of mass system. Blue: elusive reaction on quasi-free protons. Red: Exclusive reaction on quasi free neutrons. Green: Exclusive reaction on free protons. Solid lines: Theoretical predictions from [20].

6.3. Invariant Mass Distributions

This section shows the invariant mass distributions $m(N\eta)$ (top row), $m(N\pi)$ (middle row) and $m(\eta\pi)$ (bottom row) in Figs. 6.9 and 6.10. Results for reactions on quasi-free protons are shown as blue squares, neutron results are shown as red circles and free proton results are shown as green triangles. All differential cross sections are divided by the total cross section in the corresponding energy bins, to make comparison easier, by removing scaling effects due to final state interactions. The solid curves represent model calculations from [20]. For all three types of mass distributions it can be seen, that there is practically no difference in shape between the quasi-free proton and neutron data. Also, the shape of the distributions of free and quasi-free protons is in almost perfect agreement. In addition, the model calculations describe the data very well and are almost identical for all channels. There are some small differences in the sharp peak maxima of the nucleon-meson distributions between experimental data and model predictions. These are most likely caused by the finite resolution of the detector systems, which was not taken into account in the predictions.

The $N\pi$ distributions of all reaction channels show a pronounced peak at the position of the $\Delta(1232)$ resonance. Only at the very lowest energies, the distributions peak at values below 1232 MeV, which is due to the low photon energies in this range, that are not high enough to populate the $\Delta(1232)$.

Neither the $N\eta$ nor the $\eta\pi$ distributions show such pronounced peaks. Earlier results obtained from free proton data [25] show contributions from the $N(1535)1/2^-\pi$ intermediate state, but the photon energies in this work were not high enough to reproduce them. For the same reason, there is no indication of the $a_0(980)$ meson in the $\eta\pi$ distributions. The $a_0(980)$ decays into the $\eta\pi^0$ and thus, could contribute to the cross section at higher energies.

In summary, the invariant mass distributions show clear contributions of a $\Delta\eta$ intermediate state for all analyzed reaction channels, and thus clearly favor a decay chain of the form $\Delta^* \rightarrow \Delta\eta \rightarrow N\eta\pi$.

6.3.1. $\eta\pi^0$ channels

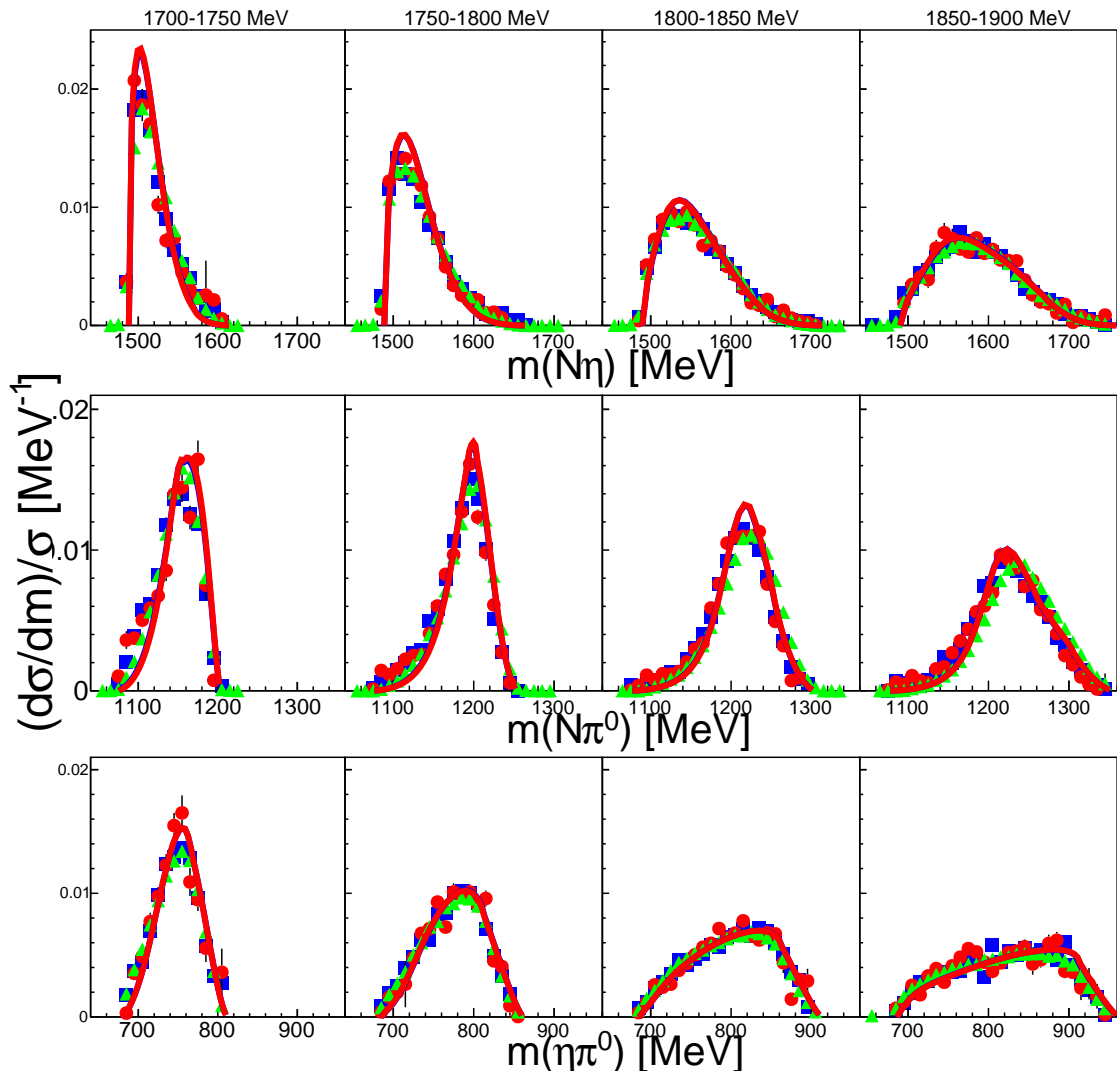


Figure 6.9.: Differential cross sections for the production of $\eta\pi^0$ pairs as function of the combined $\eta\pi^0$ invariant mass for 4 bins of final state invariant mass W . elusive reaction on quasi-free protons. Red: Exclusive reaction on quasi free neutrons. Green: Exclusive reaction on free protons. Solid lines: Theoretical predictions from [20]. The respective theoretical predictions overlap as well as the experimental results, so they might be difficult to distinguish.

6.3.2. $\eta\pi^\pm$ channels

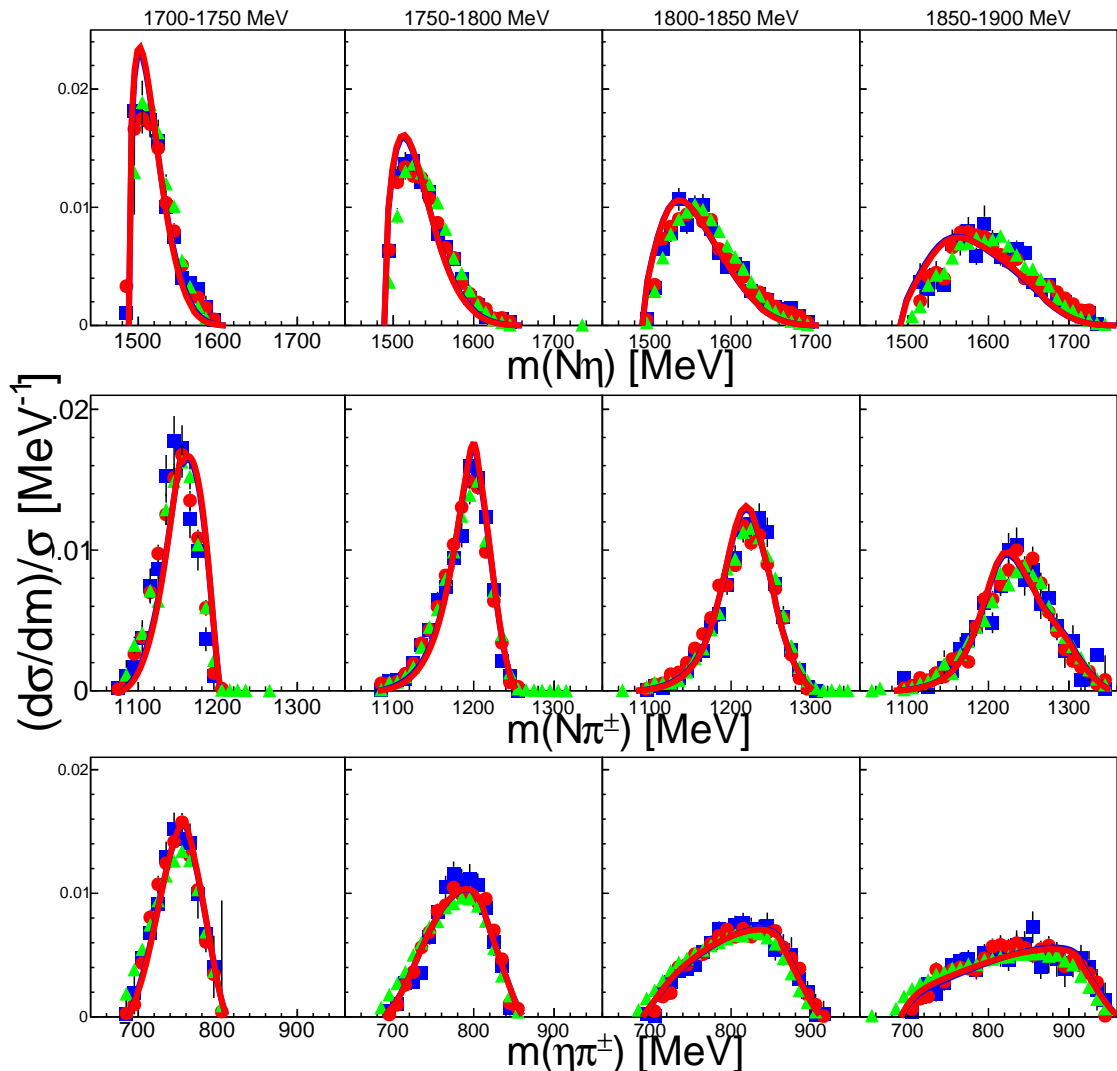


Figure 6.10.: Differential cross sections for the production of $\eta\pi^\pm$ pairs as function of the combined $\eta\pi^0$ invariant mass for 4 bins of final state invariant mass W . elusive reaction on quasi-free protons. Red: Exclusive reaction on quasi free neutrons. Green: Exclusive reaction on free protons. Solid lines: Theoretical predictions from [20]. The respective theoretical predictions overlap as well as the experimental results, so they might be difficult to distinguish.

6.4. Angular Distributions

This section shows the angular distributions of the pion in the helicity (index 'h') and canonical (index 'c') frames defined in section 5.18. Shown are results for the quasi-free exclusive reactions on protons and neutrons, and on free protons . Again, all differential cross sections are divided by the total cross section in the corresponding energy bins. As for results shown above, there is almost no difference between distributions of free and quasi-free protons and between quasi-free protons and neutrons, for all reactions. This is in accordance with the theoretical predictions, which again agree reasonably with experimental results.

6.4.1. $\eta\pi^0$ channels

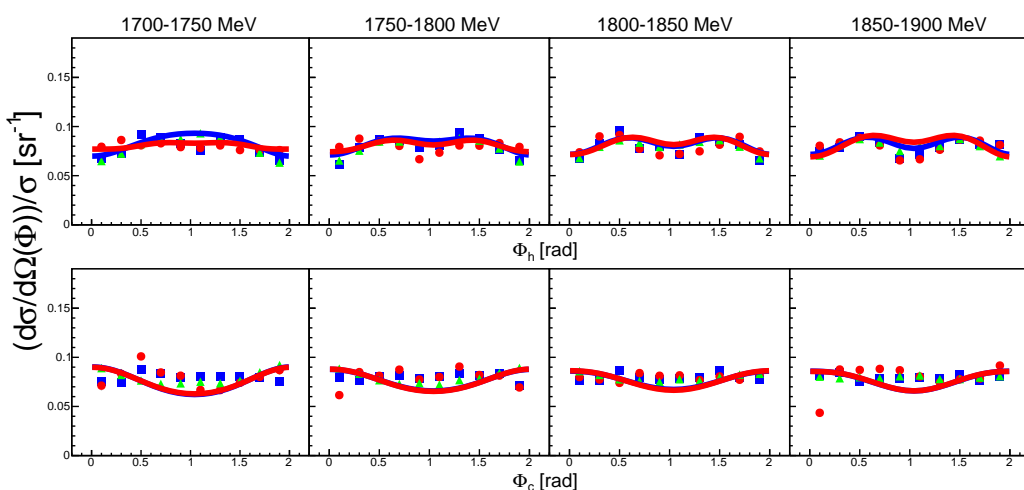


Figure 6.11.: Differential cross sections for the production of $\eta\pi^0$ pairs as function of the pions polar angle in the helicity (top row) and canonical (bottom row) frames, for 4 bins of final state invariant mass W . elusive reaction on quasi-free protons. Red: Exclusive reaction on quasi free neutrons. Green: Exclusive reaction on free protons. Solid lines: Theoretical predictions. The respective theoretical predictions overlap as well as the experimental results, so they might be difficult to distinguish.

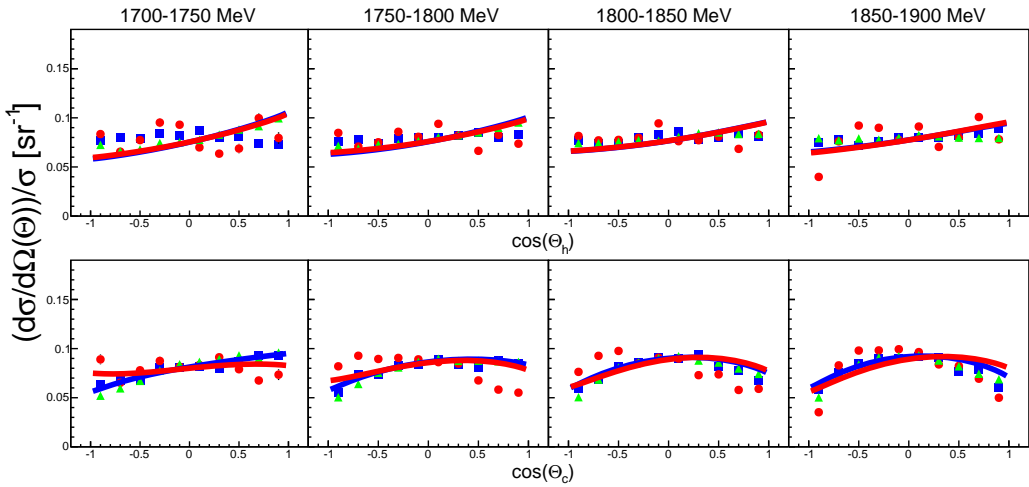


Figure 6.12.: Differential cross sections for the production of $\eta\pi^0$ pairs as function of the pions azimuthal angle in the helicity (top row) and canonical (bottom row) frames, for 4 bins of final state invariant mass W . elusive reaction on quasi-free protons. Red: Exclusive reaction on quasi free neutrons. Green: Exclusive reaction on free protons. Solid lines: Theoretical predictions. The respective theoretical predictions overlap as well as the experimental results, so they might be difficult to distinguish.

6.4.2. $\eta\pi^\pm$ channels

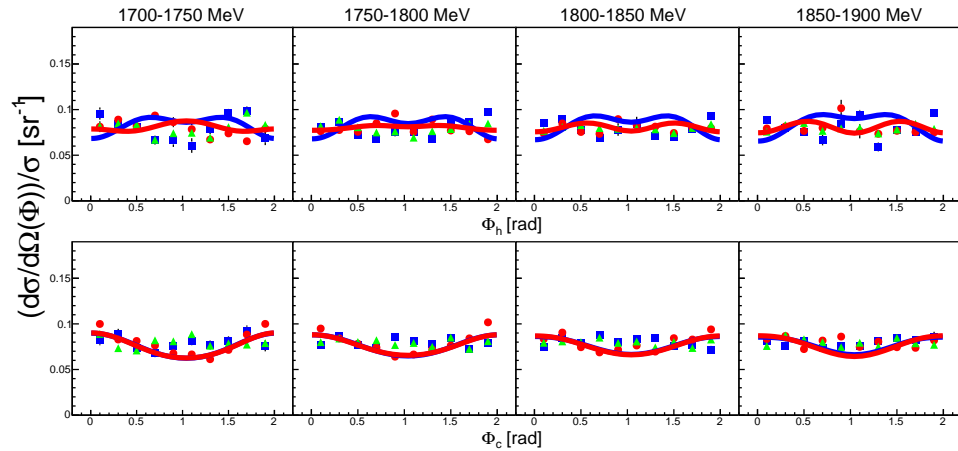


Figure 6.13.: Differential cross sections for the production of $\eta\pi^\pm$ pairs as function of the pions polar angle in the helicity (top row) and canonical (bottom row) frames, for 4 bins of final state invariant mass W . elusive reaction on quasi-free protons. Red: Exclusive reaction on quasi free neutrons. Green: Exclusive reaction on free protons. Solid lines: Theoretical predictions. The respective theoretical predictions overlap as well as the experimental results, so they might be difficult to distinguish.

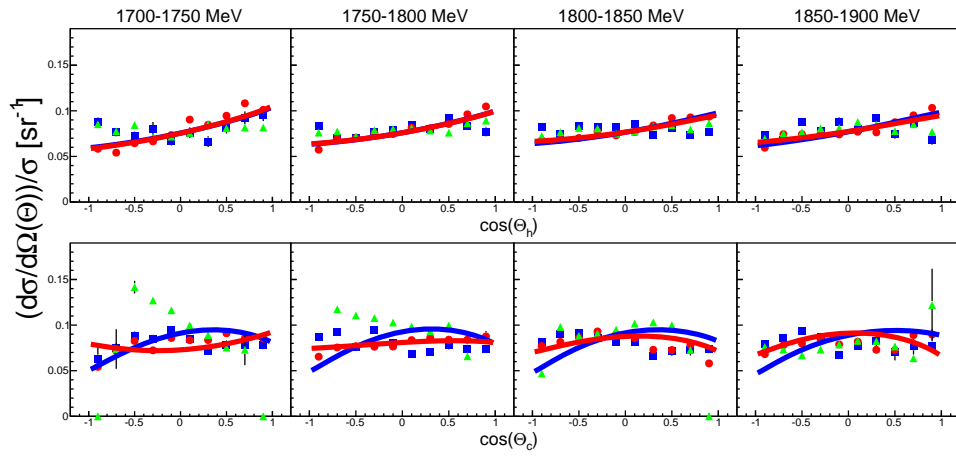


Figure 6.14.: Differential cross sections for the production of $\eta\pi^\pm$ pairs as function of the pions azimuthal angle in the helicity (top row) and canonical (bottom row) frames, for 4 bins of final state invariant mass W. elusive reaction on quasi-free protons. Red: Exclusive reaction on quasi free neutrons. Green: Exclusive reaction on free protons. Solid lines: Theoretical predictions. The respective theoretical predictions overlap as well as the experimental results, so they might be difficult to distinguish.

6.5. Helicity Asymmetries

This section shows the helicity asymmetries I_1 , I_2 and I_3 as defined above for quasi-free exclusive reactions on protons and neutrons, and on free protons. All differential cross sections are divided by the total cross sections in the corresponding energy bins. Earlier results for $I^\odot(\pi^0, p, \eta)$ on free protons can be found in [35]. The asymmetries are compared to theoretical predictions from [20] in Figs. 6.15 and 6.18. In Figs. 6.16 and 6.19 the distributions were fitted with a sine expansion according to equation 5.46, to extract the coefficients A_i . The coefficients are compared to model predictions in Figs. 6.17 and 6.20.

Again, as for the results shown above, there are only small differences between free and quasi-free proton results, indicating only minor FSI-effects on the shapes of the distributions. Quasi-free proton and neutron results are also in good agreement, as are experimental results and theoretical predictions.

An interesting aspect of the asymmetries is, that they are caused by the interference of the D_{33} decay channels, namely $D_{33} \rightarrow \pi N^*$ and $D_{33} \rightarrow \eta\Delta$. Therefore, asymmetries different from 0 are evidence for contributions of πN^* intermediate states, most likely $\pi N(1535)1/2^-$. However, these contributions are not visible in the mass distributions, and also ratios of total cross sections indicate that these contributions have to be small.

6.5.1. $\eta\pi^0$ channels

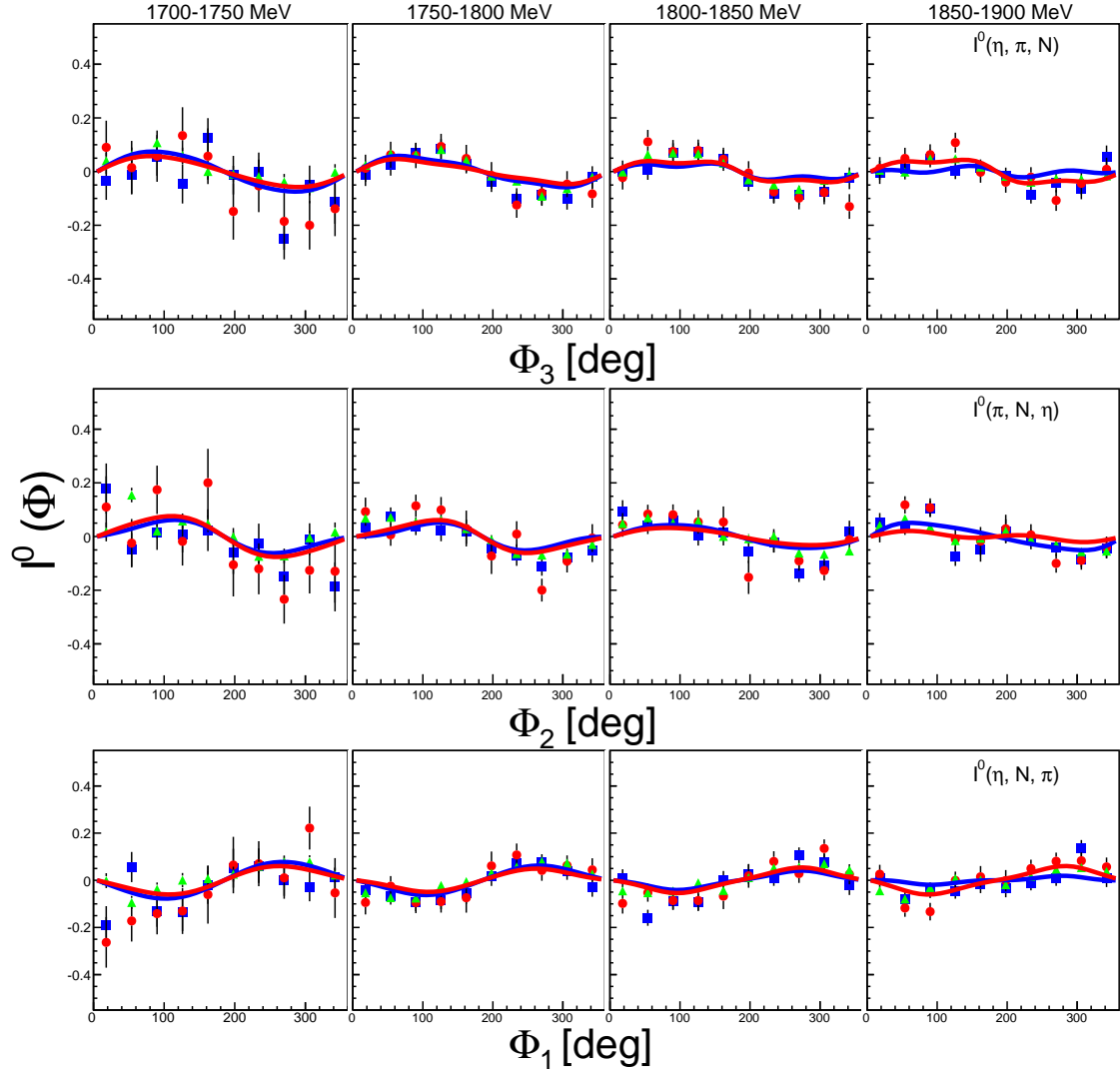


Figure 6.15.: Helicity Asymmetries for the production of $\eta\pi^0$ pairs as functions of Φ for 4 bins of final state invariant mass W . Top row: $I^\odot(\eta, \pi, N)$. Middle row: $I^\odot(\pi, N, \eta)$. Bottom row: $I^\odot(\eta, N, \pi)$. Blue squares: Exclusive reaction on quasi-free protons. Red circles: Exclusive reaction on quasi-free neutrons. Green Triangles: Exclusive reaction on free protons. Solid lines: Theoretical predictions from [20].

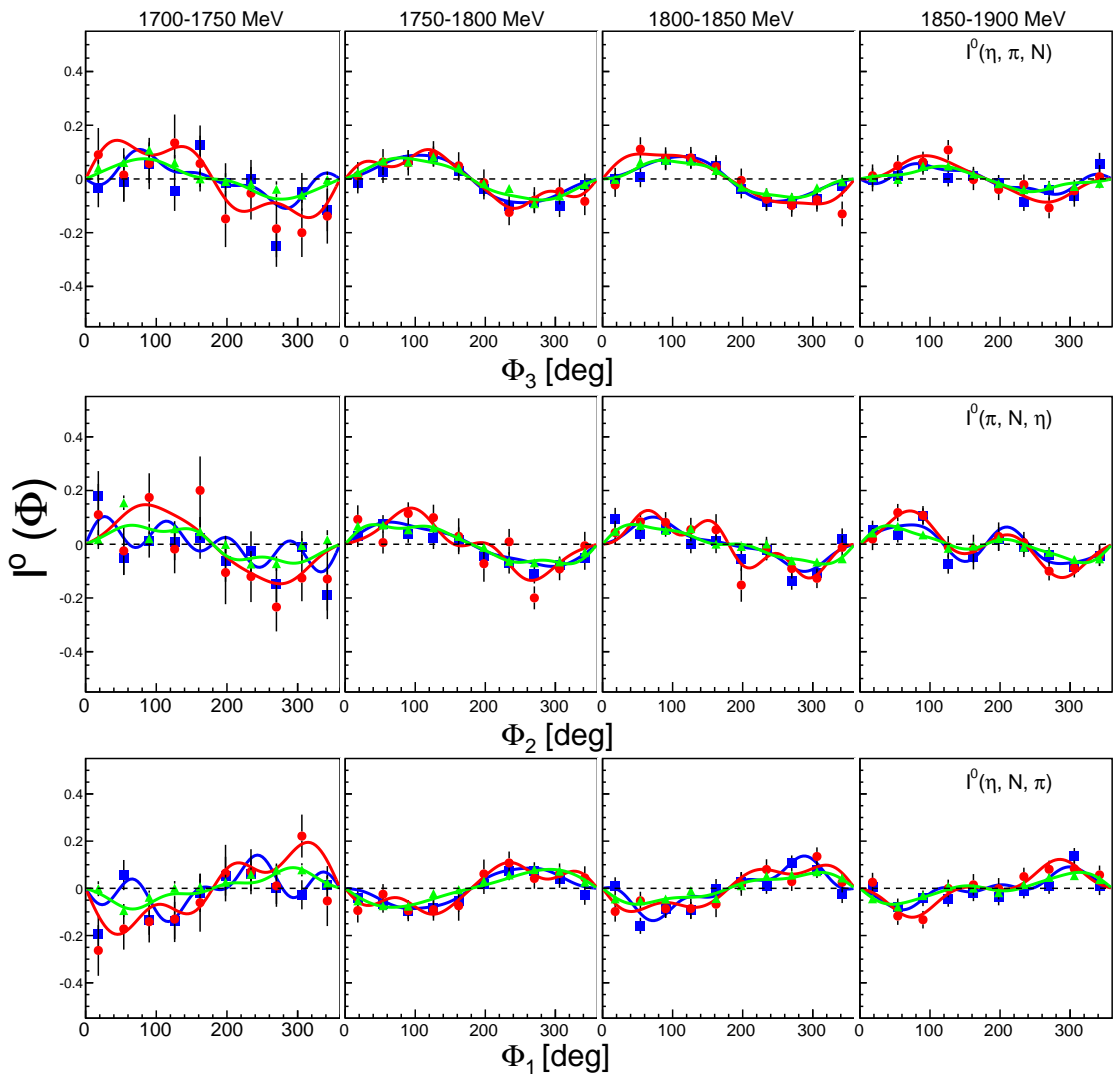


Figure 6.16.: Helicity Asymmetries for the production of $\eta\pi^0$ pairs as functions of Φ for 4 bins of final state invariant mass W . Top row: $I^\odot(\eta, \pi, N)$. Middle row: $I^\odot(\pi, N, \eta)$. Bottom row: $I^\odot(\eta, N, \pi)$. Blue squares: Exclusive reaction on quasi-free protons. Red circles: Exclusive reaction on quasi-free neutrons. Green Triangles: Exclusive reaction on free protons. Solid lines: Fits to the data with equation 5.46

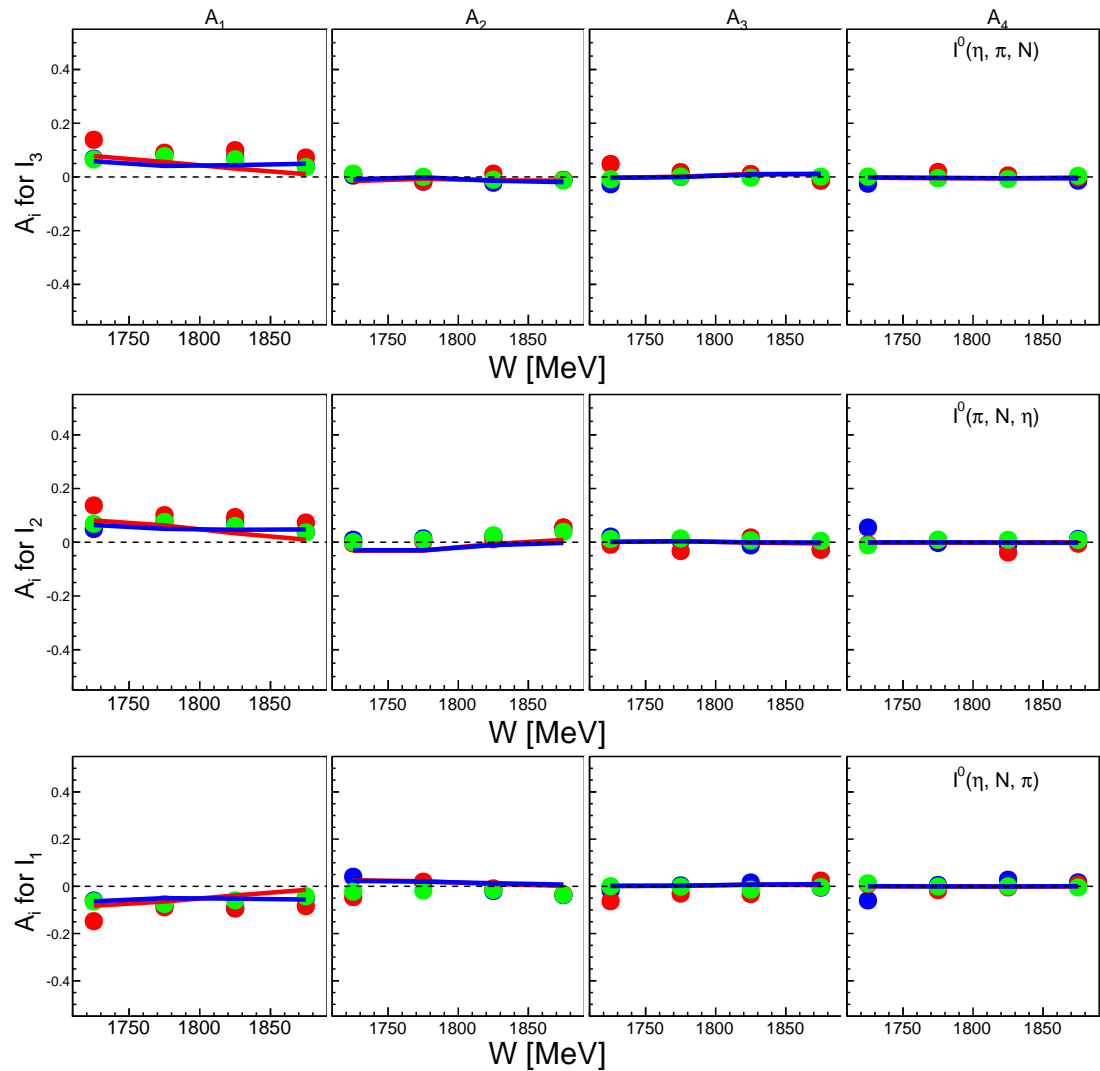


Figure 6.17.: Fit parameters of the fitted helicity asymmetries shown in Fig. 6.16 from the sine expansion 5.46, compared to predictions from [20].

6.5.2. $\eta\pi^\pm$ channels

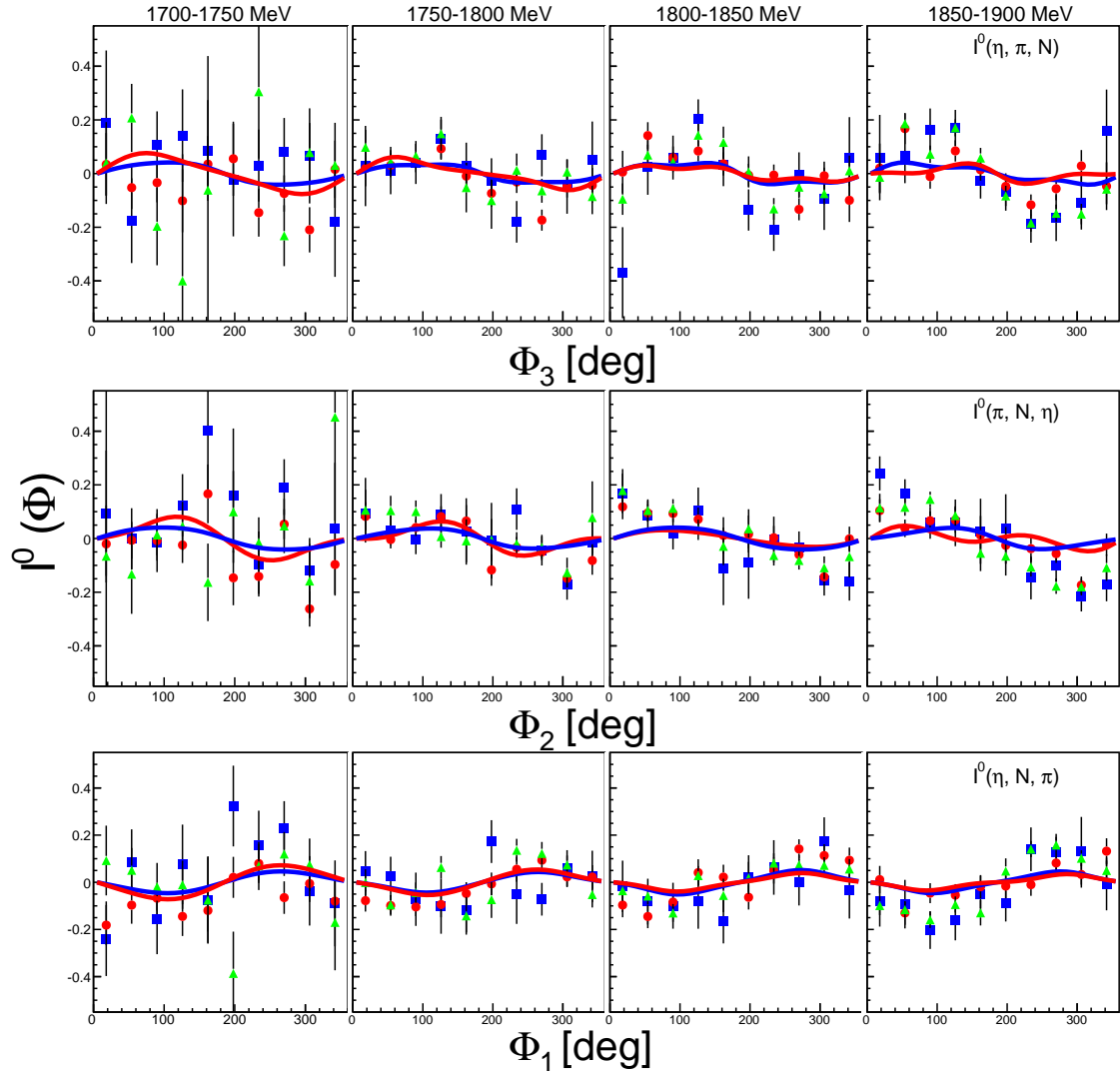


Figure 6.18.: Helicity Asymmetries for the production of $\eta\pi^0$ pairs as functions of Φ for 4 bins of final state invariant mass W . Top row: $I^\odot(\eta, \pi, N)$. Middle row: $I^\odot(\pi, N, \eta)$. Bottom row: $I^\odot(\eta, N, \pi)$. Blue squares: Exclusive reaction on quasi-free protons. Red circles: Exclusive reaction on quasi-free neutrons. Green Triangles: Exclusive reaction on free protons. Solid lines: Theoretical predictions from [20].

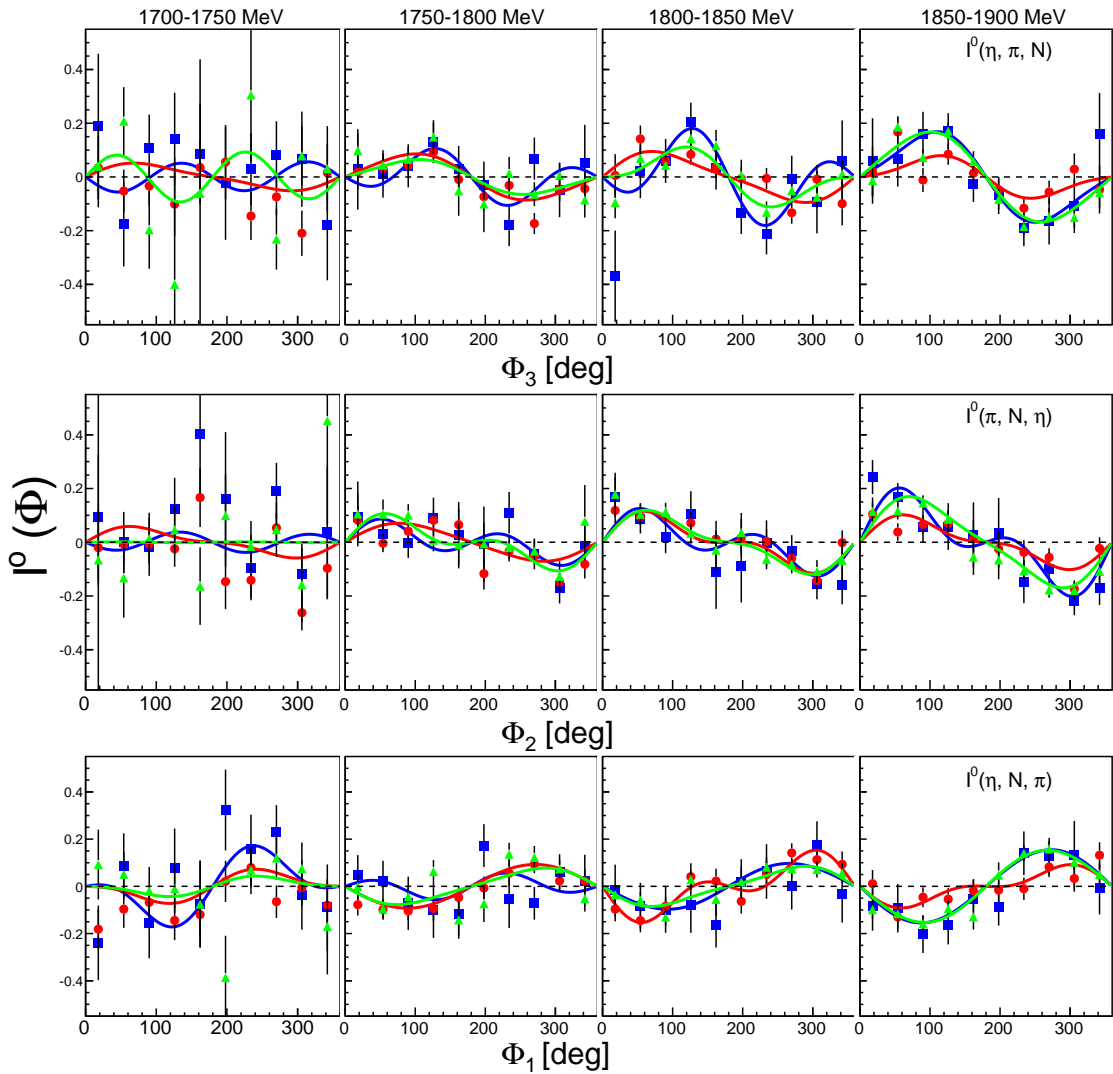


Figure 6.19.: Helicity Asymmetries for the production of $\eta\pi^\pm$ pairs as functions of Φ for 4 bins of final state invariant mass W . Top row: $I^0(\eta, \pi, N)$. Middle row: $I^0(\pi, N, \eta)$. Bottom row: $I^0(\eta, N, \pi)$. Blue squares: Exclusive reaction on quasi-free protons. Red circles: Exclusive reaction on quasi-free neutrons. Green Triangles: Exclusive reaction on free protons. Solid lines: Fits to the data with equation 5.46

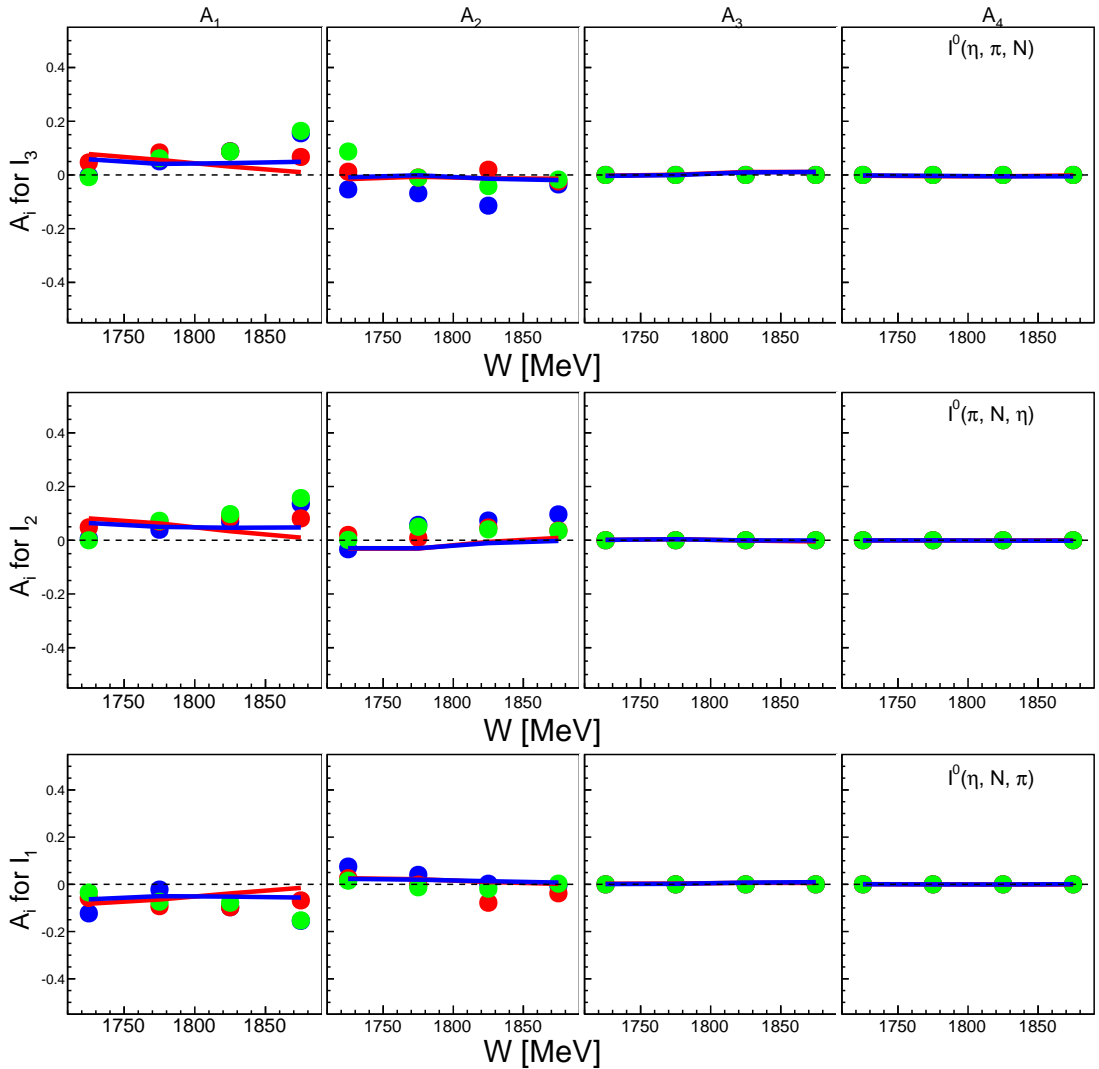


Figure 6.20.: Fit parameters of the fitted helicity asymmetries shown in Fig. 6.19 from the sine expansion 5.46 compared to predictions from [20].

6.6. Double polarization observable E

The double polarization observable E was extracted using the 3 different methods described in section 5.20. As can be seen in Fig. 6.21, the different extraction methods yield comparable results. Deviations are only visible for lower energies. This might be caused by problems with the nucleon detection efficiency, that plays a larger role at lower energies. However, since the nucleon detection efficiency is present in σ_{diff} and σ_{sum} it should cancel in the determination of E.

Another possibility are problems with the carbon subtraction. Due to the small cross

sections and limited statistics in the threshold region, it was not possible to determine the carbon contribution reliably. The quality of the carbon subtraction is shown in Fig. 6.23. For the quasi-free protons the sum of the helicity dependent cross sections agrees very well with two times the unpolarized cross sections. For the quasi-free neutron there are deviations at lower energies, that indicate an overestimation of the carbon contribution. This is mainly caused by the poor statistical quality at low energies. For values of W over 1700 MeV the sum of the helicity dependent cross sections and the unpolarized cross section agree well.

For values of $W \geq 1700$ MeV deviations between the extraction methods vanish, and E could be extracted to be ≈ 0 for the remaining energy range for reactions on quasi-free protons and neutrons. This is in accordance with the assumption that $\eta\pi^0$ production takes predominantly place via excitation of the $\Delta(1700)3/2^-$ resonance in the investigated energy range. The PDG values for the helicity couplings $A_{1/2}$ and $A_{3/2}$ of the $\Delta(1700)3/2^-$ are [96]:

$$A_{1/2} = A_{3/2} = 0.140 \pm 0.03 \text{ GeV}^{-1/2}.$$

In [20] the ratio $A_{1/2}/A_{3/2}$ was derived from their theoretical model and varies between 0.95 and 1.3.

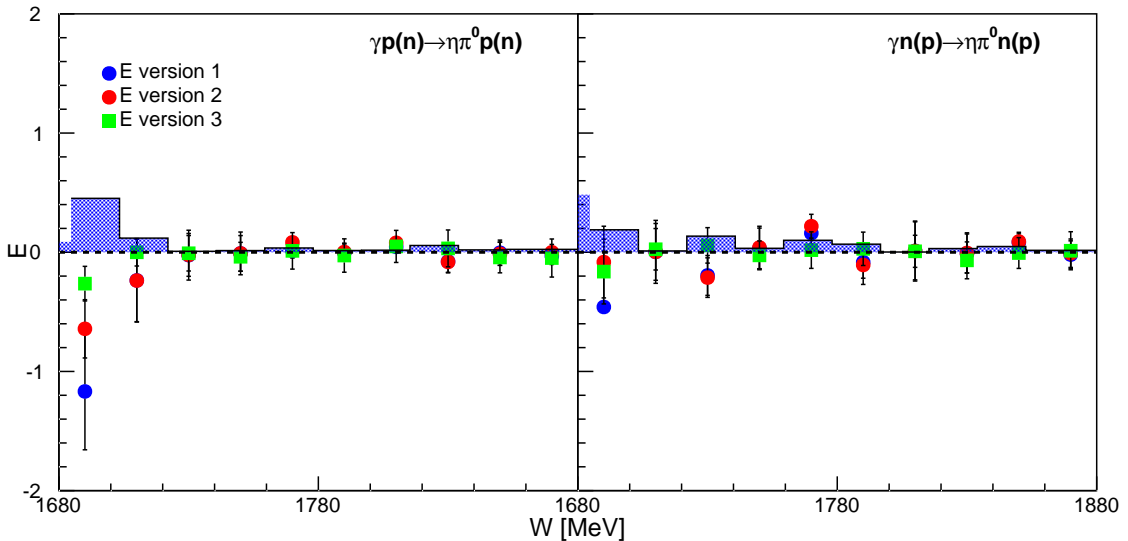


Figure 6.21.: Double polarization observable E extracted with the methods described in section 5.20. The left-hand side shows the results for quasi-free protons, the righthand side shows results for quasi-free neutrons. The shaded area shows the systematic errors.

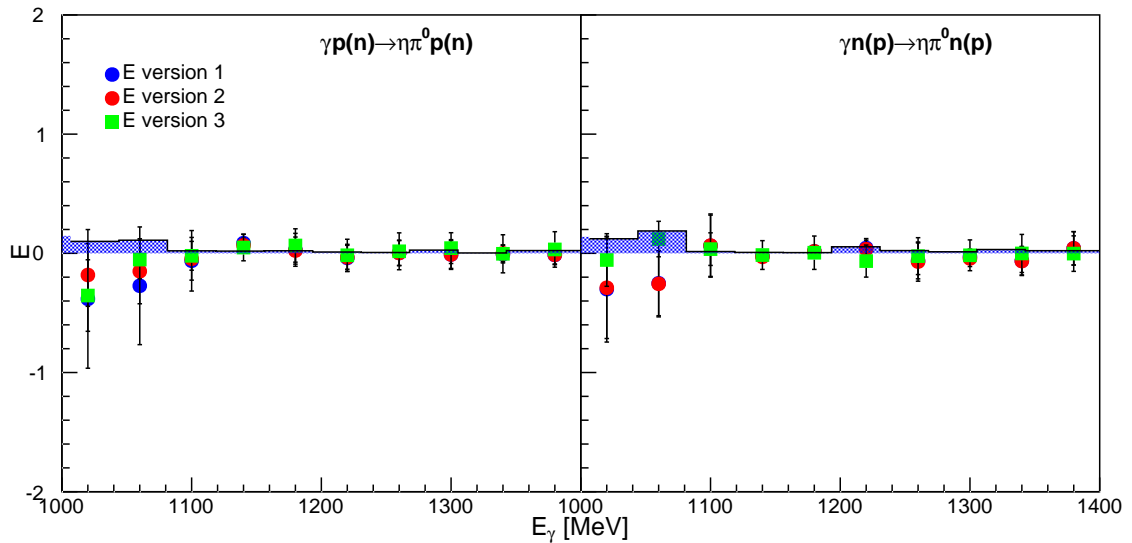


Figure 6.22.: Double polarization observable E extracted with the methods described in section 5.20, as function of the photon energy E_γ . The left-hand side shows the results for quasi-free protons, the righthand side shows results for quasi-free neutrons. The shaded area shows the systematic errors.

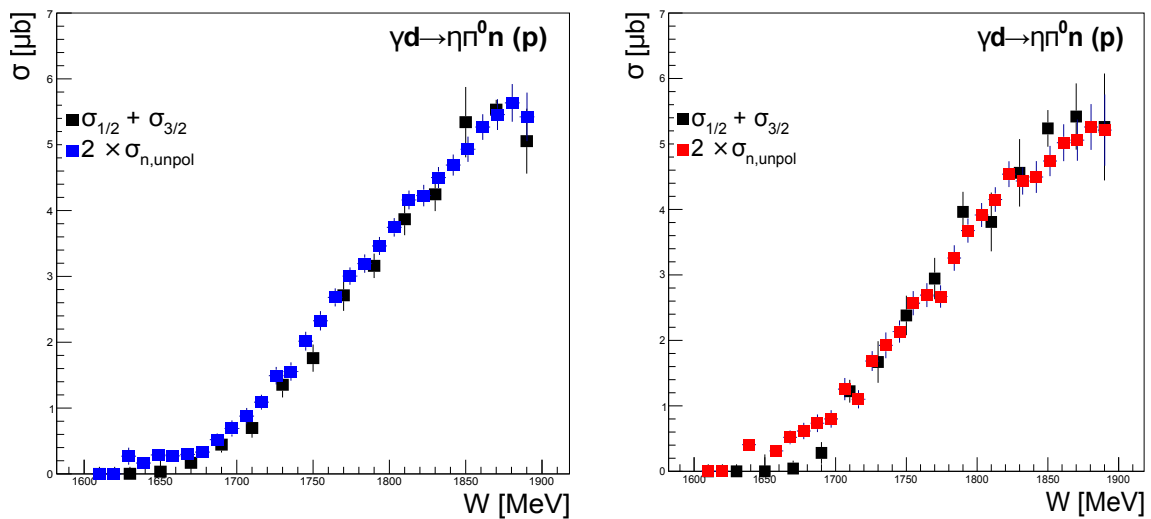


Figure 6.23.: Comparison of the sum of the helicity dependent cross sections to the unpolarized cross sections. Left-hand side: reaction on quasi-free protons. Right-hand side: reaction on quasi-free neutrons.

6.7. Helicity dependent cross sections

The helicity dependent cross sections $\sigma_{1/2}$ and $\sigma_{3/2}$ were extracted using 4 different methods described in section 5.20.2. They are shown in Fig. 6.24 and compared to the unpolarized cross sections. As described above, $E \approx 0$ and therefore $\sigma_{1/2}$ should be equal to $\sigma_{3/2}$.

Small deviations between the cross-sections are evident for reactions on quasi-free neutrons. This is most likely caused by the carbon subtraction that is less reliable for neutrons because of the lower statistical quality. However in the margin of errors the polarized and unpolarized cross section are in reasonable agreement.

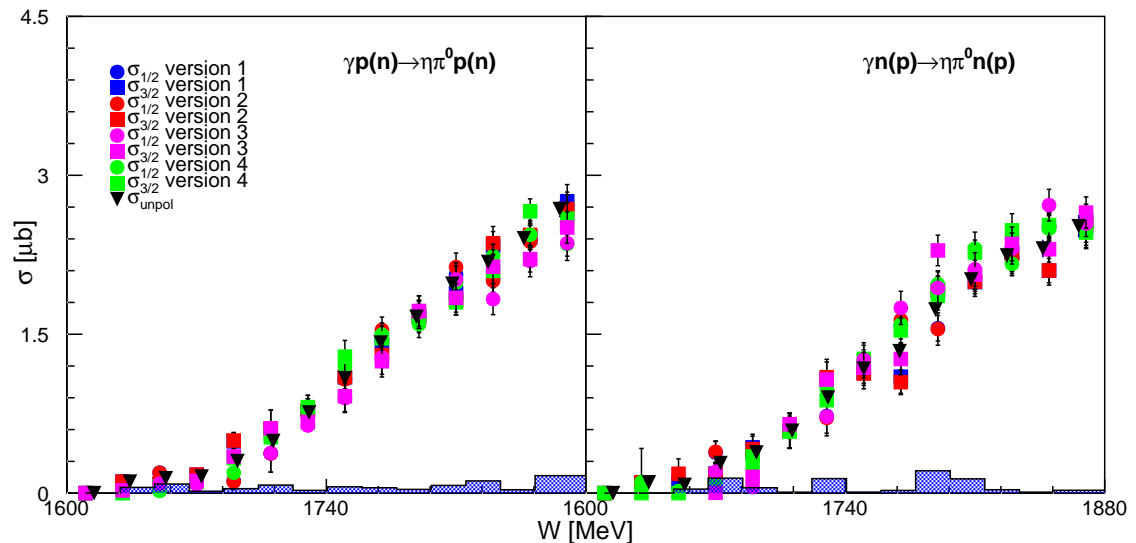


Figure 6.24.: The helicity dependent cross sections $\sigma_{1/2}$ and $\sigma_{3/2}$ extracted with different methods described in section 5.20.2. The left-hand side shows the results for quasi-free protons, the righthand side shows results for quasi-free neutrons. The shaded area shows the systematic errors.

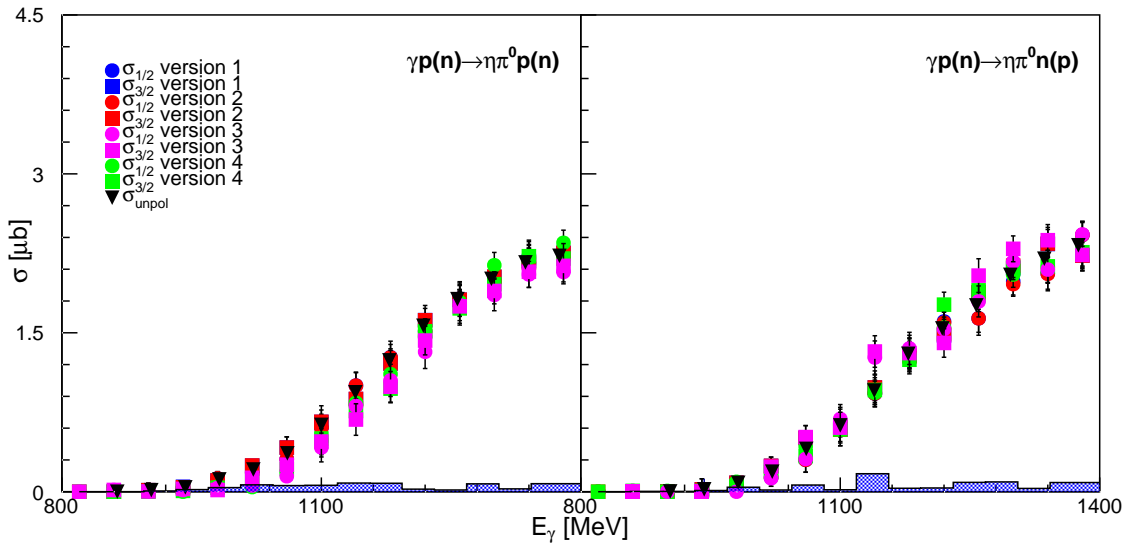


Figure 6.25.: The helicity dependent cross sections $\sigma_{1/2}$ and $\sigma_{3/2}$ extracted with different methods described in section 5.20.2, as function of the photon energy E_γ . The left-hand side shows the results for quasi-free protons, the righthand side shows results for quasi-free neutrons. The shaded area shows the systematic errors.

6.8. Conclusions

The photoproduction of $\eta\pi$ pairs has been investigated using data from experiments at the MAMI accelerator facility. Altogether 3 data sets with unpolarized deuterium data, 1 set with unpolarized hydrogen data, 3 sets with polarized dButanol data and 2 sets with carbon data were analyzed.

The data were used to extract unpolarized differential and total cross sections, invariant-mass distributions and angular distributions, helicity asymmetries as well as polarized total cross sections and the double polarization observable E.

Observables for $\eta\pi^0$ production, extracted from hydrogen data are in excellent agreement with previous measurements and served as cross-checks for the analysis procedures.

The comparison of the free and quasi-free total cross sections indicates the presence of FSI effects. For $\eta\pi^0$ pairs, the quasi-free total cross section off protons bound in the deuteron is about 25% smaller than the cross section for free protons. For the production of $\eta\pi^\pm$ pairs, the quasi-free cross section is roughly 10% smaller than the free cross section. Similar results were obtained for single π photoproduction, were reactions with charged pions in the final state are effected less by FSI [97]. Unfortunately there is no quantitative modeling of these FSI yet.

The shapes of the helicity asymmetries, invariant-mass and angular distributions of quasi-free reactions agree well with the corresponding spectra for free protons, after they were scaled with the total cross sections, indicating that FSI only affect the absolute scale of the total cross sections but not the line-shapes. All observables extracted from reactions on quasi free neutrons have the same shapes and magnitudes as their counterparts extracted from quasi free protons. This behavior is expected if dominant contributions from Δ resonances are assumed, as the photocouplings of protons and neutrons are equal in that case.

The ratios of the total cross sections are in excellent agreement with eq. 1.38, indicating a strong contribution of the decay cascade given in eq. 1.36. This is corroborated by the model calculations of [20], which is based on a strong domination of D_{33} resonances, namely $\Delta(1700)3/2^-$ in the threshold region and $\Delta(1940)3/2^-$ at higher energies. The small deviations between experimental results and model predictions could stem from decays of the form $D_{33} \rightarrow \pi S_{11}(1535)$. This is supported by the model calculations, which see the beam helicity asymmetries coming from interferences of $\eta\Delta(1232)$ states with $\pi N(1535)1/2^-$ states. Therefore, the helicity asymmetries show evidence of (small) contributions of $\pi N(1535)1/2^-$ intermediate states.

Further confirmation of the importance of the D_{33} partial wave is given by the double polarization observable E. The helicity couplings $A_{1/2}$ and $A_{3/2}$ are equal for the $\Delta(1700)3/2^-$, what leads to similar helicity dependent cross sections and therefore vanishing E, for reactions on quasi free protons and neutrons.

Together with the good agreement of the coherent cross section and the models it seems that photoproduction of $\eta\pi$ pairs is a well suited tool to investigate the properties of Δ resonances and the $\Delta(1700)3/2^-$ resonance in particular.

A. Appendix 1

A.1. Efficiencies

A.1.1. $\eta\pi^0$ channels

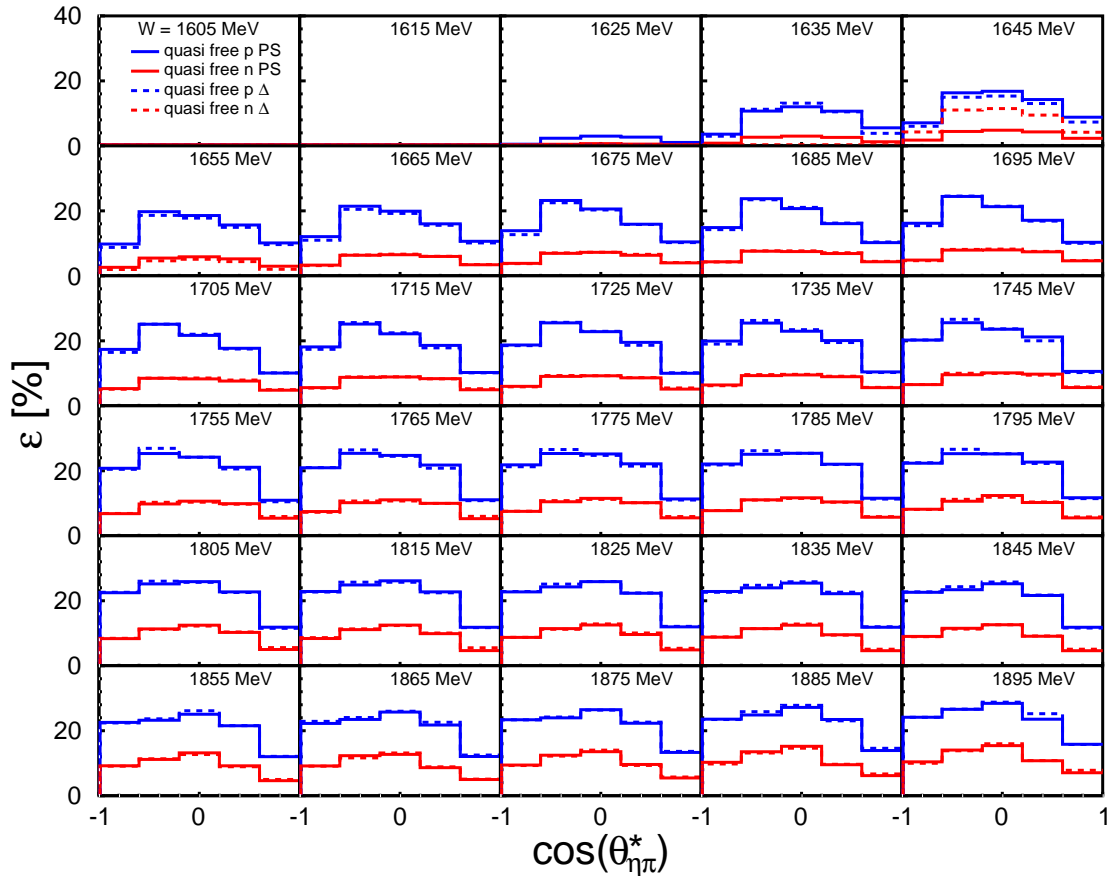


Figure A.1.: Detection efficiencies for the quasi-free reactions with neutral pions in the final state. Blue lines show reactions on the quasi-free proton, red lines show reactions on the quasi-free neutron. Solid lines show efficiencies that were extracted with MC simulations, that used pure phase space distributions. Dotted lines show efficiencies that were extracted with MC simulations that used a $\Delta\eta$ intermediate state. The efficiencies are shown as function of the polar angle of the combined $\eta\pi$ system in the global γN center-of-mass frame.

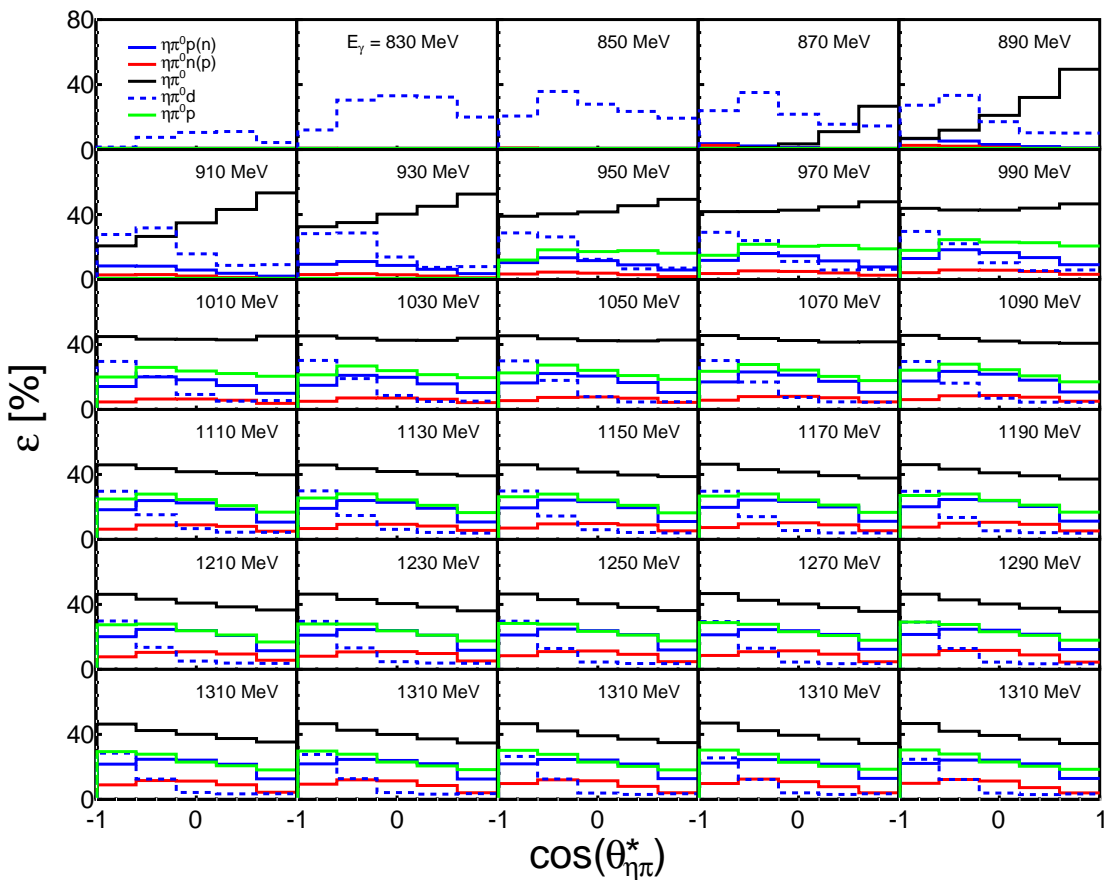


Figure A.2.: Detection efficiencies as function of $\cos(\theta_{\eta\pi}^*)$ for bins of photon energy E_γ .

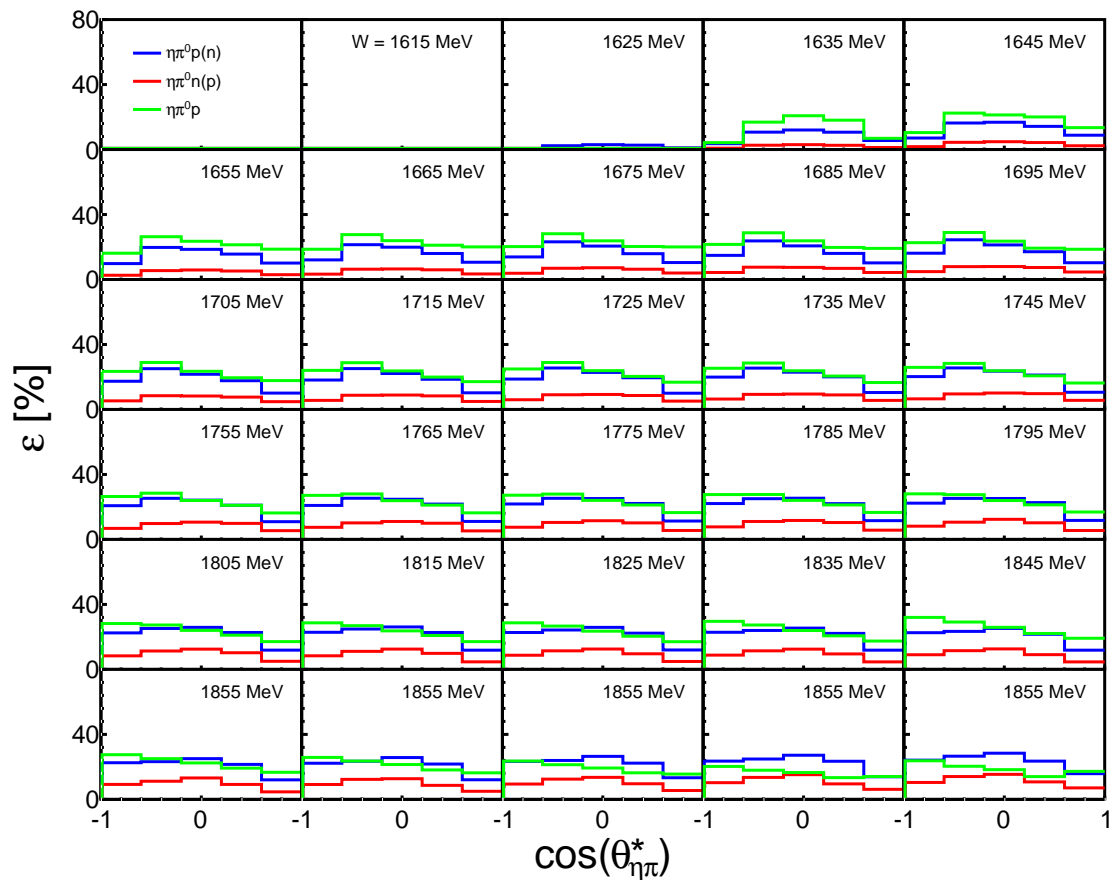


Figure A.3.: Detection efficiencies as function of $\cos(\theta_{\eta\pi}^*)$ for bins of W .

A.1.2. $\eta\pi^\pm$ channels

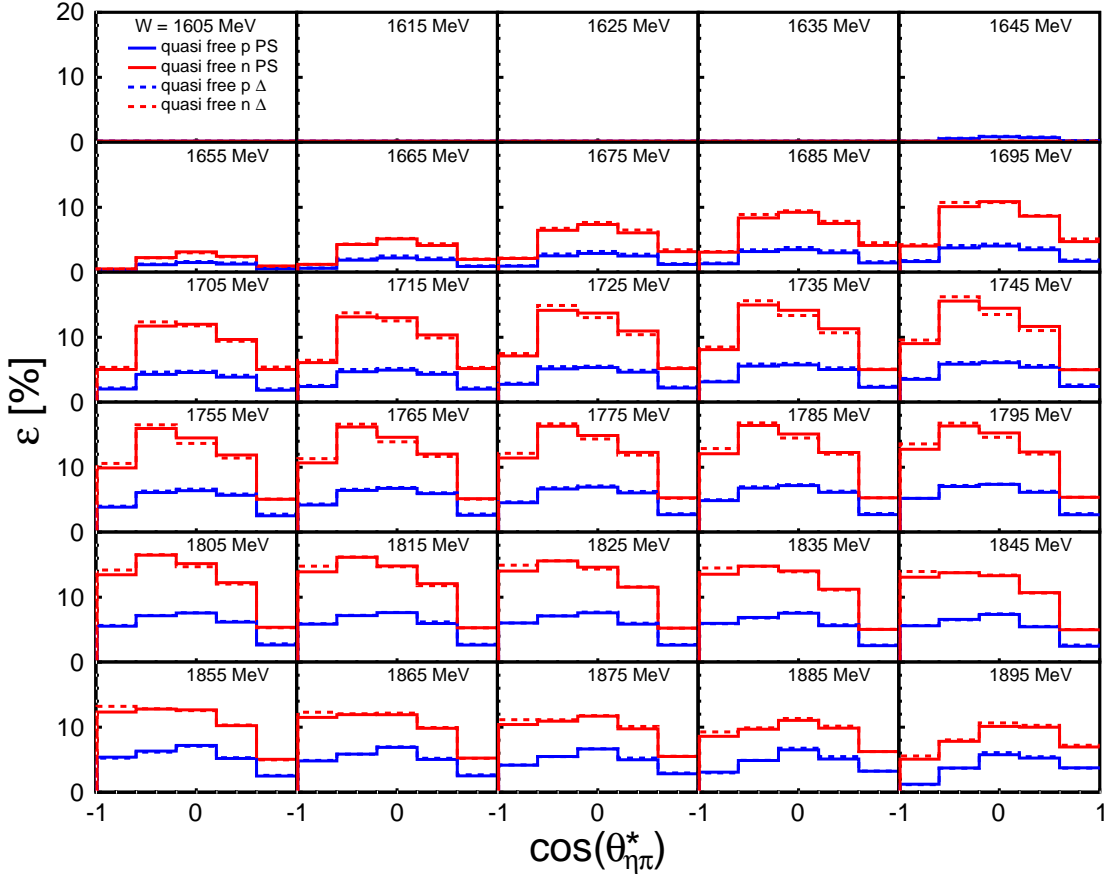


Figure A.4.: Detection efficiencies for the quasi-free reactions with charged pions in the final state. Blue lines show reactions on the quasi-free proton, red lines show reactions on the quasi-free neutron. Solid lines show efficiencies that were extracted with MC simulations, that used pure phase space distributions. Dotted lines show efficiencies that were extracted with MC simulations that used a $\Delta\eta$ intermediate state. The efficiencies are shown as function of the polar angle of the combined $\eta\pi$ system in the global γN center-of-mass frame.

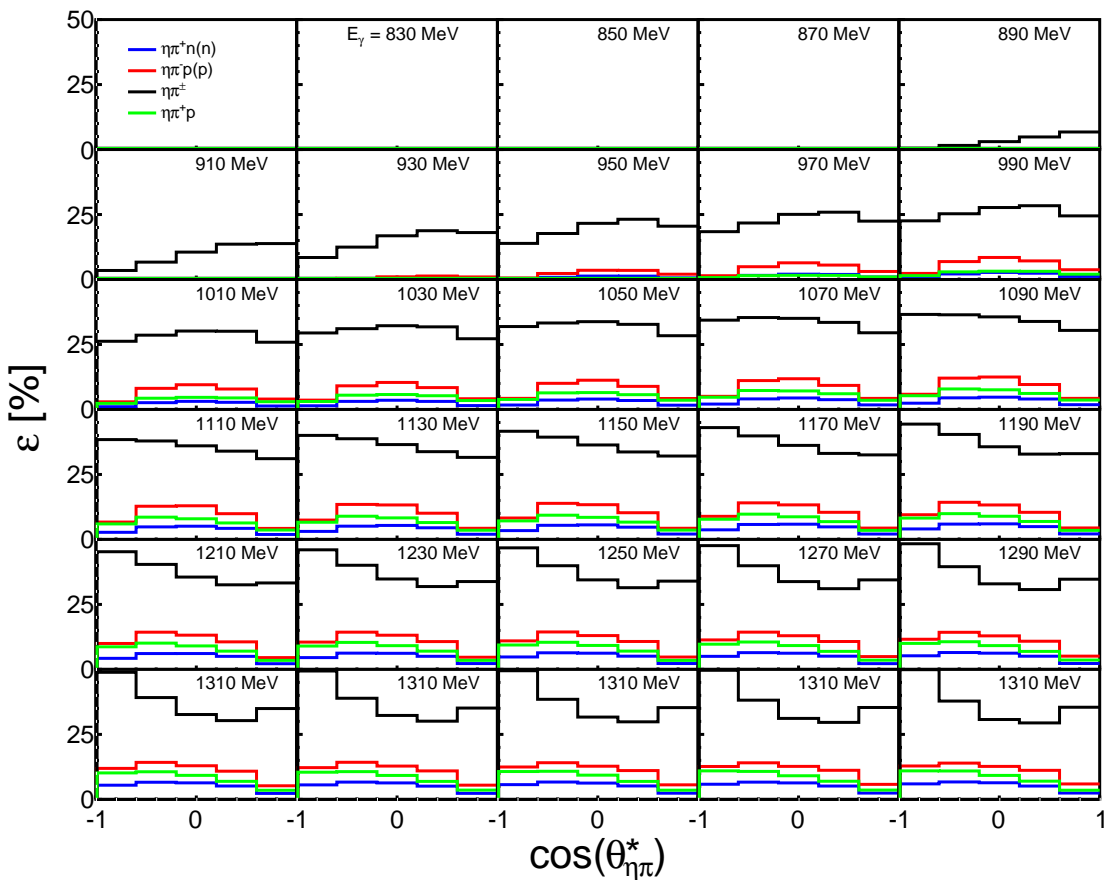


Figure A.5.: Detection efficiencies as function of $\cos(\theta_{\eta\pi}^*)$ for bins of photon energy E_γ .

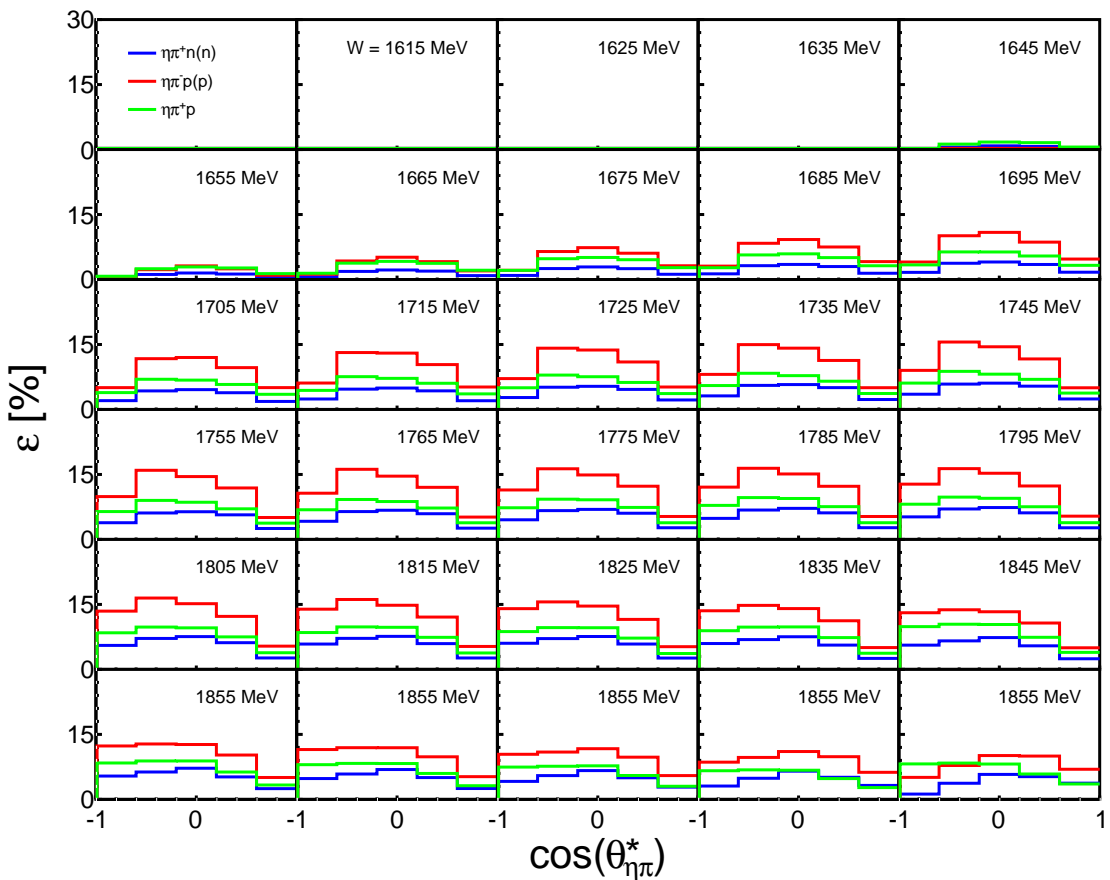


Figure A.6.: Detection efficiencies as function of $\cos(\theta_{\eta\pi}^*)$ for bins of W .

A.2. Differential Cross sections

A.2.1. $\eta\pi^0$ channels

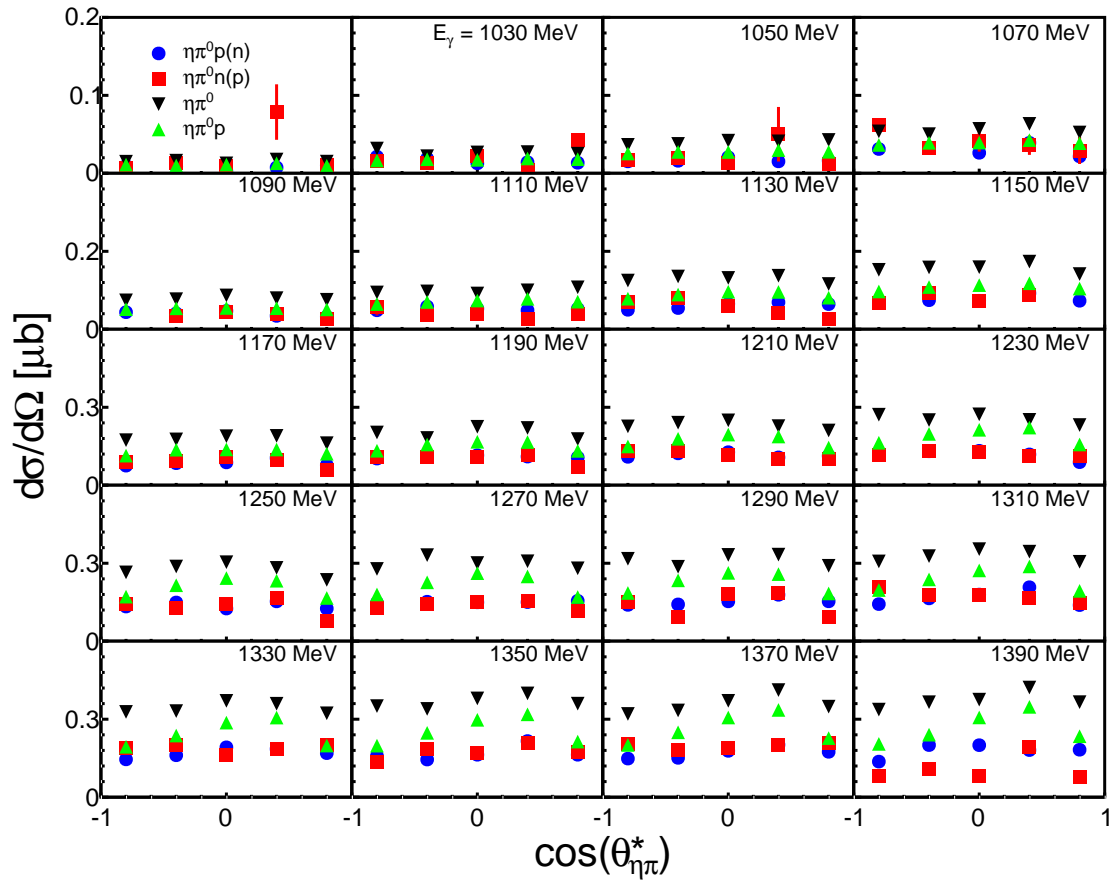


Figure A.7.: Differential cross sections as function of $\cos(\theta_{\eta\pi}^*)$ for bins of photon energy E_γ .

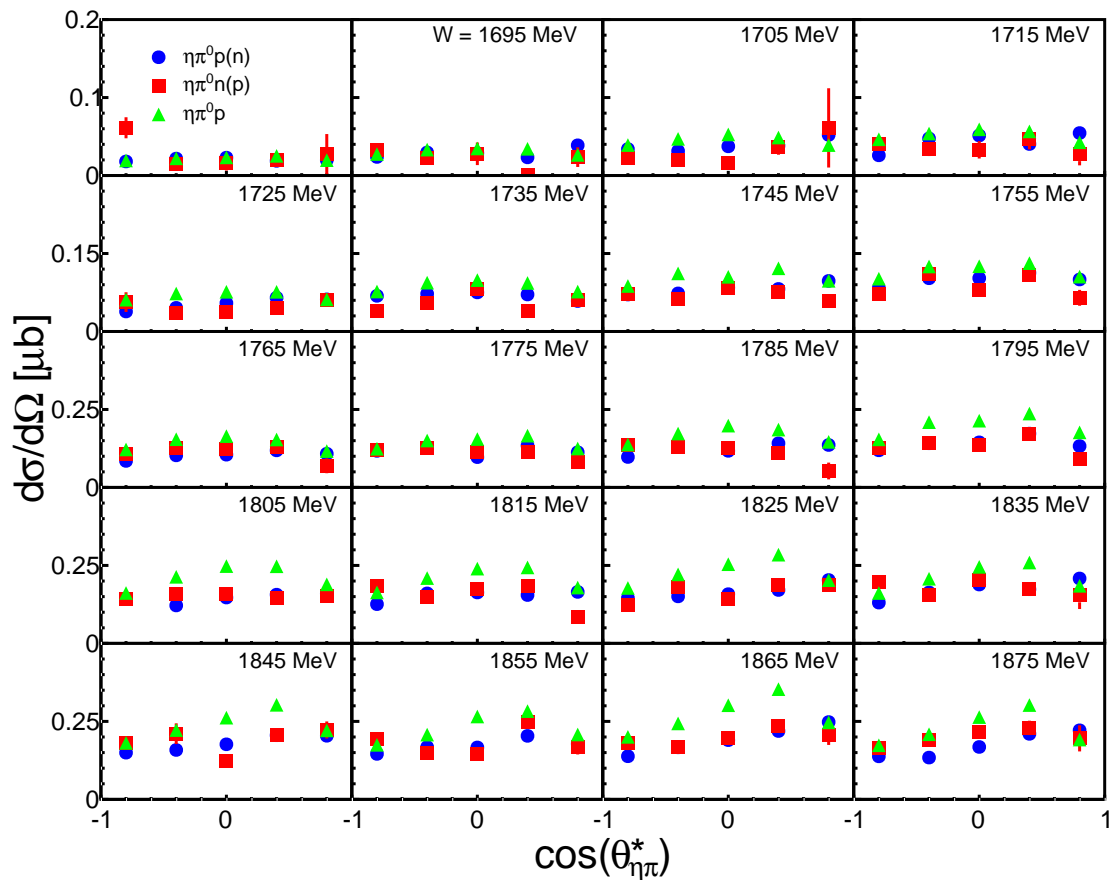


Figure A.8.: Differential cross sections as function of $\cos(\theta_{\eta\pi}^*)$ for bins W .

A.2.2. $\eta\pi^\pm$ channels

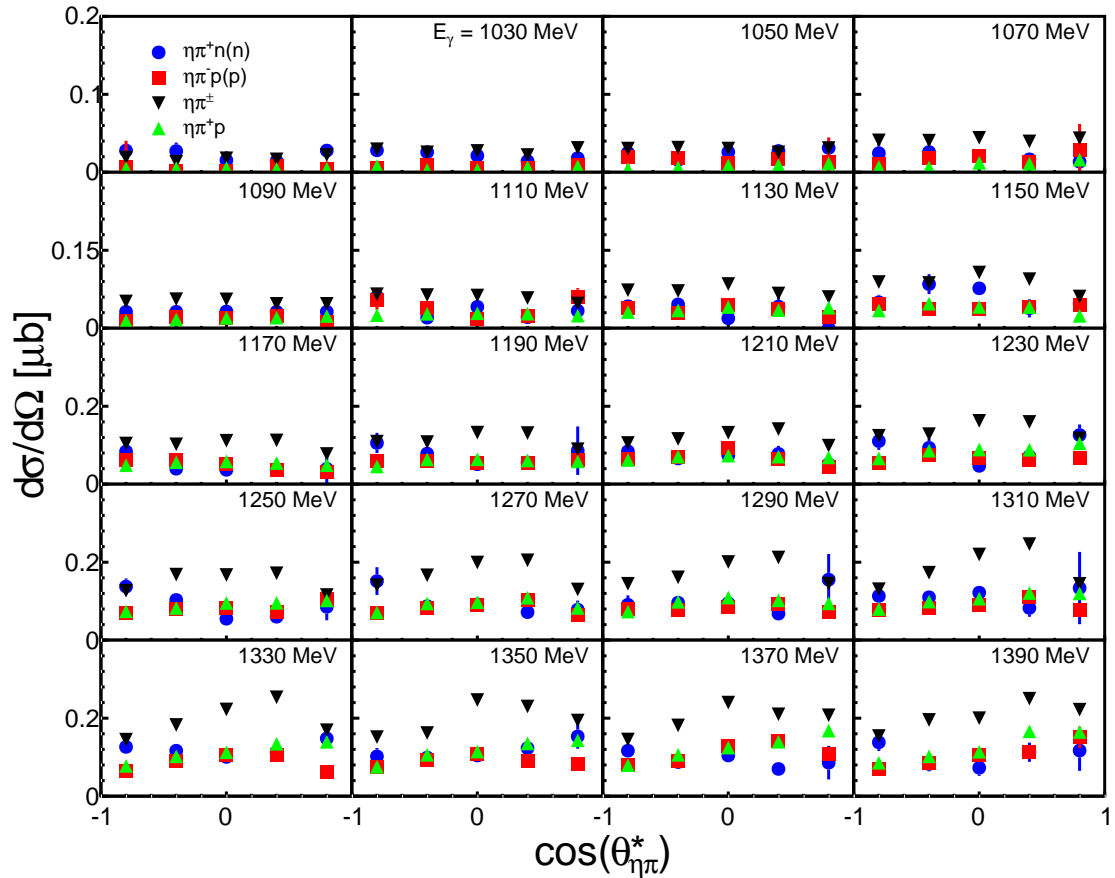


Figure A.9.: Differential cross sections as function of $\cos(\theta_{\eta\pi}^*)$ for bins of photon energy E_γ .

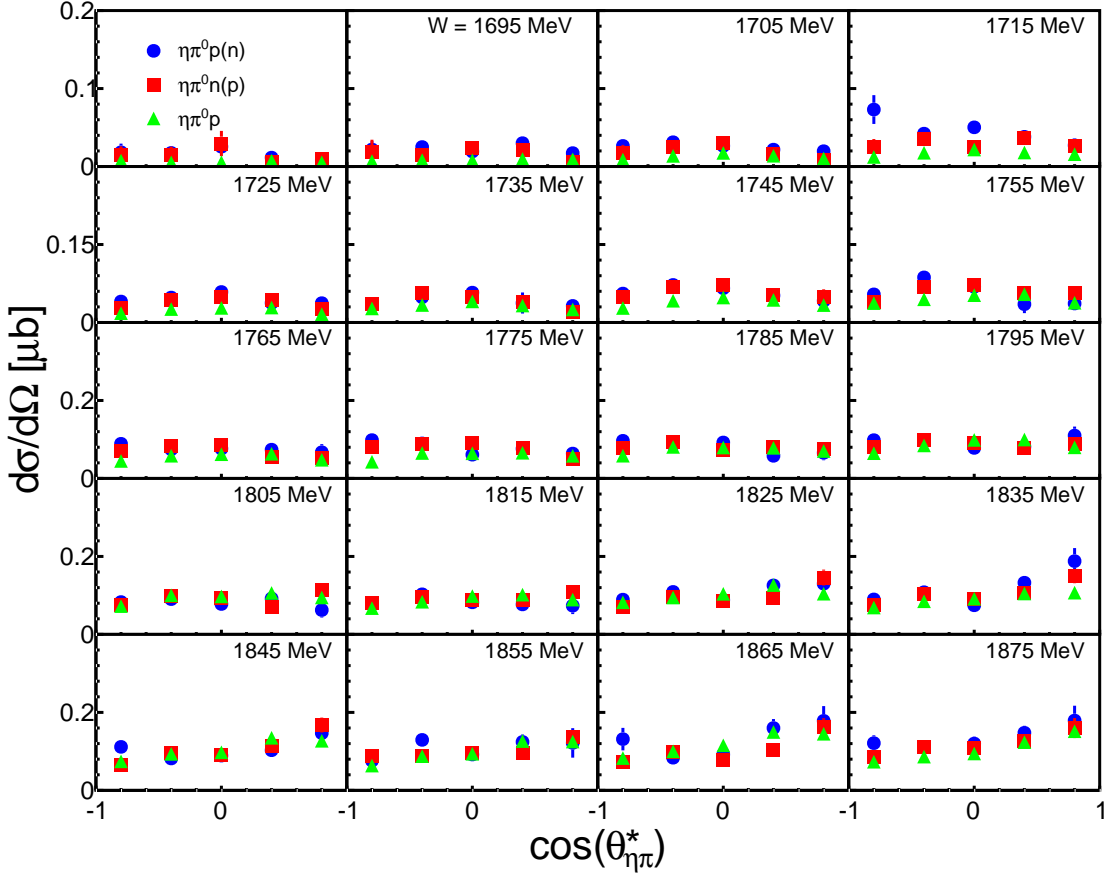


Figure A.10.: Differential cross sections as function of $\cos(\theta_{\eta\pi}^*)$ for bins W .

A.3. Determination of $\Delta m_{\gamma_i\gamma_j}$

The invariant mass of the photon pair $\gamma_1\gamma_2$, is given by

$$m_{\gamma_1\gamma_2} = \sqrt{2E_{\gamma_1}E_{\gamma_2} \cdot (1 - \cos(\phi_{\gamma_1\gamma_2}))}, \quad (\text{A.1})$$

with the opening angle of the two photons $\phi_{\gamma_1\gamma_2}$ and their energies $E_{\gamma_1}, E_{\gamma_2}$. The error $\Delta m_{\gamma_1\gamma_2}$ from equation A.1 can be determined with the Gaussian error propagation:

$$\begin{aligned} \Delta m_{\gamma_1\gamma_2} &= \sqrt{\left[\frac{\partial m_{\gamma_1\gamma_2}}{\partial \cos(\phi_{\gamma_1\gamma_2})} \cdot \Delta \cos(\phi_{\gamma_1\gamma_2}) \right]^2 + \sum_{i=1}^2 \left[\frac{\partial m_{\gamma_1\gamma_2}}{\partial E_{\gamma_i}} \cdot \Delta E_{\gamma_i} \right]^2} \\ &= \frac{1}{2} m_{\gamma_1\gamma_2} \cdot \sqrt{\left[\frac{\Delta E_{\gamma_1}}{E_{\gamma_1}} \right]^2 + \left[\frac{\Delta E_{\gamma_2}}{E_{\gamma_2}} \right]^2 + \left[\frac{\Delta \cos(\phi_{\gamma_1\gamma_2})}{1 - \cos(\phi_{\gamma_1\gamma_2})} \right]^2}, \end{aligned} \quad (\text{A.2})$$

where $\Delta \cos(\phi_{\gamma_1\gamma_2})$ is given by:

$$\Delta \cos(\phi_{\gamma_1\gamma_2}) = \sqrt{\sum_{i=1}^2 \left[\frac{\partial \cos(\phi_{\gamma_1\gamma_2})}{\partial \phi_{\gamma_i}} \Delta \phi_{\gamma_i} \right]^2 + \sum_{i=1}^2 \left[\frac{\partial \cos(\phi_{\gamma_1\gamma_2})}{\partial \theta_{\gamma_i}} \Delta \theta_{\gamma_i} \right]^2}. \quad (\text{A.3})$$

With $\cos(\phi_{\gamma_1\gamma_2})$ as

$$\begin{aligned} \cos(\phi_{\gamma_1\gamma_2}) &= \frac{\vec{p}_{\gamma_1} \cdot \vec{p}_{\gamma_2}}{|\vec{p}_{\gamma_1}| \cdot |\vec{p}_{\gamma_2}|} \\ &= \sin(\theta_{\gamma_1}) \sin(\theta_{\gamma_2}) \cos(\phi_{\gamma_1}) \cos(\phi_{\gamma_2}) + \\ &\quad \cos(\theta_{\gamma_1}) \cos(\theta_{\gamma_2}) \sin(\phi_{\gamma_1}) \sin(\phi_{\gamma_2}) + \\ &\quad \cos(\theta_{\gamma_1}) \cos(\theta_{\gamma_2}) \end{aligned} \quad (\text{A.4})$$

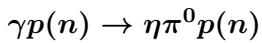
the error $\Delta \cos(\phi_{\gamma_1\gamma_2})$ is given by

$$\begin{aligned} \Delta \cos(\phi_{\gamma_1\gamma_2}) &= \{ [-\sin(\theta_{\gamma_1}) \sin(\theta_{\gamma_2}) \sin(\phi_{\gamma_1} - \phi_{\gamma_2}) \Delta \phi_{\gamma_1}]^2 + \\ &\quad [-\sin(\theta_{\gamma_1}) \sin(\theta_{\gamma_2}) \sin(\phi_{\gamma_2} - \phi_{\gamma_1}) \Delta \phi_{\gamma_2}]^2 + \\ &\quad [(\cos(\theta_{\gamma_1}) \sin(\theta_{\gamma_2}) \cos(\phi_{\gamma_1} - \phi_{\gamma_2}) - \sin(\theta_{\gamma_1}) \cos(\theta_{\gamma_2})) \Delta \phi_{\gamma_1}]^2 + \\ &\quad [(\sin(\theta_{\gamma_1}) \cos(\theta_{\gamma_2}) \cos(\phi_{\gamma_2} - \phi_{\gamma_1}) - \cos(\theta_{\gamma_1}) \sin(\theta_{\gamma_2})) \Delta \phi_{\gamma_1}]^2 \}^{1/2}. \end{aligned} \quad (\text{A.5})$$

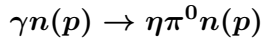
As a consequence, the error in the invariant mass of the photon pair $\gamma_1\gamma_2$ depends on the errors of the energies $\Delta E_{\gamma_{1,2}}$ and the errors of the angles $\Delta \theta_{\gamma_{1,2}}$ and $\Delta \phi_{\gamma_{1,2}}$ of the photon pair.

B. Data tables

B.0.1. Total Cross Sections



E_γ [MeV]	ΔE_γ [MeV]	σ [μ b]	Δ_{stat} [μ b]	Δ_{syst} [μ b]
800.0	20.0	0.0000	0.0000	0.0000
820.0	20.0	0.0000	0.0000	0.0000
840.0	20.0	0.0000	0.0000	0.0000
860.0	20.0	0.0002	0.0058	0.0002
880.0	20.0	0.0197	0.0097	0.0159
900.0	20.0	0.0092	0.0035	0.0053
920.0	20.0	0.0259	0.0082	0.0033
940.0	20.0	0.0562	0.0117	0.0074
960.0	20.0	0.0900	0.0162	0.0061
980.0	20.0	0.1421	0.0180	0.0168
1000.0	20.0	0.1746	0.0189	0.0128
1020.0	20.0	0.2445	0.0221	0.0205
1040.0	20.0	0.3040	0.0257	0.0282
1060.0	20.0	0.4206	0.0277	0.0294
1080.0	20.0	0.5538	0.0302	0.0335
1100.0	20.0	0.7079	0.0372	0.0302
1120.0	20.0	0.8862	0.0373	0.0456
1140.0	20.0	0.9907	0.0389	0.0410
1160.0	20.0	1.1475	0.0389	0.0317
1180.0	20.0	1.3320	0.0415	0.0645
1200.0	20.0	1.4957	0.0444	0.0443
1220.0	20.0	1.6371	0.0470	0.0578
1240.0	20.0	1.7859	0.0488	0.0604
1260.0	20.0	1.8492	0.0495	0.0680
1280.0	20.0	1.9556	0.0542	0.0535
1300.0	20.0	2.0626	0.0505	0.0491
1320.0	20.0	2.1020	0.0630	0.0611
1340.0	20.0	2.2266	0.0584	0.0328
1360.0	20.0	2.2049	0.0549	0.0450
1380.0	20.0	2.2479	0.0616	0.0254



E_γ [MeV]	ΔE_γ [MeV]	σ [μ b]	Δ_{stat} [μ b]	Δ_{syst} [μ b]
800.0	20.0	0.0000	0.0000	0.0000
820.0	20.0	0.0000	0.0000	0.0000
840.0	20.0	0.0000	0.0000	0.0000
860.0	20.0	0.0000	0.0000	0.0000
880.0	20.0	0.0054	0.0000	0.0054
900.0	20.0	0.0000	0.0000	0.0000
920.0	20.0	0.0000	0.0000	0.0000
940.0	20.0	0.0454	0.0220	0.0242
960.0	20.0	0.0776	0.0178	0.1525
980.0	20.0	0.0910	0.0222	0.0564
1000.0	20.0	0.1503	0.0251	0.0220
1020.0	20.0	0.2280	0.0307	0.0354
1040.0	20.0	0.3411	0.0363	0.0457
1060.0	20.0	0.4675	0.0403	0.0541
1080.0	20.0	0.5763	0.0411	0.0695
1100.0	20.0	0.6759	0.0536	0.0752
1120.0	20.0	0.8826	0.0518	0.0784
1140.0	20.0	1.0278	0.0562	0.0925
1160.0	20.0	1.2001	0.0550	0.0882
1180.0	20.0	1.4034	0.0582	0.1234
1200.0	20.0	1.3972	0.0613	0.0885
1220.0	20.0	1.6849	0.0679	0.1113
1240.0	20.0	1.6553	0.0674	0.0983
1260.0	20.0	1.8615	0.0674	0.1053
1280.0	20.0	2.0245	0.0729	0.1593
1300.0	20.0	2.0687	0.0726	0.1570
1320.0	20.0	2.1902	0.0868	0.1003
1340.0	20.0	2.2081	0.0763	0.1011
1360.0	20.0	2.3691	0.0770	0.1161
1380.0	20.0	2.2831	0.0882	0.1259

$\gamma N(N) \rightarrow \eta\pi^0(N)$

E_γ [MeV]	ΔE_γ [MeV]	σ [μ b]	Δ_{stat} [μ b]	Δ_{syst} [μ b]
800.0	20.0	0.0000	0.0000	0.0000
820.0	20.0	0.0000	0.0000	0.0000
840.0	20.0	0.0006	0.0084	0.0000
860.0	20.0	0.0027	0.0012	0.0000
880.0	20.0	0.0038	0.0039	0.0038
900.0	20.0	0.0223	0.0060	0.0208
920.0	20.0	0.0407	0.0068	0.0100
940.0	20.0	0.0588	0.0089	0.0025
960.0	20.0	0.0973	0.0107	0.0134
980.0	20.0	0.1719	0.0133	0.0251
1000.0	20.0	0.2684	0.0159	0.0311
1020.0	20.0	0.4092	0.0191	0.0144
1040.0	20.0	0.5751	0.0226	0.0473
1060.0	20.0	0.7798	0.0258	0.0578
1080.0	20.0	1.0021	0.0285	0.0774
1100.0	20.0	1.2694	0.0347	0.0741
1120.0	20.0	1.6117	0.0352	0.0880
1140.0	20.0	1.8359	0.0380	0.0798
1160.0	20.0	2.1752	0.0387	0.0929
1180.0	20.0	2.4830	0.0417	0.1392
1200.0	20.0	2.7529	0.0450	0.1226
1220.0	20.0	3.0504	0.0486	0.1594
1240.0	20.0	3.3364	0.0508	0.1910
1260.0	20.0	3.5635	0.0528	0.1807
1280.0	20.0	3.7713	0.0579	0.2505
1300.0	20.0	3.8939	0.0546	0.2317
1320.0	20.0	4.1862	0.0682	0.2272
1340.0	20.0	4.3251	0.0643	0.2971
1360.0	20.0	4.3068	0.0603	0.3445
1380.0	20.0	4.4369	0.0695	0.2951

$\gamma p \rightarrow \eta\pi^0 p$

E_γ [MeV]	ΔE_γ [MeV]	σ [μb]	Δ_{stat} [μb]	Δ_{syst} [μb]
800.0	20.0	0.0000	0.0000	0.0000
820.0	20.0	0.0000	0.0000	0.0000
840.0	20.0	0.0000	0.0000	0.0000
860.0	20.0	0.0000	0.0000	0.0000
880.0	20.0	0.0000	0.0000	0.0000
900.0	20.0	0.0000	0.0000	0.0000
920.0	20.0	0.0034	0.0000	0.0000
940.0	20.0	0.0114	0.0000	0.0000
960.0	20.0	0.0275	0.0000	0.0000
980.0	20.0	0.0755	0.0000	0.0000
1000.0	20.0	0.1490	0.0000	0.0000
1020.0	20.0	0.2467	0.0000	0.0000
1040.0	20.0	0.3688	0.0000	0.0000
1060.0	20.0	0.4993	0.0000	0.0000
1080.0	20.0	0.6801	0.0077	0.0000
1100.0	20.0	0.8992	0.0114	0.0061
1120.0	20.0	1.0945	0.0135	0.0050
1140.0	20.0	1.3064	0.0144	0.0067
1160.0	20.0	1.5625	0.0145	0.0190
1180.0	20.0	1.7880	0.0158	0.0222
1200.0	20.0	2.0746	0.0164	0.0276
1220.0	20.0	2.2849	0.0180	0.0299
1240.0	20.0	2.4538	0.0195	0.0420
1260.0	20.0	2.6297	0.0214	0.0530
1280.0	20.0	2.6958	0.0217	0.0526
1300.0	20.0	2.8195	0.0205	0.0622
1320.0	20.0	2.9591	0.0259	0.0681
1340.0	20.0	3.0368	0.0219	0.0791
1360.0	20.0	3.2159	0.0239	0.0889
1380.0	20.0	3.1701	0.0250	0.0804

$\gamma d \rightarrow \eta\pi^0d$

E_γ [MeV]	ΔE_γ [MeV]	σ [μb]	Δ_{stat} [μb]	Δ_{syst} [μb]
800.0	20.0	-0.0001	0.0000	-0.0000
820.0	20.0	-0.0000	0.0000	-0.0000
840.0	20.0	0.0035	0.0010	0.0003
860.0	20.0	0.0052	0.0012	0.0002
880.0	20.0	0.0084	0.0016	0.0020
900.0	20.0	0.0220	0.0024	0.0010
920.0	20.0	0.0357	0.0031	0.0037
940.0	20.0	0.0471	0.0036	0.0032
960.0	20.0	0.0650	0.0044	0.0048
980.0	20.0	0.0763	0.0051	0.0068
1000.0	20.0	0.0836	0.0055	0.0048
1020.0	20.0	0.0900	0.0060	0.0077
1040.0	20.0	0.1032	0.0066	0.0040
1060.0	20.0	0.1055	0.0067	0.0051
1080.0	20.0	0.0989	0.0067	0.0048
1100.0	20.0	0.1100	0.0077	0.0036
1120.0	20.0	0.1006	0.0069	0.0058
1140.0	20.0	0.1105	0.0075	0.0069
1160.0	20.0	0.0836	0.0064	0.0040
1180.0	20.0	0.0918	0.0067	0.0064
1200.0	20.0	0.0907	0.0070	0.0047
1220.0	20.0	0.0742	0.0067	0.0059
1240.0	20.0	0.0638	0.0062	0.0029
1260.0	20.0	0.0581	0.0057	0.0045
1280.0	20.0	0.0695	0.0066	0.0063
1300.0	20.0	0.0709	0.0070	0.0043
1320.0	20.0	0.0632	0.0076	0.0045
1340.0	20.0	0.0553	0.0066	0.0069
1360.0	20.0	0.0487	0.0064	0.0033
1380.0	20.0	0.0453	0.0068	0.0028

$\gamma p(n) \rightarrow \eta\pi^+n(n)$

E_γ [MeV]	ΔE_γ [MeV]	σ [μ b]	Δ_{stat} [μ b]	Δ_{syst} [μ b]
800.0	20.0	0.0000	0.0000	0.0000
820.0	20.0	0.0000	0.0000	0.0000
840.0	20.0	0.0000	0.0000	0.0000
860.0	20.0	0.0002	0.0058	0.0002
880.0	20.0	0.0197	0.0097	0.0159
900.0	20.0	0.0092	0.0035	0.0053
920.0	20.0	0.0259	0.0082	0.0033
940.0	20.0	0.0562	0.0117	0.0074
960.0	20.0	0.0900	0.0162	0.0061
980.0	20.0	0.1421	0.0180	0.0168
1000.0	20.0	0.1746	0.0189	0.0128
1020.0	20.0	0.2445	0.0221	0.0205
1040.0	20.0	0.3040	0.0257	0.0282
1060.0	20.0	0.4206	0.0277	0.0294
1080.0	20.0	0.5538	0.0302	0.0335
1100.0	20.0	0.7079	0.0372	0.0302
1120.0	20.0	0.8862	0.0373	0.0456
1140.0	20.0	0.9907	0.0389	0.0410
1160.0	20.0	1.1475	0.0389	0.0317
1180.0	20.0	1.3320	0.0415	0.0645
1200.0	20.0	1.4957	0.0444	0.0443
1220.0	20.0	1.6371	0.0470	0.0578
1240.0	20.0	1.7859	0.0488	0.0604
1260.0	20.0	1.8492	0.0495	0.0680
1280.0	20.0	1.9556	0.0542	0.0535
1300.0	20.0	2.0626	0.0505	0.0491
1320.0	20.0	2.1020	0.0630	0.0611
1340.0	20.0	2.2266	0.0584	0.0328
1360.0	20.0	2.2049	0.0549	0.0450
1380.0	20.0	2.2479	0.0616	0.0254

$\gamma n(p) \rightarrow \eta\pi^- p(p)$

E_γ [MeV]	ΔE_γ [MeV]	σ [μ b]	Δ_{stat} [μ b]	Δ_{syst} [μ b]
800.0	20.0	0.0000	0.0000	0.0000
820.0	20.0	0.0000	0.0000	0.0000
840.0	20.0	0.0000	0.0000	0.0000
860.0	20.0	0.0000	0.0000	0.0000
880.0	20.0	0.0054	0.0000	0.0054
900.0	20.0	0.0000	0.0000	0.0000
920.0	20.0	0.0000	0.0000	0.0000
940.0	20.0	0.0454	0.0220	0.0242
960.0	20.0	0.0776	0.0178	0.1525
980.0	20.0	0.0910	0.0222	0.0564
1000.0	20.0	0.1503	0.0251	0.0220
1020.0	20.0	0.2280	0.0307	0.0354
1040.0	20.0	0.3411	0.0363	0.0457
1060.0	20.0	0.4675	0.0403	0.0541
1080.0	20.0	0.5763	0.0411	0.0695
1100.0	20.0	0.6759	0.0536	0.0752
1120.0	20.0	0.8826	0.0518	0.0784
1140.0	20.0	1.0278	0.0562	0.0925
1160.0	20.0	1.2001	0.0550	0.0882
1180.0	20.0	1.4034	0.0582	0.1234
1200.0	20.0	1.3972	0.0613	0.0885
1220.0	20.0	1.6849	0.0679	0.1113
1240.0	20.0	1.6553	0.0674	0.0983
1260.0	20.0	1.8615	0.0674	0.1053
1280.0	20.0	2.0245	0.0729	0.1593
1300.0	20.0	2.0687	0.0726	0.1570
1320.0	20.0	2.1902	0.0868	0.1003
1340.0	20.0	2.2081	0.0763	0.1011
1360.0	20.0	2.3691	0.0770	0.1161
1380.0	20.0	2.2831	0.0882	0.1259

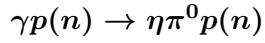
$\gamma N(N) \rightarrow \eta\pi^\pm(N)$

E_γ [MeV]	ΔE_γ [MeV]	σ [μ b]	Δ_{stat} [μ b]	Δ_{syst} [μ b]
800.0	20.0	0.0000	0.0000	0.0000
820.0	20.0	0.0000	0.0000	0.0000
840.0	20.0	0.0006	0.0084	0.0000
860.0	20.0	0.0027	0.0012	0.0000
880.0	20.0	0.0038	0.0039	0.0038
900.0	20.0	0.0223	0.0060	0.0208
920.0	20.0	0.0407	0.0068	0.0100
940.0	20.0	0.0588	0.0089	0.0025
960.0	20.0	0.0973	0.0107	0.0134
980.0	20.0	0.1719	0.0133	0.0251
1000.0	20.0	0.2684	0.0159	0.0311
1020.0	20.0	0.4092	0.0191	0.0144
1040.0	20.0	0.5751	0.0226	0.0473
1060.0	20.0	0.7798	0.0258	0.0578
1080.0	20.0	1.0021	0.0285	0.0774
1100.0	20.0	1.2694	0.0347	0.0741
1120.0	20.0	1.6117	0.0352	0.0880
1140.0	20.0	1.8359	0.0380	0.0798
1160.0	20.0	2.1752	0.0387	0.0929
1180.0	20.0	2.4830	0.0417	0.1392
1200.0	20.0	2.7529	0.0450	0.1226
1220.0	20.0	3.0504	0.0486	0.1594
1240.0	20.0	3.3364	0.0508	0.1910
1260.0	20.0	3.5635	0.0528	0.1807
1280.0	20.0	3.7713	0.0579	0.2505
1300.0	20.0	3.8939	0.0546	0.2317
1320.0	20.0	4.1862	0.0682	0.2272
1340.0	20.0	4.3251	0.0643	0.2971
1360.0	20.0	4.3068	0.0603	0.3445
1380.0	20.0	4.4369	0.0695	0.2951

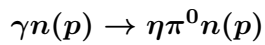
$\gamma p \rightarrow \eta\pi^+n$

E_γ [MeV]	ΔE_γ [MeV]	σ [μb]	Δ_{stat} [μb]	Δ_{syst} [μb]
800.0	20.0	0.0000	0.0000	0.0000
820.0	20.0	0.0000	0.0000	0.0000
840.0	20.0	0.0000	0.0000	0.0000
860.0	20.0	0.0000	0.0000	0.0000
880.0	20.0	0.0000	0.0000	0.0000
900.0	20.0	0.0000	0.0000	0.0000
920.0	20.0	0.0034	0.0000	0.0000
940.0	20.0	0.0114	0.0000	0.0000
960.0	20.0	0.0275	0.0000	0.0000
980.0	20.0	0.0755	0.0000	0.0000
1000.0	20.0	0.1490	0.0000	0.0000
1020.0	20.0	0.2467	0.0000	0.0000
1040.0	20.0	0.3688	0.0000	0.0000
1060.0	20.0	0.4993	0.0000	0.0000
1080.0	20.0	0.6801	0.0077	0.0000
1100.0	20.0	0.8992	0.0114	0.0061
1120.0	20.0	1.0945	0.0135	0.0050
1140.0	20.0	1.3064	0.0144	0.0067
1160.0	20.0	1.5625	0.0145	0.0190
1180.0	20.0	1.7880	0.0158	0.0222
1200.0	20.0	2.0746	0.0164	0.0276
1220.0	20.0	2.2849	0.0180	0.0299
1240.0	20.0	2.4538	0.0195	0.0420
1260.0	20.0	2.6297	0.0214	0.0530
1280.0	20.0	2.6958	0.0217	0.0526
1300.0	20.0	2.8195	0.0205	0.0622
1320.0	20.0	2.9591	0.0259	0.0681
1340.0	20.0	3.0368	0.0219	0.0791
1360.0	20.0	3.2159	0.0239	0.0889
1380.0	20.0	3.1701	0.0250	0.0804

B.0.2. Total Cross Sections as function of W



W [MeV]	ΔW [MeV]	σ [μb]	Δ_{stat} [μb]	Δ_{syst} [μb]
1600.0	10.0	0.0001	0.0000	0.0000
1610.0	10.0	0.0001	0.0000	0.0000
1620.0	10.0	0.0000	0.0000	0.0000
1630.0	10.0	0.0000	0.0000	0.0000
1640.0	10.0	0.0520	0.0192	0.0047
1650.0	10.0	0.0815	0.0206	0.0069
1660.0	10.0	0.1443	0.0300	0.0153
1670.0	10.0	0.2055	0.0439	0.0139
1680.0	10.0	0.2528	0.0500	0.0168
1690.0	10.0	0.3731	0.0542	0.0338
1700.0	10.0	0.5192	0.0547	0.0311
1710.0	10.0	0.6529	0.0500	0.0369
1720.0	10.0	0.7967	0.0494	0.0440
1730.0	10.0	0.9213	0.0540	0.0475
1740.0	10.0	1.1138	0.0508	0.0573
1750.0	10.0	1.2461	0.0569	0.0568
1760.0	10.0	1.3540	0.0490	0.0580
1770.0	10.0	1.5665	0.0534	0.0660
1780.0	10.0	1.7293	0.0535	0.0673
1790.0	10.0	1.7746	0.0533	0.0659
1800.0	10.0	1.8771	0.0531	0.0668
1810.0	10.0	1.9987	0.0584	0.0720
1820.0	10.0	2.1414	0.0564	0.0703
1830.0	10.0	2.2581	0.0629	0.0687
1840.0	10.0	2.2744	0.0588	0.0668
1850.0	10.0	2.2773	0.0655	0.0731
1860.0	10.0	2.4105	0.0696	0.0650
1870.0	10.0	2.4274	0.0805	0.0636
1880.0	10.0	2.2988	0.0960	0.0626
1890.0	10.0	2.5827	0.1247	0.0572



W [MeV]	ΔW [MeV]	σ [μ b]	Δ_{stat} [μ b]	Δ_{syst} [μ b]
1600.0	10.0	0.0001	0.0000	0.0000
1610.0	10.0	0.0001	0.0000	0.0000
1620.0	10.0	0.0003	0.0017	0.0001
1630.0	10.0	0.0000	0.0000	0.0000
1640.0	10.0	0.0249	0.0000	0.2408
1650.0	10.0	0.0717	0.0271	0.0646
1660.0	10.0	0.1056	0.0000	0.0302
1670.0	10.0	0.2007	0.0378	0.1696
1680.0	10.0	0.2913	0.0500	0.0210
1690.0	10.0	0.3957	0.0561	0.1176
1700.0	10.0	0.5260	0.0520	0.0168
1710.0	10.0	0.6534	0.0500	0.0464
1720.0	10.0	0.8405	0.0536	0.0817
1730.0	10.0	0.9955	0.0674	0.1160
1740.0	10.0	1.1482	0.0578	0.0393
1750.0	10.0	1.2446	0.0646	0.0826
1760.0	10.0	1.4158	0.0627	0.0506
1770.0	10.0	1.5590	0.0625	0.0587
1780.0	10.0	1.7151	0.0596	0.0912
1790.0	10.0	1.8179	0.0602	0.0501
1800.0	10.0	1.9477	0.0629	0.0805
1810.0	10.0	2.0772	0.0720	0.1056
1820.0	10.0	2.2213	0.0742	0.1212
1830.0	10.0	2.3086	0.0744	0.1333
1840.0	10.0	2.2498	0.0700	0.1028
1850.0	10.0	2.3021	0.0770	0.1082
1860.0	10.0	2.3821	0.0780	0.1761
1870.0	10.0	2.5449	0.0923	0.1681
1880.0	10.0	2.3224	0.1085	0.1758
1890.0	10.0	2.5336	0.1248	0.1930

$\gamma p \rightarrow \eta\pi^0 p$

W [MeV]	ΔW [MeV]	σ [μb]	Δ_{stat} [μb]	Δ_{syst} [μb]
1600.0	10.0	0.0000	0.0000	0.0000
1610.0	10.0	0.0000	0.0000	0.0000
1620.0	10.0	0.0000	0.0000	0.0000
1630.0	10.0	0.0000	0.0000	0.0000
1640.0	10.0	0.0000	0.0000	0.0000
1650.0	10.0	0.0000	0.0000	0.0000
1660.0	10.0	0.0033	0.0000	0.0001
1670.0	10.0	0.0115	0.0000	0.0004
1680.0	10.0	0.0272	0.0000	0.0008
1690.0	10.0	0.0764	0.0000	0.0023
1700.0	10.0	0.1493	0.0000	0.0038
1710.0	10.0	0.2469	0.0000	0.0060
1720.0	10.0	0.3671	0.0000	0.0082
1730.0	10.0	0.5011	0.0000	0.0104
1740.0	10.0	0.6815	0.0077	0.0129
1750.0	10.0	0.8981	0.0114	0.0160
1760.0	10.0	1.0953	0.0136	0.0184
1770.0	10.0	1.3055	0.0144	0.0203
1780.0	10.0	1.5626	0.0147	0.0235
1790.0	10.0	1.7830	0.0158	0.0256
1800.0	10.0	2.0766	0.0164	0.0270
1810.0	10.0	2.2863	0.0180	0.0350
1820.0	10.0	2.4530	0.0195	0.0297
1830.0	10.0	2.6296	0.0215	0.0308
1840.0	10.0	2.6963	0.0217	0.0302
1850.0	10.0	2.8222	0.0206	0.0319
1860.0	10.0	2.9519	0.0260	0.0340
1870.0	10.0	3.0339	0.0220	0.0316
1880.0	10.0	3.2171	0.0240	0.0315
1890.0	10.0	3.1696	0.0251	0.0292

$\gamma p(n) \rightarrow \eta\pi^+n(n)$

W [MeV]	ΔW [MeV]	σ [μ b]	Δ_{stat} [μ b]	Δ_{syst} [μ b]
1600.0	10.0	0.0001	0.0000	0.0000
1610.0	10.0	0.0001	0.0000	0.0000
1620.0	10.0	0.0001	0.0000	0.0000
1630.0	10.0	0.0001	0.0000	0.0000
1640.0	10.0	0.0000	0.0014	0.0000
1650.0	10.0	0.0136	0.0035	0.0012
1660.0	10.0	0.0236	0.0000	0.0025
1670.0	10.0	0.0290	0.0213	0.0020
1680.0	10.0	0.0795	0.0293	0.0053
1690.0	10.0	0.1787	0.0296	0.0162
1700.0	10.0	0.2309	0.0229	0.0138
1710.0	10.0	0.3648	0.0356	0.0206
1720.0	10.0	0.4417	0.0361	0.0244
1730.0	10.0	0.5121	0.0318	0.0264
1740.0	10.0	0.6441	0.0339	0.0331
1750.0	10.0	0.6759	0.0348	0.0308
1760.0	10.0	0.7948	0.0406	0.0340
1770.0	10.0	0.8798	0.0406	0.0371
1780.0	10.0	0.9167	0.0512	0.0357
1790.0	10.0	1.0195	0.0546	0.0379
1800.0	10.0	0.9827	0.0571	0.0350
1810.0	10.0	1.1064	0.0580	0.0399
1820.0	10.0	1.1574	0.0528	0.0380
1830.0	10.0	1.2084	0.0550	0.0367
1840.0	10.0	1.2300	0.0593	0.0361
1850.0	10.0	1.3081	0.0768	0.0420
1860.0	10.0	1.3014	0.0797	0.0351
1870.0	10.0	1.4596	0.0869	0.0382
1880.0	10.0	1.5148	0.0940	0.0413
1890.0	10.0	1.3886	0.1336	0.0307

$\gamma n(p) \rightarrow \eta\pi^- p(p)$

W [MeV]	ΔW [MeV]	σ [μb]	Δ_{stat} [μb]	Δ_{syst} [μb]
1600.0	10.0	0.0001	0.0000	0.0000
1610.0	10.0	0.0001	0.0000	0.0000
1620.0	10.0	0.0001	0.0000	0.0000
1630.0	10.0	0.0000	0.0027	0.0000
1640.0	10.0	0.0078	0.0113	0.0000
1650.0	10.0	0.0019	0.0133	0.0017
1660.0	10.0	0.0551	0.0176	0.0158
1670.0	10.0	0.0114	0.0136	0.0096
1680.0	10.0	0.1422	0.0183	0.0103
1690.0	10.0	0.1961	0.0158	0.0583
1700.0	10.0	0.3451	0.0189	0.0110
1710.0	10.0	0.3988	0.0214	0.0283
1720.0	10.0	0.4953	0.0230	0.0481
1730.0	10.0	0.6232	0.0265	0.0726
1740.0	10.0	0.6938	0.0275	0.0237
1750.0	10.0	0.7369	0.0275	0.0489
1760.0	10.0	0.7897	0.0309	0.0282
1770.0	10.0	0.8979	0.0303	0.0338
1780.0	10.0	0.9919	0.0327	0.0528
1790.0	10.0	1.0347	0.0335	0.0285
1800.0	10.0	1.0959	0.0346	0.0453
1810.0	10.0	1.1260	0.0360	0.0572
1820.0	10.0	1.1391	0.0379	0.0621
1830.0	10.0	1.2100	0.0413	0.0699
1840.0	10.0	1.2518	0.0436	0.0572
1850.0	10.0	1.2881	0.0486	0.0605
1860.0	10.0	1.3266	0.0474	0.0981
1870.0	10.0	1.4874	0.0604	0.0982
1880.0	10.0	1.4949	0.0697	0.1132
1890.0	10.0	1.4874	0.0836	0.1133

$\gamma p \rightarrow \eta\pi^+n$

W [MeV]	ΔW [MeV]	σ [μb]	Δ_{stat} [μb]	Δ_{syst} [μb]
1600.0	10.0	0.0000	0.0000	0.0000
1610.0	10.0	0.0000	0.0000	0.0000
1620.0	10.0	0.0000	0.0000	0.0000
1630.0	10.0	0.0000	0.0000	0.0000
1640.0	10.0	0.0000	0.0000	0.0000
1650.0	10.0	0.0000	0.0000	0.0000
1660.0	10.0	0.0000	0.0000	0.0000
1670.0	10.0	0.0000	0.0000	0.0000
1680.0	10.0	0.0084	0.0333	0.0003
1690.0	10.0	0.0260	0.0134	0.0008
1700.0	10.0	0.0483	0.0105	0.0012
1710.0	10.0	0.0706	0.0079	0.0017
1720.0	10.0	0.1405	0.0092	0.0031
1730.0	10.0	0.2060	0.0124	0.0043
1740.0	10.0	0.2903	0.0127	0.0055
1750.0	10.0	0.4094	0.0142	0.0073
1760.0	10.0	0.5357	0.0172	0.0090
1770.0	10.0	0.6204	0.0177	0.0097
1780.0	10.0	0.7782	0.0186	0.0117
1790.0	10.0	0.8791	0.0200	0.0126
1800.0	10.0	1.0154	0.0210	0.0132
1810.0	10.0	1.1833	0.0231	0.0181
1820.0	10.0	1.2451	0.0252	0.0151
1830.0	10.0	1.2660	0.0269	0.0148
1840.0	10.0	1.3281	0.0266	0.0149
1850.0	10.0	1.3919	0.0251	0.0157
1860.0	10.0	1.4134	0.0317	0.0163
1870.0	10.0	1.4153	0.0259	0.0147
1880.0	10.0	1.4937	0.0286	0.0146
1890.0	10.0	1.5254	0.0305	0.0140

B.0.3. Invariant Mass Distributions

$\gamma p(n) \rightarrow \eta\pi^0 p(n)$

$m_{\eta\pi} [MeV]$	$W=(1725.0 \pm 25.0) \text{ MeV}$		$W=(1775.0 \pm 25.0) \text{ MeV}$	
	$d\sigma/dM$ [$\mu\text{b}/\text{GeV}$]	Δ_{stat} [$\mu\text{b}/\text{GeV}$]	$d\sigma/dM$ [$\mu\text{b}/\text{GeV}$]	Δ_{stat} [$\mu\text{b}/\text{GeV}$]
650.00	0.0000	0.0000	0.0000	0.0000
660.00	0.0000	0.0000	0.0000	0.0000
670.00	0.0000	0.0000	0.0000	0.0000
680.00	1.3506	0.1713	1.4028	0.1595
690.00	2.8591	0.2254	2.9629	0.1972
700.00	3.4095	0.2500	3.8934	0.2539
710.00	5.3621	0.3152	6.1107	0.3114
720.00	7.5756	0.3523	7.5684	0.3382
730.00	9.5279	0.3965	9.7448	0.3909
740.00	9.9618	0.3895	9.7237	0.4265
750.00	10.4771	0.4330	12.9650	0.4756
760.00	9.8470	0.4049	13.1121	0.5002
770.00	7.3981	0.3734	15.6474	0.5121
780.00	4.3861	0.3324	15.8818	0.5168
790.00	2.5364	0.3770	15.5937	0.5107
800.00	2.1110	0.4846	14.3210	0.5691
810.00	0.0000	0.0000	11.1298	0.5272
820.00	0.0000	0.0000	7.6937	0.4488
830.00	0.0000	0.0000	5.1279	0.5412
840.00	0.0000	0.0000	2.8881	0.3328
850.00	0.0000	0.0000	0.0000	0.0000
860.00	0.0000	0.0000	0.0000	0.0000
870.00	0.0000	0.0000	0.0000	0.0000
880.00	0.0000	0.0000	0.0000	0.0000
890.00	0.0000	0.0000	0.0000	0.0000
900.00	0.0000	0.0000	0.0000	0.0000
910.00	0.0000	0.0000	0.0000	0.0000
920.00	0.0000	0.0000	0.0000	0.0000
930.00	0.0000	0.0000	0.0000	0.0000
940.00	0.0000	0.0000	0.0000	0.0000

$m_{\eta\pi} [MeV]$	$W=(1825.0 \pm 25.0) \text{ MeV}$		$W=(1875.0 \pm 25.0) \text{ MeV}$	
	$d\sigma/dM$ [$\mu\text{b}/\text{GeV}$]	Δ_{stat} [$\mu\text{b}/\text{GeV}$]	$d\sigma/dM$ [$\mu\text{b}/\text{GeV}$]	Δ_{stat} [$\mu\text{b}/\text{GeV}$]
650.00	0.0000	0.0000	0.0000	0.0000
660.00	0.0000	0.0000	0.0000	0.0000
670.00	0.0000	0.0000	0.0000	0.0000
680.00	1.4366	0.1671	1.1378	0.2078
690.00	2.5771	0.2307	2.6266	0.3275
700.00	4.9635	0.2820	4.4575	0.4288
710.00	5.9075	0.3202	6.4859	0.4387
720.00	7.3630	0.3744	6.5649	0.4896
730.00	9.6786	0.3916	7.2973	0.4887
740.00	8.8124	0.4034	8.3057	0.5146
750.00	9.7875	0.4233	8.2167	0.5288
760.00	10.6114	0.4491	8.4199	0.5007
770.00	12.1318	0.4811	10.5245	0.5465
780.00	11.8527	0.4860	10.9380	0.5956
790.00	13.6080	0.5209	7.3603	0.5884
800.00	13.9239	0.5293	13.1046	0.6217
810.00	14.8872	0.6238	10.1350	0.6719
820.00	13.7356	0.6099	12.0459	0.9312
830.00	15.0618	0.5764	11.3481	0.6564
840.00	14.4910	0.5652	12.5513	0.7572
850.00	12.4844	0.5778	11.5535	0.7604
860.00	10.5897	0.5977	12.3510	0.7841
870.00	7.6399	0.7721	11.7400	1.0274
880.00	6.3310	0.6386	10.4266	0.9932
890.00	1.7154	0.3677	13.7279	0.9863
900.00	0.0000	0.0000	9.4686	0.7869
910.00	0.0000	0.0000	6.8158	0.7820
920.00	0.0000	0.0000	4.9935	0.7219
930.00	0.0000	0.0000	3.6058	0.6653
940.00	0.0000	0.0000	0.4309	0.7770

$m_{N\eta}[MeV]$	$W=(1725.0 \pm 25.0) \text{ MeV}$		$W=(1775.0 \pm 25.0) \text{ MeV}$	
	$d\sigma/dM$ [$\mu\text{b}/\text{GeV}$]	Δ_{stat} [$\mu\text{b}/\text{GeV}$]	$d\sigma/dM$ [$\mu\text{b}/\text{GeV}$]	Δ_{stat} [$\mu\text{b}/\text{GeV}$]
1450.00	0.0000	0.0000	0.0000	0.0000
1460.00	0.0000	0.0000	0.0000	0.0000
1470.00	0.3705	0.1050	0.3236	0.0839
1480.00	1.5369	0.2082	0.9900	0.1303
1490.00	2.9570	0.2441	1.1667	0.1693
1500.00	4.3577	0.2669	2.3201	0.2424
1510.00	4.6310	0.2927	3.1496	0.2393
1520.00	6.2325	0.3285	4.3349	0.2666
1530.00	8.9129	0.3992	4.6629	0.3000
1540.00	10.2659	0.4135	7.9895	0.3562
1550.00	10.5636	0.4202	9.3098	0.4000
1560.00	9.5059	0.3838	12.7605	0.4640
1570.00	8.9470	0.3613	17.1485	0.5392
1580.00	5.2109	0.2708	20.9627	0.5887
1590.00	1.7423	0.2425	24.2192	0.6145
1600.00	0.2791	0.1926	21.9633	0.5804
1610.00	0.0000	0.0000	16.1981	0.5001
1620.00	0.0000	0.0000	8.1907	0.3979
1630.00	0.0000	0.0000	4.4380	0.3049
1640.00	0.0000	0.0000	0.8650	0.1355
1650.00	0.0000	0.0000	0.0277	0.4387
1660.00	0.0000	0.0000	0.0000	0.0000
1670.00	0.0000	0.0000	0.0000	0.0000
1680.00	0.0000	0.0000	0.0000	0.0000
1690.00	0.0000	0.0000	0.0000	0.0000
1700.00	0.0000	0.0000	0.0000	0.0000
1710.00	0.0000	0.0000	0.0000	0.0000
1720.00	0.0000	0.0000	0.0000	0.0000
1730.00	0.0000	0.0000	0.0000	0.0000
1740.00	0.0000	0.0000	0.0000	0.0000

$m_{N\eta}[MeV]$	$W=(1825.0 \pm 25.0) \text{ MeV}$		$W=(1875.0 \pm 25.0) \text{ MeV}$	
	$d\sigma/dM$ [$\mu\text{b}/\text{GeV}$]	Δ_{stat} [$\mu\text{b}/\text{GeV}$]	$d\sigma/dM$ [$\mu\text{b}/\text{GeV}$]	Δ_{stat} [$\mu\text{b}/\text{GeV}$]
1450.00	0.0000	0.0000	0.0000	0.0000
1460.00	0.0000	0.0000	0.0000	0.0000
1470.00	0.9324	0.0874	0.0210	0.0156
1480.00	0.2336	0.0766	1.6676	0.0855
1490.00	1.1287	0.1584	1.3284	0.3462
1500.00	1.6820	0.1927	1.5748	0.2336
1510.00	1.9927	0.1742	0.8823	0.2042
1520.00	2.9257	0.2464	1.7811	0.2911
1530.00	2.8744	0.2490	2.9342	0.3814
1540.00	4.8690	0.3009	5.8936	0.5591
1550.00	6.5902	0.3538	4.7341	0.4903
1560.00	8.6594	0.4132	7.2160	0.5189
1570.00	11.3039	0.4753	10.6858	0.5906
1580.00	16.3963	0.5617	12.5160	0.7367
1590.00	19.8799	0.6396	18.0033	0.7633
1600.00	23.3825	0.6603	18.6719	0.8861
1610.00	24.7994	0.6675	22.2032	0.8912
1620.00	23.3172	0.6588	22.4988	0.8827
1630.00	21.5197	0.6517	20.7427	0.8091
1640.00	17.3811	0.5784	18.0900	0.8204
1650.00	11.3110	0.4739	16.4211	0.7111
1660.00	7.5969	0.4070	15.2520	0.7008
1670.00	3.5977	0.2894	12.6957	0.5118
1680.00	1.7831	0.1760	9.1667	0.5518
1690.00	1.0336	0.1210	7.8264	0.5856
1700.00	0.0000	0.0000	4.9320	0.3725
1710.00	0.0000	0.0000	3.5921	0.3606
1720.00	0.0000	0.0000	0.0000	0.0000
1730.00	0.0000	0.0000	1.0170	0.0360
1740.00	0.0000	0.0000	0.3358	2.6434

$m_{N\pi}[MeV]$	$W=(1725.0 \pm 25.0) \text{ MeV}$		$W=(1775.0 \pm 25.0) \text{ MeV}$	
	$d\sigma/dM$ [$\mu\text{b}/\text{GeV}$]	Δ_{stat} [$\mu\text{b}/\text{GeV}$]	$d\sigma/dM$ [$\mu\text{b}/\text{GeV}$]	Δ_{stat} [$\mu\text{b}/\text{GeV}$]
1050.00	0.0000	0.0000	0.0000	0.0000
1060.00	0.0000	0.0000	0.0000	0.0000
1070.00	0.3705	0.1050	0.3236	0.0839
1080.00	1.5369	0.2082	0.9900	0.1303
1090.00	2.9570	0.2441	1.1667	0.1693
1100.00	4.3577	0.2669	2.3201	0.2424
1110.00	4.6310	0.2927	3.1496	0.2393
1120.00	6.2325	0.3285	4.3349	0.2666
1130.00	8.9129	0.3992	4.6629	0.3000
1140.00	10.2659	0.4135	7.9895	0.3562
1150.00	10.5636	0.4202	9.3098	0.4000
1160.00	9.5059	0.3838	12.7605	0.4640
1170.00	8.9470	0.3613	17.1485	0.5392
1180.00	5.2109	0.2708	20.9627	0.5887
1190.00	1.7423	0.2425	24.2192	0.6145
1200.00	0.2791	0.1926	21.9633	0.5804
1210.00	0.0000	0.0000	16.1981	0.5001
1220.00	0.0000	0.0000	8.1907	0.3979
1230.00	0.0000	0.0000	4.4380	0.3049
1240.00	0.0000	0.0000	0.8650	0.1355
1250.00	0.0000	0.0000	0.0277	0.4387
1260.00	0.0000	0.0000	0.0000	0.0000
1270.00	0.0000	0.0000	0.0000	0.0000
1280.00	0.0000	0.0000	0.0000	0.0000
1290.00	0.0000	0.0000	0.0000	0.0000
1300.00	0.0000	0.0000	0.0000	0.0000
1310.00	0.0000	0.0000	0.0000	0.0000
1320.00	0.0000	0.0000	0.0000	0.0000
1330.00	0.0000	0.0000	0.0000	0.0000
1340.00	0.0000	0.0000	0.0000	0.0000

$m_{N\pi} [MeV]$	$W=(1825.0 \pm 25.0) \text{ MeV}$		$W=(1875.0 \pm 25.0) \text{ MeV}$	
	$d\sigma/dM$ [$\mu\text{b}/\text{GeV}$]	Δ_{stat} [$\mu\text{b}/\text{GeV}$]	$d\sigma/dM$ [$\mu\text{b}/\text{GeV}$]	Δ_{stat} [$\mu\text{b}/\text{GeV}$]
1050.00	0.0000	0.0000	0.0000	0.0000
1060.00	0.0000	0.0000	0.0000	0.0000
1070.00	0.9324	0.0874	0.0210	0.0156
1080.00	0.2336	0.0766	1.6676	0.0855
1090.00	1.1287	0.1584	1.3284	0.3462
1100.00	1.6820	0.1927	1.5748	0.2336
1110.00	1.9927	0.1742	0.8823	0.2042
1120.00	2.9257	0.2464	1.7811	0.2911
1130.00	2.8744	0.2490	2.9342	0.3814
1140.00	4.8690	0.3009	5.8936	0.5591
1150.00	6.5902	0.3538	4.7341	0.4903
1160.00	8.6594	0.4132	7.2160	0.5189
1170.00	11.3039	0.4753	10.6858	0.5906
1180.00	16.3963	0.5617	12.5160	0.7367
1190.00	19.8799	0.6396	18.0033	0.7633
1200.00	23.3825	0.6603	18.6719	0.8861
1210.00	24.7994	0.6675	22.2032	0.8912
1220.00	23.3172	0.6588	22.4988	0.8827
1230.00	21.5197	0.6517	20.7427	0.8091
1240.00	17.3811	0.5784	18.0900	0.8204
1250.00	11.3110	0.4739	16.4211	0.7111
1260.00	7.5969	0.4070	15.2520	0.7008
1270.00	3.5977	0.2894	12.6957	0.5118
1280.00	1.7831	0.1760	9.1667	0.5518
1290.00	1.0336	0.1210	7.8264	0.5856
1300.00	0.0000	0.0000	4.9320	0.3725
1310.00	0.0000	0.0000	3.5921	0.3606
1320.00	0.0000	0.0000	0.0000	0.0000
1330.00	0.0000	0.0000	1.0170	0.0360
1340.00	0.0000	0.0000	0.3358	2.6434

$\gamma n(p) \rightarrow \eta\pi^0 n(p)$

$m_{\eta\pi} [MeV]$	$W=(1725.0 \pm 25.0) \text{ MeV}$		$W=(1775.0 \pm 25.0) \text{ MeV}$	
	$d\sigma/dM$ [$\mu\text{b}/\text{GeV}$]	Δ_{stat} [$\mu\text{b}/\text{GeV}$]	$d\sigma/dM$ [$\mu\text{b}/\text{GeV}$]	Δ_{stat} [$\mu\text{b}/\text{GeV}$]
650.00	0.0000	0.0000	0.0000	0.0000
660.00	0.0000	0.0000	0.0000	0.0000
670.00	0.0000	0.0000	0.0000	0.0000
680.00	0.2105	0.1689	0.6050	0.1653
690.00	2.4043	0.2655	2.3582	0.2337
700.00	3.3366	0.3235	2.9679	0.2789
710.00	5.2633	0.4862	3.9246	2.7575
720.00	6.6487	0.5195	7.0640	0.4561
730.00	8.3792	0.6016	10.0147	0.5667
740.00	10.5579	0.7023	10.5596	0.6432
750.00	11.2591	0.9650	13.7625	0.7342
760.00	7.4470	0.7700	10.7633	0.7201
770.00	6.4615	0.6132	14.9725	1.0389
780.00	3.7932	0.7646	14.4990	0.7901
790.00	0.0000	0.0000	14.9734	0.9196
800.00	2.4644	1.3646	13.3199	0.8662
810.00	0.0000	0.0000	14.1858	0.9672
820.00	0.0000	0.0000	6.7180	0.7356
830.00	0.0000	0.0000	6.0325	0.9742
840.00	0.0000	0.0000	1.3417	1.1959
850.00	0.0000	0.0000	0.0508	0.0000
860.00	0.0000	0.0000	0.0000	0.0000
870.00	0.0000	0.0000	0.0000	0.0000
880.00	0.0000	0.0000	0.0000	0.0000
890.00	0.0000	0.0000	0.0000	0.0000
900.00	0.0000	0.0000	0.0000	0.0000
910.00	0.0000	0.0000	0.0000	0.0000
920.00	0.0000	0.0000	0.0000	0.0000
930.00	0.0000	0.0000	0.0000	0.0000
940.00	0.0000	0.0000	0.0000	0.0000

$m_{\eta\pi} [MeV]$	$W=(1825.0 \pm 25.0) \text{ MeV}$		$W=(1875.0 \pm 25.0) \text{ MeV}$	
	$d\sigma/dM$ [$\mu\text{b}/\text{GeV}$]	Δ_{stat} [$\mu\text{b}/\text{GeV}$]	$d\sigma/dM$ [$\mu\text{b}/\text{GeV}$]	Δ_{stat} [$\mu\text{b}/\text{GeV}$]
650.00	0.0000	0.0000	0.0000	0.0000
660.00	0.0000	0.0000	0.0000	0.0000
670.00	0.0000	0.0000	0.0000	0.0000
680.00	0.6808	0.1718	1.4232	0.3843
690.00	2.2770	0.2713	2.4512	0.3983
700.00	5.0511	0.3671	5.1909	0.5800
710.00	4.6940	0.3891	3.6391	0.5916
720.00	5.1670	0.4708	6.7276	0.6594
730.00	7.3520	0.5316	7.9386	0.6210
740.00	8.4203	0.6261	5.6976	0.5575
750.00	9.7890	0.5993	8.3873	0.7021
760.00	10.9891	0.6429	9.8023	0.7165
770.00	11.6075	0.6110	11.2143	0.8563
780.00	13.9355	0.7618	10.6766	0.8065
790.00	12.3973	0.7505	8.9879	0.8464
800.00	13.2147	1.0601	7.5082	1.1608
810.00	15.1464	0.8835	8.8749	0.9842
820.00	12.7782	0.9936	10.5792	0.9420
830.00	12.1331	0.8006	10.8030	1.0932
840.00	13.2862	0.8266	11.5103	1.2090
850.00	13.0936	0.9976	8.7018	1.7549
860.00	8.5537	1.6182	9.3835	1.2658
870.00	2.7978	0.5585	12.0703	1.4411
880.00	5.8879	0.7843	12.5795	1.3795
890.00	5.6676	1.9281	7.5083	1.1532
900.00	0.0000	0.0000	7.3301	1.1123
910.00	0.0000	0.0000	4.7458	1.9769
920.00	0.0000	0.0000	5.4618	2.5793
930.00	0.0000	0.0000	3.3969	2.0222
940.00	0.0000	0.0000	0.3653	1.0037

$m_{N\eta}[MeV]$	$W=(1725.0 \pm 25.0) \text{ MeV}$		$W=(1775.0 \pm 25.0) \text{ MeV}$	
	$d\sigma/dM$ [$\mu\text{b}/\text{GeV}$]	Δ_{stat} [$\mu\text{b}/\text{GeV}$]	$d\sigma/dM$ [$\mu\text{b}/\text{GeV}$]	Δ_{stat} [$\mu\text{b}/\text{GeV}$]
1450.00	0.0000	0.0000	0.0000	0.0000
1460.00	0.0000	0.0000	0.0000	0.0000
1470.00	0.7099	0.0934	0.1714	0.9204
1480.00	2.4629	0.4296	2.1193	0.2108
1490.00	2.5564	0.2778	1.7053	0.2095
1500.00	3.4343	0.3499	2.2958	0.2241
1510.00	4.0131	0.4275	3.2977	0.4690
1520.00	4.6153	0.4807	3.6772	0.3438
1530.00	5.8411	0.5145	3.7656	0.3781
1540.00	9.5477	0.7334	5.9953	0.4018
1550.00	9.8730	0.6957	8.8631	0.6021
1560.00	8.4148	0.5731	12.1786	0.6234
1570.00	11.2447	0.9099	14.2238	0.7610
1580.00	5.1256	0.7461	18.7103	0.8163
1590.00	0.5069	0.2949	23.7051	1.0229
1600.00	0.0000	0.0000	18.1604	0.7903
1610.00	0.0000	0.0000	14.4640	0.8639
1620.00	0.0000	0.0000	8.9774	0.6471
1630.00	0.0000	0.0000	4.0225	0.6364
1640.00	0.0000	0.0000	0.8214	0.2406
1650.00	0.0000	0.0000	0.0000	0.0000
1660.00	0.0000	0.0000	0.0000	0.0000
1670.00	0.0000	0.0000	0.0000	0.0000
1680.00	0.0000	0.0000	0.0000	0.0000
1690.00	0.0000	0.0000	0.0000	0.0000
1700.00	0.0000	0.0000	0.0000	0.0000
1710.00	0.0000	0.0000	0.0000	0.0000
1720.00	0.0000	0.0000	0.0000	0.0000
1730.00	0.0000	0.0000	0.0000	0.0000
1740.00	0.0000	0.0000	0.0000	0.0000

$m_{N\eta} [MeV]$	$W=(1825.0 \pm 25.0) \text{ MeV}$		$W=(1875.0 \pm 25.0) \text{ MeV}$	
	$d\sigma/dM$ [$\mu\text{b}/\text{GeV}$]	Δ_{stat} [$\mu\text{b}/\text{GeV}$]	$d\sigma/dM$ [$\mu\text{b}/\text{GeV}$]	Δ_{stat} [$\mu\text{b}/\text{GeV}$]
1450.00	0.0000	0.0000	0.0000	0.0000
1460.00	0.0000	0.0000	0.0000	0.0000
1470.00	0.0755	1.0463	0.1395	0.0574
1480.00	0.7230	0.0950	1.3456	0.1142
1490.00	2.1615	0.1433	1.0372	0.2289
1500.00	1.5266	0.1636	2.3696	0.2848
1510.00	2.3691	0.2704	1.6007	0.3565
1520.00	2.2772	0.2965	1.2462	0.4870
1530.00	2.6787	0.3734	3.4451	0.5190
1540.00	4.0005	0.4080	3.7536	0.5202
1550.00	5.7737	0.4848	5.9839	0.3839
1560.00	6.6195	0.6448	7.8419	0.4495
1570.00	11.5018	0.7195	9.6488	0.7661
1580.00	14.8490	0.8183	12.4221	0.8004
1590.00	20.5166	0.9163	13.3552	0.9559
1600.00	21.4041	1.0347	15.4000	1.5132
1610.00	21.4460	0.9233	21.3472	1.1643
1620.00	21.5049	0.9119	20.5843	1.3389
1630.00	22.1156	0.9579	19.3260	1.1974
1640.00	14.8209	0.8307	16.3998	0.9444
1650.00	9.6314	0.6644	17.3242	0.9635
1660.00	6.2607	0.4935	12.7592	0.9753
1670.00	1.4171	0.2098	11.7783	0.7451
1680.00	1.8097	0.2727	8.9763	0.7651
1690.00	0.0000	0.0000	5.5320	0.7771
1700.00	0.0000	0.0000	4.0931	0.7998
1710.00	0.0000	0.0000	2.1708	0.6120
1720.00	0.0000	0.0000	1.0220	0.2156
1730.00	0.0000	0.0000	0.2758	0.2382
1740.00	0.0000	0.0000	0.0000	0.0000

$m_{N\pi} [MeV]$	$W=(1725.0 \pm 25.0) \text{ MeV}$		$W=(1775.0 \pm 25.0) \text{ MeV}$	
	$d\sigma/dM$ [$\mu\text{b}/\text{GeV}$]	Δ_{stat} [$\mu\text{b}/\text{GeV}$]	$d\sigma/dM$ [$\mu\text{b}/\text{GeV}$]	Δ_{stat} [$\mu\text{b}/\text{GeV}$]
1050.00	0.0000	0.0000	0.0000	0.0000
1060.00	0.0000	0.0000	0.0000	0.0000
1070.00	0.7099	0.0934	0.1714	0.9204
1080.00	2.4629	0.4296	2.1193	0.2108
1090.00	2.5564	0.2778	1.7053	0.2095
1100.00	3.4343	0.3499	2.2958	0.2241
1110.00	4.0131	0.4275	3.2977	0.4690
1120.00	4.6153	0.4807	3.6772	0.3438
1130.00	5.8411	0.5145	3.7656	0.3781
1140.00	9.5477	0.7334	5.9953	0.4018
1150.00	9.8730	0.6957	8.8631	0.6021
1160.00	8.4148	0.5731	12.1786	0.6234
1170.00	11.2447	0.9099	14.2238	0.7610
1180.00	5.1256	0.7461	18.7103	0.8163
1190.00	0.5069	0.2949	23.7051	1.0229
1200.00	0.0000	0.0000	18.1604	0.7903
1210.00	0.0000	0.0000	14.4640	0.8639
1220.00	0.0000	0.0000	8.9774	0.6471
1230.00	0.0000	0.0000	4.0225	0.6364
1240.00	0.0000	0.0000	0.8214	0.2406
1250.00	0.0000	0.0000	0.0000	0.0000
1260.00	0.0000	0.0000	0.0000	0.0000
1270.00	0.0000	0.0000	0.0000	0.0000
1280.00	0.0000	0.0000	0.0000	0.0000
1290.00	0.0000	0.0000	0.0000	0.0000
1300.00	0.0000	0.0000	0.0000	0.0000
1310.00	0.0000	0.0000	0.0000	0.0000
1320.00	0.0000	0.0000	0.0000	0.0000
1330.00	0.0000	0.0000	0.0000	0.0000
1340.00	0.0000	0.0000	0.0000	0.0000

$m_{N\pi} [MeV]$	$W=(1825.0 \pm 25.0) \text{ MeV}$		$W=(1875.0 \pm 25.0) \text{ MeV}$	
	$d\sigma/dM$ [$\mu\text{b}/\text{GeV}$]	Δ_{stat} [$\mu\text{b}/\text{GeV}$]	$d\sigma/dM$ [$\mu\text{b}/\text{GeV}$]	Δ_{stat} [$\mu\text{b}/\text{GeV}$]
1050.00	0.0000	0.0000	0.0000	0.0000
1060.00	0.0000	0.0000	0.0000	0.0000
1070.00	0.0755	1.0463	0.1395	0.0574
1080.00	0.7230	0.0950	1.3456	0.1142
1090.00	2.1615	0.1433	1.0372	0.2289
1100.00	1.5266	0.1636	2.3696	0.2848
1110.00	2.3691	0.2704	1.6007	0.3565
1120.00	2.2772	0.2965	1.2462	0.4870
1130.00	2.6787	0.3734	3.4451	0.5190
1140.00	4.0005	0.4080	3.7536	0.5202
1150.00	5.7737	0.4848	5.9839	0.3839
1160.00	6.6195	0.6448	7.8419	0.4495
1170.00	11.5018	0.7195	9.6488	0.7661
1180.00	14.8490	0.8183	12.4221	0.8004
1190.00	20.5166	0.9163	13.3552	0.9559
1200.00	21.4041	1.0347	15.4000	1.5132
1210.00	21.4460	0.9233	21.3472	1.1643
1220.00	21.5049	0.9119	20.5843	1.3389
1230.00	22.1156	0.9579	19.3260	1.1974
1240.00	14.8209	0.8307	16.3998	0.9444
1250.00	9.6314	0.6644	17.3242	0.9635
1260.00	6.2607	0.4935	12.7592	0.9753
1270.00	1.4171	0.2098	11.7783	0.7451
1280.00	1.8097	0.2727	8.9763	0.7651
1290.00	0.0000	0.0000	5.5320	0.7771
1300.00	0.0000	0.0000	4.0931	0.7998
1310.00	0.0000	0.0000	2.1708	0.6120
1320.00	0.0000	0.0000	1.0220	0.2156
1330.00	0.0000	0.0000	0.2758	0.2382
1340.00	0.0000	0.0000	0.0000	0.0000

$\gamma p(n) \rightarrow \eta\pi^+n(n)$

$m_{\eta\pi} [MeV]$	$W=(1725.0 \pm 25.0) \text{ MeV}$		$W=(1775.0 \pm 25.0) \text{ MeV}$	
	$d\sigma/dM$ [$\mu\text{b}/\text{GeV}$]	Δ_{stat} [$\mu\text{b}/\text{GeV}$]	$d\sigma/dM$ [$\mu\text{b}/\text{GeV}$]	Δ_{stat} [$\mu\text{b}/\text{GeV}$]
650.00	0.0000	0.0000	0.0000	0.0000
660.00	0.0000	0.0000	0.0000	0.0000
670.00	0.0000	0.0000	0.0000	0.0000
680.00	1.3506	0.1713	1.4028	0.1595
690.00	2.8591	0.2254	2.9629	0.1972
700.00	3.4095	0.2500	3.8934	0.2539
710.00	5.3621	0.3152	6.1107	0.3114
720.00	7.5756	0.3523	7.5684	0.3382
730.00	9.5279	0.3965	9.7448	0.3909
740.00	9.9618	0.3895	9.7237	0.4265
750.00	10.4771	0.4330	12.9650	0.4756
760.00	9.8470	0.4049	13.1121	0.5002
770.00	7.3981	0.3734	15.6474	0.5121
780.00	4.3861	0.3324	15.8818	0.5168
790.00	2.5364	0.3770	15.5937	0.5107
800.00	2.1110	0.4846	14.3210	0.5691
810.00	0.0000	0.0000	11.1298	0.5272
820.00	0.0000	0.0000	7.6937	0.4488
830.00	0.0000	0.0000	5.1279	0.5412
840.00	0.0000	0.0000	2.8881	0.3328
850.00	0.0000	0.0000	0.0000	0.0000
860.00	0.0000	0.0000	0.0000	0.0000
870.00	0.0000	0.0000	0.0000	0.0000
880.00	0.0000	0.0000	0.0000	0.0000
890.00	0.0000	0.0000	0.0000	0.0000
900.00	0.0000	0.0000	0.0000	0.0000
910.00	0.0000	0.0000	0.0000	0.0000
920.00	0.0000	0.0000	0.0000	0.0000
930.00	0.0000	0.0000	0.0000	0.0000
940.00	0.0000	0.0000	0.0000	0.0000

$m_{\eta\pi} [MeV]$	$W=(1825.0 \pm 25.0) \text{ MeV}$		$W=(1875.0 \pm 25.0) \text{ MeV}$	
	$d\sigma/dM$ [$\mu\text{b}/\text{GeV}$]	Δ_{stat} [$\mu\text{b}/\text{GeV}$]	$d\sigma/dM$ [$\mu\text{b}/\text{GeV}$]	Δ_{stat} [$\mu\text{b}/\text{GeV}$]
650.00	0.0000	0.0000	0.0000	0.0000
660.00	0.0000	0.0000	0.0000	0.0000
670.00	0.0000	0.0000	0.0000	0.0000
680.00	1.4366	0.1671	1.1378	0.2078
690.00	2.5771	0.2307	2.6266	0.3275
700.00	4.9635	0.2820	4.4575	0.4288
710.00	5.9075	0.3202	6.4859	0.4387
720.00	7.3630	0.3744	6.5649	0.4896
730.00	9.6786	0.3916	7.2973	0.4887
740.00	8.8124	0.4034	8.3057	0.5146
750.00	9.7875	0.4233	8.2167	0.5288
760.00	10.6114	0.4491	8.4199	0.5007
770.00	12.1318	0.4811	10.5245	0.5465
780.00	11.8527	0.4860	10.9380	0.5956
790.00	13.6080	0.5209	7.3603	0.5884
800.00	13.9239	0.5293	13.1046	0.6217
810.00	14.8872	0.6238	10.1350	0.6719
820.00	13.7356	0.6099	12.0459	0.9312
830.00	15.0618	0.5764	11.3481	0.6564
840.00	14.4910	0.5652	12.5513	0.7572
850.00	12.4844	0.5778	11.5535	0.7604
860.00	10.5897	0.5977	12.3510	0.7841
870.00	7.6399	0.7721	11.7400	1.0274
880.00	6.3310	0.6386	10.4266	0.9932
890.00	1.7154	0.3677	13.7279	0.9863
900.00	0.0000	0.0000	9.4686	0.7869
910.00	0.0000	0.0000	6.8158	0.7820
920.00	0.0000	0.0000	4.9935	0.7219
930.00	0.0000	0.0000	3.6058	0.6653
940.00	0.0000	0.0000	0.4309	0.7770

$m_{N\eta}[MeV]$	$W=(1725.0 \pm 25.0) \text{ MeV}$		$W=(1775.0 \pm 25.0) \text{ MeV}$	
	$d\sigma/dM$ [$\mu\text{b}/\text{GeV}$]	Δ_{stat} [$\mu\text{b}/\text{GeV}$]	$d\sigma/dM$ [$\mu\text{b}/\text{GeV}$]	Δ_{stat} [$\mu\text{b}/\text{GeV}$]
1450.00	0.0000	0.0000	0.0000	0.0000
1460.00	0.0000	0.0000	0.0000	0.0000
1470.00	0.0612	0.6349	0.0000	0.0000
1480.00	0.3913	0.1799	0.0628	0.0325
1490.00	0.6293	0.2797	0.5608	0.1831
1500.00	1.4062	0.4628	0.6145	0.2496
1510.00	2.7755	0.4650	0.6551	0.1829
1520.00	3.2225	0.4948	1.4942	0.2693
1530.00	5.6990	0.5474	2.5056	0.3741
1540.00	6.6259	0.6528	3.3033	0.4688
1550.00	6.4329	0.6000	4.9414	0.4661
1560.00	4.5625	0.5215	5.6942	0.5547
1570.00	3.7015	0.5155	7.2698	0.6278
1580.00	1.3647	0.3171	8.4756	0.6348
1590.00	0.4004	0.4269	12.2709	0.8276
1600.00	0.0000	0.0000	11.6199	0.8351
1610.00	0.0000	0.0000	9.4830	0.8642
1620.00	0.0000	0.0000	5.5281	0.7265
1630.00	0.0000	0.0000	1.6172	0.3333
1640.00	0.0000	0.0000	0.8155	0.6507
1650.00	0.0000	0.0000	0.0139	0.2228
1660.00	0.0000	0.0000	0.0000	0.0000
1670.00	0.0000	0.0000	0.0000	0.0000
1680.00	0.0000	0.0000	0.0000	0.0000
1690.00	0.0000	0.0000	0.0000	0.0000
1700.00	0.0000	0.0000	0.0000	0.0000
1710.00	0.0000	0.0000	0.0000	0.0000
1720.00	0.0000	0.0000	0.0000	0.0000
1730.00	0.0000	0.0000	0.0000	0.0000
1740.00	0.0000	0.0000	0.0000	0.0000

$m_{N\eta}[MeV]$	$W=(1825.0 \pm 25.0) \text{ MeV}$		$W=(1875.0 \pm 25.0) \text{ MeV}$	
	$d\sigma/dM$ [$\mu\text{b}/\text{GeV}$]	Δ_{stat} [$\mu\text{b}/\text{GeV}$]	$d\sigma/dM$ [$\mu\text{b}/\text{GeV}$]	Δ_{stat} [$\mu\text{b}/\text{GeV}$]
1450.00	0.0000	0.0000	0.0000	0.0000
1460.00	0.0000	0.0000	0.0000	0.0000
1470.00	0.0000	0.0000	0.0000	0.0000
1480.00	0.0000	0.0000	0.0000	0.0000
1490.00	0.0486	0.0648	0.8504	0.0290
1500.00	0.3223	0.2022	0.3187	0.2269
1510.00	0.1676	0.0928	0.0000	0.0000
1520.00	0.5163	0.1958	0.2473	0.2000
1530.00	0.7902	0.2240	0.9213	0.3618
1540.00	1.2204	0.2359	1.5595	0.3961
1550.00	2.2858	0.3504	1.3793	0.3682
1560.00	2.4901	0.3638	2.8801	0.7980
1570.00	4.0420	0.5882	3.4394	0.0005
1580.00	4.8819	0.5276	4.3371	0.6040
1590.00	6.7008	0.6346	5.9964	0.8207
1600.00	8.3794	0.8267	4.6374	0.7122
1610.00	10.1765	0.8002	7.1665	0.7084
1620.00	10.5268	0.8351	9.6284	1.1344
1630.00	10.9014	0.9557	9.9621	1.1823
1640.00	10.0217	0.9356	7.5802	1.0926
1650.00	6.7324	0.7130	8.2432	1.2434
1660.00	4.6627	0.6974	5.9081	1.0140
1670.00	2.6063	0.5915	6.3153	0.9875
1680.00	1.2940	0.4671	4.4276	0.8532
1690.00	0.2067	0.3047	2.7441	1.1893
1700.00	0.0000	0.0000	3.4210	1.0479
1710.00	0.0000	0.0000	0.7056	0.8650
1720.00	0.0000	0.0000	0.7724	0.5302
1730.00	0.0000	0.0000	2.4663	0.3440
1740.00	0.0000	0.0000	0.1238	1.1245

$m_{N\pi} [MeV]$	$W=(1725.0 \pm 25.0) \text{ MeV}$		$W=(1775.0 \pm 25.0) \text{ MeV}$	
	$d\sigma/dM$ [$\mu\text{b}/\text{GeV}$]	Δ_{stat} [$\mu\text{b}/\text{GeV}$]	$d\sigma/dM$ [$\mu\text{b}/\text{GeV}$]	Δ_{stat} [$\mu\text{b}/\text{GeV}$]
1050.00	0.0000	0.0000	0.0000	0.0000
1060.00	0.0000	0.0000	0.0000	0.0000
1070.00	0.0612	0.6349	0.0000	0.0000
1080.00	0.3913	0.1799	0.0628	0.0325
1090.00	0.6293	0.2797	0.5608	0.1831
1100.00	1.4062	0.4628	0.6145	0.2496
1110.00	2.7755	0.4650	0.6551	0.1829
1120.00	3.2225	0.4948	1.4942	0.2693
1130.00	5.6990	0.5474	2.5056	0.3741
1140.00	6.6259	0.6528	3.3033	0.4688
1150.00	6.4329	0.6000	4.9414	0.4661
1160.00	4.5625	0.5215	5.6942	0.5547
1170.00	3.7015	0.5155	7.2698	0.6278
1180.00	1.3647	0.3171	8.4756	0.6348
1190.00	0.4004	0.4269	12.2709	0.8276
1200.00	0.0000	0.0000	11.6199	0.8351
1210.00	0.0000	0.0000	9.4830	0.8642
1220.00	0.0000	0.0000	5.5281	0.7265
1230.00	0.0000	0.0000	1.6172	0.3333
1240.00	0.0000	0.0000	0.8155	0.6507
1250.00	0.0000	0.0000	0.0139	0.2228
1260.00	0.0000	0.0000	0.0000	0.0000
1270.00	0.0000	0.0000	0.0000	0.0000
1280.00	0.0000	0.0000	0.0000	0.0000
1290.00	0.0000	0.0000	0.0000	0.0000
1300.00	0.0000	0.0000	0.0000	0.0000
1310.00	0.0000	0.0000	0.0000	0.0000
1320.00	0.0000	0.0000	0.0000	0.0000
1330.00	0.0000	0.0000	0.0000	0.0000
1340.00	0.0000	0.0000	0.0000	0.0000

$m_{N\pi} [MeV]$	$W=(1825.0 \pm 25.0) \text{ MeV}$		$W=(1875.0 \pm 25.0) \text{ MeV}$	
	$d\sigma/dM$ [$\mu\text{b}/\text{GeV}$]	Δ_{stat} [$\mu\text{b}/\text{GeV}$]	$d\sigma/dM$ [$\mu\text{b}/\text{GeV}$]	Δ_{stat} [$\mu\text{b}/\text{GeV}$]
1050.00	0.0000	0.0000	0.0000	0.0000
1060.00	0.0000	0.0000	0.0000	0.0000
1070.00	0.0000	0.0000	0.0000	0.0000
1080.00	0.0000	0.0000	0.0000	0.0000
1090.00	0.0486	0.0648	0.8504	0.0290
1100.00	0.3223	0.2022	0.3187	0.2269
1110.00	0.1676	0.0928	0.0000	0.0000
1120.00	0.5163	0.1958	0.2473	0.2000
1130.00	0.7902	0.2240	0.9213	0.3618
1140.00	1.2204	0.2359	1.5595	0.3961
1150.00	2.2858	0.3504	1.3793	0.3682
1160.00	2.4901	0.3638	2.8801	0.7980
1170.00	4.0420	0.5882	3.4394	0.0005
1180.00	4.8819	0.5276	4.3371	0.6040
1190.00	6.7008	0.6346	5.9964	0.8207
1200.00	8.3794	0.8267	4.6374	0.7122
1210.00	10.1765	0.8002	7.1665	0.7084
1220.00	10.5268	0.8351	9.6284	1.1344
1230.00	10.9014	0.9557	9.9621	1.1823
1240.00	10.0217	0.9356	7.5802	1.0926
1250.00	6.7324	0.7130	8.2432	1.2434
1260.00	4.6627	0.6974	5.9081	1.0140
1270.00	2.6063	0.5915	6.3153	0.9875
1280.00	1.2940	0.4671	4.4276	0.8532
1290.00	0.2067	0.3047	2.7441	1.1893
1300.00	0.0000	0.0000	3.4210	1.0479
1310.00	0.0000	0.0000	0.7056	0.8650
1320.00	0.0000	0.0000	0.7724	0.5302
1330.00	0.0000	0.0000	2.4663	0.3440
1340.00	0.0000	0.0000	0.1238	1.1245

$\gamma n(p) \rightarrow \eta\pi^- p(p)$

$m_{\eta\pi} [MeV]$	$W=(1725.0 \pm 25.0) \text{ MeV}$		$W=(1775.0 \pm 25.0) \text{ MeV}$	
	$d\sigma/dM$ [$\mu\text{b}/\text{GeV}$]	Δ_{stat} [$\mu\text{b}/\text{GeV}$]	$d\sigma/dM$ [$\mu\text{b}/\text{GeV}$]	Δ_{stat} [$\mu\text{b}/\text{GeV}$]
650.00	0.0000	0.0000	0.0000	0.0000
660.00	0.0000	0.0000	0.0000	0.0000
670.00	0.0000	0.0000	0.0000	0.0000
680.00	0.2105	0.1689	0.6050	0.1653
690.00	2.4043	0.2655	2.3582	0.2337
700.00	3.3366	0.3235	2.9679	0.2789
710.00	5.2633	0.4862	3.9246	2.7575
720.00	6.6487	0.5195	7.0640	0.4561
730.00	8.3792	0.6016	10.0147	0.5667
740.00	10.5579	0.7023	10.5596	0.6432
750.00	11.2591	0.9650	13.7625	0.7342
760.00	7.4470	0.7700	10.7633	0.7201
770.00	6.4615	0.6132	14.9725	1.0389
780.00	3.7932	0.7646	14.4990	0.7901
790.00	0.0000	0.0000	14.9734	0.9196
800.00	2.4644	1.3646	13.3199	0.8662
810.00	0.0000	0.0000	14.1858	0.9672
820.00	0.0000	0.0000	6.7180	0.7356
830.00	0.0000	0.0000	6.0325	0.9742
840.00	0.0000	0.0000	1.3417	1.1959
850.00	0.0000	0.0000	0.0508	0.0000
860.00	0.0000	0.0000	0.0000	0.0000
870.00	0.0000	0.0000	0.0000	0.0000
880.00	0.0000	0.0000	0.0000	0.0000
890.00	0.0000	0.0000	0.0000	0.0000
900.00	0.0000	0.0000	0.0000	0.0000
910.00	0.0000	0.0000	0.0000	0.0000
920.00	0.0000	0.0000	0.0000	0.0000
930.00	0.0000	0.0000	0.0000	0.0000
940.00	0.0000	0.0000	0.0000	0.0000

$m_{\eta\pi} [MeV]$	$W=(1825.0 \pm 25.0) \text{ MeV}$		$W=(1875.0 \pm 25.0) \text{ MeV}$	
	$d\sigma/dM$ [$\mu\text{b}/\text{GeV}$]	Δ_{stat} [$\mu\text{b}/\text{GeV}$]	$d\sigma/dM$ [$\mu\text{b}/\text{GeV}$]	Δ_{stat} [$\mu\text{b}/\text{GeV}$]
650.00	0.0000	0.0000	0.0000	0.0000
660.00	0.0000	0.0000	0.0000	0.0000
670.00	0.0000	0.0000	0.0000	0.0000
680.00	0.6808	0.1718	1.4232	0.3843
690.00	2.2770	0.2713	2.4512	0.3983
700.00	5.0511	0.3671	5.1909	0.5800
710.00	4.6940	0.3891	3.6391	0.5916
720.00	5.1670	0.4708	6.7276	0.6594
730.00	7.3520	0.5316	7.9386	0.6210
740.00	8.4203	0.6261	5.6976	0.5575
750.00	9.7890	0.5993	8.3873	0.7021
760.00	10.9891	0.6429	9.8023	0.7165
770.00	11.6075	0.6110	11.2143	0.8563
780.00	13.9355	0.7618	10.6766	0.8065
790.00	12.3973	0.7505	8.9879	0.8464
800.00	13.2147	1.0601	7.5082	1.1608
810.00	15.1464	0.8835	8.8749	0.9842
820.00	12.7782	0.9936	10.5792	0.9420
830.00	12.1331	0.8006	10.8030	1.0932
840.00	13.2862	0.8266	11.5103	1.2090
850.00	13.0936	0.9976	8.7018	1.7549
860.00	8.5537	1.6182	9.3835	1.2658
870.00	2.7978	0.5585	12.0703	1.4411
880.00	5.8879	0.7843	12.5795	1.3795
890.00	5.6676	1.9281	7.5083	1.1532
900.00	0.0000	0.0000	7.3301	1.1123
910.00	0.0000	0.0000	4.7458	1.9769
920.00	0.0000	0.0000	5.4618	2.5793
930.00	0.0000	0.0000	3.3969	2.0222
940.00	0.0000	0.0000	0.3653	1.0037

$m_{N\eta}[MeV]$	$W=(1725.0 \pm 25.0) \text{ MeV}$		$W=(1775.0 \pm 25.0) \text{ MeV}$	
	$d\sigma/dM$ [$\mu\text{b}/\text{GeV}$]	Δ_{stat} [$\mu\text{b}/\text{GeV}$]	$d\sigma/dM$ [$\mu\text{b}/\text{GeV}$]	Δ_{stat} [$\mu\text{b}/\text{GeV}$]
1450.00	0.0000	0.0000	0.0000	0.0000
1460.00	0.0000	0.0000	0.0000	0.0000
1470.00	0.0473	0.1240	0.0000	0.0000
1480.00	0.2680	0.1210	0.4132	0.0568
1490.00	1.0979	0.1752	0.4070	0.0930
1500.00	1.5928	0.2167	0.4954	0.1294
1510.00	2.9344	0.2324	0.9465	0.1377
1520.00	4.0906	0.2668	1.5041	0.1575
1530.00	5.2586	0.3000	2.6334	0.1997
1540.00	6.3509	0.3072	3.3855	0.2479
1550.00	7.0319	0.3221	4.6573	0.2991
1560.00	5.6734	0.2821	6.3955	0.3085
1570.00	4.5525	0.2516	8.1063	0.3481
1580.00	2.4725	0.2343	10.1765	0.3904
1590.00	0.5244	0.1366	11.5953	0.4123
1600.00	0.0666	0.0425	11.2776	0.4109
1610.00	0.0000	0.0000	7.6929	0.3619
1620.00	0.0000	0.0000	4.9763	0.3305
1630.00	0.0000	0.0000	2.6561	0.2714
1640.00	0.0000	0.0000	0.4610	0.1400
1650.00	0.0000	0.0000	0.2236	0.2862
1660.00	0.0000	0.0000	0.0000	0.0000
1670.00	0.0000	0.0000	0.0000	0.0000
1680.00	0.0000	0.0000	0.0000	0.0000
1690.00	0.0000	0.0000	0.0000	0.0000
1700.00	0.0000	0.0000	0.0000	0.0000
1710.00	0.0000	0.0000	0.0000	0.0000
1720.00	0.0000	0.0000	0.0000	0.0000
1730.00	0.0000	0.0000	0.0000	0.0000
1740.00	0.0000	0.0000	0.0000	0.0000

$m_{N\eta}[MeV]$	$W=(1825.0 \pm 25.0) \text{ MeV}$		$W=(1875.0 \pm 25.0) \text{ MeV}$	
	$d\sigma/dM$ [$\mu\text{b}/\text{GeV}$]	Δ_{stat} [$\mu\text{b}/\text{GeV}$]	$d\sigma/dM$ [$\mu\text{b}/\text{GeV}$]	Δ_{stat} [$\mu\text{b}/\text{GeV}$]
1450.00	0.0000	0.0000	0.0000	0.0000
1460.00	0.0000	0.0000	0.0000	0.0000
1470.00	0.0000	0.0000	0.0000	0.0000
1480.00	0.0000	0.0000	0.0000	0.0000
1490.00	0.1240	0.0503	0.1761	0.1276
1500.00	0.4310	0.1235	0.3572	0.1892
1510.00	0.5139	0.1153	0.8992	0.2708
1520.00	1.1403	0.1612	0.7457	0.2114
1530.00	1.2670	0.1685	1.2405	0.2796
1540.00	1.9235	0.2104	0.9895	0.2340
1550.00	2.9166	0.2350	2.2163	0.3896
1560.00	3.9025	0.2745	2.3687	0.3537
1570.00	5.0119	0.3045	2.0254	0.3243
1580.00	7.2509	0.3751	4.4883	0.4717
1590.00	7.2543	0.3946	6.4242	0.5332
1600.00	8.6309	0.4332	6.4140	0.5717
1610.00	11.3661	0.5011	7.4379	0.7143
1620.00	10.1699	0.5297	8.4457	0.7296
1630.00	10.7092	0.5095	9.8340	0.7405
1640.00	8.7132	0.4693	8.7186	0.6934
1650.00	7.0191	0.4263	9.2647	0.8184
1660.00	4.9935	0.4039	7.5359	0.7299
1670.00	2.4722	0.3106	5.5123	0.6152
1680.00	0.8626	0.2320	4.1677	0.6353
1690.00	0.1308	0.1352	2.8817	0.5002
1700.00	0.0000	0.0000	2.0789	0.4496
1710.00	0.0000	0.0000	1.6682	0.4684
1720.00	0.0000	0.0000	1.3456	0.6547
1730.00	0.0000	0.0000	0.4661	0.6763
1740.00	0.0000	0.0000	0.7622	1.7170

$m_{N\pi}[MeV]$	$W=(1725.0 \pm 25.0) \text{ MeV}$		$W=(1775.0 \pm 25.0) \text{ MeV}$	
	$d\sigma/dM$ [$\mu\text{b}/\text{GeV}$]	Δ_{stat} [$\mu\text{b}/\text{GeV}$]	$d\sigma/dM$ [$\mu\text{b}/\text{GeV}$]	Δ_{stat} [$\mu\text{b}/\text{GeV}$]
1050.00	0.0000	0.0000	0.0000	0.0000
1060.00	0.0000	0.0000	0.0000	0.0000
1070.00	0.0473	0.1240	0.0000	0.0000
1080.00	0.2680	0.1210	0.4132	0.0568
1090.00	1.0979	0.1752	0.4070	0.0930
1100.00	1.5928	0.2167	0.4954	0.1294
1110.00	2.9344	0.2324	0.9465	0.1377
1120.00	4.0906	0.2668	1.5041	0.1575
1130.00	5.2586	0.3000	2.6334	0.1997
1140.00	6.3509	0.3072	3.3855	0.2479
1150.00	7.0319	0.3221	4.6573	0.2991
1160.00	5.6734	0.2821	6.3955	0.3085
1170.00	4.5525	0.2516	8.1063	0.3481
1180.00	2.4725	0.2343	10.1765	0.3904
1190.00	0.5244	0.1366	11.5953	0.4123
1200.00	0.0666	0.0425	11.2776	0.4109
1210.00	0.0000	0.0000	7.6929	0.3619
1220.00	0.0000	0.0000	4.9763	0.3305
1230.00	0.0000	0.0000	2.6561	0.2714
1240.00	0.0000	0.0000	0.4610	0.1400
1250.00	0.0000	0.0000	0.2236	0.2862
1260.00	0.0000	0.0000	0.0000	0.0000
1270.00	0.0000	0.0000	0.0000	0.0000
1280.00	0.0000	0.0000	0.0000	0.0000
1290.00	0.0000	0.0000	0.0000	0.0000
1300.00	0.0000	0.0000	0.0000	0.0000
1310.00	0.0000	0.0000	0.0000	0.0000
1320.00	0.0000	0.0000	0.0000	0.0000
1330.00	0.0000	0.0000	0.0000	0.0000
1340.00	0.0000	0.0000	0.0000	0.0000

$m_{N\pi} [MeV]$	$W=(1825.0 \pm 25.0) \text{ MeV}$		$W=(1875.0 \pm 25.0) \text{ MeV}$	
	$d\sigma/dM$ [$\mu\text{b}/\text{GeV}$]	Δ_{stat} [$\mu\text{b}/\text{GeV}$]	$d\sigma/dM$ [$\mu\text{b}/\text{GeV}$]	Δ_{stat} [$\mu\text{b}/\text{GeV}$]
1050.00	0.0000	0.0000	0.0000	0.0000
1060.00	0.0000	0.0000	0.0000	0.0000
1070.00	0.0000	0.0000	0.0000	0.0000
1080.00	0.0000	0.0000	0.0000	0.0000
1090.00	0.1240	0.0503	0.1761	0.1276
1100.00	0.4310	0.1235	0.3572	0.1892
1110.00	0.5139	0.1153	0.8992	0.2708
1120.00	1.1403	0.1612	0.7457	0.2114
1130.00	1.2670	0.1685	1.2405	0.2796
1140.00	1.9235	0.2104	0.9895	0.2340
1150.00	2.9166	0.2350	2.2163	0.3896
1160.00	3.9025	0.2745	2.3687	0.3537
1170.00	5.0119	0.3045	2.0254	0.3243
1180.00	7.2509	0.3751	4.4883	0.4717
1190.00	7.2543	0.3946	6.4242	0.5332
1200.00	8.6309	0.4332	6.4140	0.5717
1210.00	11.3661	0.5011	7.4379	0.7143
1220.00	10.1699	0.5297	8.4457	0.7296
1230.00	10.7092	0.5095	9.8340	0.7405
1240.00	8.7132	0.4693	8.7186	0.6934
1250.00	7.0191	0.4263	9.2647	0.8184
1260.00	4.9935	0.4039	7.5359	0.7299
1270.00	2.4722	0.3106	5.5123	0.6152
1280.00	0.8626	0.2320	4.1677	0.6353
1290.00	0.1308	0.1352	2.8817	0.5002
1300.00	0.0000	0.0000	2.0789	0.4496
1310.00	0.0000	0.0000	1.6682	0.4684
1320.00	0.0000	0.0000	1.3456	0.6547
1330.00	0.0000	0.0000	0.4661	0.6763
1340.00	0.0000	0.0000	0.7622	1.7170

$\gamma p \rightarrow \eta\pi^0 p$

$m_{\eta\pi} [MeV]$	$W = (1725.0 \pm 25.0) \text{ MeV}$		$W = (1775.0 \pm 25.0) \text{ MeV}$	
	$d\sigma/dM$ [$\mu\text{b}/\text{GeV}$]	Δ_{stat} [$\mu\text{b}/\text{GeV}$]	$d\sigma/dM$ [$\mu\text{b}/\text{GeV}$]	Δ_{stat} [$\mu\text{b}/\text{GeV}$]
650.00	0.0000	0.0000	0.0000	0.0000
660.00	0.0000	0.0000	0.0000	0.0000
670.00	0.0000	0.0000	0.0000	0.0000
680.00	1.7119	0.0672	1.5624	0.0684
690.00	3.5072	0.1007	3.6902	0.1087
700.00	5.0147	0.1231	5.5464	0.1319
710.00	6.8204	0.1453	7.4894	0.1498
720.00	8.6126	0.1599	10.2748	0.1721
730.00	10.4381	0.1690	12.3007	0.1873
740.00	11.5473	0.1703	14.8960	0.2067
750.00	12.2671	0.1732	15.8082	0.2181
760.00	11.5843	0.1687	18.1111	0.2315
770.00	9.4364	0.1497	18.7648	0.2350
780.00	6.3050	0.1258	19.7098	0.2343
790.00	3.3848	0.0978	19.5422	0.2240
800.00	0.8494	0.0721	18.3672	0.2159
810.00	0.0000	0.0000	15.8586	0.2031
820.00	0.0000	0.0000	11.3460	0.1720
830.00	0.0000	0.0000	6.8038	0.1379
840.00	0.0000	0.0000	3.5331	0.1065
850.00	0.0000	0.0000	0.8452	0.0788
860.00	0.0000	0.0000	0.0000	0.0000
870.00	0.0000	0.0000	0.0000	0.0000
880.00	0.0000	0.0000	0.0000	0.0000
890.00	0.0000	0.0000	0.0000	0.0000
900.00	0.0000	0.0000	0.0000	0.0000
910.00	0.0000	0.0000	0.0000	0.0000
920.00	0.0000	0.0000	0.0000	0.0000
930.00	0.0000	0.0000	0.0000	0.0000
940.00	0.0000	0.0000	0.0000	0.0000

$m_{\eta\pi} [MeV]$	$W=(1825.0 \pm 25.0) \text{ MeV}$		$W=(1875.0 \pm 25.0) \text{ MeV}$	
	$d\sigma/dM$ [$\mu\text{b}/\text{GeV}$]	Δ_{stat} [$\mu\text{b}/\text{GeV}$]	$d\sigma/dM$ [$\mu\text{b}/\text{GeV}$]	Δ_{stat} [$\mu\text{b}/\text{GeV}$]
650.00	0.0000	0.0000	0.5247	0.0895
660.00	0.0000	0.0000	0.0000	0.0000
670.00	0.0000	0.0000	0.0000	0.0000
680.00	1.7403	0.0813	3.2064	0.1698
690.00	4.5366	0.1336	7.8602	0.2533
700.00	6.4751	0.1551	10.7178	0.2902
710.00	8.8401	0.1815	12.6519	0.3119
720.00	11.2672	0.1971	14.0739	0.3160
730.00	13.2714	0.2129	16.1980	0.3265
740.00	14.2503	0.2142	17.0382	0.3267
750.00	15.4941	0.2213	18.4549	0.3345
760.00	16.2791	0.2245	18.6819	0.3334
770.00	17.3545	0.2293	20.0747	0.3386
780.00	18.1237	0.2374	19.9774	0.3293
790.00	19.0254	0.2475	21.7210	0.3465
800.00	19.8819	0.2577	22.0105	0.3474
810.00	19.7279	0.2581	22.7910	0.3564
820.00	20.7303	0.2626	22.9114	0.3634
830.00	20.2800	0.2509	23.9187	0.3729
840.00	19.2601	0.2379	23.9166	0.3790
850.00	17.7712	0.2254	24.0829	0.3839
860.00	14.2139	0.2105	24.1392	0.3854
870.00	10.5344	0.1799	23.1452	0.3675
880.00	6.4504	0.1461	23.5329	0.3615
890.00	3.5839	0.1163	21.3492	0.3352
900.00	1.2834	0.1383	19.8599	0.3279
910.00	0.0000	0.0000	15.5416	0.3072
920.00	0.0000	0.0000	11.3344	0.2767
930.00	0.0000	0.0000	6.7701	0.2386
940.00	0.0000	0.0000	3.2125	0.1824

$m_{N\eta} [MeV]$	$W=(1725.0 \pm 25.0) \text{ MeV}$		$W=(1775.0 \pm 25.0) \text{ MeV}$	
	$d\sigma/dM$ [$\mu\text{b}/\text{GeV}$]	Δ_{stat} [$\mu\text{b}/\text{GeV}$]	$d\sigma/dM$ [$\mu\text{b}/\text{GeV}$]	Δ_{stat} [$\mu\text{b}/\text{GeV}$]
1450.00	0.0163	0.0015	0.0205	0.0018
1460.00	0.0233	0.0017	0.0196	0.0018
1470.00	0.0994	0.0069	0.0169	0.0014
1480.00	0.8255	0.0329	0.2244	0.0134
1490.00	1.8244	0.0611	0.7864	0.0352
1500.00	3.2419	0.0875	1.4289	0.0552
1510.00	4.9284	0.1108	2.4399	0.0787
1520.00	7.2197	0.1404	3.6581	0.0955
1530.00	9.7745	0.1673	5.2935	0.1199
1540.00	12.3492	0.1936	8.0541	0.1491
1550.00	13.8886	0.2049	10.4678	0.1708
1560.00	13.2857	0.1923	14.3357	0.2031
1570.00	10.5592	0.1699	19.0704	0.2357
1580.00	7.0602	0.1303	23.9596	0.2695
1590.00	2.4437	0.0625	28.8875	0.2992
1600.00	0.0821	0.0029	29.4295	0.3063
1610.00	0.0389	0.0024	24.4926	0.2668
1620.00	0.0150	0.0016	16.4276	0.2081
1630.00	0.0000	0.0000	8.8723	0.1427
1640.00	0.0000	0.0000	3.1549	0.0720
1650.00	0.0000	0.0000	0.3949	0.0160
1660.00	0.0000	0.0000	0.0606	0.0031
1670.00	0.0000	0.0000	0.0272	0.0023
1680.00	0.0000	0.0000	0.0165	0.0018
1690.00	0.0000	0.0000	0.0000	0.0000
1700.00	0.0000	0.0000	0.0000	0.0000
1710.00	0.0000	0.0000	0.0000	0.0000
1720.00	0.0000	0.0000	0.0000	0.0000
1730.00	0.0000	0.0000	0.0000	0.0000
1740.00	0.0000	0.0000	0.0000	0.0000

$m_{N\eta} [MeV]$	$W=(1825.0 \pm 25.0) \text{ MeV}$		$W=(1875.0 \pm 25.0) \text{ MeV}$	
	$d\sigma/dM$ [$\mu\text{b}/\text{GeV}$]	Δ_{stat} [$\mu\text{b}/\text{GeV}$]	$d\sigma/dM$ [$\mu\text{b}/\text{GeV}$]	Δ_{stat} [$\mu\text{b}/\text{GeV}$]
1450.00	0.0000	0.0000	0.0000	0.0000
1460.00	0.0359	0.0026	0.0447	0.0038
1470.00	0.0248	0.0021	0.0242	0.0029
1480.00	0.0393	0.0037	0.0174	0.0022
1490.00	0.3268	0.0201	0.1779	0.0137
1500.00	0.8409	0.0436	0.7473	0.0424
1510.00	1.5615	0.0630	1.4255	0.0732
1520.00	2.4877	0.0854	2.0297	0.0959
1530.00	3.3166	0.1015	3.5232	0.1277
1540.00	4.9189	0.1234	4.9988	0.1567
1550.00	7.0473	0.1502	7.0548	0.1961
1560.00	9.5042	0.1764	9.8845	0.2304
1570.00	13.3498	0.2126	13.5051	0.2758
1580.00	17.3986	0.2440	18.4270	0.3268
1590.00	22.4701	0.2794	23.7505	0.3818
1600.00	27.6210	0.3118	30.5480	0.4380
1610.00	31.9892	0.3329	36.8394	0.4863
1620.00	32.6900	0.3336	40.6387	0.5150
1630.00	32.3008	0.3240	43.2258	0.5311
1640.00	28.9448	0.3046	42.0654	0.5116
1650.00	23.2106	0.2680	37.8475	0.4737
1660.00	16.5104	0.2200	34.3250	0.4449
1670.00	10.1866	0.1636	29.9466	0.4107
1680.00	5.5416	0.1137	24.6940	0.3769
1690.00	2.3103	0.0655	20.7476	0.3465
1700.00	0.6764	0.0264	16.3677	0.3217
1710.00	0.0276	0.0020	12.1124	0.2868
1720.00	0.0283	0.0023	7.6394	0.2270
1730.00	0.0121	0.0016	4.5767	0.1774
1740.00	0.0000	0.0000	2.4308	0.1361

$m_{N\pi}[MeV]$	$W=(1725.0 \pm 25.0) \text{ MeV}$		$W=(1775.0 \pm 25.0) \text{ MeV}$	
	$d\sigma/dM$ [$\mu\text{b}/\text{GeV}$]	Δ_{stat} [$\mu\text{b}/\text{GeV}$]	$d\sigma/dM$ [$\mu\text{b}/\text{GeV}$]	Δ_{stat} [$\mu\text{b}/\text{GeV}$]
1050.00	0.0163	0.0015	0.0205	0.0018
1060.00	0.0233	0.0017	0.0196	0.0018
1070.00	0.0994	0.0069	0.0169	0.0014
1080.00	0.8255	0.0329	0.2244	0.0134
1090.00	1.8244	0.0611	0.7864	0.0352
1100.00	3.2419	0.0875	1.4289	0.0552
1110.00	4.9284	0.1108	2.4399	0.0787
1120.00	7.2197	0.1404	3.6581	0.0955
1130.00	9.7745	0.1673	5.2935	0.1199
1140.00	12.3492	0.1936	8.0541	0.1491
1150.00	13.8886	0.2049	10.4678	0.1708
1160.00	13.2857	0.1923	14.3357	0.2031
1170.00	10.5592	0.1699	19.0704	0.2357
1180.00	7.0602	0.1303	23.9596	0.2695
1190.00	2.4437	0.0625	28.8875	0.2992
1200.00	0.0821	0.0029	29.4295	0.3063
1210.00	0.0389	0.0024	24.4926	0.2668
1220.00	0.0150	0.0016	16.4276	0.2081
1230.00	0.0000	0.0000	8.8723	0.1427
1240.00	0.0000	0.0000	3.1549	0.0720
1250.00	0.0000	0.0000	0.3949	0.0160
1260.00	0.0000	0.0000	0.0606	0.0031
1270.00	0.0000	0.0000	0.0272	0.0023
1280.00	0.0000	0.0000	0.0165	0.0018
1290.00	0.0000	0.0000	0.0000	0.0000
1300.00	0.0000	0.0000	0.0000	0.0000
1310.00	0.0000	0.0000	0.0000	0.0000
1320.00	0.0000	0.0000	0.0000	0.0000
1330.00	0.0000	0.0000	0.0000	0.0000
1340.00	0.0000	0.0000	0.0000	0.0000

$m_{N\pi} [MeV]$	$W=(1825.0 \pm 25.0) \text{ MeV}$		$W=(1875.0 \pm 25.0) \text{ MeV}$	
	$d\sigma/dM$ [$\mu\text{b}/\text{GeV}$]	Δ_{stat} [$\mu\text{b}/\text{GeV}$]	$d\sigma/dM$ [$\mu\text{b}/\text{GeV}$]	Δ_{stat} [$\mu\text{b}/\text{GeV}$]
1050.00	0.0000	0.0000	0.0000	0.0000
1060.00	0.0359	0.0026	0.0447	0.0038
1070.00	0.0248	0.0021	0.0242	0.0029
1080.00	0.0393	0.0037	0.0174	0.0022
1090.00	0.3268	0.0201	0.1779	0.0137
1100.00	0.8409	0.0436	0.7473	0.0424
1110.00	1.5615	0.0630	1.4255	0.0732
1120.00	2.4877	0.0854	2.0297	0.0959
1130.00	3.3166	0.1015	3.5232	0.1277
1140.00	4.9189	0.1234	4.9988	0.1567
1150.00	7.0473	0.1502	7.0548	0.1961
1160.00	9.5042	0.1764	9.8845	0.2304
1170.00	13.3498	0.2126	13.5051	0.2758
1180.00	17.3986	0.2440	18.4270	0.3268
1190.00	22.4701	0.2794	23.7505	0.3818
1200.00	27.6210	0.3118	30.5480	0.4380
1210.00	31.9892	0.3329	36.8394	0.4863
1220.00	32.6900	0.3336	40.6387	0.5150
1230.00	32.3008	0.3240	43.2258	0.5311
1240.00	28.9448	0.3046	42.0654	0.5116
1250.00	23.2106	0.2680	37.8475	0.4737
1260.00	16.5104	0.2200	34.3250	0.4449
1270.00	10.1866	0.1636	29.9466	0.4107
1280.00	5.5416	0.1137	24.6940	0.3769
1290.00	2.3103	0.0655	20.7476	0.3465
1300.00	0.6764	0.0264	16.3677	0.3217
1310.00	0.0276	0.0020	12.1124	0.2868
1320.00	0.0283	0.0023	7.6394	0.2270
1330.00	0.0121	0.0016	4.5767	0.1774
1340.00	0.0000	0.0000	2.4308	0.1361

$\gamma p \rightarrow \eta\pi^+n$

$m_{\eta\pi} [MeV]$	$W=(1725.0 \pm 25.0) \text{ MeV}$		$W=(1775.0 \pm 25.0) \text{ MeV}$	
	$d\sigma/dM$ [$\mu\text{b}/\text{GeV}$]	Δ_{stat} [$\mu\text{b}/\text{GeV}$]	$d\sigma/dM$ [$\mu\text{b}/\text{GeV}$]	Δ_{stat} [$\mu\text{b}/\text{GeV}$]
650.00	0.0000	0.0000	0.0000	0.0000
660.00	0.0000	0.0000	0.0000	0.0000
670.00	0.0000	0.0000	0.0000	0.0000
680.00	1.7119	0.0672	1.5624	0.0684
690.00	3.5072	0.1007	3.6902	0.1087
700.00	5.0147	0.1231	5.5464	0.1319
710.00	6.8204	0.1453	7.4894	0.1498
720.00	8.6126	0.1599	10.2748	0.1721
730.00	10.4381	0.1690	12.3007	0.1873
740.00	11.5473	0.1703	14.8960	0.2067
750.00	12.2671	0.1732	15.8082	0.2181
760.00	11.5843	0.1687	18.1111	0.2315
770.00	9.4364	0.1497	18.7648	0.2350
780.00	6.3050	0.1258	19.7098	0.2343
790.00	3.3848	0.0978	19.5422	0.2240
800.00	0.8494	0.0721	18.3672	0.2159
810.00	0.0000	0.0000	15.8586	0.2031
820.00	0.0000	0.0000	11.3460	0.1720
830.00	0.0000	0.0000	6.8038	0.1379
840.00	0.0000	0.0000	3.5331	0.1065
850.00	0.0000	0.0000	0.8452	0.0788
860.00	0.0000	0.0000	0.0000	0.0000
870.00	0.0000	0.0000	0.0000	0.0000
880.00	0.0000	0.0000	0.0000	0.0000
890.00	0.0000	0.0000	0.0000	0.0000
900.00	0.0000	0.0000	0.0000	0.0000
910.00	0.0000	0.0000	0.0000	0.0000
920.00	0.0000	0.0000	0.0000	0.0000
930.00	0.0000	0.0000	0.0000	0.0000
940.00	0.0000	0.0000	0.0000	0.0000

$m_{\eta\pi} [MeV]$	$W=(1825.0 \pm 25.0) \text{ MeV}$		$W=(1875.0 \pm 25.0) \text{ MeV}$	
	$d\sigma/dM$ [$\mu\text{b}/\text{GeV}$]	Δ_{stat} [$\mu\text{b}/\text{GeV}$]	$d\sigma/dM$ [$\mu\text{b}/\text{GeV}$]	Δ_{stat} [$\mu\text{b}/\text{GeV}$]
650.00	0.0000	0.0000	0.5247	0.0895
660.00	0.0000	0.0000	0.0000	0.0000
670.00	0.0000	0.0000	0.0000	0.0000
680.00	1.7403	0.0813	3.2064	0.1698
690.00	4.5366	0.1336	7.8602	0.2533
700.00	6.4751	0.1551	10.7178	0.2902
710.00	8.8401	0.1815	12.6519	0.3119
720.00	11.2672	0.1971	14.0739	0.3160
730.00	13.2714	0.2129	16.1980	0.3265
740.00	14.2503	0.2142	17.0382	0.3267
750.00	15.4941	0.2213	18.4549	0.3345
760.00	16.2791	0.2245	18.6819	0.3334
770.00	17.3545	0.2293	20.0747	0.3386
780.00	18.1237	0.2374	19.9774	0.3293
790.00	19.0254	0.2475	21.7210	0.3465
800.00	19.8819	0.2577	22.0105	0.3474
810.00	19.7279	0.2581	22.7910	0.3564
820.00	20.7303	0.2626	22.9114	0.3634
830.00	20.2800	0.2509	23.9187	0.3729
840.00	19.2601	0.2379	23.9166	0.3790
850.00	17.7712	0.2254	24.0829	0.3839
860.00	14.2139	0.2105	24.1392	0.3854
870.00	10.5344	0.1799	23.1452	0.3675
880.00	6.4504	0.1461	23.5329	0.3615
890.00	3.5839	0.1163	21.3492	0.3352
900.00	1.2834	0.1383	19.8599	0.3279
910.00	0.0000	0.0000	15.5416	0.3072
920.00	0.0000	0.0000	11.3344	0.2767
930.00	0.0000	0.0000	6.7701	0.2386
940.00	0.0000	0.0000	3.2125	0.1824

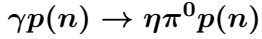
$m_{N\eta}[MeV]$	$W=(1725.0 \pm 25.0) \text{ MeV}$		$W=(1775.0 \pm 25.0) \text{ MeV}$	
	$d\sigma/dM$ [$\mu\text{b}/\text{GeV}$]	Δ_{stat} [$\mu\text{b}/\text{GeV}$]	$d\sigma/dM$ [$\mu\text{b}/\text{GeV}$]	Δ_{stat} [$\mu\text{b}/\text{GeV}$]
1450.00	0.0000	0.0000	0.0000	0.0000
1460.00	0.0000	0.0000	0.0000	0.0000
1470.00	0.0000	0.0000	0.0000	0.0000
1480.00	0.3800	0.3468	0.0784	0.5196
1490.00	1.0831	0.2009	0.5338	0.1375
1500.00	1.3627	0.1994	0.5597	0.0877
1510.00	2.3698	0.2742	0.9032	0.1649
1520.00	2.1273	0.3049	1.4990	0.1755
1530.00	4.2952	0.3700	2.7639	0.2456
1540.00	4.9683	0.3917	4.0319	0.3312
1550.00	5.4217	0.3723	5.1348	0.3614
1560.00	5.0830	0.3101	7.0639	0.4309
1570.00	3.4675	0.2159	8.7953	0.4951
1580.00	1.9769	0.1260	11.0455	0.5547
1590.00	0.7271	0.0480	12.3731	0.5895
1600.00	0.0208	0.0013	13.2671	0.5610
1610.00	0.0185	0.0013	9.5048	0.4021
1620.00	0.0177	0.0013	6.3066	0.2569
1630.00	0.0127	0.0011	3.5681	0.1382
1640.00	0.0000	0.0000	1.1540	0.0496
1650.00	0.0000	0.0000	0.1357	0.0073
1660.00	0.0000	0.0000	0.0602	0.0024
1670.00	0.0000	0.0000	0.0509	0.0023
1680.00	0.0000	0.0000	0.0399	0.0020
1690.00	0.0000	0.0000	0.0308	0.0018
1700.00	0.0000	0.0000	0.0225	0.0015
1710.00	0.0000	0.0000	0.0119	0.0011
1720.00	0.0000	0.0000	0.0000	0.0000
1730.00	0.0000	0.0000	0.0000	0.0000
1740.00	0.0000	0.0000	0.0000	0.0000

$m_{N\eta}[MeV]$	$W=(1825.0 \pm 25.0) \text{ MeV}$		$W=(1875.0 \pm 25.0) \text{ MeV}$	
	$d\sigma/dM$ [$\mu\text{b}/\text{GeV}$]	Δ_{stat} [$\mu\text{b}/\text{GeV}$]	$d\sigma/dM$ [$\mu\text{b}/\text{GeV}$]	Δ_{stat} [$\mu\text{b}/\text{GeV}$]
1450.00	0.0000	0.0000	0.0342	0.0020
1460.00	0.0584	0.0027	0.3720	0.0082
1470.00	0.0000	0.0000	0.0000	0.0000
1480.00	0.0000	0.0000	0.0000	0.0000
1490.00	0.4056	0.3296	0.1812	0.3275
1500.00	0.8250	0.6321	0.4445	0.1654
1510.00	0.7758	0.1657	1.0569	0.2509
1520.00	0.7775	0.1116	1.3779	0.3862
1530.00	1.0482	0.1630	2.2619	0.2938
1540.00	1.8628	0.1925	3.8532	1.9026
1550.00	3.1751	0.2760	2.4693	0.3491
1560.00	4.1485	0.3307	5.2055	0.6061
1570.00	6.0060	0.4041	7.0310	0.6211
1580.00	7.6270	0.5418	9.0821	0.7363
1590.00	11.9811	0.6346	10.0538	0.8039
1600.00	12.9417	0.6540	12.7143	0.9461
1610.00	15.5821	0.6999	16.7731	1.0644
1620.00	15.9759	0.6837	15.1509	0.7317
1630.00	15.0466	0.6002	17.0087	0.7791
1640.00	13.2783	0.5150	17.8412	0.9678
1650.00	11.0570	0.4050	16.4863	0.8317
1660.00	7.4031	0.2687	15.4843	0.7187
1670.00	4.4048	0.1576	12.0403	0.5583
1680.00	2.3226	0.0840	9.4042	0.4354
1690.00	1.0040	0.0366	7.6547	0.3446
1700.00	0.2726	0.0112	6.3561	0.2740
1710.00	0.0444	0.0022	4.7334	0.2067
1720.00	0.0697	0.0029	3.0222	0.1313
1730.00	0.0578	0.0026	1.7242	0.0754
1740.00	0.0472	0.0024	0.8657	0.0382

$m_{N\pi} [MeV]$	$W=(1725.0 \pm 25.0) \text{ MeV}$		$W=(1775.0 \pm 25.0) \text{ MeV}$	
	$d\sigma/dM$ [$\mu\text{b}/\text{GeV}$]	Δ_{stat} [$\mu\text{b}/\text{GeV}$]	$d\sigma/dM$ [$\mu\text{b}/\text{GeV}$]	Δ_{stat} [$\mu\text{b}/\text{GeV}$]
1050.00	0.0000	0.0000	0.0000	0.0000
1060.00	0.0000	0.0000	0.0000	0.0000
1070.00	0.0000	0.0000	0.0000	0.0000
1080.00	0.3800	0.3468	0.0784	0.5196
1090.00	1.0831	0.2009	0.5338	0.1375
1100.00	1.3627	0.1994	0.5597	0.0877
1110.00	2.3698	0.2742	0.9032	0.1649
1120.00	2.1273	0.3049	1.4990	0.1755
1130.00	4.2952	0.3700	2.7639	0.2456
1140.00	4.9683	0.3917	4.0319	0.3312
1150.00	5.4217	0.3723	5.1348	0.3614
1160.00	5.0830	0.3101	7.0639	0.4309
1170.00	3.4675	0.2159	8.7953	0.4951
1180.00	1.9769	0.1260	11.0455	0.5547
1190.00	0.7271	0.0480	12.3731	0.5895
1200.00	0.0208	0.0013	13.2671	0.5610
1210.00	0.0185	0.0013	9.5048	0.4021
1220.00	0.0177	0.0013	6.3066	0.2569
1230.00	0.0127	0.0011	3.5681	0.1382
1240.00	0.0000	0.0000	1.1540	0.0496
1250.00	0.0000	0.0000	0.1357	0.0073
1260.00	0.0000	0.0000	0.0602	0.0024
1270.00	0.0000	0.0000	0.0509	0.0023
1280.00	0.0000	0.0000	0.0399	0.0020
1290.00	0.0000	0.0000	0.0308	0.0018
1300.00	0.0000	0.0000	0.0225	0.0015
1310.00	0.0000	0.0000	0.0119	0.0011
1320.00	0.0000	0.0000	0.0000	0.0000
1330.00	0.0000	0.0000	0.0000	0.0000
1340.00	0.0000	0.0000	0.0000	0.0000

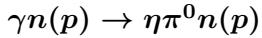
$m_{N\pi} [MeV]$	$W=(1825.0 \pm 25.0) \text{ MeV}$		$W=(1875.0 \pm 25.0) \text{ MeV}$	
	$d\sigma/dM$ [$\mu\text{b}/\text{GeV}$]	Δ_{stat} [$\mu\text{b}/\text{GeV}$]	$d\sigma/dM$ [$\mu\text{b}/\text{GeV}$]	Δ_{stat} [$\mu\text{b}/\text{GeV}$]
1050.00	0.0000	0.0000	0.0342	0.0020
1060.00	0.0584	0.0027	0.3720	0.0082
1070.00	0.0000	0.0000	0.0000	0.0000
1080.00	0.0000	0.0000	0.0000	0.0000
1090.00	0.4056	0.3296	0.1812	0.3275
1100.00	0.8250	0.6321	0.4445	0.1654
1110.00	0.7758	0.1657	1.0569	0.2509
1120.00	0.7775	0.1116	1.3779	0.3862
1130.00	1.0482	0.1630	2.2619	0.2938
1140.00	1.8628	0.1925	3.8532	1.9026
1150.00	3.1751	0.2760	2.4693	0.3491
1160.00	4.1485	0.3307	5.2055	0.6061
1170.00	6.0060	0.4041	7.0310	0.6211
1180.00	7.6270	0.5418	9.0821	0.7363
1190.00	11.9811	0.6346	10.0538	0.8039
1200.00	12.9417	0.6540	12.7143	0.9461
1210.00	15.5821	0.6999	16.7731	1.0644
1220.00	15.9759	0.6837	15.1509	0.7317
1230.00	15.0466	0.6002	17.0087	0.7791
1240.00	13.2783	0.5150	17.8412	0.9678
1250.00	11.0570	0.4050	16.4863	0.8317
1260.00	7.4031	0.2687	15.4843	0.7187
1270.00	4.4048	0.1576	12.0403	0.5583
1280.00	2.3226	0.0840	9.4042	0.4354
1290.00	1.0040	0.0366	7.6547	0.3446
1300.00	0.2726	0.0112	6.3561	0.2740
1310.00	0.0444	0.0022	4.7334	0.2067
1320.00	0.0697	0.0029	3.0222	0.1313
1330.00	0.0578	0.0026	1.7242	0.0754
1340.00	0.0472	0.0024	0.8657	0.0382

B.0.4. Angular Distributions of the η in the CM System



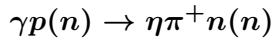
$\cos(\theta_\eta^*)$	$W=(1725.0 \pm 25.0) \text{ MeV}$		$W=(1775.0 \pm 25.0) \text{ MeV}$	
	$d\sigma/d\Omega$	Δ_{stat}	$d\sigma/d\Omega$	Δ_{stat}
	[$\mu\text{b}/\text{sr}$]	[$\mu\text{b}/\text{sr}$]	[$\mu\text{b}/\text{sr}$]	[$\mu\text{b}/\text{sr}$]
-0.90	0.0704	0.0027	0.1405	0.0037
-0.70	0.0681	0.0027	0.1410	0.0043
-0.50	0.0625	0.0026	0.1326	0.0042
-0.30	0.0703	0.0028	0.1342	0.0039
-0.10	0.0691	0.0028	0.1324	0.0039
0.10	0.0648	0.0027	0.1398	0.0040
0.30	0.0708	0.0029	0.1343	0.0040
0.50	0.0674	0.0029	0.1429	0.0037
0.70	0.0670	0.0030	0.1489	0.0038
0.90	0.0667	0.0029	0.1515	0.0040

$\cos(\theta_\eta^*)$	$W=(1825.0 \pm 25.0) \text{ MeV}$		$W=(1875.0 \pm 25.0) \text{ MeV}$	
	$d\sigma/d\Omega$	Δ_{stat}	$d\sigma/d\Omega$	Δ_{stat}
	[$\mu\text{b}/\text{sr}$]	[$\mu\text{b}/\text{sr}$]	[$\mu\text{b}/\text{sr}$]	[$\mu\text{b}/\text{sr}$]
-0.90	0.2015	0.0051	0.2373	0.0083
-0.70	0.1816	0.0075	0.1994	0.0084
-0.50	0.1784	0.0053	0.1736	0.0068
-0.30	0.1697	0.0046	0.1802	0.0064
-0.10	0.1642	0.0046	0.1765	0.0054
0.10	0.1806	0.0051	0.1856	0.0060
0.30	0.1847	0.0048	0.2149	0.0069
0.50	0.1983	0.0050	0.2600	0.0076
0.70	0.2108	0.0053	0.2812	0.0078
0.90	0.2208	0.0058	0.3042	0.0081



$\cos(\theta_\eta^*)$	$W=(1725.0 \pm 25.0) \text{ MeV}$		$W=(1775.0 \pm 25.0) \text{ MeV}$	
	$d\sigma/d\Omega$	Δ_{stat}	$d\sigma/d\Omega$	Δ_{stat}
	[$\mu\text{b}/\text{sr}$]	[$\mu\text{b}/\text{sr}$]	[$\mu\text{b}/\text{sr}$]	[$\mu\text{b}/\text{sr}$]
-0.90	0.0759	0.0044	0.1600	0.0054
-0.70	0.0737	0.0039	0.1486	0.0059
-0.50	0.0601	0.0037	0.1440	0.0048
-0.30	0.0671	0.0040	0.1434	0.0048
-0.10	0.0637	0.0041	0.1446	0.0053
0.10	0.0702	0.0044	0.1298	0.0051
0.30	0.0664	0.0043	0.1318	0.0051
0.50	0.0594	0.0041	0.1423	0.0055
0.70	0.0651	0.0047	0.1367	0.0060
0.90	0.0529	0.0043	0.1430	0.0064

$\cos(\theta_\eta^*)$	$W=(1825.0 \pm 25.0) \text{ MeV}$		$W=(1875.0 \pm 25.0) \text{ MeV}$	
	$d\sigma/d\Omega$	Δ_{stat}	$d\sigma/d\Omega$	Δ_{stat}
	[$\mu\text{b}/\text{sr}$]	[$\mu\text{b}/\text{sr}$]	[$\mu\text{b}/\text{sr}$]	[$\mu\text{b}/\text{sr}$]
-0.90	0.2178	0.0076	0.2370	0.0064
-0.70	0.1970	0.0070	0.2075	0.0070
-0.50	0.1872	0.0060	0.1852	0.0089
-0.30	0.1803	0.0047	0.1696	0.0080
-0.10	0.1840	0.0057	0.1709	0.0066
0.10	0.1813	0.0066	0.1996	0.0086
0.30	0.1870	0.0065	0.2158	0.0095
0.50	0.2015	0.0068	0.2496	0.0093
0.70	0.1979	0.0065	0.2714	0.0099
0.90	0.2151	0.0075	0.2757	0.0116



$\cos(\theta_\eta^*)$	$W=(1725.0 \pm 25.0) \text{ MeV}$		$W=(1775.0 \pm 25.0) \text{ MeV}$	
	$d\sigma/d\Omega$	Δ_{stat}	$d\sigma/d\Omega$	Δ_{stat}
	[$\mu\text{b}/\text{sr}$]	[$\mu\text{b}/\text{sr}$]	[$\mu\text{b}/\text{sr}$]	[$\mu\text{b}/\text{sr}$]
-0.90	0.0341	0.0029	0.0895	0.0062
-0.70	0.0354	0.0046	0.0809	0.0080
-0.50	0.0331	0.0037	0.0795	0.0053
-0.30	0.0390	0.0035	0.0635	0.0045
-0.10	0.0416	0.0039	0.0731	0.0051
0.10	0.0371	0.0041	0.0672	0.0049
0.30	0.0420	0.0039	0.0672	0.0050
0.50	0.0313	0.0066	0.0609	0.0049
0.70	0.0395	0.0045	0.0750	0.0058
0.90	0.0312	0.0065	0.0715	0.0063

$\cos(\theta_\eta^*)$	$W=(1825.0 \pm 25.0) \text{ MeV}$		$W=(1875.0 \pm 25.0) \text{ MeV}$	
	$d\sigma/d\Omega$	Δ_{stat}	$d\sigma/d\Omega$	Δ_{stat}
	[$\mu\text{b}/\text{sr}$]	[$\mu\text{b}/\text{sr}$]	[$\mu\text{b}/\text{sr}$]	[$\mu\text{b}/\text{sr}$]
-0.90	0.0952	0.0056	0.1186	0.0101
-0.70	0.1011	0.0088	0.0933	0.0106
-0.50	0.0977	0.0064	0.0776	0.0090
-0.30	0.0948	0.0071	0.0846	0.0082
-0.10	0.0884	0.0065	0.0829	0.0086
0.10	0.0910	0.0061	0.1006	0.0087
0.30	0.0826	0.0063	0.1316	0.0101
0.50	0.0898	0.0070	0.1356	0.0100
0.70	0.1025	0.0071	0.1649	0.0128
0.90	0.1122	0.0097	0.1689	0.0122

$\gamma n(p) \rightarrow \eta\pi^- p(p)$

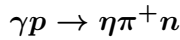
$\cos(\theta_\eta^*)$	$W=(1725.0 \pm 25.0) \text{ MeV}$		$W=(1775.0 \pm 25.0) \text{ MeV}$	
	$d\sigma/d\Omega$	Δ_{stat}	$d\sigma/d\Omega$	Δ_{stat}
	[$\mu\text{b}/\text{sr}$]	[$\mu\text{b}/\text{sr}$]	[$\mu\text{b}/\text{sr}$]	[$\mu\text{b}/\text{sr}$]
-0.90	0.0374	0.0017	0.0714	0.0023
-0.70	0.0331	0.0016	0.0773	0.0025
-0.50	0.0413	0.0022	0.0731	0.0027
-0.30	0.0429	0.0020	0.0713	0.0025
-0.10	0.0486	0.0025	0.0704	0.0027
0.10	0.0438	0.0024	0.0657	0.0025
0.30	0.0298	0.0018	0.0670	0.0026
0.50	0.0327	0.0024	0.0737	0.0029
0.70	0.0261	0.0018	0.0657	0.0027
0.90	0.0272	0.0019	0.0685	0.0029

$\cos(\theta_\eta^*)$	$W=(1825.0 \pm 25.0) \text{ MeV}$		$W=(1875.0 \pm 25.0) \text{ MeV}$	
	$d\sigma/d\Omega$	Δ_{stat}	$d\sigma/d\Omega$	Δ_{stat}
	[$\mu\text{b}/\text{sr}$]	[$\mu\text{b}/\text{sr}$]	[$\mu\text{b}/\text{sr}$]	[$\mu\text{b}/\text{sr}$]
-0.90	0.0879	0.0031	0.1130	0.0061
-0.70	0.0840	0.0033	0.0774	0.0056
-0.50	0.0817	0.0033	0.0676	0.0050
-0.30	0.0876	0.0034	0.0803	0.0052
-0.10	0.0914	0.0034	0.0889	0.0052
0.10	0.0892	0.0033	0.0963	0.0054
0.30	0.0866	0.0034	0.1254	0.0059
0.50	0.0994	0.0037	0.1395	0.0065
0.70	0.0994	0.0038	0.1528	0.0067
0.90	0.0962	0.0038	0.1544	0.0063

$\gamma p \rightarrow \eta\pi^0 p$

$\cos(\theta_\eta^*)$	$W=(1725.0 \pm 25.0) \text{ MeV}$		$W=(1775.0 \pm 25.0) \text{ MeV}$	
	$d\sigma/d\Omega$	Δ_{stat}	$d\sigma/d\Omega$	Δ_{stat}
	[$\mu\text{b}/\text{sr}$]	[$\mu\text{b}/\text{sr}$]	[$\mu\text{b}/\text{sr}$]	[$\mu\text{b}/\text{sr}$]
-0.90	0.0704	0.0011	0.1569	0.0017
-0.70	0.0711	0.0011	0.1530	0.0017
-0.50	0.0686	0.0011	0.1442	0.0017
-0.30	0.0709	0.0012	0.1424	0.0017
-0.10	0.0681	0.0012	0.1413	0.0017
0.10	0.0663	0.0012	0.1367	0.0016
0.30	0.0688	0.0012	0.1439	0.0017
0.50	0.0709	0.0012	0.1447	0.0017
0.70	0.0656	0.0012	0.1435	0.0018
0.90	0.0542	0.0011	0.1440	0.0019

$\cos(\theta_\eta^*)$	$W=(1825.0 \pm 25.0) \text{ MeV}$		$W=(1875.0 \pm 25.0) \text{ MeV}$	
	$d\sigma/d\Omega$	Δ_{stat}	$d\sigma/d\Omega$	Δ_{stat}
	[$\mu\text{b}/\text{sr}$]	[$\mu\text{b}/\text{sr}$]	[$\mu\text{b}/\text{sr}$]	[$\mu\text{b}/\text{sr}$]
-0.90	0.2212	0.0022	0.2574	0.0029
-0.70	0.2086	0.0022	0.2328	0.0028
-0.50	0.1957	0.0021	0.2178	0.0042
-0.30	0.1903	0.0020	0.2124	0.0040
-0.10	0.1873	0.0031	0.2066	0.0025
0.10	0.1897	0.0020	0.2234	0.0026
0.30	0.2009	0.0021	0.2526	0.0028
0.50	0.2160	0.0043	0.2828	0.0047
0.70	0.2287	0.0041	0.3235	0.0047
0.90	0.2366	0.0038	0.3379	0.0021



$\cos(\theta_\eta^*)$	$W=(1725.0 \pm 25.0) \text{ MeV}$		$W=(1775.0 \pm 25.0) \text{ MeV}$	
	$d\sigma/d\Omega$	Δ_{stat}	$d\sigma/d\Omega$	Δ_{stat}
	[$\mu\text{b}/\text{sr}$]	[$\mu\text{b}/\text{sr}$]	[$\mu\text{b}/\text{sr}$]	[$\mu\text{b}/\text{sr}$]
-0.90	0.0344	0.0018	0.0800	0.0022
-0.70	0.0315	0.0018	0.0844	0.0023
-0.50	0.0314	0.0016	0.0884	0.0022
-0.30	0.0334	0.0020	0.0772	0.0022
-0.10	0.0301	0.0020	0.0688	0.0024
0.10	0.0345	0.0020	0.0702	0.0021
0.30	0.0292	0.0019	0.0707	0.0025
0.50	0.0286	0.0020	0.0728	0.0022
0.70	0.0271	0.0019	0.0772	0.0023
0.90	0.0257	0.0019	0.0731	0.0021

$\cos(\theta_\eta^*)$	$W=(1825.0 \pm 25.0) \text{ MeV}$		$W=(1875.0 \pm 25.0) \text{ MeV}$	
	$d\sigma/d\Omega$	Δ_{stat}	$d\sigma/d\Omega$	Δ_{stat}
	[$\mu\text{b}/\text{sr}$]	[$\mu\text{b}/\text{sr}$]	[$\mu\text{b}/\text{sr}$]	[$\mu\text{b}/\text{sr}$]
-0.90	0.1236	0.0031	0.1388	0.0042
-0.70	0.1288	0.0035	0.1275	0.0037
-0.50	0.1123	0.0032	0.1144	0.0039
-0.30	0.1059	0.0030	0.1076	0.0037
-0.10	0.1031	0.0029	0.1097	0.0022
0.10	0.1085	0.0031	0.1214	0.0032
0.30	0.1095	0.0032	0.1375	0.0041
0.50	0.1193	0.0034	0.1595	0.0046
0.70	0.1223	0.0032	0.1689	0.0050
0.90	0.1156	0.0033	0.1765	0.0053

B.0.5. Angular Distributions of the π in the Helicity System

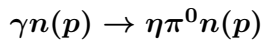
$\gamma p(n) \rightarrow \eta\pi^0 p(n)$

ϕ_π	$W=(1725.0 \pm 25.0) \text{ MeV}$		$W=(1775.0 \pm 25.0) \text{ MeV}$	
	$d\sigma/d\Omega$ [$\mu\text{b}/\text{sr}$]	Δ_{stat} [$\mu\text{b}/\text{sr}$]	$d\sigma/d\Omega$ [$\mu\text{b}/\text{sr}$]	Δ_{stat} [$\mu\text{b}/\text{sr}$]
0.00	0.0375	0.0014	0.0721	0.0016
0.20	0.0405	0.0016	0.0926	0.0024
0.40	0.0513	0.0019	0.1022	0.0027
0.60	0.0496	0.0022	0.1005	0.0030
0.80	0.0462	0.0023	0.0927	0.0034
1.00	0.0418	0.0022	0.0950	0.0032
1.20	0.0496	0.0021	0.1105	0.0025
1.40	0.0482	0.0019	0.1038	0.0027
1.60	0.0408	0.0017	0.0901	0.0025
1.80	0.0364	0.0014	0.0776	0.0023

ϕ_π	$W=(1825.0 \pm 25.0) \text{ MeV}$		$W=(1875.0 \pm 25.0) \text{ MeV}$	
	$d\sigma/d\Omega$ [$\mu\text{b}/\text{sr}$]	Δ_{stat} [$\mu\text{b}/\text{sr}$]	$d\sigma/d\Omega$ [$\mu\text{b}/\text{sr}$]	Δ_{stat} [$\mu\text{b}/\text{sr}$]
0.00	0.1043	0.0023	0.1298	0.0045
0.20	0.1276	0.0027	0.1378	0.0027
0.40	0.1485	0.0031	0.1569	0.0057
0.60	0.1202	0.0032	0.1466	0.0047
0.80	0.1225	0.0039	0.1178	0.0054
1.00	0.1097	0.0036	0.1244	0.0053
1.20	0.1363	0.0037	0.1380	0.0054
1.40	0.1314	0.0033	0.1509	0.0046
1.60	0.1253	0.0025	0.1429	0.0033
1.80	0.1014	0.0030	0.1420	0.0031

$\cos(\theta_\pi)$	$W=(1725.0 \pm 25.0) \text{ MeV}$		$W=(1775.0 \pm 25.0) \text{ MeV}$	
	$d\sigma/d\Omega$ [$\mu\text{b}/\text{sr}$]	Δ_{stat} [$\mu\text{b}/\text{sr}$]	$d\sigma/d\Omega$ [$\mu\text{b}/\text{sr}$]	Δ_{stat} [$\mu\text{b}/\text{sr}$]
-0.90	0.0591	0.0019	0.1222	0.0037
-0.70	0.0613	0.0027	0.1255	0.0037
-0.50	0.0611	0.0026	0.1202	0.0036
-0.30	0.0651	0.0028	0.1279	0.0039
-0.10	0.0629	0.0027	0.1296	0.0040
0.10	0.0670	0.0030	0.1299	0.0046
0.30	0.0617	0.0029	0.1325	0.0044
0.50	0.0623	0.0032	0.1370	0.0046
0.70	0.0570	0.0032	0.1287	0.0062
0.90	0.0560	0.0032	0.1336	0.0051

$\cos(\theta_\pi)$	$W=(1825.0 \pm 25.0) \text{ MeV}$		$W=(1875.0 \pm 25.0) \text{ MeV}$	
	$d\sigma/d\Omega$ [$\mu\text{b}/\text{sr}$]	Δ_{stat} [$\mu\text{b}/\text{sr}$]	$d\sigma/d\Omega$ [$\mu\text{b}/\text{sr}$]	Δ_{stat} [$\mu\text{b}/\text{sr}$]
-0.90	0.1657	0.0044	0.1850	0.0061
-0.70	0.1595	0.0042	0.1934	0.0062
-0.50	0.1597	0.0047	0.1782	0.0066
-0.30	0.1725	0.0047	0.1866	0.0073
-0.10	0.1805	0.0052	0.1976	0.0070
0.10	0.1857	0.0054	0.1983	0.0078
0.30	0.1684	0.0054	0.1979	0.0088
0.50	0.1722	0.0057	0.2018	0.0083
0.70	0.1819	0.0060	0.2081	0.0096
0.90	0.1763	0.0067	0.2216	0.0096



ϕ_π	$W=(1725.0 \pm 25.0) \text{ MeV}$		$W=(1775.0 \pm 25.0) \text{ MeV}$	
	$d\sigma/d\Omega$ [$\mu\text{b}/\text{sr}$]	Δ_{stat} [$\mu\text{b}/\text{sr}$]	$d\sigma/d\Omega$ [$\mu\text{b}/\text{sr}$]	Δ_{stat} [$\mu\text{b}/\text{sr}$]
0.00	0.0409	0.0024	0.0873	0.0032
0.20	0.0444	0.0026	0.0966	0.0033
0.40	0.0416	0.0023	0.0935	0.0033
0.60	0.0427	0.0025	0.0885	0.0036
0.80	0.0407	0.0027	0.0736	0.0034
1.00	0.0402	0.0028	0.0809	0.0036
1.20	0.0415	0.0021	0.0890	0.0034
1.40	0.0391	0.0023	0.0887	0.0032
1.60	0.0392	0.0023	0.0916	0.0032
1.80	0.0391	0.0025	0.0874	0.0033

ϕ_π	$W=(1825.0 \pm 25.0) \text{ MeV}$		$W=(1875.0 \pm 25.0) \text{ MeV}$	
	$d\sigma/d\Omega$ [$\mu\text{b}/\text{sr}$]	Δ_{stat} [$\mu\text{b}/\text{sr}$]	$d\sigma/d\Omega$ [$\mu\text{b}/\text{sr}$]	Δ_{stat} [$\mu\text{b}/\text{sr}$]
0.00	0.1126	0.0032	0.1402	0.0049
0.20	0.1374	0.0031	0.1462	0.0054
0.40	0.1394	0.0046	0.1539	0.0054
0.60	0.1182	0.0035	0.1407	0.0052
0.80	0.1079	0.0042	0.1142	0.0053
1.00	0.1099	0.0042	0.1162	0.0054
1.20	0.1141	0.0040	0.1330	0.0055
1.40	0.1243	0.0042	0.1512	0.0048
1.60	0.1367	0.0039	0.1493	0.0050
1.80	0.1140	0.0034	0.1416	0.0041

$\cos(\theta_\pi)$	$W=(1725.0 \pm 25.0) \text{ MeV}$		$W=(1775.0 \pm 25.0) \text{ MeV}$	
	$d\sigma/d\Omega$ [$\mu\text{b}/\text{sr}$]	Δ_{stat} [$\mu\text{b}/\text{sr}$]	$d\sigma/d\Omega$ [$\mu\text{b}/\text{sr}$]	Δ_{stat} [$\mu\text{b}/\text{sr}$]
-0.90	0.0588	0.0041	0.1303	0.0051
-0.70	0.0461	0.0046	0.1089	0.0048
-0.50	0.0544	0.0043	0.1156	0.0056
-0.30	0.0670	0.0051	0.1320	0.0058
-0.10	0.0655	0.0043	0.1242	0.0057
0.10	0.0492	0.0044	0.1445	0.0054
0.30	0.0447	0.0041	0.1263	0.0067
0.50	0.0484	0.0054	0.1022	0.0055
0.70	0.0701	0.0054	0.1271	0.0085
0.90	0.0560	0.0065	0.1133	0.0084

$\cos(\theta_\pi)$	$W=(1825.0 \pm 25.0) \text{ MeV}$		$W=(1875.0 \pm 25.0) \text{ MeV}$	
	$d\sigma/d\Omega$ [$\mu\text{b}/\text{sr}$]	Δ_{stat} [$\mu\text{b}/\text{sr}$]	$d\sigma/d\Omega$ [$\mu\text{b}/\text{sr}$]	Δ_{stat} [$\mu\text{b}/\text{sr}$]
-0.90	0.1737	0.0058	0.0897	0.0052
-0.70	0.1641	0.0058	0.1710	0.0087
-0.50	0.1651	0.0064	0.2072	0.0092
-0.30	0.1697	0.0065	0.2021	0.0099
-0.10	0.2009	0.0063	0.1742	0.0096
0.10	0.1623	0.0070	0.2050	0.0116
0.30	0.1643	0.0085	0.1583	0.0095
0.50	0.1722	0.0077	0.1798	0.0127
0.70	0.1456	0.0083	0.2267	0.0150
0.90	0.1765	0.0076	0.1757	0.0133

$\gamma p(n) \rightarrow \eta\pi^+n(n)$

ϕ_π	$W=(1725.0 \pm 25.0) \text{ MeV}$		$W=(1775.0 \pm 25.0) \text{ MeV}$	
	$d\sigma/d\Omega$ [$\mu\text{b}/\text{sr}$]	Δ_{stat} [$\mu\text{b}/\text{sr}$]	$d\sigma/d\Omega$ [$\mu\text{b}/\text{sr}$]	Δ_{stat} [$\mu\text{b}/\text{sr}$]
0.00	0.0401	0.0044	0.0678	0.0049
0.20	0.0352	0.0033	0.0718	0.0039
0.40	0.0338	0.0030	0.0602	0.0040
0.60	0.0279	0.0033	0.0570	0.0048
0.80	0.0278	0.0047	0.0633	0.0067
1.00	0.0254	0.0053	0.0627	0.0064
1.20	0.0332	0.0040	0.0563	0.0051
1.40	0.0403	0.0031	0.0722	0.0044
1.60	0.0413	0.0032	0.0722	0.0041
1.80	0.0287	0.0050	0.0815	0.0057

ϕ_π	$W=(1825.0 \pm 25.0) \text{ MeV}$		$W=(1875.0 \pm 25.0) \text{ MeV}$	
	$d\sigma/d\Omega$ [$\mu\text{b}/\text{sr}$]	Δ_{stat} [$\mu\text{b}/\text{sr}$]	$d\sigma/d\Omega$ [$\mu\text{b}/\text{sr}$]	Δ_{stat} [$\mu\text{b}/\text{sr}$]
0.00	0.0918	0.0053	0.1217	0.0081
0.20	0.0963	0.0046	0.1089	0.0073
0.40	0.0831	0.0059	0.1030	0.0089
0.60	0.0744	0.0079	0.0912	0.0123
0.80	0.0839	0.0117	0.1149	0.0179
1.00	0.0906	0.0132	0.1297	0.0110
1.20	0.0757	0.0074	0.0810	0.0105
1.40	0.0746	0.0054	0.1062	0.0089
1.60	0.0843	0.0048	0.1032	0.0073
1.80	0.0994	0.0062	0.1316	0.0084

$\cos(\theta_\pi)$	$W=(1725.0 \pm 25.0) \text{ MeV}$		$W=(1775.0 \pm 25.0) \text{ MeV}$	
	$d\sigma/d\Omega$ [$\mu\text{b}/\text{sr}$]	Δ_{stat} [$\mu\text{b}/\text{sr}$]	$d\sigma/d\Omega$ [$\mu\text{b}/\text{sr}$]	Δ_{stat} [$\mu\text{b}/\text{sr}$]
-0.90	0.0382	0.0034	0.0698	0.0044
-0.70	0.0331	0.0033	0.0596	0.0039
-0.50	0.0315	0.0033	0.0592	0.0043
-0.30	0.0348	0.0052	0.0649	0.0046
-0.10	0.0291	0.0035	0.0661	0.0047
0.10	0.0330	0.0040	0.0708	0.0050
0.30	0.0287	0.0041	0.0673	0.0051
0.50	0.0353	0.0043	0.0775	0.0054
0.70	0.0401	0.0049	0.0704	0.0051
0.90	0.0416	0.0049	0.0650	0.0069

$\cos(\theta_\pi)$	$W=(1825.0 \pm 25.0) \text{ MeV}$		$W=(1875.0 \pm 25.0) \text{ MeV}$	
	$d\sigma/d\Omega$ [$\mu\text{b}/\text{sr}$]	Δ_{stat} [$\mu\text{b}/\text{sr}$]	$d\sigma/d\Omega$ [$\mu\text{b}/\text{sr}$]	Δ_{stat} [$\mu\text{b}/\text{sr}$]
-0.90	0.0873	0.0049	0.1047	0.0069
-0.70	0.0800	0.0048	0.0968	0.0078
-0.50	0.0885	0.0056	0.1259	0.0090
-0.30	0.0877	0.0060	0.1115	0.0094
-0.10	0.0877	0.0060	0.1257	0.0113
0.10	0.0917	0.0065	0.1143	0.0092
0.30	0.0786	0.0074	0.1319	0.0099
0.50	0.0866	0.0061	0.1064	0.0115
0.70	0.0788	0.0055	0.1248	0.0132
0.90	0.0817	0.0065	0.0974	0.0116

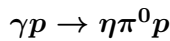
$\gamma n(p) \rightarrow \eta\pi^- p(p)$

ϕ_π	$W=(1725.0 \pm 25.0) \text{ MeV}$		$W=(1775.0 \pm 25.0) \text{ MeV}$	
	$d\sigma/d\Omega$ [$\mu\text{b}/\text{sr}$]	Δ_{stat} [$\mu\text{b}/\text{sr}$]	$d\sigma/d\Omega$ [$\mu\text{b}/\text{sr}$]	Δ_{stat} [$\mu\text{b}/\text{sr}$]
0.00	0.0476	0.0055	0.0775	0.0051
0.20	0.0522	0.0034	0.0788	0.0037
0.40	0.0478	0.0028	0.0768	0.0035
0.60	0.0548	0.0038	0.0863	0.0045
0.80	0.0505	0.0051	0.0972	0.0062
1.00	0.0460	0.0055	0.0768	0.0053
1.20	0.0394	0.0035	0.0905	0.0040
1.40	0.0433	0.0029	0.0783	0.0035
1.60	0.0383	0.0032	0.0774	0.0038
1.80	0.0464	0.0051	0.0685	0.0050

ϕ_π	$W=(1825.0 \pm 25.0) \text{ MeV}$		$W=(1875.0 \pm 25.0) \text{ MeV}$	
	$d\sigma/d\Omega$ [$\mu\text{b}/\text{sr}$]	Δ_{stat} [$\mu\text{b}/\text{sr}$]	$d\sigma/d\Omega$ [$\mu\text{b}/\text{sr}$]	Δ_{stat} [$\mu\text{b}/\text{sr}$]
0.00	0.0905	0.0057	0.1182	0.0102
0.20	0.1039	0.0044	0.1214	0.0107
0.40	0.0925	0.0042	0.1142	0.0068
0.60	0.0899	0.0058	0.1190	0.0120
0.80	0.1097	0.0087	0.1512	0.0218
1.00	0.1019	0.0072	0.1136	0.0185
1.20	0.0997	0.0061	0.1095	0.0103
1.40	0.0911	0.0041	0.1143	0.0104
1.60	0.0982	0.0043	0.1124	0.0063
1.80	0.0977	0.0057	0.1117	0.0075

$\cos(\theta_\pi)$	$W=(1725.0 \pm 25.0) \text{ MeV}$		$W=(1775.0 \pm 25.0) \text{ MeV}$	
	$d\sigma/d\Omega$ [$\mu\text{b}/\text{sr}$]	Δ_{stat} [$\mu\text{b}/\text{sr}$]	$d\sigma/d\Omega$ [$\mu\text{b}/\text{sr}$]	Δ_{stat} [$\mu\text{b}/\text{sr}$]
-0.90	0.0286	0.0022	0.0537	0.0026
-0.70	0.0266	0.0019	0.0645	0.0029
-0.50	0.0316	0.0024	0.0658	0.0031
-0.30	0.0326	0.0021	0.0708	0.0032
-0.10	0.0360	0.0023	0.0698	0.0029
0.10	0.0444	0.0023	0.0763	0.0031
0.30	0.0416	0.0025	0.0757	0.0032
0.50	0.0464	0.0023	0.0801	0.0030
0.70	0.0531	0.0023	0.0900	0.0030
0.90	0.0496	0.0026	0.0981	0.0028

$\cos(\theta_\pi)$	$W=(1825.0 \pm 25.0) \text{ MeV}$		$W=(1875.0 \pm 25.0) \text{ MeV}$	
	$d\sigma/d\Omega$ [$\mu\text{b}/\text{sr}$]	Δ_{stat} [$\mu\text{b}/\text{sr}$]	$d\sigma/d\Omega$ [$\mu\text{b}/\text{sr}$]	Δ_{stat} [$\mu\text{b}/\text{sr}$]
-0.90	0.0790	0.0033	0.0817	0.0057
-0.70	0.0795	0.0038	0.1020	0.0058
-0.50	0.0819	0.0034	0.1019	0.0058
-0.30	0.0902	0.0035	0.1019	0.0054
-0.10	0.0852	0.0037	0.1016	0.0053
0.10	0.0893	0.0041	0.1057	0.0056
0.30	0.0979	0.0039	0.1047	0.0077
0.50	0.1073	0.0036	0.1200	0.0064
0.70	0.1082	0.0035	0.1304	0.0069
0.90	0.1091	0.0040	0.1416	0.0085



ϕ_π	$W=(1725.0 \pm 25.0) \text{ MeV}$		$W=(1775.0 \pm 25.0) \text{ MeV}$	
	$d\sigma/d\Omega$ [$\mu\text{b}/\text{sr}$]	Δ_{stat} [$\mu\text{b}/\text{sr}$]	$d\sigma/d\Omega$ [$\mu\text{b}/\text{sr}$]	Δ_{stat} [$\mu\text{b}/\text{sr}$]
0.00	0.0578	0.0011	0.1297	0.0016
0.20	0.0645	0.0010	0.1495	0.0016
0.40	0.0733	0.0012	0.1679	0.0018
0.60	0.0765	0.0013	0.1679	0.0021
0.80	0.0777	0.0015	0.1676	0.0023
1.00	0.0829	0.0015	0.1677	0.0023
1.20	0.0788	0.0013	0.1746	0.0021
1.40	0.0756	0.0012	0.1698	0.0018
1.60	0.0654	0.0010	0.1539	0.0016
1.80	0.0564	0.0011	0.1276	0.0016

ϕ_π	$W=(1825.0 \pm 25.0) \text{ MeV}$		$W=(1875.0 \pm 25.0) \text{ MeV}$	
	$d\sigma/d\Omega$ [$\mu\text{b}/\text{sr}$]	Δ_{stat} [$\mu\text{b}/\text{sr}$]	$d\sigma/d\Omega$ [$\mu\text{b}/\text{sr}$]	Δ_{stat} [$\mu\text{b}/\text{sr}$]
0.00	0.1954	0.0022	0.3134	0.0037
0.20	0.2284	0.0021	0.3609	0.0036
0.40	0.2473	0.0024	0.3881	0.0040
0.60	0.2405	0.0027	0.3725	0.0045
0.80	0.2280	0.0029	0.3344	0.0050
1.00	0.2352	0.0030	0.3576	0.0051
1.20	0.2429	0.0027	0.3568	0.0044
1.40	0.2480	0.0024	0.3888	0.0041
1.60	0.2287	0.0021	0.3564	0.0036
1.80	0.1947	0.0022	0.3104	0.0037

$\cos(\theta_\pi)$	$W=(1725.0 \pm 25.0) \text{ MeV}$		$W=(1775.0 \pm 25.0) \text{ MeV}$	
	$d\sigma/d\Omega$	Δ_{stat}	$d\sigma/d\Omega$	Δ_{stat}
	[$\mu\text{b}/\text{sr}$]	[$\mu\text{b}/\text{sr}$]	[$\mu\text{b}/\text{sr}$]	[$\mu\text{b}/\text{sr}$]
-0.90	0.0640	0.0012	0.1407	0.0018
-0.70	0.0581	0.0011	0.1353	0.0017
-0.50	0.0600	0.0012	0.1431	0.0018
-0.30	0.0657	0.0012	0.1443	0.0018
-0.10	0.0664	0.0012	0.1501	0.0019
0.10	0.0685	0.0012	0.1581	0.0019
0.30	0.0732	0.0012	0.1620	0.0019
0.50	0.0777	0.0012	0.1674	0.0018
0.70	0.0808	0.0012	0.1767	0.0019
0.90	0.0878	0.0015	0.1873	0.0022

$\cos(\theta_\pi)$	$W=(1825.0 \pm 25.0) \text{ MeV}$		$W=(1875.0 \pm 25.0) \text{ MeV}$	
	$d\sigma/d\Omega$	Δ_{stat}	$d\sigma/d\Omega$	Δ_{stat}
	[$\mu\text{b}/\text{sr}$]	[$\mu\text{b}/\text{sr}$]	[$\mu\text{b}/\text{sr}$]	[$\mu\text{b}/\text{sr}$]
-0.90	0.2134	0.0023	0.3536	0.0043
-0.70	0.2137	0.0023	0.3440	0.0041
-0.50	0.2177	0.0023	0.3527	0.0040
-0.30	0.2223	0.0024	0.3468	0.0039
-0.10	0.2205	0.0024	0.3560	0.0040
0.10	0.2320	0.0025	0.3680	0.0042
0.30	0.2423	0.0025	0.3621	0.0042
0.50	0.2448	0.0024	0.3568	0.0040
0.70	0.2400	0.0023	0.3546	0.0039
0.90	0.2408	0.0026	0.3546	0.0043

$\gamma p \rightarrow \eta\pi^+n$

ϕ_π	$W=(1725.0 \pm 25.0) \text{ MeV}$		$W=(1775.0 \pm 25.0) \text{ MeV}$	
	$d\sigma/d\Omega$	Δ_{stat}	$d\sigma/d\Omega$	Δ_{stat}
	[$\mu\text{b}/\text{sr}$]	[$\mu\text{b}/\text{sr}$]	[$\mu\text{b}/\text{sr}$]	[$\mu\text{b}/\text{sr}$]
0.00	0.0348	0.0031	0.0828	0.0038
0.20	0.0362	0.0023	0.0899	0.0030
0.40	0.0356	0.0017	0.0816	0.0023
0.60	0.0285	0.0015	0.0759	0.0025
0.80	0.0316	0.0022	0.0769	0.0034
1.00	0.0318	0.0022	0.0701	0.0032
1.20	0.0295	0.0016	0.0772	0.0025
1.40	0.0345	0.0016	0.0796	0.0023
1.60	0.0412	0.0025	0.0852	0.0029
1.80	0.0355	0.0030	0.0857	0.0038

ϕ_π	$W=(1825.0 \pm 25.0) \text{ MeV}$		$W=(1875.0 \pm 25.0) \text{ MeV}$	
	$d\sigma/d\Omega$ [$\mu\text{b}/\text{sr}$]	Δ_{stat} [$\mu\text{b}/\text{sr}$]	$d\sigma/d\Omega$ [$\mu\text{b}/\text{sr}$]	Δ_{stat} [$\mu\text{b}/\text{sr}$]
0.00	0.1214	0.0044	0.1827	0.0067
0.20	0.1280	0.0034	0.2002	0.0055
0.40	0.1313	0.0031	0.2058	0.0054
0.60	0.1262	0.0034	0.1849	0.0061
0.80	0.1250	0.0047	0.1916	0.0084
1.00	0.1262	0.0046	0.1931	0.0084
1.20	0.1240	0.0034	0.1781	0.0059
1.40	0.1173	0.0029	0.1885	0.0052
1.60	0.1265	0.0035	0.2037	0.0056
1.80	0.1330	0.0045	0.1904	0.0066

$\cos(\theta_\pi)$	$W=(1725.0 \pm 25.0) \text{ MeV}$		$W=(1775.0 \pm 25.0) \text{ MeV}$	
	$d\sigma/d\Omega$ [$\mu\text{b}/\text{sr}$]	Δ_{stat} [$\mu\text{b}/\text{sr}$]	$d\sigma/d\Omega$ [$\mu\text{b}/\text{sr}$]	Δ_{stat} [$\mu\text{b}/\text{sr}$]
-0.90	0.0362	0.0019	0.0775	0.0024
-0.70	0.0329	0.0018	0.0787	0.0025
-0.50	0.0358	0.0019	0.0731	0.0025
-0.30	0.0302	0.0018	0.0800	0.0027
-0.10	0.0304	0.0019	0.0815	0.0028
0.10	0.0321	0.0020	0.0824	0.0029
0.30	0.0362	0.0021	0.0797	0.0029
0.50	0.0343	0.0021	0.0773	0.0030
0.70	0.0346	0.0022	0.0878	0.0032
0.90	0.0346	0.0023	0.0908	0.0034

$\cos(\theta_\pi)$	$W=(1825.0 \pm 25.0) \text{ MeV}$		$W=(1875.0 \pm 25.0) \text{ MeV}$	
	$d\sigma/d\Omega$ [$\mu\text{b}/\text{sr}$]	Δ_{stat} [$\mu\text{b}/\text{sr}$]	$d\sigma/d\Omega$ [$\mu\text{b}/\text{sr}$]	Δ_{stat} [$\mu\text{b}/\text{sr}$]
-0.90	0.1148	0.0030	0.1698	0.0047
-0.70	0.1215	0.0032	0.1836	0.0053
-0.50	0.1288	0.0034	0.1870	0.0055
-0.30	0.1281	0.0035	0.1973	0.0059
-0.10	0.1191	0.0035	0.1983	0.0063
0.10	0.1225	0.0037	0.2143	0.0068
0.30	0.1315	0.0039	0.2073	0.0069
0.50	0.1336	0.0041	0.1900	0.0068
0.70	0.1263	0.0041	0.2084	0.0074
0.90	0.1370	0.0044	0.1880	0.0072

B.0.6. Angular Distributions of the Pion in the Canonical System

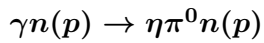
$$\gamma p(n) \rightarrow \eta\pi^0 p(n)$$

ϕ_π	$W=(1725.0 \pm 25.0) \text{ MeV}$		$W=(1775.0 \pm 25.0) \text{ MeV}$	
	$d\sigma/d\Omega$ [$\mu\text{b}/\text{sr}$]	Δ_{stat} [$\mu\text{b}/\text{sr}$]	$d\sigma/d\Omega$ [$\mu\text{b}/\text{sr}$]	Δ_{stat} [$\mu\text{b}/\text{sr}$]
0.00	0.0578	0.0029	0.1268	0.0046
0.20	0.0573	0.0029	0.1219	0.0044
0.40	0.0676	0.0028	0.1284	0.0043
0.60	0.0643	0.0027	0.1295	0.0039
0.80	0.0608	0.0027	0.1257	0.0038
1.00	0.0616	0.0027	0.1280	0.0036
1.20	0.0618	0.0027	0.1331	0.0038
1.40	0.0619	0.0029	0.1297	0.0043
1.60	0.0608	0.0030	0.1330	0.0048
1.80	0.0576	0.0031	0.1140	0.0049

ϕ_π	$W=(1825.0 \pm 25.0) \text{ MeV}$		$W=(1875.0 \pm 25.0) \text{ MeV}$	
	$d\sigma/d\Omega$ [$\mu\text{b}/\text{sr}$]	Δ_{stat} [$\mu\text{b}/\text{sr}$]	$d\sigma/d\Omega$ [$\mu\text{b}/\text{sr}$]	Δ_{stat} [$\mu\text{b}/\text{sr}$]
0.00	0.1632	0.0063	0.2016	0.0086
0.20	0.1617	0.0058	0.2087	0.0085
0.40	0.1839	0.0051	0.1855	0.0075
0.60	0.1690	0.0047	0.1943	0.0067
0.80	0.1650	0.0045	0.1933	0.0065
1.00	0.1664	0.0046	0.1977	0.0063
1.20	0.1688	0.0046	0.1935	0.0066
1.40	0.1837	0.0052	0.2048	0.0077
1.60	0.1689	0.0059	0.1904	0.0092
1.80	0.1646	0.0066	0.2004	0.0093

$\cos(\theta_\pi)$	$W=(1725.0 \pm 25.0) \text{ MeV}$		$W=(1775.0 \pm 25.0) \text{ MeV}$	
	$d\sigma/d\Omega$ [$\mu\text{b}/\text{sr}$]	Δ_{stat} [$\mu\text{b}/\text{sr}$]	$d\sigma/d\Omega$ [$\mu\text{b}/\text{sr}$]	Δ_{stat} [$\mu\text{b}/\text{sr}$]
-0.90	0.0498	0.0025	0.0897	0.0033
-0.70	0.0530	0.0023	0.1199	0.0034
-0.50	0.0531	0.0024	0.1200	0.0036
-0.30	0.0630	0.0024	0.1337	0.0037
-0.10	0.0637	0.0026	0.1370	0.0040
0.10	0.0643	0.0028	0.1439	0.0042
0.30	0.0629	0.0031	0.1369	0.0044
0.50	0.0678	0.0034	0.1304	0.0050
0.70	0.0732	0.0043	0.1429	0.0056
0.90	0.0729	0.0052	0.1383	0.0066

$\cos(\theta_\pi)$	$W=(1825.0 \pm 25.0) \text{ MeV}$		$W=(1875.0 \pm 25.0) \text{ MeV}$	
	$d\sigma/d\Omega$ [$\mu\text{b}/\text{sr}$]	Δ_{stat} [$\mu\text{b}/\text{sr}$]	$d\sigma/d\Omega$ [$\mu\text{b}/\text{sr}$]	Δ_{stat} [$\mu\text{b}/\text{sr}$]
-0.90	0.1272	0.0040	0.1428	0.0061
-0.70	0.1457	0.0042	0.1858	0.0064
-0.50	0.1736	0.0045	0.2074	0.0068
-0.30	0.1837	0.0047	0.2196	0.0072
-0.10	0.1933	0.0051	0.2200	0.0075
0.10	0.1919	0.0054	0.2259	0.0080
0.30	0.2007	0.0055	0.2232	0.0080
0.50	0.1737	0.0058	0.1879	0.0082
0.70	0.1655	0.0065	0.1937	0.0092
0.90	0.1442	0.0069	0.1473	0.0095

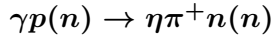


ϕ_π	$W=(1725.0 \pm 25.0) \text{ MeV}$		$W=(1775.0 \pm 25.0) \text{ MeV}$	
	$d\sigma/d\Omega$ [$\mu\text{b}/\text{sr}$]	Δ_{stat} [$\mu\text{b}/\text{sr}$]	$d\sigma/d\Omega$ [$\mu\text{b}/\text{sr}$]	Δ_{stat} [$\mu\text{b}/\text{sr}$]
0.00	0.0512	0.0053	0.0935	0.0080
0.20	0.0599	0.0056	0.1291	0.0069
0.40	0.0726	0.0037	0.1234	0.0055
0.60	0.0609	0.0044	0.1329	0.0055
0.80	0.0585	0.0044	0.1177	0.0053
1.00	0.0480	0.0037	0.1216	0.0050
1.20	0.0480	0.0035	0.1377	0.0050
1.40	0.0533	0.0044	0.1246	0.0061
1.60	0.0576	0.0053	0.1237	0.0071
1.80	0.0626	0.0052	0.1053	0.0073

ϕ_π	$W=(1825.0 \pm 25.0) \text{ MeV}$		$W=(1875.0 \pm 25.0) \text{ MeV}$	
	$d\sigma/d\Omega$ [$\mu\text{b}/\text{sr}$]	Δ_{stat} [$\mu\text{b}/\text{sr}$]	$d\sigma/d\Omega$ [$\mu\text{b}/\text{sr}$]	Δ_{stat} [$\mu\text{b}/\text{sr}$]
0.00	0.1688	0.0088	0.0939	0.0080
0.20	0.1636	0.0079	0.1890	0.0115
0.40	0.1562	0.0071	0.1881	0.0094
0.60	0.1773	0.0065	0.1904	0.0084
0.80	0.1716	0.0061	0.1874	0.0080
1.00	0.1725	0.0058	0.1737	0.0083
1.20	0.1623	0.0059	0.1605	0.0104
1.40	0.1701	0.0075	0.1675	0.0102
1.60	0.1630	0.0083	0.1691	0.0118
1.80	0.1753	0.0078	0.1977	0.0114

$\cos(\theta_\pi)$	$W=(1725.0 \pm 25.0) \text{ MeV}$		$W=(1775.0 \pm 25.0) \text{ MeV}$	
	$d\sigma/d\Omega$ [$\mu\text{b}/\text{sr}$]	Δ_{stat} [$\mu\text{b}/\text{sr}$]	$d\sigma/d\Omega$ [$\mu\text{b}/\text{sr}$]	Δ_{stat} [$\mu\text{b}/\text{sr}$]
-0.90	0.0577	0.0052	0.1188	0.0057
-0.70	0.0423	0.0035	0.1343	0.0065
-0.50	0.0505	0.0045	0.1296	0.0061
-0.30	0.0567	0.0046	0.1311	0.0063
-0.10	0.0529	0.0036	0.1290	0.0050
0.10	0.0541	0.0038	0.1249	0.0051
0.30	0.0591	0.0043	0.1228	0.0062
0.50	0.0512	0.0043	0.0980	0.0054
0.70	0.0438	0.0046	0.0844	0.0058
0.90	0.0476	0.0057	0.0799	0.0059

$\cos(\theta_\pi)$	$W=(1825.0 \pm 25.0) \text{ MeV}$		$W=(1875.0 \pm 25.0) \text{ MeV}$	
	$d\sigma/d\Omega$ [$\mu\text{b}/\text{sr}$]	Δ_{stat} [$\mu\text{b}/\text{sr}$]	$d\sigma/d\Omega$ [$\mu\text{b}/\text{sr}$]	Δ_{stat} [$\mu\text{b}/\text{sr}$]
-0.90	0.1552	0.0079	0.0774	0.0068
-0.70	0.1885	0.0069	0.1823	0.0105
-0.50	0.1986	0.0072	0.2154	0.0092
-0.30	0.1727	0.0064	0.2158	0.0113
-0.10	0.1847	0.0066	0.2184	0.0094
0.10	0.1829	0.0077	0.2120	0.0091
0.30	0.1485	0.0063	0.1844	0.0096
0.50	0.1501	0.0068	0.1810	0.0111
0.70	0.1178	0.0072	0.1524	0.0115
0.90	0.1201	0.0079	0.1098	0.0093



ϕ_π	$W=(1725.0 \pm 25.0) \text{ MeV}$		$W=(1775.0 \pm 25.0) \text{ MeV}$	
	$d\sigma/d\Omega$ [$\mu\text{b}/\text{sr}$]	Δ_{stat} [$\mu\text{b}/\text{sr}$]	$d\sigma/d\Omega$ [$\mu\text{b}/\text{sr}$]	Δ_{stat} [$\mu\text{b}/\text{sr}$]
0.00	0.0386	0.0041	0.0680	0.0054
0.20	0.0417	0.0045	0.0762	0.0062
0.40	0.0347	0.0037	0.0681	0.0058
0.60	0.0320	0.0034	0.0650	0.0055
0.80	0.0356	0.0034	0.0752	0.0045
1.00	0.0381	0.0034	0.0713	0.0051
1.20	0.0362	0.0037	0.0689	0.0056
1.40	0.0384	0.0038	0.0748	0.0054
1.60	0.0436	0.0043	0.0640	0.0059
1.80	0.0358	0.0046	0.0700	0.0057

ϕ_π	$W=(1825.0 \pm 25.0) \text{ MeV}$		$W=(1875.0 \pm 25.0) \text{ MeV}$	
	$d\sigma/d\Omega$ [$\mu\text{b}/\text{sr}$]	Δ_{stat} [$\mu\text{b}/\text{sr}$]	$d\sigma/d\Omega$ [$\mu\text{b}/\text{sr}$]	Δ_{stat} [$\mu\text{b}/\text{sr}$]
0.00	0.0868	0.0074	0.1204	0.0121
0.20	0.0982	0.0073	0.1130	0.0107
0.40	0.0926	0.0072	0.1201	0.0089
0.60	0.1024	0.0072	0.1083	0.0086
0.80	0.0932	0.0064	0.1117	0.0093
1.00	0.0969	0.0062	0.1122	0.0081
1.20	0.0982	0.0073	0.1203	0.0095
1.40	0.0882	0.0076	0.1248	0.0093
1.60	0.0895	0.0062	0.1218	0.0104
1.80	0.0835	0.0083	0.1268	0.0137

$\cos(\theta_\pi)$	$W=(1725.0 \pm 25.0) \text{ MeV}$		$W=(1775.0 \pm 25.0) \text{ MeV}$	
	$d\sigma/d\Omega$ [$\mu\text{b}/\text{sr}$]	Δ_{stat} [$\mu\text{b}/\text{sr}$]	$d\sigma/d\Omega$ [$\mu\text{b}/\text{sr}$]	Δ_{stat} [$\mu\text{b}/\text{sr}$]
-0.90	0.0286	0.0086	0.0770	0.0053
-0.70	0.0337	0.0042	0.0823	0.0051
-0.50	0.0396	0.0037	0.0676	0.0038
-0.30	0.0385	0.0032	0.0843	0.0044
-0.10	0.0425	0.0030	0.0709	0.0040
0.10	0.0381	0.0035	0.0602	0.0041
0.30	0.0325	0.0031	0.0626	0.0049
0.50	0.0353	0.0036	0.0698	0.0074
0.70	0.0352	0.0039	0.0655	0.0024
0.90	0.0350	0.0032	0.0657	0.0054

$\cos(\theta_\pi)$	$W=(1825.0 \pm 25.0) \text{ MeV}$		$W=(1875.0 \pm 25.0) \text{ MeV}$	
	$d\sigma/d\Omega$ [$\mu\text{b}/\text{sr}$]	Δ_{stat} [$\mu\text{b}/\text{sr}$]	$d\sigma/d\Omega$ [$\mu\text{b}/\text{sr}$]	Δ_{stat} [$\mu\text{b}/\text{sr}$]
-0.90	0.0900	0.0047	0.1069	0.0072
-0.70	0.1005	0.0055	0.1166	0.0076
-0.50	0.1007	0.0051	0.1262	0.0088
-0.30	0.0956	0.0054	0.1175	0.0089
-0.10	0.0906	0.0053	0.0908	0.0094
0.10	0.0897	0.0067	0.1050	0.0101
0.30	0.0738	0.0084	0.1119	0.0156
0.50	0.0791	0.0090	0.0955	0.0197
0.70	0.0805	0.0104	0.1042	0.0194
0.90	0.0813	0.0080	0.1050	0.0096

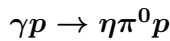
$\gamma n(p) \rightarrow \eta\pi^- p(p)$

ϕ_π	$W=(1725.0 \pm 25.0) \text{ MeV}$		$W=(1775.0 \pm 25.0) \text{ MeV}$	
	$d\sigma/d\Omega$ [$\mu\text{b}/\text{sr}$]	Δ_{stat} [$\mu\text{b}/\text{sr}$]	$d\sigma/d\Omega$ [$\mu\text{b}/\text{sr}$]	Δ_{stat} [$\mu\text{b}/\text{sr}$]
0.00	0.0504	0.0026	0.0880	0.0028
0.20	0.0418	0.0019	0.0779	0.0025
0.40	0.0410	0.0020	0.0726	0.0026
0.60	0.0385	0.0023	0.0686	0.0032
0.80	0.0341	0.0023	0.0594	0.0032
1.00	0.0335	0.0019	0.0617	0.0034
1.20	0.0309	0.0021	0.0667	0.0036
1.40	0.0360	0.0020	0.0708	0.0027
1.60	0.0445	0.0020	0.0780	0.0026
1.80	0.0504	0.0025	0.0943	0.0027

ϕ_π	$W=(1825.0 \pm 25.0) \text{ MeV}$		$W=(1875.0 \pm 25.0) \text{ MeV}$	
	$d\sigma/d\Omega$ [$\mu\text{b}/\text{sr}$]	Δ_{stat} [$\mu\text{b}/\text{sr}$]	$d\sigma/d\Omega$ [$\mu\text{b}/\text{sr}$]	Δ_{stat} [$\mu\text{b}/\text{sr}$]
0.00	0.0971	0.0041	0.1167	0.0072
0.20	0.1054	0.0033	0.1213	0.0065
0.40	0.0867	0.0038	0.1012	0.0061
0.60	0.0801	0.0042	0.1143	0.0059
0.80	0.0835	0.0037	0.1204	0.0068
1.00	0.0889	0.0042	0.1046	0.0072
1.20	0.0811	0.0039	0.1126	0.0076
1.40	0.0983	0.0039	0.1041	0.0055
1.60	0.0966	0.0031	0.1032	0.0054
1.80	0.1095	0.0041	0.1147	0.0096

$\cos(\theta_\pi)$	$W=(1725.0 \pm 25.0) \text{ MeV}$		$W=(1775.0 \pm 25.0) \text{ MeV}$	
	$d\sigma/d\Omega$ [$\mu\text{b}/\text{sr}$]	Δ_{stat} [$\mu\text{b}/\text{sr}$]	$d\sigma/d\Omega$ [$\mu\text{b}/\text{sr}$]	Δ_{stat} [$\mu\text{b}/\text{sr}$]
-0.90	0.0256	0.0027	0.0621	0.0041
-0.70	0.0339	0.0028	0.0717	0.0025
-0.50	0.0389	0.0024	0.0730	0.0025
-0.30	0.0341	0.0021	0.0724	0.0025
-0.10	0.0405	0.0025	0.0726	0.0030
0.10	0.0394	0.0024	0.0794	0.0028
0.30	0.0394	0.0024	0.0817	0.0026
0.50	0.0429	0.0023	0.0798	0.0032
0.70	0.0404	0.0033	0.0798	0.0075
0.90	0.0402	0.0035	0.0831	0.0089

$\cos(\theta_\pi)$	$W=(1825.0 \pm 25.0) \text{ MeV}$		$W=(1875.0 \pm 25.0) \text{ MeV}$	
	$d\sigma/d\Omega$ [$\mu\text{b}/\text{sr}$]	Δ_{stat} [$\mu\text{b}/\text{sr}$]	$d\sigma/d\Omega$ [$\mu\text{b}/\text{sr}$]	Δ_{stat} [$\mu\text{b}/\text{sr}$]
-0.90	0.0864	0.0043	0.0948	0.0064
-0.70	0.0914	0.0029	0.1083	0.0055
-0.50	0.0963	0.0029	0.1108	0.0047
-0.30	0.1042	0.0035	0.1183	0.0064
-0.10	0.1009	0.0030	0.1096	0.0050
0.10	0.0959	0.0031	0.1138	0.0059
0.30	0.0817	0.0038	0.1014	0.0070
0.50	0.0814	0.0042	0.1008	0.0094
0.70	0.0877	0.0100	0.1239	0.0112
0.90	0.0650	0.0071	0.1247	0.0128



ϕ_π	$W=(1725.0 \pm 25.0) \text{ MeV}$		$W=(1775.0 \pm 25.0) \text{ MeV}$	
	$d\sigma/d\Omega$ [$\mu\text{b}/\text{sr}$]	Δ_{stat} [$\mu\text{b}/\text{sr}$]	$d\sigma/d\Omega$ [$\mu\text{b}/\text{sr}$]	Δ_{stat} [$\mu\text{b}/\text{sr}$]
0.00	0.0788	0.0014	0.1745	0.0021
0.20	0.0727	0.0011	0.1644	0.0018
0.40	0.0677	0.0011	0.1512	0.0018
0.60	0.0646	0.0012	0.1439	0.0018
0.80	0.0651	0.0012	0.1454	0.0018
1.00	0.0666	0.0012	0.1424	0.0018
1.20	0.0652	0.0012	0.1515	0.0018
1.40	0.0674	0.0011	0.1544	0.0018
1.60	0.0750	0.0012	0.1659	0.0018
1.80	0.0816	0.0015	0.1760	0.0021

ϕ_π	$W=(1825.0 \pm 25.0) \text{ MeV}$		$W=(1875.0 \pm 25.0) \text{ MeV}$	
	$d\sigma/d\Omega$ [$\mu\text{b}/\text{sr}$]	Δ_{stat} [$\mu\text{b}/\text{sr}$]	$d\sigma/d\Omega$ [$\mu\text{b}/\text{sr}$]	Δ_{stat} [$\mu\text{b}/\text{sr}$]
0.00	0.2476	0.0027	0.3588	0.0045
0.20	0.2366	0.0023	0.3517	0.0039
0.40	0.2237	0.0023	0.3563	0.0039
0.60	0.2187	0.0023	0.3517	0.0040
0.80	0.2161	0.0023	0.3609	0.0042
1.00	0.2238	0.0024	0.3646	0.0042
1.20	0.2192	0.0023	0.3481	0.0040
1.40	0.2296	0.0024	0.3481	0.0039
1.60	0.2375	0.0023	0.3548	0.0039
1.80	0.2398	0.0027	0.3611	0.0045

$\cos(\theta_\pi)$	$W=(1725.0 \pm 25.0) \text{ MeV}$		$W=(1775.0 \pm 25.0) \text{ MeV}$	
	$d\sigma/d\Omega$	Δ_{stat}	$d\sigma/d\Omega$	Δ_{stat}
	[$\mu\text{b}/\text{sr}$]	[$\mu\text{b}/\text{sr}$]	[$\mu\text{b}/\text{sr}$]	[$\mu\text{b}/\text{sr}$]
-0.90	0.0473	0.0010	0.1008	0.0014
-0.70	0.0541	0.0009	0.1279	0.0015
-0.50	0.0610	0.0010	0.1507	0.0016
-0.30	0.0705	0.0011	0.1615	0.0017
-0.10	0.0764	0.0012	0.1728	0.0018
0.10	0.0786	0.0012	0.1793	0.0019
0.30	0.0811	0.0013	0.1750	0.0020
0.50	0.0846	0.0015	0.1752	0.0022
0.70	0.0821	0.0016	0.1740	0.0025
0.90	0.0872	0.0019	0.1728	0.0029

$\cos(\theta_\pi)$	$W=(1825.0 \pm 25.0) \text{ MeV}$		$W=(1875.0 \pm 25.0) \text{ MeV}$	
	$d\sigma/d\Omega$	Δ_{stat}	$d\sigma/d\Omega$	Δ_{stat}
	[$\mu\text{b}/\text{sr}$]	[$\mu\text{b}/\text{sr}$]	[$\mu\text{b}/\text{sr}$]	[$\mu\text{b}/\text{sr}$]
-0.90	0.1453	0.0018	0.2228	0.0030
-0.70	0.1966	0.0019	0.3174	0.0035
-0.50	0.2317	0.0022	0.3711	0.0037
-0.30	0.2462	0.0023	0.4029	0.0040
-0.10	0.2588	0.0024	0.4091	0.0041
0.10	0.2650	0.0025	0.4123	0.0043
0.30	0.2523	0.0025	0.3891	0.0043
0.50	0.2464	0.0027	0.3631	0.0045
0.70	0.2292	0.0030	0.3293	0.0047
0.90	0.2133	0.0035	0.3045	0.0056

$\gamma p \rightarrow \eta\pi^+n$

ϕ_π	$W=(1725.0 \pm 25.0) \text{ MeV}$		$W=(1775.0 \pm 25.0) \text{ MeV}$	
	$d\sigma/d\Omega$	Δ_{stat}	$d\sigma/d\Omega$	Δ_{stat}
	[$\mu\text{b}/\text{sr}$]	[$\mu\text{b}/\text{sr}$]	[$\mu\text{b}/\text{sr}$]	[$\mu\text{b}/\text{sr}$]
0.00	0.0377	0.0023	0.0813	0.0031
0.20	0.0311	0.0020	0.0853	0.0030
0.40	0.0300	0.0019	0.0814	0.0028
0.60	0.0348	0.0020	0.0834	0.0028
0.80	0.0343	0.0019	0.0780	0.0026
1.00	0.0376	0.0020	0.0803	0.0026
1.20	0.0322	0.0018	0.0761	0.0026
1.40	0.0333	0.0020	0.0864	0.0029
1.60	0.0327	0.0021	0.0737	0.0029
1.80	0.0334	0.0022	0.0823	0.0031

ϕ_π	$W=(1825.0 \pm 25.0) \text{ MeV}$		$W=(1875.0 \pm 25.0) \text{ MeV}$	
	$d\sigma/d\Omega$ [$\mu\text{b}/\text{sr}$]	Δ_{stat} [$\mu\text{b}/\text{sr}$]	$d\sigma/d\Omega$ [$\mu\text{b}/\text{sr}$]	Δ_{stat} [$\mu\text{b}/\text{sr}$]
0.00	0.1249	0.0040	0.1825	0.0068
0.20	0.1273	0.0038	0.2108	0.0068
0.40	0.1260	0.0036	0.2004	0.0062
0.60	0.1338	0.0036	0.1926	0.0057
0.80	0.1247	0.0033	0.1794	0.0053
1.00	0.1272	0.0033	0.1912	0.0054
1.20	0.1169	0.0033	0.1809	0.0055
1.40	0.1262	0.0037	0.2042	0.0063
1.60	0.1159	0.0038	0.1898	0.0067
1.80	0.1305	0.0041	0.1857	0.0067

$\cos(\theta_\pi)$	$W=(1725.0 \pm 25.0) \text{ MeV}$		$W=(1775.0 \pm 25.0) \text{ MeV}$	
	$d\sigma/d\Omega$ [$\mu\text{b}/\text{sr}$]	Δ_{stat} [$\mu\text{b}/\text{sr}$]	$d\sigma/d\Omega$ [$\mu\text{b}/\text{sr}$]	Δ_{stat} [$\mu\text{b}/\text{sr}$]
-0.90	0.0000	0.0000	0.0000	0.0000
-0.70	0.0254	0.0119	0.0949	0.0055
-0.50	0.0487	0.0038	0.0894	0.0029
-0.30	0.0437	0.0021	0.0870	0.0024
-0.10	0.0400	0.0016	0.0831	0.0022
0.10	0.0343	0.0014	0.0795	0.0022
0.30	0.0306	0.0013	0.0753	0.0021
0.50	0.0259	0.0013	0.0805	0.0023
0.70	0.0251	0.0093	0.0532	0.0036
0.90	0.0000	0.0000	0.0000	0.0000

$\cos(\theta_\pi)$	$W=(1825.0 \pm 25.0) \text{ MeV}$		$W=(1875.0 \pm 25.0) \text{ MeV}$	
	$d\sigma/d\Omega$ [$\mu\text{b}/\text{sr}$]	Δ_{stat} [$\mu\text{b}/\text{sr}$]	$d\sigma/d\Omega$ [$\mu\text{b}/\text{sr}$]	Δ_{stat} [$\mu\text{b}/\text{sr}$]
-0.90	0.0616	0.0058	0.1927	0.0159
-0.70	0.1287	0.0045	0.1854	0.0060
-0.50	0.1157	0.0031	0.1694	0.0047
-0.30	0.1192	0.0029	0.1854	0.0048
-0.10	0.1248	0.0029	0.1996	0.0048
0.10	0.1336	0.0029	0.2096	0.0052
0.30	0.1355	0.0030	0.2087	0.0056
0.50	0.1312	0.0034	0.1939	0.0066
0.70	0.0955	0.0052	0.1612	0.0107
0.90	0.0000	0.0000	0.3090	0.1601

B.0.7. Helicity Asymmetries

$$\gamma p(n) \rightarrow \eta\pi^0 p(n)$$

ϕ_1	$W=(1725.0 \pm 25.0) \text{ MeV}$		$W=(1775.0 \pm 25.0) \text{ MeV}$	
	I^\odot	Δ_{stat}	I^\odot	Δ_{stat}
0.00	-0.1921	0.0825	-0.0409	0.0409
0.20	0.0562	0.0639	-0.0681	0.0351
0.40	-0.1323	0.0649	-0.0947	0.0361
0.60	-0.1366	0.0789	-0.0835	0.0390
0.80	-0.0196	0.0806	-0.0553	0.0446
1.00	0.0512	0.0823	0.0185	0.0424
1.20	0.0619	0.0733	0.0720	0.0378
1.40	-0.0004	0.0658	0.0747	0.0357
1.60	-0.0273	0.0617	0.0378	0.0358
1.80	0.0131	0.0810	-0.0289	0.0409

ϕ_1	$W=(1825.0 \pm 25.0) \text{ MeV}$		$W=(1875.0 \pm 25.0) \text{ MeV}$	
	I^\odot	Δ_{stat}	I^\odot	Δ_{stat}
0.00	0.0087	0.0381	0.0071	0.0389
0.20	-0.1590	0.0340	-0.0784	0.0351
0.40	-0.0895	0.0341	-0.0423	0.0331
0.60	-0.0938	0.0364	-0.0448	0.0333
0.80	-0.0007	0.0402	-0.0179	0.0364
1.00	0.0266	0.0408	-0.0351	0.0370
1.20	0.0094	0.0329	-0.0117	0.0309
1.40	0.1057	0.0338	0.0101	0.0336
1.60	0.0777	0.0341	0.1367	0.0341
1.80	-0.0225	0.0399	0.0097	0.0384

ϕ_2	$W=(1725.0 \pm 25.0) \text{ MeV}$		$W=(1775.0 \pm 25.0) \text{ MeV}$	
	I^\odot	Δ_{stat}	I^\odot	Δ_{stat}
0.00	0.1788	0.0935	0.0319	0.0421
0.20	-0.0499	0.0635	0.0761	0.0324
0.40	0.0133	0.0630	0.0380	0.0327
0.60	0.0082	0.0675	0.0219	0.0396
0.80	0.0236	0.0777	0.0176	0.0452
1.00	-0.0606	0.0791	-0.0429	0.0463
1.20	-0.0250	0.0731	-0.0692	0.0400
1.40	-0.1478	0.0684	-0.1125	0.0334
1.60	-0.0099	0.0593	-0.0782	0.0326
1.80	-0.1876	0.0913	-0.0510	0.0441

ϕ_2	$W=(1825.0 \pm 25.0) \text{ MeV}$		$W=(1875.0 \pm 25.0) \text{ MeV}$	
	I^\odot	Δ_{stat}	I^\odot	Δ_{stat}
0.00	0.0950	0.0404	0.0512	0.0364
0.20	0.0392	0.0300	0.0347	0.0284
0.40	0.0582	0.0303	0.1038	0.0300
0.60	0.0022	0.0358	-0.0742	0.0354
0.80	0.0137	0.0469	-0.0469	0.0468
1.00	-0.0546	0.0446	0.0196	0.0448
1.20	-0.0207	0.0391	-0.0111	0.0366
1.40	-0.1381	0.0313	-0.0414	0.0310
1.60	-0.1085	0.0301	-0.0850	0.0294
1.80	0.0203	0.0388	-0.0429	0.0376

ϕ_3	$W=(1725.0 \pm 25.0) \text{ MeV}$		$W=(1775.0 \pm 25.0) \text{ MeV}$	
	I^\odot	Δ_{stat}	I^\odot	Δ_{stat}
0.00	-0.0340	0.0713	-0.0132	0.0405
0.20	-0.0119	0.0717	0.0261	0.0413
0.40	0.0557	0.0711	0.0703	0.0372
0.60	-0.0457	0.0732	0.0834	0.0374
0.80	0.1266	0.0725	0.0299	0.0366
1.00	-0.0133	0.0718	-0.0378	0.0383
1.20	-0.0003	0.0711	-0.1004	0.0384
1.40	-0.2510	0.0761	-0.0867	0.0378
1.60	-0.0479	0.0702	-0.1010	0.0407
1.80	-0.1144	0.0800	-0.0214	0.0414

ϕ_3	$W=(1825.0 \pm 25.0) \text{ MeV}$		$W=(1875.0 \pm 25.0) \text{ MeV}$	
	I^\odot	Δ_{stat}	I^\odot	Δ_{stat}
0.00	-0.0004	0.0415	-0.0031	0.0429
0.20	0.0074	0.0381	0.0101	0.0394
0.40	0.0705	0.0351	0.0492	0.0335
0.60	0.0730	0.0343	0.0028	0.0308
0.80	0.0468	0.0343	0.0127	0.0325
1.00	-0.0376	0.0347	-0.0168	0.0316
1.20	-0.0843	0.0349	-0.0853	0.0337
1.40	-0.0884	0.0360	-0.0423	0.0350
1.60	-0.0736	0.0387	-0.0647	0.0384
1.80	-0.0251	0.0405	0.0556	0.0416

$\gamma n(p) \rightarrow \eta\pi^0 n(p)$

ϕ_1	$W=(1725.0 \pm 25.0) \text{ MeV}$		$W=(1775.0 \pm 25.0) \text{ MeV}$	
	I^\odot	Δ_{stat}	I^\odot	Δ_{stat}
0.00	-0.2632	0.1073	-0.0941	0.0507
0.20	-0.1722	0.0875	-0.0250	0.0429
0.40	-0.1414	0.0879	-0.0946	0.0446
0.60	-0.1302	0.0974	-0.0904	0.0466
0.80	-0.0606	0.1232	-0.0741	0.0632
1.00	0.0645	0.1198	0.0611	0.0609
1.20	0.0704	0.0954	0.1075	0.0484
1.40	0.0104	0.0887	0.0417	0.0438
1.60	0.2214	0.0910	0.0625	0.0430
1.80	-0.0534	0.1065	0.0443	0.0491
ϕ_1	$W=(1825.0 \pm 25.0) \text{ MeV}$		$W=(1875.0 \pm 25.0) \text{ MeV}$	
	I^\odot	Δ_{stat}	I^\odot	Δ_{stat}
0.00	-0.0982	0.0429	0.0258	0.0400
0.20	-0.0526	0.0382	-0.1174	0.0374
0.40	-0.0861	0.0396	-0.1330	0.0372
0.60	-0.0859	0.0423	-0.0005	0.0374
0.80	-0.0673	0.0547	0.0148	0.0456
1.00	0.0188	0.0504	-0.0016	0.0451
1.20	0.0798	0.0434	0.0499	0.0376
1.40	0.0286	0.0396	0.0806	0.0367
1.60	0.1349	0.0386	0.0830	0.0354
1.80	0.0254	0.0426	0.0568	0.0397
ϕ_2	$W=(1725.0 \pm 25.0) \text{ MeV}$		$W=(1775.0 \pm 25.0) \text{ MeV}$	
	I^\odot	Δ_{stat}	I^\odot	Δ_{stat}
0.00	0.1100	0.1145	0.0925	0.0525
0.20	-0.0246	0.0901	0.0063	0.0408
0.40	0.1742	0.0900	0.1144	0.0417
0.60	-0.0180	0.0901	0.0991	0.0481
0.80	0.2003	0.1266	0.0298	0.0668
1.00	-0.1054	0.1178	-0.0726	0.0671
1.20	-0.1204	0.0950	0.0092	0.0479
1.40	-0.2338	0.0908	-0.1997	0.0426
1.60	-0.1259	0.0863	-0.0917	0.0423
1.80	-0.1294	0.1171	-0.0057	0.0518

ϕ_2	$W=(1825.0 \pm 25.0) \text{ MeV}$		$W=(1875.0 \pm 25.0) \text{ MeV}$	
	I^\odot	Δ_{stat}	I^\odot	Δ_{stat}
0.00	0.0433	0.0441	0.0193	0.0412
0.20	0.0835	0.0351	0.1180	0.0321
0.40	0.0812	0.0386	0.1074	0.0348
0.60	0.0545	0.0438	-0.0099	0.0402
0.80	0.0539	0.0581	-0.0171	0.0526
1.00	-0.1521	0.0621	0.0290	0.0523
1.20	-0.0157	0.0433	0.0061	0.0399
1.40	-0.0906	0.0369	-0.1002	0.0346
1.60	-0.1270	0.0363	-0.0889	0.0347
1.80	-0.0117	0.0450	-0.0407	0.0406

ϕ_3	$W=(1725.0 \pm 25.0) \text{ MeV}$		$W=(1775.0 \pm 25.0) \text{ MeV}$	
	I^\odot	Δ_{stat}	I^\odot	Δ_{stat}
0.00	0.0904	0.0994	0.0124	0.0506
0.20	0.0148	0.0995	0.0629	0.0484
0.40	0.0575	0.0955	0.0597	0.0469
0.60	0.1343	0.1056	0.0937	0.0471
0.80	0.0573	0.1038	0.0489	0.0507
1.00	-0.1485	0.1052	-0.0142	0.0497
1.20	-0.0533	0.0979	-0.1247	0.0475
1.40	-0.1855	0.1060	-0.0791	0.0486
1.60	-0.2000	0.0906	-0.0467	0.0484
1.80	-0.1386	0.1021	-0.0834	0.0513

ϕ_3	$W=(1825.0 \pm 25.0) \text{ MeV}$		$W=(1875.0 \pm 25.0) \text{ MeV}$	
	I^\odot	Δ_{stat}	I^\odot	Δ_{stat}
0.00	-0.0222	0.0446	0.0119	0.0421
0.20	0.1110	0.0443	0.0491	0.0396
0.40	0.0752	0.0426	0.0631	0.0385
0.60	0.0787	0.0405	0.1080	0.0370
0.80	0.0458	0.0432	-0.0023	0.0392
1.00	-0.0054	0.0441	-0.0395	0.0391
1.20	-0.0753	0.0410	-0.0207	0.0372
1.40	-0.0989	0.0418	-0.1074	0.0390
1.60	-0.0778	0.0440	-0.0439	0.0408
1.80	-0.1302	0.0461	0.0085	0.0432

$\gamma p(n) \rightarrow \eta\pi^+n(n)$

ϕ_1	$W=(1725.0 \pm 25.0) \text{ MeV}$		$W=(1775.0 \pm 25.0) \text{ MeV}$	
	I^\odot	Δ_{stat}	I^\odot	Δ_{stat}
0.00	-0.2393	0.1581	0.0466	0.0857
0.20	0.0860	0.1385	0.0239	0.0845
0.40	-0.1574	0.1475	-0.0719	0.1130
0.60	0.0757	0.1689	-0.1019	0.1163
0.80	-0.0749	0.1853	-0.1164	0.0963
1.00	0.3234	0.1712	0.1726	0.0908
1.20	0.1561	0.1475	-0.0523	0.1242
1.40	0.2312	0.1129	-0.0718	0.0693
1.60	-0.0362	0.1472	0.0595	0.0767
1.80	-0.0894	0.1822	0.0245	0.1094

ϕ_1	$W=(1825.0 \pm 25.0) \text{ MeV}$		$W=(1875.0 \pm 25.0) \text{ MeV}$	
	I^\odot	Δ_{stat}	I^\odot	Δ_{stat}
0.00	-0.0172	0.1090	-0.0814	0.1064
0.20	-0.0818	0.0971	-0.0926	0.1030
0.40	-0.0993	0.0974	-0.2025	0.0801
0.60	-0.0784	0.1186	-0.1620	0.0841
0.80	-0.1654	0.0937	-0.0524	0.0800
1.00	0.0201	0.0945	-0.0866	0.0796
1.20	0.0629	0.1157	0.1400	0.0926
1.40	0.0000	0.0983	0.1270	0.0782
1.60	0.1739	0.1015	0.1335	0.1436
1.80	-0.0316	0.1220	-0.0072	0.1117

ϕ_2	$W=(1725.0 \pm 25.0) \text{ MeV}$		$W=(1775.0 \pm 25.0) \text{ MeV}$	
	I^\odot	Δ_{stat}	I^\odot	Δ_{stat}
0.00	0.0943	0.2336	0.0941	0.0877
0.20	-0.0008	0.1138	0.0305	0.0549
0.40	-0.0166	0.1085	-0.0020	0.0564
0.60	0.1239	0.1161	0.0899	0.0759
0.80	0.4012	0.2269	0.0264	0.1237
1.00	0.1597	0.2504	-0.0083	0.1412
1.20	-0.0949	0.1212	0.1097	0.0773
1.40	0.1916	0.1039	-0.0434	0.0571
1.60	-0.1180	0.1200	-0.1701	0.0580
1.80	0.0374	0.2450	-0.0139	0.0885

ϕ_2	$W=(1825.0 \pm 25.0) \text{ MeV}$		$W=(1875.0 \pm 25.0) \text{ MeV}$	
	I^\odot	Δ_{stat}	I^\odot	Δ_{stat}
0.00	0.1680	0.0738	0.2428	0.0636
0.20	0.0868	0.0542	0.1677	0.0531
0.40	0.0184	0.0589	0.0581	0.0589
0.60	0.1055	0.0844	0.0585	0.0870
0.80	-0.1125	0.1357	0.0270	0.1213
1.00	-0.0874	0.1371	0.0360	0.1290
1.20	-0.0037	0.0852	-0.1464	0.0804
1.40	-0.0337	0.0601	-0.0989	0.0629
1.60	-0.1562	0.0563	-0.2177	0.0541
1.80	-0.1602	0.0710	-0.1693	0.0644

ϕ_3	$W=(1725.0 \pm 25.0) \text{ MeV}$		$W=(1775.0 \pm 25.0) \text{ MeV}$	
	I^\odot	Δ_{stat}	I^\odot	Δ_{stat}
0.00	0.1889	0.2698	0.0282	0.1496
0.20	-0.1755	0.1579	0.0113	0.0884
0.40	0.1081	0.1237	0.0413	0.0801
0.60	0.1416	0.1722	0.1284	0.0726
0.80	0.0864	0.1876	0.0282	0.0870
1.00	-0.0240	0.2100	-0.0285	0.0855
1.20	0.0299	0.1341	-0.1797	0.0775
1.40	0.0820	0.1253	0.0681	0.0785
1.60	0.0660	0.1772	-0.0480	0.1017
1.80	-0.1786	0.2062	0.0515	0.1424

ϕ_3	$W=(1825.0 \pm 25.0) \text{ MeV}$		$W=(1875.0 \pm 25.0) \text{ MeV}$	
	I^\odot	Δ_{stat}	I^\odot	Δ_{stat}
0.00	-0.3694	0.1697	0.0596	0.1591
0.20	0.0239	0.1029	0.0663	0.1021
0.40	0.0597	0.0818	0.1616	0.0810
0.60	0.2035	0.0730	0.1701	0.0672
0.80	0.0335	0.0804	-0.0266	0.0665
1.00	-0.1357	0.0768	-0.0686	0.0696
1.20	-0.2107	0.0777	-0.1882	0.0693
1.40	-0.0062	0.0853	-0.1658	0.0857
1.60	-0.0939	0.1161	-0.1092	0.0994
1.80	0.0580	0.1524	0.1596	0.1535

$\gamma n(p) \rightarrow \eta\pi^- p(p)$

ϕ_1	$W=(1725.0 \pm 25.0) \text{ MeV}$		$W=(1775.0 \pm 25.0) \text{ MeV}$	
	I^\odot	Δ_{stat}	I^\odot	Δ_{stat}
0.00	-0.1816	0.0852	-0.0777	0.0464
0.20	-0.0967	0.0789	-0.0986	0.0432
0.40	-0.0677	0.0673	-0.1044	0.0389
0.60	-0.1447	0.0830	-0.0942	0.0542
0.80	-0.1196	0.0895	-0.0475	0.0479
1.00	0.0210	0.0870	-0.0070	0.0482
1.20	0.0795	0.0824	0.0553	0.0531
1.40	-0.0650	0.0690	0.0935	0.0384
1.60	-0.0055	0.0779	0.0230	0.0434
1.80	-0.0800	0.0984	0.0223	0.0502
ϕ_1	$W=(1825.0 \pm 25.0) \text{ MeV}$		$W=(1875.0 \pm 25.0) \text{ MeV}$	
	I^\odot	Δ_{stat}	I^\odot	Δ_{stat}
0.00	-0.0965	0.0518	0.0113	0.0582
0.20	-0.1450	0.0496	-0.1300	0.0503
0.40	-0.0840	0.0398	-0.0461	0.0423
0.60	0.0410	0.0567	-0.0546	0.0468
0.80	0.0221	0.0524	-0.0190	0.0496
1.00	-0.0636	0.0518	-0.0161	0.0519
1.20	0.0498	0.0554	-0.0102	0.0472
1.40	0.1414	0.0410	0.0818	0.0427
1.60	0.1134	0.0481	0.0331	0.0557
1.80	0.0935	0.0537	0.1320	0.0546
ϕ_2	$W=(1725.0 \pm 25.0) \text{ MeV}$		$W=(1775.0 \pm 25.0) \text{ MeV}$	
	I^\odot	Δ_{stat}	I^\odot	Δ_{stat}
0.00	-0.0202	0.1437	0.0823	0.0532
0.20	-0.0065	0.0685	-0.0039	0.0330
0.40	-0.0077	0.0545	0.0409	0.0310
0.60	-0.0243	0.0668	0.0816	0.0387
0.80	0.1664	0.1095	0.0652	0.0595
1.00	-0.1465	0.1021	-0.1171	0.0589
1.20	-0.1414	0.0655	-0.0330	0.0387
1.40	0.0534	0.0558	-0.0499	0.0308
1.60	-0.2623	0.0659	-0.1483	0.0330
1.80	-0.0969	0.1158	-0.0820	0.0530

ϕ_2	$W=(1825.0 \pm 25.0) \text{ MeV}$		$W=(1875.0 \pm 25.0) \text{ MeV}$	
	I^\odot	Δ_{stat}	I^\odot	Δ_{stat}
0.00	0.1183	0.0464	0.1038	0.0427
0.20	0.0952	0.0316	0.0381	0.0326
0.40	0.0935	0.0328	0.0664	0.0348
0.60	0.0718	0.0433	0.0692	0.0482
0.80	0.0115	0.0681	0.0126	0.0717
1.00	0.0166	0.0690	-0.0256	0.0688
1.20	0.0030	0.0439	-0.0377	0.0456
1.40	-0.0599	0.0325	-0.0564	0.0341
1.60	-0.1428	0.0320	-0.1736	0.0320
1.80	-0.0013	0.0456	-0.0230	0.0414

ϕ_3	$W=(1725.0 \pm 25.0) \text{ MeV}$		$W=(1775.0 \pm 25.0) \text{ MeV}$	
	I^\odot	Δ_{stat}	I^\odot	Δ_{stat}
0.00	0.0341	0.1171	0.0187	0.0660
0.20	-0.0523	0.0798	0.0310	0.0448
0.40	-0.0339	0.0732	0.0430	0.0380
0.60	-0.1014	0.1173	0.0927	0.0411
0.80	0.0352	0.1048	-0.0094	0.0492
1.00	0.0554	0.1380	-0.0737	0.0493
1.20	-0.1455	0.0894	-0.0314	0.0409
1.40	-0.0742	0.0676	-0.1735	0.0393
1.60	-0.2096	0.0842	-0.0449	0.0442
1.80	0.0159	0.1069	-0.0436	0.0648

ϕ_3	$W=(1825.0 \pm 25.0) \text{ MeV}$		$W=(1875.0 \pm 25.0) \text{ MeV}$	
	I^\odot	Δ_{stat}	I^\odot	Δ_{stat}
0.00	0.0055	0.0794	0.0207	0.0912
0.20	0.1417	0.0498	0.1676	0.0579
0.40	0.0595	0.0416	-0.0114	0.0448
0.60	0.0840	0.0385	0.0845	0.0395
0.80	0.0361	0.0434	0.0141	0.0403
1.00	-0.0061	0.0426	-0.0476	0.0390
1.20	-0.0056	0.0394	-0.1165	0.0387
1.40	-0.1333	0.0408	-0.0564	0.0431
1.60	-0.0082	0.0528	0.0286	0.0591
1.80	-0.0995	0.0808	-0.0470	0.0889

$\gamma p \rightarrow \eta\pi^0 p$

ϕ_1	$W=(1725.0 \pm 25.0) \text{ MeV}$		$W=(1775.0 \pm 25.0) \text{ MeV}$	
	I^\odot	Δ_{stat}	I^\odot	Δ_{stat}
0.00	-0.0016	0.0316	-0.0529	0.0161
0.20	-0.0940	0.0277	-0.0733	0.0152
0.40	-0.0377	0.0284	-0.0752	0.0157
0.60	0.0009	0.0301	-0.0219	0.0165
0.80	0.0070	0.0322	-0.0055	0.0175
1.00	0.0260	0.0315	0.0307	0.0172
1.20	0.0592	0.0290	0.0565	0.0163
1.40	0.0776	0.0276	0.0798	0.0155
1.60	0.0786	0.0278	0.0730	0.0152
1.80	0.0225	0.0310	0.0264	0.0162
ϕ_1	$W=(1825.0 \pm 25.0) \text{ MeV}$		$W=(1875.0 \pm 25.0) \text{ MeV}$	
	I^\odot	Δ_{stat}	I^\odot	Δ_{stat}
0.00	-0.0446	0.0149	-0.0443	0.0134
0.20	-0.0526	0.0144	-0.0787	0.0129
0.40	-0.0451	0.0149	-0.0306	0.0131
0.60	-0.0104	0.0158	0.0074	0.0132
0.80	-0.0430	0.0165	0.0011	0.0145
1.00	0.0113	0.0166	-0.0184	0.0144
1.20	0.0522	0.0156	0.0159	0.0131
1.40	0.0565	0.0148	0.0462	0.0133
1.60	0.0704	0.0144	0.0539	0.0129
1.80	0.0440	0.0151	0.0374	0.0134
ϕ_2	$W=(1725.0 \pm 25.0) \text{ MeV}$		$W=(1775.0 \pm 25.0) \text{ MeV}$	
	I^\odot	Δ_{stat}	I^\odot	Δ_{stat}
0.00	0.0172	0.0351	0.0682	0.0172
0.20	0.1547	0.0270	0.0717	0.0140
0.40	0.0203	0.0264	0.0542	0.0144
0.60	0.0579	0.0280	0.0613	0.0163
0.80	0.0475	0.0308	0.0295	0.0180
1.00	-0.0006	0.0323	-0.0115	0.0183
1.20	-0.0736	0.0288	-0.0635	0.0164
1.40	-0.0721	0.0272	-0.0690	0.0146
1.60	-0.0045	0.0265	-0.0656	0.0141
1.80	0.0169	0.0355	-0.0296	0.0173

ϕ_2	$W=(1825.0 \pm 25.0) \text{ MeV}$		$W=(1875.0 \pm 25.0) \text{ MeV}$	
	I^\odot	Δ_{stat}	I^\odot	Δ_{stat}
0.00	0.0485	0.0157	0.0420	0.0136
0.20	0.0703	0.0130	0.0667	0.0115
0.40	0.0513	0.0136	0.0349	0.0120
0.60	0.0581	0.0161	-0.0150	0.0142
0.80	0.0006	0.0179	-0.0063	0.0164
1.00	-0.0081	0.0181	0.0211	0.0167
1.20	0.0011	0.0160	-0.0111	0.0141
1.40	-0.0613	0.0136	-0.0303	0.0120
1.60	-0.0661	0.0131	-0.0564	0.0117
1.80	-0.0540	0.0157	-0.0542	0.0135

ϕ_3	$W=(1725.0 \pm 25.0) \text{ MeV}$		$W=(1775.0 \pm 25.0) \text{ MeV}$	
	I^\odot	Δ_{stat}	I^\odot	Δ_{stat}
0.00	0.0405	0.0300	0.0237	0.0164
0.20	0.0614	0.0284	0.0666	0.0162
0.40	0.1077	0.0286	0.0628	0.0157
0.60	0.0603	0.0289	0.0823	0.0156
0.80	0.0005	0.0307	0.0421	0.0162
1.00	-0.0094	0.0308	-0.0168	0.0164
1.20	-0.0185	0.0296	-0.0354	0.0158
1.40	-0.0382	0.0295	-0.0920	0.0158
1.60	-0.0600	0.0290	-0.0635	0.0161
1.80	-0.0022	0.0300	-0.0206	0.0170

ϕ_3	$W=(1825.0 \pm 25.0) \text{ MeV}$		$W=(1875.0 \pm 25.0) \text{ MeV}$	
	I^\odot	Δ_{stat}	I^\odot	Δ_{stat}
0.00	-0.0015	0.0157	0.0051	0.0143
0.20	0.0634	0.0159	-0.0016	0.0144
0.40	0.0694	0.0149	0.0478	0.0131
0.60	0.0664	0.0146	0.0482	0.0126
0.80	0.0314	0.0152	0.0171	0.0131
1.00	-0.0304	0.0151	-0.0174	0.0131
1.20	-0.0497	0.0147	-0.0396	0.0128
1.40	-0.0665	0.0150	-0.0254	0.0132
1.60	-0.0326	0.0157	-0.0279	0.0142
1.80	-0.0102	0.0166	-0.0162	0.0152

$\gamma p \rightarrow \eta\pi^+n$

ϕ_1	$W=(1725.0 \pm 25.0) \text{ MeV}$		$W=(1775.0 \pm 25.0) \text{ MeV}$	
	I^\odot	Δ_{stat}	I^\odot	Δ_{stat}
0.00	0.0923	0.1479	-0.0009	0.0561
0.20	0.0509	0.0943	-0.0957	0.0405
0.40	-0.0191	0.1012	-0.0439	0.0431
0.60	-0.0105	0.1025	0.0630	0.0483
0.80	-0.0754	0.1816	-0.1422	0.0798
1.00	-0.3863	0.1771	-0.0734	0.0777
1.20	0.0694	0.1022	0.1359	0.0485
1.40	0.1199	0.0932	0.1225	0.0485
1.60	0.0744	0.1112	0.0737	0.0398
1.80	-0.1700	0.2031	-0.0520	0.0549

ϕ_1	$W=(1825.0 \pm 25.0) \text{ MeV}$		$W=(1875.0 \pm 25.0) \text{ MeV}$	
	I^\odot	Δ_{stat}	I^\odot	Δ_{stat}
0.00	-0.0356	0.0427	-0.0986	0.0404
0.20	-0.0584	0.0347	-0.1161	0.0337
0.40	-0.1301	0.0378	-0.1591	0.0344
0.60	0.0284	0.0404	-0.0942	0.0341
0.80	-0.0557	0.0709	-0.1294	0.0537
1.00	0.0182	0.0683	0.0476	0.0538
1.20	0.0815	0.0411	0.1407	0.0343
1.40	0.0740	0.0412	0.1581	0.0343
1.60	0.0718	0.0348	0.1020	0.0339
1.80	0.0562	0.0425	0.0502	0.0422

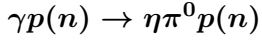
ϕ_2	$W=(1725.0 \pm 25.0) \text{ MeV}$		$W=(1775.0 \pm 25.0) \text{ MeV}$	
	I^\odot	Δ_{stat}	I^\odot	Δ_{stat}
0.00	-0.0657	0.6173	0.1055	0.1206
0.20	-0.1327	0.1478	0.1040	0.0551
0.40	0.0136	0.0962	0.1006	0.0413
0.60	0.0459	0.0911	0.0074	0.0417
0.80	-0.1633	0.1444	-0.0087	0.0802
1.00	0.0996	0.1524	-0.0058	0.0786
1.20	-0.0153	0.0943	-0.0197	0.0432
1.40	0.0469	0.1012	-0.0331	0.0415
1.60	-0.1583	0.1384	-0.1272	0.0557
1.80	0.4523	0.3861	0.0781	0.1351

ϕ_2	$W=(1825.0 \pm 25.0) \text{ MeV}$		$W=(1875.0 \pm 25.0) \text{ MeV}$	
	I^\odot	Δ_{stat}	I^\odot	Δ_{stat}
0.00	0.1784	0.0804	0.1144	0.0525
0.20	0.1045	0.0415	0.1165	0.0315
0.40	0.1123	0.0344	0.1459	0.0288
0.60	0.0324	0.0378	0.0856	0.0346
0.80	-0.0291	0.0701	-0.0550	0.0664
1.00	0.0362	0.0729	-0.0656	0.0724
1.20	-0.0633	0.0373	-0.1064	0.0352
1.40	-0.0817	0.0339	-0.1774	0.0288
1.60	-0.1089	0.0423	-0.1799	0.0318
1.80	-0.0674	0.0776	-0.1085	0.0490

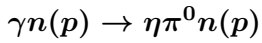
ϕ_3	$W=(1725.0 \pm 25.0) \text{ MeV}$		$W=(1775.0 \pm 25.0) \text{ MeV}$	
	I^\odot	Δ_{stat}	I^\odot	Δ_{stat}
0.00	0.0393	0.1525	0.0981	0.0649
0.20	0.2074	0.1269	0.0435	0.0441
0.40	-0.1963	0.1453	0.0657	0.0450
0.60	-0.3998	0.4718	0.1486	0.0629
0.80	-0.0614	0.4995	-0.0521	0.0924
1.00	0.6781	0.4509	-0.1006	0.1051
1.20	0.3051	0.2493	0.0127	0.0619
1.40	-0.2314	0.1135	-0.0641	0.0446
1.60	0.0783	0.1103	0.0058	0.0461
1.80	0.0308	0.1584	-0.0855	0.0658

ϕ_3	$W=(1825.0 \pm 25.0) \text{ MeV}$		$W=(1875.0 \pm 25.0) \text{ MeV}$	
	I^\odot	Δ_{stat}	I^\odot	Δ_{stat}
0.00	-0.0952	0.0586	-0.0137	0.0603
0.20	0.0690	0.0387	0.1858	0.0384
0.40	0.0431	0.0377	0.0722	0.0323
0.60	0.1430	0.0418	0.1706	0.0319
0.80	0.1163	0.0587	0.0580	0.0378
1.00	0.0062	0.0579	-0.0832	0.0377
1.20	-0.1315	0.0403	-0.1844	0.0319
1.40	-0.0505	0.0362	-0.1479	0.0323
1.60	-0.0747	0.0396	-0.1509	0.0382
1.80	0.0104	0.0567	-0.0580	0.0562

B.0.8. Double Polarization Observable E as Function of E_γ



E_γ [MeV]	ΔE_γ [MeV]	E	Δ_{stat}	Δ_{syst}
800.0	40.0	0.0000	0.0392	0.0000
840.0	40.0	0.0052	0.2337	0.0001
880.0	40.0	0.0000	0.0498	0.0072
920.0	40.0	-0.1037	0.2440	0.0200
960.0	40.0	0.2103	0.4151	0.0380
1000.0	40.0	-0.2710	0.3629	0.0691
1040.0	40.0	-0.1429	0.3050	0.0491
1080.0	40.0	0.0110	0.1824	0.0533
1120.0	40.0	0.0594	0.0785	0.0846
1160.0	40.0	0.0368	0.1254	0.0842
1200.0	40.0	-0.0417	0.1157	0.0134
1240.0	40.0	0.0005	0.1213	0.0111
1280.0	40.0	0.0188	0.1215	0.0554
1320.0	40.0	-0.0016	0.1011	0.0228
1360.0	40.0	0.0111	0.1021	0.0615



E_γ [MeV]	ΔE_γ [MeV]	E	Δ_{stat}	Δ_{syst}
800.0	40.0	0.0000	0.0392	0.0000
840.0	40.0	0.1101	0.0437	0.0030
880.0	40.0	0.0000	0.0510	0.0028
920.0	40.0	-0.0000	0.0522	0.0108
960.0	40.0	0.0924	0.1756	0.0422
1000.0	40.0	-0.1348	0.2802	0.0052
1040.0	40.0	0.0524	0.0505	0.0075
1080.0	40.0	0.0170	0.2150	0.0099
1120.0	40.0	-0.0473	0.0412	0.1698
1160.0	40.0	0.0129	0.0471	0.0327
1200.0	40.0	0.0067	0.0960	0.0313
1240.0	40.0	-0.0518	0.1563	0.0941
1280.0	40.0	-0.0309	0.0868	0.0926
1320.0	40.0	-0.0427	0.1334	0.0311
1360.0	40.0	0.0270	0.1426	0.0616

B.0.9. Double Polarization Observable E as Function of W

$\gamma p(n) \rightarrow \eta\pi^0 p(n)$

W [MeV]	ΔW [MeV]	E	Δ_{stat}	Δ_{syst}
1600.0	20.0	0.0054	0.0392	0.0001
1620.0	20.0	-0.0028	0.0437	0.0541
1640.0	20.0	1.0586	0.1346	0.0794
1660.0	20.0	-0.2330	0.2057	0.0127
1680.0	20.0	-0.0651	0.2623	0.0471
1700.0	20.0	-0.0286	0.2171	0.0145
1720.0	20.0	-0.0788	0.1761	0.0234
1740.0	20.0	-0.0536	0.1413	0.0851
1760.0	20.0	-0.1159	0.1225	0.0900
1780.0	20.0	-0.0063	0.0941	0.0416
1800.0	20.0	0.0313	0.1146	0.2115
1820.0	20.0	0.0512	0.0955	0.0590
1840.0	20.0	-0.0137	0.0840	0.0686
1860.0	20.0	-0.0323	0.1282	0.0469
1880.0	20.0	0.0006	0.0823	0.1117

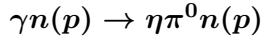
$\gamma n(p) \rightarrow \eta\pi^0 n(p)$

W [MeV]	ΔW [MeV]	E	Δ_{stat}	Δ_{syst}
1600.0	20.0	0.0050	0.0392	0.0001
1620.0	20.0	0.0000	0.0708	0.0509
1640.0	20.0	-0.2248	0.0498	0.0069
1660.0	20.0	0.4346	0.4452	0.1363
1680.0	20.0	0.0919	0.3907	0.0895
1700.0	20.0	-0.2116	0.1721	0.0965
1720.0	20.0	0.0668	0.1750	0.0141
1740.0	20.0	-0.0038	0.1531	0.0040
1760.0	20.0	0.1291	0.1192	0.0250
1780.0	20.0	-0.0504	0.1489	0.1304
1800.0	20.0	-0.0860	0.1657	0.0750
1820.0	20.0	-0.0267	0.1521	0.1995
1840.0	20.0	0.0483	0.0959	0.0215
1860.0	20.0	-0.0011	0.1084	0.0508
1880.0	20.0	0.0028	0.0873	0.0259

B.0.10. Helicity Dependent Cross Sections as Function of E_γ
 $\gamma p(n) \rightarrow \eta\pi^0 p(n)$

E_γ [MeV]	ΔE_γ [MeV]	$\sigma_{1/2}$ [μ b]	Δ_{stat} [μ b]	Δ_{syst} [μ b]
800.0	40.0	0.0000	0.0009	0.0000
840.0	40.0	0.0042	0.0063	0.0001
880.0	40.0	0.0073	0.0322	0.0072
920.0	40.0	0.0224	0.0227	0.0200
960.0	40.0	0.0850	0.0439	0.0380
1000.0	40.0	0.1109	0.0325	0.0691
1040.0	40.0	0.2457	0.0616	0.0491
1080.0	40.0	0.5612	0.1226	0.0533
1120.0	40.0	0.9676	0.1292	0.0846
1160.0	40.0	1.2076	0.1380	0.0842
1200.0	40.0	1.4306	0.1421	0.0134
1240.0	40.0	1.7809	0.1377	0.0111
1280.0	40.0	2.0360	0.1282	0.0554
1320.0	40.0	2.1519	0.1467	0.0228
1360.0	40.0	2.2224	0.1218	0.0615

E_γ [MeV]	ΔE_γ [MeV]	$\sigma_{3/2}$ [μ b]	Δ_{stat} [μ b]	Δ_{syst} [μ b]
800.0	40.0	0.0000	0.0009	0.0000
840.0	40.0	0.0042	0.0063	0.0000
880.0	40.0	0.0073	0.0322	0.0071
920.0	40.0	0.0304	0.0222	0.0197
960.0	40.0	0.0662	0.0429	0.0343
1000.0	40.0	0.1715	0.0337	0.0921
1040.0	40.0	0.3255	0.0692	0.0932
1080.0	40.0	0.5507	0.1405	0.0598
1120.0	40.0	0.8552	0.1347	0.0598
1160.0	40.0	1.1272	0.1349	0.1011
1200.0	40.0	1.5619	0.1258	0.0671
1240.0	40.0	1.7861	0.1521	0.0530
1280.0	40.0	1.9668	0.1229	0.0141
1320.0	40.0	2.1605	0.1473	0.0224
1360.0	40.0	2.1851	0.1391	0.0171



E_γ [MeV]	ΔE_γ [MeV]	$\sigma_{1/2}$ [μ b]	Δ_{stat} [μ b]	Δ_{syst} [μ b]
800.0	40.0	0.0000	0.0000	0.0000
840.0	40.0	0.0042	0.0032	0.0030
880.0	40.0	0.0034	0.0034	0.0028
920.0	40.0	0.0137	0.0248	0.0108
960.0	40.0	0.0656	0.0167	0.0422
1000.0	40.0	0.1576	0.0444	0.0052
1040.0	40.0	0.4176	0.0156	0.0075
1080.0	40.0	0.6358	0.1226	0.0099
1120.0	40.0	0.9821	0.1292	0.1698
1160.0	40.0	1.3147	0.1380	0.0327
1200.0	40.0	1.5812	0.1421	0.0313
1240.0	40.0	1.7254	0.1377	0.0941
1280.0	40.0	2.0346	0.1282	0.0926
1320.0	40.0	2.0840	0.1467	0.0311
1360.0	40.0	2.3984	0.1218	0.0616

E_γ [MeV]	ΔE_γ [MeV]	$\sigma_{3/2}$ [μ b]	Δ_{stat} [μ b]	Δ_{syst} [μ b]
800.0	40.0	0.0000	0.0000	0.0000
840.0	40.0	0.0024	0.0033	0.0048
880.0	40.0	0.0014	0.0034	0.0013
920.0	40.0	0.0137	0.0248	0.0108
960.0	40.0	0.0554	0.0041	0.0422
1000.0	40.0	0.2110	0.0475	0.0172
1040.0	40.0	0.3834	0.0156	0.0306
1080.0	40.0	0.6176	0.1405	0.0169
1120.0	40.0	1.0940	0.1347	0.1698
1160.0	40.0	1.2783	0.1349	0.0169
1200.0	40.0	1.5382	0.1258	0.1516
1240.0	40.0	1.9294	0.1521	0.0837
1280.0	40.0	2.1701	0.1229	0.0926
1320.0	40.0	2.2951	0.1473	0.1054
1360.0	40.0	2.2551	0.1391	0.0407

B.0.11. Helicity Dependent Cross Sections as Function of W

$\gamma p(n) \rightarrow \eta\pi^0 p(n)$

W [MeV]	ΔW [MeV]	$\sigma_{1/2}$ [μ b]	Δ_{stat} [μ b]	Δ_{syst} [μ b]
1600.0	20.0	0.0002	0.0000	0.0001
1620.0	20.0	0.0548	0.0000	0.0541
1640.0	20.0	0.0958	0.0236	0.0794
1660.0	20.0	0.0960	0.0514	0.0127
1680.0	20.0	0.2544	0.0571	0.0471
1700.0	20.0	0.4646	0.0874	0.0145
1720.0	20.0	0.6841	0.1086	0.0234
1740.0	20.0	1.0341	0.1226	0.0851
1760.0	20.0	1.2319	0.1292	0.0900
1780.0	20.0	1.6780	0.1380	0.0416
1800.0	20.0	2.0896	0.1421	0.2115
1820.0	20.0	2.3297	0.1377	0.0590
1840.0	20.0	2.3755	0.1282	0.0686
1860.0	20.0	2.4420	0.1467	0.0469
1880.0	20.0	2.6682	0.1218	0.1117

W [MeV]	ΔW [MeV]	$\sigma_{3/2}$ [μ b]	Δ_{stat} [μ b]	Δ_{syst} [μ b]
1600.0	20.0	0.0002	0.0000	0.0001
1620.0	20.0	0.0548	0.0000	0.0543
1640.0	20.0	0.0622	0.0300	0.0369
1660.0	20.0	0.1396	0.0498	0.0530
1680.0	20.0	0.2807	0.0572	0.0139
1700.0	20.0	0.4934	0.0865	0.0244
1720.0	20.0	0.8047	0.1079	0.0124
1740.0	20.0	1.1542	0.1405	0.0570
1760.0	20.0	1.5890	0.1347	0.0935
1780.0	20.0	1.6857	0.1349	0.0216
1800.0	20.0	1.8932	0.1258	0.1512
1820.0	20.0	2.1094	0.1521	0.0436
1840.0	20.0	2.4286	0.1229	0.0201
1860.0	20.0	2.6246	0.1473	0.1725
1880.0	20.0	2.6747	0.1391	0.1088

$\gamma n(p) \rightarrow \eta\pi^0n(p)$

W [MeV]	ΔW [MeV]	$\sigma_{1/2}$ [μ b]	Δ_{stat} [μ b]	Δ_{syst} [μ b]
1600.0	20.0	0.0002	0.0000	0.0001
1620.0	20.0	-0.0166	0.0042	0.0509
1640.0	20.0	-0.0000	0.0674	0.0069
1660.0	20.0	0.2847	0.0700	0.1363
1680.0	20.0	0.3729	0.1031	0.0895
1700.0	20.0	0.4582	0.0930	0.0965
1720.0	20.0	0.9456	0.1300	0.0141
1740.0	20.0	1.2129	0.1226	0.0040
1760.0	20.0	1.6262	0.1292	0.0250
1780.0	20.0	1.7075	0.1380	0.1304
1800.0	20.0	1.8637	0.1421	0.0750
1820.0	20.0	2.1863	0.1377	0.1995
1840.0	20.0	2.5481	0.1282	0.0215
1860.0	20.0	2.5520	0.1467	0.0508
1880.0	20.0	2.5902	0.1218	0.0259

W [MeV]	ΔW [MeV]	$\sigma_{3/2}$ [μ b]	Δ_{stat} [μ b]	Δ_{syst} [μ b]
1600.0	20.0	0.0002	0.0000	0.0001
1620.0	20.0	-0.0166	0.0041	0.0509
1640.0	20.0	0.0642	0.0674	0.0653
1660.0	20.0	0.0947	0.0525	0.0779
1680.0	20.0	0.2997	0.1044	0.0168
1700.0	20.0	0.7358	0.0946	0.0809
1720.0	20.0	0.8303	0.1278	0.0149
1740.0	20.0	1.2103	0.1405	0.0801
1760.0	20.0	1.2371	0.1347	0.2811
1780.0	20.0	1.9135	0.1349	0.0136
1800.0	20.0	2.2210	0.1258	0.0378
1820.0	20.0	2.3515	0.1521	0.1149
1840.0	20.0	2.2923	0.1229	0.2222
1860.0	20.0	2.5492	0.1473	0.0545
1880.0	20.0	2.6154	0.1391	0.1677

Bibliography

- [1] R. Frisch and O. Stern. Über die magnetische Ablenkung von Wasserstoffmolekülen und das magnetische Moment des Protons. I, Zeitschrift für Physik 85, 4–16, 1933.
- [2] L. W. Alvarez, F. Bloch. A quantitative determination of the neutron magnetic moment in absolute nuclear magnetons, Physical Review. 57: 111–122, 1940.
- [3] R. W. McAllister and R. Hofstadter. Elastic Scattering of 188-Mev Electrons from the Proton and the Alpha Particle, Phys. Rev. 102, 851, 1956.
- [4] H. L. Anderson et al. Total Cross Sections of Positive Pions in Hydrogen, Phys. Rev. 85, 936, 1952.
- [5] C. Patrignani et al. (Particle Data Group). 2015 Review of Particle Physics, Chin. Phys. C, 40, 100001, 2016.
- [6] M. Gell-Mann. Symmetries of Baryons and Mesons”, Phys. Rev. 125, 1067–1084, 1962.
- [7] S. Capstick and W. Roberts. Quark Models of Baryon Masses and Decays, Prog. Part. Nucl. Phys. 45, S241, 1940.
- [8] C. Hanretty. Measurement of the Polarization Observables I^S and I^C for $\vec{\gamma}p \rightarrow p\pi^+\pi^-$ using the CLAS Spectrometer, PhD Thesis, Florida State University, 2011.
- [9] U. Löring, B. C. Metsch, and H. R. Petry. The light-baryon spectrum in a relativistic quark model with instanton-induced quark forces . The non-strange-baryon spectrum and ground states, The European Physical Journal A 10, 395–446, 2001.
- [10] B. Krusche. Photoproduction of mesons off nuclei, The European Physical Journal Special Topics 198, 2011.
- [11] G. F. Chew, M. L. Goldberger, F. E. Low and Y. Nambu. Relativistic Dispersion Relation Approach to Photomeson Production, Phys. Rev. 106, 1345–1355, 1957.
- [12] B. Krusche and S, Schadmand. Study of Non-Strange Baryon Resonance with Meson Photoproduction, Progress in Particle and Nuclear Physics 51 (2) 399, 2003.
- [13] R. L. Walker. Phenomenological Analysis of Single-Pion Photoproduction, Phys. Rev. 182, 1729–1748, 1969.
- [14] I. S. Barker, A. Donnachie, and J. K. Storrow. Complete experiments in pseudoscalar photoproduction, Nuclear Physics 95, 347–356 , 1975.

- [15] A. M. Sandorfi et al. Calculations of Polarization Observables in Pseudoscalar Meson Photo-production Reactions, <https://arxiv.org/abs/0912.3505> , 2009.
- [16] W.T. Chiang and F. Tabakin. Completeness rules for spin observables in pseudoscalar meson photoproduction, Physical Review C55, 1997.
- [17] A.Fix and H. Arenhövel . Partial wave expansion for photoproduction of two pseudoscalars on a nucleon, Phys. Rev. C 85, 035502, 2012.
- [18] W. Roberts and T. Oed. Polarization observables for two-pion production off the nucleon, Phys. Rev. C 71, 055201 , 2005.
- [19] A.Fix and H. Arenhövel. Polarization observables in $\pi^0\eta$ -photoproduction on the proton, Phys. Rev. C 83, 015503, 2011.
- [20] A. Fix, V.L. Kashevarov, A. Lee, and M. Ostrick. Isobar model analysis of $\pi^0 - \eta$ photoproduction on protons, Phys. Rev. C 82 035207, 2010.
- [21] M. Egorov and A. Fix. Coherent $\pi^0\eta$ photoproduction on s-shell nuclei, Phys. Rev. C 88 054611, 2013.
- [22] V.L. Kashevarov et al. Photoproduction of $\pi^0\eta$ on protons and the $\Delta(1700)D_{33}$ resonance, Eur. Phys. J. A 42, 141–149 , 2009.
- [23] J.R.M. Annand et al. . First measurement of target and beam-target asymmetries in the $\gamma p \rightarrow \pi^0\eta p$ reaction, Phys. Rev. C91, 5, 055208, 2015.
- [24] A.Fix, V.L. Kashevarov and M. Ostrick. Study of the partial wave structure of $\pi^0\eta$ photoproduction on protons, 2013.
- [25] E. Gutz et al. High statistics study of the reaction $\gamma p \rightarrow p\pi^0\eta$, Eur. Phys. J. A 50, 74, 2013.
- [26] E. Gutz et al. Measurement of the beam asymmetry Σ in $\pi^0\eta$ production off the proton with the CBELSA/TAPS experiment, Eur. Phys. J. A 35, 291, 2008.
- [27] E. Gutz et al. Photoproduction of meson pairs: First measurement of the polarization observable I^S , Phys. Let. B 687, 11, 2010.
- [28] I. Horn et al. Study of the reaction $\gamma p \rightarrow p\pi^0\eta$, Eur. Phys. J. A 38, 173 , 2008.
- [29] Ajaka et al. Simultaneous Photoproduction of π^0 and η Mesons on the Proton Phys. Rev. Lett. 100, 052003 , 2008.
- [30] T. Nakabayashi et al. Photoproduction of η mesons off protons for $E_\gamma \leq 1.15$ GeV, Phys. Rev. C 74, 035202 , 2006.
- [31] A.V.Anisovich et al. Partial wave decomposition of pion and photoproduction amplitudes, Eur.Phys.J. A24, 111 , 2005.

- [32] M. Döring, E. Oset, and D. Strottman. Chiral dynamics in the $\gamma p \rightarrow \pi^0 \eta p$ and $\gamma p \rightarrow \pi^0 K^0 \Sigma^+$ reactions, Phys. Rev. C 73, 045209, 2006.
- [33] M. Döring, E. Oset, and D. Strottman. Clues to the nature of the $\Delta^*(1700)$ resonance from pion- and photon-induced reactions, Phys. Rev. C 73, 045209, 2006.
- [34] B. Krusche and C. Wilkin. Production of η and η' Mesons on Nucleons and Nuclei, Progress in Particle and Nuclear Physics 80, 43 , 2015.
- [35] V.L. Kashevarov et al. First measurement of the circular beam asymmetry in the $\vec{\gamma}p \rightarrow \pi^0 \eta p$ reaction, Phys. Lett. B 693, 551, 2010.
- [36] A. Jankowiak. The Mainz Microtron MAMI —Past and future, Eur. Phys. J. A 28, s01, 149–160, 2006.
- [37] K.-H. Kaiser et al. The 1.5 GeV harmonic double-sided microtron at Mainz University, Nucl. Instr. Meth. A 593, 159, 2008.
- [38] J. C. McGeorge et al. Upgrade of the Glasgow photon tagging spectrometer for Mainz MAMI-C, Eur. Phys. J. A 37, 129, 2008.
- [39] J. R. M. Annand. The Glasgow/Mainz Bremsstrahlung Tagger Operations Manual , 2008.
- [40] D. Watts. The Crystal Ball and TAPS Detectors at the MAMI electron beam facility, Proceedings of the 11th International Conference, 116-123, 2005.
- [41] A. Starostin et al. Measurement of $K^- p \rightarrow \eta \Lambda$ near threshold, Physical Review C 64, 055205, 2001.
- [42] E. D. Bloom et al. A Proposal For A Large Solid Angle Neutral Detector For Spear 2 (The Crystal Ball), SLAC Proposal SP-024, 1975.
- [43] Pauline Hall Barrientos. First Measurement of F Double Polarisation Obeservable in Pion Photoproduction, PhD Thesis, University of Edinburgh, 2012.
- [44] R. Novotny. The BaF₂ photon spectrometer TAPS, IEEE Trans. Nucl. Sci. 38, 379, 1991.
- [45] A. R. Gabler et al. Response of TAPS to monochromatic photons with energies between 45 and 790 MeV, Nucl. Instr. Meth. A 346, 168 , 1994.
- [46] S.Janssen, W.Döring, V.Metag and R.Novotny. The New Charged-Particle Veto Detector for the Photon Spectrometer TAPS, Nucl. Sci., vol. 47, no. 3, pp. 798-801, 2000.
- [47] D. Werthmüller. Experimental study of nucleon resonance contributions to η -photoproduction on the neutron, Ph.D. thesis, Universität Basel, 2013.

- [48] K. Aulenbacher et al. The MAMI source of polarized electrons, Nuclear Instruments and Methods in Physics Research Section A: Accelerators, Spectrometers, Detectors and Associated Equipment 391, 498–506 , 1997.
- [49] H. Euteneuer et al. Experience with the 855-MeV RTM-Cascade MAMI, Conf. Proc. C920324, 418–420, 1992.
- [50] U. Timm. Coherent Bremsstrahlung of Electrons in Crystals, Fortschritte der Physik 17, 765–808, 1969.
- [51] S. Schumann. Strahlungsbegleitete π^0 -Photoproduktion am Proton, Ph.D. thesis, Universität Bonn, 2007.
- [52] Hornidge D. and Downie E.J. and Annand J.R.M. and MacGregor I.J.D. Measurement of the Proton Spin Polarizabilities. An A2 Collaboration Proposal for an Experiment at MAMI, 2009.
- [53] H. Olsen and L.C. Maximon. Photon and Electron Polarization in High- Energy Bremsstrahlung and Pair Production with Screening, Phys. Rev. 114, 887, 1959.
- [54] H. W. Koch and J. W. Motz. Bremsstrahlung Cross-Section Formulas and Related Data, Rev. Mod. Phys. 31, 920, 1959.
- [55] W. Heitler. Quantum theory of radiation, 3rd edition, Oxford Univ. Press, London, 1954.
- [56] Mark J. Oreglia. A Study of the Reactions $\Psi' \rightarrow \gamma\gamma\Psi$, Phd Thesis, Department of Physics of Stanford University, 1980.
- [57] A. Thomas. Crystal Ball Hydrogen (Deuterium) Target manual, 2013.
- [58] M. Schiemann. Polarisationsmessungen an mit Trityl-Radikalen dotiertem D-Butanol, Diploma thesis (Ruhr-Universität Bochum, Bochum, 2006.
- [59] P. J. Mohrm, B. N. Taylor, and D. B. Newell. The 2014 CODATA Recommended Values of the Fundamental Physical Constants, <http://physics.nist.gov/constants>, 2016.
- [60] S. T. Goertz. The dynamic nuclear polarization process, Nuclear Instruments and Methods in Physics Research Section A: Accelerators, Spectrometers, Detectors and Associated Equipment 526, 28-42, 2003.
- [61] A. Thomas. Polarised targets for 4π detectors at MAMI, Eur. Phys. J. ST 198, 171–180, 2011.
- [62] A. Thomas. Review on the last developments on polarized targets at Mainz, Annual Meeting of the GDR PH-QCD, 1–40 ,<https://indico.in2p3.fr/event/9046/session/3/contribution/27/material/0/0.pdf> , 2013.

- [63] M. Dieterle. Measurement of Polarization Obesrvables in π^0 and $\pi^0\pi^0$ Photoproduction from Protons and Neutrons at MAMI and ELSA. Ph.D. thesis, Universität Basel , 2015.
- [64] P.-B. Otte. Aufbau und Test eines Möllerpolarimeters für das Crystal-Ball Experiment an MAMI-C, Diploma thesis (Johannes Gutenberg-Universität Mainz, 2008.
- [65] V. Tioukine, K. Aulenbacher, and E. Riehn. A Mott polarimeter operating at MeV electron beam energies, Review of Scientific Instruments 82, 033303-9, 2011.
- [66] P.-B. Otte. Erste Messung der π^0 -Photoproduktion an transversal polarisierten Protonen nahe der Schwelle, PhD thesis, Johannes Gutenberg Universität Mainz , 2015.
- [67] . Webpage of the A2 collaboration, <http://www.a2.kph.uni-mainz.de>, 2015.
- [68] J. R. M. Annand. Data Analysis within an AcquRoot Framework, <http://www.nuclear.gla.ac.uk/~acqusys/doc/AcquRoot.11.08.pdf> , 2008.
- [69] R. Brun and F. Rademakers. ROOT - An Object Oriented Data Analysis Framework, Nucl. Instr. and Meth. A 389, 81 , 1997.
- [70] D. Glazier. A Geant4 simulation for the CrystalBall@MAMI Setup, <http://www2.ph.ed.ac.uk/nuclear/G4/G4A2CBSimulation-06-12.pdf> , 2012.
- [71] S. Agostinelli et al. Geant4 - a simulation toolkit, Nucl. Instr. Meth. A 506, 2003.
- [72] J. Allison et al. Geant4 developments and applications, IEEE Trans. Nucl.Sci. 53, 270, 2006.
- [73] GEANT4. Reference Physics Lists, http://geant4.cern.ch/support/proc_mod_catalog/physics_lists/referencePL.shtml, 05.2016.
- [74] I. Froehlich. Pluto: A Monte Carlo Simulation Tool for Hadronic Physics, 11th International Workshop on Advanced Computing and Analysis Techniques in Physics Research, 2007.
- [75] L. Witthauer. Measurement of Cross Sections and Polarisation Observables in η Photoproduction from Neutrons and Protons Bound in Light Nuclei, Ph.D. thesis, Universität Basel, 2015.
- [76] E. Rickert. Untersuchung der Ortsabhängigkeit der Polarisation des Mainzer Frozen-Spin-Targets, BA thesis, Johannes Gutenberg-Universität Mainz, 2015.
- [77] A. Thomas. Frozen Spin Target, Presentation at the 26th A2 collaboration meeting, 2015.
- [78] H. Rochholz. Diplomarbeit: Entwicklungsarbeiten für einen Freie-Elektronen-Laser auf der Basis des Smith-Purcell-Effektes im infraroten Spektralbereich, Diploma Thesis, Johannes Gutenberg Universität Mainz, 2002.

- [79] T. C. Awes et al. A simple method of shower localization and identification in laterally segmented calorimeters, Nucl. Instr. Meth. A311, 130, 1992.
- [80] F. M. Marques et al. Identification of photons and particles in the segmented electromagnetic calorimeter TAPS, Nucl. Instrum. Meth. A365, 392-409, 1995.
- [81] F. Zehr. Double pion photoproduction off the proton at threshold and the second resonance region, Ph.D. thesis, Universität Basel , 2010.
- [82] M. Martemianov et al. A new measurement of the neutron detection efficiency for the NaI Crystal Ball detector, Journal of Instrumentation, Volume 10, 2015.
- [83] C. Patrignani et al. (Particle Data Group). PDG, Kinematics, pdg.lbl.gov/2016/reviews/rpp2016-rev-kinematics.pdf, 2016.
- [84] M. Unverzagt. Energie-Eichung des Crystal Ball-Detektors am MAMI, Diploma thesis, Johannes Gutenberg–Universität Mainz, Mainz, 2004.
- [85] M. Unverzagt. Bestimmung des Dalitz-Plot-Parameters α für den Zerfall $\eta \rightarrow 3\pi^0$ mit dem Crystal Ball am MAMI, Ph.D. thesis, Universität Bonn, 2008.
- [86] M. E. Röbig. Eichung des TAPS-Detektorsystems mit Höhenstrahlung, Diploma thesis, Universität Giessen, 1991.
- [87] T. Jude. Strangeness Photoproduction off the Proton at Threshold Energies, PhD thesis, University of Edinburgh, 2010.
- [88] M. Oberle. Photoproduction of pion pairs off nucleons, Ph.D. thesis, Universität Basel , 2014.
- [89] E. F. McNicoll et al. Experimental study of the $\gamma p \rightarrow \eta p$ reaction with the Crystal Ball detector at the Mainz Microtron (MAMI-C), Phys. Rev. C 82, 035208 , 2010.
- [90] S. Brandt. Data analysis: Using statistical methods and computer programs, Spektrum Akademischer Verlag, 1999.
- [91] V. Hejny. Photoproduction von η -mesonen an Helium 4, Ph.D. thesis, Universität Giessen , 1998.
- [92] M. Lacombe et al. Parametrization of the deuteron wave function of the Paris N–N potential, Phys. Lett. B 101, 139 , 1981.
- [93] R. O. Owens. Statistical treatment of tagged photon experiments, Nucl. Instr. and Meth. A 288, 574, 1990.
- [94] H. Olsen and L.C. Maximon. Highlights of Crystal Ball Physics. Phys. Rev. 114 887, 1959.
- [95] B. Krusche et al. Photoproduction of π^0 -mesons from nuclei, The European Physical Journal A 22, 277–291 , 2004.

- [96] C. Patrignani et al. (Particle Data Group). 2015 Review of Particle Physics, Chin. Phys. C, 40, 100001, <http://www-pdg.lbl.gov/2016/listings/rpp2016-list-Delta-1700.pdf>, 2016.
- [97] M. Dieterle et al. Photoproduction of π^0 -mesons off neutrons in the nucleon resonance region, Phys. Rev. Lett. 112, 2014.